ADVANCED NUCLEAR POWER PROGRAM

Integrated FHR Technology Development: Tritium Management, Materials Testing, Salt Chemistry Control, Thermal Hydraulics and Neutronics, Associated Benchmarking and Commercial Basis

C. W. Forsberg(MIT), P. F. Peterson (UCB)
K. Sridharan (UW), Lin-wen Hu(MIT),
M. Fratoni (UCB), A. Kant Prinja (UNM)

MIT-ANP-TR-180
October 2018
For Public Distribution

CENTER FOR
ADVANCED NUCLEAR
ENERGY SYSTEMS

CANES

Massachusetts Institute of Technology
77 Massachusetts Avenue, 24-215
Cambridge, MA 02139-4307

(617) 452-2660
canes@mit.edu
mit.edu/canes

U.S. Department of Energy

MIT CANES: ANP-TR-180
UCBTH-18-001
UW-INES-18-050

Final Project Report

Integrated FHR Technology Development: Tritium Management, Materials Testing, Salt Chemistry Control, Thermal Hydraulics and Neutronics, Associated Benchmarking and Commercial Basis

Charles Forsberg[1]
Per F. Peterson[2]
Kumar Sridharan[3]
Lin-wen Hu[1]
Massimiliano Fratoni[2]
Anil Kant Prinja[4]

[1]Massachusetts Institute of Technology (MIT)

[2]University of California at Berkeley (UCB)

[3]University of Wisconsin at Madison (UW)

[4]University of New Mexico (UNM)

September 30, 2018

For Public Distribution

Abstract

This report summarizes the results of a 3-year Integrated Research Project (IRP) sponsored by the U.S. Department of Energy to address major technical challenges in the development of the Fluoride-salt-cooled High-temperature Reactor (FHR). The IRP universities included the Massachusetts Institute of Technology (MIT), the University of California at Berkeley (UCB), the University of Wisconsin (UW), and the University of New Mexico (UNM). The FHR is a new reactor concept less than 20 years old that combines (1) a clean fluoride salt coolant, (2) the graphite-matrix coated-particle fuel originally developed for High-Temperature Gas-Cooled Reactors and (3) passive decay heat removal systems from sodium fast reactors. The base-line design is a pebble-bed FHR that delivers heat between 600 to 700°C with a $^7Li_2BeF_4$ (flibe) salt coolant to the power cycle or industrial users.

The Executive Summary describes what was accomplished and summarizes major conclusions. The main report contains stand-alone sections in each major area of work. Highlights are summarized below.

Tritium. The coolant salt produces tritium necessitating understanding and control of tritium. Experimental work included measuring hydrogen uptake on carbon, tritium uptake during irradiation of graphite in 700°C salt and the permeability of tritium through metals with and without coatings. An FHR systems model was developed to predict tritium behavior and enable design of tritium control systems. The leading candidate for tritium removal from the flibe salt is carbon bed outside the reactor core.

Thermal hydraulics and Neutronics. A 10-meter high FHR integral effects test facility, using Dowtherm A®, has been built and used to simulate the integral response of a representative FHR to improve understanding of FHR thermal hydraulics and validate thermal hydraulics codes used for the FHR. Neutronic analysis included code-to-code benchmarking, multiphysics modeling, uncertainty analysis for nuclear data uncertainties and shielding analysis. Twisted-tube heat exchangers were examined that may provide significant cost reductions because of their improved heat-transfer performance with liquid salts. The impacts on safety and design caused by uncertainties in physical properties of the salt were assessed with recommendations on where added physical property measurements are needed. Work began on understanding radiative heat transfer that becomes important in salt systems at higher temperatures.

Materials. Static corrosion tests were conducted on graphite and materials in 700°C salt—both in the UW laboratory and in the MIT reactor. In addition to static corrosion testing, a circulating salt corrosion loop was built and is operating. Methods to measure salt properties including redox were developed. The presence of carbon increases corrosion. With good redox control, the evidence indicates stainless steel can be used as a material of construction.

Benchmarking. An additional series of workshops where held to enable benchmarking and comparison of results between different investigators.

Commercialization. The FHR delivers higher average-temperature (~650°C) heat to the power cycle or industry than other reactors. This enables power cycles with lower-cost heat storage for variable electricity to the grid while the reactor operates at base-load—providing a major competitive advantage by maximizing revenue from electricity sales. In October, 2016, a new startup company named Kairos Power was formed, and opened its first office in Jack London Square, Oakland, California, in January 2017. Kairos Power exists largely due to the work that was accomplished by this IRP and the previous DOE-funded FHR IRP that performed research on FHR technology from 2012 to 2015. In September, 2018, as this IRP is concluding, Kairos Power was staffed at 60 full time employees, working to develop technology derived from this IRP. Many of these employees worked with the IRP before joining Kairos Power

(*https://kairospower.com*). Other students and researchers from this IRP have joined other startup companies, including the Terrapower Molten Chloride Fast Reactor and the Terrestrial Energy development efforts.

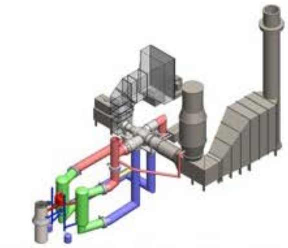

Conceptual Design Studies

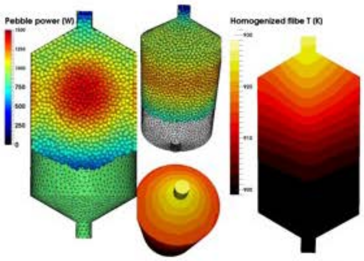

Coupled Neutronics and Thermal Hydraulics

Separate and integral effect tests

Corrosion Test Loops

In Reactor Materials Testing

Benchmarking

Major IRP Activities

Acknowledgements

We would like to thank (1) the U.S. Department of Energy Office of Nuclear Energy for their support of this project through the Nuclear Energy University Program, (2) Oak Ridge National Laboratory for support including providing fluoride salts with isotopically separated lithium-7 for reactor experiments and (3) our Technical Advisory Panel chaired by Dr. Regis Matzie for good advice.

CANES PUBLICATIONS

Topical and progress reports are published under seven series:

Advances in Nuclear Energy Disciplines (ANED) Series
Advanced Nuclear Power Technology (ANP) Series
Nuclear Fuel Cycle Technology and Policy (NFC) Series
Nuclear Systems Enhanced Performance (NSP) Series
MIT Reactor Redesign (MITRR) Series
Nuclear Energy and Sustainability (NES) Series
Nuclear Space Applications (NSA) Series

Please visit our website (mit.edu/canes/) to view more publication lists.

MIT-ANP-TR-179	C. W. Forsberg, N. Sepulveda and K. Dawson ***Implications of Carbon Constraints on Electricity Generation Mix For the United States, China, France and United Kingdom*** (August 2018).
MIT-ANP-TR-178	C. W. Forsberg, N. Sepulveda and K. Dawson ***Commercialization Basis for Fluoride-salt-cooled High-Temperature Reactors (FHRs): Base-load Reactor with Heat Storage for Variable Electricity and High-Temperature Heat to Industry*** (August 2018).
MIT-ANP-TR-177	S.T. Lam, C. W. Forsberg, and R. Ballinger ***Understanding Hydrogen/Tritium Behavior on Carbon to Predict and Control Tritium in Salt Reactors: Experiments, Modeling and Simulation*** (August 2018).
MIT-ANP-TR-176	J. Conway, N. Todreas, and J. Buongiorno ***Security and the Offshore Nuclear Plant (ONP): Security Simulation Testing and Analysis of the Multi-Layer Security System*** (August 2018).
MIT-ANP-TR-175	P. A. Champlin, D. Petti, and J. Buongiorno ***Techno-Economic Evaluation of Cross-Cutting Technologies for Cost Reduction in Nuclear Power Plants*** (August 2018).
MIT-ANP-TR-174	L. T. Rush, D. Petti, and J. Buongiorno ***Critical Assessment of Techniques, Markets and Overall Economics of Generation III+ and IV Reactors*** (August 2018).
MIT-ANP-TR-173	C. W. Forsberg, et al. ***Technoeconomic Modeling of Heat Storage and Added Assured Capacity for Steam Cycle Nuclear Power Plants*** (September 2018).
MIT-ANP-TR-172	G. Locatelli, University of Leeds ***WHY ARE MEGAPROJECTS, INCLUDING NUCLEAR POWER PLANTS, DELIVERED OVERBUDGET AND LATE?*** (January 2018).
MIT-ANP-TR-171	C. W. Forsberg, et al. ***MIT-Japan Study Future of Nuclear Power in a Low-Carbon World: The Need for Dispatchable Energy*** (September 2017).
MIT-ANP-TR-170	C. W. Forsberg, et al. **Light Water Reactor Heat Storage for Peak Power and Increased Revenue: Focused Workshop on Near-Term Options** (July 2017).

MIT-ANP-TR-169	J. Conway, N. Todreas, **Offshore Floating Nuclear Plant (OFNP):** Published as report MIT-ANP-TR-176.
MIT-ANP-TR-168	G. N. Genzman, N. Todreas, R. Abeyaratne, and M. Dahleh, **Ship Collision and the Offshore Floating Nuclear Plant (OFNP): Analysis of Possible Threats and Security Measures** (September 2016).
MIT-ANP-TR-167	K. Shirvan, G. Daines, K. P. So, A. Mieloszyk, Y. Sukjai, and Ju Li, **Silicon Carbide Performance as Cladding for Advanced Uranium and Thorium Fuels for Light Water Reactors,** (August 2016).
MIT-ANP-TR-166	C. W. Forsberg, S. Lam, D. M. Carpenter, D. G. Whyte, R. Scarlat, C. Contescu, L. Wei, J. Stempien, and E. Blandford, **Tritium Control and Capture in Salt-Cooled Fission and Fusion Reactors: Status, Challenges and Path Forward** (May 2016).
MIT-ANP-TR-165	C. Forsberg, D. Carpenter, D. Whyte, R. Scarlat, and L. Wei, **Tritium Control and Capture in Salt-Cooled Fission and Fusion Reactors: Experiments, Models, and Benchmarking** (January 2016).
MIT-ANP-TR-164	J. Zhang, J. Buongiorno, M.W. Golay, N.E. Todreas, **Safety Analysis of OFNP-300 and OFNP-1100 (for design basis events)** (November 2015).
MIT-ANP-TR-163	J. Stempien, R. Ballinger, C. Forsberg, M. Kazimi, **Tritium Transport, Corrosion, and Fuel Performance Modeling in the Fluoride Salt-Cooled High-Temperature Reactor (FHR)** (September 2015).
MIT-ANP-TR-162	C. Forsberg, **Strategies for a Low-Carbon Electricity Grid with Full use of Nuclear, Wind and Solar Capacity to Minimize Total Costs** (August 2015).
MIT-ANP-TR-161	A. Briccetti, J. Buongiorno, M.W. Golay. N.E. Todreas, **An Analysis of the Spreading of Radionuclides from a Vent of an Offshore Floating Nuclear Power Plant** (2015).
MIT-ANP-TR-160	J. Jurewicz, J. Buongiorno, M.W. Golay, N.E. Todreas, **Design and Construction of an Offshore Floating Nuclear Power Plant** (June 2015).
MIT-ANP-TR-159	Matthew Brian Strother, J. Buongiorno, M.W. Golay, N.E. Todreas, **Hydrodynamic Analysis of the Offshore Floating Nuclear Power Plant** (2015).
MIT-ANP-TR-158	Jacob DeWitte, N.E. Todreas, R. Ballinger, **Maximizing Nuclear Power Plant Performance via Mega-Uprates and Subsequent License Renewal** (January 2015).
MIT-ANP-TR-157	Charles Forsberg, Lin-Wen Hu, Per Peterson and Kumar Sridharan, **Fluoride-Salt-Cooled High-Temperature Reactor (FHR) for Power and Process Heat** (December 2014).
MIT-ANP-TR-156	Nghia T. Nguyen and Neil E. Todreas, **An Inverted Pressurized Water Reactor Design With Twisted-Tape Swirl** (June 2014).
MIT-ANP-TR-155	K. Shirvan, R. Ballinger, J. Buongiorno, C Forsberg, M.S. Kazimi, N.E. Todreas, **Advanced Offshore Seabed Reactors** (April 2014).
MIT-ANP-TR-154	C. Forsberg, L-W. Hu, J. Richard, R. Romatoski, B. Forget, J. Stempien, R. Ballinger, **Fluoride-Salt-Cooled High-Temperature Test Reactor (FHTR): Goals, Options, Ownership, Requirements, Design, Licensing, and Support Facilities** (December 2014).

Project Description

Integrated FHR Technology Development: Tritium Management, Materials Testing, Salt Chemistry Control, Thermal Hydraulics and Neutronics with Associated Benchmarking

Project Title:	Integrated FHR Technology Development: Tritium Management, Materials Testing, Salt Chemistry Control, Thermal Hydraulics, and Neutronics with Associated Benchmarking
Date of Report:	September 30, 2018
Recipient:	Massachusetts Institute of Technology, 77 Massachusetts Ave., Cambridge, MA 02139
Award Number:	NEUP14-7476
Principal Investigator:	Charles Forsberg, 617-324-4010, cforsber@mit.edu
Co-PI:	Lin-wen Hu, lwhu@mit.edu Per F. Peterson, peterson@nuc.berkeley.edu Massimiliano Fratoni, maxfratoni@berkeley.edu Kumar Sridharan, kumar@engr.wisc.edu Anil Kant Prinja, prinja@unm.edu

Project Objectives: The objective of the Integrated Research Project (IRP) is to address major challenges in the development of commercial Fluoride-salt-cooled High-temperature Reactor (FHR) technology: tritium control; fluoride-salt corrosion control and materials selection; thermal-hydraulics and neutronics; and evaluation model benchmarking. The work with other activities addressed other challenges including the commercial case and key requirements for FHR instrumentation and control.

Table of Contents

Executive Summary

This report summarizes the results of a 3-year Integrated Research Project (IRP) sponsored by the U.S. Department of Energy to address major technical challenges in the development of the Fluoride-salt-cooled High-temperature Reactor (FHR). The IRP universities included the Massachusetts Institute of Technology (MIT), the University of California at Berkeley (UCB), the University of Wisconsin (UW), and the University of New Mexico (UNM). The report includes activities fully funded by the IRP and activities that may have had multiple funding sources. The large amount of progress that was made is partly a consequence of this being the second IRP where much of the initial learning curve occurred during the first IRP.

The FHR is a new reactor concept less than 20 years old that combines a clean fluoride salt coolant, the graphite-matrix coated-particle fuel originally developed for High-Temperature Gas-Cooled Reactors (HTGRs) and passive decay heat removal systems from sodium fast reactors. For most of the base-line studies, the IRP examined a pebble-bed FHR that delivers heat between 600 to 700°C with a $^{7}Li_2BeF_4$ (flibe) salt coolant. There are alternative FHR designs. There are multiple incentives for development of the FHR based on our current understanding of the technology.

- *Economics*. Revenue per unit of thermal heat output is increased because the average temperature of delivered heat to the power cycle is ~650°C, higher than the average temperature of delivered heat from helium, sodium and water cooled reactors. Higher temperatures enable (1) higher heat-to-electricity efficiency, (2) higher temperature delivered heat to industry, and (3) more efficient coupling to heat storage technologies that enable variable electricity to the grid from a base-load reactor to enhance revenue. Costs may be reduced by operating at low pressures and passive safety systems.
- *Safety*. The FHR is a low-pressure reactor with HTGR fuel that minimizes stored energy in the reactor core that can drive accidents. Safety is aided by the very high-temperature capabilities of the HTGR fuel, a salt coolant with a boiling point above 1200°C, and a coolant that dissolves most fission products if there are fuel failures.
- *Technology Status*. While the FHR is a new reactor concept, it is built upon existing technologies that can reduce development risk and time. The Next Generation Nuclear Plant (NGNP) program has developed a detailed understanding of HTGR fuel and demonstrated its performance—the fuel used by the FHR. The use of a clean liquid salt rather than the molten salt reactor (MSR) with fuel dissolved in the salt minimizes technology risks and uncertainties. Last, the development of higher-temperature Rankine (steam) and Brayton power cycles enables efficient use of higher-temperature delivered heat. When the MSR was originally being developed in the 1970s, peak power cycle temperatures were near 550°C. It was not possible to fully utilize the higher temperature of delivered heat.

There are development challenges. The report is organized as a series of stand-alone sections on different activities to address these challenges with references including thesis and publications that resulted from this work. This summary includes the major conclusions from this work. Sections within this summary correspond to sections in the main report.

Tritium Control and the Role of Carbon

Understanding Hydrogen/Tritium Behavior on Carbon to Predict and Control Tritium in Salt Reactors and Modeling Tritium System Behavior (MIT)

Liquid salts, particularly flibe, generate significant quantities of tritium that must be captured to avoid its release to the environment. The primary emphasis of the MIT work on tritium is understanding its interactions with carbon to predict behavior and ultimately control tritium releases. The fuel contains large quantities of carbon and carbon beds can be used to remove tritium from the liquid salt. Carbon is a leading candidate for tritium removal from salt at 700°C because (1) it can adsorb significant amounts of tritium as demonstrated in the molten salt reactor experiment where 15% of the tritium remained with the nuclear-grade carbon moderator and (2) carbon is chemically compatible with fluoride salts. Carbon comes in many forms. The processing of graphite to withstand neutron irradiation with limited dimensional changes creates a carbon form that limits tritium uptake. If a carbon bed is used for tritium removal from the liquid salt outside the reactor core, there is no requirement for the carbon bed to withstand high neutron fluences. The experimental work explored alternative carbon forms that yield high hydrogen adsorption. Combined with system-level modeling, it was shown that carbon materials in an adsorption bed outside the reactor core can be effectively used as tritium getters to control radioactive releases and manage corrosion. The improved understanding of hydrogen adsorption on carbon may also enable design of carbons with lower tritium uptake—a characteristic that may be desired for the fuel and other carbon components in the core to reduce potential release of tritium in an over-temperature transient.

From 2015 – 2018, an experimental laboratory has been established using hydrogen and deuterium surrogate for materials exploration. Tritium system-level modeling and a variety of experiments probing different physical properties of materials were conducted to 1) analyze system wide tritium behavior in the FHR, 2) understand the thermodynamic behavior of tritium on FHR materials and 3) demonstrate that alternative carbon-based materials can reduce tritium levels at prototypic FHR conditions. MIT has continued development and improvement of system level code TRIDENT (Tritium DiffusioN Evolution and Transport). Using a carbon adsorption column, it has been found that tritium capture performance can be optimized by varying the design and operating conditions, namely the size of the adsorptive pebbles, the dimensions of the column, and regeneration rate of the spent carbon adsorber. Experimentally, it has been found that above all, graphite and carbon-based materials with greater narrow micropore (< 0.7 nm width) and micropore (<2 nm width) volumes adsorb more tritium even at high temperatures of 700^{o}C, where the adsorption appears to occur via a combination of molecular attraction and dissociative chemical bonding. Using these new materials, specifically granular activated carbon OVC 4x8, simulations have shown that release rates for the 236 MWth prototype reactor can be reduced from 2410 Ci/d to less than 40 Ci/d. Further, it was found that this can be accomplished with a modestly-sized small column of 1.5 R x 4.5 m.

With the use of typical nuclear-grade carbons designed for high neutron fluxes, solubility-limited carbon limits the rate of tritium removal from the salt and thus controls system performance. In contrast, with carbon forms such as OVC 4x8 mass transfer of tritium through the salt to the carbon surface controls system performance—the carbon adsorption no longer limits tritium removal, While further experiments must be conducted to examine long-term performance of adsorbers, early simulation and modeling efforts show great potential.

Irradiation Experiments with Tritium (MIT)

The MIT NRL conducted a series of experiments utilizing the MIT Research Reactor (MITR) to investigate the generation, transport, and partitioning of tritium from flibe salt. The experiments, names FS-1 through FS-4, involved the irradiation of materials in liquid flibe from 600-700°C for up to 1000 hours. Tritium generated in the flibe is transported to an inert sweep gas just as it would be in a commercial FHR. Both real-time (compensated ion chamber) and integrated (bubbler/catalyst) systems were then used to collect and quantitatively evaluate both the chemical speciation and activity of the tritium. The first three irradiations used positions within the core of the MITR. These represented the first irradiations of enriched flibe under FHR conditions since the MSRE in the 1960s. The FS-4 experiment utilized an MITR vertical graphite reflector position to maximize volume and thermal neutron flux in order to generate a steady-state supply of tritium from unenriched liquid flibe. The lessons learned from the design, operation, and post-irradiation examination of these facilities provides valuable information for the future direction of FHR irradiation research and the measurement of tritium in FHR conditions. In particular it addresses the challenges of tritium parasitic capture/catalyzed reactions, static capsule irradiations at 700°C, fluoride radiolysis, and flibe-bearing specimen handling.

Fig. S.1. FS-3 Irradiation in the MIT Reactor

Experimental Measurements of Tritium Permeation through Metals (MIT)

Tritium permeation through metallic walls of tanks, pipes, and heat exchangers is one of the main challenges in the development of molten salt nuclear reactors, and in particular FHRs. Flibe is being considering as the primary loop fluid for modern FHRs; it will be used to transfer heat from the core to heat exchangers. However, tritium is generated in the molten salt due to the neutron interactions with salt components such as Li, Be, and F. This tritium, with a half-life of 12.6 years, can then easily permeate through metal alloys at high temperature. If uncontrolled, this will result in the spread of radioactive material throughout the FHR system and eventual environmental releases. Among several tritium control strategies being considered for FHRs is adding an alumina coating on surface of metals as tritium permeation barrier (TPB). Alumina TPBs appear to be an efficient solution with respect to the real-world engineering practicability, availability, and reliability. In this study, a layer of alumina coating was added onto the surface of commercial 316 stainless steel tubing via plasma thermal spray. An intermediate bond layer of NiCr and a transit layer of NiCr+alumina was applied to the outer surface of the tube in order to enhance the adhesion between alumina coating and stainless steel, especially at high temperatures. The efficacy of the coating to reducing tritium transport was investigated by experimentally measuring the tritium permeation rate through coated tube and bare stainless tubes at the prototypical FHR temperature of 700°C. In order to generate a continuous source of tritium, 35g of purified natural Flibe salt (not Li-7 enriched) was irradiated by thermal neutron flux at 620°C in the Massachusetts Institute of Technology Research Reactor (MITR). The preliminary results suggest that the coatings on tube surface significantly reduced the tritium permeation rate at high temperature. To get better understanding of the TPB, the microstructure of the coated tubes was characterized using various techniques.

Uptake and Release of Tritium from Irradiated Graphite (MIT)

Under neutron irradiation in an FHR, tritium is continuously generated from all three elemental components of flibe salt. This tritium may then interact with the large amounts of graphite present in the FHR primary system as both fuel matrix and neutron reflectors. Graphite is known to have a high potential for uptake of tritium, and so it is also under consideration as tritium capture media. In order to understand the interaction between fluoride salt, tritium and graphite at FHR conditions, graphite specimens were irradiated in the MITR core at 700°C in flibe in a series of experiments. After irradiation these specimens were extracted and analyzed using a variety of techniques. In particular, nuclear-grade graphite samples (both high-density structural and fuel matrix graphite) from the FS-1 and FS-2 in-core irradiations were extracted and analyzed for tritium content using a custom designed thermal desorption furnace. Tritium desorption as a function of temperature and the total tritium content of sample subsections suggests that tritium retention was predominantly a surface effect. A majority of desorbed tritium was measured in an insoluble form (HT/T_2).

Experimental Investigation of Ultrasonic-Enhanced Gas Sparging to Remove Tritium and Other Gas Impurities from High-Temperature Salts (UNM)

Tritium in a FHR is generated in liquid salts as a dissolved gas. Tritium removal is required to prevent escape to the environment. One method to remove the tritium is gas sparging with either an inert gas or a hydrogen/inert gas mixture. The rate of tritium removal from the liquid is controlled by the mass transfer through the liquid salt to the sparging gas. Mass transfer is increased by using smaller gas bubbles with more surface area per unit volume of gas sparing. Ultrasonic agitation of the gas-liquid mixture can increase the number of bubbles and create non-spherical bubbles of changing dimensions—methods that increase tritium mass transfer from liquid to gas phase. Ultrasonic gas sparging was experimentally investigated using dissolved oxygen in glycerol to simulate hydrogen in liquid salts.

The Small Ultrasonic Mass Transfer (SUMATRA) experiments demonstrated proof-of-concept of ultrasonic mass transfer enhancement. The results were used to develop a mass transfer correlation for ultrasonically enhanced mass transfer. The second experiment, the Prototype Ultrasonic Mass Transfer (PULST) was designed as a scaled up version of SUMATRA with the goal of investigating indirect ultrasonic-enhanced mass transfer and the viability of using commercial off-the-shelf components. The PULST experiments did not conclusively show mass transfer enhancement but did (1) establish the limits of using off-the-shelf components with indirect ultrasonic mass transfer enhancement and (2) quantified the changes required to optimize flow-cell design. The requirement is to efficiently transfer ultrasonic energy from the ultrasonic generator through the wall to the hot salt with large temperature differences between the salt and ultrasonic generator.

FHR Corrosion Control with Redox Control, Impurity Control, and Materials Selection (UW)

A significant step in FHR research was the implementation and improvement of methods for producing and controlling the properties of FLiBe salt. Methods have been perfected for purifying salt and then testing its elemental and electrochemical characteristics. The interaction of important structural materials with FLiBe salt was evaluated in long term static corrosion experiments. To better understand FLiBe salt's thermohydraulic nature a large natural convection circulation loop has been constructed at UW. Salts specifically designed for irradiated environments were re-purified at UW-Madison and sent to MIT for in-reactor experimentation.

A vital resource to the success of salt research in irradiated environments is ^{7}Li enriched MSRE FLiBe. This salt which contains less of the isotope ^{6}Li than natural lithium has a much lower probability of producing tritium under irradiation. The United States currently does not produce large quantities of enriched ^{7}Li for nuclear environments. What remained of the valuable ^{7}Li enriched FLiBe left over from the MSRE sat dormant in less than ideal conditions since its retirement in 1969. In 2015, the University of Wisconsin-Madison successfully re-purified roughly 54.4 kg of spent ^{7}Li enriched MSRE FLiBe from ORNL that had circulated in the MSRE's secondary loop for over 23,000 hours. The salt was re-purified by a process call hydrofluorination. In this process, hydrogen fluoride and hydrogen gas are sparged through the molten mixture (melt) in order to remove common salt impurities such as oxygen, moisture and some metallic impurities.

The re-purification of MSRE FLiBe helped build the expertise to produce large quantities of purified natural lithium FLiBe salt for further out-of-reactor experimentation. Using the same batch hydrofluorination unit, UW-Madison produced another 38.7 kg of natural lithium FLiBe salt. This salt has been used extensively in both laboratory and natural convection circulation loop environments at UW-Madison. Analytical chemistry methods developed with the help of the Wisconsin State Laboratory of Hygiene show that the natural lithium FLiBe has similar make-up as the ^{7}Li enriched reference salt.

An in-situ electrochemical method was developed to expedite the measurement of corrosion product concentrations and help better predict the longevity of a reactor primary loop. A simple yet robust electrochemical probe was designed for laboratory and circulation loop environments. Two electrochemical techniques have been implemented at the laboratory scale to help characterize FLiBe salts and understand corrosion results. The fluoride salt redox potential is a simple electrochemical method that gives insight into how oxidizing FLiBe salt can be to a given material. The fluoride salt redox potential was used to characterize salts used in corrosion experiments. The redox potential is sensitive to corrosion control methods such as beryllium metal addition. Corrosion results show that corrosion rate of common structural materials, such as 316L stainless steel and Hastelloy N, are modestly correlated with the value of the fluoride salt redox potential. Cyclic voltammetry (CV) and Linear Sweep Voltammetry (LSV) are useful methods for investigating and measuring common corrosion products found in FLiBe salt. CV has been used extensively to study the behavior of chromium fluoride, the dominant corrosion product of most preferred alloys.

In preliminary salt exposure studies, 316L stainless steel and Hastelloy N were exposed to as-purified ^{7}Li-enriched FLiBe for 3000 hours and 1000 hours, respectively. 316 stainless steel was exposed to molten FLiBe in both 316L stainless steel and graphite capsules. 316 stainless steel performed well when tested in 316 stainless steel capsules with a predicted attack depth of 17.1 µm per year. In graphite capsules, the corrosion was accelerated with a predicted attack depth of 31.2 µm per year. Corrosion in both capsules occurred by the dissolution of chromium from the stainless steel into the salt which led to the depletion of chromium, predominantly along the grain boundaries the material. Carburization in the subsurface of 316 stainless steel occurred during corrosion tests in graphite crucibles. Cr_7C_3 precipitate particles were observed in the corrosion layer. The corrosion results showed promising evidence that very pure or slightly reducing FLiBe may reduce the corrosion rate of 316 stainless steel to acceptable rates for use in the FHR.

Hastelloy N showed outstanding corrosion resistance in FLiBe when tested in a pure Ni crucible. Similar to the corrosion of 316 stainless steel in graphite, the graphite crucible accelerates corrosion of Hastelloy N in FLiBe. Carburization occurred in the subsurface of Hastelloy N during the 1000 hour corrosion test at 700˚C. Results also indicate that, while graphite accelerates the corrosion in the short-term, this may not be the case for the long-term.

To gauge the influence of irradiation on corrosion, in-reactor tests of both 316L stainless steel and Hastelloy N in ^{7}Li enriched FLiBe salt and identical capsules were conducted in the Massachusetts Institute of Technology Nuclear Research Reactor. Overall comparisons suggest that both effects of graphite and neutron radiation accelerate the corrosion rate by 2 to 10 times for the two tested alloys.

The corrosion resistance of a broader array of candidate structural materials was tested in molten natural lithium FLiBe salt produced at the University of Wisconsin-Madison. A static corrosion experiment was conducted for 2,000 hours at 700˚C. Materials tested include 316L stainless steel, Mo-Hf-C, W-Zr-C Cermet, silicon carbide, siC-siC composites and nuclear graphite. The influence of salt chemistry on the corrosion performance of these materials was investigated by chemically altering the salt to make it less oxidizing. Metallic beryllium was added to the salt to increase its thermodynamic stability by removing salt impurities thought to contribute to corrosion. These salts were benchmarked electrochemically using a test called the fluoride salt redox potential measurement. In addition, the influence of dissimilar materials on corrosion was evaluated. 316L stainless steel was exposed to FLiBe salts contained in both 316 stainless steel and graphite capsules.

Beryllium addition to FLiBe salt increases the thermodynamic stability of the salt and reduces corrosion of 316 stainless steel samples substantially. Approximately 10% less weight loss was experienced by samples exposed to Be-reduced salt compared to as-purified salt. Graphite-encapsulated samples exhibited about 50% greater depth of attack than 316-encapsulated samples. Samples exposed to Be-reduced salt showed less severe grain boundary corrosion than samples exposed to as-purified salt. Chromium is severely depleted in grain boundaries near the surface of all samples. A similar depth of attack of about 10-15μm was observed in 316L stainless steel in both reduced and as-purified salt when exposed in 316L capsule material. Stainless steel samples contained in graphite experienced a slightly higher depth of attack from corrosion. Profilometry shows that the surface of stainless steel samples encapsulated in graphite was up to 30% rougher than those encapsulated in stainless steel liners. ICP-OES results of post-corrosion salt samples showed that the chromium concentration is only increased in the salt contained in graphite capsules. The salt in the stainless steel-encapsulated samples did not have any noticeable increase in chromium concentration.

MoHfC samples showed negligible corrosion after exposure to molten FLiBe. Hafnium carbides (HfC) dispersed on the surface of as-polished MoHfC dissolved into FLiBe during exposure, leaving behind pits. Overall, the matrix Mo metal did not experience any major corrosion effects in molten fluoride salt.

WZrC samples performed poorly in molten salt due to the thermodynamically favorable dissolution of zirconium, as well as high bulk porosity of WZrC samples. Beryllium addition to FLiBe salt resulted in exposed samples experiencing twice the mass-loss relative to samples in as-purified salt. Tungsten carbide (W_2C) formation was prevalent in all post-corrosion samples, likely due to the increased relative carbon content in the samples as a product of zirconium dissolution.

The two type of graphite, A3 and IG-110, were completely unaffected following corrosion testing in molten FLiBe. Be-reduced salt showed higher corrosion of graphite, however results are inconclusive. While, bulk silicon-carbide as a material performed very well in molten FLiBe salt, silicon carbide coated SiC-SiC composite samples experienced some spallation or erosion of the coating after exposure to 700°C molten FLiBe. This resulted in a high mass-loss and exposure of the underlying composite. This suggests that further improvements in coating procedures may be needed to coating SiC on SiC-SiC composite. The polished SiC-SiC composite underneath the coating showed no signs of corrosion. The SiC samples joined by solid state bonding using an aluminum precursor bond layer are failed at the bond line during exposure to molten FLiBe salt. The smooth surface of the bonded silicon carbide samples showed very low surface corrosion in molten FLiBe salt, despite a failure of the bonded region. The failure at the bond is caused by the high solubility of aluminum in molten FLiBe. The bulk surface of both CVD SiC and SC-30 SiC-SiC composite showed no signs of corrosion, despite the formation of SiF_4 at high temperatures. XPS results show that a carbon thin film forms on the surface of SiC samples after corrosion, which indicates silicon dissolution and possible protection of the underlying SiC by a carbon thin film. Carbon materials show very high nobility in molten fluorides salts. Further optimization of coating procedures and bond procedures are clearly needed before such composites are used to make components used in molten FLiBe salt.

A molten salt flow loop has been designed and constructed at the University of Wisconsin and is now operational. This is the first FLiBe loop to operate since the 1970s and it is the first natural circulation FLiBe loop instrumented for thermal hydraulic measurements. The system is currently undergoing tests to measure heat transfer coefficients before starting materials testing. The flow environment is stable but shows several unique flow phenomena, including strong thermal stratification and short temperature jumps or spikes. The heat transfer measurements made so far show reasonable agreement with correlations but include an unexplained split in the data for heated salt, which requires further study. A new set of tests will rerun several operating states using a clean batch of FLiBe to examine the impact of salt impurity concentrations on heat transfer. After this, corrosion studies will be run to examine candidate FHR materials under expected operating conditions for 1000 or more hours. These tests are designed to mimic the static testing performed at UW so comparisons can be made between corrosion test methods.

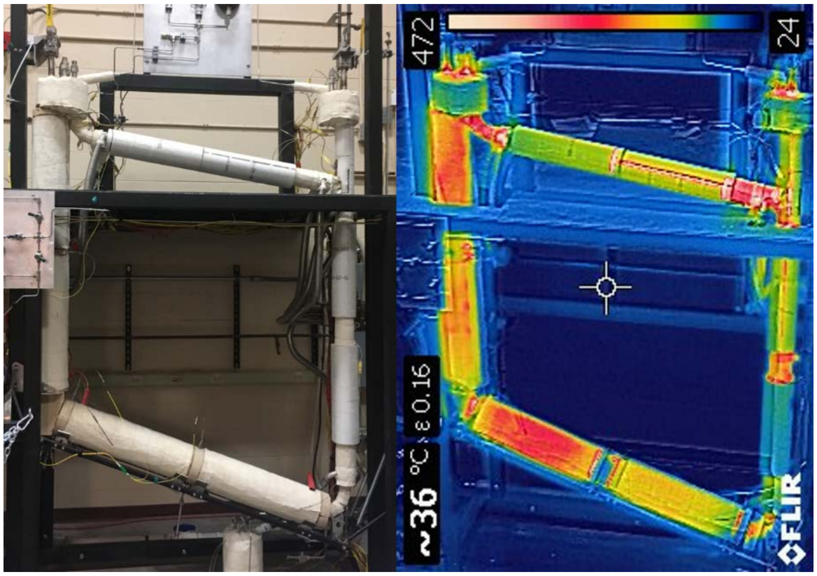

Fig. S.2. Natural Convection Molten Salt Corrosion Test Loop (Left: Loop and Right: Infrared)

In-Reactor FHR Materials Corrosion Testing (MIT)

The MIT NRL designed its first three in-core FHR irradiations to duplicate the conditions of the autoclave testing conducted by UW. The graphite holder, salt, and specimens were produced from the same batches of materials to matching dimensions. This is intended to give as direct a comparison as possible to help identify those corrosion effects that are affected by the presence of neutron and gamma irradiation, or how materials' susceptibility to corrosion is changed by accumulated radiation damage. The three MITR in-core irradiations (FS-1, -2, and -3) exposed various graphite, carbon fiber, SS316, Hastelloy, SiC, and SiC composite materials to enriched static flibe at 700°C for 300-1000 hours. After irradiation the specimens were extracted from the salt and analyzed for weight and dimensional changes, as well as microstructural characterization. The unique effects of irradiation (in particular activation/transmutation and generation and adsorption of tritium) added a further complexity to the handling and analysis of these samples. Using facilities at MIT and Idaho National Laboratory, information on the changes to the surface microstructure of the specimens was analyzed. For graphite specimens, frozen salt on samples' surface displays various crystalline shapes, including needle, dendrite, plate, petal, and nuggets. Some hexagonal and snow-like crystals were observed on surfaces cleaned with DI water. These crystals have relatively high concentration of Fe, Ti, Cr, O and F, which are probably associated with the impurities in molten salt. Fractional oxides also formed on the edges of the pores of the cleaned graphite and C/C composite samples. Compared to out-of-reactor specimens, nano carbide particles were not found in the near-surface layer of in-core corrosion samples, possibly due to the presence of tritium. A large number of line dislocation and dislocation loops, evidence of neutron irradiation-induced structural damage, were observed in grains and near to grain boundaries in metal specimens. The precipitates in the alloys probably inhibit the movement of the line dislocations.

Experiments and Modeling for Thermal Hydraulics, Neutronics and Structural Materials

FHR Experiments and Modeling for Thermal Hydraulics (UCB)

The UCB goals in thermal hydraulics were to improve the technical and scientific basis to predict the thermal hydraulics and neutronics response of FHRs. A class of heat transfer oils was used, that in the temperature range of 50°C to 120°C allow simulation of the thermal hydraulics of 700°C liquid salt while matching the Reynolds, Froude, Prandtl, and Grashof numbers. This remarkable good fortune allows low-cost, low-temperature experiments to simulate the thermal hydraulic behavior of high-temperature salts. The Compact Integral Effects Test (CIET) test facility (Fig. S.3), using Dowtherm A, was originally designed to drastically reduce the time and effort to experimentally simulate the system-level thermal hydraulic phenomena in FHRs. Experimental results can be used to validate system thermal hydraulic models for modeling and simulation purposes as well as for licensing applications. Since its inception, the CIET Research Program has expanded its reach by building new capabilities that allow the CIET Facility to act as a small-scale reactor simulator, coupled to a reactor control room. Now, additional areas of research and development related to FHRs and advanced reactors more generally include operation and performance, licensing, system design, human-machine interface, and fault detection. This new research is important for FHR understanding and development not only at UCB but for other organizations as well, such as DOE national laboratories and commercial organizations, such as Kairos Power.

Fig. S.3. Compact Integral Effects Test Facility

This work is separated into sections to describe the physical enhancements to the CIET Facility including the addition of the Advanced Reactor Control and Operations (ARCO) Facility, experiments and analysis in the CIET Facility, separate effects test (SET) research efforts to support the CIET Facility and other areas of FHR technology development, and thermal hydraulics simulation models and analysis. Major conclusions for this project include:

- *CIET Facility Modifications:* Several physical modifications have been made to the CIET Facility primarily to improve the facility performance and to decrease scaling distortions between the model facility and a prototypical FHR. Physical modifications have led to the operation of the CIET Facility as a small test-scale nuclear reactor rather than a thermal fluids system, including the important addition of the ARCO Facility to allow the study of human-machine interfaces, operator performance, system optimization, and a range of other interesting fields of study such as critical infrastructure cyber security. Further thought and research is being performed to identify areas of development possible with advanced integral effects tests, such as the CIET Facility, to establish clear plans of commercial technology development and licensing, such as for digital instrumentation and control systems and control and operation facilities in advanced reactors.

- *Frequency Response Testing:* Over the course of this work, a technique known as frequency response testing was implemented and studied with the CIET Facility. Frequency response testing provides a useful way of extracting information about reactors during operation. Among other things, it can be used for empirical model development, stability analysis, and parameter identification. Possible applications were tested with CIET to better understand the limitations and capabilities of this technique. The heater power control was then updated with simulated neutronic feedback control. This gives the ability to use a simulated control rod position and temperature feedback coefficients of reactivity with point reactor kinetics to calculate the heater output power. Fuel and coolant feedback coefficients were varied and a large variety of frequency response tests were used to extract information regarding the behavior of the CIET simulated reactor. Frequency response testing was able to show the stability of the reactor, as well as an understanding of the magnitude of temperature feedback

FHR Neutronics Analysis (UCB)

In the scope of the IRP, efforts on understanding and modeling the core neutronics for FHRs include code-to-code benchmark to verify the credibility of neutronics codes in modeling reactors with TRISO particle type fuel, development of numerical models for FHR cores, uncertainty and sensitivity study of Monte Carlo models due to nuclear data, and analyzing the activation process and gamma radiation shielding of the FHR coolant. The major projects are:

- *Code-to-code benchmark:* To date, no fueled experiments using pebbles immersed in salt have been conducted. Early-stage benchmarking of FHRs must rely heavily on code-to-code comparisons. The design of test cases for the IRP FHR neutronics benchmark starts with a simple, infinite cell containing pebbles and is examined with varying levels of homogenization. And the second scenario includes a graphite reflector and black boundaries to simulate a simplified reactor geometry, allowing for leakage and reflector effects.

- *Multiphysics modeling for FHR cores:* This project developed dedicated models for FHRs with different levels of spatial and energy resolution for the broad need in reactor design and analysis, including coupled heat diffusion and point kinetics unit cell models, Monte Carlo neutronics models, and coupled multi-group neutron diffusion and multi-scale porous media model. The methodology was applied to the TMSR SF-1 and Mk1 design to simulate both steady state and transient scenarios.

- *Investigation of uncertainties in Monte Carlo models due to nuclear data*: Sensitivity and uncertainty analyses for effective multiplication factor and coolant density reactivity coefficient due to nuclear data were performed for the Mark-1 pebble-bed fluoride-salt-cooled high-temperature reactor (Mk1 PB-FHR).

- *Salt activation and shielding analysis:* This project analyzed the shielding property of the Mark-1 PB-FHR reactor design, in three steps: burnup calculation, shielding calculation and flux to dose conversion. The calculations serve as an initial analysis on the shielding properties of the materials used in Mark-1 PB-FHR.

Experimental and Computational Investigation of Twisted Tube Heat Exchangers (UNM)

Liquid salts as heat transfer fluids compared to other reactor coolants have greater volumetric heat capacities, have higher Prandtl numbers and are expensive coolants. While total pumping power is low because of the high heat capacity, there is relatively poor heat transfer compared to other coolants for the same pumping power. These characteristics may result in decay heat cooling systems operating in the transitional flow regime. Under such operational conditions, alternative heat exchanger designs may provide better performance at lower costs. The use of twisted-tube versus straight-tube heat exchangers were experimentally evaluated in a test loop using Dowtherm A to simulate flibe salt coolants. Parallel computational investigations were conducted.

Fig. S.4. Twisted Elliptical and Plain Wall Heat Exchangers Tested in Heat Transfer Facility (Photo Credit: Hipex PTY. Ltd.)

The twisted elliptical tubes were found to have significant performance advantages in both the experimental and computational studies for use in FHR decay heat cooling systems. Experimental comparisons for buoyancy-affected and low forced-convection flow regimes showed up to 55% heat transfer coefficient enhancement on the shell side for natural circulation flow and greater than 250% heat transfer coefficient enhancement on the shell side for transitional forced convection flow. Results from the computational analysis showed that twisted elliptical heat exchangers can provide a 23 to 51% cost savings compared to a standard shell-and-tube heat exchanger for the intermediate heat exchanger used in a FHR.

Methodology for Thermal-hydraulic Uncertainty Propagation Licensing Analysis for a FHR Test Reactor – Uncertainty Propagation of Coolant Properties (MIT)

An important FHR development step is to design, build, and operate a test reactor. Through a literature review, liquid-salt coolant thermophysical properties have been recommended along with their uncertainties of 2-20%. The study addressed these high uncertainties by developing a methodology to incorporate uncertainty propagation in a thermal-hydraulic safety analysis for test reactor licensing. A hot channel model, Monte Carlo statistical sampling uncertainty propagation, and limiting safety systems settings (LSSS) approach were combined to ensure sufficient margin to fuel and material thermal limits during steady-state operation and to incorporate margin for high uncertainty inputs. The method calculates LSSS parameters to define safe operation. The methodology has been applied to two test reactors currently considered, the Chinese TMSR-SF1 pebble bed design and MIT's Transportable FHR prismatic core design; two candidate coolants, flibe ($LiF-BeF_2$) and nafzirf ($NaF-ZrF_4$); and forced flow and natural circulation conditions to compare operating regions and LSSS power (maximum power not exceeding any thermal limits). The calculated operating region accounts for uncertainty (2σ) with LSSS power (MW) for forced flow of 25.37±0.72, 22.56±1.15, 21.28±1.48, and 11.32±1.35 for pebble flibe, pebble nafzirf, prismatic flibe, and prismatic nafzirf, respectively. The pebble bed has superior heat transfer with an operating region reduced by 10% when switching coolants and 50% smaller uncertainty than the prismatic. The maximum fuel temperature constrains the pebble bed FHR while the maximum coolant temperature constrains the prismatic FHR due to different dominant heat transfer modes. Sensitivity analysis revealed 1) thermal conductivity and thus conductive heat transfer dominates in the prismatic design while convection is superior in the pebble bed, and 2) the impact of thermophysical property uncertainties are ranked and should be considered for experimental measurements in the following order: thermal conductivity, heat capacity, density, and lastly viscosity. Broadly, the methodology developed incorporates uncertainty propagation that can be used to evaluate parametric uncertainties to satisfy guidelines for non-power reactor licensing applications, and method application shows the pebble bed is more attractive for thermal-hydraulic safety. Although the method was developed and evaluated for coolant property uncertainties, it is readily applicable for any parameters of interest.

Effects of Radiative Heat Transfer in High-Temperature Liquids-Salts (MIT/UCB)

New FHR designs utilize high-temperature fluoride salts that may experience the effects of participating media radiative heat transfer. While radiative heat transfer has not been extensively studied for LWRs, its effects become significant at temperatures over 600-700°C due to its dependence on the absolute temperature to the fourth power [T^4] in liquid salts. This effect is not seen in high-temperature helium that is transparent. Radiative absorption and emission can increase energy transfer and increase temperature uniformity within the liquid-salt, which has large implications in accident scenarios where better heat transfer can reduce peak temperatures. MIT is creating a methodology to understand the effects of radiative heat transfer in high-temperature liquid-salts by: (1) performing opacity measurements on a variety of halide (fluoride and chloride) salts between 600-1000°C and (2) performing detailed modeling and simulation of the complex phenomena of radiative heat transfer in halide salts for key, representative flow geometries and structure surface emissivities. Figure S.5 shows the black body emission spectrum at 800°C where the adsorption coefficients are at the wavelengths to begin to make radiative heat transfer important.

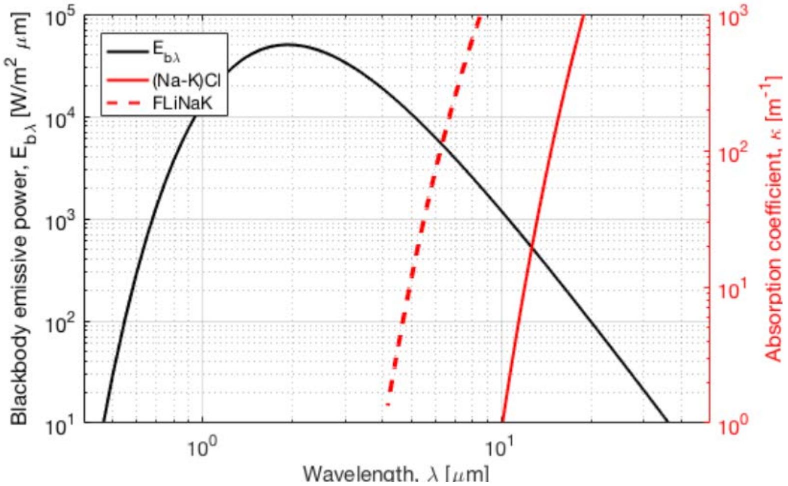

Figure S.5. Black body emission spectrum at 800C for index of refraction, n=1.4 and theoretical, pure (Na-K)Cl and FLiNaK absorption coefficients.

FHR Evaluation Model Benchmarking and Validation Workshops

A series of workshops throughout the duration of this IRP were held that included IRP members (faculty, staff, and students) and external experts from other academic institutions, national laboratories, and commercial companies in the U.S. and abroad. The goal of the workshops was to coordinate a broad benchmarking campaign to provide input for the development of advanced modeling and simulation tools for FHR development and analysis. Further description is provided below.

- *Workshop 1:* The primary results were the formation of technical area working groups (neutronics, thermal hydraulics, and materials corrosion, activation, tritium and transport (MATT)), the close collaboration with the second FHR IRP led by the Georgia Institute of Technology, and the establishment of a path forward for the benchmarking campaign including future workshop planning. White paper available on UCB's FHR website as UCBTH-15-006 (http://fhr.nuc.berkeley.edu/references/fhr-white-papers/).

- *Workshop 2:* The benchmarking workshop resulted in a variety of plans for moving forward, with a common theme being the need for delineating collaboration options between IRP members and identifying specific benchmarking needs. White papers from each working group have been compiled that summarize discussions, conclusions, and paths forward for each working group. White papers available at http://fhr.nuc.berkeley.edu/references/fhr-white-papers/.

- *Workshop 3:* Development of modern, powerful modeling and simulation toolsets are underway at many levels, paving the way for future design and development of nuclear reactors and systems without heavy reliance on expensive and relatively limited experiments. However, a significant, cross-cutting need was identified: high-quality validation data for these new tool sets. Closer coordination is needed between modeling and experimental groups at the national and international level. Workshop results are available at https://smartech.gatech.edu/handle/1853/58808. The MATT working group concluded that there was a need for a review paper on methods to control redox (and thus corrosion) in high-temperature fluoride salts. The goal was to assemble what is currently known to help focus future work. The review paper “Redox Potential Control in Molten Salt Systems for Corrosion Mitigation,” authored by J. Zhang et al was prepared and published in *Corrosion Science*. https://doi.org/10.1016/j.corsci.2018.08.035

Integrated Subcritical Experiments (MIT)

There are multiple pathways going forward. All involve test loops and lead to a full reactor test. MIT investigated an intermediate option—building an integrated subcritical experiment where the research reactor provides neutrons to drive the experiment. MIT developed the concept and proposed a large integrated experiment in a subcritical facility that contains TRISO particle fuel compacts and circulation Flibe salt operating at 600-700°C at MITR. This integrated experiment can provide valuable neutronic, thermal hydraulic and tritium management data, and is potentially a low-cost, accelerated path to demonstrate the technical feasibility of FHR.

Economics: Commercialization Basis for FHRs: Base-load Reactor with Heat Storage for Variable Electricity and High-Temperature Heat to Industry (MIT)

The question for any advanced reactor is: *What is the compelling economic case to justify the development of the reactor?* For the FHR an economic case was developed based on the ability of a base-load FHR to provide (1) economic variable dispatchable electricity to the grid and (2) high-temperature heat to industry with high reliability. Salt-cooled reactors deliver higher average-temperature (~650°C) heat to the power cycle or industry relative to other advanced reactors. This translates into lower-cost heat storage systems for variable electricity production and larger industrial heat markets.

Electricity markets are changing because of (1) the large-scale addition of wind and solar that results in times of low electricity prices [excess wind or solar and/or low demand] and times of high electricity prices [limited wind or solar and/or high demand] and (2) the goal of a low-carbon economy. This creates incentives to operate nuclear reactors at base-load to minimize production cost while using heat storage to vary electricity output to match electricity demand. At times of low electricity prices, the minimum amount of heat is sent to the turbine to keep it operating for rapid return to higher power levels while the remainder of the heat goes to storage. At times of high electricity prices, all heat from the reactor and heat from storage go to the power cycle to produce peak power that is above the base-load electricity output of the reactor.

The cost of heat storage is lower for reactors that deliver high-temperature heat to storage than low-temperature heat. The heat storage capacity of sensible heat storage systems depends upon the temperature swing from hot to cold that may be twice as large for an FHR compared to a light-water reactor (LWR); thus, reducing FHR heat storage cost for the same amount of heat storage media. The heat-to-electricity conversion efficiency for stored heat from an LWR is 20 to 30% versus 40% or higher for an FHR because of the higher efficiency of converting high-temperature heat to electricity—reducing heat storage costs per unit of electricity. Heat storage can be incorporated (1) in the steam cycle with multiple options or (2) in the intermediate loop between the reactor and the power cycle using nitrate, chloride or other salts. Nitrate-salt heat storage is used in existing concentrated solar power systems and is proposed by several salt-cooled reactor startup companies. Very-low-cost chloride salts for heat storage are being developed for the next generation of high-temperature (700°C) concentrated solar power systems with the same peak temperature as an FHR. If heat storage is depleted, it can be backed up by a combustion heater to provide assured peak electricity generating capacity at a cost less than the alternative of a stand-alone gas turbine.

Because of its high average temperature of delivered heat, the FHR can couple to Brayton power cycles with auxiliary-fuel (fossil fuels, biofuels, hydrogen or high-temperature stored heat) thermodynamic topping cycles. These power cycles have incremental heat-to-electricity efficiencies near 70%, greater than stand-alone gas turbines. The FHR provides heat to ~700°C for base-load electricity production with thermodynamic topping cycles using auxiliary fuel for peak power production that can raise peak turbine inlet temperatures to between 1100 to 1500°C. If there is excess low-price electricity, it can be converted into high-temperature stored heat for such topping cycles. Brayton power cycle options include (1) nuclear air-Brayton combined cycles and (2) nuclear steam-injected Brayton cycles with base-load steam cycles.

1. Introduction

This report summarizes the results of a 3-year Integrated Research Project (IRP) sponsored by the U.S. Department of Energy to address major technical challenges in the development of the Fluoride-salt-cooled High-temperature Reactor (FHR). The IRP universities included the Massachusetts Institute of Technology (MIT), the University of California at Berkeley (UCB), the University of Wisconsin (UW), and the University of New Mexico (UNM). The report includes activities fully funded by the IRP and activities that had multiple funding sources. The large amount of progress that was made is partly a consequence of this being the second IRP where much of the initial learning curve occurred during the first IRP. It also enabled the development of major experimental facilities.

The Fluoride-salt-cooled High-temperature Reactor (FHR) is a new reactor concept[1, 2, 3] that uses graphite-matrix coated-particle fuel developed for high-temperature gas-cooled reactors (HTGRs) and clean liquid fluoride salt coolants originally developed for molten salt reactors (MSRs). In an MSR the fuel is dissolved in the coolant. The use of a salt coolant enables delivery of heat to the power cycle or industrial process at a temperature between 600 and 700°C. For most of the base-line studies, the IRP examined a pebble-bed FHR with a $^7Li_2BeF_4$ (flibe) salt coolant. There are alternative FHR designs

There are several coolant choices[4] with the leading candidates shown in Table 1. All coolants are mixtures of multiple salts to reduce melting points. For comparison, water properties under LWR conditions are given. The requirement to minimize neutron adsorption in a thermal spectrum limits the coolant choices used to cool the reactor core. If the salt contains lithium, it must be isotopically-separated lithium-7 which has a low neutron absorption cross section. Flibe is the leading candidate among the possible salts because of its superior nuclear and heat transfer characteristics.

TABLE I. Candidate Reactor Coolant Properties

Coolant	T_{melt} (°C)	T_{boil} (°C)	ρ (kg/m^3)	ρC_p (kJ/m^3 °C)
$^7Li_2BeF_4$ (Flibe)	459	1430	1940	4670
59.5 NaF-40.5 ZrF_4	500	1290	3140	3670
26 ^{7}LiF-37 NaF-37 ZrF_4	436		2790	3500
51 ^{7}LiF-49 ZrF_4	509		3090	3750
Water (7.5 MPa)	0	290	732	4040
Water (15.5 MPa)	0	345	709	4049

Salt compositions in mole percent. Salt properties at 700°C and 1 atm. Sodium-zirconium fluoride salt conductivity is estimated—not measured. For comparison water data is shown at 290°C (7.5 MPa, boiling point) and PWR conditions with water properties at 309°C (average core temperature).

---

[1] C. W. FORSBERG and P. F. PETERSON, "Basis for Fluoride-Salt-Cooled High-Temperature Reactors with Nuclear Air-Brayton Combined Cycles and Firebrick Resistance-Heated Energy Storage", *Nucl. Technol.*, **196**, 1, 13 (October 2016) http://dx.doi.org/10.13182/NT16-28

[2] C. ANDREADES et al. "Design Summary of the Mark-I Pebble-Bed, Fluoride Salt–Cooled, High-Temperature Reactor Commercial Power Plant", *Nucl. Technol.*, **195**, 3 (September 2016) http://dx.doi.org/10.13182/NT-16-2

[3] Added FHR reports : http://web.mit.edu/nse/people/research/forsberg.html and http://fhr.nuc.berkeley.edu/

[4] D. F. WILLIAMAS, L. M. TOTH, K. T. CLARNO, "Assessment of Candidate Molten Salt Coolants for the Advanced High-Temperature Reactor (AHTR)," ORNL/TM-2006/12, Oak Ridge National Laboratory (2006).

From a thermo-mechanical design perspective, the defining characteristic of these salts relative to other nuclear reactor coolants is the high melting point. The practical implication is that typical reactor designs have reactor core coolant inlet temperatures near 600°C to minimize the risk of salt freezing and exit temperatures near 700°C based on limits of economic materials for the construction of the heat exchangers.

The fuel is the graphite-matrix coated-particle fuel used for HTGRs. As a consequence, the FHR is a thermal spectrum reactor with the same fuel cycle options as the HTGR. The Next Generation Nuclear Plant (NGNP) program to develop modular HTGRs includes a large fuel development and testing program. Most of the fuels technology for the FHR is built upon the NGNP fuels program.

The report is organized as a series of stand-alone sections that addressed major challenges associated with the development of the FHR. Most of the work was in the following categories that are sections within this report.

- Tritium control (Chapter 2)
- Materials testing and selection (Chapter 3)
- Experiments and Modeling of Thermal Hydraulics, Neutronics, and Structural Mechanics (Chapter 4)
- Evaluation Model Benchmarking and Validation Workshops (Chapter 5)
- Reactor test options (Chapter 6)
- Commercialization basis for FHR (Chapter 7)

2. Tritium Control

The objective of this task was to understand the production, transport, control, and recovery of tritium in FHRs and to develop cost effective methods to minimize release of tritium to the environment, minimize exposure to workers, and prevent release of stored tritium during accidents. The base-line reactor salt coolant is Flibe ($^{7}Li_2BeF_4$). Under neutron generation the lithium fluoride is converted to tritium fluoride (^{3}HF) that is highly corrosive. With appropriate chemical redox control[5], the HF is converted into hydrogen ($^{3}H_2$) and another fluoride. If the redox control agent is beryllium, the second chemical reaction product is BeF_2. If the tritium is in the form of hydrogen, it can potentially diffuse through metal heat exchangers and be released to the environment. Because of the central role of tritium in terms of plant corrosion and radionuclide releases to the environment, understanding its behavior and control is central to development of an FHR.

Most of this work involves hydrogen (tritium) sorption on carbon because (1) the fuel is a carbon-based fuel implying tritium sorption on carbon in the reactor core and where tritium could be released in an over-temperature transient and (2) other forms of carbon have potentially excellent characteristics for tritium removal from the liquid salt on carbon beds outside the reactor core. A carbon bed outside the reactor core for tritium removal does not have the requirement to withstand high neutron fluences; thus, carbon forms can be chosen to maximize tritium removal. The work is divided into several components: understanding hydrogen uptake on graphitic materials, MIT reactor tritium experiments to understand tritium uptake in systems with graphite and salt under neutron irradiation, experiments to measure tritium permeation through various barriers, and experiments with simulants to understand tritium removal by gas sparging. The following reports describe work in each of these areas.

- Understanding Hydrogen/Tritium Behavior on Carbon to Predict and Control Tritium in Salt Reactors and Modeling Tritium System Behavior (MIT)
- Uptake of Tritium by Graphite During Neutron Irradiation in Flibe Salt (MIT)
- Tritium Permeation Experiment (Zheng: MIT)
- Experimental Investigation of Ultrasonic-Enhanced Gas Sparging to Remove Tritium and Other Gas Impurities from High-Temperature Salts (UNM)

There is an alternative strategy for capturing tritium from the FHR to prevent its release to the environment—an option that is now being considered partly because of changes in electricity markets. Tritium can be removed with an intermediate heat transfer loop with nitrate salts between the reactor and power cycle. Tritium diffuses through the heat exchangers, is oxidized in the nitrate salts and removed as steam from the nitrate salts. This option was investigated at Oak Ridge National Laboratory[6] in the 1970s but abandoned because of the cost penalties associated with an additional intermediate heat transfer loop.

However, in the last several years there have been major changes in electricity markets with (1) the addition of large-scale wind and solar and (2) the goal of a low-carbon electricity grid. These changes result

---

[5] J. Zhang et al. "Redox Potential Control in Molten Salt Systems for Corrosion Mitigation", *Corrosion Science,* https://doi.org/10.1016/j.corsci.2018.08.035

[6] E. G. Bohlmann, *Heat Transfer Salt for High Temperature Steam Generation,* ORNL-TM-3777, Oak Ridge National Laboratory, Oak Ridge, Tennessee (December 1972).

in large variations in electricity prices over time and create large incentives provide variable electricity to the grid to maximize revenue while operating the reactor at base-load to minimize costs. This can be accomplished by adding heat storage. At times of low electricity prices, some reactor heat is sent to storage while some heat is sent to the power cycle. At times of high electricity prices, heat from the reactor and heat from storage is sent to the power cycle to produce electricity at a rate greater than the base-load capability of the power plant. Initial economic analysis (Chapter 7) indicate large economic incentives to couple the FHR to heat storage[7]. The leading heat storage system uses nitrate salts for heat storage—the same systems used in concentrated solar power systems with heat storage capabilities in excess of one gigawatt hour. As a consequence, many FHR and MSR designs now include an intermediate nitrate loop that serves two functions: (1) heat storage for variable electricity to the market with a base-load reactor and (2) catch any tritium leaking through heat exchangers. This development does not change the need to understand and control tritium in the reactor system because of its impact on corrosion, impact on operations (health physics) and potential release in an accident—but does create another option to prevent tritium releases to the environment.

---

[7] C. W. Forsberg, N. Sepulveda and K. Dawson, Commercialization Basis for Fluoride-salt-cooled High-Temperature Reactors (FHRs): Base-load Reactor with Heat Storage for Variable Electricity and High-Temperature heat to Industry, MIT-ANP-TR-178, Center for Advanced Nuclear Energy Systems, Massachusetts Institute of Technology (August 2018)

2.1. Understanding Hydrogen/Tritium Behavior on Carbon to Predict and Control Tritium in Salt Reactors and Modeling Tritium System Behavior (MIT)

Understanding Hydrogen/Tritium Behavior on Carbon to Predict and Control Tritium in Salt Reactors and Modelling Tritium System Behavior (MIT)[8]

Summary

Liquid salts, particularly flibe, generate significant quantities of tritium that must be captured to avoid its release to the environment. The primary emphasis of the MIT work on tritium is understanding its interactions with carbon to predict behavior and ultimately control tritium releases. The fuel contains large quantities of carbon and carbon beds can be used to remove tritium from the liquid salt. Carbon is a leading candidate for tritium removal from salt at 700°C because (1) it can adsorb significant amounts of tritium as demonstrated in the molten salt reactor experiment where 15% of the tritium remained with the nuclear-grade carbon moderator and (2) carbon is chemically compatible with fluoride salts. Carbon comes in many forms. The processing of graphite to withstand neutron irradiation with limited dimensional changes creates a carbon form that limits tritium uptake. If a carbon bed is used for tritium removal from the liquid salt outside the reactor core, there is no requirement for the carbon bed to withstand high neutron fluences. The experimental work conducted includes exploration of carbon properties that yield high hydrogen adsorption. Combined with system-level modeling, it was shown that carbon materials in an adsorption bed outside the reactor core can effectively be used as tritium getters to significantly reduce radioactive release and manage corrosion. The improved understanding of hydrogen adsorption on carbon may also enable design of carbons with lower tritium uptake—a characteristic that may be desired for the fuel and other carbon components in the core to reduce potential release of tritium in an over-temperature transient.

An experimental laboratory has been established using hydrogen and deuterium surrogate for materials exploration. Tritium system-level modeling and experiments probing different physical properties of materials were conducted to 1) analyze system wide tritium behavior in the FHR, 2) understand the thermodynamic behavior of tritium on FHR materials and 3) demonstrate that alternative carbon-based materials can reduce tritium levels at prototypic FHR conditions. MIT has continued development of system level code TRIDENT (Tritium DiffusioN Evolution and Transport) with several code improvements. Using a carbon adsorption column, it has been found that tritium capture performance can be optimized by varying the design and operating conditions, namely the size of the adsorptive pebbles, the dimensions of the column, and regeneration rate of the spent carbon adsorber. Experimentally, it has been found that above all, graphite and carbon-based materials with higher narrow micropore (< 0.7 nm width) and micropore (<2 nm width) volumes adsorb more tritium even at high temperatures of 700^{o}C, where the adsorption appears to

---

[8] S. Lam

occur via a combination of molecular attraction and dissociative chemical bonding. Using these new materials, specifically granular activated carbon OVC 4x8 simulations have shown that release rates for the 236 MWth prototype reactor can be reduced from 2410 Ci/d to less than 40 Ci/d. Further, it was found that this can be accomplished with a modestly sized small column of 1.5 R x 4.5 m.

With nuclear-grade carbons designed for high neutron fluxes, solubility-limited carbon limits the rate of tritium removal from the salt and thus controls system performance. In contrast, with carbon forms such as OVC 4x8 mass transfer of tritium through the salt to the carbon surface controls system performance—the carbon adsorption no longer limits tritium removal, While further experiments must be conducted to examine long-term performance of adsorbers, early simulation and modeling efforts show great potential.

Background

It has been demonstrated in literature that adsorption of hydrogen isotopes have been higher than expected in graphite materials. During the molten salt reactor experiment (MSRE), it was shown that almost 15% of the generated tritium was captured in the graphite stringers [1]. At the surface, it was shown that POCO graphite that was used had a concentration as high as 0.0156 cm^3STP/g. In fusion material applications, solubility information has been found to show a similar magnitude for isograph-88 at high temperatures above 700ºC [2]. It was further shown that different grades and types of carbon materials have significantly differing adsorption capacities [3]. In the FHR, large quantities of carbon materials (~50, 000 kg of graphite and carbon-fiber composites) have been proposed for use [4], which will be a significant tritium sink.

The objective of this work is to understand the production, transport, control, and recovery of tritium in FHRs and to develop cost effective methods to minimize release of tritium to the environment, minimize exposure to workers, and prevent release of stored tritium during accidents. To achieve control, we have proposed to use carbon-based materials, which will already exist in large parts of the reactor system. The work is primarily divided into two components: 1) Experimental work to determine micro- and macroscopic hydrogen adsorption behavior on carbon that can potentially be used in the FHR, and 2) Development of models and simulation to predict the behavior of tritium in the system. These activities are complimentary in that results from both from both are mutually informative. The work is summarized below.

Experimental Methods and Materials

In order to quantify the interaction between tritium, a lab was built with constant volumetric and dynamic adsorption capabilities, gas handling, and sample preparation facilities. The adsorption apparatus used was a Quantachrome IQ-C . In experiments, hydrogen is used a surrogate for tritium as it has a similar valence and thus should exhibit chemical behavior. Where, the diffusion rate is required, it is scaled by the square root masses as per classical rate theory. The use of hydrogen experiments is validated by deuterium experiments combined with tritium experiments in the MIT reactor core. The general schematic of this system is shown in Fig. 1, where the sample is interacted with a volume of gas that is introduced through the manifold. The volumes in the manifold and sample cell are calibrated so that changes in pressure can be used to accurately determine the injected volume. Further, differences in the expected pressure without adsorption versus actual pressure can be used to calculate the adsorption volume on a material. Three pressure gauges of maximum pressures of 0.1, 10, and 1000 torr with errors of 1.5, 1.5 and 1% of the measured value respectively combined with a turbo-molecular pump capable of reaching 10^{-8} Pa in pressure. This allows the system to reach low partial pressure measurements similar to the actual conditions of the FHR system. Further, a temperature-controlled furnace that is capable of reaching 1100°C is used to control the sample temperature. The outlet of the sample chamber is fed to analyzers including a mass spectrometer and thermal conductivity detector which can be used for measuring the quantity and species of evolving gases during temperature controlled desorption for determining surface reactions, adsorption mechanisms and rates. The same experimental system, with slight modification can be used for low temperature adsorption, which allows the study of surface morphology. The furnace can be interchanged with a low-temperature control bath suitable for characterization studies that involve condensation of adsorbing gases.

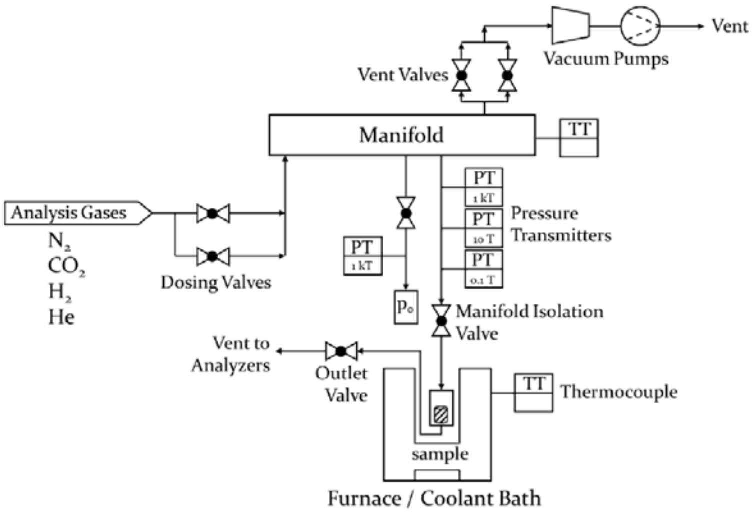

Figure 1 Piping schematic of experimental for adsorption analyses

Carbon surface area and pore volume are determined using N_2 adsorption at 77K while a combination of N_2 at 77K and CO_2 at 273K are used to determine the micro and meso-pore size distribution. Surface area is calculated using the BET method with Rouquerel's procedure for measurement of BET in microporous materials [5]. The total pore volume and average pore radius are determined by measuring the adsorbed liquid volume at N_2 at saturation assuming a constant liquid density. The average pore size is determined by assuming a cylindrical geometry and using the measured BET surface area and liquid volume. The pore size distribution is calculated using liquid density functional theory methods, non-local density functional theory (NLDFT) for CO_2 for the micropore range [6] and quenched solid density functional theory (QSDFT) for N_2 in the micro-mesopore range [7][8]. In addition, scanning electron microscopy images were collected using JEOL 5910.

The materials tested consist of graphite and other carbon-based materials summarized in the Table 1, which consists of a variety of amorphous material, graphene nanoplatelets and nuclear graphite.

Table 1 Material name and manufacturer summary

	Material Name	Manufacturer/Vendor
Nuclear Graphite	IG-110U	Toyo Tanso Inc.
Granular AC*	CAL TR 12x40 (CTR 12x40)	CalgonCarbon
GAC (continued)	OLC 12x40	CalgonCarbon
	OVC 4x8	
	Norit Vapur 612 (NV 612)	Cabot Corporation
Powdered AC*	Norit PAC 200 (PAC 200)	Cabot Corporation
	MAXSORB (MSC-30)	Kansai Coke and Chemicals Co. Ltd.
Extruded AC*	Norit RB 40M (NRB 40M)	Cabot Corporation
Graphene Oxide	Graphenit-OX	Nanoinnova Technologies SL

*AC: Activated carbon

Material Characterization and Morphology

The BET surface areas for materials examined are summarized in Table 2.

Table 2 BET surface areas of tested materials

Material	BET Surface Area	C-Value
IG-110U	0.588	38.865
OVC 4x8	1153.531	2201.599
NV 612	923.641	983.921
CAL TR 12x40	993.224	1026.43
OLC 12x40	1113.998	1449.539
PAC 200	1033.576	783.873
MSC-30	3125.557	145.390
RB-40M	1094.006	386.397
Graphenit OX	113.041	263.315

As expected from the N_2 adsorption isotherms, the superactivated carbon MSC-30 exhibited the highest surface area at 3126 m^2/g while the nuclear graphite IG-110U showed the lowest surface area at 0.588 m^2/g. Nearly all other types of activated carbons showed similar surface areas between 900 – 1200 m^2/g independent of type (granular, powder or extruded), form or particle size, which suggests that the contribution to surface area lies largely in the accessible microporosity and not in the apparent bulk area of the particle. The grapheme nanoplates (GNP) such as Graphenit OX showed a higher surface area than the IG-110U at 113 m^2/g, but significantly lower surface area than the AC materials.

The observations for total pore volume were similar to that of BET surface area shown in the previous section. The MSC-30 material had the highest (by more than 3X) volume compared to all other materials at 1.7 cm^3/g in comparison to the ACs which had volumes close to 0.5 cm^3/g. The GNP had a pore volume of 0.1828 cm^3/g. The average pore size was also calculated. The calculation of the average pore size assumed a constant bulk density, which has been shown by theory and simulation to be a non-rigorous simplification. Further, the average pore size calculation used the BET surface area, which does not apply strictly apply to porous material.

Table 3 *Average pore radius (Å) and pore volume for pores smaller than 200 Å, taken at a relative pressure of 0.95 P/P_0*

Material	**Average Pore Size (A)**	**Average Pore Volume (cm^3/g)**
IG-110U	33.7038	$0.9909*10^{-3}$
OVC 4x8	8.71103	0.5024
NV 612	10.9385	0.5052
CAL TR 12x40	10.1126	0.5022
OLC 12x40	8.25987	0.4601
PAC 200	10.7479	0.554
MSC-30	11.0156	1.721
RB-40M	10.1082	0.5529
Graphenit OX	32.0211	0.1828

The average pore sizes were largest for IG-110U and Graphenit-OX both at ~33 Å. This makes sense based on the adsorption isotherms of these materials that suggested significant meso and macroporosity. Most of the activated carbons had average pore sizes near 10 Å, while OLC 12x40 and OVC 4x8 had the lowest average pore sizes of 8.26 and 8.7 Å respectively.

Three brackets for pore width were used to discuss the pore size distribution, which is recommended by IUPAC: Narrow Micropores (< 0.7 nm), micropores (< 2nm) and mesopores (2 - 50 nm). The measured volume in narrow micropore region ranged from 0.0004 cm^3/g for IG-110U to 0.17 cm^3/g for the GAC OVC 4x8. Graphenit-OX had a relatively low surface area of 0.014 cm^3/g while most of the ACs showed high narrow micropore surface areas between 0.1 – 0.15 cm^3/g. More variation was observed in the micropores compared to the narrow micropores in the other activated carbons ranging from 0.2 cm^3/g for OLC 12x40 to 0.33 cm^3/g for OVC 4x8. Graphenit-OX had a relatively low microporous area again at 0.02 cm^3/g. The variation was again larger when comparing different materials' mesopore distributions. IG-110U also had the lowest mesopore surface area at 0.51 m^2/g while MSC-30 had the highest surface area again at 1021.10 m^2/g. Graphenit-OX had more mesoporosity at 71.29 m^2/g than some other activated carbons such as OLC 12x40 and OVC 4x8, which had areas of 38.9 and 45.10 m^2/g respectively. The other activated carbons had surface areas between 100 to 200 m^2/g. The results are summarized in Table 4.

Table 4 *Volume contribution (cm^3) of narrow micropores (<2 nm), mesopores (2 – 50 nm) and mesopores (> 50 nm)*

Material	Narrow Micropore (< 0.7 nm)	Micropore (<2 nm)	Mesopore (2 – 50 nm)
IG-110U	0.0004	0.0010	0.0021
OVC 4x8	0.1676	0.3280	0.0332

NV 612	0.1239	0.2418	0.1812
CAL TR 12x40	0.1404	0.2743	0.1566
OLC 12x40	0.1014	0.2112	0.0340
PAC 200	0.1270	0.2689	0.2039
MSC-30	0.1579	0.6834	0.8640
RB-40M	0.1027	0.3504	0.1080
Graphenit OX	0.0136	0.0196	0.2030

Note that the pore size distribution can also be expressed in surface area (cm^3/g). The conversion between surface area and volume is simply performed using an assumed pore geometry (cylindrical / spherical) and the fluid density in the pores calculated from liquid DFT. Thus, the specific volume shows similar trends to the surface area contributions shown in Table 4.

Scanning electron microscopy images of various types of carbon materials are shown in Fig. 2. Images a) to c) show the images for granular activated carbons CTR 12x40, OVC 4x8 and NV 612, which were found to have relatively high hydrogen solubility in comparison to other types of materials. These images all show that the surfaces of granular carbons had highly three-dimensional microstructures. CTR 12x40 and OVC 4x8 both showed highly heterogeneous material grains and porosity on the surface with a high degree of roughness while the NV 612 had a more stacked planar structure with large open cylindrical pores (<1 μm), which allows direct access to the internal structure. **Error! Reference source not found.**. d) shows the powdered activated carbon MSC-30, which had a much smoother surface morphology with long slit-like pores. MSC-30 had the third lowest hydrogen solubility of all the materials tested next to Graphenit-OX and IG-110U which are shown in **Error! Reference source not found.** e) and f). In the Graphenit-OX image, individual nanoplatelets can be seen on the 2-3 micron level. The surface of these platelets appear to be relatively smooth and non-porous. Fig. 2f) shows that IG-110U had a smooth two-dimensional surface with few meso and macropores. Of all carbons, IG-110U had the lowest hydrogen solubility by a couple orders of magnitude in comparison to the granular activated carbons. Experimentally, the carbons which had rough surfaces tended towards high chemisorption and generally appeared to obey the assumption used in DFT calculations that the mesopores were roughly cylindrical. While MSC-30 had the highest calculated BET surface area of 3000+ m^2/g, it exhibited substantially lower chemisorption (2-3X) and had a much smoother surface on the micron level. Additionally, the relatively non-porous two-dimensional structures of Graphenit-OX and IG-110U had both the lowest measured surface area and chemisorption capacity, which is discussed further in the next section.

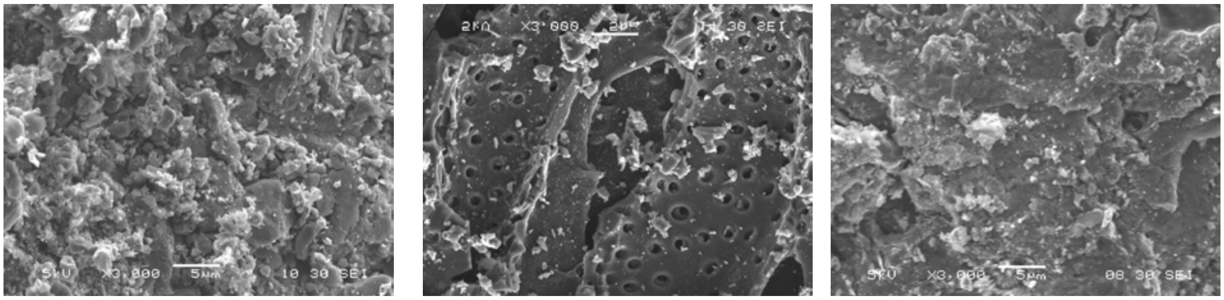

a) **b)** **c)**

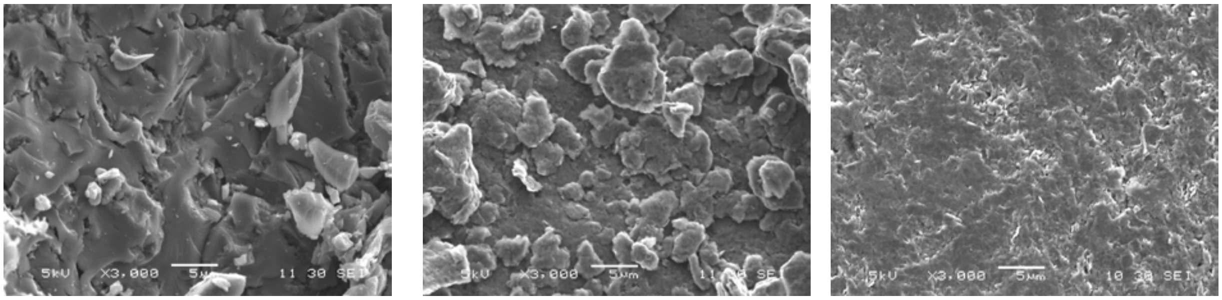

d) **e)** **f)**

Figure 2 Scanning electron microscopy of different carbon types at 5 kV, 3000X magnification. a) GAC CTR 12x40, b) GAC OVC 4x8, c) GAC NV 612, d) PAC MSC-30, e) Graphenit-OX, f) IG-110U

Hydrogen Chemisorption Measurement and Modeling

Measurement and Modeling of Different Chemisorption Interactions

Hydrogen chemisorption measurements were conducted at 700°C. Two different types of chemisorption were determined by desorbing hydrogen from the surface after measuring the total adsorption. The adsorption isotherm that is measured after desorption, is referred to as the weak chemisorption owing to the weak interactions with the surface. This data is shown in Fig. 3 where a range of adsorption is shown across the materials. No significant adsorption was measured on IG-110U. With the exception of MSC-30, all the activated carbons exhibited a hydrogen solubility at 4 kPa and 700°C of between 2 – 4 cm^3/g with the highest being GAC OVC 4x8 and lowest being CTR 12x40.

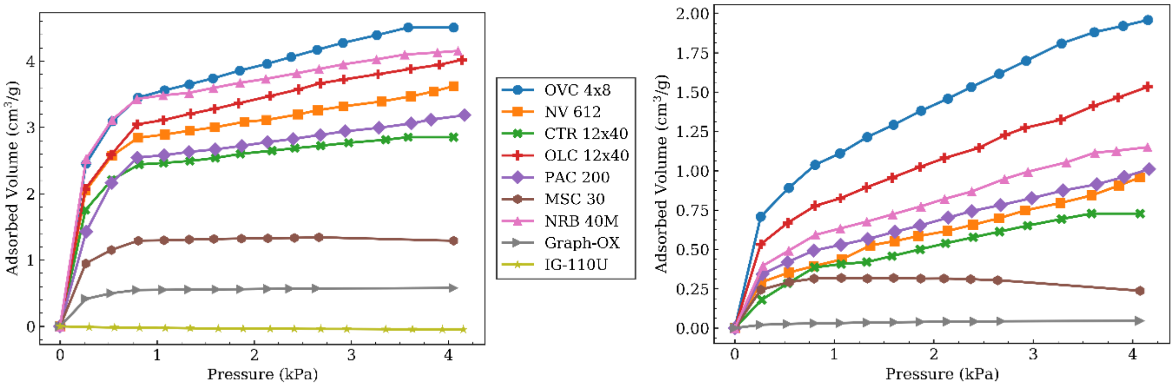

a) b)

Figure 3 a) Total and b) weak chemisorption data for nine different materials

The difference in the total and weak isotherms therefore represents an isotherm of adsorbed hydrogen which is strongly bond the materials surface. The proportion of weak and strong adsorption is shown in Figure 4:

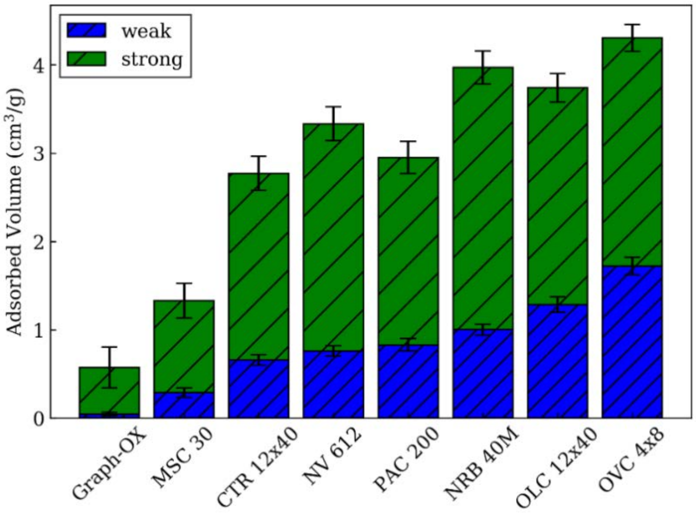

Figure 4 Adsorption on Different Materials at 700 °C and hydrogen partial pressure of 3kPa

These isotherms can be thermodynamically modeled to infer information regarding the surface reactions. Various models were applied to the different isotherms, including homogeneous surface models which assume a constant adsorption energy with increasing pressure and heterogeneous models which assume a change in energy due to different or interacting adsorption sites during saturation. For example, the least-squares error was minimized with Sips model:

$$V_{ads} = \mathrm{V_m} \frac{\mathrm{KP}^{1/\mathrm{n}}}{1 + \mathrm{KP}^{1/\mathrm{n}}}$$

Where V_{ads} is the adsorbed volume, V_m is the monolayer volume, K is the reaction constant, P is pressure, and n is the reaction order. From applying Sips model, total adsorption is shown to have a mixed order between 1.0 and 2.0 implying multi-state or heterogeneous adsorption. The model is shown in Fig. 4.

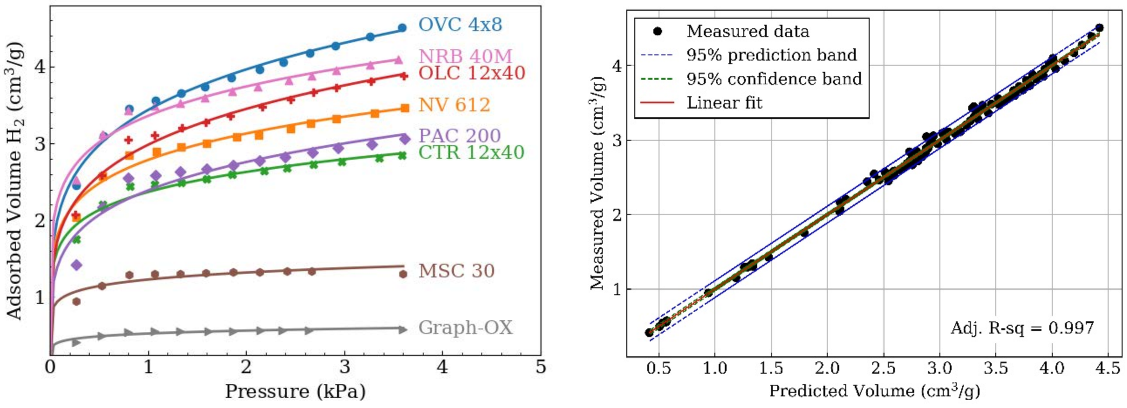

a) b)

Figure 5 Heterogeneous surface model for different types of carbon materials shows relatively good fit

The model used above shows a relatively good for all of the different materials. Similarly, the analysis can be done for the weak adsorption, which suggests a second order dissociative adsorption.

Material Properties and Physical Descriptors for Maximizing Hydrogen Solubility

Despite having the highest micropore and mesopore volumes and surface areas, MSC-30 was found to underperform compared to other carbons with a solubility of 1.2 cm^3/g, which is almost 3x smaller than other ACs. Similarly, GNP, which had a relatively low microporous surface area and volume exhibited low hydrogen adsorption at close to 0.5 cm^3/g. Overall however, materials with higher surface tended to have higher total adsorption as shown in Fig. 5a). With respect to pore size distribution, it was found that increased small porosity in materials significantly increased both the total and weak adsorption. For example, the relationship between weak adsorption and micropore volume is shown in Fig. 6b), where a relatively good correlation is observed and R = 0.93. The p-value for this correlation was 0.0005, and the standard error was relatively low at 0.6. This indicates that carbon materials that have a greater volume fraction of micropores are able to weakly adsorb greater amounts of hydrogen.

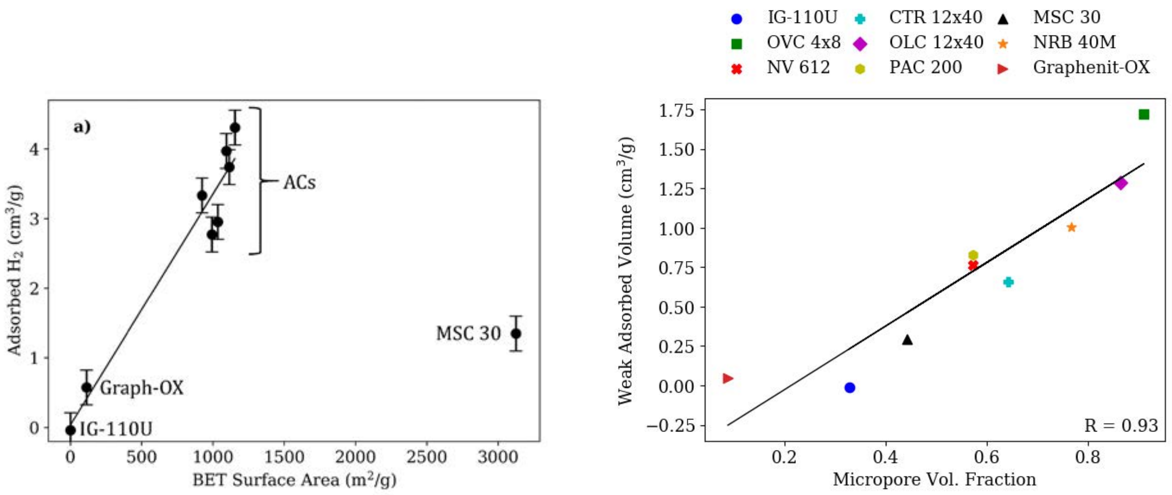

a) b)

Figure 6 a) Total Adsorbed Volume versus BET Surface Area and b) Weak adsorbed volume versus the micropore volume fraction

The understanding of what carbon properties determines hydrogen sorption enables one to better design carbon forms to minimize or maximize hydrogen sorption on carbon—depending upon the reactor designer's goals. The designer may choose to minimize tritium uptake in the fuel to avoid large-scale release of tritium in a temperature over-transient while wanting to maximize tritium uptake in an adsorber bed. Equally important, such knowledge enables modeling tritium system behavior.

Tritium Modeling and Simulation

The tritium modeling theory and techniques have been previously outlined [9][10]. In order to predict tritium behavior in an FHR, a code named Tritium Diffusion Evolution and Transport (TRIDENT) was developed to model these coupled reaction and transport phenomena.

The main purpose of TRIDENT is to track the generation and migration of tritium through the system while accounting for the reactions which act as tritium sources and sinks. Tritium generation due to impurities in the graphite and structural materials is neglected as it is relatively small compared to the tritium generated by reactions in the flibe. Globally, a redox potential in the system can be imposed as a user input by fixing the fluorine potential or allowed to be transient in the system based on the natural un-controlled tritium speciation in the system. Tritium is generated in the core from neutron reactions while simultaneous uptake and release from the graphite and structural components occur in the core. At each point in the system, the corrosion and deposition of structural metals is accounted for, which causes transformation of TF into T_2 and vice versa. Corrosion is based on selective attack of chromium, in which the equilibrium condition is set by the solution redox potential. The kinetics are limited by chromium diffusion along grain boundaries in the metallic structural components. The code allows a user option to input one of three different mechanisms that remove tritium: 1) transfer to gas in a multi-stage absorption column, 2) diffusion through a tritium-permeable window, and 3) uptake by graphite material in a solid adsorption column. Finally, the code calculates the tritium flux and mass lost through the heat exchangers by diffusion of T_2. The flibe coolant circulates through the system and returns any remaining tritium to the reactor core. The workflow is shown in Figure 7.

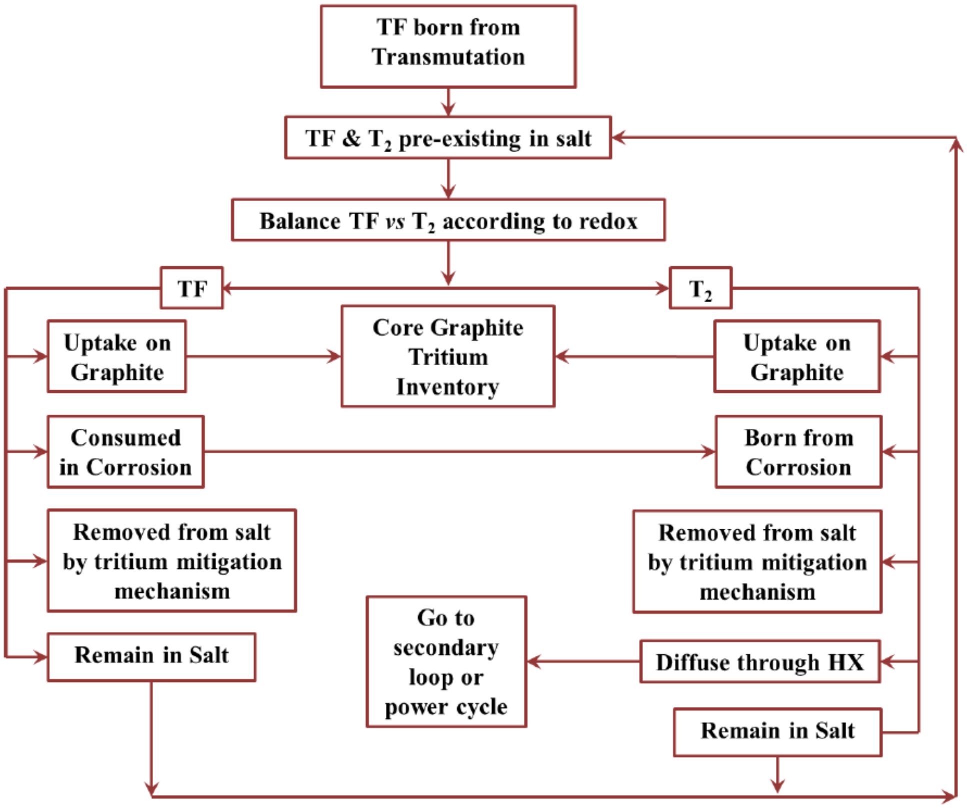

Figure 7 TRIDENT modeling workflow schematic

An adsorption column placed downstream of the reactor core was proposed to capture tritium to minimize environmental losses through the heat exchanger shown in Fig. 6.

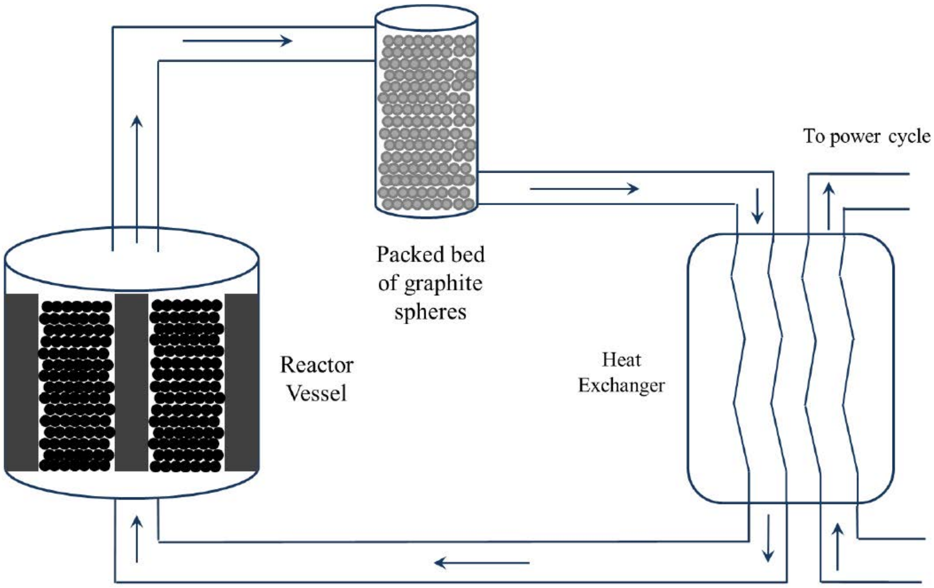

Figure 8 Schematic of pebble-bed simulation

The main performance parameters evaluated were the peak release rates (Ci/day) and the tritium inventory in the system. Without the carbon packed bed to remove tritium shown in Figure 6, the total tritium inventory and release rates as a function of time from reactor startup were calculated and the results are shown in Fig. 7 a) and b) respectively. The inventory stabilizes at 68, 365 Ci, with the majority of this made up by the inventory in the reactor core graphite, which is 2-3 orders magnitude larger than the tritium in the heat exchanger and 4-5 orders of magnitude larger than the tritium in the molten salt. The maximum release rate occurs at approximately 2400 Ci/day. Release rates are initially small as tritium that is generated is adsorbed on the carbon. As the graphite becomes saturated with tritium, more tritium is released. The tritium release rate levels off as tritium production equals tritium release with a small adjustment for tritium decay. The tritium production rate over the time period shown slightly decreases because of the burnout of Li-6 in the coolant. It is assumed that the reactor core is refueled at an a rate such that 1/30th of the reactor bed is replaced per day. The reactor core graphite uptake characteristics are assumed to be similar to that of Isograph-88 for which experimental data is available.

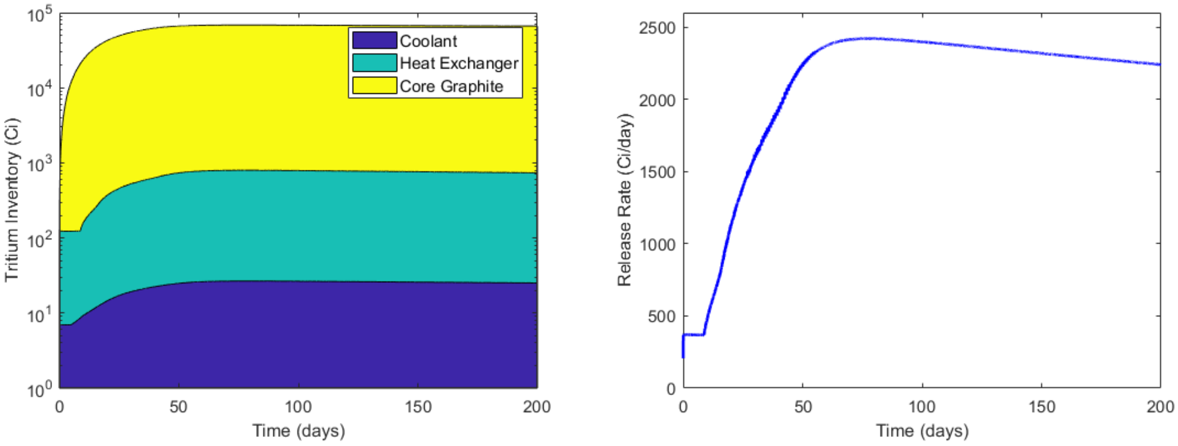

a) **b)**

Figure 9 *Baseline simulation with no mitigation mechanism in place. a) The tritium inventories in the coolant, heat exchanger and core graphite and b) the release rate during a 200 day simulation*

For comparison, nuclear graphite ISO-88 previously examined by Atsumi [11] was compared to GAC OVC 4x8 for use in a carbon tritium-removal adsorption column. The parameters found to most greatly influence the release rate and inventory were found to be the pebble radius of the adsorbents and the regeneration cycle, ie. average number of days per full bed regeneration. The column size used for analyses was 1.5 m R x 4.5 m H.

Tritium Release Rate to Environment

The minimum of release rates were found for the lowest pebble radius and shortest regeneration cycle, due to a maximization of the surface area and concentration gradient respectively. The minimum release rate achievable for IG-110U was close to 70 Ci/day at the pressure-limiting pebble size of 0.9 cm and practical regeneration cycle length of 7 days. In contrast, the same performance was achieved in OVC 4x8 at a pebble size of 1.2 cm (lowering pressure drop by up to 10 kPa/m) and a much longer cycle past 30 days (reducing the operational demand, wear on adsorbent and operating cost). For OVC 4x8, the release rate reduced to lower than 40 Ci/day with the pebble size of 0.9 cm at any cycle length < 31 days. Plots of the release rates versus the design / operating parameters are shown in Figure 8.

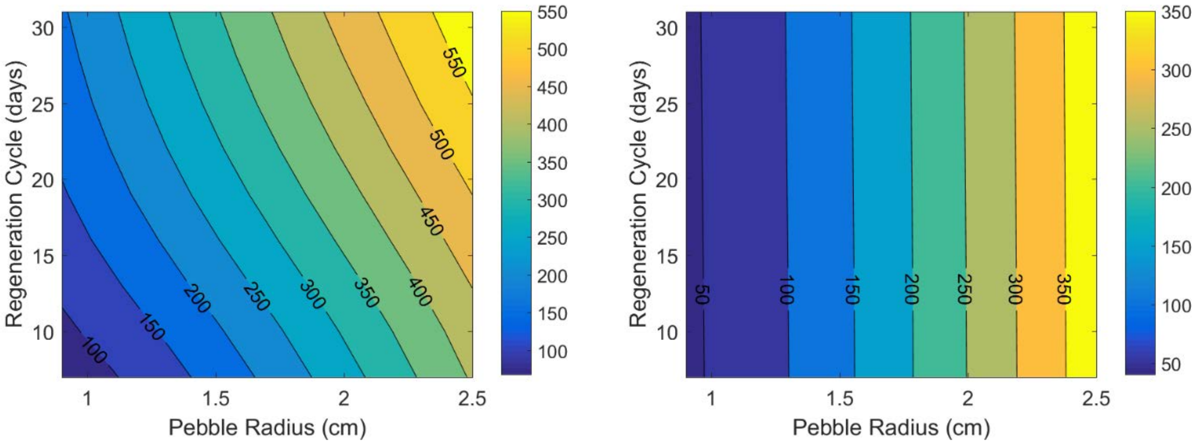

a) ISO – 88 **b) OVC 4x8**

Figure 10 *Regeneration cycle and pebble radius versus release rates (Curies/day) into power cycle for a) nuclear graphite ISO-88 and b) Granular Activated OVC 4x8. The color scales of the two figures are different-- OVC 4x8 has much better performance*

The very different performance between ISO-88 (nuclear grade graphite designed for in-core use) and OVC 4x8 reflect a fundamental change in what is controlling system performance. With ISO-88 the adsorption capability of the carbon is partly controlling system performance. With OVC 4x8 the carbon has a large capacity to adsorb hydrogen; thus, system performance is controlled by rate of diffusion of tritium to the carbon surface.

Minimizing Tritium Inventory

As shown in Figure 9, core graphite was by far the largest sink of tritium in primary system (excluding the adsorption bed). The inventory trends were similar to those of the release rates, where the lowest inventory was achieved with the smallest pebble size and fastest regenerating rate in the tritium removal bed. The inventory of tritium ranged from 2.2 to 4.0 x 10^4 Ci in ISO-88 and from 2.0 to 3.4 x 10^4 Ci in OVC 4x8. For a typical pebble radius of 1.5 cm and regeneration cycle of 14 days, the inventory was reduced from 30, 000 Ci to 26, 000, a 13% reduction by switching from ISO-88 to OVC 4x8 adsorbent in the external carbon bed for tritium removal. Although the tritium inventories in core graphite remained considerably high, a substantial amount of this inventory could potentially be retained on the core graphite in a transient depending on the maximum temperature and duration of the transient since tritium has a higher binding energy to graphite than other materials. Thus, Figure 9 and Figure 10 are shown for the coolant and heat exchanger tubing inventories.

The total inventory held in the coolant shown in Figure 8 was low since flibe has a relatively low tritium solubility that obeys Henry's law. At the limiting conditions for ISO-88, the minimum inventory in coolant was just 4 Ci, but was less than 3 Ci for OVC 4x8. The inventory in HX tubing is shown in Figure 9. The stainless steel tubing of the HX adsorbs more tritium than the coolant with the minimum being close to 40 Ci when using adsorbent ISO-88 at best case scenario. By using OVC 4x8 and the pebble size of approximately 1 cm, this inventory reduced to less than 20 Ci while maintaining a flexible cycle length.

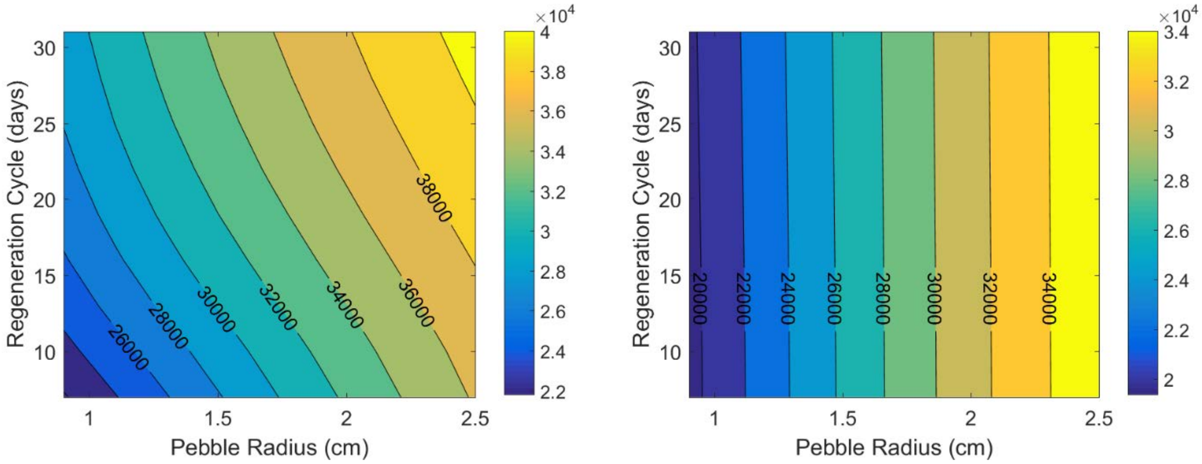

a) ISO – 88 **b) OVC 4x8**

Figure 11 *Regeneration cycle and pebble radius versus core graphite tritium inventory for a) nuclear graphite ISO-88 and b) granular activated carbon OVC 4x8. The two color scales are different.*

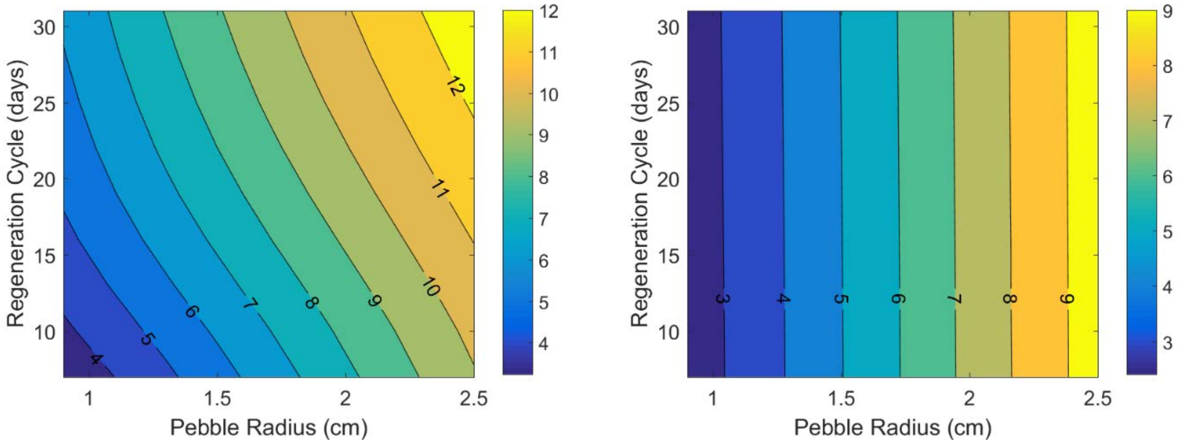

a) ISO – 88 **b) OVC 4x8**

Figure 12 *Regeneration cycle and pebble radius versus primary coolant tritium inventory for a) nuclear graphite ISO-88 and b) granular activated carbon OVC 4x8. The two color scales are different.*

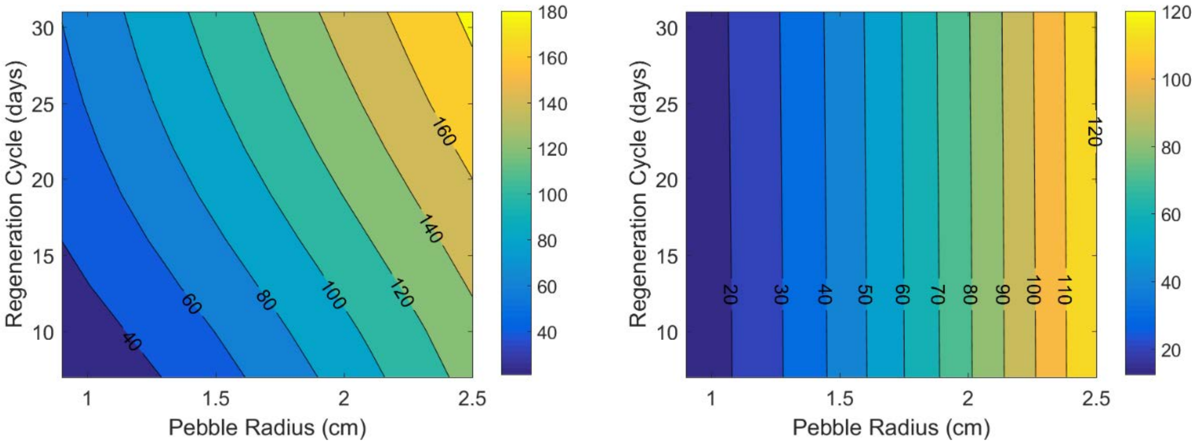

a) ISO – 88

b) OVC 4x8

Figure 13 *Regeneration cycle and pebble radius versus primary HX tritium inventory for a) nuclear graphite ISO-88 and b) granular activated carbon OVC 4x8. The two color scales are different.*

In all of the contour plots discussed above, it was shown that within the chosen bounds of design, reducing the pebble radius and the cycle length reduced the total tritium release and inventory for ISO - 88, while it did result in an appreciable difference in OVC 4x8. The difference came primarily because of solubility limitations of ISO – 88, which is on the order of 0.1 cm^3/g at 5 kPa H_2 partial pressure. It is shown in Figure 12a), that tritium, particularly in the form of TF began to saturate the graphite relatively quickly in operation, thus resulting in a decreased concentration gradient and mass flux to the pebble. For comparison, the adsorbed concentration relative to the solubility during the 200-day simulation on an OVC 4x8 adsorption column is shown in Figure 12 b). The cycle length used for this simulation was 31 days and pebble size was 0.9 cm, to illustrate the conditions that would yield the maximum concentration in the adsorbent.

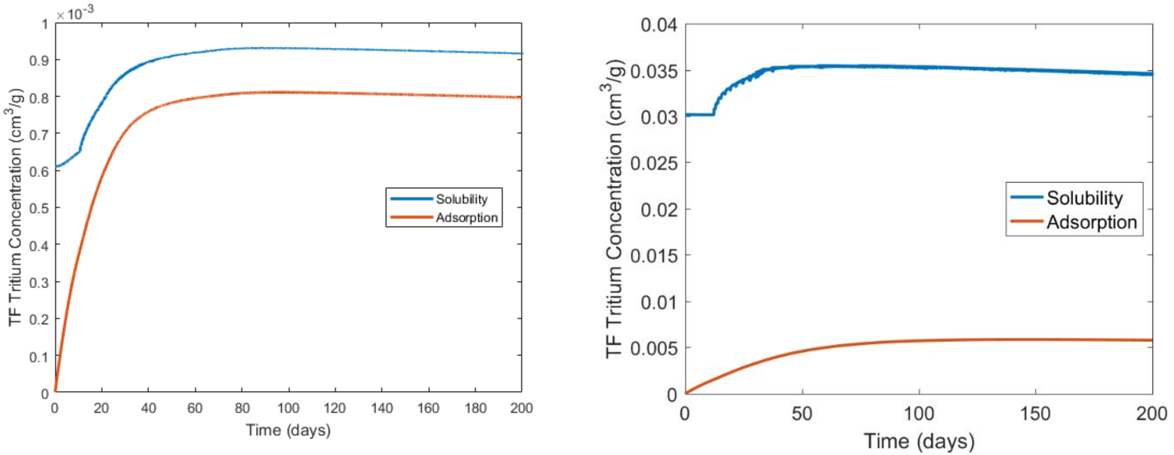

a) ISO-88

b) OVC 4x8

Figure 14 *Solubility versus adsorption of TF in a) ISO-88 and b) activated carbon OVC 4x8 on graphite bed during 200 days of operation with 0.9 cm pebbles, regenerated at a cycle length of 31 days*

Controlling Corrosion and Tritium Management

In controlling the tritium concentration in the system, one necessary consideration that is strongly coupled is the presence of corrosion. Since corrosion reaction transforms TF (corrosive) into T_2 (diffusive), the mitigation mechanism must consider this effect. In an American Nuclear Society Winter Conference summary paper [12], an evaluation of various options were given. Since the TF/T_2 is the redox-controlling species, changing their relative ratio affects corrosion and redox potential as shown in Fig. 13

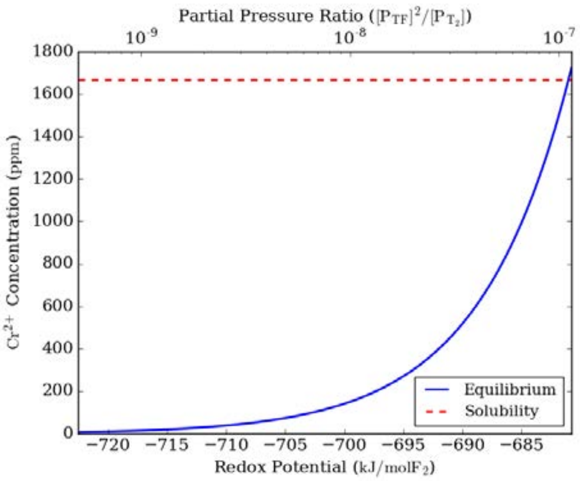

Figure 15 Equilibrium Concentration of CrF_2 in flibe if Type 316 SS is exposed to flibe at 650°C over a range of redox (fluorine) potentials determined by $[P_{TF}]^2$:$[P_{T2}]$

The corrosion (chromium concentration) was calculated using equilibrium data from Baes [13], assuming activity coefficients are unity. This assumption has yet to be verified experimentally. The mitigation mechanisms considered for tritium removal were (1) tritium permeation through a window, (2) tritium adsorption on getter—carbon, and (3) removal by inert gas sparging. The corrosion control (redox) mechanisms considered that are applicable to the FHR are (1) hydrogen gas sparging and (2) major metal control (reaction with Be). Hydrogen sparging is simple and known to work as it has been used extensively for salt-purification and is therefore considered a viable short-term option. One advantage of hydrogen sparging is that the tritium concentration can be kept almost entirely in TF, which does not diffuse through stainless steel piping. That is because one is controlling the HF/H_2 ratio by H_2 addition. In contrast, since Be control requires the reaction of TF into T_2, the release rates will necessarily be higher. *However, this assumes a relatively low isotopic exchange that depends upon the energetics of the reaction—where we have been unable to identify appropriate confirmatory experimental data.*

With redox control using hydrogen sparging, the T_2 concentration is negligible (mostly in TF), which implies that gas permeation is not capable of removing tritium in the system and can be readily eliminated as a potential option. This leaves solid adsorption (carbon or some other material) and inert gas absorption. In both cases, if hydrogen gas sparging is used for redox control, efficiencies would be relatively low since H and T compete on adsorption sites and in the gas phase. For adsorption to work, the getter material must have sufficient hydrogen/tritium solubility to remove both hydrogen and tritium. Based on results from previous sections, this is believed to be a viable, but may not be an optimal solution. For gas absorption, the Henry's coefficient H_2 is approximately three orders of magnitude greater than HF/TF [14][15], which indicates that tritium absorption requires large gas flows and vessel volumes in the presence of redox control. In summary, no known options to date are clearly superior to the others, and further research must continue to understand binary interaction between TF and T_2, improve quality of tritium equilibrium data in molten salts and examine feasibility of different redox control.

Notes on Further Tritium Work

Further experimentation and modeling must be completed in order to fully characterize adsorption and desorption of tritium in these materials, understand the effects on transient behavior the FHR system, and design a mitigation mechanism that optimizes performance and economics. This includes a full analysis of adsorption characteristics including the both the short-term, long-term behavior, reversibility of hydrogen adsorption, isotopic effect on adsorption surfaces and probing specific reactions by mass spectrometry, and first principles analysis. The material changes over time must be evaluated as tritium is cycled by analyzing changes in physical properties with gas adsorption and x-ray diffraction and chemical changes evaluated using x-ray photo electron spectroscopy. Effect of irradiation using materials from MITR must be investigated. Further, those experiments can be compared to hydrogen experiments out-of-core. Finally, more detailed engineering and simulation of the single pebble to column-level must be conducted using a combination of in-house codes and commercial multiphysics software.

Relevant Publications and Conference Papers

Lam, S., Ballinger, R., Forsberg, C., "Modeling and Predicting Total Hydrogen Solubility in Nanoporous Carbon Materials for Advanced Molten-Salt Nuclear Systems", Submitted to *Journal of Nuclear Materials*, April 2017.

Lam, S., Ballinger, R., Forsberg, C., Conference Proceeding, *Controlling corrosion and tritium in a fluoride-salt-cooled high-temperature reactor*, American Nuclear Society Winter Meeting, Washington DC, Oct. 29 – Nov. 2, 2017.

Stephen T Lam, "Managing Tritium Inventory and Release with Carbon Materials in a Fluoride Salt-Cooled High-Temperature Reactor", S.M. Thesis, Massachusetts Institute of Technology, 2017.

Lam, S., Ballinger, R., Stempien, J., Forsberg, C. (2016), "Tritium Management and Control Using Carbon in a Fluoride Salt-Cooled High-Temperature Reactor" *Fusion Science and Technology*, Vol. 71, No. 4 (2017).

Forsberg, C., Lam, S., Carpenter, D., Scarlat, R., Contescu C., Wei, L., Stempien, J., Blandford, E., "Tritium Control and Capture in Salt-Cooled Fission and Fusion Reactors: Status, Challenges, and Path Forward", *Nuclear Technology*, Vol. 197, No. 2 (2017).

J. D. Stempien, "Tritium Transport and Corrosion Modeling in the Fluoride Salt-Cooled High-Temperature Reactor," Ph.D. Thesis, Massachusetts Institute of Technology, 2015.

References

[1] R. B. (ORNL) Briggs, "Tritium in Molten-Salt Reactors," *React. Technol.*, vol. 14, pp. 335–352, 1971.

[2] H. Atsumi, M. Iseki, and T. Shikama, "Hydrogen solubility and diffusivity in neutron-irradiated graphite," *J. Nucl. Mater.*, vol. 191–194, pp. 368–372, 1992.

[3] H. Atsumi, T. Tanabe, and T. Shikama, "Trapping state of hydrogen isotopes in carbon and graphite investigated by thermal desorption spectrometry," *Fusion Sci. Technol.*, vol. 67, no. 2, pp. 245–249, 2015.

[4] C. Andreades *et al.*, "Mark--1 PB--FHR Technical Description Technical Description of the 'Mark 1' Pebble-Bed Fluoride-Salt-Cooled High-Temperature Reactor (PB-FHR) Power Plant," pp. 1–153, 2014.

[5] J. Rouquerol and P. Llewellyn, "Is the BET Equation Applicable to Microporous Adsorbents?," *Stud. Surf. Sci. Catal.*, vol. 160, pp. 49–56, 2007.

[6] P. I. Ravikovitch, A. Vishnyakov, R. Russo, and A. V. Neimark, "Unified Approach to Pore Size Characterization of Microporous Carbonaceous Materials from N 2 , Ar, and CO 2 Adsorption Isotherms," *Langmuir*, vol. 16, no. 5, pp. 2311–2320, 2000.

[7] A. V. Neimark, Y. Lin, P. I. Ravikovitch, and M. Thommes, "Quenched solid density functional theory and pore size analysis of micro-mesoporous carbons," *Carbon N. Y.*, vol. 47, no. 7, pp. 1617–1628, 2009.

[8] G. Y. Gor, M. Thommes, K. A. Cychosz, and A. V. Neimark, "Quenched solid density functional theory method for characterization of mesoporous carbons by nitrogen adsorption," *Carbon N. Y.*, vol. 50, no. 4, pp. 1583–1590, 2012.

[9] J. D. Stempien, "Tritium Transport and Corrosion Modeling in the Fluoride Salt-Cooled High-Temperature Reactor," Ph.D. Thesis, Massachusetts Institute of Technology, 2015.

[10] S. T. Lam, “Managing Tritium Inventory and Release with Carbon Materials in a Fluoride Salt-Cooled High-Temperature Reactor by,” Massachusetts Institute of Technology, 2017.

[11] H. Atsumi, M. Iseki, and T. Shikama, “Hydrogen solubility and diffusivity in neutron-irradiated graphite,” *J. Nucl. Mater.*, vol. 191–194, pp. 368–372, 1992.

[12] C. F. S. Lam, R. Ballinger, “Controlling Corrosion and Tritium in a Fluoride-Salt-Cooled High-Temperautre Reactor,” in *American Nuclear Society Winter Meeting*, 2017.

[13] C. F. F. Baes, “The chemistry and thermodynamics of molten salt reactor fuels,” *J. Nucl. Mater.*, vol. 51, no. 1, pp. 149–162, 1969.

[14] P. E. Field and J. H. Shaffer, “The Solubilities of Hydrogen Fluoride and Deuterium Fluoride in Molten Fluorides,” *J. Phys. Chem.*, vol. 71, no. 10, pp. 3218–3222, 1967.

[15] A. P. Malinauskas and D. M. Richardson, “The Solubilities of Hydrogen, Deuterium, and Helium in Molten Li 2 BeF 4,” *Ind. Eng. Chem. Fundam.*, vol. 13, no. 3, pp. 242–245, 1974.

2.2. Uptake of Tritium by Graphite During Neutron Irradiation in Flibe Salt (MIT)

Uptake of Tritium by Graphite During Neutron Irradiation in Flibe Salt (MIT)[9]

Summary

Under neutron irradiation in an FHR, tritium is continuously generated from all three elemental components of flibe salt. This tritium may then interact with the large amounts of graphite present in the FHR primary system as both fuel matrix and neutron reflectors. Graphite is known to have a high potential for uptake of tritium, and so it is also under consideration as tritium capture media.

In order to understand the interaction between fluoride salt, tritium and graphite at FHR conditions, graphite specimens were irradiated in the MITR core at 700°C in flibe in a series of experiments. After irradiation these specimens were extracted and analyzed using a variety of techniques. In particular, nuclear-grade graphite samples (both high-density structural and fuel matrix graphite) from the FS-1 and FS-2 in-core irradiations were extracted and analyzed for tritium content using a custom designed thermal desorption furnace. Tritium desorption as a function of temperature and the total tritium content of sample subsections suggests that tritium retention was predominantly a surface effect. A majority of desorbed tritium was measured in an insoluble form (HT/T_2).

---

[9] K. Dolan and D. M. Carpenter (david_c@mit.edu)

Introduction

An important metric for FHR design is the expected quantity and distribution of tritium in the reactor graphite components. Tritium will be continuously generated in the flibe primary coolant, which is in intimate contact with large surface areas of graphite from both the fuel (as either pebbles or blocks) and neutron reflectors. This graphite has long residence times in the reactor and so may have a substantial loading of tritium. In addition, the affinity of graphite to adsorb tritium may be utilized in a tritium cleanup and capture system where specially designed graphite beds are placed in the salt flow. Therefore, interaction of tritium with graphite is of primary importance for the development of FHRs, however understanding tritium uptake in graphite requires experimental investigation since few studies have examined the combined effects of molten flibe, tritium, and graphite at relevant FHR temperatures and tritium partial pressures. Towards this end, the in-core fluoride salt irradiations at the Massachusetts Institute of Technology Nuclear Reactor Laboratory were undertaken to understand expected tritium uptake behavior in an FHR environment.

For post-irradiation examination (PIE) of sample materials irradiated in flibe, a custom-designed thermal desorption furnace was used to the heat graphite samples in order to release and measure the adsorbed tritium. Desorption verses temperature was monitored with a compensated ion chamber system while tritium chemical form was also examined by liquid scintillation counting (LSC) of the water vial traps. In addition to evaluating the total tritium loading of materials, the combination of these systems allowed exploration of probable tritium trapping sites and mechanisms, as well as an understanding of the tritium/salt/graphite system chemistry.

Experiment Setup

The desorption furnace setup consists of several components, broadly a furnace control system, gas supply and measurement system, and data acquisition system. The design of the furnace is based on early work as part of this IRP to identify critical experimental needs. The ability to measure tritium uptake in materials was seen as particularly important, however difficult to accomplish. The first three NRL irradiation experiments that produced tritium (the first irradiations of enriched flibe since the MSRE in the 1960s) were designed around the constraints of the MITR core. These experiments were also intended to cover a variety of topics, including corrosion and radiolysis in addition to tritium transport and partitioning [1]. It was desirable to have a high-sensitivity tritium measurement system capable of handling any of the materials exposed to tritium from this test, but in particular the larger in-core crucibles and capsule parts. In addition to their size, they would have considerable gamma activity from activation or contamination. Various analytical techniques, including film imaging, chemical dissolution, and pyrolization were considered, however thermal desorption was selected as the most practicable and cost-effective technique. After a survey of available commercial furnace systems, it was decided to construct a custom system that would provide sufficient volume while minimizing the volume of materials in the hot zone of the furnace that might be a parasitic sink for tritium. Ultimate containment of tritium was also a major concern in order to prevent loss of tritium from the counting and collection system. The final furnace design is shown in Figure 1. The outer wall of the furnace is shielded from the heating element by internal Mo baffles, and actively cooled by a copper water jacket in order to make it impermeable to tritium. The furnace has ports for gas inlet and outlet as well as thermocouples for monitoring the furnace and jacket temperature. [2]

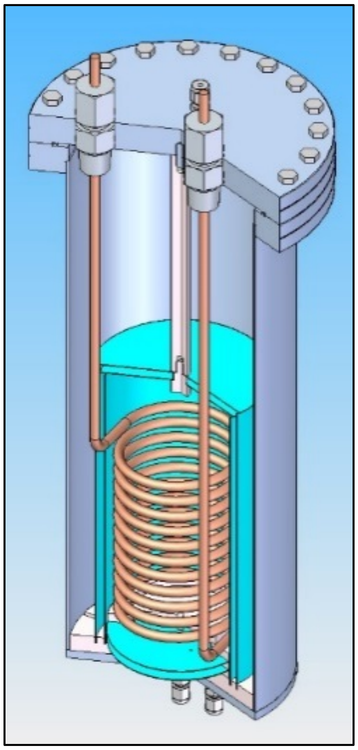

Figure 1. Custom tritium desorption furnace design.

Inert gas (pre-mixed Ar4%H_2) is supplied into the bottom of the furnace. The argon helps to insulate the furnace, while the hydrogen saturates surfaces is the gas system and furnace chamber to reduce parasitic loss or tritium during the desorption test. The outlet gas from the furnace goes through a compensated ion chamber system then to a combined water bubbler/oxidation furnace. The ion chambers provide real-time indication of the tritium activity, while the bubbler captures the tritium for later analysis using liquid scintillation counting. The combined furnace, ion chamber system, and water bubbler setup is shown in Figure 2.

Figure 2. Thermal desorption measurement setup with the furnace, ion chamber, and tritium bubbler in the experimental configuration.

Desorption Tests

The initial desorption analysis focused on IG-110U and ARB graphite test specimens from the second flibe irradiation experiment (FS-2) at the MIT Reactor (MITR). Samples were extracted after the experiment and discs of each graphite type were sectioned into ten pieces to allow for various PIE testing. An example subsection labeling diagram for the ARB graphite disc is shown in Figure 3 along with the salt-filled crucibles before the irradiation. In total, the FS-2 capsule was irradiated for an integrated MITR power of 74.2 MWd, and the total tritium activity produced was calculated to be 566.9 mCi according to an MCNP model of the MITR core and flibe experimental facility. [3] The goal of the desorption testing program is to quantify the amount of generated tritium that was retained in the graphite and other materials from the in-core capsule. While some tritium was detected in the capsule sweep gas during irradiation, it was anticipated that a significant amount could be held up in the capsule graphite, either on the surface or diffused into the bulk. This tritium may have been ionic species in the salt or in the gas phase; the specimens were completely submersed in the flibe during the test, while some sections of the graphite crucible would have had no direct salt contact. By heating the graphite to at or above the irradiation temperature (700°C), the goal is to re-mobilize the trapped tritium and entrain it in the furnace sweep gas for measurement and collection.

Figure 3. Graphite crucibles filled with Li-7 enriched flibe salt and test samples for the FS-2 experiment (left). After the experiment, an ARB graphite sample was extracted, cleaned for residual salt, and sectioned (right).

In the thermal desorption procedure, an initial ramp was completed from room temperature to 1000℃ at a fixed rate (0.1 °C/s for most samples). The temperature never fully reached the 1000 °C set point, but leveled out at a typical maximum of 960-970 °C. After the initial ramp section, a 20-minute ramp down to 800 °C along with a 10-minute hold was used. After the first round, the sample was heated with the same ramp profile, however the initial ramp was sped up to 0.14 °C/s. The faster ramp is justifiable since the majority of tritium is desorbed at high temperatures towards the end and after the ramp. An example desorption procedure is shown in Figure 4 as completed for the ARB-4 sample.

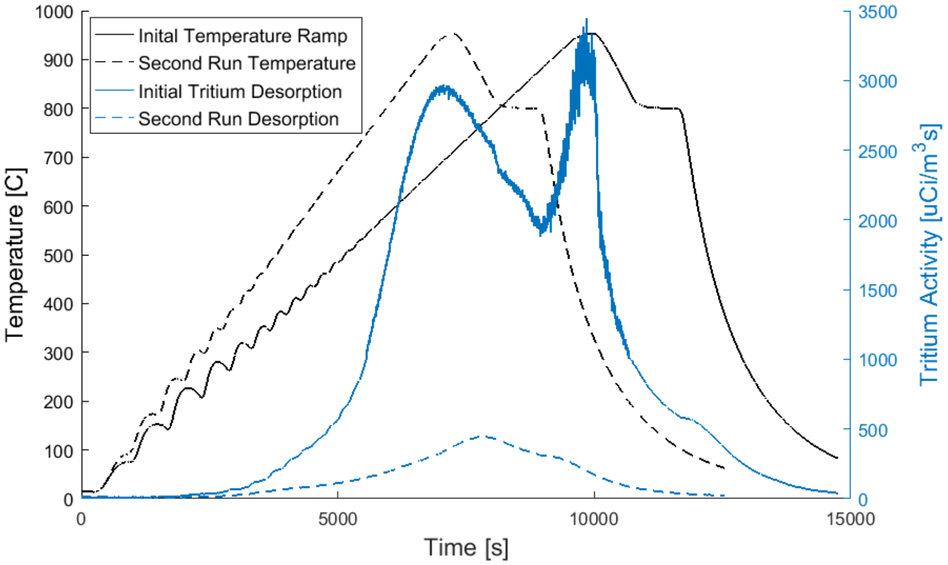

Figure 4. Desorption heating ramp procedure showing an initial temperature ramp of 0.1 °C/s, a 20-minute ramp down to 800 °C and a 10-minute hold. Results from the AR2-4 section are used in this example. The second ramp uses a faster ramp of 0.14 °C/s followed by the same ramp down and hold.

Overall tritium thermal desorption completeness can be assessed by comparing the tritium collected in the second ramp to the two run total, which was 11% on average for the 7 samples. Activity from each sample's first and second rounds of desorption testing according to the ion chamber measurement are shown in

Table 1. Assuming the same fractional decrease for an infinite amount of runs, the 11% suggests that the total tritium collected from each sample should be within 1-2% of the maximum releasable value. The sum of the first and second desorption activity was taken as the tritium content from each sample. As previously discussed, total tritium inventory can be estimated by both the ion chamber in the off-gas system and LSC analysis of the water vial traps. The ion chamber measurement was taken as the reference value in this work because of more consistent result of carryover from first to second runs (

Table 1) and a decreased standard deviation of activity measurements of each graphite type (Table 2). However, some consistency was observed from both tritium measurement systems. The first and second activity measurements from all of the furnace trials are shown in Figure 5; a 0.988 r^2 value was observed with both measurements over several orders of tritium activity with a factor of 1.792 applied to the LSC measurement. The decreased LSC tritium activity relative to the ion chamber measurement could be caused by tritium losses in the tubing between the ion chamber and water bubbler, or incomplete oxidation of HT/T_2 in the bubbler system catalyst furnace.

Table 1. Total tritium release from samples after the first and second rounds of desorption based on the integrated ion chamber measurements.

Sample	*Initial Release [mCi]*	*Second Ramp [mCi]*	*Second/First*
IG-5	0.1053	0.0142	13%
IG-6	0.0868	0.0102	12%
IG-8	0.1345	0.0129	10%
ARB-4	0.0748	0.0093	12%
ARB-6	0.0717	0.0047	7%
ARB-8	0.1781	0.0142	8%
ARB-9	0.0554	0.0070	13%

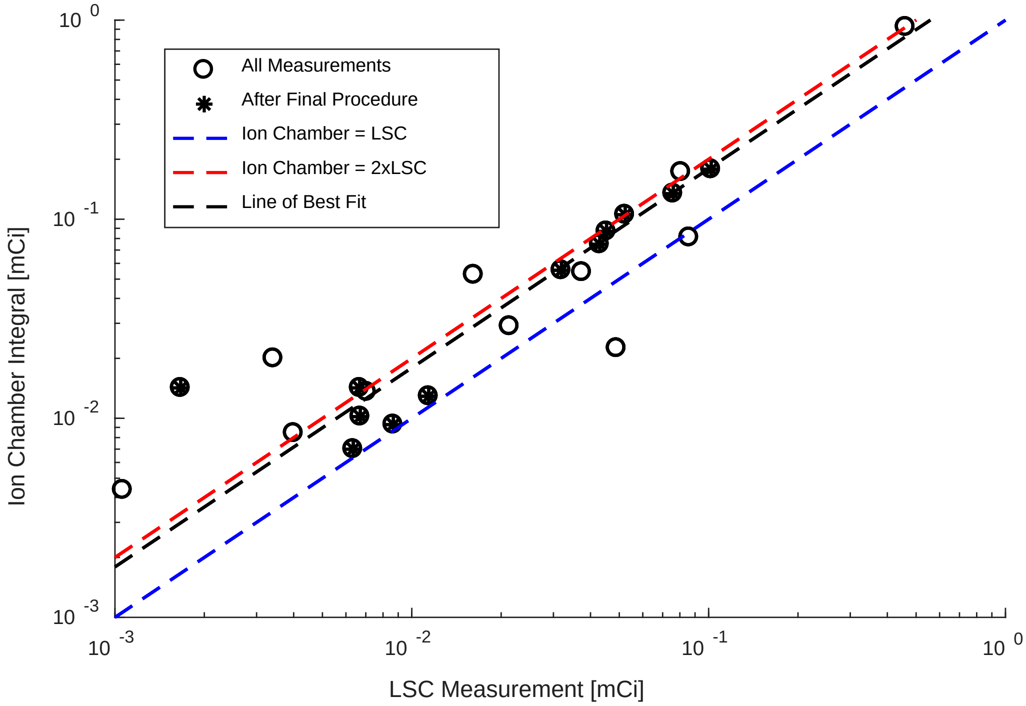

Figure 5. Comparison of LSC tritium bubbler measurements and the integral of the ion chamber profile. The blue dashed line indicates a perfect agreement between the two measurements, however the ion

chamber measured higher typically. Measurements taken with the finalized procedure can be fit by $y=1.792x$ with an r^2 value of 0.988.

Tritium Trapping

In addition to measuring total tritium content, a goal of the thermal desorption system was to gain fundamental information about how tritium was retained in the flibe-graphite environment during the irradiation. Testing multiple sections from each sample disc can reveal characteristics about how tritium is retained within the graphite. Since sample subsections were not uniform in size or shape, the amount of tritium released varied between each test. The sample salt-facing surface area and sample mass are two possible options for normalizing total tritium measurements from the subsections. The samples themselves were cut from a uniform graphite block. If the samples were saturated homogenously throughout their entire volume, then sample mass should provide the most consistent normalization. In contrast, if tritium retention was mainly limited to the sample exterior, then surface area would be the more representative metric. The desorbed tritium and normalizations are shown in Table 2. The results demonstrate that tritium retention was better predicted by sample salt-facing area than by sample mass based on the relative standard deviations from the measurements of each graphite type. For both IG-110U and ARB, there was a noticeable decrease in standard deviation for tritium activity normalized by area instead of mass.

Table 2. Total tritium from samples along with measurements normalized by salt-facing surface area and by mass. Diving by area produced more consistent measurements within the sample group.

Sample	*Total Tritium [mCi]*	*Tritium/Area [mCi/mm^2]*	*Tritium/Mass [mCi/g]*
IG-5	0.1195	2.91E-03	1.686
IG-6	0.097	2.69E-03	1.578
IG-8	0.1474	3.38E-03	2.405
	Average:	2.99E-03	1.890
	$\sigma_{relative}$:	10%	19%
AR-4	0.0841	2.01E-03	1.107
AR-6	0.1923	1.57E-03	1.260
AR-8	0.0624	2.34E-03	2.293
AR-9	0.0764	1.59E-03	0.876
	Average:	1.88E-03	1.384
	$\sigma_{relative}$:	17%	39%

The observed desorption of tritium from the FS-2 samples as a function of temperature also suggested that tritium retention was a surface related phenomenon. Desorption measurements in this study, like previous research with hydrogen and deuterium, displayed release peak structures that are indicative of multiple trapping mechanisms with graphite. [4, 5] Measured tritium release as a function of temperature is shown for ARB samples desorbed at 0.1 °C/s in Figure 6. The exact trapping mechanisms from the FS-2 graphite cannot be identified without additional testing. However, the increase of the central desorption peak with salt-facing area suggests that the phenomenon responsible for the 700°C peak is surface related, such as surface chemisorption. The salt-facing area per sample mass was 552 mm^2/g, 801 mm^2/g, and 979 mm^2/g for ARB-4, ARB-8, and ARB-9 respectively. Moreover, because the central peak structure appears to comprise most of the desorption profile, the bulk of tritium retention can be inferred to be a result of a surface trapping effect.

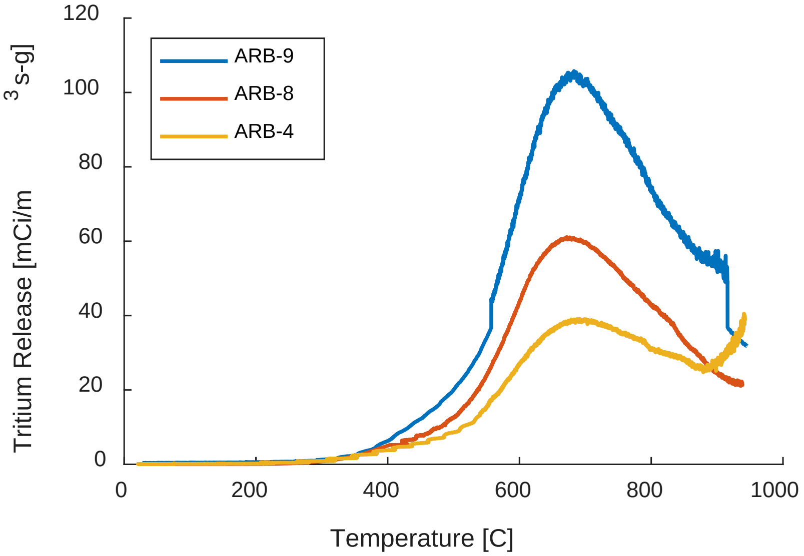

Figure 6. Measured tritium desorption rate as a function of temperature for samples of ARB graphite.

Another interesting observation was the chemical form of the thermally desorbed tritium. Liquid scintillation measurements of the water vial traps can distinguish between soluble and insoluble forms of tritium by collection before and after a catalyzer furnace. In this case, soluble forms are TF, HTO, and T_2O while insoluble forms are most likely HT and T_2. The fraction of soluble and insoluble tritium in the total tritium release by each sample is displayed in Figure 7, where a clear preference for insoluble tritium was observed. In all cases, a majority of tritium was measured as an insoluble form – for all samples except IG-5 the amount of insoluble tritium was greater than 80%. The desorption furnace utilizes an Ar-4%H_2 sweep gas to saturate surfaces with excess hydrogen and decrease tritium losses. If the excess hydrogen was reacting with released tritium, then the measured chemical form could be biased towards insoluble forms from isotopic exchange reactions. A pure argon sweep gas was used for the ARB-6 sample to test the effect of hydrogen on isotopic exchange in the furnace. The similarly low soluble fraction for the ARB-6 measurement shows that isotopic exchange was not responsible for the large fraction of insoluble tritium measured.

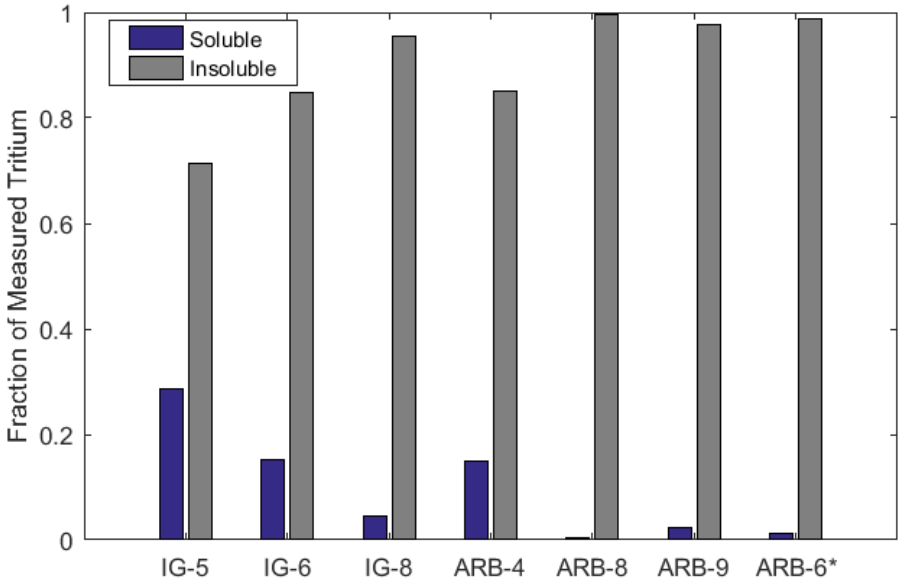

Figure 7. Fraction of soluble (TF, T2O, HTO) and insoluble (T2, H2) tritium measured from the desorption of each sample subsection. The ARB-6 sample was desorbed in argon gas while other samples used Ar-4%H_2. With both types of sweep gas a majority of insoluble tritium was measured.

Conclusions

The tritium adsorbed onto graphite under neutron irradiation in flibe at 700°C has been successfully released and measured using a custom thermal desorption system. This system consists of a furnace to heat and release tritium from specimens and gas system with ion chambers and water bubblers to count and collect the tritium after release. Specimens of graphite from the MITR FS-2 irradiation were heated in the furnace at various ramp rates to investigate both their total tritium uptake and the mechanisms of tritium trapping. Significant tritium activity was found to be released from the graphite at or above the irradiation temperature. Based on the release rates and normalization of tritium source term between similar specimens, it is believed that a majority of the tritium trapping occurs at the surface of the graphite. Additional details of these experiments can be found in references 1-3.

References

1. D. Carpenter, M. Ames, G. Zheng, G. Kohse and L.-w. Hu, "Tritium Production and Partitioning from the Irradiation of Lithium-Beryllium Fluoride Salt," *Fusion Science and Technology* **71**, no. 4, pp. 549-554, 2017.
2. K. Dolan, "Tritium Thermal Desorption Testing of Nuclear Graphites Irradiated at Fluoride-Salt-Cooled High-Temperature Reactor Conditions," MS thesis, Massachusetts Institute of Technology, Cambridge, MA, 2018.
3. D. Carpenter, M. Ames, G. Kohse, Y. Ostrovsky, and L. Hu, “Findings of the Second Round of Fluoride Salt High Temperature Reactor Materials Irradiation Tests at the MIT Research Reactor,” *Proceedings of the 2015 International Conference on Advances in Nuclear Power Plants: ICAPP 2015*, Nice, France, May 3-6 2015.
4. H. Atsumi, Y. Takemura, T. Miyabe, T. Konishi, T. Tanabe and T. Shikama, "Desorption of hydrogen trapped in carbon and graphite," *Journal of Nuclear Materials* **442**, pp. S746-S750, 2013.
5. H. Atsumi, T. Tanabe and T. Shikama, "Trapping State of Hydrogen Isotopes in Carbon and Graphite Investigated by Thermal Desorption Spectrometry," *Fusion Science and Technology* **67:2**, pp. 245-249, 2015.

2.3. Tritium Permeation Experiment (MIT)

Tritium Permeation Experiment (MIT)[10]

Summary:

Tritium permeation through metallic walls of tanks, pipes, and heat exchangers is one of the main challenges in the development of molten salt nuclear reactors, and in particular fluoride salt -cooled high-temperature nuclear reactors (FHRs). $2LiF\text{-}BeF_2$ (flibe) is being considering as the primary loop fluid for modern FHRs; it will be used to transfer heat from the core to heat exchangers. However, tritium is generated in the molten salt due to the neutron interactions with salt components such as Li, Be, and F. This tritium, with a half-life of 12.6 years, can then easily permeate through metal alloys at high temperature. If uncontrolled, this will result in the spread of radioactive material throughout the FHR system and eventual environmental releases. Among several tritium control strategies being considered for FHRs is adding an alumina coating on surface of metals as tritium permeation barrier (TPB). Alumina TPBs appear to be an efficient solution with respect to the real-world engineering practicability, availability, and reliability. In this study, a layer of alumina coating was added onto the surface of commercial 316 stainless steel tubing via plasma thermal spray. An intermediate bond layer of NiCr and a transit layer of NiCr+alumina were applied to the outer surface of the tube in order to enhance the adhesion between alumina coating and stainless steel, especially at high temperatures. The efficacy of the coating to reducing tritium transport was investigated by experimentally measuring the tritium permeation rate through coated tube and bare stainless tubes at the prototypical FHR temperature of 700°C. In order to generate a continuous source of tritium, 35g of purified natural Flibe salt (not Li-7 enriched) was irradiated by thermal neutron flux at 620°C in the Massachusetts Institute of Technology Research Reactor (MITR). The preliminary results suggest that the coatings on tube surface significantly reduced the tritium permeation rate at high temperature. To obtain a better understanding of the TPB, the microstructure of the coated tubes was characterized using various techniques.

---

[10] Guiqiu (Tony) Zheng, Kieran Dolan, and David Carpenter.

Introduction

Tritium permeation through structural alloys at high temperature is one of the challenges in the development of fluoride salt-cooled high-temperature nuclear reactor (FHR) that is emerging as a leading reactor concept for the next generation nuclear reactors[1]–[3]. In the design of modern FHRs, $2LiF\text{-}BeF_2$ (flibe) salt is being considered as the primary coolant to transfer heat from reactor core to heat exchangers. Under neutron irradiation, tritium is continuously generated via the following neutron reactions with all three elemental components of flibe salt, however the primary pathway is the neutron capture in Li-6 as shown in reaction 1 [4], [5]:

(1) Li^6 (n, t) He^4
(2) Li^7 (n, n+t) He^4
(3) Be^9 (n, t) Li^7
(4) F^{19} (n, t) O^{17}

To reduce tritium production, FHRs can utilize Li-7 enriched flibe. For instance, the MSRE utilized 99.995% Li-7 enriched flibe in its fueled primary loop, and 99.99% Li-7 enriched flibe in its clean secondary loop and flush systems. However, even if Li-6 were removed entirely from the flibe, an equilibrium level of Li-6 will be reached due to its generation from the $Be^9(n,\alpha)He^6$ reaction. This combination of reactions ensures that flibe under neutron irradiation will always be a significant tritium generator. Due to its relative long half-life of 12.6 years and low solubility in the salt, the tritium will be easily transported around and build up in the FHR primary system. At high temperatures tritium can then easily diffuse into and permeate through solid metallic structures, including the metal FHR vessel, piping, and heat exchangers. If unchecked, this diffusion creates an undesirable pathway for tritium transport out of the primary system and eventually to the environment.

Among several materials, the type 316 stainless steel is a promising structural alloy for the FHR because of its good corrosion resistance to molten fluoride salts and mechanical properties at high temperature[6]–[8]. Because of its favorable properties and wide experience and code qualification base, it is desirable to use 316 for many FHR primary system components. To reduce tritium permeation through stainless steel, several coating materials have been previously investigated as a tritium permeation barrier (TPB)[9]–[14]. Such a barrier could be applied on the surface of the 316 without affecting its important structural properties, but significantly reduce the transport of tritium, therefore helping to keep in contained within the system. It has been reported that an alumina coating can be an effective solution to reduce hydrogen permeation through structural materials at high temperature, and has positive attributes including available fabrication techniques, thermal stability, compatibility with the substrate, reduction of tritium permeation, etc. [10], [13], [14].

In this study, an alumina coating was added on the outer surface of 316 stainless steel tubes by the plasma thermal spray technique in order to investigate the barrier efficiency of tritium permeation rate at high temperature. The final coating microstructure was also analyzed using various characterization techniques in order to understand the behavior of the coating after thermal cycling. To conduct tritium permeation experiments, a dynamic tritium gas source was produced by neutron irradiating flibe in a specifically designed capsule in the MITR. Tritium in the gas stream on either side of the heated 316 barrier tube was then measured under various conditions in order to gain understanding on the transport of tritium through 316 with and without an alumina TPB.

Experimental

Microstructural characterizations of coating layers

Alumina coating was added on the cleaned and blasted surface of 316 stainless steel tubing (25.4mm in outer diameter, and 0.9mm in the wall thickness procured from TW Metals) by using the plasma thermal spray technique (Falmer Thermal Spray, Massachusetts, USA). To enhance the adhesion between the alumina coating and the stainless steel substrate, an intermediate bonding layer of NiCr and a transit layer of 50%NiCr+50%alumina was sprayed on tube's surface in advance. The real thickness of the coating layers from inner to outer is 83±8µm, 66±7µm, and 140±23µm for NiCr bonding layer, NiCr+alumina transit layer, and alumina barrier layer, respectively. The microstructure of the coating layers was characterized by using SEM-EDS and XRD techniques.

Molten salt neutron irradiation

To gain tritium source online for the permeation experiments, natural flibe salt (35g) was loaded into a specifically designed system at the MITR. The irradiation utilized on of the six vertical neutron irradiation facilities (3GV6) in MITR graphite reflector (Figure 8). A triple-layer capsule, loaded with salt at the center, was positioned at the middle height of reactor core where the thermal neutron flux is at a maximum. This facility has three separate gas inlet and outlet systems corresponding to each zone in the triple-capsule. The theoretical tritium production rate for 35g of natural flibe salt in the 3GV facility of the MITR was calculated to be approximately 200mCi/MWd. As shown in Figure 9 and Figure 10, a triple-layer capsule with salt loaded in inner capsule was maintained at ~620°C, higher than the salt melting point of 459°C, using electric heater. The electric heater was concentrically inserted into the center hole of the triple-layer capsule (shown in Figure 10 (b)). It should be noted that each capsule has a separate sweep gas system, all using 3.5%H_2 balance He. This mixture ensures that all of the gas system surfaces are saturated with hydrogen, significantly reducing parasitic adsorption of tritium before it reaches the detection and collection system. When the power of the MITR was brought to 200kW, an ion chamber (Model 7045 Room Tritium In-Air Monitor, TYNE engineering Inc.) detected significant radioactive isotopes in the sweep gas (150cc/min) from the inner capsule. This ion chamber was set up in the gas lines prior to the cascade water bubbler and catalyst that absorbs tritium from the reactor tritium generator.

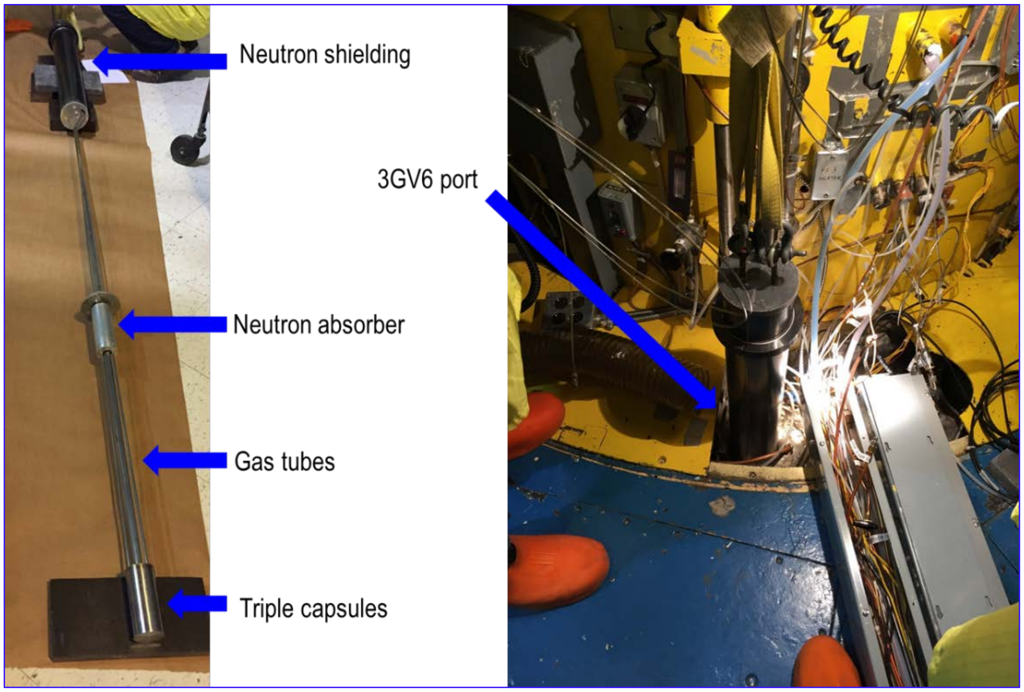

Figure 8: Assembled gas lines and salt capsule for irradiating natural FLiBe molten salt in a 3GV port of the MITR.

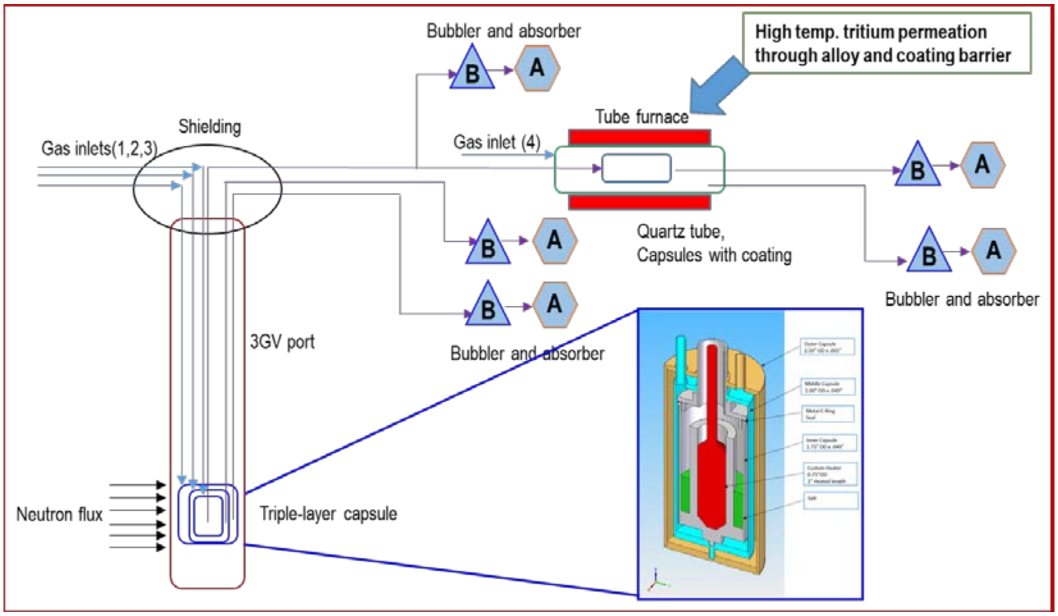

Figure 9: schematic of the main parts and gas lines of natural Flibe salt neutron irradiation and high-temperature tritium permeation experiment. Cross-sectional view in lower inset showing inner configuration of triple-layer capsule.

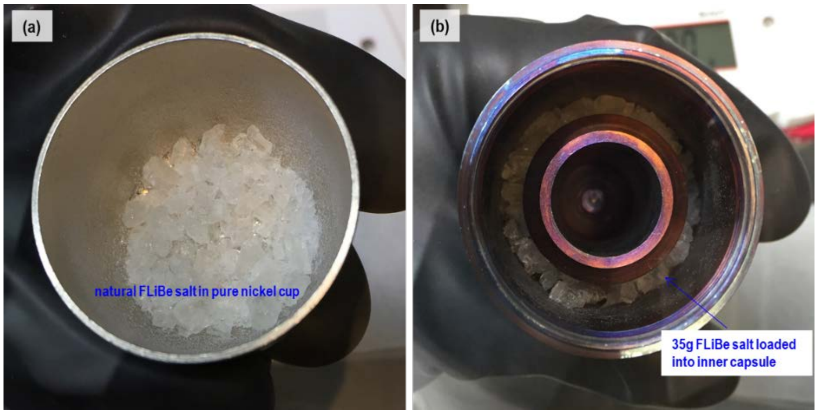

Figure 10: solid natural Flibe salt preparation and loading (a) granulated salt particles in nickel cup, and (b) loaded into inner capsule of irradiation assembly.

High-temperature tritium permeation

The main components of salt irradiation capsules and high-temperature tube furnace for tritium permeation experiment are shown in Figure 11. Photos show the configuration of capsules, heater, shielding plugs and gas lines for neutron irradiation subsystem that is inserted into the neutron irradiation facility (3GV6). With neutron irradiation (mainly thermal neutrons), tritium is generated from the molten flibe salt in this system in the same was as a commercial FHR. In addition to the tritium in in innermost encapsulation outlet gas (released directly from the liquid salt to the sweep gas), fractional tritium permeated through the inner capsule wall to middle capsule at ~620°C under irradiation. The right photos show the tube furnace and the out gas lines containing the tritium gas. This tube furnace system was set up on a stage without irradiation for testing tritium permeation at high temperature. The outer quartz tube and inner stainless steel tube have been vacuumed and filled with Ar gas repeatedly prior to heating up and flowing any tritium containing gases. The heating zone of the tube furnace is 8” from left to right. Quartz wool was applied on both ends of the heating zone to mitigate radiation heat losses from furnace. The temperature on the stainless steel tube out of heating zone was ~200°C while heating zone temperature was 700°C. Therefore, only the stainless steel tube within the 8” heating zone was considered as the tritium permeation area.

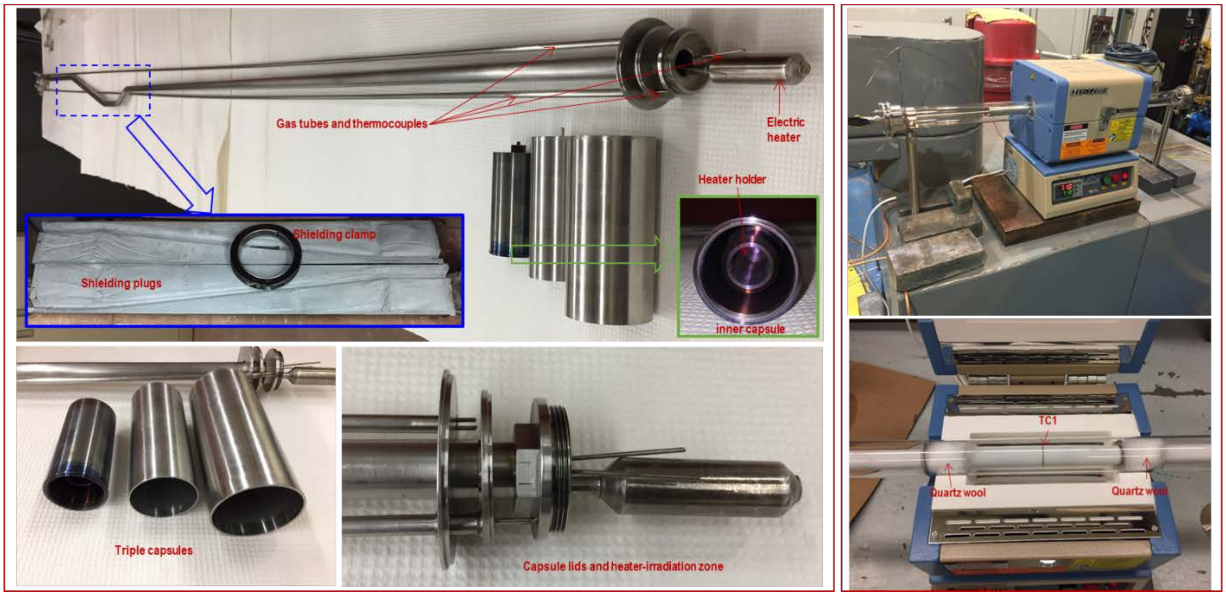

Figure 11: (left) main components for salt neutron irradiation and (right) high-temperature tube furnace.

There are two instruments to measure the tritium in the gas. One is an ion chamber for monitoring tritium online. This ion chamber is sensitive to the beta radiation released from the tritium and directly reports activity in real-time. Another is a bubbling system that has six vials, each filled with ~80 ml deionized water. The first three vials water absorbs soluble tritium such as HTO, T_2O or TF. Insoluble tritium such as HT and T_2 passes through these first bubblers and through a cylindrical furnace containing catalyst. An oxygen (1vol.%) balanced helium gas (50ccm) is mixed into the furnace to oxidize the insoluble tritium and create soluble tritium (HTO and T_2O). Then the oxidized tritium was absorbed in last three water bubbling vials. For each testing period, these six vials were replaced with a new set filled with fresh deionized water. During each neutron irradiation and permeation testing period, 0.1ml tritiated water sample was extracted from each vial to mix with 18ml liquid scintillation cocktail (PerkinElmer). If the tritium concentration is too high (>10^6dpm/100µl water), the tritiated water was further diluted then mixed with LSC cocktail.

Post-irradiation processing

The tritiated water samples were mechanically agitated to ensure good mixing between the water and scintillation fluid. They were then analyzed using a calibrated liquid scintillation counting (LSC) system. According to the measured tritium activity in each sample, the original tritium concentration in water vials at each sample collection point was calculated for plotting the profiles of the tritium activity in out gas as a function of time. The soluble tritium and insoluble tritium in the gas were obtained based on the counted tritium from the first three vials and the second three vials, respectively. The trend of plotted profiles of total tritium (soluble and insoluble) was then compared with the recorded activity data. In addition, the recorded data of temperatures, gas flowing rates, and reactor power during the periods of tritium generation and permeation experiments were extracted from the facility data acquisition system.

Results and discussion

Microstructure of coating layers

The right lower photo in Figure 11 shows a coated 316 stainless steel tube, 24” in length, 1” in outer diameter and 0.035” in wall thickness. Figure 12 shows the cross-section of the coated stainless steel tube. From inner to outer surface shown on the cross-sectional SEM image, there are, sequentially, 316 stainless steel tube wall, NiCr bonding layer, NiCr/Al_2O_3 transit layer, Al_2O_3 layer (main tritium barrier), and mounting powder. The interface between each coating layer is relatively rough, which favors the enhanced adhesion of the coating layers on the stainless steel surface at high temperature. The mixture of NiCr and Al_2O_3 transit layers in the middle not only enhances bonding but also improves the tolerance of thermal expansion differences between the metal and ceramic layers. In addition, many pores with various dimensions were observed in Al_2O_3-containing layers. These pores are mainly due to mechanical polishing during SEm preparation (some Al_2O_3 grains were removed). However, some pores are probably relevant to the volume shrink during plasma thermal spray. The interior microstructure was further observed in the following ion milled cross-section (Figure 14).

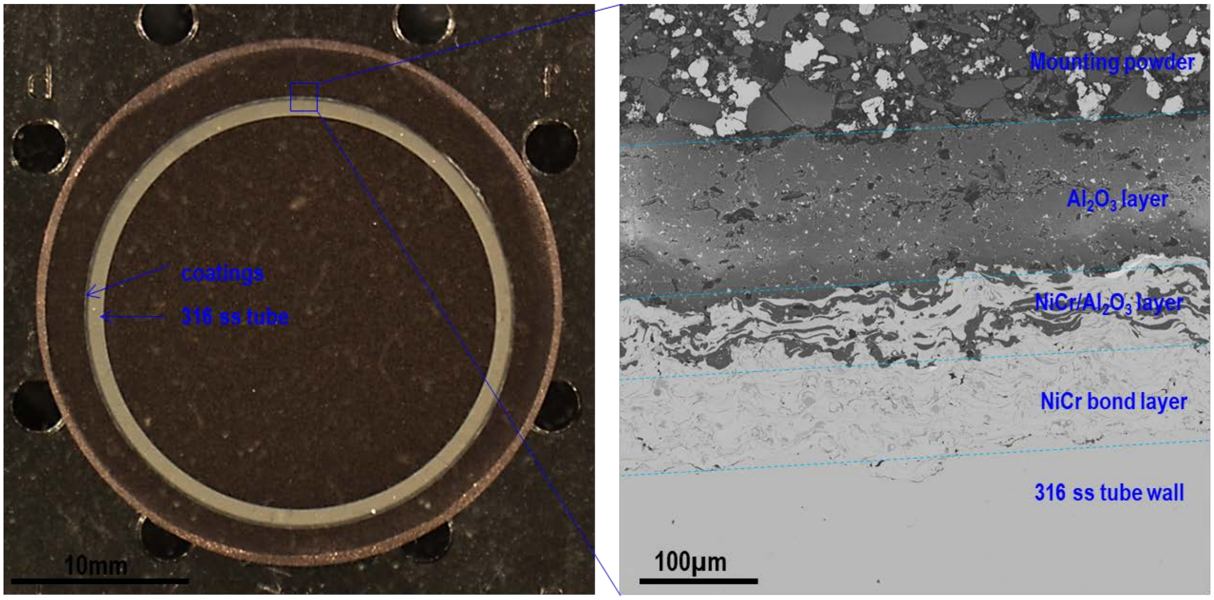

Figure 12: optical image (left) and SEM image (right) on the cross-section of the coated 316 stainless steel tube.

The distribution of the main elements Al, O, Ni, Cr, Fe, Si, Cu and C in coatings, mounting powder and stainless steel tube are shown in the EDS mappings in Figure 13. The Fe mapping clearly distinguishes the interface between tube and the first NiCr layer. The blasted tube surface is relatively rough. The relatively high concentration of both Ni and Cr elements were detected on the NiCr bonding layer and transit layer. The Al- and O-rich areas in the EDS mappings display the Al2O3 coating layer. Si, Cu and C are the main components of mounting powder. The distinct Al and Ni distributions in the coating layers indicate the high purity of coating materials. The small quantities of Cu and C in the Al_2O_3 layer are due to the mounting powders left in pores during polishing.

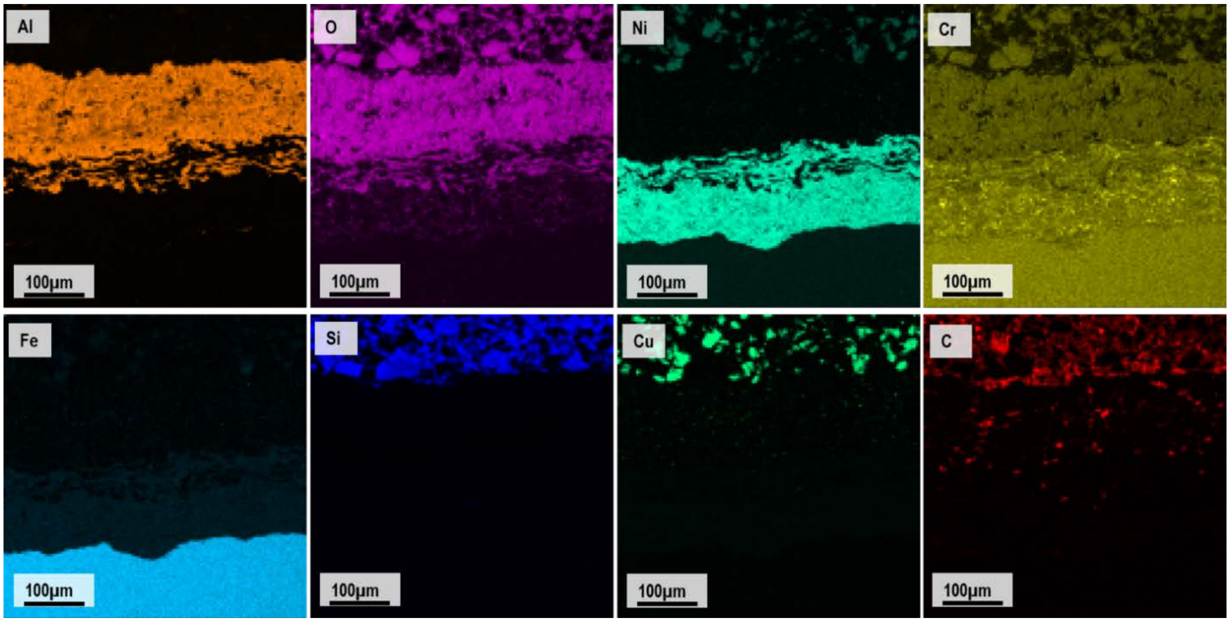

Figure 13: EDS mapping on the cross-section of the coatings on 316 stainless steel tube surface, showing the main elements distribution.

As shown in Figure 14, an area on the cross-section of Al_2O_3 layer was vertically milled down using FIB technique for revealing the interior microstructure of Al_2O_3 coating layer without polishing damage. Figure 14 (b) and Figure 14 (c) are the SEM images on the polished and ion milled Al_2O_3 coating layer, respectively. There are many micro cracks on the polished cross-section in addition to some irregular pores. The FIB-milled cross-section clearly shows the real development of these micro cracks originated in the Al_2O_3 layer. According to the SEM observation, the depth of these cracks is in a wide range, from several microns to tenth microns even longer. These two images suggest that many micro cracks exist inherently in the Al_2O_3 coating.

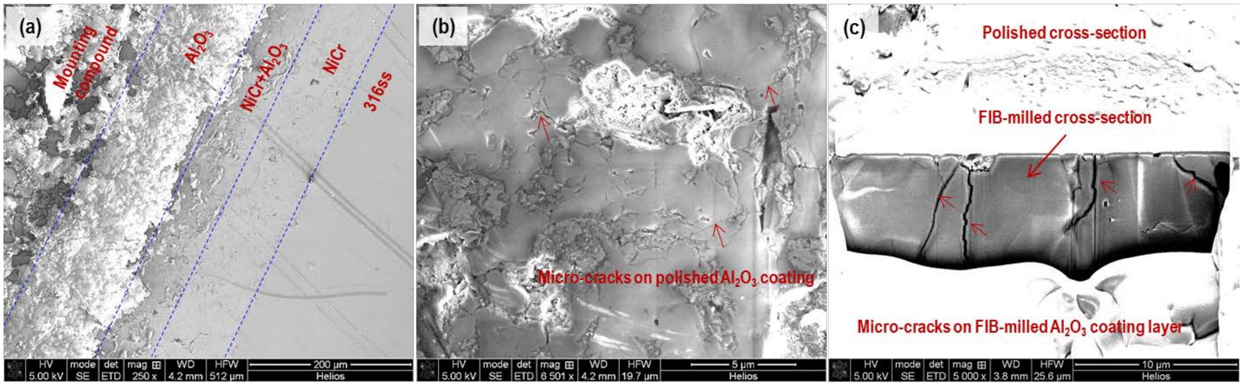

Figure 14: SEM images on the cross-section of multiple coating layers before (a, b) and after (c) FIB milling.

Before conducting the tritium permeation experiment, the coated 316 stainless steel tubes were pre-heated in an Ar filled quartz tube at 700°C for 2 hours to examine coating adhesion at high temperature. After the heat-treatment, the microstructure of the coated tube was characterized using the same SEM and EDS analyses as above. There is no distinguishable difference between heat-treated and as-fabricated tubes. This suggests the excellent stability of the coatings' microstructure at high temperature. In addition, the phase stability at high temperature was analyzed by comparing their X-ray diffraction patterns. As shown in Figure 15, the main peaks of as-fabricated and heat treated alumina coating are identical on the XRD patterns, suggesting the good thermal stability of the coating material at 700°C.

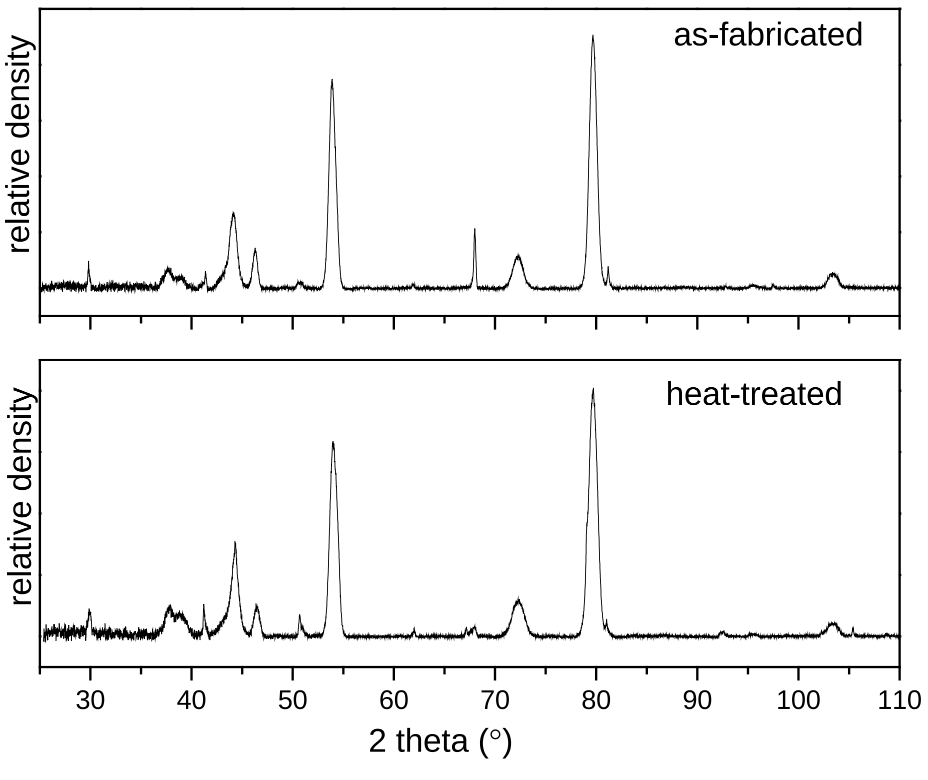

Figure 15: XRD diffraction patterns on the outer alumina coating before and after heat-treatment at 700C for 2 hours.

Tritium generation and permeation

The results of tritium generation rate from the natural Flibe salt under neutron irradiation and the tritium permeation rate through various materials are described and discussed as follow. Two specific experiment periods were selected to represent these two typical phenomena: (1) the tritium in the outlet gas from the inner salt capsule, and (2) the tritium permeated through coated 316 stainless steel tube at 700°C. The profiles for these two phenomena at equilibrium state are shown in the following Figure 16 and Figure 17.

As shown in Figure 16, the temperatures, gas flowing rate and radioactivity were recorded while measuring the equilibrium tritium in the outlet gas from salt capsule under neutron irradiation. The profiles temperature and gas flowing rates share left Y-axis (same value with different units), but the activity measured via ion chamber corresponds to right Y-axis. The stable salt capsule temperature of 620°C suggests an excellent temperature control for the inner salt capsule under neutron irradiation. The radioactivity of the outlet gas from the salt capsule is approximately 9600 $\mu Ci/m^3$. The oxygen/helium gas for the catalyst furnace inside bubbler was suspended while collecting tritiated water samples. As shown on the gas flowing profiles, the He/O_2 flowing rate is zero before starting point and after the end point of each experiment period. According to the difference in the tritium measured with LSC method before and after the period of ~60 minutes, the increased tritium in the water vials of bubbler is approximately 6.92×10^{-2} mCi. Since the flowing rate of the sweeping gas through salt capsule is about 150 ccm, the LSC measured radioactivity of the tritium in the outlet gas of salt capsule can be converted to 7700 $\mu Ci/m^3$ which is close to the data recorded by ion chamber. It should be noted that the accuracy of the ion chamber at high range (≥ 1000 $\mu Ci/m^3$) is much lower than low range (0-1000 $\mu Ci/m^3$). This tritium-contained gas (7700 $\mu Ci/m^3$) is the dynamic tritium source for the following tritium permeation experiments.

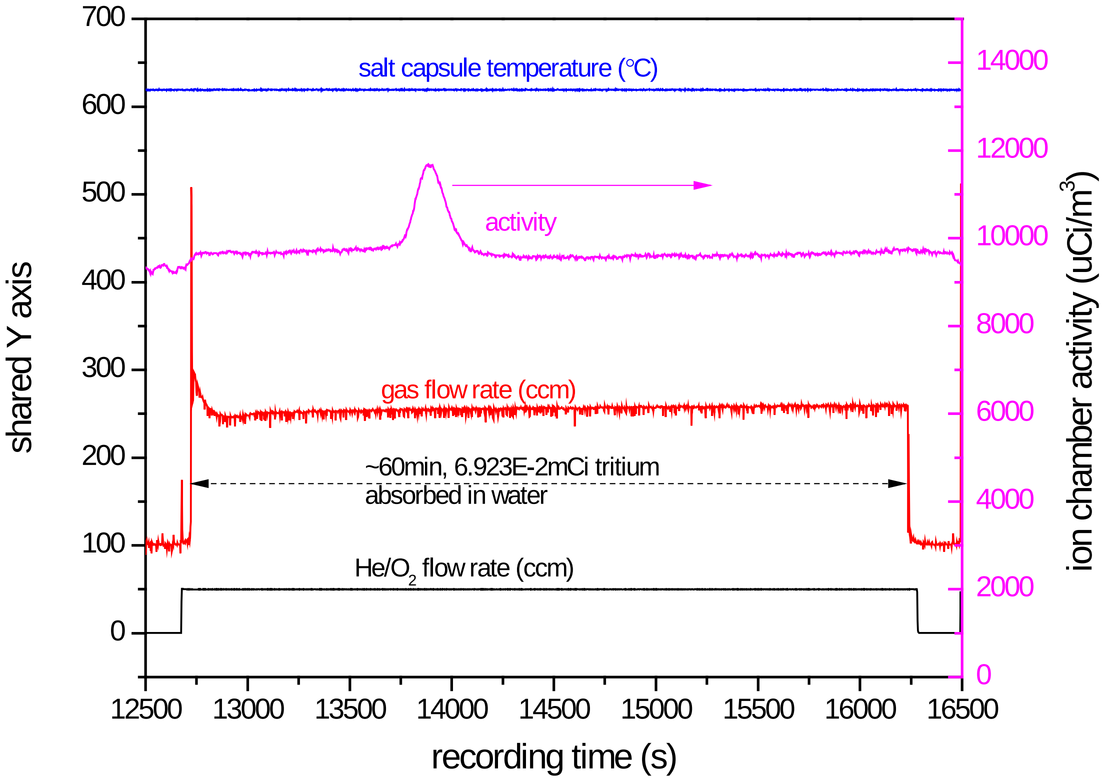

Figure 16: Profiles of the inner salt capsule temperature (°C, left Y-axis), gas flow rates (ccm, left Y-axis), and the activity of the outlet gas (right Y-axis) from salt capsule during neutron irradiation.

Figure 17 shows the profiles of tube furnace temperature, gas flowing rates, and ion chamber recorded radioactivity of the sweeping gas through quartz tube while the tritium-contained outlet gas of salt capsule passed through the inside of the coated 316 stainless steel tube. An 8” zone of coated stainless steel tube and outer quartz tube both were in the heating zone of tube furnace that was maintained at 700°C. Fractional tritium permeated through the wall and coatings of the stainless steel tube while the tritium-contained gas flowing through the inside of the tube. When the permeation reached an equilibrium state, Figure 17 presents the recorded data for a period of about 27.5 minutes. The radioactivity of the sweeping gas from outer quartz tube corresponds to the content of the tritium permeated through coated stainless steel tube, in a range of 370-380 µCi/m^3. The LSC measured tritium in the bubbler water is approximately 1.45x10^{-3} mCi during this period. Since the flowing rate of the sweeping gas through quartz tube is 150 ccm, the measured tritium radioactivity of about 350 µCi/m^3 in the gas through the quartz tube is calculated, very close to the radioactivity reading on ion chamber. Furthermore, this also means that about

4.5% (350 µCi/m^3 per 7700 µCi/m^3) of the tritium in the flowing gas continuously permeated through the coated 316 stainless steel tube at 700°C. With this tritium source gas, the permeation rate per unit area through coated stainless steel tube is approximately 5.82x10^{-6} µCi/s·cm^2, as summarized in Table 3, which is significantly lower than that through the bare tubing at same temperature. The permeation rate at 600°C is about half of the value at 700°C. The radioactivity reading on ion chamber is low and inconstant while the temperature was set at 400°C and 500°C, suggesting the undetectable tritium permeated through coated tube at these temperatures.

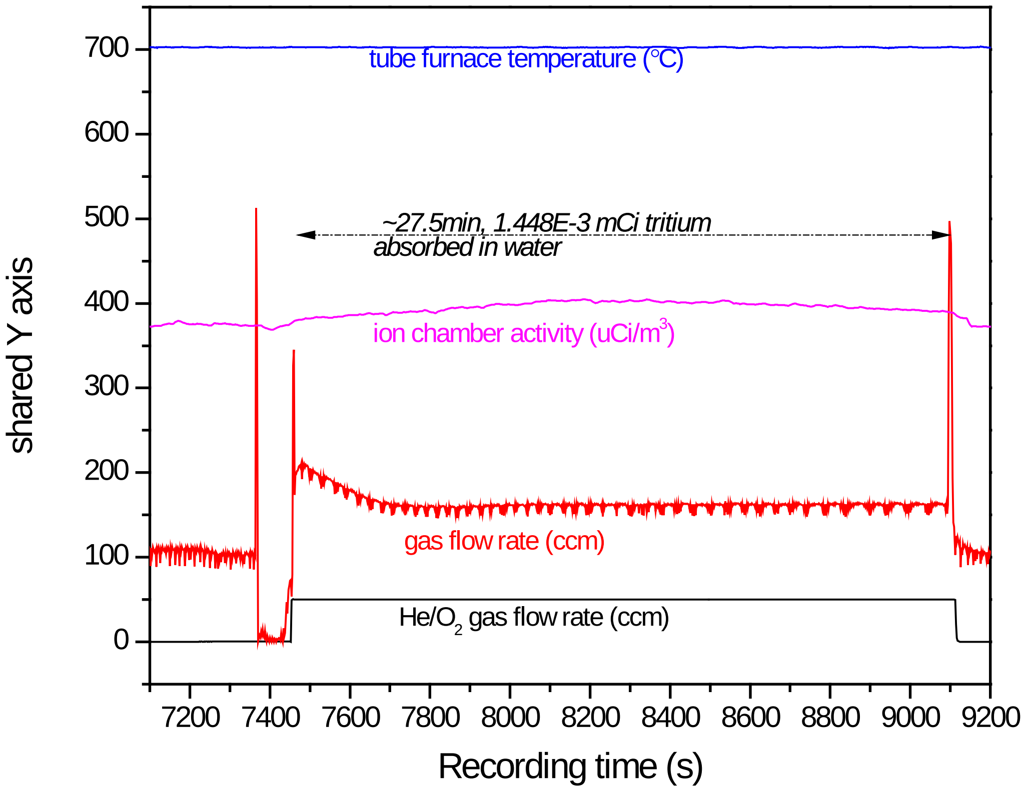

Figure 17: Profiles of tube furnace temperature (°C), gas flow rates (ccm), and the activity of the gas from quartz tube (µCi/m^3) while tritium permeating through coated 316 stainless steel tube at 700°C. All profiles share left Y axis.

Table 3: Summary of the LSC measured tritium in the outlet gas at different conditions, and the calculated tritium permeation rate.

Description	**LSC measured tritium (μCi/min)**	**Tritium permeation rate (μCi/s·cm^2)**
Tritium in the gas of salt capsule at 620°C under neutron irradiation	1.154	
Tritium in the gas of quartz tube, permeating through bare stainless steel tube at 700°C	0.738	8.162E-5
Tritium in the gas of quartz tube, permeating through coated stainless steel tube at 700°C	0.053	5.823E-6
Tritium in the gas of quartz tube, permeating through coated stainless steel tube at 600°C	0.026	2.844E-6

The soluble (HTO, T_2O and TF) and insoluble (HT and T_2) tritium species in the gas lines can be identified by measuring the tritium absorbed in the water of 1-3 vials and 4-6 vials on the bubbler, respectively. As shown in Figure 18, the LSC measurements of six sets of tritiated water samples suggest that higher than 98.5% tritium is insoluble, including the tritium gas from salt capsule and quartz tube. These insoluble tritium species are the main source that permeates through materials at high temperature. Such high insoluble tritium species in the outlet gas might be relevant to the addition of hydrogen in sweeping gas. The hydrogen not only saturates the inner surface of gas tubing but also reduces certain soluble tritium at high temperature.

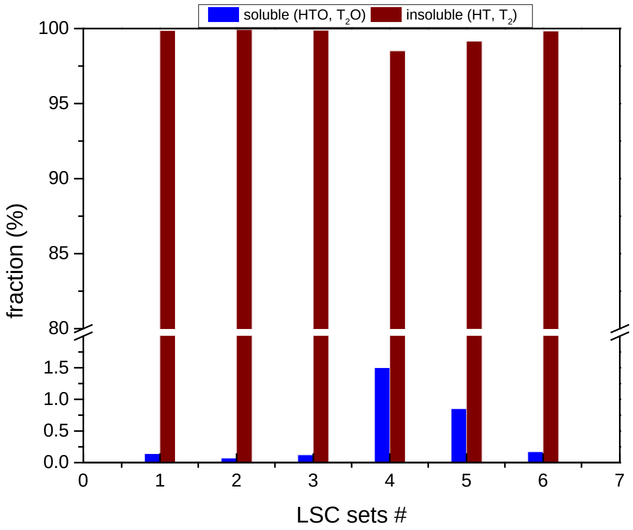

Figure 18: the fraction of soluble tritium (HTO, T2O, and TF) and insoluble tritium (HT, T2) in the outlet gas based on the LSC results of collected tritiated water samples. Note that the broken Y axis clearly presents the small fraction of the solution tritium.

It should be noted that the hydrogen (H_2<4%) in the pre-mixed He+H_2 sweeping gas theoretically has similar thermal permeation behavior as the tritium. A competition mechanism between hydrogen permeation and tritium permeation through same material probably exists in this study. Therefore, the true value of the tritium permeation rates should multiply a number to obtain real permeation data in practice.

Conclusions

This study experimentally investigated the efficiency of alumina coating as tritium permeation barrier at high temperature by using the tritium gas source generated from the natural flibe molten salt under neutron irradiation in the MITR. The microstructure analysis of the coating layers on 316 stainless steel tube surface shows good adhesion and phase stability of alumina coating added on with plasma thermal spray technique, even after thermal cycling. Under thermal neutron irradiation in an MITR facility, permeation was measured with a continuously generated tritium source from the flibe maintained at 620°C. The tritium measurement systems consisted of ion chamber for online radioactivity reading and bubbler for absorbing the tritium in outlet gas provide accurate integrated data for studying tritium permeation rates. Approximately 7700 µCi/m^3 tritium source was obtained for testing the tritium permeation through 316 stainless steel tube with and without the alumina TPB coating. It was found that the application of alumina coating on tube surface significantly decreases tritium permeation rate from 8.162x10^{-5} to 5.823x10^{-6} μCi/s·cm^2 at 700°C. It is also found that the micro-cracks in the alumina coating likely release some tritium at high temperature. It is inferred that the tritium barrier efficiency can be further improved by more advanced coating techniques that reduce porosity and cracking.

References

[1] C. W. Forsberg, P. F. Peterson, and P. S. Pickard, "Molten-Salt-Cooled Advanced High-Temperature Reactor for Production of Hydrogen and Electricity," in *Nuclear Technology, American Nuclear Society*, 2003, pp. 1–25.

[2] C. W. Forsberg, P. F. Peterson, and R. A. Kochendarfer, "Design options for the advanced high-temperature reactor," in *2008 International Congress on Advances in Nuclear Power Plants : ICAPP '08 : embedded topical meeting,* 2008, vol. 2.

[3] C. W. Forsberg, L. W. Hu, P. F. Peterson, M. Fratoni, K. Sridharan, and E. Blandford, "Progress in development of fluoride-salt-cooled high-temperature reactors (FHRs)," in *Transactions of the American Nuclear Society*, 2017, vol. 116, p. 21808.

[4] D. Carpenter, M. Ames, G. Zheng, G. Kohse, and L. Hu, "Tritium Production and Partitioning from the Irradiation of Lithium-Beryllium Fluoride Salt," *Fusion Sci. Technol.*, vol. 71, no. 4, pp. 549–554, May 2017.

[5] J. D. Stempien, "Tritium Transport, Corrosion, and Fuel Performance Modeling in the Fluoride Salt-Cooled High-Temperature Reactor (FHR)," Massachusetts Institute of Technology, 2015.

[6] G. Zheng, B. Kelleher, G. Cao, M. Anderson, T. Allen, and K. Sridharan, "Corrosion of 316 stainless steel in high temperature molten Li2BeF4 (Flibe) salt," *J. Nucl. Mater.*, vol. 461, pp. 143–150, Jun. 2015.

[7] Y. Oya *et al.*, "Effect of surface oxide layer on deuterium permeation behaviors through a type 316 stainless steel," *Fusion Eng. Des.*, vol. 87, no. 5–6, pp. 580–583, Aug. 2012.

[8] J. R. Keiser, J. H. DeVan, and D. L. Manning, "The Corrosion Resistance of Type 316 Stainless Steel to Li2BeF4, ORNL/TM-5782," 1977.

[9] G. W. Hollenberg, E. P. Simonen, G. Kalinin, and A. Terlain, "Tritium/hydrogen barrier development," *Fusion Eng. Des.*, vol. 28, pp. 190–208, 1995.

[10] G. Benamati, C. Chabrol, A. Perujo, E. Rigal, and H. Glasbrenner, "Development of tritium permeation barriers on Al base in Europe," *J. Nucl. Mater.*, vol. 271–272, pp. 391–395, May 1999.

[11] R. A. Causey, R. A. Karnesky, and C. San Marchi, "Tritium Barriers and Tritium Diffusion in Fusion Reactors," in *Comprehensive Nuclear Materials*, Elsevier, 2012, pp.

511–549.

[12] Z. Yao, J. Hao, C. Zhou, C. Shan, and J. Yu, “The permeation of tritium through 316L stainless steel with multiple coatings,” *J. Nucl. Mater.*, vol. 283–287, pp. 1287–1291, Dec. 2000.

[13] G. K. Zhang, C. A. Chen, D. L. Luo, and X. L. Wang, “An advance process of aluminum rich coating as tritium permeation barrier on 321 steel workpiece,” *Fusion Eng. Des.*, vol. 87, pp. 1370–1375, 2012.

[14] F. Yang *et al.*, “Tritium permeation characterization of Al2O3/FeAl coatings as tritium permeation barriers on 321 type stainless steel containers,” *J. Nucl. Mater.*, vol. 478, pp. 144–148, Sep. 2016.

2.4. Experimental Investigation of Ultrasonic-Enhanced Gas Sparging to Remove Tritium and Other Gas Impurities from High-Temperature Salts (UNM)

Experimental Investigation of Ultrasonic-Enhanced Gas Sparging to Remove Tritium and Other Gas Impurities from High-Temperature Salts (UNM) [1]

Executive Summary

Tritium in a FHR is generated in liquid salts as a dissolved gas. Tritium removal is required to prevent escape to the environment. One method to remove the tritium is gas sparging with either an inert gas or a hydrogen/inert gas mixture. The rate of tritium removal from the liquid is controlled by the mass transfer through the liquid salt to the sparging gas. Mass transfer is increased by using smaller gas bubbles with more suriface area per unit volume of gas sparing. Ultrasonic agitation of the gas-liquid mixture can increase the number of bubbles and create non-spherical bubbles of changing dimensions—methods that increase tritium mass transfer from liquid to gas phase. Ultrasonic gas sparging was experimentally investigated using dissolved oxygen in glycerol to simulate hydrogen in liquid salts.

The Small Ultrasonic Mass Transfer (SUMATRA) experiments demonstrated proof-of-concept of ultrasonic mass transfer enhancement. The results were used to develop a mass transfer correlation for ultrasonically enhanced mass transfer. The second experiment, the Prototype Ultrasonic Mass Transfer (PULST) was designed as a scaled up version of SUMATRA with the goal of investigating indirect ultrasonic-enhanced mass transfer and the viability of using commercial off-the-shelf components. The PULST experiments did not conclusively show mass transfer enhancement but did (1) establish the limits of using off-the-shelf components with indirect ultrasonic mass transfer enhancement and (2) quantified the changes required to optimize flow-cell design. The requirement is to efficiently transfer ultrasonic energy from the ultrasonic generator through the wall to the hot salt with large temperature differences between the salt and ultrasonic generator.

---

[1] F. Rubio (rubiofv@unm.edu or rubiofv@gmail.com) and E. Blandford (edb@unm.edu)

Contents

1 Introduction

The Integrated Research Project fell into two major themes in support of Fluoride-salt-cooled High-temperature Reactor (FHR) development: heat transfer work and mass transfer work. These two major themes helped to explore potential limitations of the FHR technology: economic and performance penalties associated with high viscosity and expensive coolants and the use of twisted elliptical tubes as a potential solution, and the use of acoustically-enhanced inert gas sparging to reduce tritium concentration in the circulating flibe coolant, which has economic, safety, and licensing implications. The major findings of the mass transfer work is detailed below, and the findings of the heat transfer work are detailed in a sister report.

High-power ultrasonics have been used in many industrial process streams such as food processing, metal production, chemical production, and pharmaceutical manufacturing. The Integrated Research Project had investigated integrating these techniques and concepts for application in tritium control in flibe through scaled mass transfer experiments. The activities documented are two scaled mass transfer experiments and a parameter comparison study of the two experiments. The first mass transfer experiment was the Small Ultrasonic Mass Transfer (SUMATRA) experiment. This experiment demonstrated proof-of-concept that high power ultrasonics can enhance sparging mass transfer. The experiment did identify a significant trade-off with acoustic horn erosion.

The second experiment, the Prototype Ultrasonic Mass transfer experiment was designed as a scaled up version of the SUMATRA experiment with the goal of investigating indirect ultrasonic enhanced mass transfer and investigating the viability of utilizing commercial-off-the-shelf (COTS) components. At the conclusion of the PULST experiment a parameter study was performed to compare the results from the PULST experiment and the SUMATRA experiment. The results of which established the limits of COTS components with indirect ultrasonic mass transfer enhancement as well as highlighing the parameter changes that would be necessary to optimize a flow cell design.

2 Theory

2.1 Sparging Mass Transfer

Inert gas sparging is the injection of a gas into a fluid in order to diffuse dissolved gas into the inert gas bubble for the purpose of removing dissolved non-condensible gases. For the work presented the mass transfer is in the form of two-phase concurrent flow. From Kress' work [1] an empirical correlation was developed for bubbles in turbulent concurrent bubbly flow. The correlation was in the form of two phase flow described by Sherwood [2]. The correlation that was developed is shown in equation (1).

$$Sh = 0.34\ Sc^{1/2} Re^{0.94} \left(\frac{d}{D}\right)^{1.0} \tag{1}$$

2.2 Acoustic Intensity and Transmission

The energy range involved in acoustic intensity spans several orders of magnitude. The perceived loudness of sound is the sound intensity, which is defined as the energy passing perpendicular to an area per unit time. So, a higher intensity would be perceived as a louder sound. Due to the large range of orders of magnitude that are relevant acoustics the decibel, dB, was adopted as a unit of measure. The dB is a unitless and comparative metric. The decibel unit of note is the decibel sound power level, $dB(SPL)$, which can be related to sound pressure, P, or intensity, I, as shown in equation (2). The reference point ($0\ dB$) is defined based on the minimum human ear sensitivity at $P_0 = 10\ \mu Pa$ in air and $I_0 = 10^{-12}\ W/m^2$. Additionally, the reference for sound pressure in solids and liquids is $P_0 = 10^{-6}\ Pa$ [3].

$$dB(SPL) = 20 \log \left(\frac{P}{P_0}\right) = 10 \log \left(\frac{I}{I_0}\right) \tag{2}$$

Acoustic transmission energy through one medium to a second is affected by several factors. One is the acoustic impedances of the interfacing media. Acoustic impedance is defined in equation (3). Acoustic impedance has the units of $Rayl$ is the product of the speed of sound in a material and the density of the material. Acoustic transmission through an interface of media is described by equations (4) and (5).

$$Z = \rho c \tag{3}$$

$$T_P = 2 \frac{Z_2}{Z_1 + Z_2} \tag{4}$$

$$\frac{I_T}{I} = \frac{Z_1}{Z_2} \left| T_P \right|^2 \tag{5}$$

To maximize the transmission of acoustic energy between two media, the acoustic impedance must be matched. In a case where it is desired to transmit acoustic energy through materials with very dissimilar impedances, a matching layer can be utilized to be able to transmit the maximum energy possible between the two media. Kino [4] describes the matching impedance of this layer as (6). For the example of finding a matching layer between water and aluminum the maximum transmission fraction and matching impedance is illustrated in Figure 2.

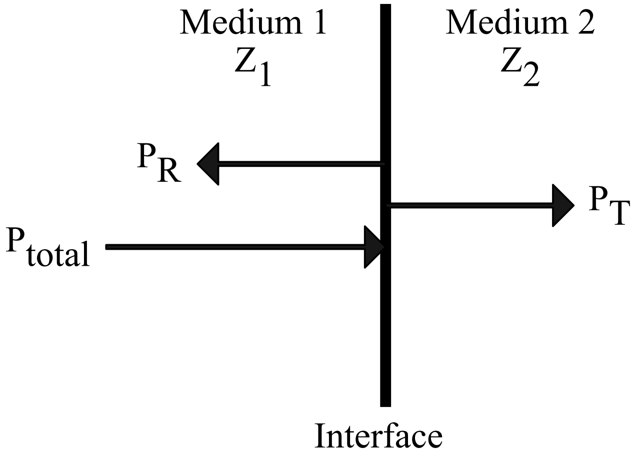

Figure 1: Diagram of an infinite plane pressure wave perpendicularly incident on an interface.

$$Z_{match} = \sqrt{Z_1 \ Z_2} \tag{6}$$

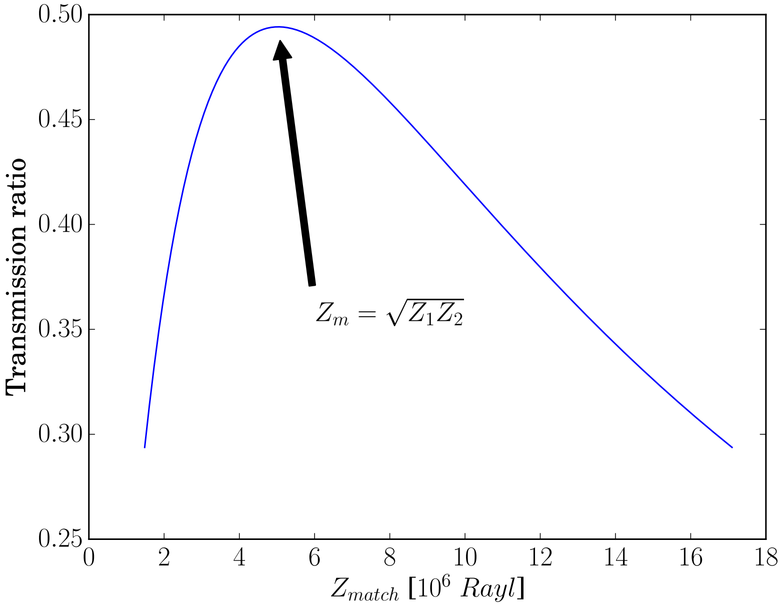

Figure 2: Intensity transmission between water ($Z_{water} = 1.483\ MRayl$) and aluminum ($Z_{Al} = 17.10\ MRayl$) for a range of matching layer impedances.

2.3 Sonomechanical Theory

Most of the demonstrated non-medical applications of sonoprocessing processing with high power ultrasonics take advantage of sonically induced cavitation [5, 6]. The bubble formation and related energy exchange are transient, involve high pressures and temperatures. The behavior is nonlinear by nature and challenging to describe, particularly when multi-phase (slurry or catalytic particles) and multi-bubble phenomena occur [5, 7, 8, 9, 10]. Ultrasonics is in essence a tool that can be used to deliver energy into a medium. This sonic energy can then be manifested in interactions as vibrations and mechanical motion (acoustic streaming), heat (through rapid bubble compression and absorption), and light (sonoluminescence) all through cavitation and the related absorption and dissipation of the sonic energy.

Cavitation is the most important effect of high power ultrasonics for the enhancement of mass transfer. Bubble breakup and the rapid vapor bubble formation and collapse forms a mechanism that can facilitate the removal of dissolved gases. Acoustic cavitation is illustrated in Figure 3 The collapse event results in very high temperatures and pressure on the order of 5000 $^{\circ}C$ and 2000 atm, illustrated in Figure 3. This phenomenon has been investigated and documented extensively [5, 7, 8, 9, 10, 11]. The threshold of cavitation can be affected by many factors, specifically applied acoustic intensity and frequency as shown in Figure 4.

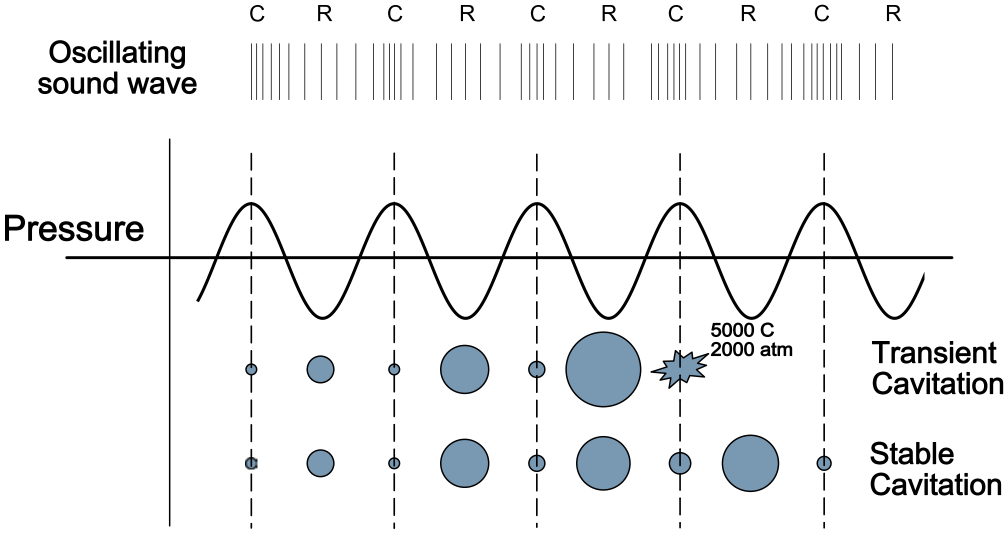

Figure 3: Illustration of stable cavitation bubbles and the lifetime of transient cavitation bubbles in relation to an oscillating sound wave represented visually as compression (C) and rarefaction cycles (R). [12]

The Rayleigh-Plesset equation, as shown in equation (7), describes the simple motion of a pulsing spherical bubble [8, 11, 14]. This equation was developed from the work of many authors, but it is now simply referred to as the “Rayleigh-Plesset Equation” [8]. It explains the time relation of a bubble radius (R) in an oscillating pressure field with a source at some distance away. The important pressures of note are the static pressure on the fluid (p_0) as well as the oscillating pressure ($p(t)$). Other factors that affect the behavior of the forced

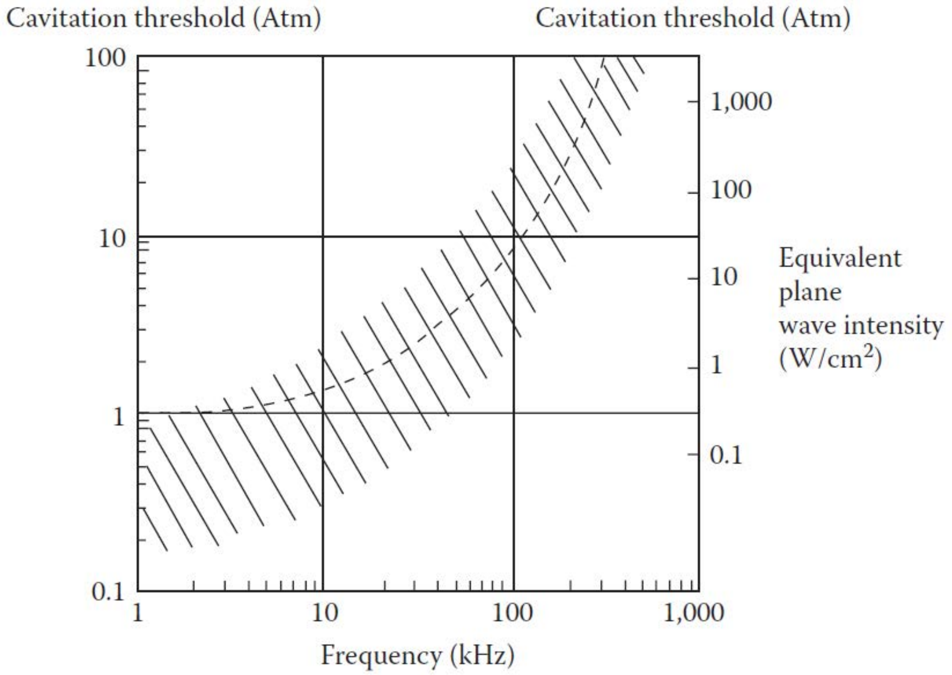

Figure 4: Frequency dependence for the cavitation threshold with continuous wave applied to fresh water at atmospheric pressure. [5, 13]

bubble are fluid properties, namely, density (ρ), surface tension (σ), sheer viscosity (η), the polytropic constant (κ), and the vapor pressure (p_v).

$$R\ddot{R} + \frac{3}{2}\dot{R}^2 = \frac{1}{\rho}\left[\left(p_0 + \frac{2\sigma}{R_0} - p_v\right)\left(\frac{R_0}{R}\right)^{3\kappa} + p_v - \frac{2\sigma}{R} - \frac{4\eta\dot{R}}{R} - p_0 - p(t)\right] \tag{7}$$

The resonant radius of a bubble in an acoustic field can be related to a freely oscillating (not in an acoustic field) bubble. A freely oscillating bubble radius to frequency relation can be describe by equation (8), as noted by [15]. The Minnaert resonance relates the frequency (f) to the polytropic coefficient (κ), ambient pressure (p_0), and fluid density (ρ).

$$f = \frac{1}{2\pi R_0}\left(\frac{3\kappa p_0}{\rho}\right)^{1/2} \tag{8}$$

The Rayleigh-Plesset equation, which describes an oscillating bubble in an acoustic field (7), can be compared to the freely oscillating bubble. The forced bubble given a small applied wave field amplitude assumption yields a resonance frequency of:

$$\omega_0^2 = \frac{1}{\rho R_0^2}\left[3\kappa\left(p_0 + \frac{2\sigma}{R_0}\right) - \frac{2\sigma}{R_0}\right] \tag{9}$$

When surface tension is negligible, equation (9) reduces to equation (8) [8, 11].

Given the assumptions and conditions of an ideal gas ($\kappa \approx 1.4$) and the fluid is 20°C water, the solution between the frequencies of 10 kHz and 10 MHz are shown in Figure 5. This result is compared to the local conditions of Albuquerque, New Mexico ($P_a = 84.2\ kPa$). It can be seen that the change in atmospheric pressure is significant to the resonance diameter.

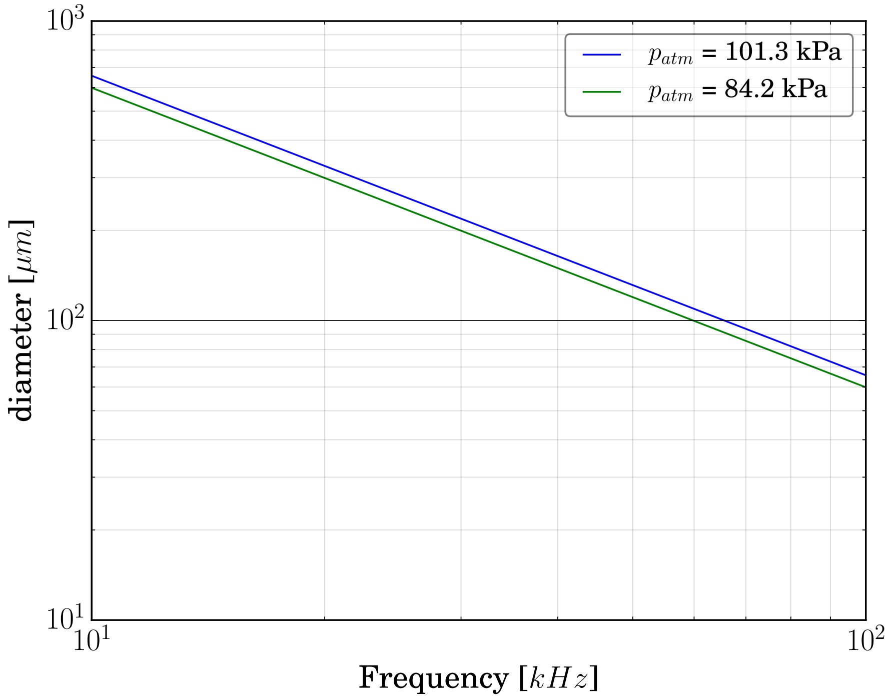

Figure 5: Minnaert Resonance diameters calculated for standard conditions at $p_{atm} = 101.3\ kPa$ and local conditions (Albuquerque, NM $p_{atm} = 84.2\ kPa$)

2.4 Similitude

To show that the current experimental efforts are commensurate to prototypical conditions, scaling arguments were made through the characteristic non-dimensional numbers for mass transfer. As described by Kline [16], similitude can be established by matching non-dimensional numbers and scaling ratios between the prototype and model systems. Scaled model experiments are attractive because they can provide meaningful data at convenient lab conditions when the prototype conditions are difficult to achieve. This has been done successfully for scaled heat transfer experiments supporting the FHR by using Dowtherm A as a surrogate fluid for flibe [17]. In this, and the subsequent work, the key non-dimensional numbers matched were Re, Pr and Nu. For mass transfer, the key non-dimensional numbers that need to be matched are Re, Sc, and Sh. One more non-dimensional number, the Weber number (We) is required to fully describe the behavior, because of the importance of the surface tension forces. The surrogate for mass transfer to match a flibe/tritium system is a mixture of water and glycerol and the liquid and oxygen as the gas [1, 18].

The non-dimensional numbers and parameters will be designated as model (m) and prototype (p). The model will denote that that parameter is for the scaled down glycerol/water mixture and the prototype will denote the FHR conditions for flibe at operating temperature. Note that L is a characteristic length corresponding to D (duct diameter) in equation (1).

$$Re_m = Re_p \rightarrow \frac{U_m L_m}{U_p L_p} = \frac{\nu_m}{\nu_p} = \frac{\mu_m \rho_p}{\mu_p \rho_m} \tag{10}$$

$$Sc_m = Sc_p \rightarrow \frac{\mu_m}{\mu_p}\frac{\rho_p}{\rho_m} = \frac{\mathscr{D}_m}{\mathscr{D}_p} \tag{11}$$

$$We_m = We_p \rightarrow \frac{U_m^2 L_m}{U_p^2 L_p} = \frac{\sigma_m \rho_p}{\sigma_p \rho_m} \tag{12}$$

$$\frac{d_m}{L_m} = \frac{d_p}{L_p} \rightarrow \frac{d_m}{d_p} = \frac{L_p}{L_m} \tag{13}$$

The relations in equations (10), (11), (12), and (13) can be rearranged to find the length and flow velocity relation as shown in equations (14) and (15).

$$\frac{L_p}{L_m} = \frac{\sigma_p \rho_m}{\sigma_m \rho_p} \left(\frac{\mathscr{D}_m}{\mathscr{D}_p} \right)^2 \tag{14}$$

$$\frac{U_m}{U_p} = \left(\frac{L_p \ \sigma_m \ \rho_p}{L_m \ \sigma_p \ \rho_m} \right)^{1/2} \tag{15}$$

The length and flow velocity ratios are shown in figures 6 and 7. Over the range of the FHR operating range, the scaling factor for the length and velocity are about 0.6 and 0.94. This shows that the scaling factor for these experiments are viable models for the prototype FHR conditions.

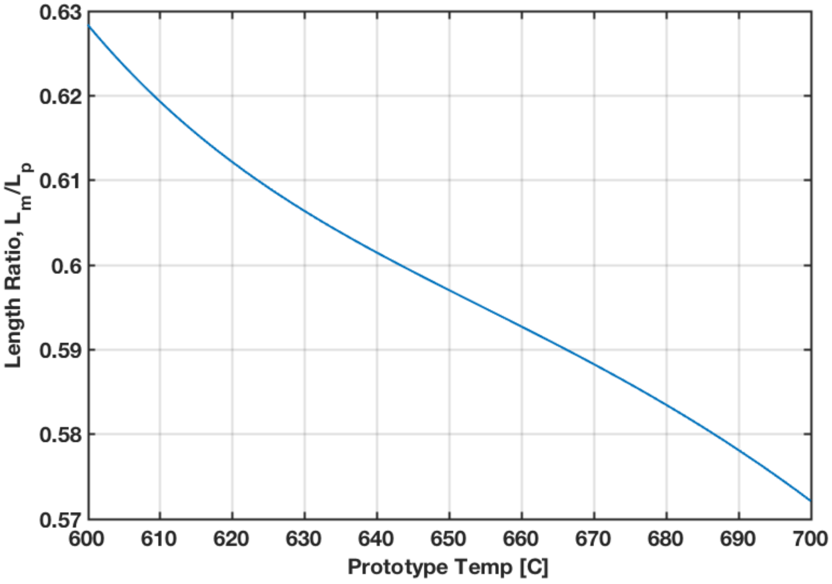

Figure 6: Model to prototype length ratio for the model water/glycerol model with respect to the prototype operating range of the FHR conditions.

The acoustic contribution to mass transfer can be captured by dimensional analysis, even though the specific contributions of each parameter is unknown. The formal method of development of an acoustic non-dimensional number is the Buckingham Pi theorem [19]. This theorem state that given some physically meaningful statement with k variables with the same units as shown in equation (16).

$$u_1 = f(u_2, u_3, ..., u_k) \tag{16}$$

$$\Pi_1 = \phi(\Pi_2, \Pi_3, ..., \Pi_{k-r}) \tag{17}$$

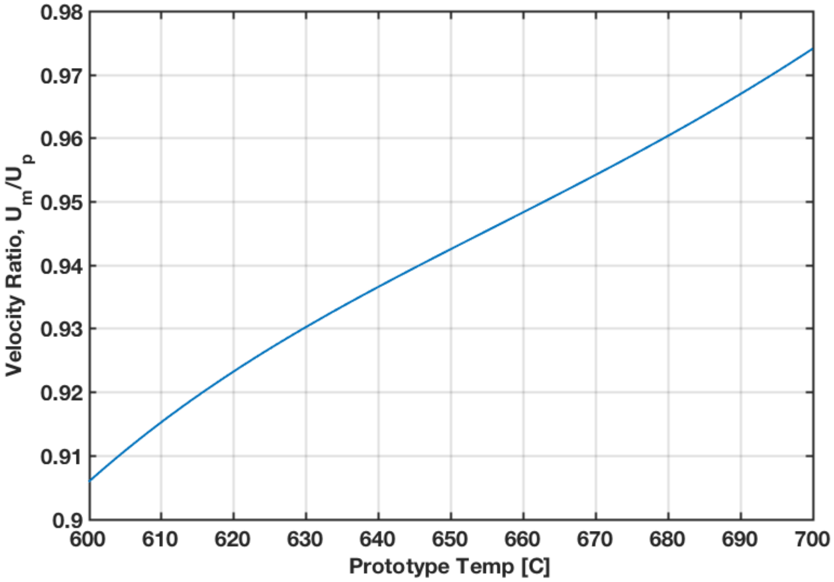

Figure 7: Model to prototype flow velocity ratio for the model water/glycerol model with respect to the prototype operating range of the FHR conditions.

It shows that equation (16) can be rewritten as a set of dimensionless products or "Π terms" as shown in equation (17) where k is the number of variables, r is the minimum number of reference dimensions, $k - r$ is the required number of Π terms, and $\phi(\Pi_2, Pi_3, ..., Pi_{k-r})$ is some function of Π_2 through Π_{k-r}. This method is used in development of an acoustic term for the SUMATRA experiment and is detailed in Rubio's dissertation [20] and the results are reported in Section 3.5.

3 SUMATRA Experiment

The first experiment detailed (SUMATRA) experiment. The goal of the SUMATRA experiment was to build and evaluate a scaled prototype for an ultrasonic sparging cell, which was submitted for archival publication [18]. This investigation began with two exploratory studies. These studies demonstrated applying acoustic energy can tune bubble size and acoustic pulsing is required to ensure bubbles get into the near field. The insights from the exploratory studies were employed in the SUMATRA experiment which had demonstrated initial proof-of-concept of sonomechanically enhanced mass transfer.

3.1 Exploratory Studies

The exploratory studies consist of two exploratory experiments. The first experiment was designed to provide operational knowledge and expertise in using ultrasonics coupled with sparging, as well as to characterize the behavior of ultrasonics and bubbles in a static flow setting. The second experiment was a first attempt at making a laboratory scale mass transfer loop with ultrasound. Subsequently, the SUMATRA experiment was designed and developed.

The purpose of the bubble resonance studies was to investigate the behavior of injected bubbles. The bubbles in an ultrasonic field were expected to maintain a predictable bubble radius [8, 15]. Furthermore, this study is to develop the capabilities needed to produce and visualize bubbles of the appropriate diameter and subject them to an ultrasonic field. The experimental configuration is illustrated in Figure 8 and 9. This configuration gives an acoustic standing wave between the horn and the bottom of the test section. This captured a single acoustic wavelength with the insertion of bubbles on the order of the resonance diameter for 20 kHz.

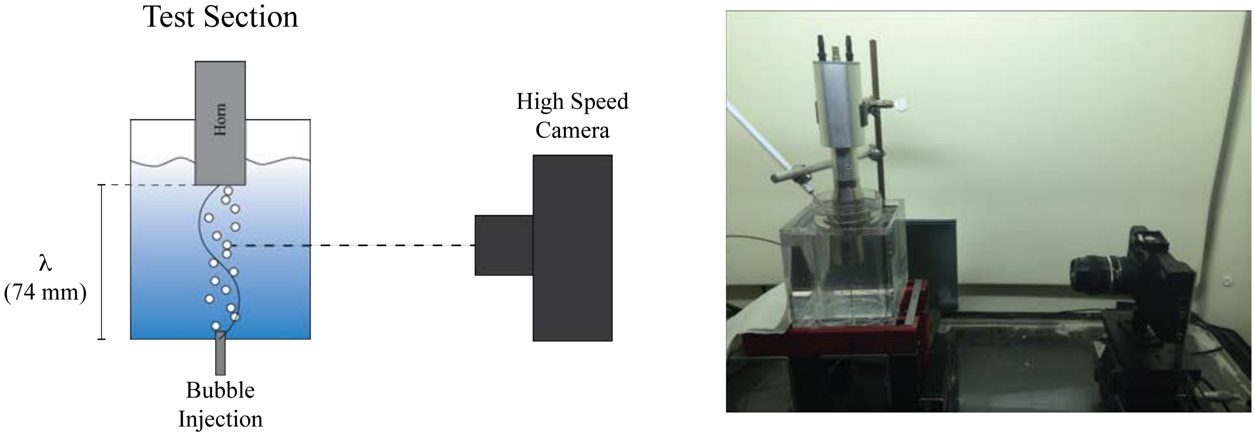

(a)

(b)

Figure 8: Bubble Resonance Experiment: a) Experiment cross section view. b) Side view of the bubble resonance experiment.

The experience was that the bubbles tried to maintain a resonant radius when acoustic energy was applied as shown by Figure 10. The sonicated bubbles oscillated between an estimated 400 μm and 600 μm, which are larger than the calculated resonant diameter of 200 μm. This is understandable because the high speed camera will only record the maximum diameter due to the frame rate restrictions. The camera was only able to reach 5600 fps, much slower than the 20 kHz applied. The key conclusion is that the bubbles will tend to a specific size. This is evident in Figure 10 because of the behavior of the bubbles coalescing and breaking apart around an observed diameter.

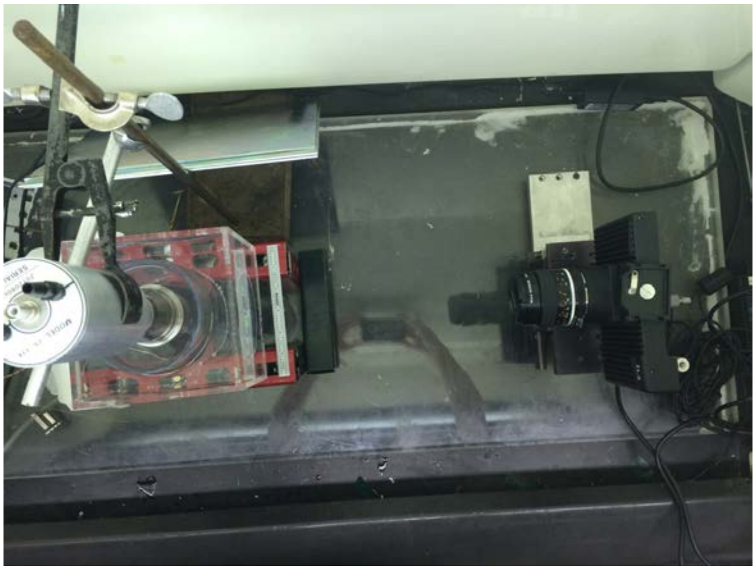

Figure 9: Top View of the bubble resonance experiment.

Using the resonance study platform, an exploratory study to pump bubbles into the near field confirmed that the streaming effect reported in the literature [5, 8, 7, 10, 21, 22] would prevent bubbles from being pushed into the near-field with the supplied pumping power. This is evident in Figure 11 frames C, D, E, and F. These frames show the bubbles are unable to be pumped into the near-field. During the pulsing, the bubbles traveled to nodes which confirms the behavior where a standing waves are able to sort and stratify particles and bubbles as shown in frames D, E, and F of Figure 11.

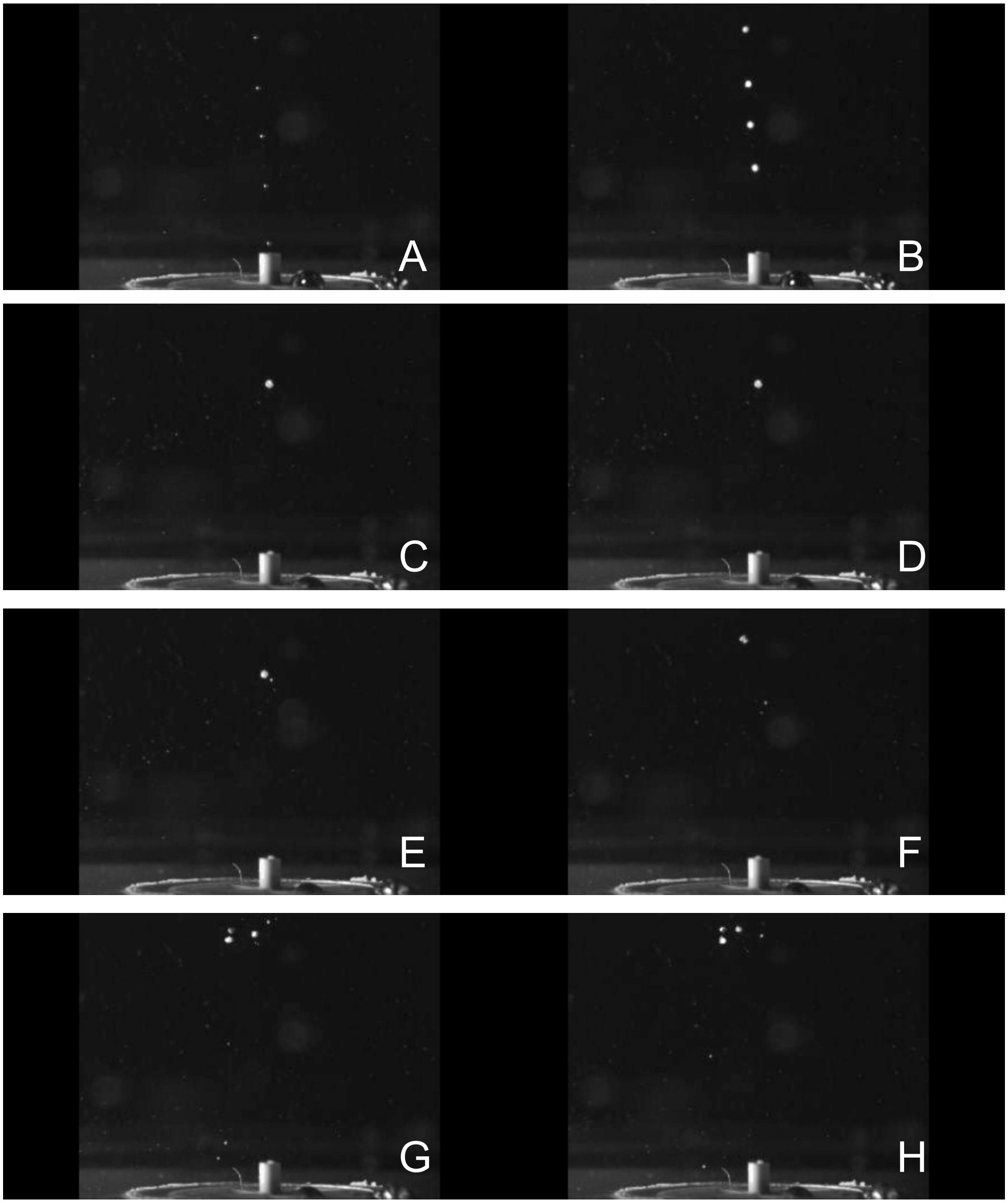

Figure 10: The 12.7 mm (1/2 in) horn is placed 1 wavelength (74 mm) above the bottom of the test section. Frame A shows 4 bubbles before pulsing. Frame B shows the start of the pulse. Frame C shows the bottom three bubbles combine due to acoustic forces and continues to grow through frames F. Frames G and H show bubbles hovering, breaking apart, and re-coalescing.

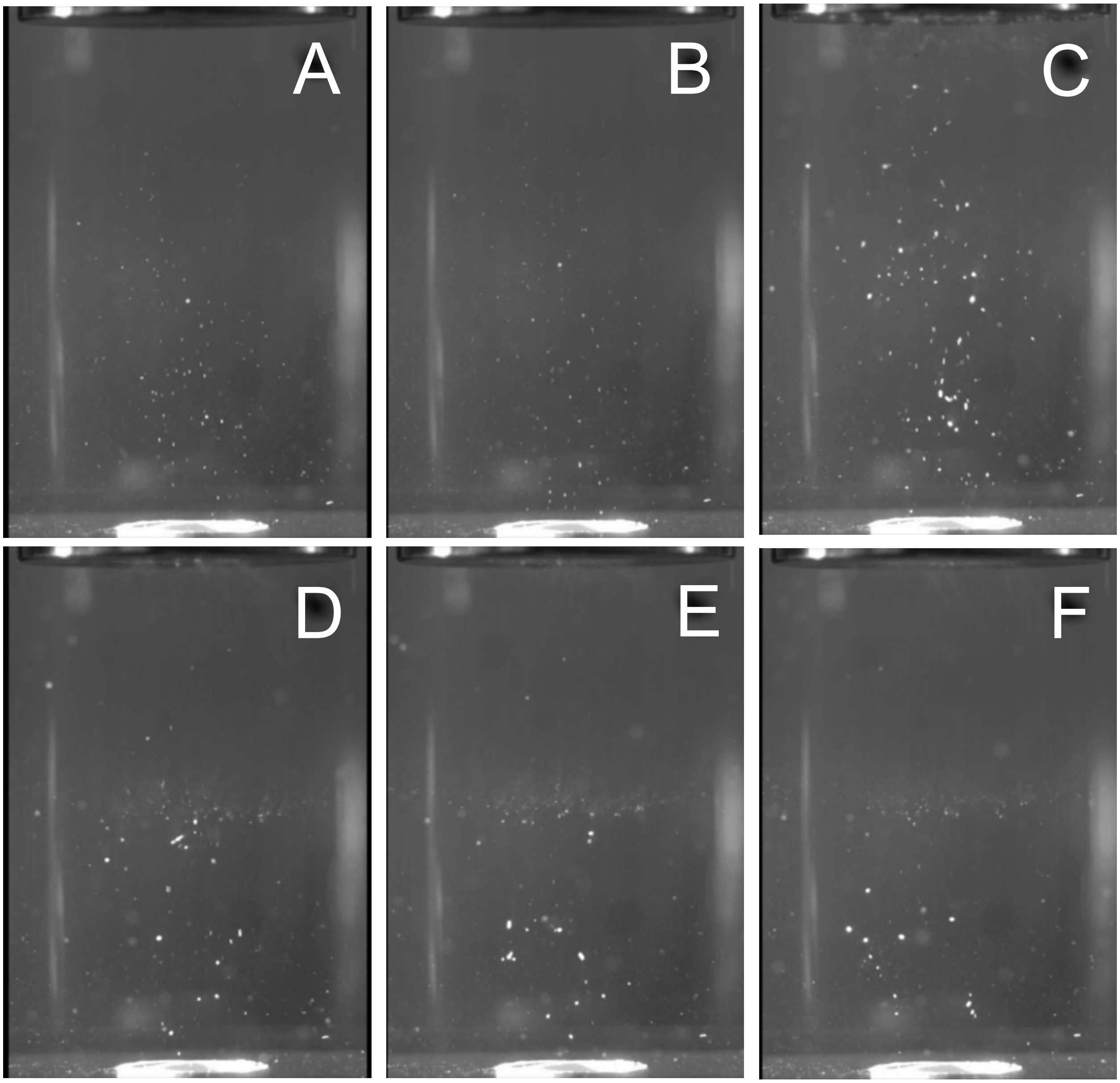

Figure 11: The 47.6 *mm* (1.875 *in*) horn is situated 1 wavelength (74 *mm*) above the bottom of the test section with bubbly flow being pumped up towards the horn. Frame A and B show bubbly flow before the ultrasonic pulse. Frame C shows the start of the pulse. Frame D through F show the streaming region under the horn to half the wavelength. At half the wavelength, there is a node where small bubbles congregate. At 3/4 wavelength, there is an anti-node where bubbles oscillate around.

The next exploratory study was a flowing fluid study provided insight into the relationships between ultrasonic energy, two-phase flow, and DO concentration. This experiment was designed to have a significant increase in pumping power and fluid volume. The loop consisted of a venturi bubble injector, ultrasonic test section, cyclone separator, variable frequency pump, cooler, thermocouples, and dissolved oxygen (DO) probe, as shown in Figure 12. The pumping power was increased to force bubbles into the near-field of ultrasonics, and the inlet piping was sized so the horn covers most of the pipe area in order to ensure bubbles will impinge into the face of the horn, as shown in Figure 13.

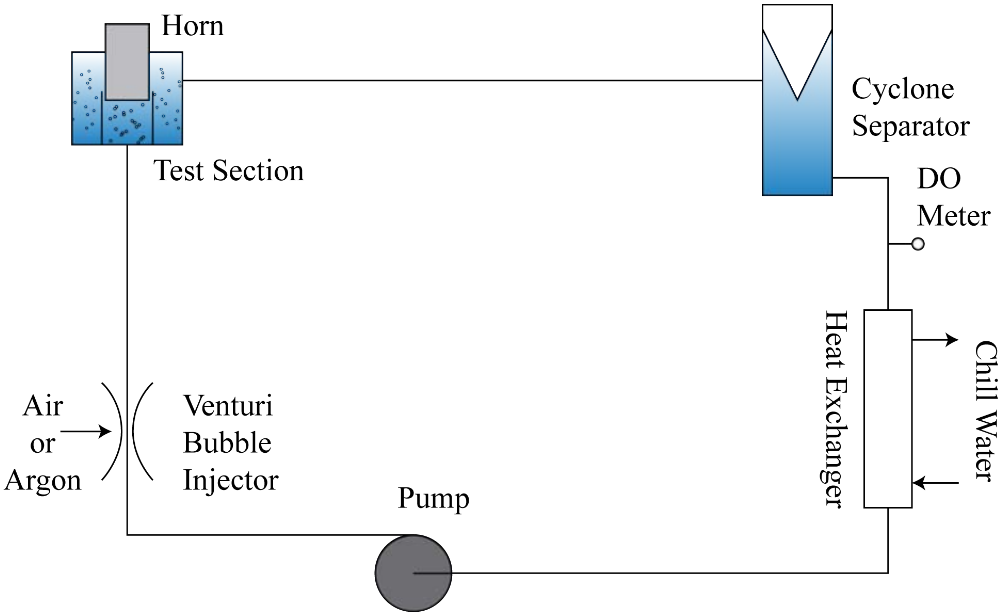

Figure 12: Schematic of the Flowing Fluid Study loop.

Figure 13: Flowing fluid study test section with no bubbles. It is possible to see how the flow must pass by the ultrasonic horn and how small the flow cross section is past the horn

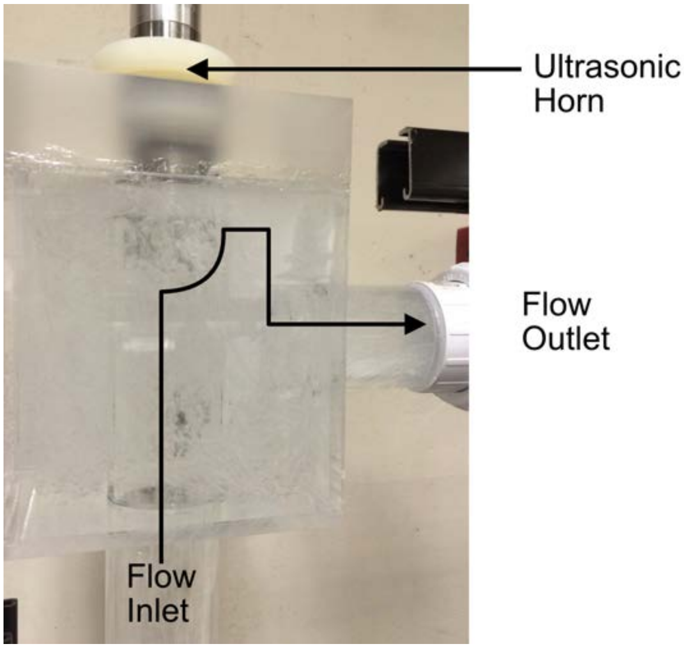

Figure 14: Rev 2 with bubbly flow. Flow direction is highlighted.

The operation of this loop was to first cool the fluid to $5°C$ in order to increase the oxygen saturation concentration, then strip the DO with an inert gas, Ar. The liquid flow rate range of the experiment was 18.9 LPM to 26.5 LPM (5 GPM to 7 GPM), and the gas injection rate was 0.24 LPM (0.5 $SFCM$). The experiment did not produce the desired effects. While watching the bubble flow interact with the ultrasonic near-field, it was apparent that the bubbles were not being pushed into the near-field. Figure 14 shows the preferred flow path of bubbles, which bypasses the near-field. The horn that was used was the 47.6 mm diameter horn. The estimated intensity of this horn was 0.085 W/cm^2 which is defined as the power supplied to the horn from the drive divided by the area of the horn face. The results from this experiment is shown in Figure 15. All runs comparing the DO vs time with and without ultrasonics overlapped within the error of the DO meter (0.4 mg/ml).

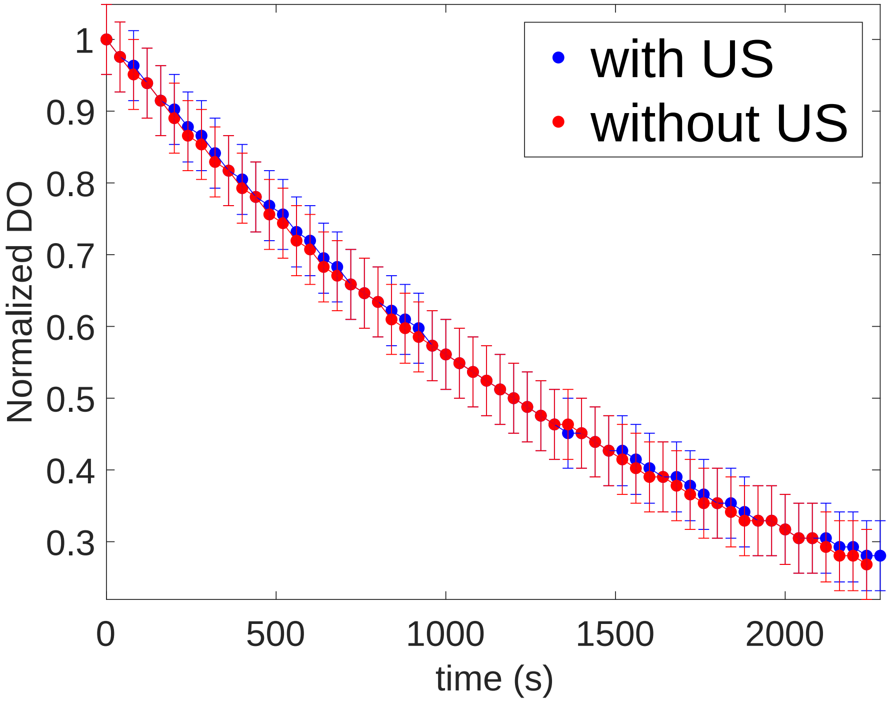

Figure 15: Typical results from the flowing fluid study. The control and ultrasonic runs overlap consistently.

Although these results did not show an increase in mass transfer, these observations were key to the design of next iteration of this study. It was observed that bubbles would not enter the ultrasonic near-field. Due to the higher flow rates, the convective contribution to mass transfer would have been so large that any contribution of ultrasonics were being masked. These conclusions pointed to the need for a smaller experiment that would minimize the contribution of convective mass transfer and isolate the contribution of sonomechanically enhanced mass transfer.

3.2 SUMATRA Experimental Description

The configuration of the SUMATRA loop was bench top scaled to the flowing fluid studies loop. The flow loop consisted of a pump, capillary tubes for bubble injection, thermocouples, a DO sensor, cyclone separator, a heat exchanger, and a flow meter. It also operated by cooling and oxygen saturating the fluid, then strip the DO with and without ultrasonics. A schematic of the experiment reflecting both the low intensity and high intensity experiments is shown in Figure 16 and 17, respectively.

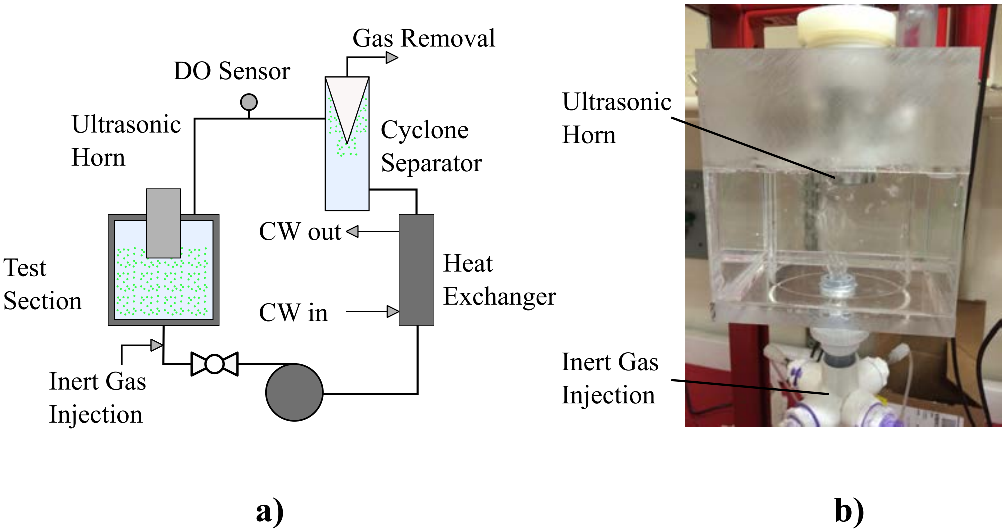

Figure 16: a) Schematic of the SUMATRA experiment with low intensity test section. b) SUMATRA test section with low intensity horn (47 *mm* diameter).

The results split for the two tests performed on this platform. The low intensity test is presented in Section 3.3, and the high intensity test is presented in Section 3.4.

3.3 Low Intensity Test

The DO stripping results are shown in Figure 18. These results are the raw, normalized average data 9 runs, and only demonstrate a marginal increase in performance of an approximately 20% reduction in degassing time. Because, as noted earlier, bubbles could not be pumped into the near field, ultrasonic pulsing was utilized. The visual data that bubbles were in the near field due to the pulsing. The bubbles that were in the near field remained inside the near field and demonstrated a "wicking" behavior. An example of the visual data is shown in Figure 19.

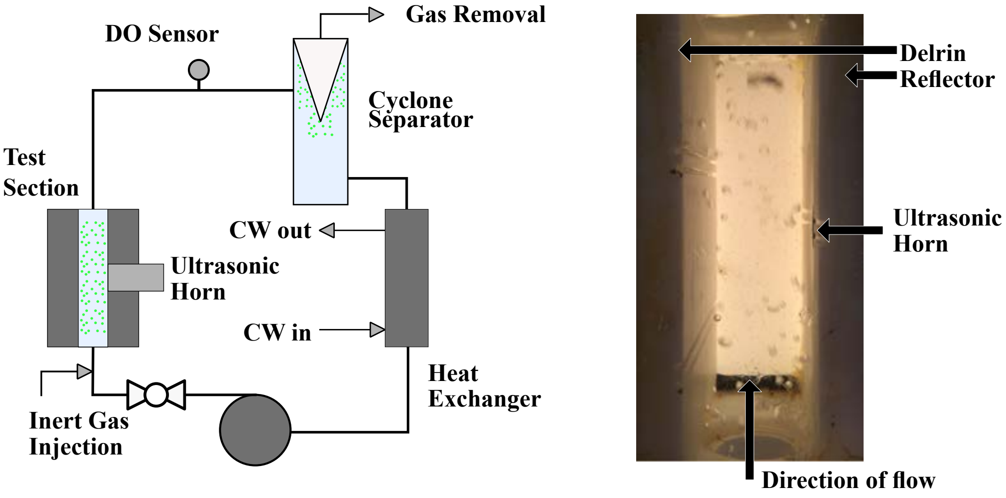

a) b)

Figure 17: a) Schematic of the SUMATRA experiment with high intensity test section. b) SUMATRA test section with high intensity horn (12.7 mm diameter). Dimensions: Height = 116 mm, Width = 28 mm, Depth = 83 mm.

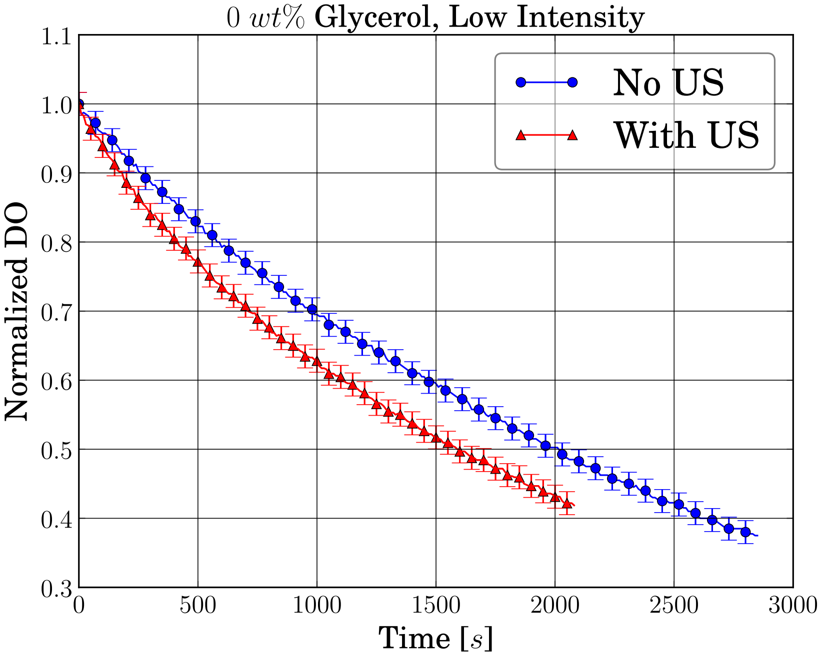

Figure 18: Results of the low intensity testing.

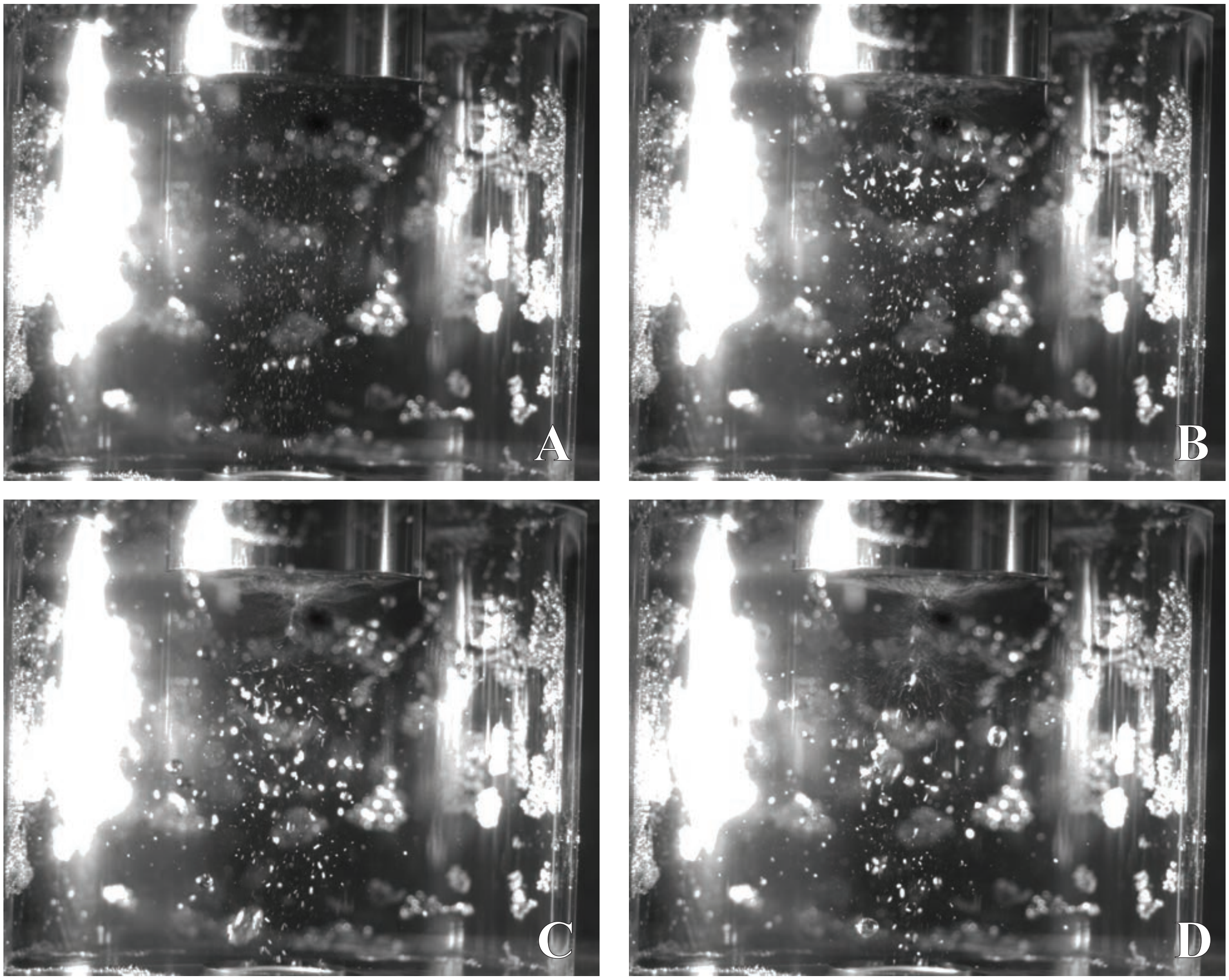

Figure 19: Visual results from the low intensity SUMATRA experiment. Frame A shows bubbles in the test section without ultrasonics applied. Frame B shows the instant the ultrasonics pulses on with bubbles trapped into the near field. Frame C shows the beginning of the wicking behavior near the horn face. Frame D shows the lasting structure of the wicking filaments and the attracting of bubbles and gases into the filament.

3.4 High Intensity Test

As mentioned before, these were first performed with water, and because the results were favorable, the experiment was continued with water and glycerol mixtures which encompass the Sc of flibe at normal operating temperatures for the FHR. From the normalized DO data from each of the runs, the volumetric mass transfer coefficient, k_La, can be calculated. The basic model of changes in concentration is equation (18). The solution for k_La is the slope of equation (19). The DO results are shown in Figure 20. From these data k_La can be obtained by using equation (19), and these data are shown in relation to glycerol concentration in Figure 21. To evaluate of mass transfer performance, the experimental Sh and mass transfer coefficient (k_L) will be determined, and a Sh correlation will be developed. The experimental Sh function is shown in equation (20).

$$\frac{dC}{dt} = k_La(C^* - C) \tag{18}$$

$$-\ln\left(\frac{C_1}{C_2}\right) = k_La(t_2 - t_1) \tag{19}$$

$$Sh = \frac{k_La}{a}\,\frac{D}{\mathscr{D}} \tag{20}$$

Visual results show a much different behavior in terms of bubbles interacting with the near-field of the ultrasonics. Figure 22 shows an example of the visual data taken for each glycerol concentration without ultrasonics, and Figure 23 shows an example of what is seen when ultrasonics is applied. Although it is difficult to see through pictures, the high speed camera footage in Figure 23 shows, that bubbles do get swept into the near-field and do not avoid the ultrasonics. Also, the footage shows that the bubbles that do get entrained into the near-field do get broken up into smaller bubbles. Another observation was that was made was there was more circulation and movement compared to the low intensity standing wave design.

In order to calculate the k_L from the k_La, the interfacial area (a) must be determined [23]. Classically, interfacial area is found by using equation (21). This was attempted, but due to the equipment limitations in terms of optical resolution, the individual bubble diameters were not able to be directly measured. This attempt to measure bubble diameters directly was performed by using a combination of image processing software (Affinity Photo) and imageJ [24]. The analysis of the visual data concluded that the resolution on the high speed camera was not sharp enough to give the bubble sizes accurately. The limit of the visual resolution was on the order of 100 $\mu m/pixel$. Another way of inferring interfacial area was found in the work by Kress [1] where the interfacial area can be determined through the holdup (ε) and the bubble number density (N) as shown in equation (22). Although the direct measurement of bubble diameter was impractical, the bubbles were still able to be

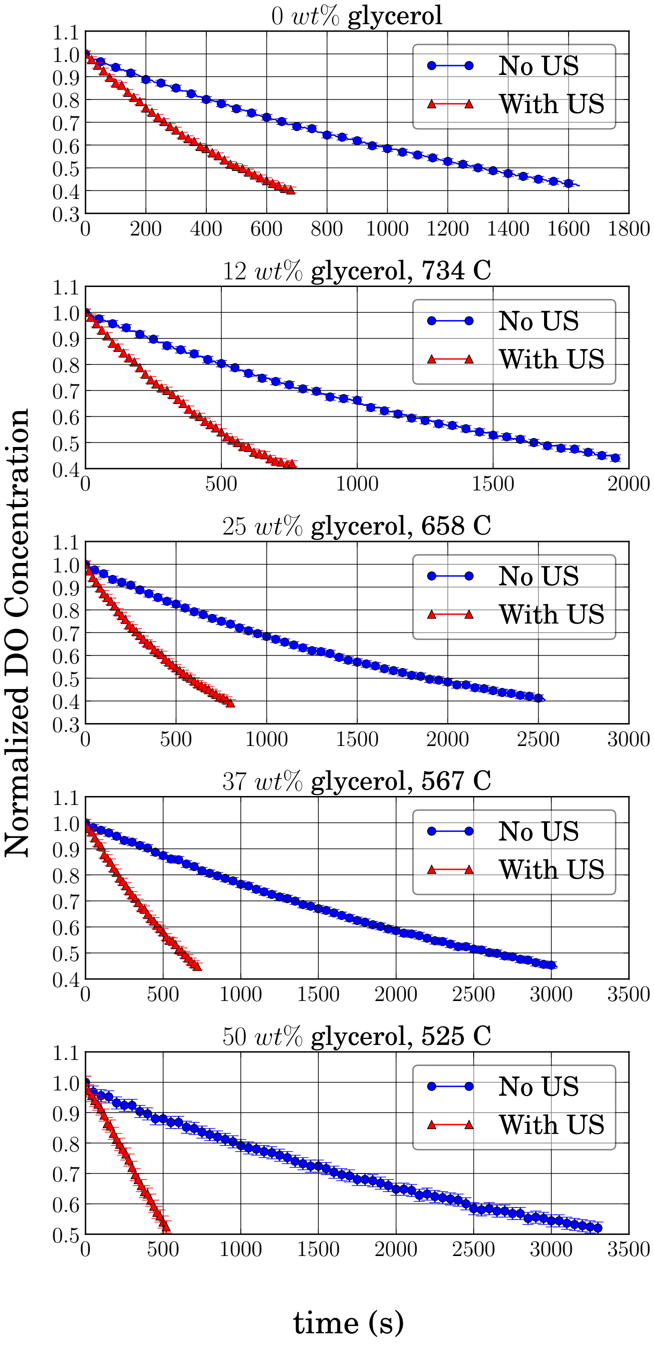

Figure 20: DO data for the SUMATRA experiment. Glycerol concentrations are matched with the corresponding flibe temperatures. The 0 $wt\%$ has no corresponding flibe temperature.

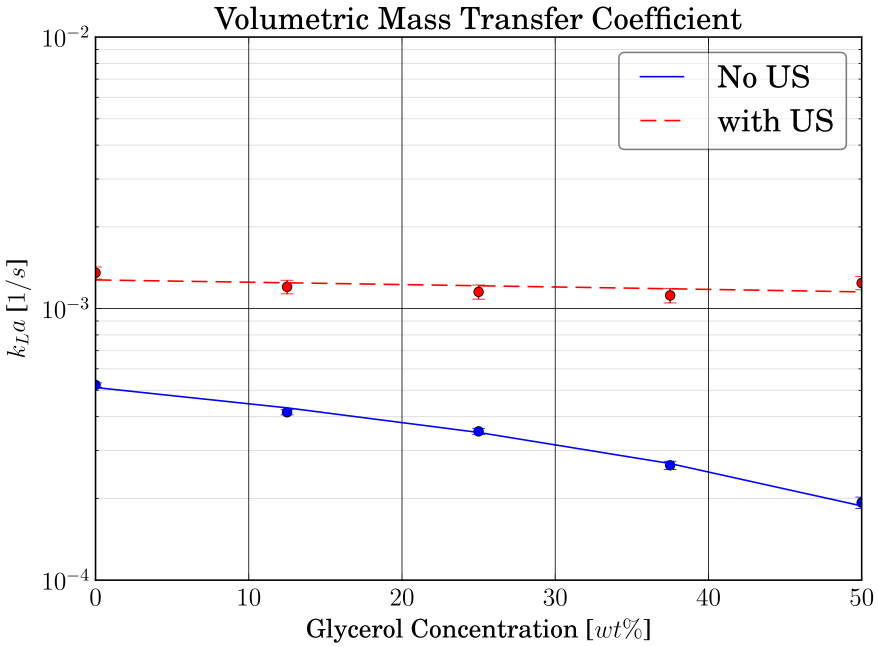

Figure 21: Volumetric mass transfer coefficient comparison.

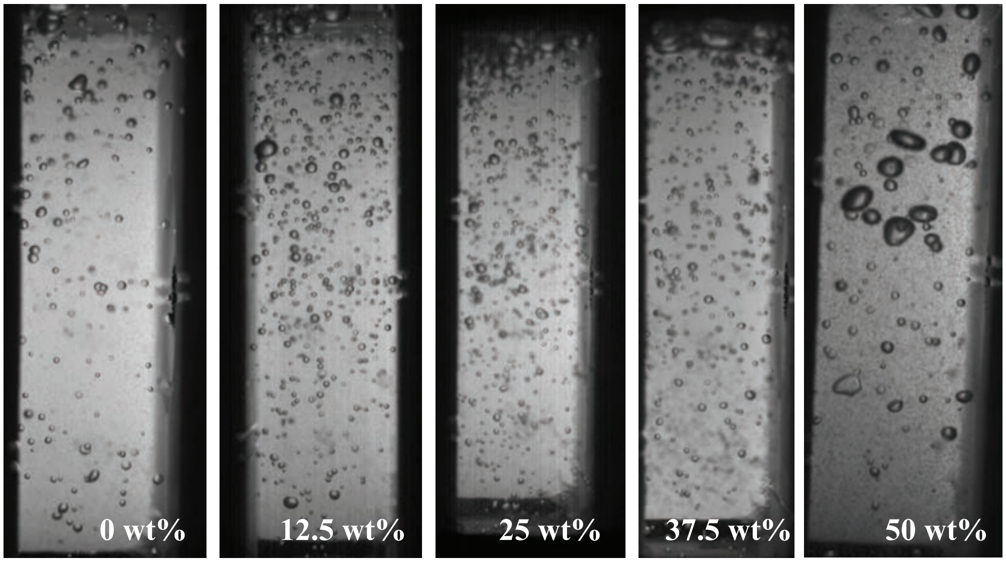

Figure 22: SUMATRA high intensity test section with no ultrasonics. This is an example of the visual data used for bubble measurements and counting.

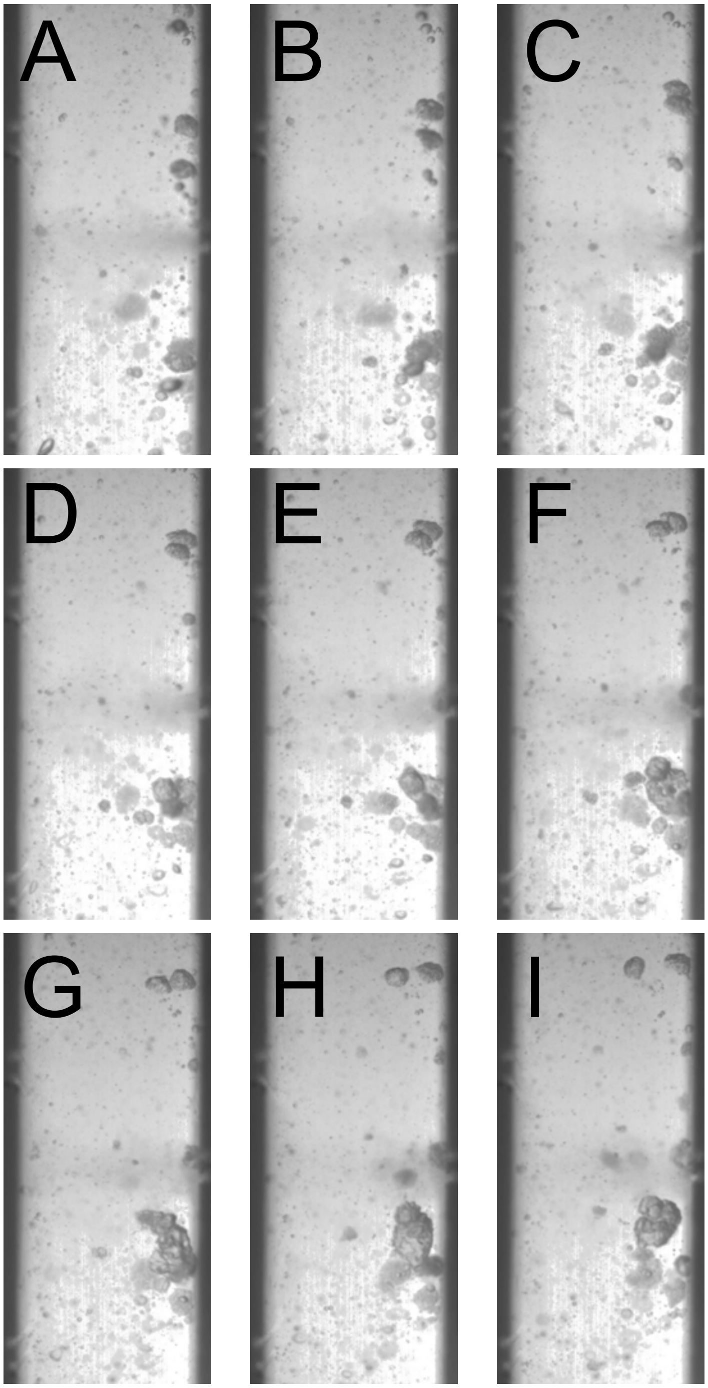

Figure 23: SUMATRA high intensity test section during enhanced DO stripping. It shows increased convection and bubble breakup, which was not seen in the low intensity test section for each glycerol concentration.

counted visually, making use of this relationship a viable method to determine interfacial area given the limitations of the laboratory equipment. This method is discussed in more detail in the Rubio's dissertation [20]. The results of direct diameter measurement and the diameter inference analysis are shown in Figure 24 and included in the results of interfacial areas. The average bubble diameters can also be determined by the relationship given in equation (23). These data are also included for reference. For the sonomechanically enhanced runs, equation (21) was used to determine interfacial area under the assumption that the resonance radius is the average bubble diameter. In this case, the resonance radius [8, 15] is calculated using equation (24). The interfacial areas can be compared and these data are given in Figure 25. This shows that the measured ultrasonic interfacial area and the expected interfacial area agree within an order of magnitude.

$$a_{classic} = \frac{6\varepsilon}{d_{avg}} \tag{21}$$

$$a_{inferred} = \frac{3}{2}\left(\frac{6\pi}{4}\right)^{2/3} N^{1/3}\varepsilon^{2/3} \tag{22}$$

$$d_{avg} = 2\sqrt{\frac{\sigma}{g\Delta\rho}} \tag{23}$$

$$d_{res} = \frac{1}{\pi f}\sqrt{\frac{3\kappa p_0}{\rho}} \tag{24}$$

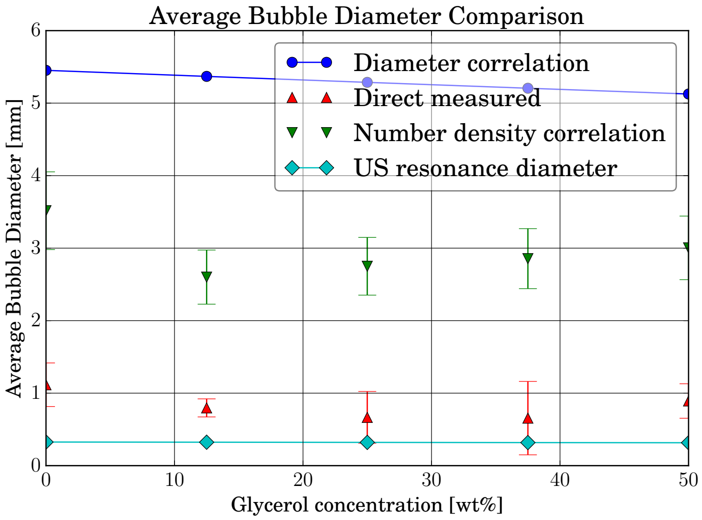

Figure 24: Comparison between correlated, directly measured, inferred, and ultrasonic resonance diameters

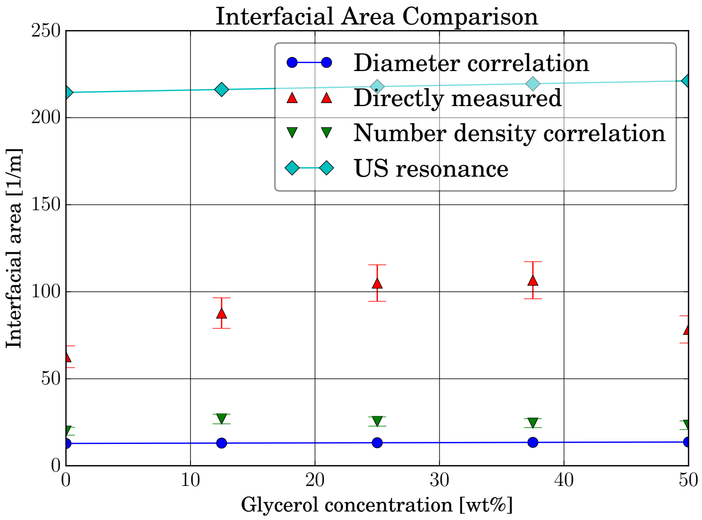

Figure 25: Comparison of correlated, directly measured, inferred, and ultrasonic interfacial areas

The experimentally determined Sh numbers are shown and compared with to the established correlation reported in the literature and the data are given in Figures 26 and 27. The experimental k_L results are shown in Figures 28 and 29. The results suggest that the lower the Sh, the better the performance. This was counter to the initial hypothesis because the introduction of ultrasonics was expected to increase the convective mass transfer component. The comparison with the experimental data and the established correlation from equation (1), shows a closeness in the form of the relationship and it would appear that the correlation can be scaled to match the SUMATRA experimental conditions.

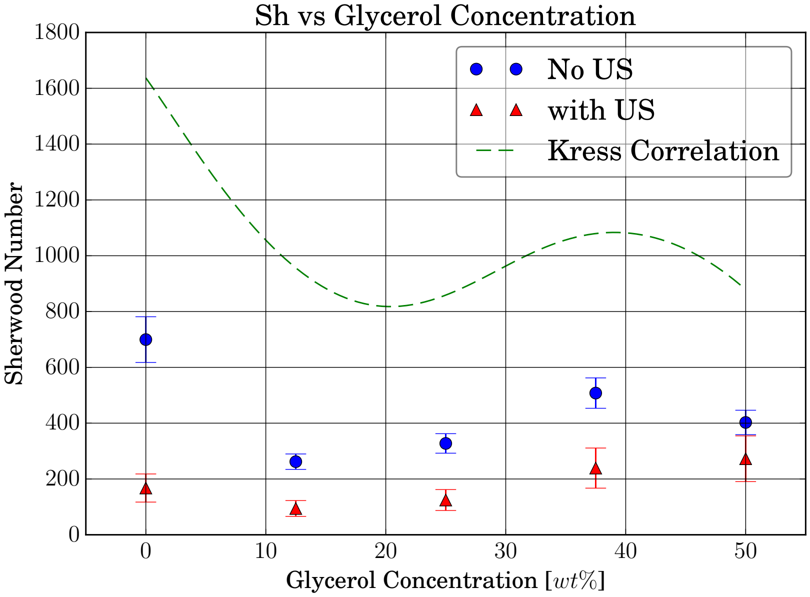

Figure 26: Sherwood number comparison to equation (1) correlation.

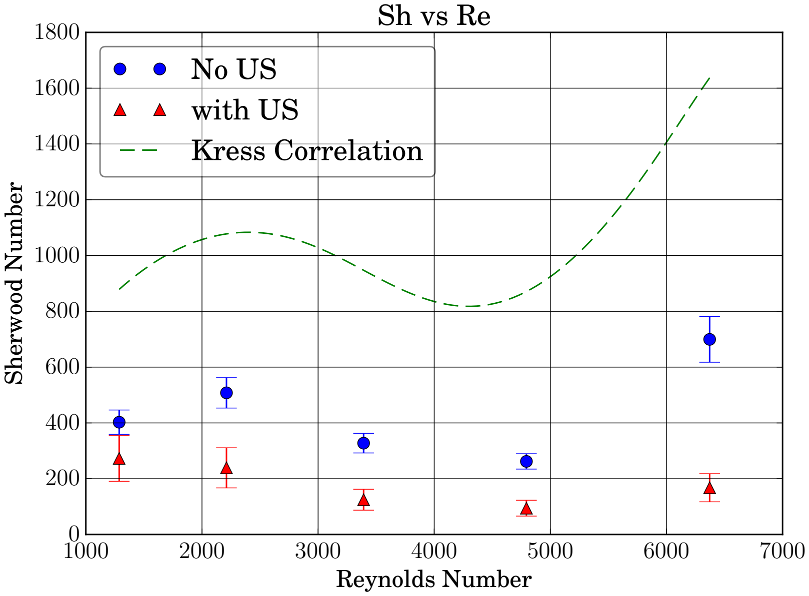

Figure 27: Sherwood number comparison to equation (1) correlation.

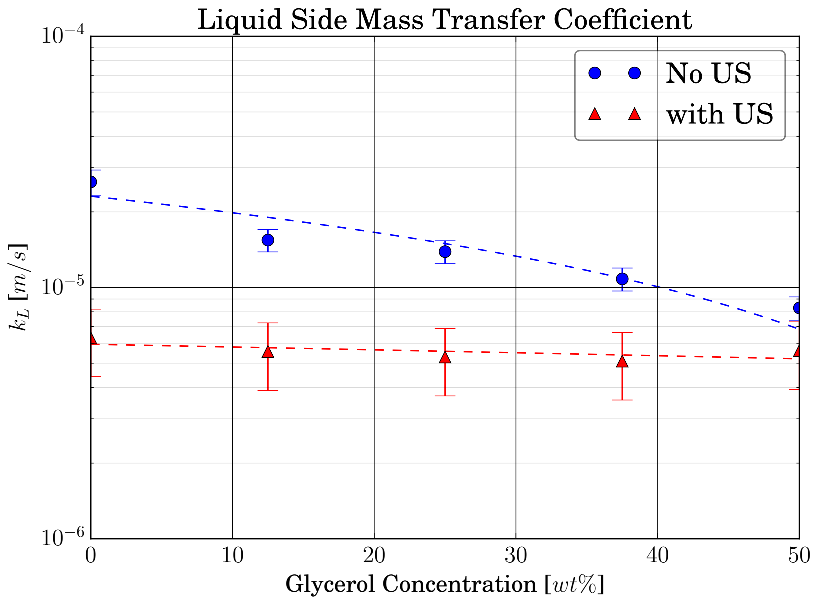

]

Figure 28: Liquid side mass transfer coefficient vs glycerol concentration.

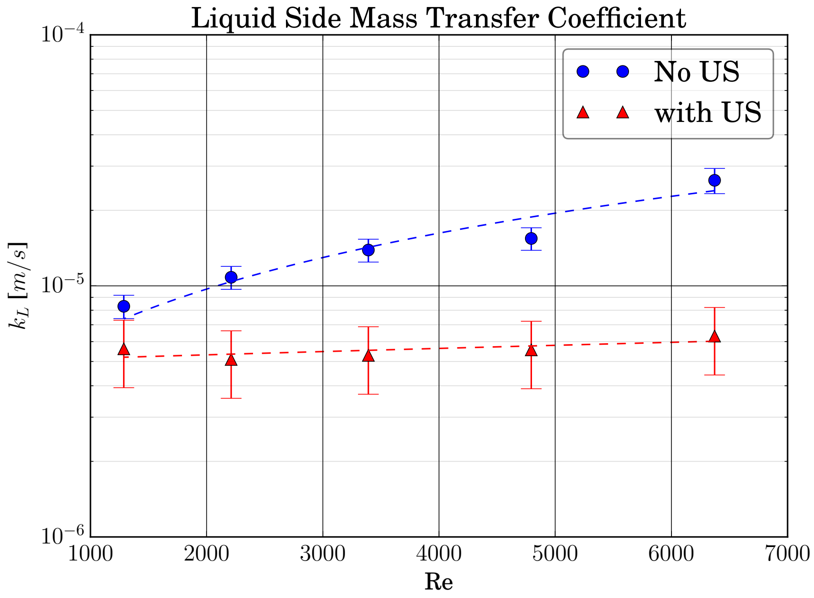

Figure 29: Liquid side mass transfer coefficient vs Re number.

In Perry's Engineer's handbook [25], the Sh correlation for sparging concurrent to flow is in the form of equation (25), and the constants and exponents were previously found to be (1). In order to fit the correlation to the SUMATRA data, a least squares optimization was performed using the leading coefficient (C) and Re exponent (x) as variables. This yielded equation (26). In an attempt to predict the Sh for ultrasonic enhancement to a first approximation, the resonance diameter was used in equation (26). This result gives a measure of the predicted ultrasonic enhancement. These results are shown in Figures 30 and 31. Looking at the ultrasonic predicted results do not accurately follow the experimental data. This suggests that an acoustic term must be developed to capture the ultrasonic contribution.

$$Sh = C\ Re^{x} Sc^{y} \left(\frac{d}{D}\right)^{z} \tag{25}$$

$$Sh = 0.28\ Re^{0.86} Sc^{1/2} \left(\frac{d}{D}\right)^{1.0} \tag{26}$$

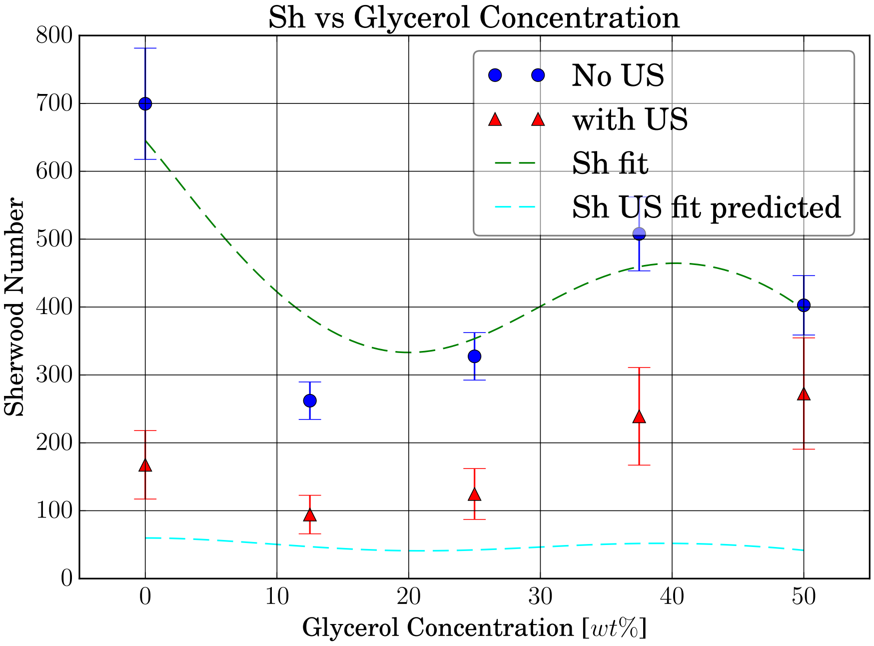

Figure 30: Sherwood number vs glycerol concentration

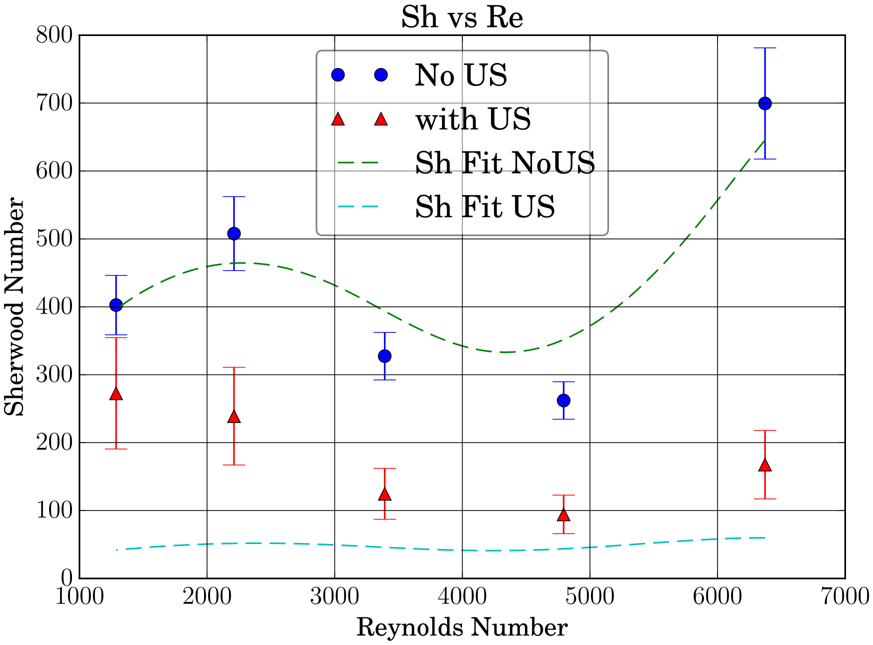

Figure 31: Sherwood number vs Re number

3.5 Acoustic Correlation

The construction of the ultrasonic portion of the Sh correlation utilized the Buckingham Pi theorem. The first step was to identify important acoustic parameters that would have an effect on the mass transfer. These parameters are listed in Table 1. These terms were selected because of its importance to the acoustic interaction. Intensity was selected because of the direct relation of energy to the mass transfer enhancement. Specifically applied intensity was chosen because this parameter is known. Horn impedances were selected to take into account the transmission phenomenology. The residence time takes into account the interaction time. Finally, the number density and frequency take into account the physical dimensions of the bubbles in the two-phase flow. Also, the presence of the bubbly flow will add some additional acoustic impedance, which can be superficially captured. The correlation form is shown in equation (27). The experimental data was fitted to the form, which yielded the following correlation shown in equation (28) [20].

Table 1: Selected Acoustic Parameters

Parameter	Term	Units
Intensity applied	I	W/m^2
Frequency	f	Hz
Horn acoustic impedance	Z_1	$Pa\ s/m^3$
Liquid acoustic impedance	Z_2	$Pa\ s/m^3$
Residence time in ultrasonic volume	τ	s
Number density of bubbles	N	$1/m^3$

$$Sh = C\ Re^w Sc^x \left(\frac{d}{D}\right)^y \left(\frac{f}{I^{1/2}\ N^{1/3}} \frac{Z_1}{Z_2^{1/2}}\right)^z \tag{27}$$

$$Sh = 1.62 \times 10^{-6}\ Re^{0.31} Sc^{0.5} \left(\frac{d}{D}\right)^1 \left(\frac{f}{I^{1/2}\ N^{1/3}} \frac{Z_1}{Z_2^{1/2}}\right)^{1.47} \tag{28}$$

The correlation fits the experimental data well within the experimental error as seen in Figure 32. In order to test the mechanistic performance a sensitivity study was performed by perturbing the key acoustic parameters. A sensitivity study was performed on the developed correlation. This study is reported Rubio's dissertation [20].

3.6 SUMATRA Conclusions

This SUMATRA experiment demonstrated the proof-of-concept that high power ultrasonics can sonomechanically enhance sparging mass transfer over a range of Sc that encompass the

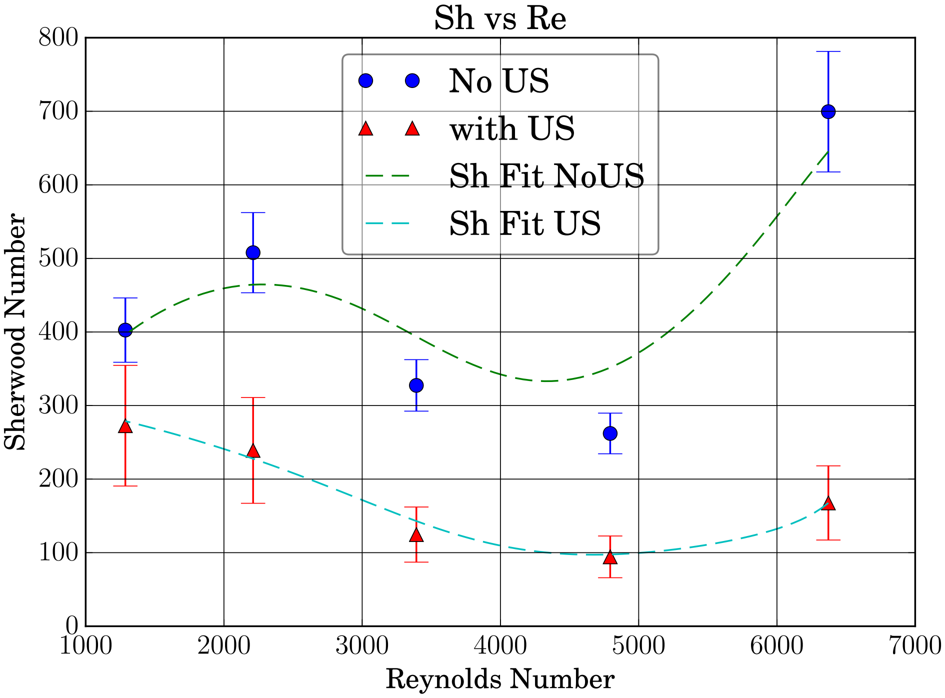

Figure 32: Experimental *Sh* for both ultrasonic and non-ultrasonic SUMATRA conditions with the developed ultrasonic and non-ultrasonic correlations.

operation temperatures of the FHR. There are some challenges that should be addressed while in the scaled experiment level of this investigation. Due to the high intensity of the ultrasonics, excessive wear occurred on the horn tip. The supplied horn from Sonics and Materials was a titanium alloy (Ti-6Al-4V). To illustrate this, Figure 33 shows a comparison of a new horn and the horn used in the SUMATRA experiment. The subsequent study will attempt to address this erosion, and the viability of employing commercial-off-the-shelf components.

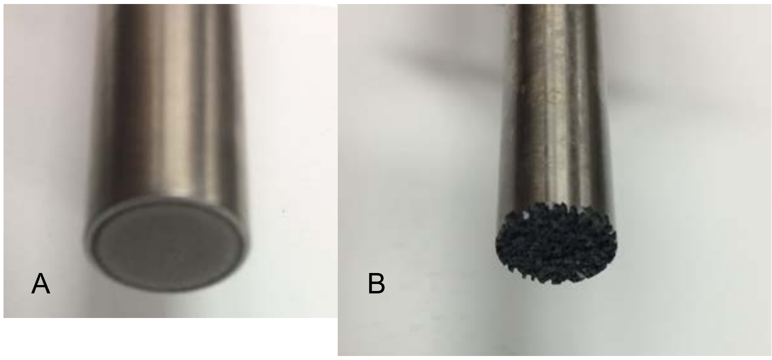

Figure 33: Comparison ultrasonic horn tips. Tip A was only used in low power applications and is relatively pristine. Tip B was used for the high power SUMATRA experiments and is very visibly eroded.

4 PULST Experiment

The Prototype Ultrasonic Mass Transfer (PULST) Experiment was designed to be a scaled-up version of the SUMATRA experiment which would investigate techniques that would make sonomechanical enhancement of sparging an attractive option to manage tritium removal from FHR salt. The objectives of this experiment was to address the horn erosion that SUMATRA had demonstrated and to investigate the viability of utilizing commercial-off-the-shelf (COTS) components for "indirect" sonication.

The notional diagram PULST loop is shown in Figure 34 and the loop is shown in Figure 35. It is of similar design as the SUMATRA loop and is constructed using clear and white 1″ schedule 40 PVC. The operation, similar to the SUMATRA loop, was to saturate the volume with oxygen and subsequently strip the DO with argon with and without sonomechanical enhancement. The important differences between the SUMATRA and PULST experiments are the test section geometry, bubble separator strategy, and bubble injection mechanism.

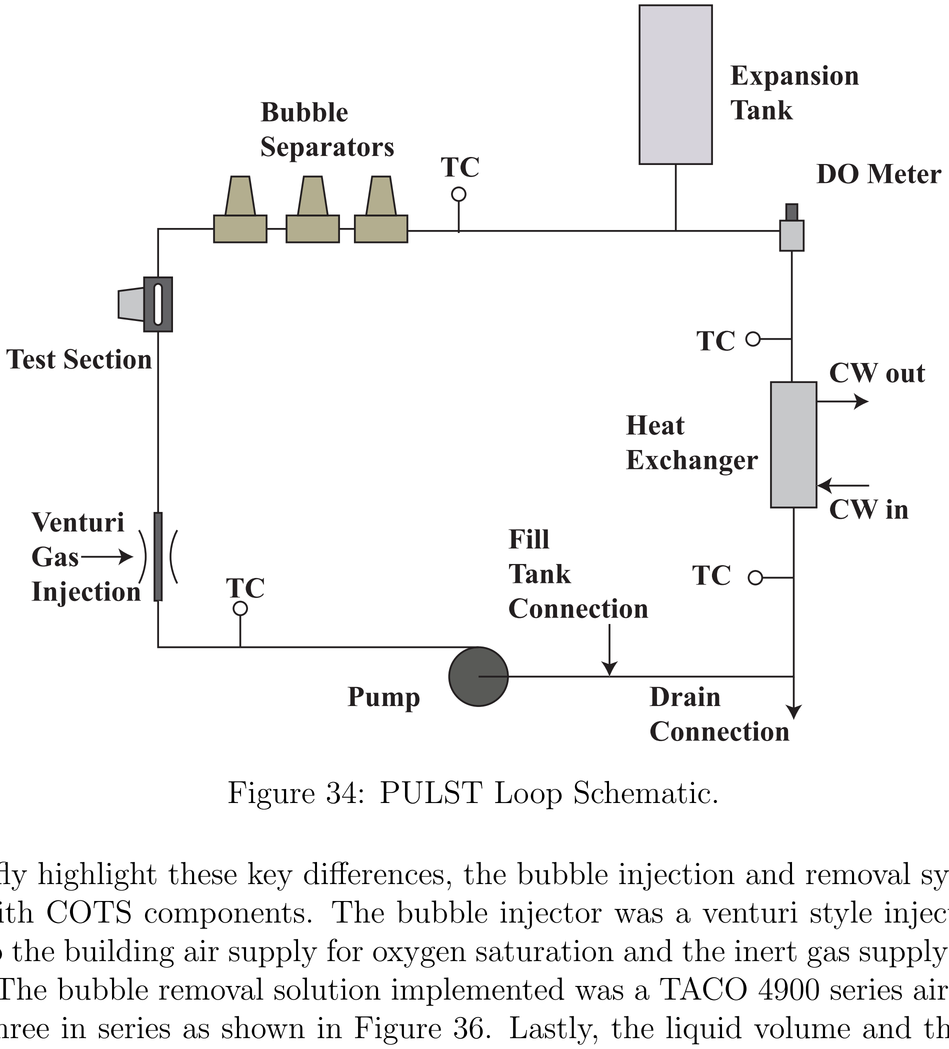

Figure 34: PULST Loop Schematic.

To briefly highlight these key differences, the bubble injection and removal systems were replaced with COTS components. The bubble injector was a venturi style injector. It was attached to the building air supply for oxygen saturation and the inert gas supply for oxygen stripping. The bubble removal solution implemented was a TACO 4900 series air separators arranged three in series as shown in Figure 36. Lastly, the liquid volume and the pumping power was increased from the bench top SUMATRA experiment.

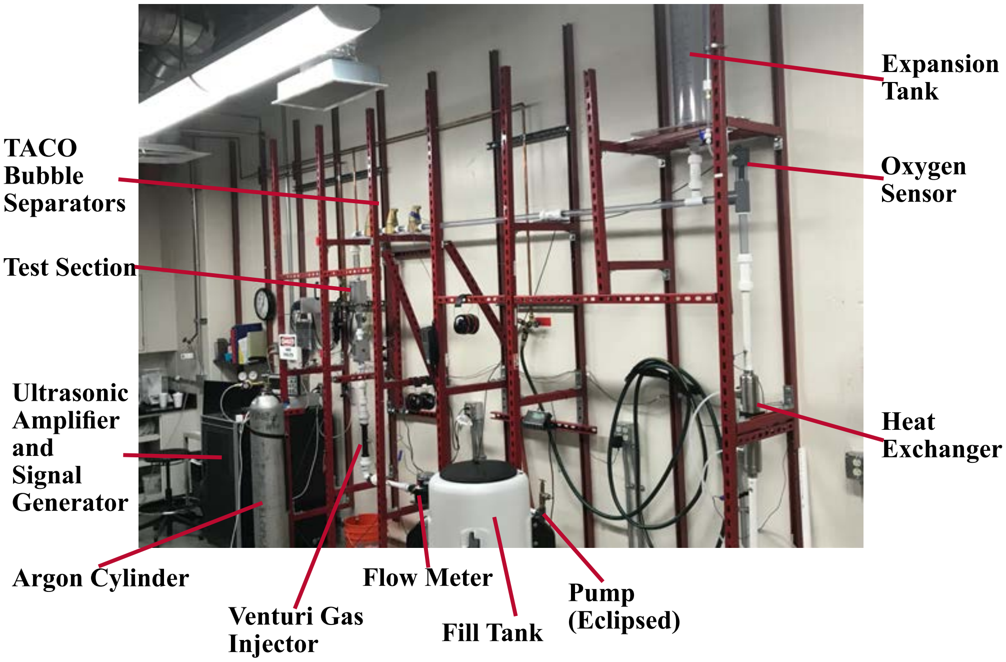

Figure 35: PULST Loop.

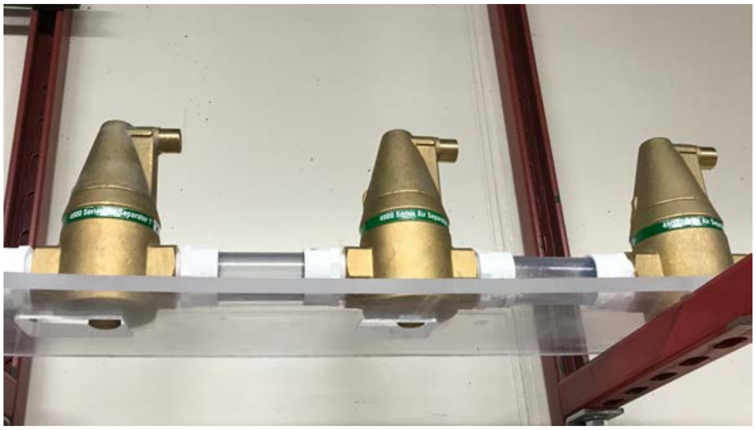

Figure 36: The set of TACO 4900 bubble separators installed in series.

4.1 PULST Test Section

There were two test sections fabricated for this study. The both test sections were of aluminum construction with visual ports. They were designed to accommodate 120 W STEm-INC acoustic transducers. The first test section was designed for two match the flow area of a 1″ schedule 40 pipe and allow flow to fully develop when the ultrasonic energy is applied.

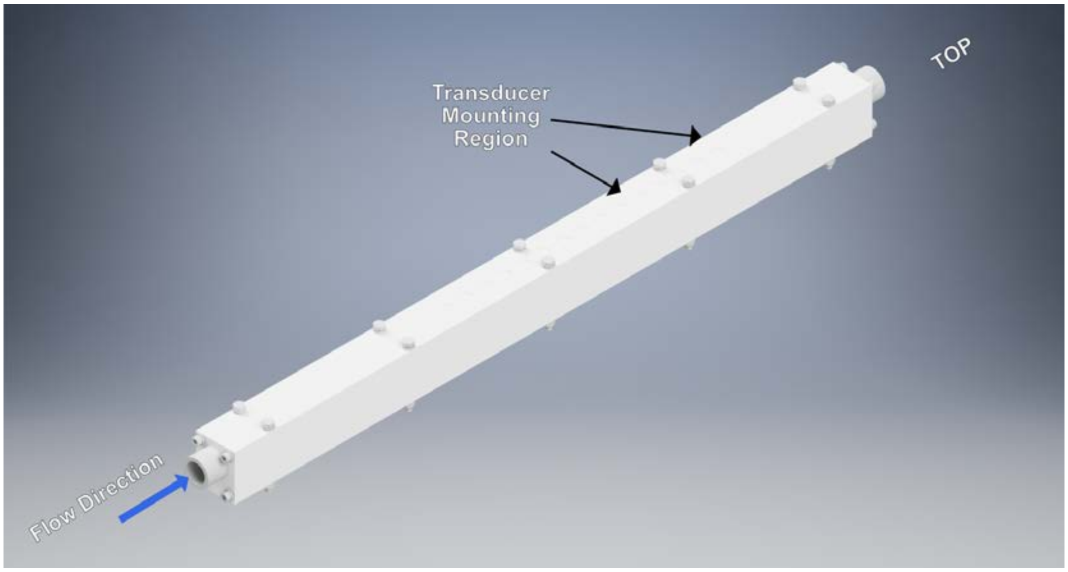

Figure 37: Notional CAD rendering of the PULST long test section.

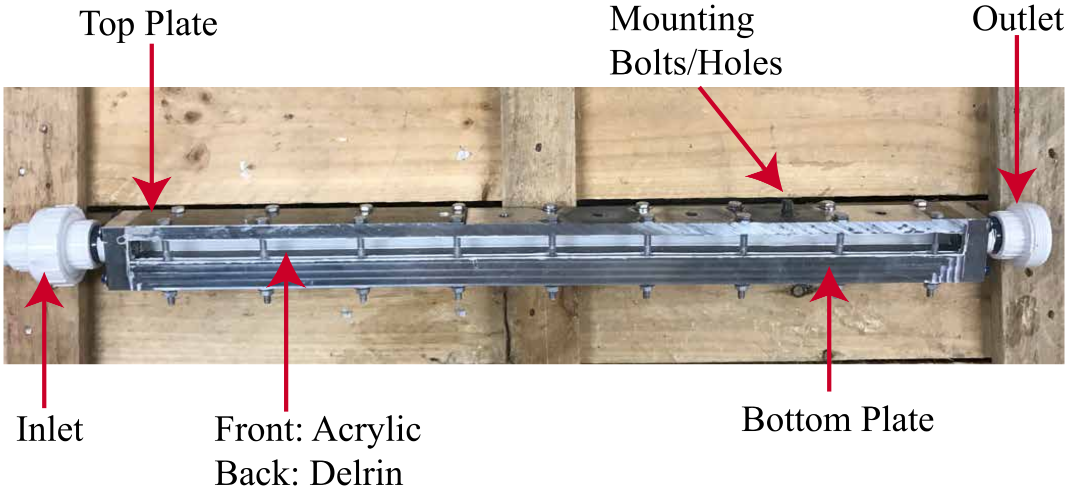

Figure 38: PULST long test section.

The second test section utilized took the experience and results from the first test section as the design input. The thickness of the mounting plate was minimized to increase the transmission of acoustic intensity. Also, the overal length was shorted because experience showed that fully developed flow was not necessary because the application of ultrasonics added significant disruption to the flow profile. They were also designed to be modular and

Figure 39: Revision 1 of the PULST test section installed.

accommodate either a 120 W or a 1 kW transducer. One module was instrumented with a Valpey Fisher VP-3 pinducer to measure acoustic intensity.

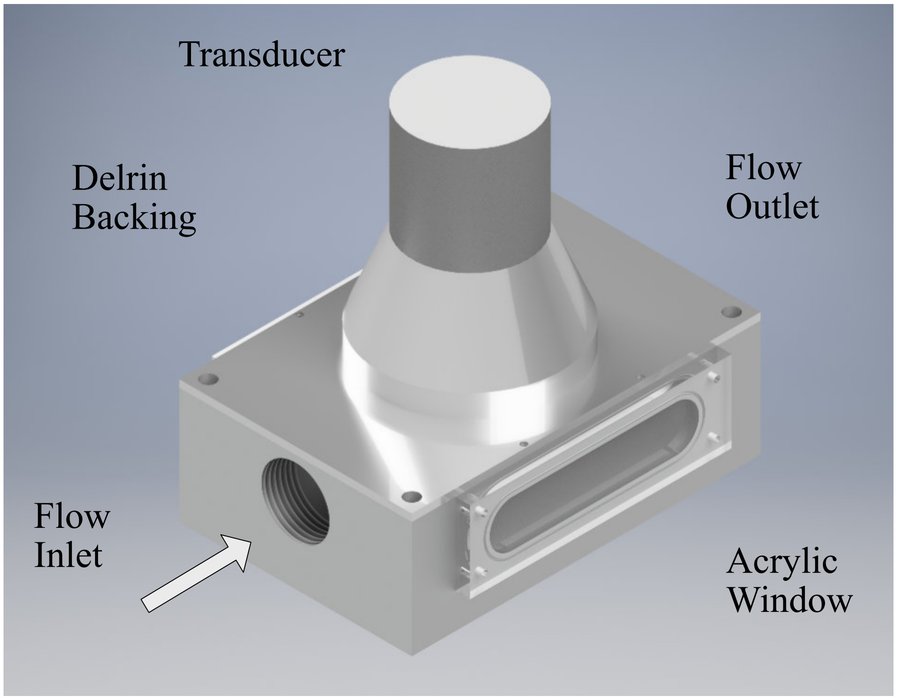

Figure 40: Third design of the PULST test section.

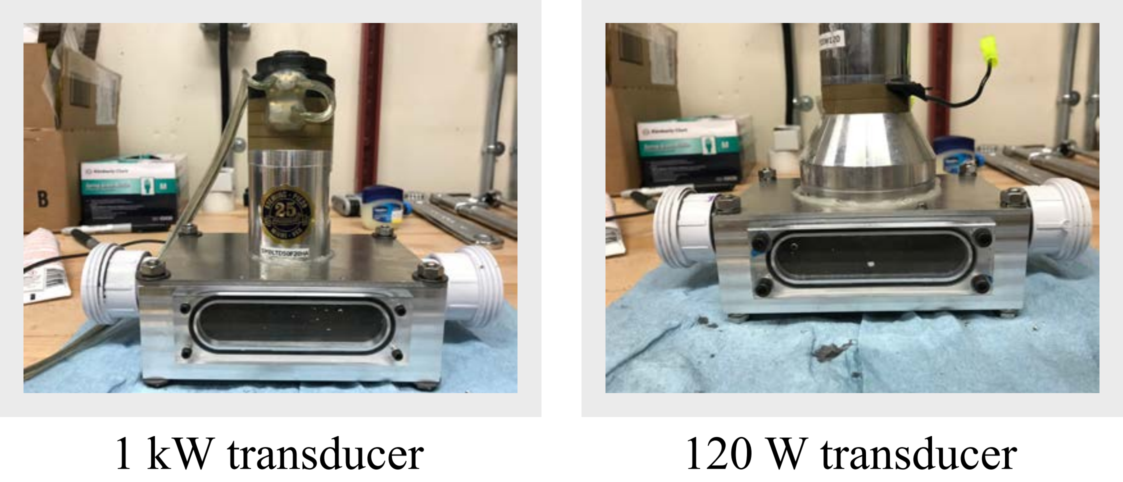

Figure 41: Modular test sections fitted with 1 kW and 120 W transducers.

Figure 42: PULST test section body modified for VP-3 Pinducer.

4.2 Results

The standard PULST test matrix is shown in Table 2. This test matrix was applied to three configurations, one 120 W transducer, two 120 W transducers, and one 1 kW transducer. For the single 120 W transducer case, tests were performed at 15 $wt\%$ and 35 $wt\%$ and Re of 3000 to confirm mass transfer performance trends. Figures 46 through 48 show the $k_L a$ enhancement between the ultrasonic enhanced and non-enhanced runs indicated by a positive differences. A closer look at these results show the majority of points do show a positive enhancement. The uncertainty in the data is derived from the variation in the individual runs, even though the runs were conducted as identically as possible. Some data showed a relatively small increase in efficiency, but others showed a largely negative effect of ultrasonics.

Table 2: Standard Test Matrix for the PULST experiment

		Re			
Glycerol *wt%*	Corresponding flibe temp (C)	3500	4000	4500	5000
17.4	700				
24.7	650				
33.4	600				

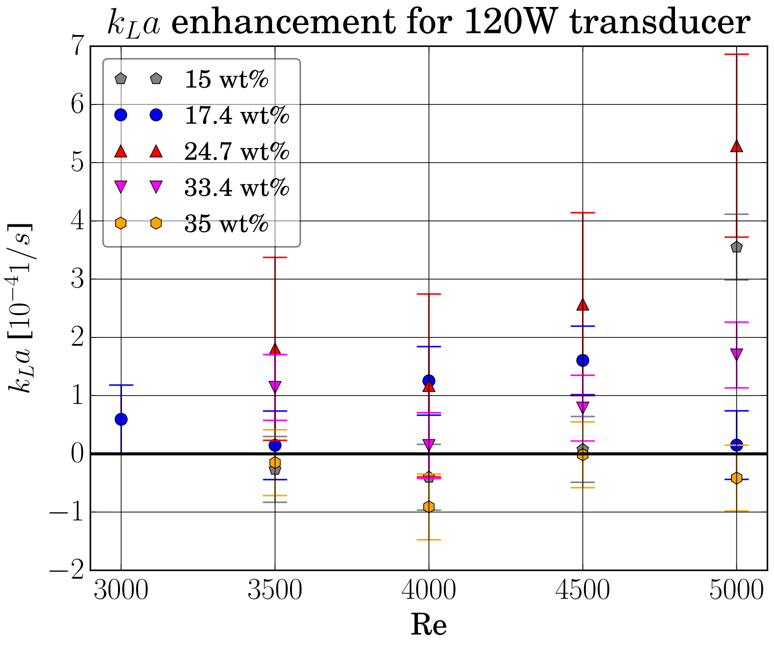

Figure 43: $k_L a$ enhancement for the single 120 W transducer.

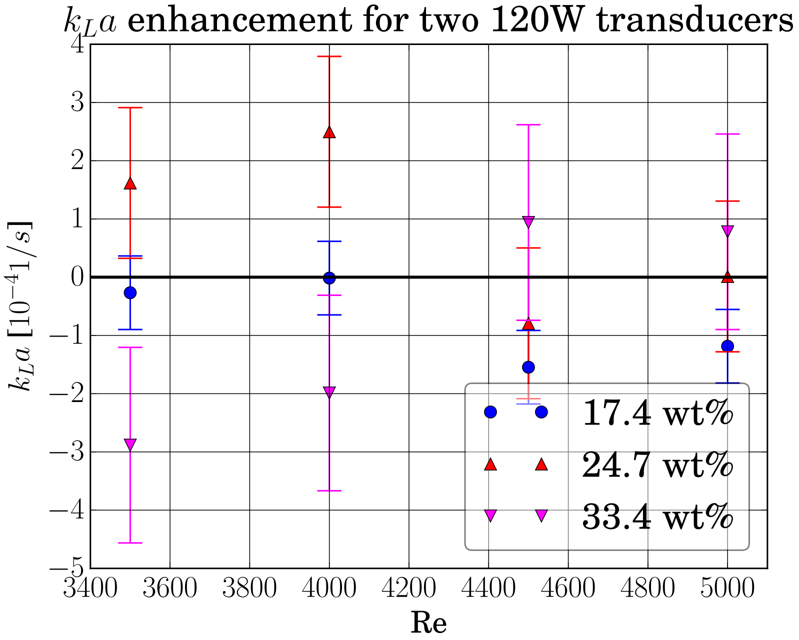

Figure 44: k_La enhancement for the two 120 W transducers.

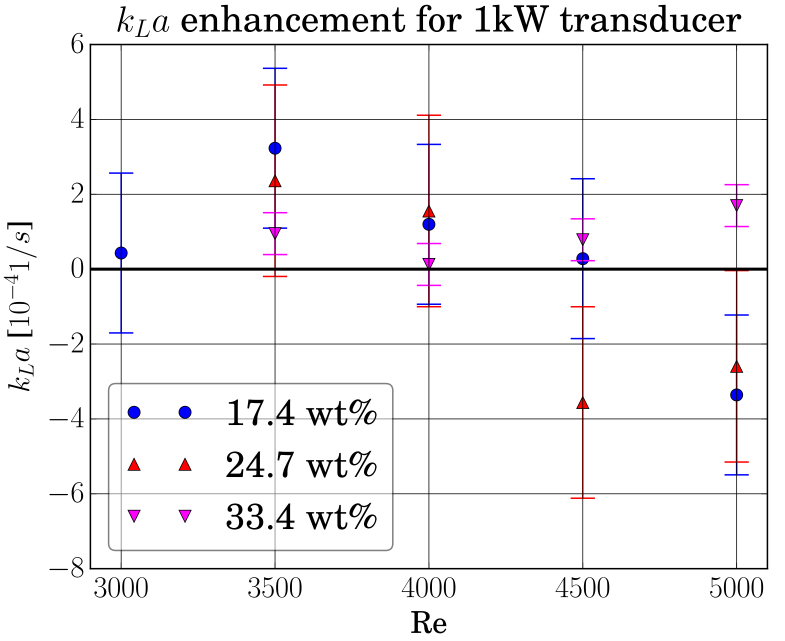

Figure 45: k_La enhancement for the 1 kW transducer.

Sh was calculated from the experimental $k_L a$ using the same procedure as the SUMATRA experiments. The necessary parameters, namely the number density and interfacial area, were derived using the procedure used in the SUMATRA experiment and this is procedure is reported in detail in Rubio's dissertation [20]. The Sh results are presented in Figures 46 through 48.

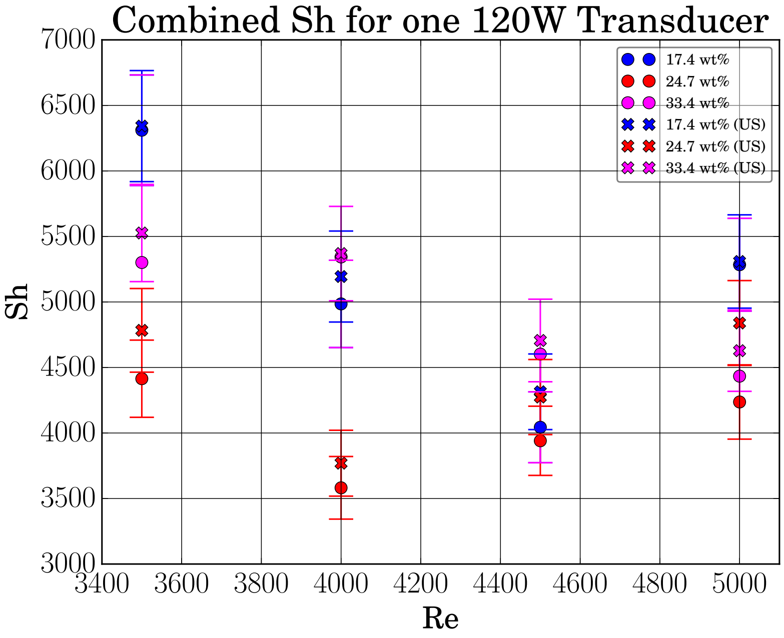

Figure 46: Sh comparison for the 120 W case.

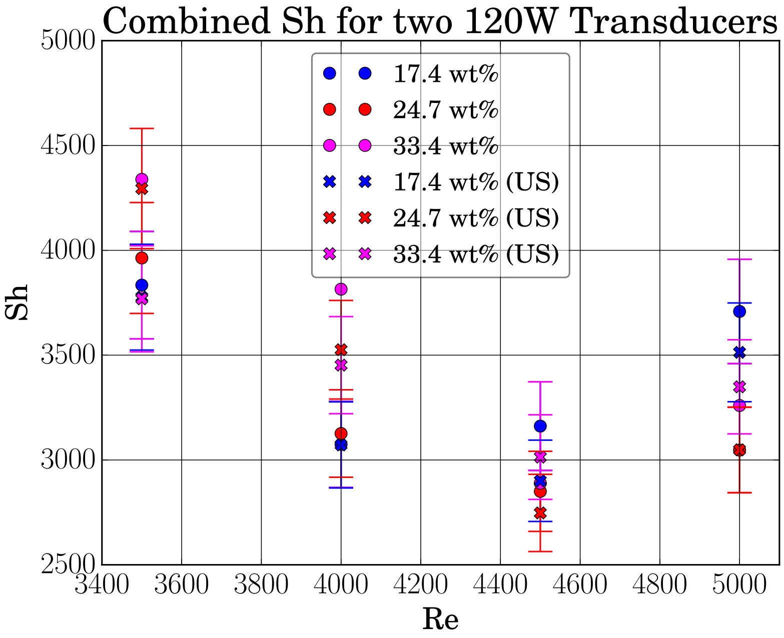

Figure 47: Sh comparison for the two 120 W module case.

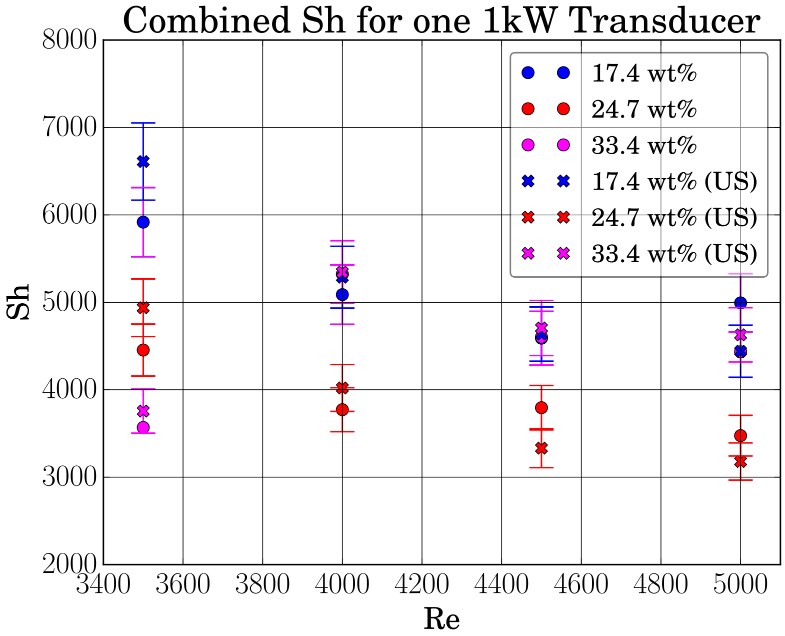

Figure 48: Sh comparison for the 1 kW case.

With the addition of the indirect application of the ultrasonic energy, the transmitted acoustic energy needed to be measured. The measurements from the instrumented module are shown in Figures 49 through 51. These results show that there is significant attenuation of the acoustic energy from the horn face to what is seen measured in the fluid. The calculated acoustic intensities at the horn faces are 2.44 W/cm^2 for the 120 W transducer and 50.9 W/cm^2 for the 1 kW transducer.

At the conclusion of testing, the test section modules did show some erosion due to ultrasonics. As seen in Figures 52 and 53, pitting erosion and metal discoloration can be observed. The surface texture of the discolored aluminum has been matted. This suggests that a different configuration of power, geometry, and materials would be required to address the erosion issue.

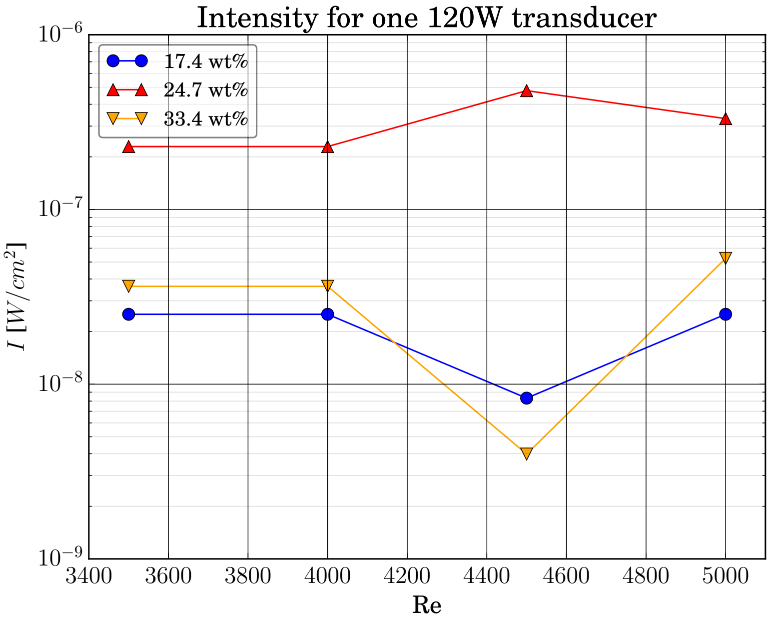

Figure 49: Measured acoustic intensity for one 120 W transducer.

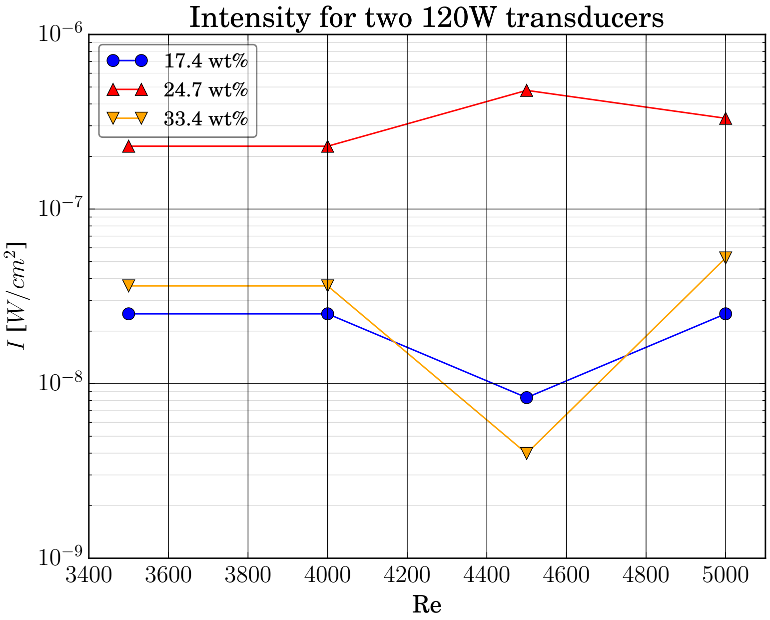

Figure 50: Measured acoustic intensity for two 120 W transducer.

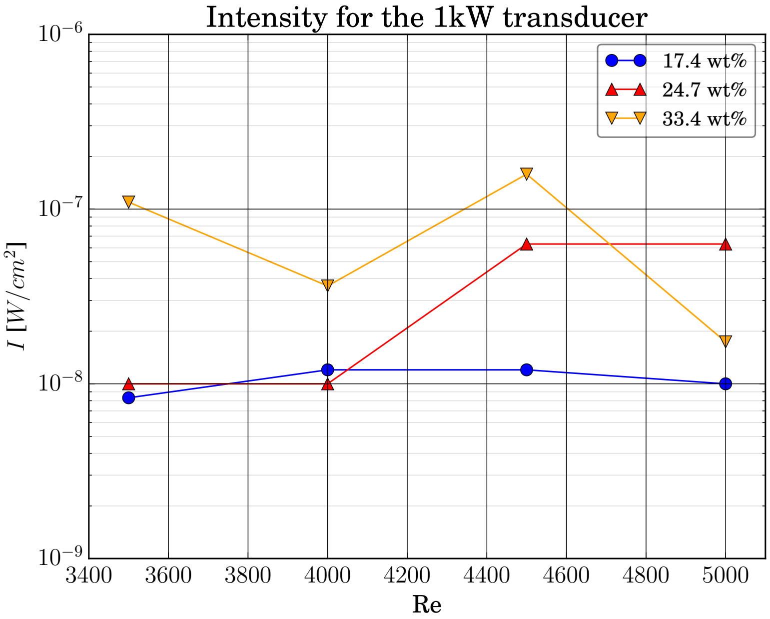

Figure 51: Measured acoustic intensity for the 1 kW transducer.

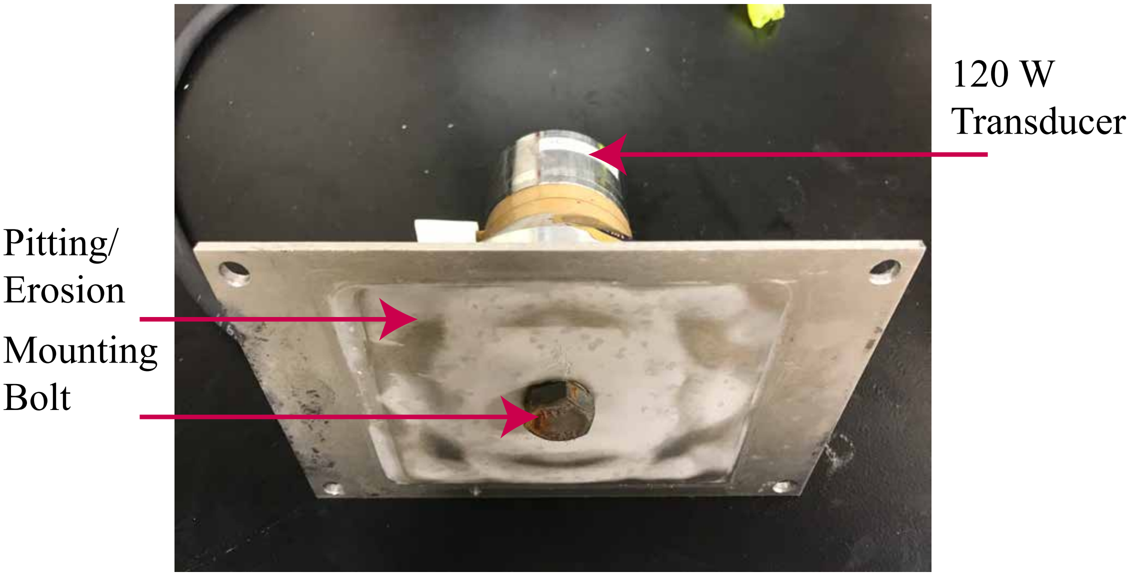

Figure 52: Underside of the top plate for 120 W after 60 hrs of testing.

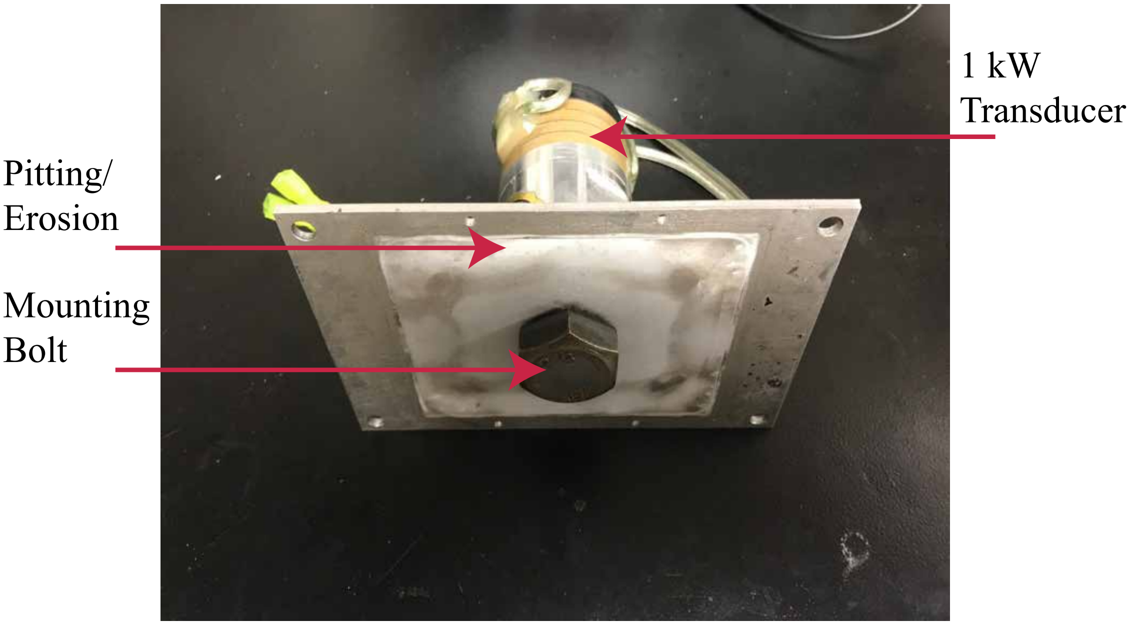

Figure 53: Underside of the top plate for 1 kW after after 20 hrs testing.

5 Parameter Comparison

The experiments performed were intended to push the technology of inert gas sparging mass transfer by use of scaled experiments and investigate the application of ultrasonics to enhance two-phase mass transfer. The first experiment (SUMATRA) had demonstrated the proof-of-concept of sonomechanical enhancement of sparging mass transfer, the second experiment (PULST) had been inconclusive in showing the viability of indirect sonomechanical enhancement of sparging mass transfer, a key parameter comparison of these experiments do give valuable insight into the development of this technology.

The list of important parameters contrasted between the two experiments in the following Table 3. They are broken up between fluid properties and acoustic properties. Naturally some parameters overlap between fluid and acoustic properties, namely bubble density and fluid density (which is manifested in impedance ratio). It would also be important to mention that the two experiments are different categories of acoustic reactors. The SUMATRA experiment is a probe reactor, and the PULST experiment is a bath reactor. Because of this, commensurate data are not superficially apparent in comparisons, and conclusions must be considered carefully.

Through the parameter study performed by Rubio in [20], the key parameters that must be matched became apparent. The study showed the necessity to add an acoustic matching layer between the horn material and the test fluid. In Figure 54 the applied intensity was compared to the interface impedance ratio for the PULST experiment. This shows significant distance in the parameter space between the PULST and SUMATRA experiments. A different look at this data, Figure 55 shows the calculated transmitted intensity over the interface. This also shows a significant distance between the experiments in the parameter space. This suggests that a horn material that more closely matches the fluid impedance will be necessary and the applied intensity must be significantly increased.

Table 3: List of Comparison Parameters for the PULST and SUMATRA experiments

SUMATRA	**PULST**
Fluid Properties	
Re	Re
Sc	Sc
Bubble Diameter	Bubble Diameter
Temperature	Temperature
Denisty	Density
Viscosity	Viscosity
Glycerol Concentration	Glycerol Concentration
Flow Velocity	Flow Velocity
Bubble Injection Rate	Bubble Injection Rate
Test Section Volume	Test Section Volume
	Number of Modules
Acoustic Properties	
Probe Reactor	Bath Reactor
Intensity Applied	Intensity Applied
Intensity Transmitted	Intensity Sensed
Impedance Ratio	Impedance Ratio
Frequency	Frequency
Bubble Diameter (Resonance)	Bubble Diameter
Bubble Density	Bubble Density
Ambient Pressure	Ambient Pressure
Acoustic Residence Time	Acoustic Residence Time
Horn Mass	Horn/Test Section Mass
Horn Geometry	Horn/Test Section Geometry

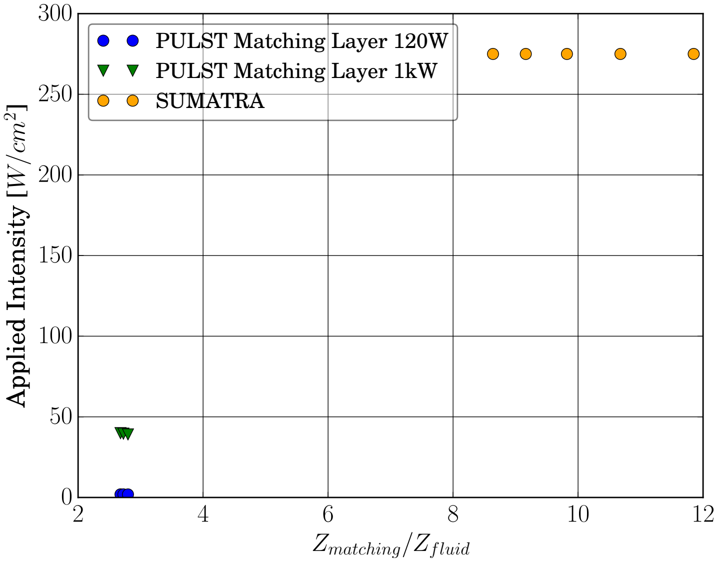

Figure 54: Applied intensity plotted on the matching layer impedance ratio for the PUSLT experiment compared to the SUMATRA applied intensity and impedance ratio.

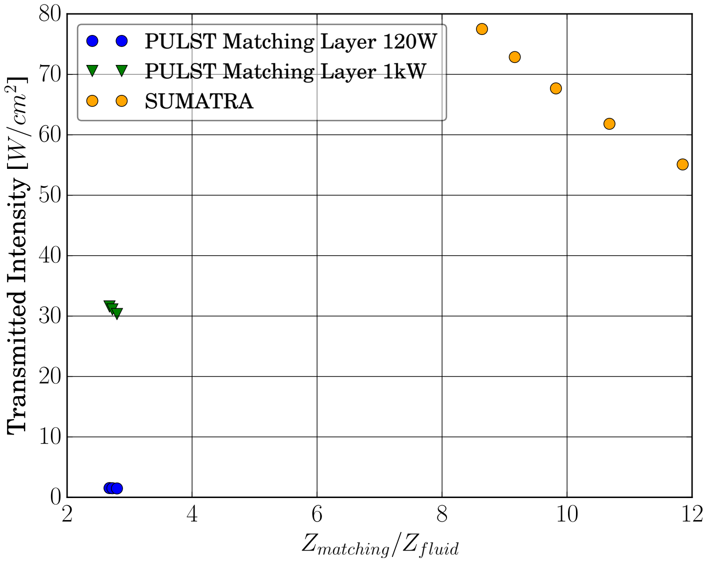

Figure 55: Calculated transmitted intensity for PULST assuming a matching layer is introduced compared to the calculated transmission of intensity in the SUMATRA experiment.

One more key parameter stood out in the study was the number density of bubbles between the two experiments. The presence of bubbles in a fluid acts as an acoustic attenuator, and has been used as one in very loud underwater construction to protect the hearing of nearby aquatic life [26, 27, 28]. As shown in Figure 56, the PULST experiment had higher number densities of bubbles. It was concluded that a lower number density of bubbles will benefit more from ultrasonic enhancement.

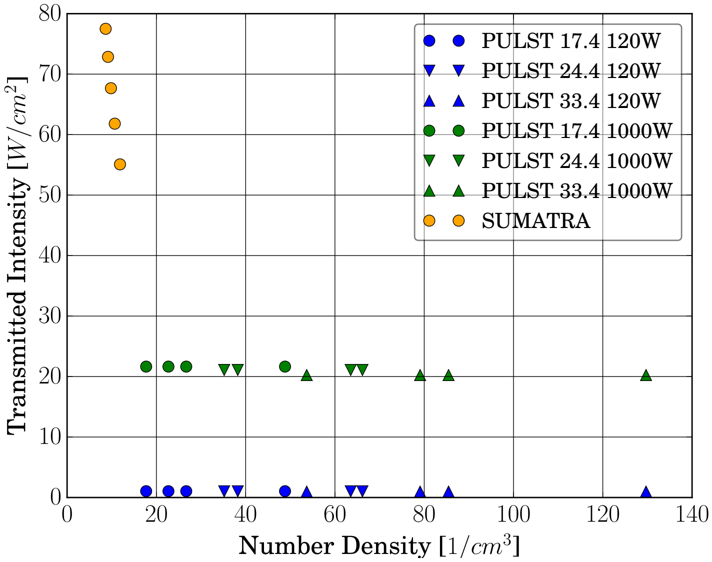

Figure 56: Number density and transmitted intensity comparison for the PULST and SMATRA experiments.

6 Conclusion

The two experiments in this report investigated the viability and value of on ultrasonic enhancement of sparging mass transfer, in scaled experiments. SUMATRA showed that it is viable on the bench top scale and with direct sonication. This experiment demonstrated the proof-of-concept of this idea. Which lead to the PULST experiment, which attempted to scale up the SUMATRA experiment while utilizing indirect sonication. PULST showed that the enhancement was inconclusive when the experiment was scaled up with indirect sonication. In order to understand the reasons that the PULST experiment did not show the same results as SUMATRA, a parameter study was performed and the conclusions of which show the boundaries of the design space for an sonomechancially enhanced mass transfer cell. The results of the parameter study suggested that higher acoustic intensities with the use of an acoustic matching layer and a lower bubble density are necessary to match the conditions of the proof-of-concept SUMATRA experiment.

6.1 Future Work

Future work in for this technology will be to address the results of the parameter study to continue in the experimental, iterative direction. More custom components should be investigated to achieve these goals. One design tool that was not leveraged in this work was the use of modeling and simulation. Due to the highly chaotic nature of ultrasonics coupled with two-phase mass transfer, an experimental approach was taken. Simulations using CFD have been done comparing mass transfer enhancements due to ultrasonics [29, 30, 31]. When studies like these can be benchmarked and validated with commensurate experimental data, this can be a powerful design tool for sonoenhanced sparging cells and sonochemical reactors.

Several major challenges that need to be addressed using appropriate scaled experiments before any implementation on a larger scale or with tritium. These include how to effectively impart acoustic energy of an appropriate intensity into the process stream without introducing wear and erosion products into the reactor flibe. One key challenge for the ultrasonic component is to find a piezoelectric material in the ultrasonic transducers that can survive a radiation field and high temperature environment. There is ongoing work by other groups that may potentially be leveraged to address the transducer requirements in a radiation environment. [32, 33, 34, 35, 36].

7 References and Further Reading

Floren V. Rubio, Leonard J. Bond, Edward D. Blandford "Summary of Sonoprocessing Applications for Nuclear Technologies and Potential Future Applications". In: Transactions of the American Nuclear Society. Anaheim, CA: American Nuclear Society, 2014, pp. 1068-

1071. [37]

Conference proceeding that explore the possible applications of high power ultrasonics in nuclear process streams.

Floren Rubio, Edward D. Blandford, and Leonard J. Bond. "Survey of advanced nuclear technologies for potential applications of sonoprocessing". In: Ultrasonics 71 (Sept. 2016), pp. 211–222. issn: 0041624X. doi: 10.1016/j.ultras.2016.06.017. url: http://linkinghub.elsevier.com/retriev
[12]

Journal paper investigating the potential benefits of high power ultrasonics in nuclear process streams.

Floren Rubio, Leonard Bond, and Edward Blandford. "Scaled experiment investigating sonomechanically enhanced inert gas sparging mass transfer". In: Nuclear Engineering and Design 324 (Dec. 2017), pp. 171–180. issn: 00295493. doi: 10.1016/j.nucengdes.2017.08.016. url: http://www.sciencedirect.com/science/article/pii/ S0029549317303904. [18]

Journal paper detailing the SUMATRA experiment and the demonstration of ultrasonic sparging mass transfer enhancement.

Floren V. Rubio and Edward D. Blandford. "Mass Transfer and Ultrasonic Scaling Parameters for Sparging Mass Transfer for High Temperature Fluoride Salt Tritium Control". In: NURETH 17. Xi'an, Shaanxi, 2017. [38]

Conference proceedings discussing the scaling arguments of matching Sc of flibe with a water/glycerol surrogate fluid, as well as matching acoustic parameters in flibe to water/glycerol mixtures.

Floren V. Rubio. "Sonomechanical Enhanced Sparging Techniques for Advanced Reactor Applications". PhD. University of New Mexico, 2018. [20].

Dissertation supported by the IRP which encompasses the included papers and conference proceedings detailing the ultrasonically enhanced mass transfer experiments and studies. It details the SUMATRA and PULST experimental results with a comparison parameter study which highlights the parameters necessary for an optimized indirect ultrasonic flow cell.

Nomenclature

C_m	Glycerol concentration $(wt\%)$
DO	Dissolved oxygen (mg/L)
I	Acoustic intensity (W/m^2)
L	Length (m) or (in)
R	Bubble radius (m)
T_P	Transmission coefficient $*$
V	Volume (m^3) or (gal)
Z	Acoustic impedance $(Rayl)$ or $(Pa\ s/m^2)$
$\mathscr{D}$	Diffusivity (m^2/s)
a	Interfacial area (m^2/m^3)
c	Speed of sound (m/s)
$dB(SPL)$	Decibel sound power level $*$
f	Frequency (Hz)
k_L	Mass transfer coefficient (m/s)
k_La	Volumetric mass transfer coefficient $(1/s)$

Greek symbols

α	Thermal diffusion rate (m^2/s)
η	Sheer viscosity (mPa/s)
κ	Polytropic constant $*$
ω	Period (s)
σ	Surface tension (N/m)
τ	Residence time (s)
ε	holdup $*$

Non-dimensional numbers

Re_b	Bubble Reynolds

$Sc = \frac{\mu}{\rho \mathscr{D}}$	Schmidt number
$Sh = \frac{k_L \ L}{\mathscr{D}}$	Sherwood number
$We = \frac{\rho \ U^2 \ L}{\sigma}$	Weber number

Other subscripts

L	Length m or in

References

[1] T. S. Kress. “Mass transfer between small bubbles and liquids in concurrent turbulent pipeline flow”. Doctor of Philosophy. University of Tennessee, 1972, p. 170. URL: `http://moltensalt.org/references/static/downloads/pdf/ORNL-TM-3718.pdf`.

[2] Thomas K. Sherwood, Robert L. Pigford, and Charles R. Wilke. *Mass transfer*. McGraw-Hill, 1975, p. 677. ISBN: 0070566925.

[3] Gracey and Associates. *Acoustic Glossary, Sound and Vibration Definitions, Terms, Units, Measurements*. URL: `http://www.acoustic-glossary.co.uk/` (visited on 01/18/2018).

[4] Gordon S. Kino. *Acoustic waves : devices, imaging, and analog signal processing*. Englewood Cliffs, New Jersey: Prentice-Hall, 1987, p. 601. ISBN: 0130030473.

[5] Dale Ensminger and Leonard Bond. *Ultrasonics*. 3rd. Dekker Mechanical Engineering. New York: CRC Press, Sept. 2011, p. 723. ISBN: 978-0-8247-5889-9.

[6] Gerald Harvey, Anthony Gachagan, and Tapiwa Mutasa. “Review of high-power ultrasound-industrial applications and measurement methods.” In: *IEEE transactions on ultrasonics, ferroelectrics, and frequency control* 61.3 (Mar. 2014), pp. 481–95. ISSN: 1525-8955. DOI: `10.1109/TUFFC.2014.2932`. URL: `http://www.ncbi.nlm.nih.gov/pubmed/24569252`.

[7] L. H. Thompson and L. K. Doraiswamy. “Sonochemistry: Science and Engineering”. In: *Industrial & Engineering Chemistry Research* 38.4 (Apr. 1999), pp. 1215–1249. ISSN: 0888-5885. DOI: `10.1021/ie9804172`. URL: `http://pubs.acs.org/doi/abs/10.1021/ie9804172`.

[8] Timothy G. Leighton. *The Acoustic Bubble*. London: Academica Press, 1994, p. 613. ISBN: 0-12-441920-8.

[9] R. E. Apfel. “Acoustic cavitation prediction”. In: *The Journal of the Acoustical Society of America* 69.6 (June 1981), pp. 1624–1633. ISSN: 00014966. DOI: `10.1121/1.385939`. URL: `http://scitation.aip.org/content/asa/journal/jasa/69/6/10.1121/1.385939`.

[10] Robert T. Beyer. *Nonlinear Acoustics*. Woodbury, NY: Acoustical Society of America, 1997, pp. 207–231. ISBN: 9780123218605.

[11] T. J. Mason and J. P. Lorimer. *Sonochemistry: Theory, Applications and Uses of Ultrasound in Chemistry*. Ellis Horwood series in physical chemistral. New York: John Wiley & Sons, 1988, p. 252. ISBN: 9780470213735.

[12] Floren Rubio, Edward D. Blandford, and Leonard J. Bond. “Survey of advanced nuclear technologies for potential applications of sonoprocessing”. In: *Ultrasonics* 71 (Sept. 2016), pp. 211–222. ISSN: 0041624X. DOI: `10.1016/j.ultras.2016.06.017`. URL: `http://linkinghub.elsevier.com/retrieve/pii/S0041624X16301019`.

[13] Robert J. Urick. *Principles Of Underwater Sound*. McGraw-Hill Ryerson, Limited, 1983, p. 423. ISBN: 0070660875.

[14] Kenneth Sanders Suslick. *Ultrasound : its chemical, physical, and biological effects / edited by Kenneth S. Suslick.* New York, N.Y. : VCH Publishers, c1988., 1988. ISBN: 0895733285.

[15] M. Minnaert. "XVI. On musical air-bubbles and the sounds of running water". In: *The London, Edinburgh, and Dublin Philosophical Magazine and Journal of Science* 16.104 (Aug. 1933), pp. 235–248. ISSN: 1941-5982. DOI: `10.1080/14786443309462277`. URL: `http://www.tandfonline.com/doi/abs/10.1080/14786443309462277`.

[16] S. J. Kline. *Similitude and approximation theory.* New York: McGraw-Hill, 1965, xiii, 229 pages.

[17] Philippe M. Bardet and Per F. Peterson. "Options for Scaled Experiments for High Temperature Liquid Salt and Helium Fluid Mechanics and Convective Heat Transfer". In: *Nuclear Technology* 163.3 (Sept. 2008), pp. 344–357. ISSN: 0029-5450. DOI: `10.13182/NT163-344`. URL: `https://www.tandfonline.com/doi/full/10.13182/NT163-344`.

[18] Floren Rubio, Leonard Bond, and Edward Blandford. "Scaled experiment investigating sonomechanically enhanced inert gas sparging mass transfer". In: *Nuclear Engineering and Design* 324 (Dec. 2017), pp. 171–180. ISSN: 00295493. DOI: `10.1016/j.nucengdes.2017.08.016`. URL: `http://www.sciencedirect.com/science/article/pii/S0029549317303904`.

[19] Bruce Roy Munson. *Fundamentals of fluid mechanics.* Wiley, 2009. ISBN: 9780470926536.

[20] Floren V. Rubio. "Sonomechanical Enhanced Sparging Techniques for Advanced Reactor Applications". PhD. University of New Mexico, 2018.

[21] N. Cheeke and J. David. *Fundamentals and applications of ultrasonic waves.* CRC series in pure and applied physics. Boca Raton : CRC Press, c2002., 2012, p. 462. ISBN: 0849301300.

[22] Kenneth S. Suslick and Gareth J. Price. "Applications of Ultrasound to Materials Chemistry". en. In: *Annual Review of Materials Science* 29.1 (Aug. 1999), pp. 295–326. ISSN: 0084-6600. DOI: `10.1146/annurev.matsci.29.1.295`. URL: `http://www.annualreviews.org/doi/10.1146/annurev.matsci.29.1.295`.

[23] Wolf-Dieter Deckwer and Robert W. Field. *Bubble column reactors.* Wiley, 1992, p. 533. ISBN: 9780471918110.

[24] Johannes Schindelin et al. "The ImageJ ecosystem: An open platform for biomedical image analysis". In: *Molecular Reproduction and Development* 82.7-8 (July 2015), pp. 518–529. ISSN: 1040452X. DOI: `10.1002/mrd.22489`. URL: `http://www.ncbi.nlm.nih.gov/pubmed/26153368`.

[25] Robert H. Perry and Don W. Green. *Perry's chemical engineers' handbook.* McGraw-Hill, 2008. ISBN: 0071422943.

[26] S. N. Domenico. "Acoustic wave propagation in air-bubble curtains in water-Part I: History and theory". In: *GEOPHYSICS* 47.3 (Mar. 1982), pp. 345–353. ISSN: 0016-8033. DOI: `10.1190/1.1441340`. URL: `http://library.seg.org/doi/10.1190/1.1441340`.

[27] James A Reyff. “Reducing Underwater Sounds with Air Bubble Curtains Protecting Fish and Marine Mammals from Pile-Driving Noise”. In: *TR News* 262 (2009). URL: `http://onlinepubs.trb.org/onlinepubs/trnews/trnews262rpo.pdf`.

[28] B. Würsig, C. R. Greene, and T. A. Jefferson. “Development of an air bubble curtain to reduce underwater noise of percussive piling”. In: *Marine Environmental Research* 49.1 (Feb. 2000), pp. 79–93. ISSN: 01411136. DOI: `10.1016/S0141-1136(99)00050-1`. URL: `http://linkinghub.elsevier.com/retrieve/pii/S0141113699000501`.

[29] Baharak Sajjadi et al. “Investigation of mass transfer intensification under power ultrasound irradiation using 3D computational simulation: A comparative analysis”. In: *Ultrasonics Sonochemistry* 34 (2017), pp. 504–518. ISSN: 18732828. DOI: `10.1016/j.ultsonch.2016.06.026`. URL: `http://dx.doi.org/10.1016/j.ultsonch.2016.06.026`.

[30] Baharak Sajjadi, Abdul Aziz Abdul Raman, and Shaliza Ibrahim. “Influence of ultrasound power on acoustic streaming and micro-bubbles formations in a low frequency sono-reactor: Mathematical and 3D computational simulation”. In: *Ultrasonics Sonochemistry* 24 (2015), pp. 193–203. ISSN: 18732828. DOI: `10.1016/j.ultsonch.2014.11.013`. URL: `http://dx.doi.org/10.1016/j.ultsonch.2014.11.013`.

[31] Baharak Sajjadi, Abdul Aziz Abdul Raman, and Shaliza Ibrahim. “A comparative fluid flow characterisation in a low frequency/high power sonoreactor and mechanical stirred vessel”. In: *Ultrasonics Sonochemistry* 27 (Nov. 2015), pp. 359–373. ISSN: 13504177. DOI: `10.1016/j.ultsonch.2015.04.034`. URL: `http://linkinghub.elsevier.com/retrieve/pii/S1350417715001273`.

[32] R Kažys, Algirdas Voleišis, and B Voleišienė. “High temperature ultrasonic transducers: review”. In: *Ultragarsas (Ultrasound)* 63.2 (2008), pp. 7–17. URL: `http://www.ultragarsas.ktu.lt/index.php/USnd/article/view/17063`.

[33] J. W. Griffin et al. “High temperature ultrasonic transducers for in-service inspection of liquid metal fast reactors”. In: *2011 IEEE International Ultrasonics Symposium*. IEEE, Oct. 2011, pp. 1924–1927. ISBN: 978-1-4577-1252-4. DOI: `10.1109/ULTSYM.2011.0479`. URL: `http://ieeexplore.ieee.org/document/6293627/`.

[34] J. L. Rempe et al. “Advanced In-Pile Instrumentation for Materials Testing Reactors”. In: *IEEE Trans. Nucl. Sci.* 61.4 (Aug. 2014), pp. 1984–1994. ISSN: 0018-9499. DOI: `10.1109/TNS.2014.2335616`. URL: `http://ieeexplore.ieee.org/lpdocs/epic03/wrapper.htm?arnumber=6869028`.

[35] Prathamesh N. Bilgunde and Leonard J. Bond. “Effect of Thermal Degradation on High Temperature Ultrasonic Transducer Performance in Small Modular Reactors”. In: *Physics Procedia* 70 (2015), pp. 433–436. ISSN: 18753892. DOI: `10.1016/j.phpro.2015.08.137`. URL: `http://www.sciencedirect.com/science/article/pii/S1875389215008780`.

[36] A.N. Sinclair and A.M. Chertov. “Radiation endurance of piezoelectric ultrasonic transducers – A review”. In: *Ultrasonics* 57.July (Mar. 2015), pp. 1–10. ISSN: 0041624X. DOI: `10.1016/j.ultras.2014.10.024`. URL: `http://www.sciencedirect.com/science/article/pii/S0041624X14003096`.

[37] Floren V. Rubio, Edward D. Blandford, and Leonard J. Bond. “Summary of Sonoprocessing Applications for Nuclear Technologies and Potential Future Applications”. In: *2014 ANS Winter Meet. Nucl. Technol. Expo.* Vol. 111. Anaheim, CA, 2014, pp. 1068–1071.

[38] Floren V. Rubio and Edward D. Blandford. “Mass Transfer and Ultrasonic Scaling Parameters for Sparging Mass Transfer for High Temperature Fluoride Salt Tritium Control”. In: *NURETH 17.* Xi’an, Shaanxi, 2017.

3. Corrosion Control with Redox Control, Impurity Control, and Materials Selection

The objective of this task was to develop strategies to assure good long-term structural materials behavior in FHRs by selection of appropriate salt chemistry and materials. The IRP had two interconnected activities. The University of Wisconsin led work on testing different materials in flibe salt at 700°C. This included preparation of clean salts, various static corrosion tests and building of a circulating salt corrosion test loop. MIT conducted irradiation tests on different materials in flibe salt at 700°C to determine the effect of irradiation on materials. These were the first irradiation tests of materials in salt since the ORNL molten salt reactor program in the early 1970s; thus, a major part of this work was developing modern methods to irradiate materials in salt.

This work involved close coordination between the two universities where identical samples and capsules were prepared for out-of-reactor corrosion tests conducted at UW and in-reactor corrosion tests conducted at MIT. For each step, one or the other university conducted the operations to assure as far as possible identical systems. For example, all salt loading was done at UW. This type of testing program enables separation of the effects of just corrosion from the combined effects of corrosion and irradiation. Two reports of these activities were prepared that summarize results and contain the detailed references.

- FHR Corrosion Control with Redox Control, Impurity Control, and Materials Selection (UW)
- In-Reactor FHR Materials Corrosion Testing (MIT)

3.1. FHR Corrosion Control with Redox Control, Impurity Control, and Materials Selection (UW)

FHR Corrosion Control with Redox Control, Impurity Control, and Materials Selection (UW)[1]

Summary

A significant step in FHR research was the implementation and improvement of methods for producing and controlling the properties of FLiBe salt. Methods have been perfected for purifying salt and then testing its elemental and electrochemical characteristics. The interaction of important structural materials with FLiBe salt was evaluated in long term static corrosion experiments. To better understand FLiBe salt's thermohydraulic nature a large natural convection circulation loop has been constructed at UW. Salts specifically designed for irradiated environments were re-purified at UW-Madison and sent to MIT for in-reactor experimentation.

A vital resource to the success of salt research in irradiated environments is ^{7}Li enriched MSRE FLiBe. This salt which contains less of the isotope ^{6}Li than natural lithium has a much lower probability of producing tritium under irradiation. The United States currently does not produce large quantities of enriched ^{7}Li for nuclear environments. What remained of the valuable ^{7}Li enriched FLiBe left over from the MSRE sat dormant in less than ideal conditions since its retirement in 1969. In 2015, the University of Wisconsin-Madison successfully re-purified roughly 54.4 kg of spent ^{7}Li enriched MSRE FLiBe from ORNL that had circulated in the MSRE's secondary loop for over 23,000 hours. The salt was re-purified by a process call hydrofluorination. Hydrogen fluoride and hydrogen gas are sparged through the molten mixture (melt) in order to remove common salt impurities such as oxygen, moisture and some metallic impurities.

The re-purification of MSRE FLiBe helped build the expertise to produce large quantities of purified natural lithium FLiBe salt for further out-of-reactor experimentation. Using the same batch hydrofluorination unit, UW-Madison produced another 38.7 kg of natural lithium FLiBe salt. This salt has been used extensively in both laboratory and natural convection circulation loop environments at UW-Madison. Analytical chemistry methods developed with the help of the Wisconsin State Laboratory of Hygiene show that the natural lithium FLiBe has similar make up to the ^{7}Li enriched reference salt.

An in-situ electrochemical method was developed to expedite the measurement of corrosion product concentrations and help better predict the longevity of a reactor primary loop. A simple yet robust electrochemical probe was designed for laboratory and circulation loop environments. Two electrochemical techniques have been implemented at the laboratory scale to help characterize FLiBe salts and understand corrosion results. The fluoride salt redox potential is a simple electrochemical method that gives insight into how oxidizing FLiBe salt can be to a given material. The fluoride salt redox potential was used to characterize salts used in corrosion experiments. The redox potential is sensitive to corrosion control methods such as beryllium metal addition. Corrosion results show that corrosion rate of common structural materials, such as 316L stainless steel and Hastelloy N, are modestly correlated with the value of the fluoride salt redox potential. Cyclic voltammetry (CV) and Linear Sweep Voltammetry (LSV) are useful methods for investigating and measuring common corrosion products found in FLiBe

[1] K. Sridharan (kumar.sridharan@wisc.edu) and W. Doniger (doniger@wisc.edu)

salt. CV has been used extensively to study the behavior of chromium fluoride, the dominant corrosion product of most preferred alloys.

In preliminary salt exposure studies, 316L stainless steel and Hastelloy N were exposed to as-purified ^{7}Li-enriched FLiBe for 3000 hours and 1000 hours, respectively. 316 stainless steel was exposed to molten FLiBe in both 316L stainless steel and graphite capsules. 316 stainless steel performed well when tested in 316 stainless steel capsules with a predicted attack depth of 17.1 µm per year. In graphite capsules, the corrosion was accelerated with a predicted attack depth of 31.2 µm per year. Corrosion in both capsules occurred by the dissolution of chromium from the stainless steel into the salt which led to the depletion of chromium, predominantly along the grain boundaries the material. Carburization in the subsurface of 316 stainless steel occurred during corrosion tests in graphite crucibles. Cr_7C_3 precipitate particles were observed throughout the depth of the corrosion layer. The corrosion results showed promising evidence that very pure or slightly reducing FLiBe may reduce the corrosion rate of 316 stainless steel to acceptable rates for us in the FHR.

Hastelloy N showed outstanding corrosion resistance in FLiBe when tested in a pure Ni crucible. Similar to the corrosion of 316 stainless steel in graphite, the graphite crucible accelerates corrosion of Hastelloy N in FLiBe. Carburization occurred in the subsurface of Hastelloy N during the 1000 hour corrosion test at 700˚C. Results also indicate that, while graphite accelerates the corrosion in the short-term, this may not be true over a period of years.

To gauge the influence of irradiation on corrosion, in-reactor tests of both 316L stainless steel and Hastelloy N in ^{7}Li enriched FLiBe salt and identical capsules were conducted in the Massachusetts Institute of Technology Nuclear Research Reactor. Overall comparisons suggest that both effects of graphite and neutron radiation accelerate the corrosion rate by 2 to 10 times for the two tested alloys.

The corrosion resistance of a broader array of candidate structural materials was tested in molten natural lithium FLiBe salt produced at the University of Wisconsin-Madison. A static corrosion experiment was conducted for 2,000 hours at 700˚C. Materials tested include 316L Stainless Steel, Mo-Hf-C, W-Zr-C Cermet, Silicon Carbide, SiC-SiC Composites and nuclear graphite. The influence of salt chemistry on the corrosion performance of these materials was investigated by chemically altering the salt to make it less oxidizing. Metallic beryllium was added to the salt to increase its thermodynamic stability by removing salt impurities thought to contribute to corrosion. These salts were benchmarked electrochemically using a test called the fluoride salt redox potential measurement. In addition, the influence of dissimilar materials on corrosion was evaluated. 316L Stainless steel was exposed to FLiBe salts contained in both 316 stainless steel and graphite capsules.

Beryllium addition to FLiBe salt increases the thermodynamic stability of the salt and reduces corrosion of 316 stainless steel samples substantially. Approximately 10% less weight loss was experienced by samples exposed to Be-reduced salt compared to as-purified salt. Graphite-encapsulated samples exhibited about 50% greater depth of attack than 316-encapsulated samples. Samples exposed to Be-reduced salt showed less severe grain boundary corrosion than samples exposed to as-purified salt. Chromium is severely depleted in grain boundaries near the surface of all samples. A similar depth of attack of about 10-15µm is observed in 316L stainless steel in both reduced and as-purified salt when exposed in a 316L capsule material. Stainless steel samples contained in graphite experienced a slightly higher depth of attack of about 15-20μm after corrosion. Profilometry shows that the surface of stainless steel samples encapsulated in graphite was up to 30% rougher than those encapsulated in stainless steel liners. ICP-OES results of post-corrosion salt samples show that the chromium concentration is only increased in the salt contained in graphite capsules. The salt in the stainless steel-encapsulated samples does not have any increase in chromium concentration.

MoHfC samples showed negligible corrosion after exposure to molten FLiBe. Hafnium carbides (HfC) dispersed on the surface of as-polished MoHfC dissolved into FLiBe during exposure, leaving behind pits. Overall, the bulk Mo metal was not affected by the corrosive molten fluoride salt.

WZrC samples performed poorly in molten salt due to the thermodynamically favorable dissolution of zirconium, as well as high bulk porosity of WZrC samples. Beryllium addition to FLiBe salt resulted in exposed samples experiencing twice the mass-loss relative to samples in as-purified salt. Tungsten carbide (W_2C) formation was prevalent in all post-corrosion samples, likely due to the increased relative carbon content in the samples as a product of zirconium dissolution.

The two type of graphite, A3 and IG-110, were completely untouched following corrosion in molten FLiBe. Be-reduced salt is potentially more corrosive to graphite, however results are inconclusive. Silicon carbide coated SiC-SiC composite samples experienced some spallation or erosion of the coating after exposure to 700°C FLiBe. This resulted in a high mass-loss and exposure of the underlying composite. The polished SiC-SiC composite underneath the coating showed no signs of corrosion. The smooth surface of the bonded silicon carbide samples showed very low surface corrosion in molten FLiBe salt, despite a failure of the bonded region. The bond was comprised of aluminum, which has a high solubility in FLiBe. The bulk surface of both CVD SiC and SC-30 SiC-SiC composite showed no signs of corrosion, despite the formation of SiF_4 at high temperatures. XPS results show that a carbon thin film forms on the surface of SiC samples after corrosion, which indicates silicon dissolution and possible protection of the underlying SiC by a carbon thin film. Carbon materials show very high nobility in molten fluorides salts.

A molten salt flow loop has been constructed and is operating at UW. This is the first FLiBe loop to operate since the 1970s and it is the first natural circulation FLiBe loop instrumented for thermal hydraulic measurements. The system is currently undergoing tests to measure heat transfer coefficients before starting materials testing. The flow environment is stable but shows several unique flow phenomena, including strong thermal stratification and short temperature jumps or spikes. The heat transfer measurements made so far show reasonable agreement with correlations but include an unexplained split in the data for heated salt, which requires further study. A new set of tests will rerun several operating states using a clean batch of FLiBe to examine the impact of salt impurity concentrations on heat transfer. After this, corrosion studies will be run to examine candidate FHR materials under expected operating conditions for 1000 or more hours. These tests are designed to mimic the static testing performed at UW so comparisons can be made between corrosion test methods.

Table of Contents

FHR Corrosion Control with Redox Control, Impurity Control, and Materials Selection

1. Introduction

The objective of FLiBe salt chemistry and materials compatibility research is to develop strategies to assure good long-term structural materials behavior in FHRs. Like most fluoride based coolants the introduction of salt impurities such as moisture or corrosion products has the potential to make salts more corrosive [1]. Purification has been performed on both ^{7}Li enriched MSRE and UW-made natural lithium FLiBe salt to remove potentially corrosive oxides, moisture and impurities. Analytical chemistry methods of FLiBe salt have been investigated for comparison of electrochemistry and corrosion results. To monitor and control salt chemistry effectively in a reactor environment in situ electrochemical techniques have been developed. The FLiBe salt redox potential and cyclic voltammetry have become primary indicators of the overall corrosive potential and the solute content of FLiBe, respectively. The influence of salt chemistry and the combination of a variety of materials has been investigated by materials testing in FLiBe at 700°C. A molten salt flow loop has been constructed and tested with an initial batch of FLiBe salt. This represents the first time since the 1970s that a FLiBe loop has been operational in the US and therefore a significant amount of initial thermal-hydraulic testing is being performed to create datasets for thermal hydraulic modeling or simulation purposes.

2. FLiBe Salt Purification (UW)

^{7}Li Enriched MSRE FLiBe Re-purification

In 2012, the University of Wisconsin-Madison received 57.4 kg of spent ^{7}Li enriched MSRE FLiBe from Oak Ridge National Laboratory. Natural lithium fluoride contains 7.5 atomic percent ^{6}Li which has a much higher probability of producing tritium under irradiation. The United States currently does not produce large quantities of ^{7}Li enriched LiF suitable for nuclear environments. It was agreed that the sole purpose of this salt would be for nuclear environments where tritium production by natural lithium would be unacceptable. This included corresponding out-of-reactor experiments which mirror in reactor experiments. The salt was originally produced in 1964 and circulated in the secondary loop for over 23,566 hours. It was drained and stored in the system dump tank after MSRE shutdown in December 1969 [2]. For various reasons, it was suspected that over the course of its time in storage this salt was exposed to moister that could make the salt non-ideal for study in its current form. UW-Madison successfully re-purified this spent MSRE FLiBe in three batches in order to produce salts suitable for research of FLiBe salt chemistry and corrosion both out-of-reactor and in-reactor environments [3].

The first re-purification of MSRE coolant salt was conducted in a small test purification system which could produce 550±25 g of salt. This purifier, shown in Fig. 1, was constructed of nickel 200/201. A hydrogen fluoride and hydrogen sparging gas mixture was prepared with gas flow rates of 110 ml min^{-1} and 1.13 L min^{-1}. This experience helped identify potential problems for the scaled up batch purifier [3].

Fig. 1 The small nickel purification vessel used for the purification of the MSRE FLiBe [3].

The two final purifications of MSRE salt were conducted in a larger batch purification unit constructed of nickel 200/201. The hyrdofluorination system, shown in Fig. 2, is designed to process up to 40 kg of FLiBe from raw materials. It can accommodate up to 100 kg of liquid FLiBe. Fig. 2 (a) and (b) depict the nickel vessel being inserted into the stainless steel pressure vessel. The final completed hydrofluorination system is shown in Fig. 2 (c) [3].

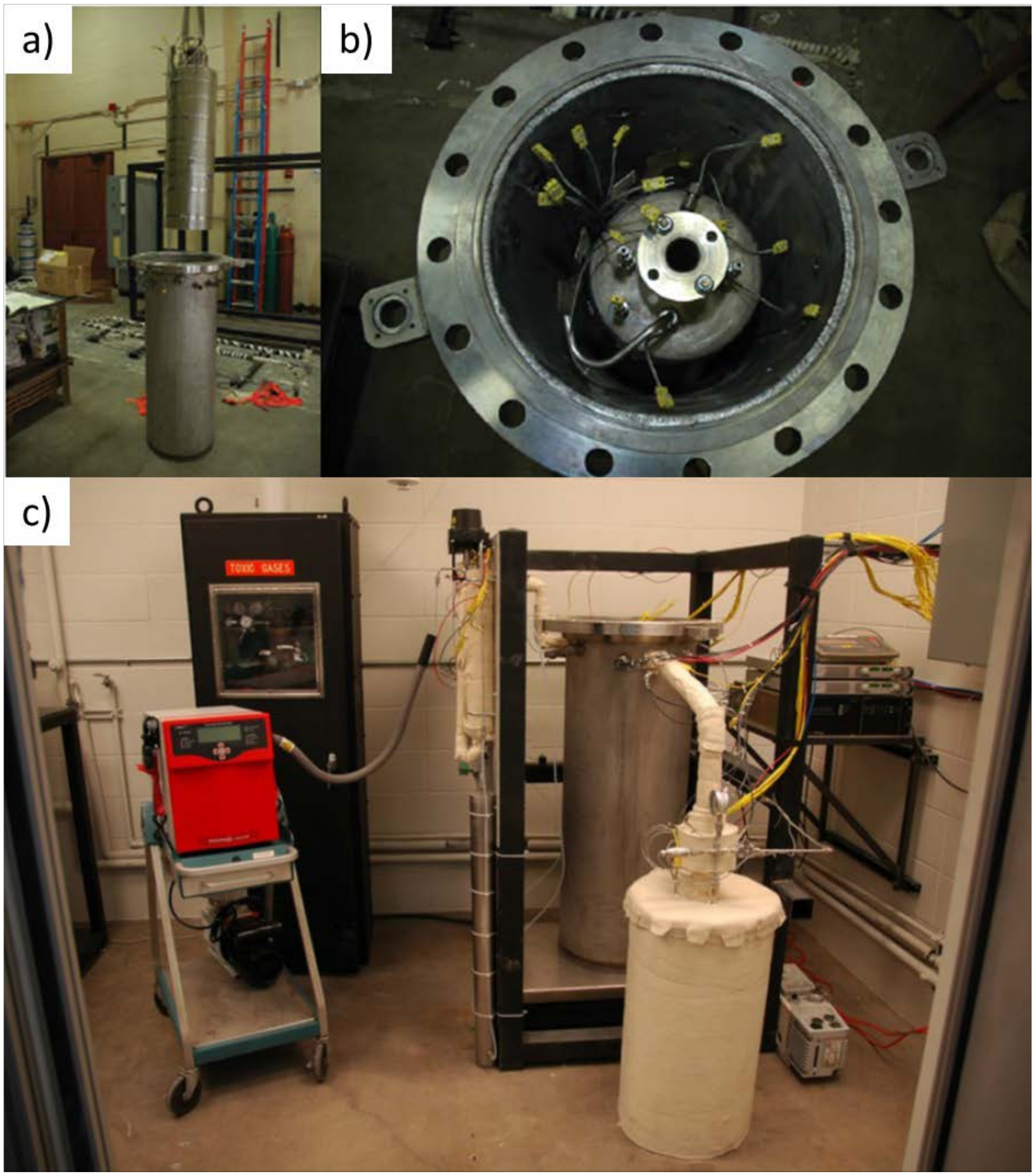

Fig. 2 (a) Lifting the purification vessel into position. (b) The purification vessel nested inside of the stainless steel vessel. (c) The competed hydrofluorination system with attached stainless steel salt storage vessel from MSRE [3].

In the second purification attempt, 16.2 kg of MSRE salt was purified. The coolant salt was sparged with AHF and hydrogen at 193 mL min^{-1} AHF and 1.93 L min^{-1} H_2 for 48 hours at 550˚C. Hydrofluorination was terminated when the pH in the online neutralizer carboy dropped below 6. The hydrofluorinated salt was then hydrogen sparged at 2.25 L min^{-1} at 550˚C for 36 hours. 3 kg of this salt was transferred to inert atmosphere gloveboxes for experimentation by way of smaller nickel transfer vessels [3]. This salt was used for both in-reactor corrosion and tritium research at MIT as well as out-of-reactor corrosion experimentation at UW-Madison [4].

In the final re-purification campaign, the remaining 39.5 kg of MSRE salt was re-purified along with the 13.2 kg of MSRE salt in the purifier. Hydrofluorination was conducted at a total flow rate of 2.5 L

min^{-1}, with 250 mL min^{-1} AHF and 2.25 L min^{-1} hydrogen. Hydrofluorination was performed for 76 hours. Hydrogen sparging was performed following the hydrofluorination at a flow rate of 2.5 L min^{-1} for three days at an average temperature of 631˚C. The re-purified MSRE salt was then stored in a nickel container under constant argon cover gas. The two nickel containers constructed for MSRE salt and natural lithium FLiBe salt produced later are shown in Fig. 3. [3]

Fig. 3 Nickel storage vessels for both natural and 7Li enriched FLiBe.

In comparison to unpurified FLiBe produced from raw materials, the cleaned MSRE was much whiter in color. Salt produced without purification has ranged in color from gray to yellow-white and is shown in Fig. 4 [3].

Fig. 4 A comparison of University of Wisconsin FLiBe and MSRE FLiBe. From left to right: re-purified MSRE FLiBe, salt melted in open atmosphere from raw components, salt melted in a glove box from raw components [3].

Natural Lithium FLiBe Production

Natural lithium FLiBe was produced at UW-Madison in March 2015 to support out-of-reactor corrosion and electrochemistry research. Lithium-fluoride of 99.8% purity was procured from Noah Technologies and 98.8% pure beryllium-fluoride was obtained from Materion. The salt components were layered to accelerate melting. Each layer was weighed on a 1 g accuracy scale. Beryllium fluoride chips used had a large variance in size. The purification vessel was then heated incrementally to 110°C. Water vapor was observed to escaping at a salt temperature of 100°C. The vessel was kept at 110°C for 20 hours, after which no water was observed in the effluent. At this point, the salt was heated up to 200°C, 300°C, and then set to 500°C to melt. Water was observed in the effluent stream after each temperature change. Melting took about ten hours. Fig. 5 shows the temperature profile during heating. A depression in temperature at 48 hours is due to the latent heat of FLiBe and signifies melting. The temperature was briefly increased to 520°C to melt any remaining components [3].

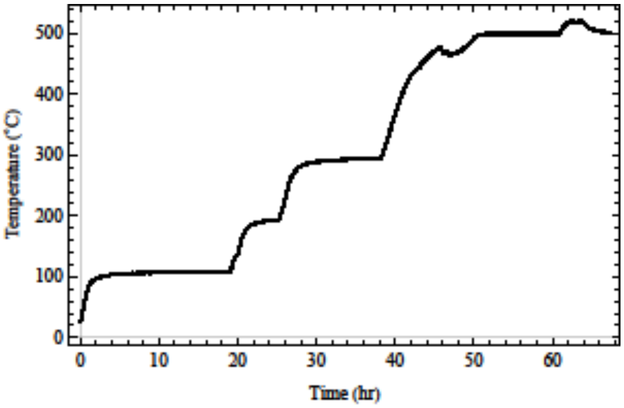

Fig. 5 Melting FLiBe from raw components. The large depression at roughly 48 hours and 460°C is caused by the latent heat of melting LiF-BeF_2 [3].

The hydrofluorination of natural lithium FLiBe used parameters similar to those used for purifying the MSRE coolant salt. A total flow rate of 2.5 L/m was selected with a 1:10 HF:H_2 ratio. Hydrofluorination was performed at 597ºC for around 80 hours. The total purification time was 72 hours. A total batch size of 38.7 kg was purified – a sample of the resulting molten and solidified salt is shown in Fig. 6. The molten salt is very transparent. The frozen salt had a slight green tint, which is likely caused by metal fluoride impurities. The composition of the purified FLiBe was measured with ICP-OES and ICP-MS techniques. These results are shown in Table 1. Elements in bold are considered to be the most stable impurity fluorides, so their effect on redox potential or corrosion can be profound. A total of 3.5 kilograms of the salt will be used for electrochemistry and static corrosion tests, with the majority of salt being saved for a natural convection flow loop [3].

Fig. 6 Purified natural lithium FLiBe prepared from raw materials, lithium-fluoride and beryllium-fluoride: (a) the molten salt after extraction in inert atmosphere. (b) solidified FLiBe salt [3].

Table 1 Composition of as-purified FLiBe salt measured by measured with ICP-OES and ICP-MS techniques [3].

Analyte	Result [mg kg^{-1}]	Analyte	Result [mg kg^{-1}]
Lithium	135000	**Chromium**	53.3
Beryllium	88200	Aluminum	28
Potassium	544	**Nickel**	10.7
Sodium	469	Thallium	10.6
Magnesium	139	Barium	9.51
Calcium	132	Strontium	3.7

In various out-of-reactor experiments the salt chemistry was modified to study the effect on salt electrochemistry and corrosion. It has been established that an addition of Be metal is required to further remove impurity cations, specifically Ni, Fe, and Cr, dissolved in the salt as fluoride compounds. Fig. 7 shows examples of ^{7}Li enriched MSRE FLiBe salt at various stages of the purification process: As-received (grey), hydrogen fluoride sparged (green), hydrogen sparged and beryllium reduced FLiBe (pure). Salts produced in the final two steps, hydrogen gas sparging and beryllium reduction, were characterized electrochemically and used in static corrosion experiments [3].

The impact of each salt production step is summarized by electrochemical and chemical analysis tools in Fig. 7. The fluoride salt redox potential is an electrochemical measurement of the melts redox condition. Generally, a smaller redox potential is indicative of a less oxidizing salt. Nuclear activation analysis (NAA) is a precise metals content analysis method. Hydrofluorination is designed mainly to remove moisture from the salt. The process, however, can be corrosive to the purifier vessel. The HF oxidizes the Ni vessel causing an increase in salt Ni content. These impurities are thought to give the as purified salt its greenish color. As a result, the poorly reduced hydrofluorinated salt is slightly more oxidizing than the as-received MSRE. The fluctuation in the metallic impurity content of the salt has a well characterized influence on the fluoride salt redox potential. Ni is very chemically active in FLiBe and increases the fluoride salt redox potential. NAA shows that Fe is easily removed by the H_2 sparge [3].

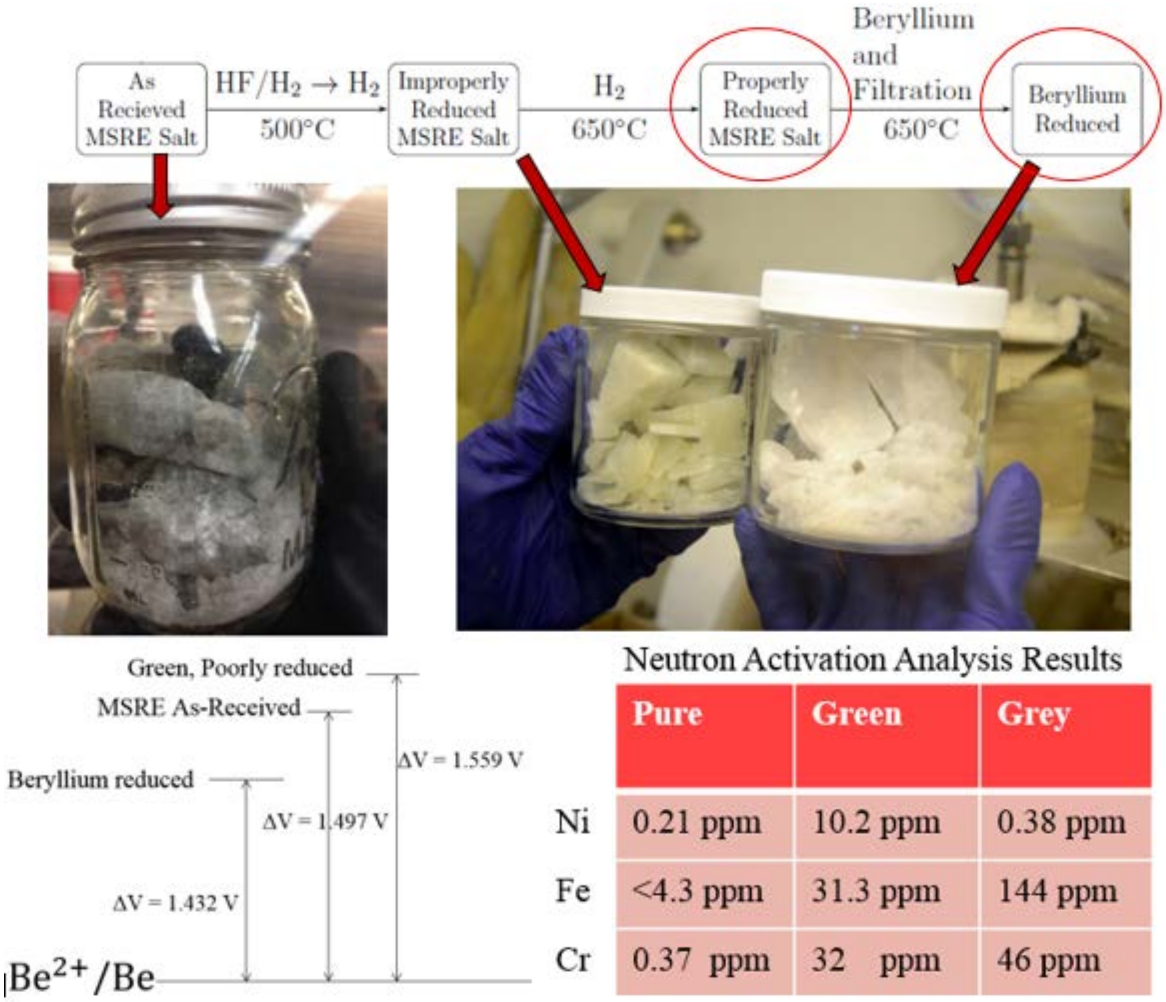

Neutron Activation Analysis Results

	Pure	Green	Grey
Ni	0.21 ppm	10.2 ppm	0.38 ppm
Fe	<4.3 ppm	31.3 ppm	144 ppm
Cr	0.37 ppm	32 ppm	46 ppm

Fig. 7 MSRE FLiBe at different stages chemistry control. Red circles signify equivalent reduction stages of UW-made FLiBe to be used in future corrosion tests. Fluoride salt redox potentials are estimated to be -1.7V and -1.4V, respectively [3].

To further reduce the natural lithium FLiBe made at UW-Madison, beryllium metal was added to FLiBe to reduce impurity metal fluorides to metals. Based on ppm amounts of Cr, Ni and Fe in UW raw materials FLiBe measured with Neutron Activation Analysis (NAA) shown in Fig. 7, an estimated .0681mg of Be per 50g batch of FLiBe would sufficiently reduce impurities, assuming that they are fluorides. Further work in FLiBe purification will be the development of a batch-wise Be-reduction procedure to prepare reduced salt for comparison to un-reduced salt in corrosion test [5].

To remove the metallic impurities that had been reduced by the Be addition, a filtration system was constructed. The gravity filtration system was consisted of a 2-3/8” diameter and 5” tall 316 stainless steel pipe. A 25-micron stainless steel mesh filter procured from Porous Metal Filter was TIG welded to the pipe bottom. The filter is suspended on top of an alumina cylinder to seat the filter inside the glassy carbon crucible. A glassy carbon crucible was placed below the filter to collect the filtered salt. The filter was able to contain two ~70 g pucks at a time. It was observed that the efficacy of the filtration process decreases with the number of filtration steps, presumably due to clogging of the filter mesh with metallic particles. Approximately 40g of Be-reduced FLiBe salt remained in the filter after the filtration process [5].

Fig. 8 Photographs of 316 stainless steel filter-bottomed crucible used for filtering metallic particulates generated from Be reduction [5].

Analytical Chemistry Methods

In addition to electrochemical characterization techniques used in this research, analytical chemistry of the metals content of FLiBe was performed by the Wisconsin State Laboratory of Hygiene (WSLH) using inductively coupled plasma-optical emission spectroscopy (ICP-OES). Table 2 shows the result for as-purified FLiBe produced at the University of Wisconsin-Madison. In general, the technique excels at quantifying dilute metal impurities such as chromium and nickel. The main salt constituents, however, require large dilution to be within the equipment's detectable range. The error of Be and Li measurements are usually on the order of 1 and 2 mole %, respectively. Therefore, ICP-OES is not properly suited for studying changes in beryllium content in the context of beryllium reduction experiments. The measurement confirms, however, that as-received FLiBe is close to the theoretical 0.66LiF-0.33BeF$_2$ mole percent composition [6], [7].

Table 2 Salt composition and metals content of purified FLiBe determined by ICP-OES at the Wisconsin State Laboratory of Hygiene [7].

	LiF	BeF_2	Al	As	Ba	Ca	Cr	Mg	Mn	Ni	K	Na	Sr	Tl
	(mol %)		(ppm)											
Purified Li_2BeF_4	65 ± 2	34 ± 1	34 ± 21	11 ± 1	9.9 ± 0.2	114 ± 4	6 ± 1	136 ± 6	4.1 ± 0.4	15 ± 2	448 ± 38	493 ± 47	3.8 ± 0.1	9.8 ± 0.5

Two salt sampling methods were experimented with. Salt samples were first obtained from solid FLiBe by cleaving the salt with a steel axe. When the salt was molten, salt samples were also gathered by coating a molybdenum dip rod at 500˚C. A comparison of the two methods showed that the solid method reported values for the main salt constituents that were closer to the theoretical value. For this reason, only solid sampling methods were used to validate electrochemical methods[7].

Using the default ICP-OES software method, spectral interference was encountered between Be and Cr for certain wavelengths of light. By adjusting the method for Cr from 205.56 nm to 283.563 nm, the measured value of chromium metal for pure UW Flibe dropped from 80 ± 7 ppm to 6 ± 1 ppm [7]. The new chromium values are more comparable to salts produced by the same methods in the literature [2]. ICP-OES shows excellent accuracy when measuring important impurities such as chromium. The standard deviation of most ICP-OES measurements of Cr is approximately ±3 ppm. In Table 3, the chromium concentration of several samples used in voltammetry studies of CrF_2 are shown [7].

Table 3 Concentration of chromium metal in FLiBe after additions of CrF_2 to purified FLiBe determined by ICP-OES [7].

Sample	Cr (±3 ppm)
1	6
2	88
3	100
4	156
5	185
6	286
7	352

3. FLiBe Electrochemistry Measurements (UW)

An in-situ electrochemical method can expedite the measurement of corrosion product concentrations and help better predict the longevity of a reactor primary loop. A sensor for FLiBe must deal with several challenges. The high-temperature, corrosive environment renders many traditional electrochemical cells impractical for the study of molten fluoride salts. Electrochemical cells for FLiBe must be designed with the important consideration of beryllium toxicity. It must be an adequate beryllium and moisture barrier so that it is practical for use in both laboratory and industrial systems[6]–[9].

The experimental apparatus is shown in Fig. 9. Electrochemistry experiments are carried out inside of an Omega 36/115 ceramic radiant full cylinder heater. The cylindrical heater sits on 1” thick 6 ½” by 6 ½” Zircar rigid insulation base inside of a ¼” deep circular hole cut in the center. Salt is melted in the heater inside of a GAT 13 glassy carbon crucible obtained from HTW Hochtemperatur-Werkstoffe

GmbH. This carbon crucible is nested inside of a 2 ½” OD stainless steel crucible, which is used to contain salt in the event of a crucible fracture and also provides an electrical ground through a vertical wire that extends through the heater lid. The glassy carbon and steel crucibles are both nested inside of a larger alumina crucible. This crucible provides electrical insulation between the inner crucibles and heater coils [9].

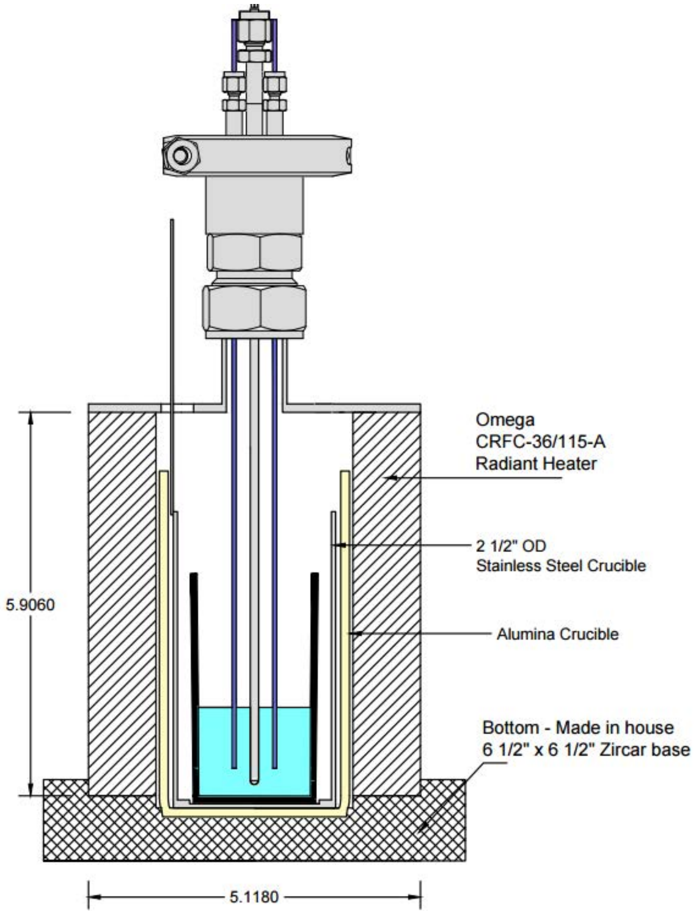

Fig. 9 Electrochemistry heater CAD drawing. Dimensions are shown in inches.

The UW electrochemistry probe is shown in Fig. 10 resting on top of the heater with its electrodes extending down into the salt melt. A picture of the separated probe, along with a cutaway drawing is included in Fig. 10. The numbered items are described below [9].

1. **Glassy Carbon Anode**. Used as anode material due to stability under polarization.
2. **Molybdenum Cathode and Indicator Electrodes**. Used due to high corrosion resistance, electro-positive nature, and availability.
3. **Swageloks with Teflon Ferrules**. Swageloks allow the depth of the electrodes to be adjusted while the Teflon maintains electrical isolation between electrodes.

4. **KF Connections**. Allows the probe to be easily disassembled for maintenance.
5. **Viton O-Ring**. Provides a gas seal for probe's tube stub.
6. **Boron Nitride Space**. Keeps electrodes aligned vertically and electrically isolated.

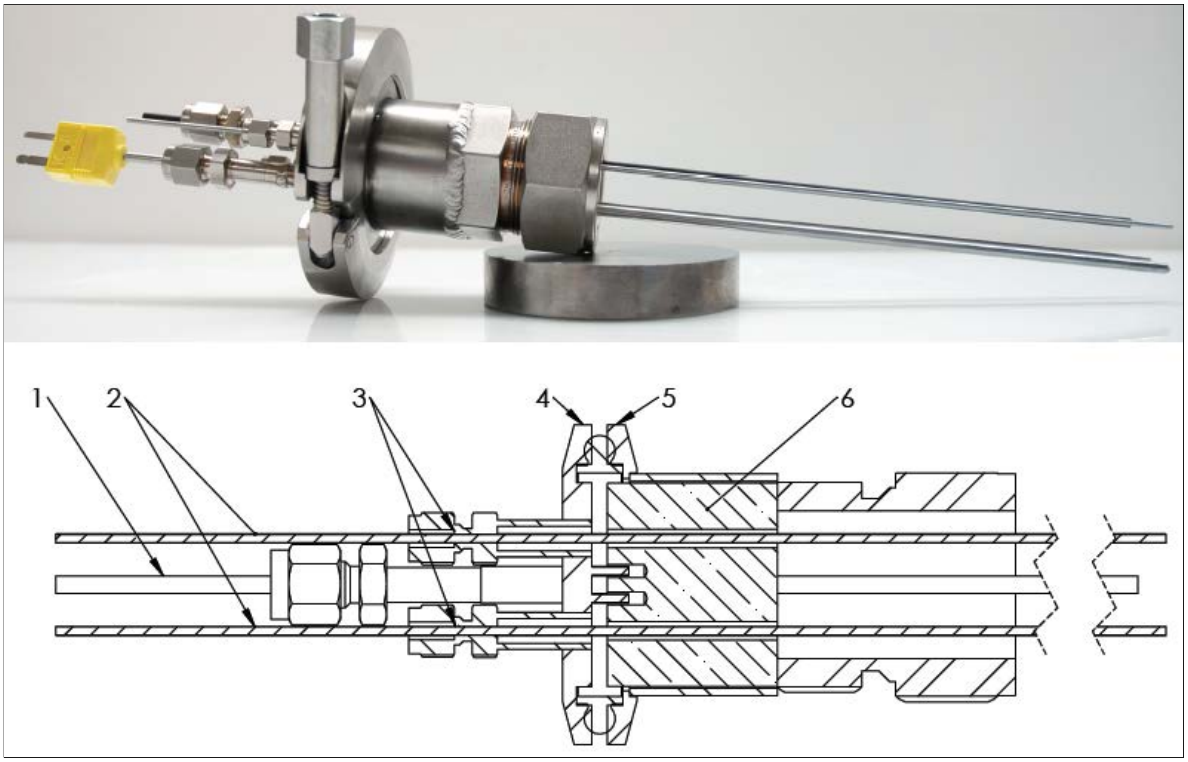

Fig. 10 UW FLiBe redox probe used for dynamic reference electrode measurements [9].

Determining the Be/Be^{2+} Reference Potential

Establishing a repeatable reference electrode for voltammetry experiments is considerable challenge for FLiBe salt electrochemistry. Development of a reliable thermodynamic reference electrode remains a challenge in fluoride melts [10]. An inert electrode, or quasi-reference electrode, is not an adequate reference electrode because its potential can depend on many factors. Fortunately, in molten FLiBe, a better reference electrode can be manufactured in situ. The following Be/Be^{2+} reference reaction is formed by reducing beryllium from solution onto the molybdenum WE.

$$Be^{2+} + 2e^{-} \leftrightarrow Be^{0}$$

When Be covers the surface of the electrode, the apparent reduction potential of this half-cell reaction is defined as follows:

$$E_{(Be^{0},Be^{2+})} = E^{o}_{(Be^{0},Be^{2+})} + \frac{RT}{nF} ln\, a_{Be^{2+}}$$

where $E^{o}_{(Be^{0},Be^{2+})}$ is the standard potential of the Be/Be^{2+} couple with respect to an arbitrary thermodynamic reference point, R is the gas constant, T the temperature, n is the number of electrons per mole of reaction, and F is Faraday's constant. As a concentrated species, Be^{2+} is theorized to greatly influence the ionic strength of the solution and have a relatively stable activity [11]. This electrode has adequate repeatability for identification of other chemical species and qualitative measurements of their reduction potentials. The electrode is referred to as a dynamic beryllium reference electrode (DBRE). The term '*dynamic*' characterizes the method of forming a Be/Be^{2+} couple as one that is not far from a thermodynamically reversible (quasi-static) process [8], [9].

Methods for production of the DBRE

Establishing the Be/Be^{2+} reference potential generally involves two steps: an electrolysis step to form the dynamic beryllium reference electrode (DBRE) and a cell potential measurement to characterize the Mo QRE. There are several approaches to the electrolysis step. Several authors have proposed galvanostatic (constant current) methods for the electrolysis step [12], [13]. Due to equipment constraints UW-Madison initially perfected potentiostatic (constant potential) methods [3], [8], [9]. Later a potentiostat was used to perform potentiodynamic (swept potential) methods for the electrolysis step. In all cases, the potential of the DBRE is characterized following the electrolysis step using an open circuit potential measurement to acquire the cell potential between the inert indicator electrode (Mo QRE) and the DBRE [6], [7].

Potentiostatic DBRE production methods were conducted with a HP 3616A power supply used in constant potential mode. This produced repeatable DBRE behavior. Care was needed to select the appropriate plating voltage for the electrolysis phase to produce the DBRE. An electrode that is sufficiently plated with Be will have a relatively constant (nonpolarizable) characteristic voltage. A statistically significant measurement can be made with a plateau voltage of roughly 10 seconds or greater. The behavior of DBREs produced with different plating potentials are shown in Fig. 11. The potential needed to produce adequate DBREs is largely dependent on salt chemistry and the design of the electrochemical cell. Too small a plating potential will not produce a distinct voltage plateau because the Be deposit formed is too short lived. Drawing too much current at the electrode will result in a thick beryllium coating and a much longer delay time between measurements as the Be metal is redissolved [7], [9].

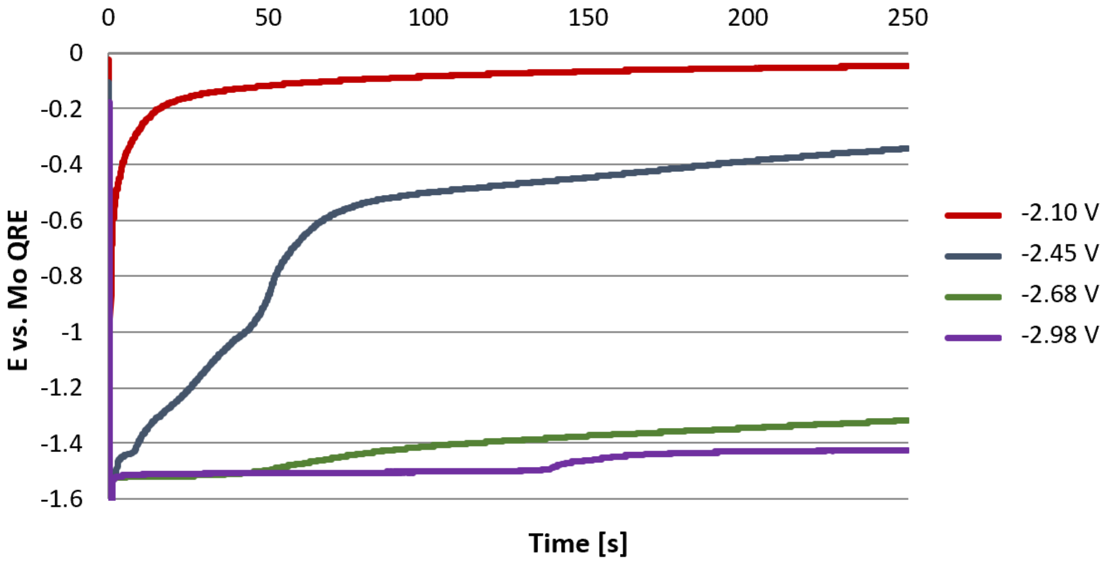

Fig. 11 Voltage relaxation measurements for various applied plating voltages [9].

Later, the electrolysis step of DBRE production was conducted with an Metrohm Autolab 128N potentiostat operated in potentiodynamic mode. In Fig. 12, a linear sweep voltammogram (LSV) is conducted with a potential can rate of 100 mV/sec. The potential of the molybdenum working electrode (WE) with respect to the Mo QRE is swept in the negative direction until the reduction of beryllium is observed. An advantage of the LSV method is that other reactions due to dilute FLiBe salt impurities can be observed. Fig. 12 shows LSVs of a salt conducted at various temperatures between 500˚C and 700˚C. This salt has been purposefully contaminated with 286 ppm CrF_2 to simulate corrosion. Reactions 2c and 3c are attributed to dilute CrF_2 and AlF_3, respectively. AlF_3 is a relatively stable fluoride that is difficult to remove by most purification methods. As a result, some trace AlF_3 is expected in purified FLiBe [7].

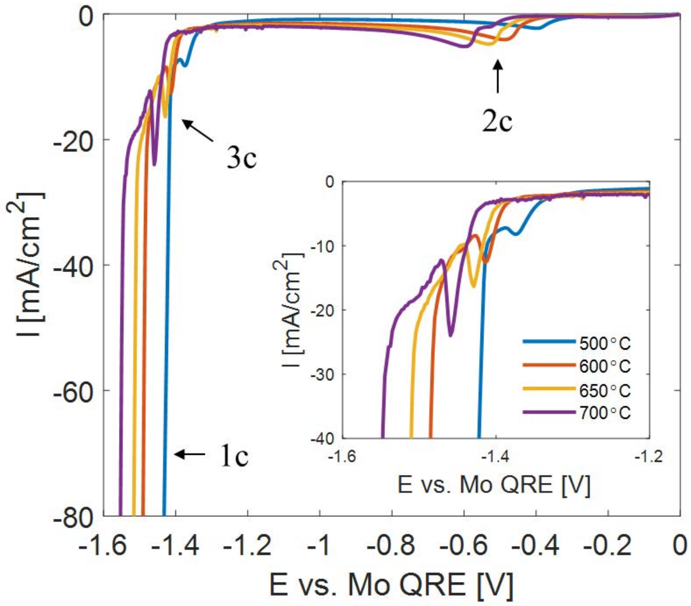

Fig. 12 Linear sweep voltammogram (LSV) of FLiBe salt with 286 ppm Cr at various temperatures. Scan rate is 100 mV/sec [7].

When using the LSV method, the length of the DBRE voltage plateau can be controlled by setting a current or charge transfer cutoff that terminates the LSV and ques an open circuit potential. For an electrode with an exposed surface area around 1 cm^2 the current density cutoff was usually between -80 mA/cm^2 and -150 mA/cm^2. The value needed is thought to depend mainly on the size of the electrode surface and the salt chemistry. Once the right cutoff was selected, the LSV method produced the most consistent DBREs. Fig. 13 shows the resulting voltage plateau in the cell potentials between the Mo QRE and DBRE at various temperatures between 500˚C and 700˚C [7].

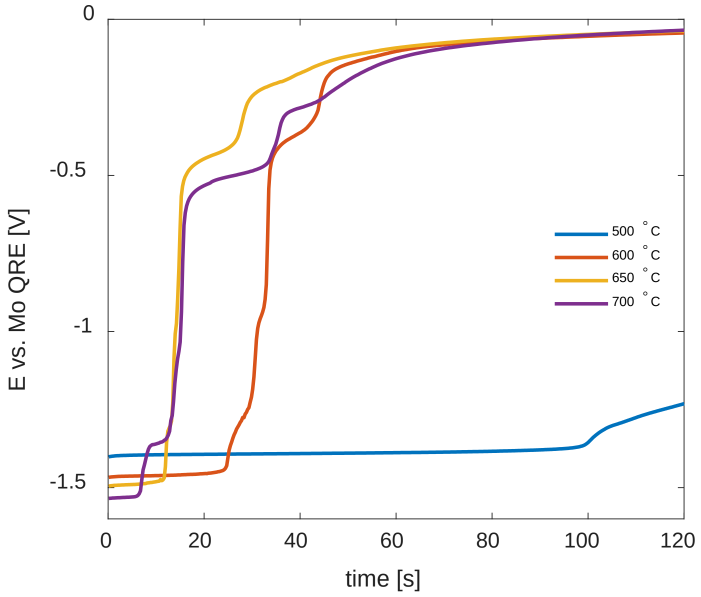

Fig. 13 Open circuit potential between the dynamic beryllium reference electrode (DBRE) and the Mo QRE as a function of time in FLiBe salt with 286 ppm Cr following the LSV plating step at various temperatures [7].

Application of the Dynamic Beryllium Reference Electrode

The dynamic beryllium reference electrode (DBRE) has been used in two type of electrochemical FLiBe salt characterization methods. The fluoride salt redox potential is a cell potential measurement related to the salts overall redox condition and is theorized to be directly tied to the salt's tendency to oxidize a foreign species. The DBRE can also be used in other voltammetry experiments as a relatively stable quasi-reference electrode.

Fluoride Salt Redox Potential

UW-Madison has conducted extensive research on the influence of common FLiBe impurities on the fluoride salt redox potential. The goal was to develop a simple in situ test which could determine how oxidizing FLiBe salt could be to a container material. Fluoride salt redox potential is a simple open circuit potential measurement between a molybdenum indicator electrode at the potential of the solution and the DBRE. In Fig. 14, several salt chemistries are compared using the fluoride salt redox potential. Salts with a higher cell potential are thought to have more chemical potential energy and may be capable causing more corrosive damage to a given material then a salt with a smaller cell potential. Figure 14, shows that as-purified (as-received) has a relatively high cell potential of 1.6 V vs. the DBRE. Adding beryllium to as-purified FLiBe lowers the cell potential (chemical potential energy) of the salt making it less likely to corrode common structural materials. Adding an oxidizing agent such as FeF_2 can increase the cell potential of a reduced salt back to the levels of an as-purified FLiBe salt.

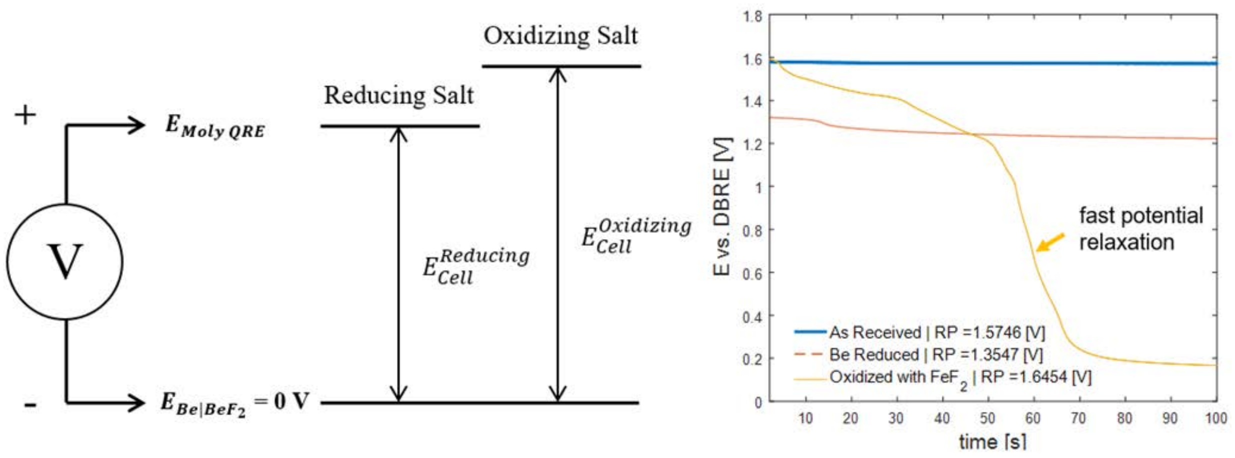

Fig. 14 Typical cell potential measurements with time of salts with various chemistries following formation of the dynamic beryllium reference electrode (DBRE) [6].

Common corrosion products, such as CrF_2, FeF_2 and NiF_2, were dissolved in separate melts to predict the behavior of FLiBe salts after extensive corrosion. Each salt impurity was added to two different batches of FLiBe with different initial fluoride salt redox potentials. Fig. 15 shows that relatively reducing salts with small cell potentials show a higher response to metal impurity addition. Nickel and iron fluorides have a clear oxidizing effect. The strong dependence of the cell potential on the concentration of NiF_2 and FeF_2 indicates that the FLiBe salt redox condition is strongly influenced by a combination of their redox reactions. One theory is that in an as received salt the amount of impurity fluorides added is comparable to the amount already in the salt, while in a reduced salt the amount of fluoride impurities added is some order of magnitude greater than what is initially in the salt. Thus, there is a greater response to additions of a few hundred ppm of iron and nickel fluoride in a reducing salt [6], [9].

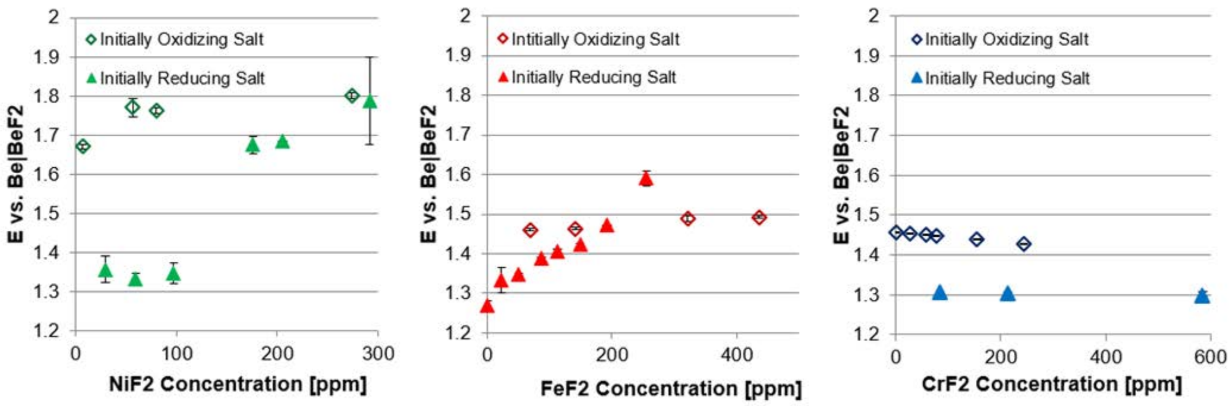

Fig. 15 FLiBe salt redox potential measurements as a function of NiF_2, FeF_2, and CrF_2 concentration [6], [9].

The cell potential is nominally affected by the addition of CrF_2. In Fig. 15, both as-purified and beryllium reduced FLiBe are somewhat reduced by chromium fluoride. Chromium fluoride is more stable than fluorides formed by iron, molybdenum or nickel. Due to the stability of chromium fluorides, it may be energetically unfavorable for chromium to undergo redox reactions on the molybdenum QRE that could affect its potential. On the other hand, chromium may have some capacity to reduce other less stable impurities, such as iron and nickel fluorides. Reduction of metal fluorides whose redox reactions more heavily influence the cell potential could account for the observed decrease in the cell potential [6], [9].

Cyclic Voltammetry

Cyclic voltammetry (CV) was used to investigate the behavior of electroactive components of FLiBe, such as Cr^{2+} and Fe^{2+}. CV was selected for study of corrosion products for several reasons. The technique offers a large amount of information about the thermodynamics and kinetics of the chemical system. There are several well-developed theories for CV which describe either potential, current or charge in terms of concentration. Theories are available for both soluble-soluble and soluble-insoluble reactions. To validate CV as an in situ diagnostic for monitoring corrosion, FLiBe salts with varying quantities of metallic impurities were investigated [7].

Preliminary studies of FLiBe using cyclic voltammetry focused on identification and characterization of common corrosion products. In Fig. 16, the cathodic peak, 1c, represents the onset of beryllium reduction according to the reaction, beryllium reduction is observed at negative potentials and is generally the limit of the usable negative potential range. Anodic current peaks 2a and 4a are attributed to the oxidation of chromium and iron, respectively. The cathodic current peaks 2c and 4c are attributed to the reduction of chromium and iron, respectively. Based on the literature both of these reactions involve a two electron reaction [14].

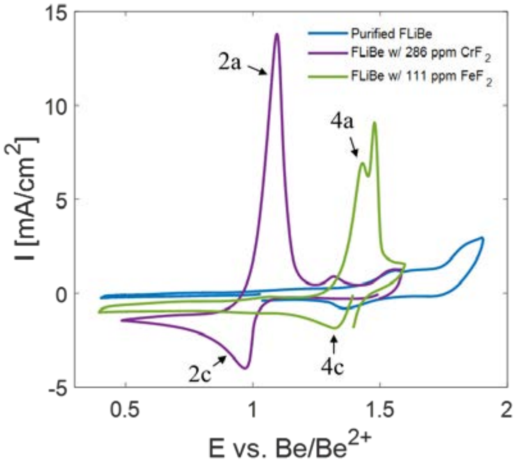

Fig. 16 Cyclic voltammograms of molten FLiBe salt samples with various impurity additions at 650˚C. Scan rate was 80 mV/sec.

The reduction of soluble Cr^{2+} on the working electrode forms insoluble Cr^0. In this case, an expression for the reduction potential of Cr^{2+} is derived by assuming the activity of the metal deposit is unity.

$$E_{(Cr^0/Cr^{2+})} = E^{\circ}_{(Cr^0/Cr^{2+})} - \frac{RT}{nF}\ln\frac{1}{\gamma_{Cr^{2+}}} - \frac{RT}{nF}\ln\frac{1}{[Cr^{2+}]} \qquad (1)$$

where $E^{\circ}_{(Cr^0/Cr^{2+})}$ is the standard potential. The activity coefficient of Cr^{2+}, $\gamma_{Cr^{2+}}$, is not known at this time. In Fig. 17(a), the shift in the reduction potential of the Cr/Cr^{2+} couple with temperatures appears to agree with equation 1 when normalized to the Be/Be^{2+} couple.

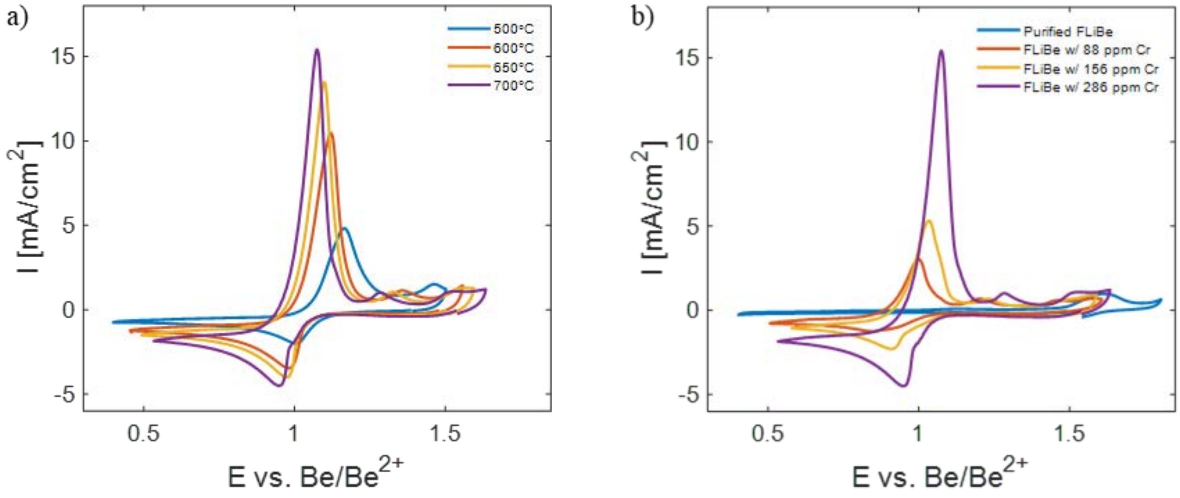

Fig. 17 CVs of a) FLiBe containing 286 ppm Cr at various temperatures and b) FLiBe containing various Cr concentrations at 700˚C. Scan rate is 80 mV/sec.

Quantitative methods based on peak current density are attractive, in part, because they do not rely on a thermodynamic reference electrode. For a soluble-insoluble reaction, a relation between the voltammogram cathodic peak current and the concentration of the electroactive species was solved by Berzins and Delahay [15], [16].

$$i_p = 0.61A[Cr^{2+}]\sqrt{\frac{F^3 n^3 D_{Cr^{2+}} v}{RT}} \tag{2}$$

A is the area of the working electrode, n is the charge transfer coefficient equal to 2, $D_{Cr^{2+}}$ is the diffusion coefficient of Cr^{2+}, and v is the potential scan rate. In Fig. 17(b), the shift in the reduction potential of the Cr/Cr^{2+} couple with Cr^{2+} concentration appears to agree with equation 1 when normalized to the Be/Be^{2+} couple. This couple also produces distinct peaks with peak current densities proportional to Cr^{2+} concentration. The direct proportionality between faradaic peak current density and species concentration, rather than a logarithmic dependence, may enable accurate concentration measurement and eliminate potential errors at low concentrations [7].

4. Out-of-Reactor Materials Corrosion Testing (UW)

Design of Static Corrosion Experiment

The corrosion capsules used in both ^7Li enriched and natural lithium FLiBe salt static corrosion experiments are identical to the corrosion capsules used in the in-reactor experiments at MIT. An example of a graphite corrosion capsule is shown in Fig. 18. To compare corrosion behavior of samples as a function of redox potential identical samples were placed in separate capsule wells containing one of two salt chemistries. To study how the presence of graphite effects corrosion of structural materials, 316 stainless steel was tested with and without a 316 stainless steel liner. To avoiding galvanic corrosion due to the dissimilar materials affects, samples were electrically isolated from the corrosion capsule by Boron Nitride (BN) capsule caps. A figure of the corrosion system is shown in Fig. 18 [4], [5].

Fig. 18 Computer Aided Drawings of corrosion crucibles and sample locations [4], [5].

A primary goal of this corrosion study is to understand the effect of redox potential on corrosion of structural materials. It would be expected that lower (less negative) redox potential salt would exhibit less corrosion in materials, whereas a higher (more negative) redox potential salt would exhibit more corrosion in materials. Two different/separate salts have been prepared and two identical sets of samples were prepared for corrosion. The as-purified (no added beryllium) FLiBe has a well-characterized redox potential of -1.706V, and will serve as the baseline salt for comparison. The other crucible (identical sample arrangement) will contain a filtered, Be-reduced FLiBe. Since the Be metal reduces fluoride impurities such as FeF_2 and NiF_2 to their metallic constituents. These metallic species can easily be removed by filtration. Based on ppm amounts of Cr, Ni and Fe in UW raw materials FLiBe measured with Neutron Activation Analysis (NAA) shown in Fig. 7, an estimated .0681mg of Be per 50g batch of FLiBe would sufficiently reduce dilute impurity fluorides. To prepare the reduced FLiBe, four ~70 g batches were melted in glassy carbon crucibles, and 0.05 mg Be-flake was added before setting the temperature to 600^{o}C and allowing the Be to dissolve for 24 hours. The final redox potential after beryllium addition was 1.41V vs. the DBRE [4], [5].

Materials Performance in ^{7}Li Enriched FLiBe Salt (UW)

Binary Ni-Cr alloys

Ni-Cr binary alloys were studied to gain a fundamental understanding of corrosion in molten FLiBe salt at 700^{o}C. Since chromium is a major player in structural metals corrosion, alloys with varying concentrations of Cr were exposed to FLiBe to understand the impact of bulk Cr concentration on corrosion. Two binary alloys, Ni-5%Cr and Ni-20%Cr, were tested in FLiBe at 700^{o}C for up to 1000 hours. The weight loss of the two alloys after corrosion is shown in Fig. 19. The weight loss results from the Cr depletion from alloys and then dissolution into molten salt in form of chromium fluoride. Due to the higher concentration of Cr in Ni-20%Cr this alloy experienced more weight loss than the Ni-5%Cr alloy [4].

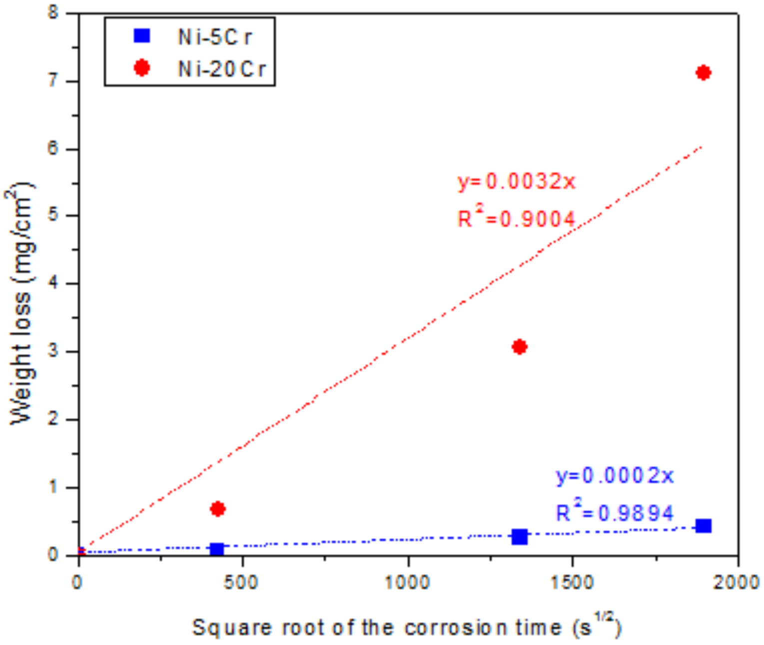

Fig. 19 Weight loss as a function of square root of the corrosion time for Ni-5%Cr (blue) and Ni-20%Cr (red) alloys that were exposed to molten FLiBe at 700°C for 50, 500 and 1000 hours. Linear trend lines (dashed lines) and R-squared values are included for both alloys [4].

Fig. 20 shows the surface morphology of samples tested in molten FLiBe for varying durations. The intergranular corrosion attack was observed on the surface of all samples, and the attack becomes deeper and wider with increased of exposure time. This is indicative of preferential Cr leaching along grain boundaries in the near-surface region. From these corrosion images, it is obvious that the fraction of grain boundaries per unit area on the surface of Ni-20%Cr is larger than that on Ni-5%Cr, which also contributes to the overall Cr depletion rate. Using ImageJ, the area fraction of attacked grain boundaries is 3.85% and 28.42% for Ni-5%Cr and Ni-20%Cr, respectively after 1000 hours corrosion in molten FLiBe. In general, the density of grain boundaries is inversely proportional to grain size for polycrystalline materials. Therefore, the Ni-20%Cr with a relatively smaller grain size has higher fraction of grain boundaries per unit area [4].

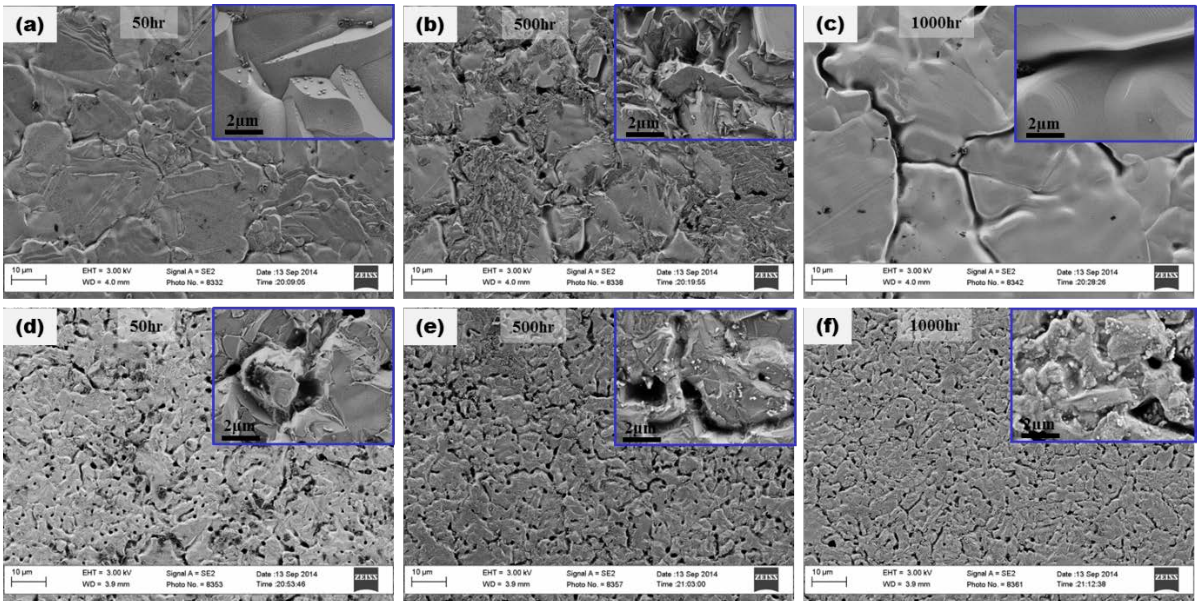

Fig. 20 Surface SEM images of (a, b, c) Ni-5%Cr and (d, e, f) Ni-20%Cr tested in molten FLiBe for 50, 500 and 1000 hours (from left to right) respectively. Inset on upper right corner shows the morphology of grain boundaries [4].

The cross-section of the near-surface layer of post-corrosion Ni-5%Cr and Ni-20%Cr model alloys is shown in Fig. 21. The corrosion surface (denoted with red arrow in SEM images) was protected by a layer of electroplated Cu prior to polishing. The voids with a couple of microns in diameter randomly distribute within the near-surface layer of Ni-20%Cr alloys, but they are not observable in post-corrosion Ni-5%Cr alloy. Furthermore, the void size in Ni-20%Cr slightly increased with increasing corrosion time [4].

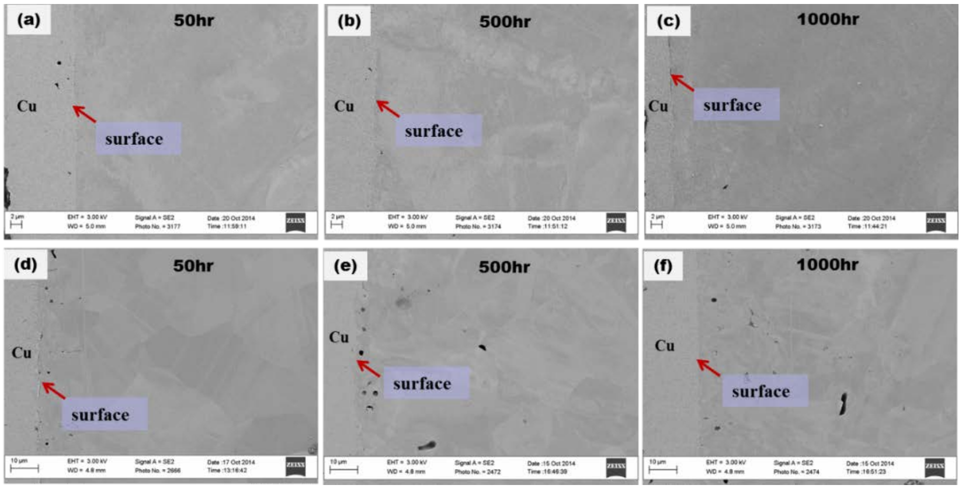

Fig. 21 Cross-sectional SEM images of (a, b, c) Ni-5%Cr and (d, e, f) Ni-20%Cr exposed to molten FLiBe for 50, 500 and 1000 hours. A layer of Cu was electroplated on all samples surface for edge protection during polishing. Arrow denotes corrosion surface [4].

Figures Fig. 22 and Fig. 23 show the elemental distributions of main constituents Ni and Cr in the cross-section of the near-surface region in FLiBe-exposed Ni-5%Cr and Ni-20%Cr for 50, 500 and 1000 hours. The relatively low concentration of Cr was observed in the near-surface region for all corrosion samples. Unlike the corrosion surface where preferential grain boundary attack was observed, the Cr depletion is also observed in the grains. It is likely that the Cr depleted grain boundaries are too thin to be identified by EDS imaging technique. This is consistent with above cross-sectional observation. Additionally, the Cr depletion is not uniform in same depth. To evaluate corrosion attack depth, the maximum Cr depletion distance was measured and labeled in EDS Cr mappings. With the increasing of corrosion time, from 50 hours to 1000 hours, the maximum Cr depletion distance increases from 5.4μm to 21.7μm and from 18.2μm to 140.8μm for Ni-5%Cr and Ni-20%Cr respectively [4].

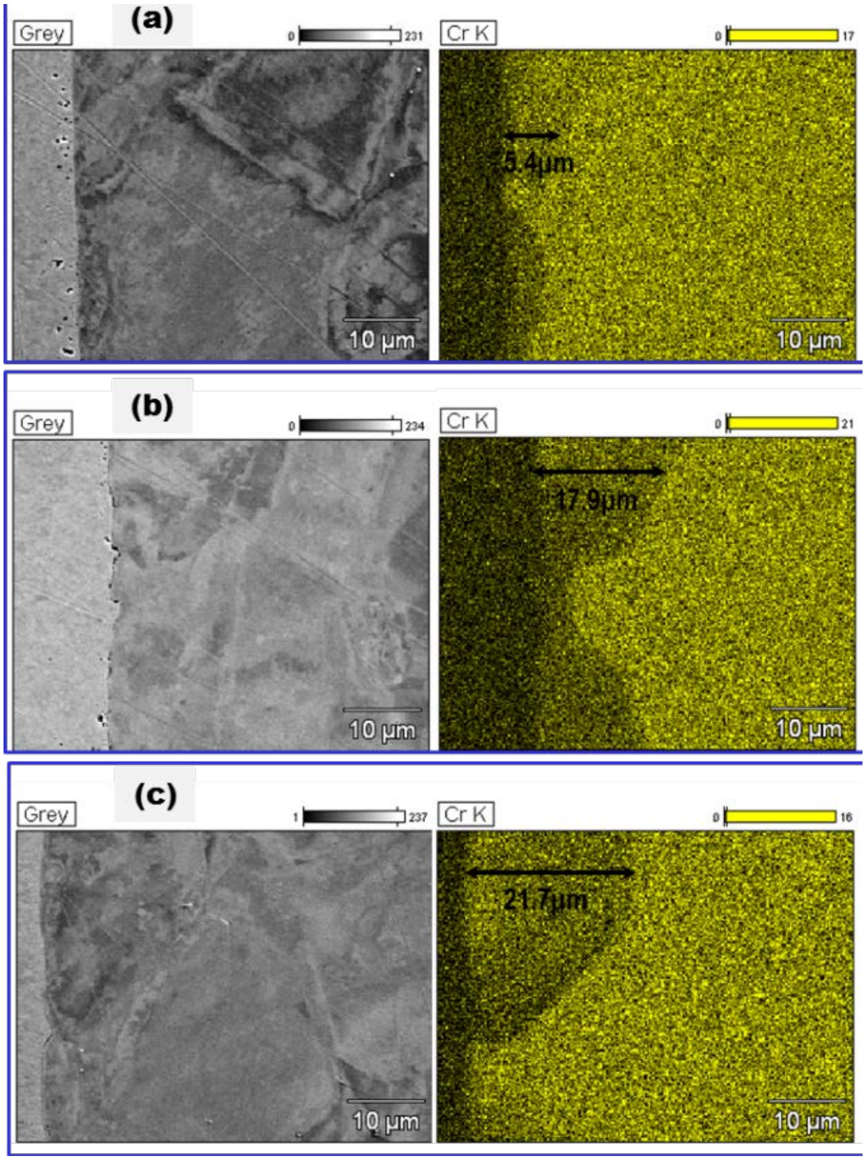

Fig. 22 EDS mapping of Cr elemental distribution in the near surface layer of the Ni-5%Cr samples tested in molten FLiBe for (a) 50 hours, (b) 500 hours and (c) 1000 hours [4].

The Cr depletion in Ni-5%Cr only occurred in certain grains adjacent to the surface. Actually, only partial Cr depletion occurred within those grains. In Ni-20%Cr, the Cr depletion occurred in a wide range crossing multiple connected grains. This is because the grain size in Ni-5Cr (~100μm-200μm) is much larger than Ni-20Cr (~10μm-30μm), even larger than the maximum Cr depletion distance. The reason why Cr depletion preferentially occurred in certain grains, not in all the grains to the same depth, will be further analyzed using EBSD technique [4].

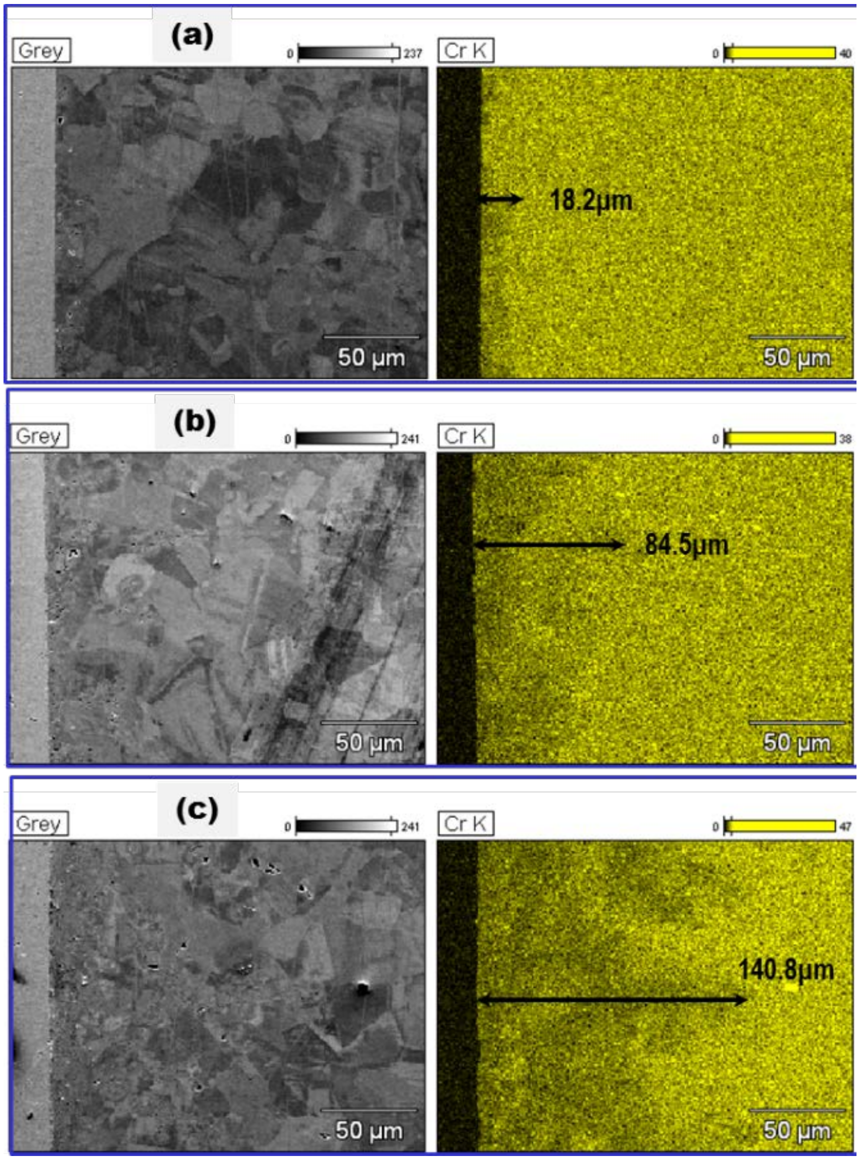

Fig. 23 EDS mapping of Cr, Ni and Cu elemental distribution in the near surface layer of the Ni-20%Cr samples tested in molten FLiBe for (a) 50 hours, (b) 500 hours and (c) 1000 hours [4].

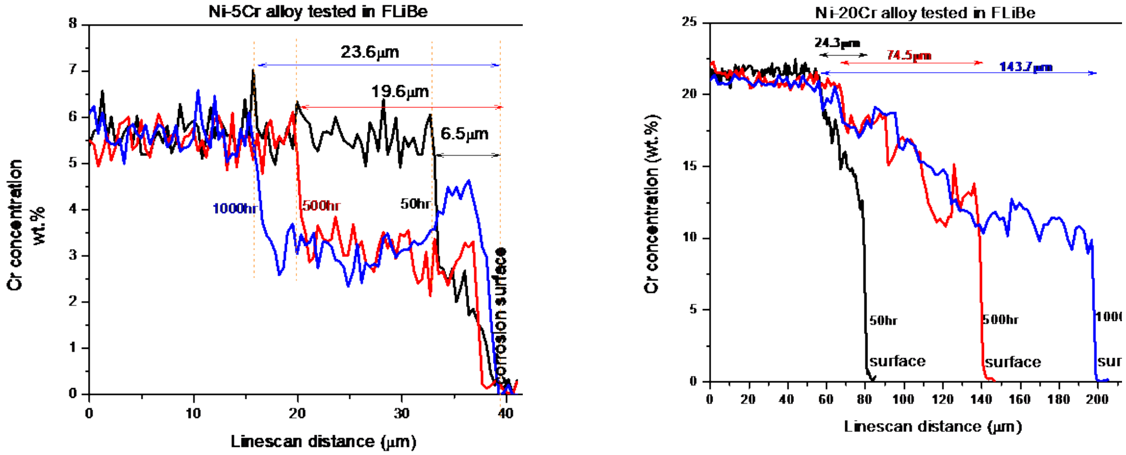

(a) (b)

Fig. 24 Cr concentration profiles (EDS linescan after exposure to molten FLiBe salt at 700°C for 50, 500 and 1000 hours (a) Ni-5%Cr and (b) Ni-20%Ni [4].

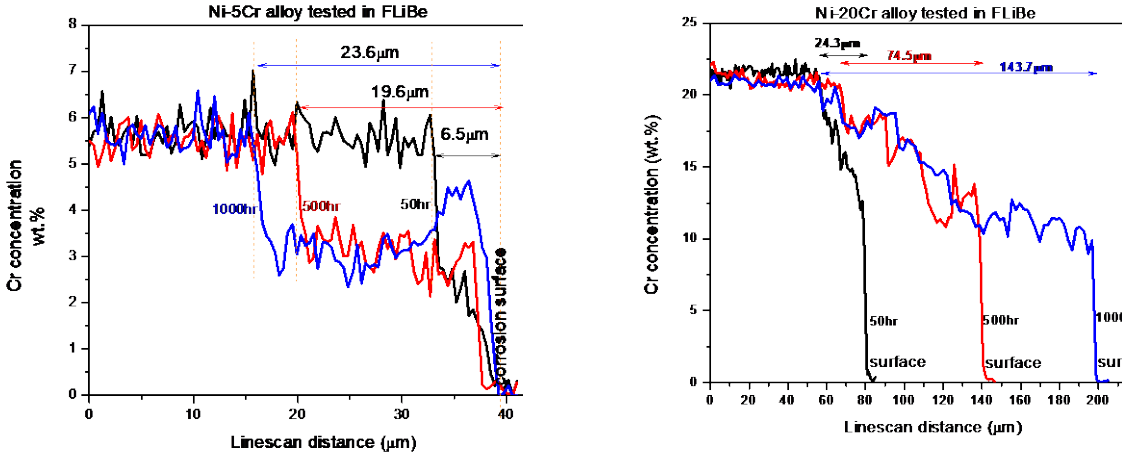
(a) (b)

Fig. 24 shows quantitative results of Cr concentration profiles in post-corrosion Ni-Cr alloys based on EDS linescan. Each linescan path crosses the maximum Cr depletion region that is referred to the observation of EDS Cr mappings. The linescan direction is from the unaffected substrate to corrosion surface. From these Cr concentration profiles, the Cr depletion distance is 6.5μm, 19.6μm, and 23.6μm for Ni-5%Cr, and 24.3μm, 74.5μm, and 143.7μm for Ni-20Cr, exposed to molten FLiBe for 50 hours, 500 hours and 1000 hours respectively. From these Cr concentration profiles, it was observed that the Cr concentration drops down dramatically from the unaffected substrate (no Cr depletion) to the Cr depleted region and then maintains at about half of initial Cr concentration in Ni-5%Cr, but gradually decreases in Ni-20% Cr [4].

Hastelloy N

Hastelloy N sample coupons were exposed to ^{7}Li enriched FLiBe for 1000 hours at 700˚C. To test the effect of dissimilar metals, samples were exposed in graphite capsules, such as the one shown in Fig. 25, and capsules that were lined with pure nickel. The weight loss of Hastelloy N samples after corrosion tests in the pure nickel capsule was only 0.124mg/cm^2 which translates to about 1.226μm/year assuming uniform corrosion. This low corrosion rate is attributed to the lack of dissimilar materials and the purity of the salt used in this study. However, the samples tested in graphite capsule showed a weight gain of about 0.165 mg/cm^2 [4].

Figure 25(a) shows photograph of these samples and no significant corrosion attack was observed in these initial visual examinations. Higher magnification surface examinations (Fig. 25(c) and Fig. 25(d)) of the Hastelloy N samples after corrosion tests showed conclusive evidence of corrosion attack. The initially polished surface (Fig. 25(b)) exhibited an increase in surface roughness and developed a porous structure for the samples tested in pure nickel capsule (Fig. 25(c)). For the samples tested in graphite containment, particle phases with diameter ranging from several tens of nano-meters to about 1.5μm covered the entire surface (Fig. 25(d)) [4].

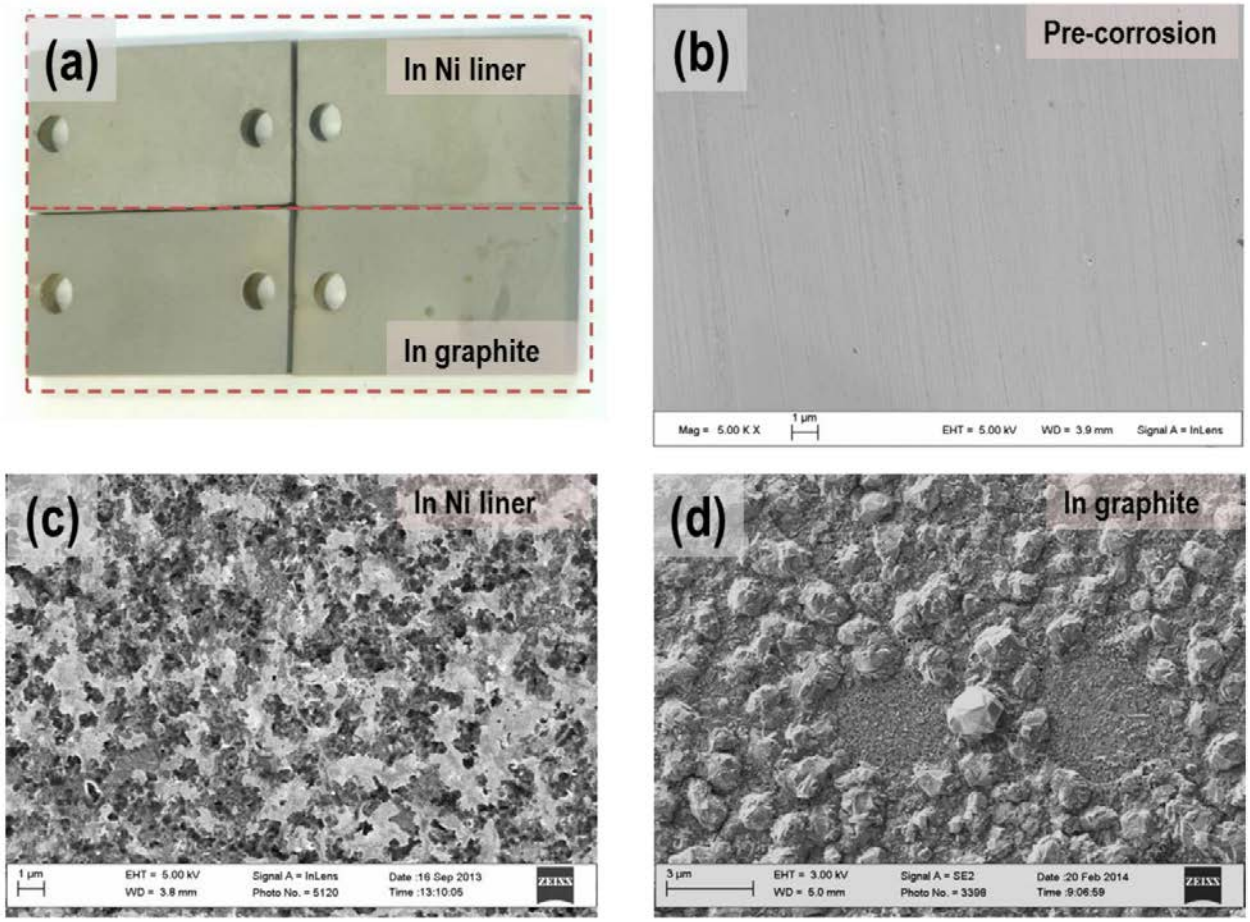

Fig. 25 (a) Hastelloy N samples after corrosion testing in FLiBe salt in nickel and graphite capsule at 700°C for 1000 hours. (b), (c) and (d) SEM images showing surface morphology of Hastelloy N before and after corrosion tests in nickel and graphite capsules, respectively [4].

The compositions of the surface features shown in Fig. 26(c) and (d) were analyzed using SEM-EDS and the results are shown in Fig. 26 As shown in Fig. 26(a), this porous layer formed on the samples tested in nickel capsule consisted of nickel enriched surface with Mo and Si rich precipitates in the size range from hundreds nanometers to several microns. For the samples tested in graphite capsules (Fig. 26(b)), relatively high Cr concentration was observed on the particulate phases and Mo and Si was not detected in the particulates. This suggests that the particulate phases are Cr-carbide particles formed due to the reaction between carbon from graphite source and Cr in the salt. Similar to samples tested in nickel capsules, Mo and Si rich precipitates were also observed on the sample surface [4].

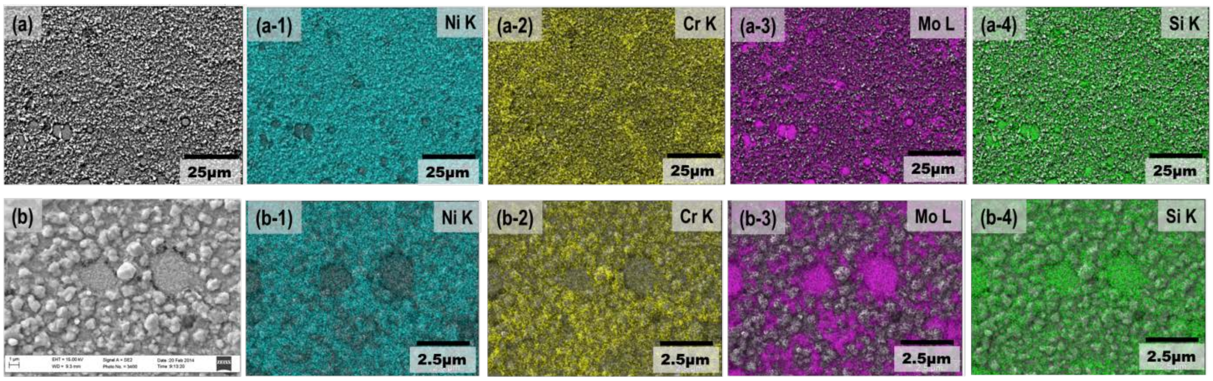

Fig. 26 EDS elemental mappings of Hastelloy N corrosion surface after testing molten FLiBe in nickel (a, scale bar 25μm) and in graphite capsule (b, scale bar 2.5μm) [4].

XRD was employed to investigate the phases in the near-surface regions of samples after corrosion tests. Fig. 27 shows XRD patterns of Hastelloy N before and after corrosion tests in nickel and graphite capsules. The characteristic peaks of the matrix FCC austenite phase are clearly identifiable on the three types of samples[17], [18]. Additionally, the characteristic peaks of $MoSi_2$ (PDF card 01-072-6181) phase were detected on both types of post-corrosion Hastelloy N samples. In addition to $MoSi_2$ precipitates, the carbides of Cr_3C_2, Cr_7C_3, and Mo_2C were identified by the XRD pattern in the samples tested in graphite capsule (Fig. 27(c)) [19]–[24]. This analysis is consistent with EDS analysis of post-corrosion alloy surface shown in Fig. 27(b). The Ni_3Fe was speculated to form in sample near-surface layer due to the severe depletion of Cr from Hastelloy N and thermal diffusion of Mo toward either surface or grain boundary [4].

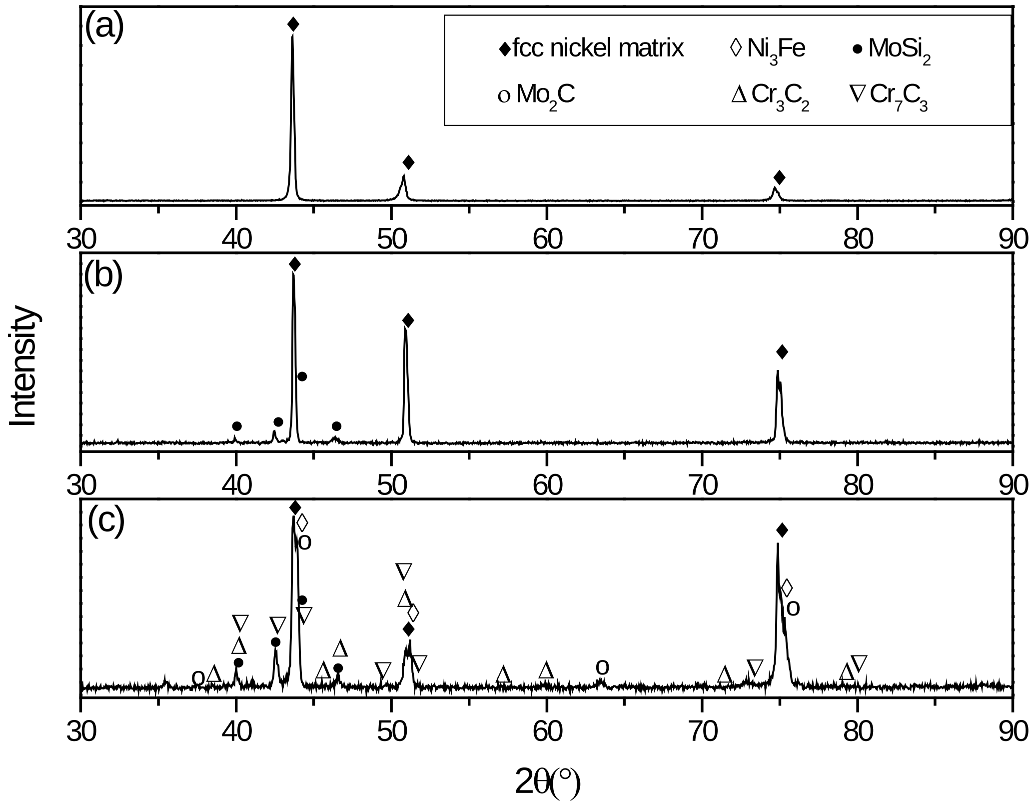

Fig. 27 X-ray diffraction patterns of the near-surface regions of Hastelloy N (a) as-received condition, and (b) and (c) after corrosion testing in FLiBe salt at 700°C for 1000 hours in nickel and graphite capsule, respectively [4].

Fig. 28 shows cross-sectional SEM images and EDS elemental mappings of as-received Hastelloy N and annealed Hastelloy N samples. In as-received alloy, the Mo- and Si-rich round phases with diameter varying from hundreds nanometers to about five microns are randomly distributed in grains. After annealing, the precipitates with relatively high concentration of Mo and Si formed at grain boundary. The precipitates coarsened and became discontinuous network at grain boundary with increasing annealing time. This observation of Mo-rich precipitates nucleating and coarsening at grain boundary indicates the microstructural instability of Hastelloy N at high temperature. This Mo- and Si-rich precipitate evolution at high temperature might changes the corrosion resistance of Hastelloy N in molten fluoride salts. In recent publications, the effect of Mo content in Hastelloy N on corrosion was reported by F. Ouyang et.al.[25], [26]. It was concluded that long-term corrosion rate of Hastelloy N and Hastelloy B3 in molten FLiNaK was controlled by the outward diffusion of Cr and Mo. The study only discussed the relationship between Mo content in alloys and corrosion rate. The mechanism of Mo effect on corrosion behavior is not well understood. From this annealing test, the migration of Mo-rich phase to grain boundary during high temperature exposure certainly mitigates Cr outward diffusion particularly along grain boundary [4].

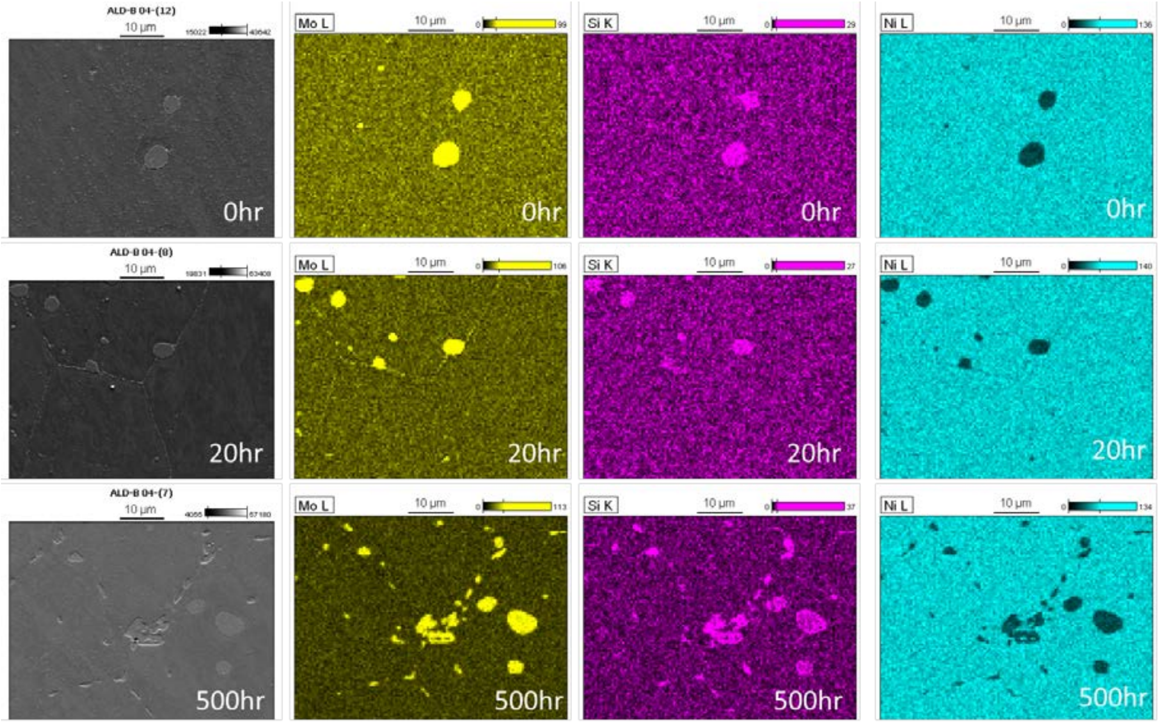

Fig. 28 Cross-sectional SEM images and EDS mappings showing the Mo rich precipitates and the elemental distribution of Mo, Si and Ni of as-received and annealed Hastelloy N samples. Annealing temperature was 850°C. Scale bar is 10μm [4].

Further examination of the near-surface regions of post-corrosion Hastelloy N samples was performed by focused ion beam (FIB) milling of the surface (Fig. 29). As observed in these FIB-SEM images, pores extend to ~200 nm into the substrate of the sample tested in pure nickel capsule (Fig. 29(b)), indicating that the porous structure shown in plan-view image in Fig. 29(a) extends to this depth below the surface. The void formation mainly results from outward diffusion of Cr and vacancy condensation analogous due to the Kirkendall effect observed in diffusion couples. As shown in Fig. 29(c) and (d), the samples tested in graphite capsule exhibited a different near-surface microstructure. High magnification SEM image (Fig. 29(c)) clearly showed three different shapes of carbides particles on corrosion surface, corresponding to Cr_3C_2, Cr_7C_3 and Mo_2C as identified by XRD. Large size particles on surface have different response to FIB milling electrons from alloy matrix, which caused rough cross-section as shown in Fig. 29(d). Underneath the corroded surface, cavities were observed in the vicinity of $MoSi_2$ precipitates. The formation of these cavities is a result from the massive depletion of Cr from the region underneath the precipitates. Meanwhile, the Cr and some of the Mo in Hastelloy N matrix in near-surface region also thermally diffused to the sample surface to react with carbon and formed carbides particles. As a consequence of substantial Cr depletion and Mo diffusion outward, a layer of Ni_3Fe compound formed underneath the surface at 700°C. These microstructural observations are in agreement with XRD analysis (Fig. 29(c)). Additionally, carbide containing layer was observed under Ni_3Fe phase layer. The dark features shown in Fig. 29(d) were identified as $Cr_{23}C_6$ particles and had a diameter of tens nanometers by scanning transmission electron microscopy (STEM) analysis (Fig. 29(d)) [4].

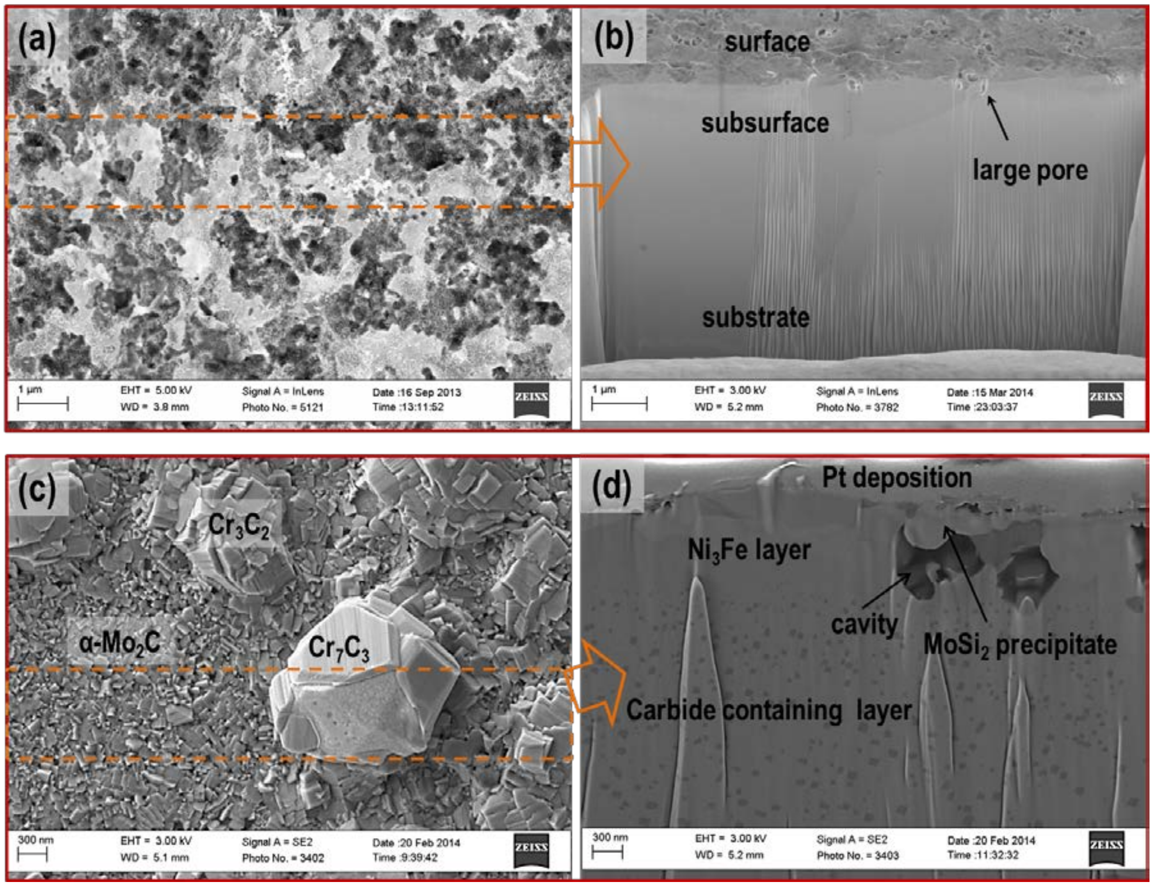

Fig. 29 SEM images showing corrosion surface and FIB milled cross section underneath framed area (orange line) for the Hastelloy N tested in FLiBe salt at 700ºC for 1000 hours in (a, b) nickel capsule and (c, d) graphite capsule, respectively [4].

Under STEM, multiple layers from surface to substrate were clearly observed in the Hastelloy N sample tested in graphite capsule. As shown in Fig. 30(a), a FIB lift-out samples encompassed about 7μm depth below the corrosion surface. In near-surface layer (Fig. 30(b)), TEM diffraction patterns identified regions 1 and 2 to be Ni_3Fe phase and nickel matrix. Fig. 30(b) also presents the distribution of carbide particles formed underneath Ni_3Fe layer, becoming larger and more scattered in deeper regions. A close view in Fig. 30(c) shows the spherical morphology of these particles within Hastelloy N matrix. The elemental compositions of these particles were quantitatively identified using STEM-EDS technique (Fig. 30(c)). High concentration of Cr, Mo and C was detected on a particle and the nominal compositions of Cr and Mn to C was approximately 23 to 6 in atom%. Combining these analyses, the nanosized particles formed in Hastelloy N matrix were identified as $(Cr, Mn)_{23}C_6$. A few Mn substituted Cr lattice sites in $Cr_{23}C_6$. Therefore, it was referred to $Cr_{23}C_6$ in this paper rather than $(Cr, Mn)_{23}C_6$ [4].

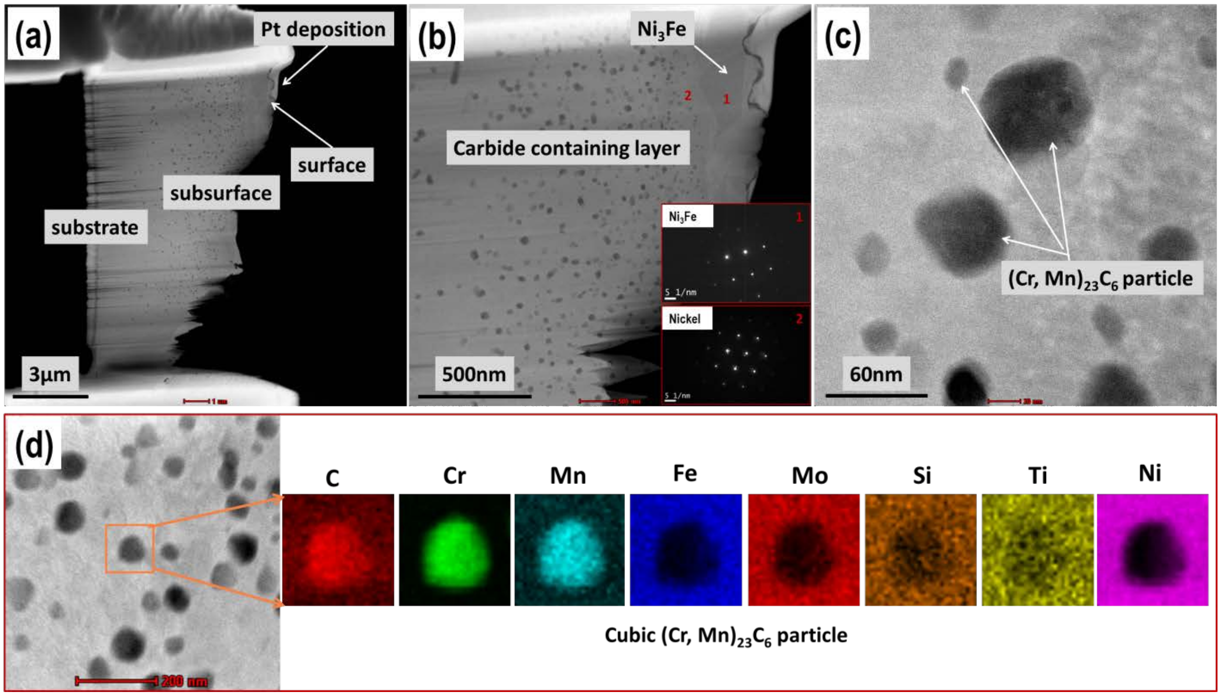

Fig. 30 STEM images and EDS mapping showing the microstructure features in near-surface layer of the Hastelloy N tested in graphite capsule. (a) full view of a FIB lift-out sample, (b) a region in near-surface layer with TEM diffraction patterns in region 1 of Ni_3Fe layer and region 2 of Hastelloy N matrix, (c) close view of nanosized carbide particles within Hastelloy N matrix, and (d) quantitative elemental mapping (C, Cr, Mn, Fe, Mo, Si, Ti and Ni) of a particle marked by a square [4].

Cross-sectional SEM-EDS examination was performed to quantify the depth of corrosion attack in Hastelloy N tested in pure nickel and graphite capsule. Fig. 31(a) shows a cross-sectional SEM image and EDS maps on the same region of the sample tested in pure nickel capsule. Mo and Si rich precipitates were observed both at grain boundary and in the vicinity of grain boundaries. EDS maps also identified Mo and Si shown earlier in Fig. 31(a). Cr depletion preferentially along grain boundary was only observed to a depth of about 3.5µm. This observation suggests that the Cr depletion occurred predominantly through grain boundary diffusion D_{gb}.

The samples tested in graphite capsule showed dramatically different microstructure in the near-surface regions. Fig. 31(b) shows a cross-sectional SEM image in the near-surface region of the material. Grain boundary attack was clearly observed, and Mo- and Si-rich precipitates were also observed both at grain boundaries and on the corrosion surface. This is similar to the observations made for samples tested in the nickel capsule. However, carbide particles ($Cr_{23}C_6$) were observed at depths ranging from approximately 2µm to 9µm from corrosion surface. These particles correspond to the black features observed in FIB milled cross-sectional SEM image shown in Fig. 31(d) and STEM images in Fig. 31(b). This carbide containing layer results from the reaction between the Cr in Hastelloy N matrix and the inward diffusing carbon from the molten FLiBe. The carbon in molten salt originally emanated from graphite crucible.

A layer of about 1.4μm in thickness underneath surface was devoid of any precipitate particles. This layer was identified as Ni_3Fe compound by XRD and STEM analyses. EDS mappings of principal elements also showed higher concentration of Fe in this layer. It is speculated that the Cr in the near-surface region diffuses outward to react with the inwardly diffusing carbon in the initial stage of corrosion and forms the chromium carbide phase.

In Figures Fig. 31(d) and Fig. 31(c), SEM indicate that Mo thermally diffuses toward either the grain boundary or surface, and then forms carbide phase particles on surface. In the EDS maps, high concentrations of Cr and Mo were observed on corrosion surface, which corresponds to the Cr_3C_2, Cr_7C_3, Mo_2C, and $MoSi_2$ precipitate phases. Furthermore, high concentration of Cr was observed at the near-surface grain boundaries suggesting that Cr in Hastelloy N preferentially diffuses toward grain boundaries.

In the case of exposure of Hastelloy N to graphite capsules, there is evidence that carbon transport can lead to chromium carbide formation and stabilization of the reactive chromium in the bulk matrix. Literature suggests that the diffusion rate of carbon through nickel matrix $D_{C/Ni}$ ($\sim10^{-10}$ m^2/sec) is much faster than Cr $D_{Cr/Ni}$ ($\sim10^{-15}$ m^2/sec)[27]–[29]. Therefore, the carbon that is transported from graphite to Hastelloy N through FLiBe salt can diffused inwardly and reacted with Cr deep within the Hastelloy N matrix. As a result, after the initial stage of corrosion, the newly-formed chromium carbide particles ($Cr_{23}C_6$) stabilize Cr in Hastelloy N matrix. No Cr is observed in the Ni_3Fe layer even though Cr concentration gradient existed [4].

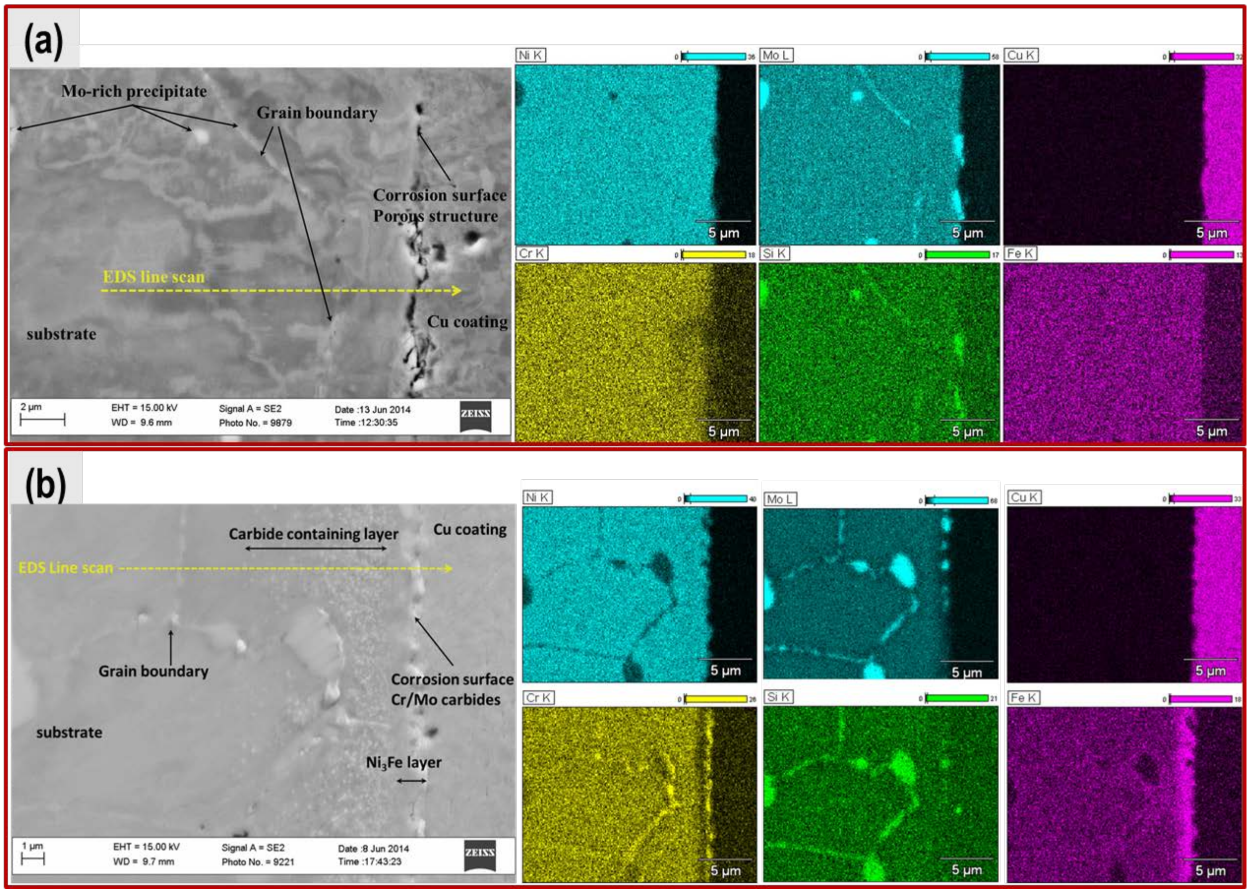

Fig. 31 SEM-EDS analysis of Hastelloy N samples tested in (a) nickel capsule and (b) graphite capsule. Cu coating was electroplated on sample surface prior to polishing. Yellow dashed arrows in cross-sectional SEM images denote the traces of EDS line-scan [4].

316L Stainless Steel

The results of weight change measurements after corrosion tests are shown in Fig. 32. In all cases the samples experienced a loss in weight due to corrosion indicating a material dissolution mechanism. This weight loss increased with exposure time. Up to 2000 hours, the weight loss was higher for the samples tested in graphite capsules as compared to the samples tested in stainless steel capsules, while at 3000 hours, the weight loss for the two capsule material tests were approximately identical. This effect can result from the introduction of carbon into the alloy at the later stages of corrosion resulting in the formation of Cr-carbide in the near-surface regions of the alloy. This will be discussed later through microstructure analyses [4].

As the depletion of Cr becomes pronounced in the near-surface, the chromium inside the sample diffuses outwards due to a concentration gradient. The rate of Cr depletion therefore depends on its thermal diffusion coefficient in 316 stainless steel. As Cr is depleted deeper within the sample, grain boundaries rather than grains, become the preferred path of Cr migration because of their higher diffusion coefficient [30], [31]. The effective diffusion coefficient (D_{eff}) of Cr in the 316 stainless steel samples tested in 316 stainless steel capsules, without graphite, was calculated to be 4.2×10^{-19} m^2/s at 700ºC, which is in the range of the reported $D_{Cr/316ss}=10^{-19}\sim10^{-17}$ m^2/s at 700ºC[30], [31]. In Fig. 32, The weight loss of 316 stainless steel in FLiBe is proportional to the square root of corrosion time indicating that corrosion is thermal diffusion-controlled [32].

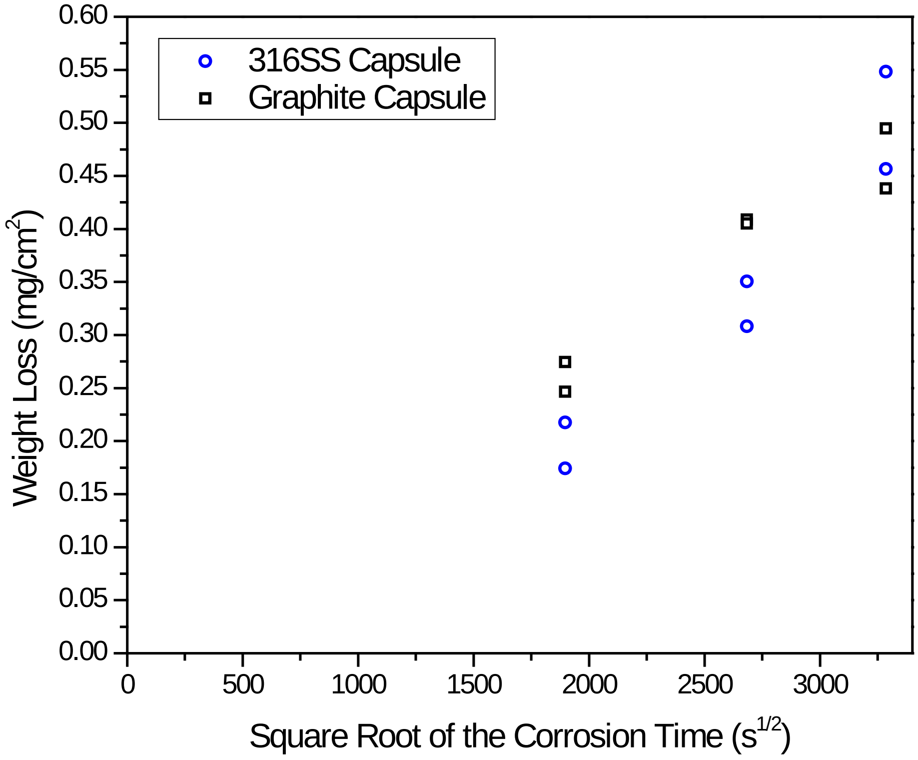

Fig. 32 Weight measurements for 316 stainless steel samples tested at 700°C in molten FLiBe salt in 316 stainless steel and graphite corrosion capsules (two samples in each capsule) as a function of square root of corrosion time [4].

The surface images of samples from each testing condition are shown after the corrosion tests in Fig. 33. All samples clearly showed evidence of corrosion attack particularly along the grain boundaries, although there is evidence of attack on the grains as well. As expected, the degree of attack increases with exposure time. The samples tested in the graphite capsules had more extensive grain boundary attack than those tested in 316 stainless steel capsules. These initial observations indicate that graphite accelerates the corrosion attack to 316 stainless steel and is to some extent consistent with the trends in weight loss measurements shown in Fig. 32. Additionally, pitting is observed on the grains of all samples and there is evidence of round particulate phases adhered to the surface [4].

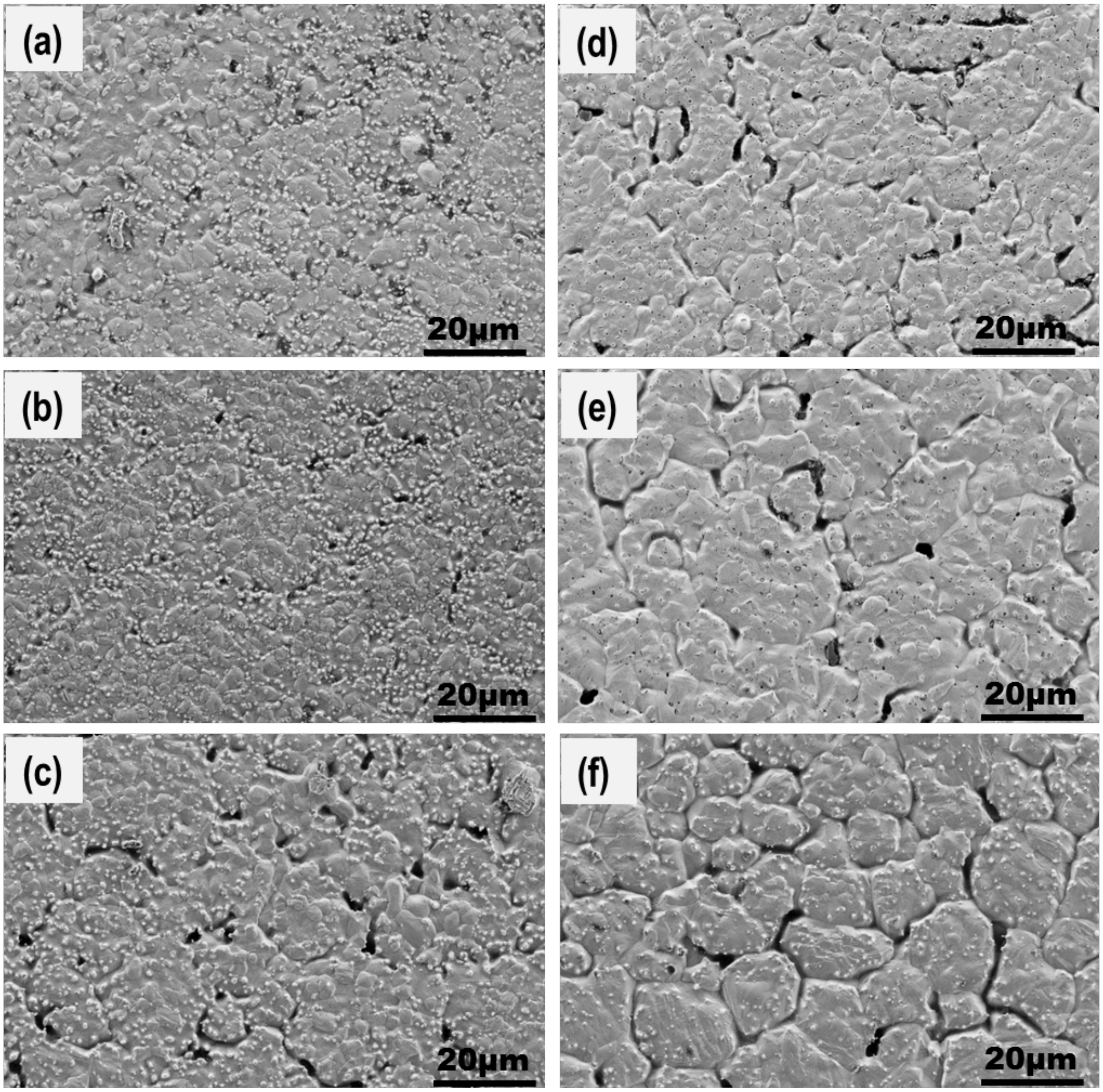

Fig. 33 Surface SEM images of 316 stainless steel samples after corrosion testing under different conditions. a, b, and c in 316 stainless steel capsules, and d, e, and f in graphite capsules for 1000, 2000, and 3000 hours, respectively [4].

The pitting and surface particulate were further investigated. Fig. 34 shows SEM images of the surface of the samples exposed for 3000 hours in 316 stainless steel and graphite capsule tests, along with Mo element EDS x-ray mapping of the surface. Mo-rich precipitate particles were detected on the corrosion surface regardless of capsule material. The formation of these precipitates appears to be a consequence of Cr depletion at the surface which increases the activity of Mo and Si in the near-surface regions and promotes the precipitation of $MoSi_2$ phase. Molybdenum is known to be quite inert to molten fluoride salts, however pure silicon is prone to attack in this environment [33]. The formation of $MoSi_2$ precipitates may prevent some fluoridation of Si [4].

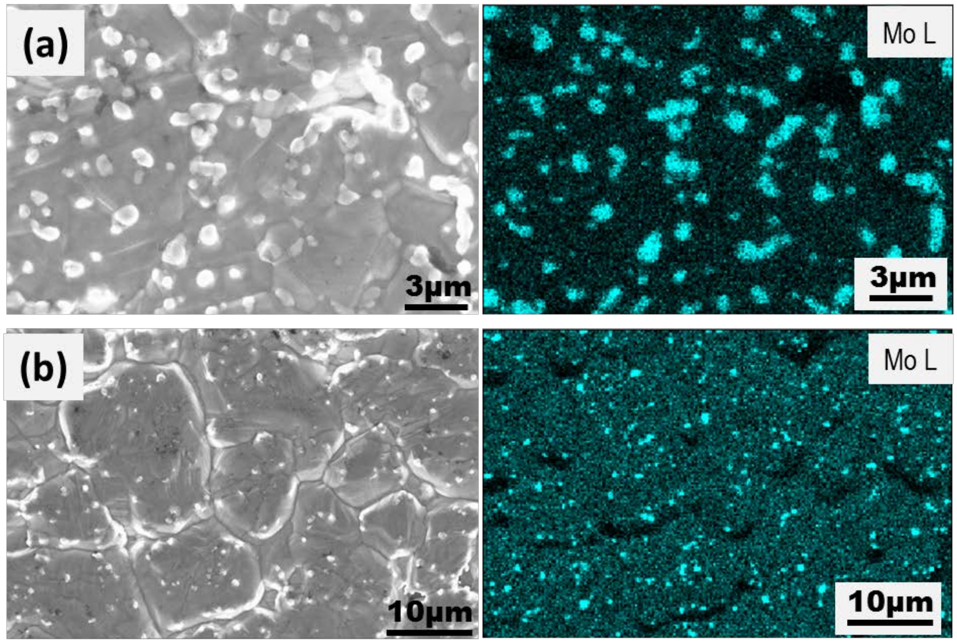

Fig. 34 EDS maps showing Mo-rich precipitates on the corrosion surface of 316 stainless steel samples tested in (a) 316 stainless steel lined capsule and (b) graphite capsule after 3000 hours exposure to molten FLiBe salt at 700°C [4].

The phase content of the corrosion layer was analyzed using XRD technique. Fig. 35 shows the XRD patterns of the as-received samples and samples tested for 3000 hours in the two capsule materials. After corrosion, the characteristic peak intensity of austenite phase (γ phase) decreased with the (220) peak shrinking and the (111) and (200) peaks completely disappearing. The characteristic peaks of α-ferrite phase generated as indicated by the appearance of (200), (211) and (110) peaks. Main peak (110) of both α-ferrite phase and α'-martensite phase overlapped on XRD pattern. The α'-martensite phase in the as-received sample might have been introduced during the cold-working of the alloy during sheet fabrication [34], [35]; the formation of α-ferrite phase is attributable to the corrosion process, but the exact mechanism for the emergence of this phase is not clear.

The XRD patterns (Fig. 35) successfully identified tetragonal $MoSi_2$ (PDF card 01-072-6181) on the corrosion test samples' surface from both types of capsules material. Cr_7C_3 (PDF card 04-002-2449) was detected only on the corrosion surface tested in graphite capsules[36]. This may have the beneficial effect of mitigating long-term-corrosion.

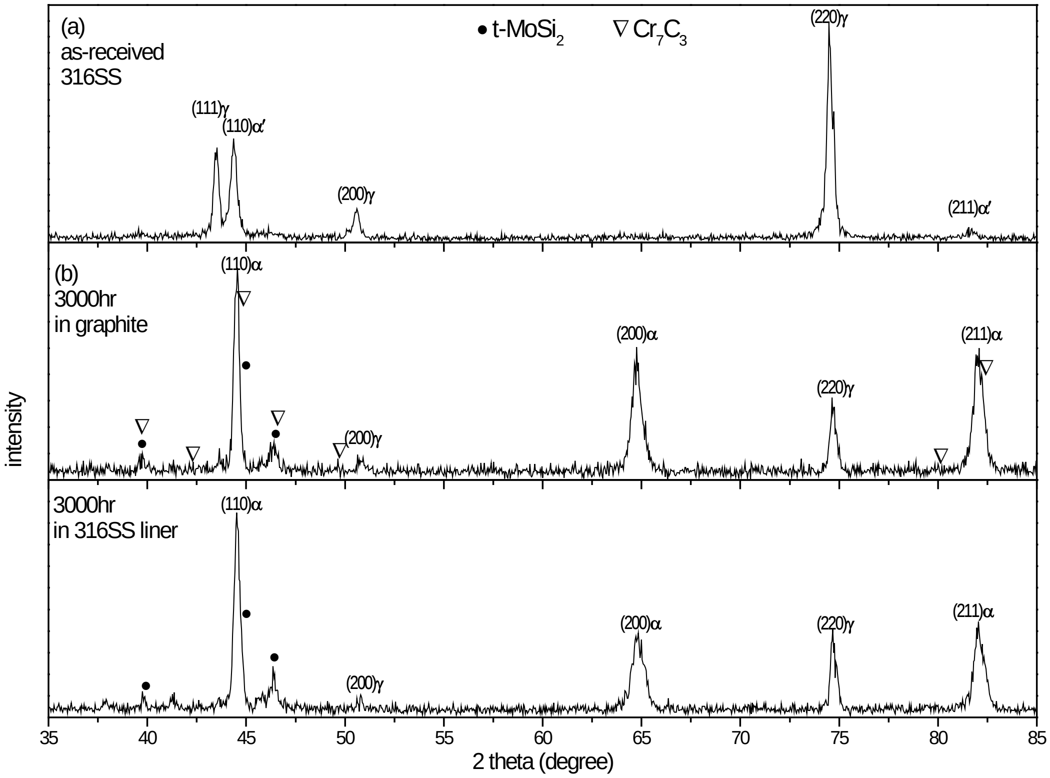

Fig. 35 XRD patterns collected from the surface of (a) as-received 316 stainless steel, (b) 316 stainless steel tested in a graphite capsule, and (c) 316 stainless steel tested in a 316 stainless steel capsule. (b) and (c): both tested for 3000 hours [4].

The depth of the corrosion attack and the internal microstructure of the corrosion layer were examined in sample cross-sections under the SEM. Fig. 36(a-c) shows the images of samples tested in 316 stainless steel capsules and Fig. 36(d-f) shows the samples tested in graphite capsules, each for 1000, 2000 and 3000 hours respectively. For the samples tested in graphite capsules, the randomly distributed particulate phases in the 316 stainless steel matrix are chromium carbide particles which were previously observed protruding from the grain boundaries in the plan view images (Fig. 36(b)). These particles are thought to form as inwardly diffusing carbon reacted with outwardly diffusing chromium. Longer exposure time resulted in an increase in depth of the region containing these particles from approximately 5µm at 1000 hours, to deeper than 50µm after 3000 hours. As expected, these chromium carbide particles were not observed in the samples tested in 316 stainless steel capsules due to the absence of carbon source in the molten salt. Additionally, in all of the cross-sectional SEM images, $M_{23}C_6$ type carbide precipitates were observed at grain boundaries, which usually formed in 316 stainless steel during high temperature aging[37]–[39]. The samples exposed to salt for 3000 hours in the graphite capsule were marked by the recession of corrosion surface, particularly at the grain boundary. As shown in Fig. 36(f), a crack developed several microns deep into alloy along grain boundary. This heavy attack at the grain boundary was not observed in the samples tested in 316 stainless steel capsules [4].

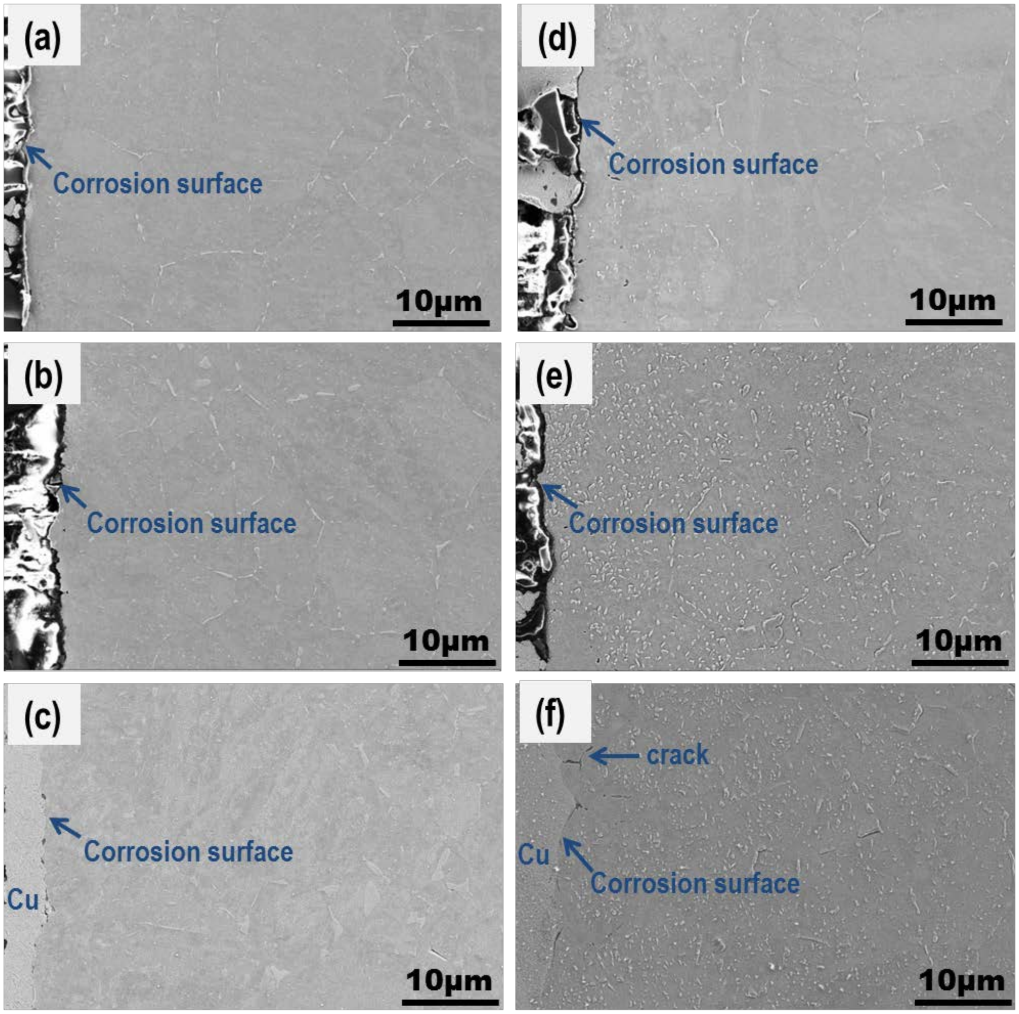

Fig. 36 Cross-sectional SEM images of 316 stainless steel samples after corrosion tests; (a), (b), and (c) tested in 316 stainless steel capsules, and (d), (e) and (f) tested in graphite capsules for 1000, 2000, and 3000 hours respectively. Please note that samples in (c) and (f) were electroplated a Cu layer for edge protection [4].

The depth of corrosion attack was measured in terms of the maximum Cr depletion distance using EDS elemental maps for Cr as shown in Fig. 37. Based on this criterion, the corrosion attack depth for exposures between 1000 hours and 3000 hours was between 6.4μm and 11.5μm for the samples tested in 316 stainless steel capsules, and between 13.7μm and 22.5μm for the samples tested in graphite capsules. As expected, increasing the corrosion test time increased the affected depth; testing in graphite capsules doubled the maximum Cr depletion depth. The EDS maps also showed Cr depletion through volume diffusion in a shallow region near the corrosion surface. This can be seen in Fig. 37(d) where volume Cr depletion accounts for a layer approximately 3μm thick. This observation indicates that volume diffusion is dominant mechanism for the Cr depletion during initial corrosion stage due to the large projected area ratio of grain to grain boundary on corrosion surface. Additionally, the contrast between Cr concentration in the grain boundary and substrate is higher for the samples in graphite capsule than those in 316 stainless steel capsule, which corresponds to the more severe Cr depletion in grain boundary. This difference further suggests the acceleration effect of graphite on Cr depletion [4].

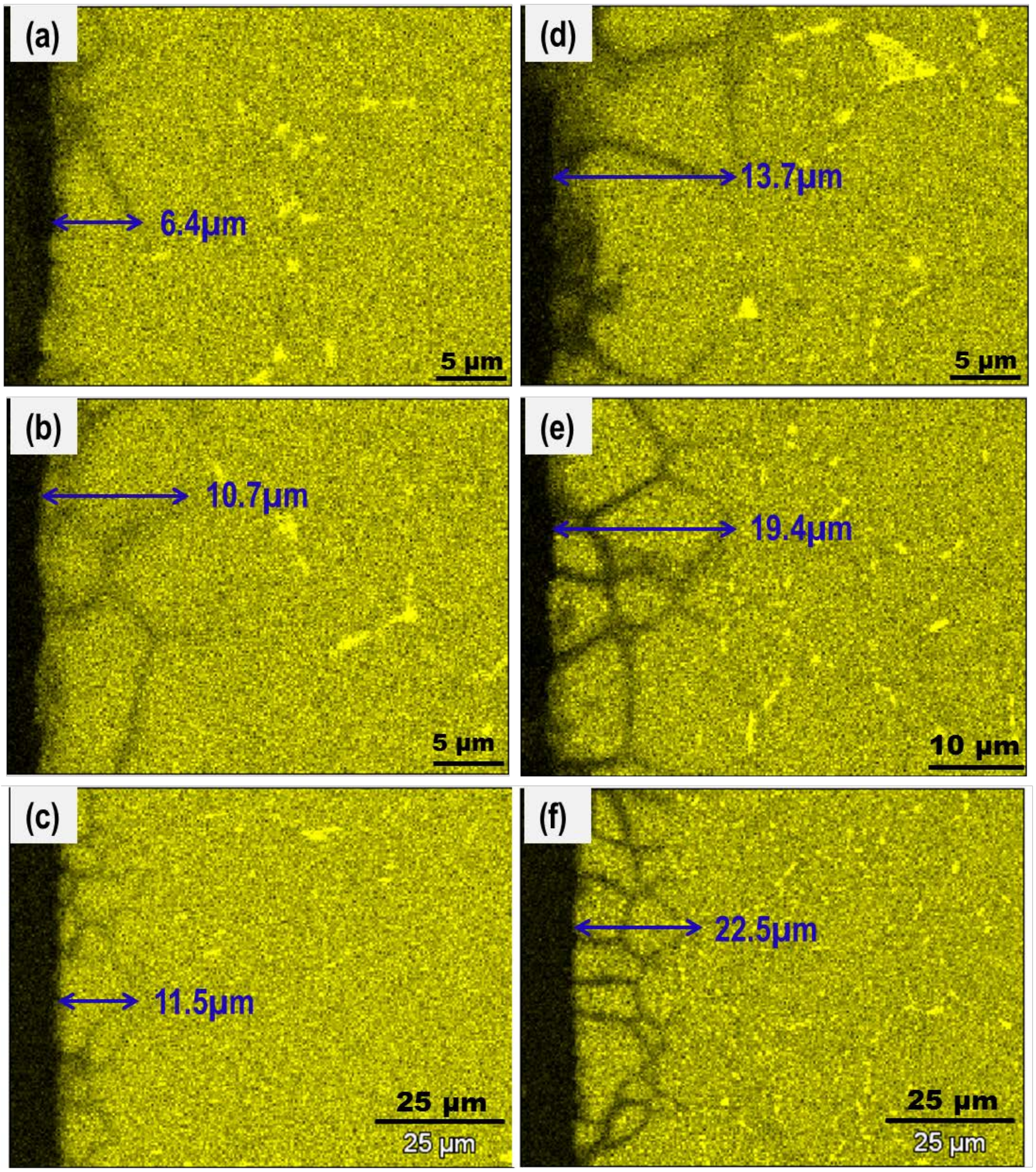

Fig. 37 EDS maps showing Cr distribution in near surface layer of corroded 316 stainless steel samples: (a), (b), and (c) tested in 316 stainless steel capsules and (d), (e), and (f) tested in graphite capsules at 700°C for 1000, 2000, and 300 hours. Maximum Cr depletion distance was labeled in each EDS Cr map [4].

Fig. 38 shows the concentration profiles of main elements Fe, Cr and Ni in 316 stainless steel. From Cr profiles, the Cr depletion distance is about 14μm and 20μm for the samples tested in 316 stainless steel capsule and graphite capsule respectively for 3000 hours. The Cr depletion profile was observed as gradually decreasing from initial concentration of [Cr]=17% to zero on corrosion surface. A plateau ([Cr] = 8%) appeared in the Cr profile in Fig. 38(b) suggests Cr depletion from the grains in near surface region of the sample tested in graphite capsule. This observation further confirms the corrosion accelerating effect of graphite in molten salt by way of Cr depletion. The profiles of EDS line-scan are highly dependent on the selection of scanning path, particularly for the inhomogeneous Cr distribution due to preferential grain boundary corrosion [4].

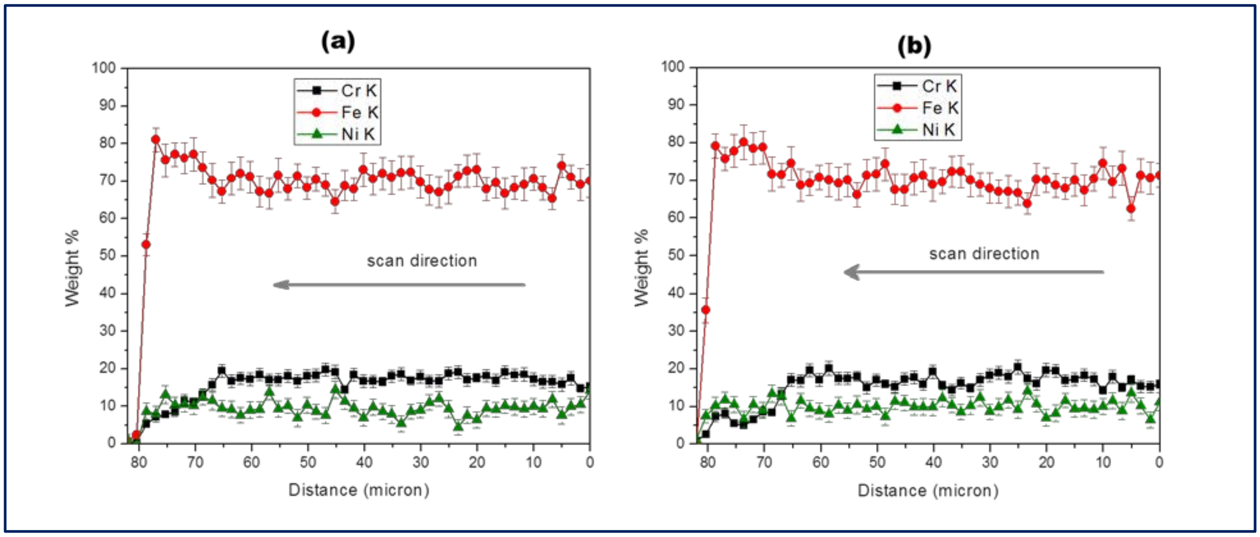

Fig. 38 Main elements Cr, Fe and Ni concentration profiles in the near-surface region of 316 stainless steel samples (a) tested in 316 stainless steel capsule and (b) tested in graphite capsule for 3000 hours [4].

The complicated Cr distribution map also suggests the complexity of corrosion rate calculation. The conventional corrosion rate calculation from the weight loss assumed uniform Cr depletion, by the means of $x = \frac{\Delta M}{AC_0\rho}$. From above observations, Cr depletion is not uniform within alloys. Therefore, the conventional calculation method underestimates the real corrosion rate in terms of the maximum Cr depletion distance [4].

Based on the maximum Cr depletion distance measured from EDS Cr mappings, the long-term corrosion attack depth can be predicted at least to a first approximation from the logarithmically fitting curves as shown in Fig. 39. The fits predicted an attack depth of 17.1μm/year and 31.2μm/year for the samples tested in 316 stainless steel capsules and graphite capsules respectively[40].

In the MSRE literature, the void layer observed under an optical microscope was considered to be Cr depletion layer, and the attack depth was calculated based on weight loss by assuming uniform Cr depletion from tested alloy[41]. Our studies using SEM and EDS to identify the depth of corrosion attack indicates that MSRE literature underestimated the corrosion attack depth values. The reported corrosion rate of Hastelloy-N in liquid FLiBe salts is approximately 25μm/year at 704ºC. In comparison, the corrosion attack depth of 316 stainless steel in FLiBe at 700ºC of 17.1μm/year and 31.2μm/year is in an acceptable range[32], [42].

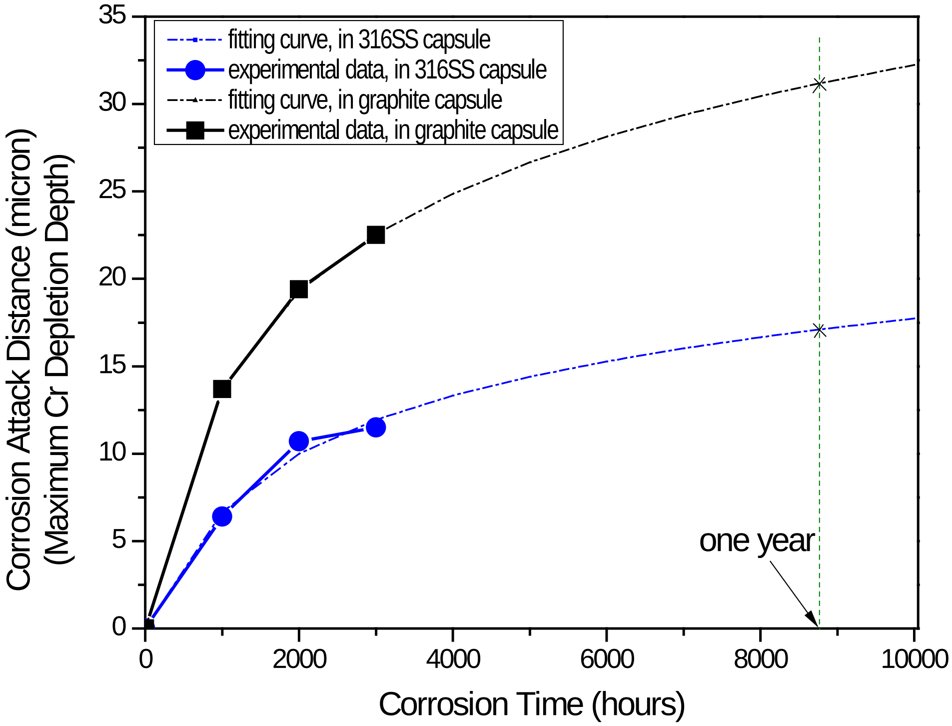

Fig. 39 The depth of corrosion attack, in terms of maximum Cr depletion depth, as a function of corrosion time. Experimental data is indicated by a solid line, while the fit is indicated by the dashed line. The fit predicted 17.1μm/year of corrosion in 316 stainless steel capsules and 31.2μm/year in graphite capsules [4].

As shown in Fig. 40, the cross-sectional microstructure, elemental distribution, grain size distribution, grain orientation and phase distribution as well as grain boundary map in the same region were obtained by combining SEM-EDS with EBSD techniques. In this same region, SEM images and EDS mappings were first collected prior to EBSD scanning. Fig. 40(a) presents precipitates at grain boundaries and the grains with different contrast. Fig. 40(b-d) exhibits EDS mappings of Cr, Fe and Ni. Concentration of Fe and Ni is relatively higher at the grain boundaries where Cr significantly depleted. Fig. 40(e-h) displays EBSD results including auto grain map, inverse polar figure (IPF), α phase (red) distribution, and image quality combined with grain boundary maps and α phase, at the same region as cross-sectional SEM and EDS mappings. These images suggest that (1) Cr only depleted along high angle grain boundaries (15-180º, blue lines), not in coincident sites lattice (CSL) grain boundaries such as Σ3 (orange lines), and (2) α phase particularly developed in the area where Cr substantially depleted, in a distance from 2μm to 6μm to surface. These results correlate the Cr depletion, phase transformation with grain boundary types. Massive Cr depletion in high angle grain boundaries enriched Fe and Ni components and then induced the formation of secondary α-ferrite phase at 700ºC. The misorientation angle between the two adjacent grains (signified by grain boundaries in orange) was calculated to be 60º, which further identifies the Σ3 grain boundary. Based on these findings, Σ3 grain boundary has the relative high corrosion resistance to molten fluoride salts at high temperature with respects to the Cr depletion [4]. In practice, a grain boundary engineering solution is applicable to improve high temperature corrosion resistance of 316 stainless steel in FLiBe. Moreover, the newly-formed α phase might change alloy radiation resistance in practical application because of the different radiation response between α-ferrite and γ-austenite phase[43], [44].

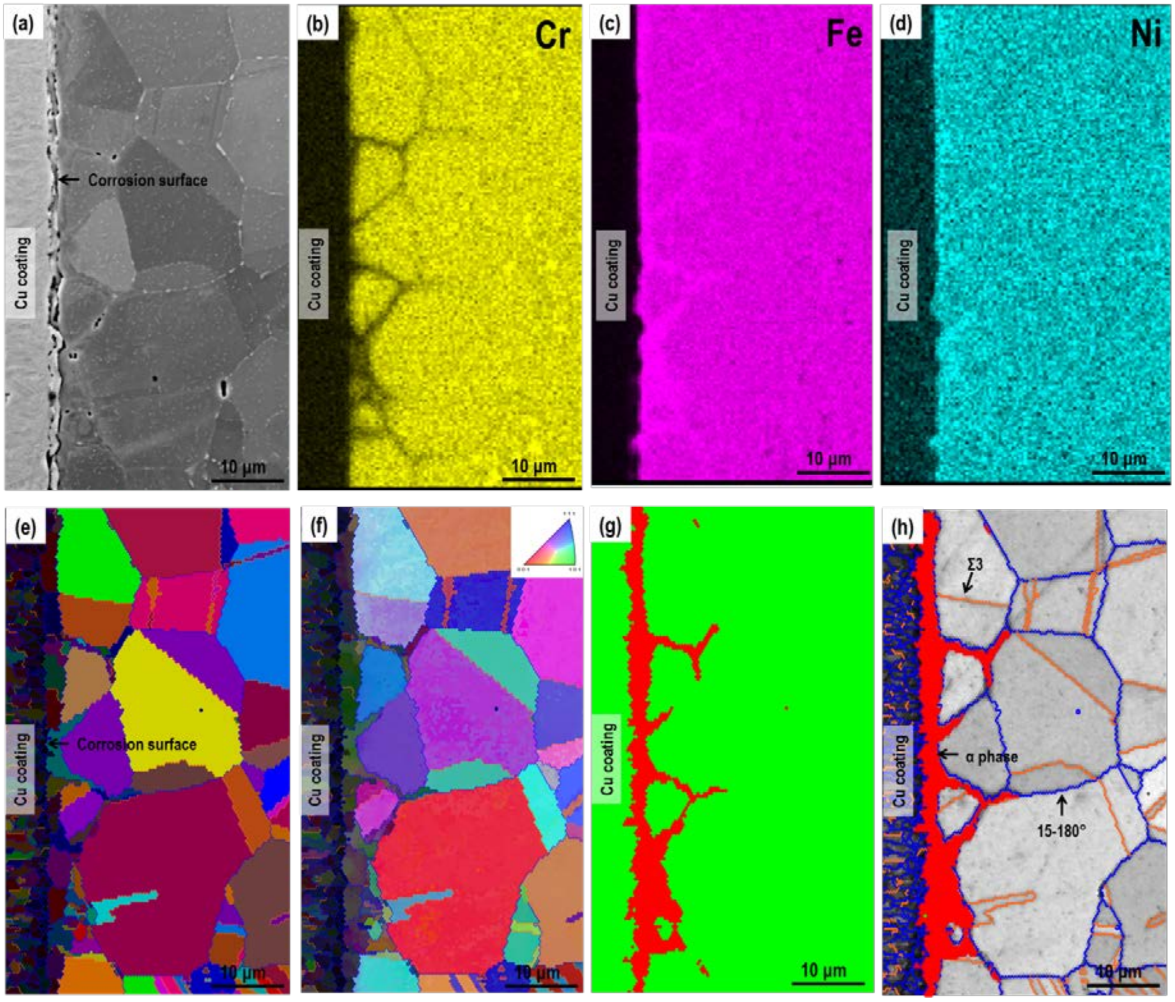

Fig. 40 (a) cross-sectional SEM image, (b-d) EDS Cr, Fe and Ni map and (e-h) EBSD images in same near-to-surface area of 316 stainless steel tested in graphite capsule for 1000 hours. (e) grain distribution, (f) inverse polar figure [001], (g) α phase (red) distribution and (h) grain boundary and α phase maps overlapped on image quality (blue lines and orange lines denote 15-180° and Σ3 grain boundaries respectively) [4].

Materials Performance in Natural Lithium FLiBe Salt (UW)

The corrosion resistance of a broader array of candidate structural materials was tested in molten natural lithium FLiBe salt produced at the University of Wisconsin-Madison. New and conventional materials were exposed to as received and beryllium reduced salts with redox potentials of -1.706 V and --1.45 V vs. Be|BeF$_2$, respectively. A static corrosion experiment was conducted for 2,000 hours at 700˚C. Materials tested include 316L Stainless Steel, Mo-Hf-C, W-Zr-C Cermet, Silicon Carbide, SiC-SiC Composites and nuclear graphite. Again, the influence of stainless steel lined capsules and graphite capsules was investigated in 316L stainless steel. In addition to common materials characterization methods, new salt analysis methods were implemented to characterize the influence of salt chemistry on corrosion. An electrochemical analysis technique called the fluoride salt redox potential was used to characterize the influence of salt chemistry control methods, such as beryllium reduction. The analytical chemistry method inductively coupled plasma optical emission spectroscopy (ICP-OES) was also used to measure the concentration of important corrosion products in the salt, such as chromium, before and after corrosion.

Metals Exposed to Natural Lithium FLiBe

The performance of the metallic materials is compared using weight change results in Fig. 42. Overall, 316 stainless steel showed relatively uniform weight loss across various corrosion conditions. MoHfC showed the least amount of weight change of the metallic samples. WZrC samples performed worst with massive weight loss due to Zr dissolution [5].

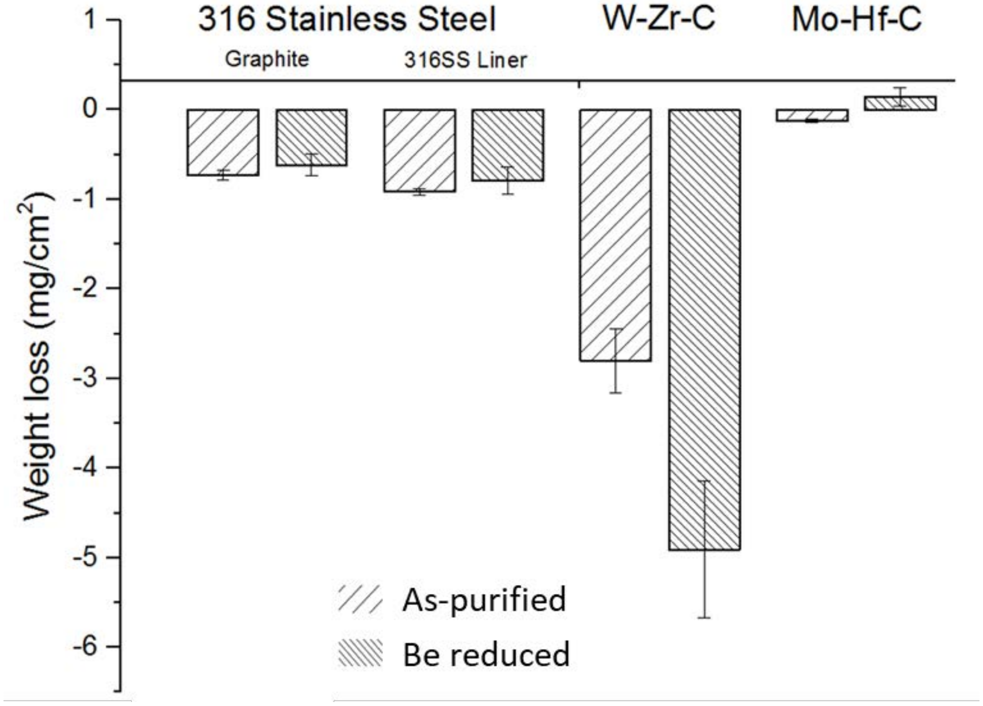

Fig. 41 Weight change results of metallic samples shown are an average of the three samples in each chamber, with error bars being their standard deviation [5].

316L Stainless Steel

Twelve coupons of the low carbon variant of 316 stainless steel were exposed to two varieties of molten FLiBe salt for 2,000 hours. Fig. 42 shows optical images of 316 stainless steel samples (a) and (b) before and (c) and (d) after corrosion depicting the surface coloration and morphology change. The stainless steel surface after corrosion in all cases has a matte finish, and scratches are no longer visible with the naked eye. Fig. 42(c) shows a 316 stainless steel sample after corrosion in graphite. Arrows denote discoloration near the mounting holes which was common for all graphite-encapsulated samples. Fig. 42(d) shows a 316 stainless steel sample after corrosion in a stainless steel capsule. It does not have the same discoloration but the same matte surface. More FLiBe was stuck to the samples in graphite after removal. This is likely due to a slightly rougher surface.

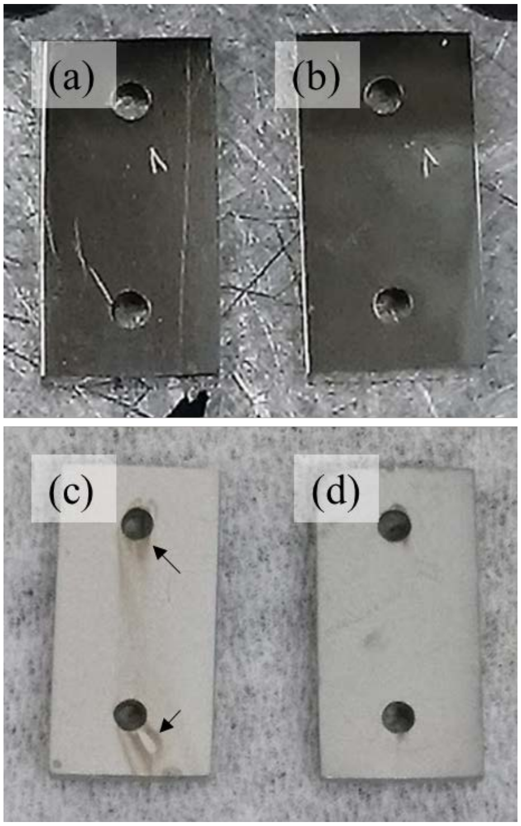

Fig. 42 Photographs of 316 stainless steel samples before (a), (b) and after (c), (d) corrosion in 700°C as-purified molten FLiBe salt. Sample (c) was graphite-encapsulated, whereas sample (d) was stainless-steel encapsulated [5].

The results of weight change in 316 stainless steel are shown in Fig. 43. The average weight change per surface area (mg/cm^2) of 3 samples in identical capsules reveals a trend that supports the hypothesis and reaffirms previous results from 1979 [45]. Samples exposed to beryllium reduced FLiBe experienced on average 10% less weight loss than samples exposed to as-purified FLiBe in 2,000 hours.

Remarkably, the samples encapsulated in stainless steel observed a slightly higher weight loss than the graphite-encapsulated samples after 2,000 hours at 700°C. This is likely due to the interaction of graphite and stainless steel, which tends to form carbides at the surface and near surface grain boundaries. Chromium carbides were found in cross sections of 316 stainless steel samples inserted into graphite capsules, but not in samples exposed to stainless steel capsules. This is consistent with the previous results of both in-reactor and out-of-reactor corrosion experiments which show evidence that carbon migration resulting in carbide formation that may affect chromium diffusion and thus its depletion from the alloy [5].

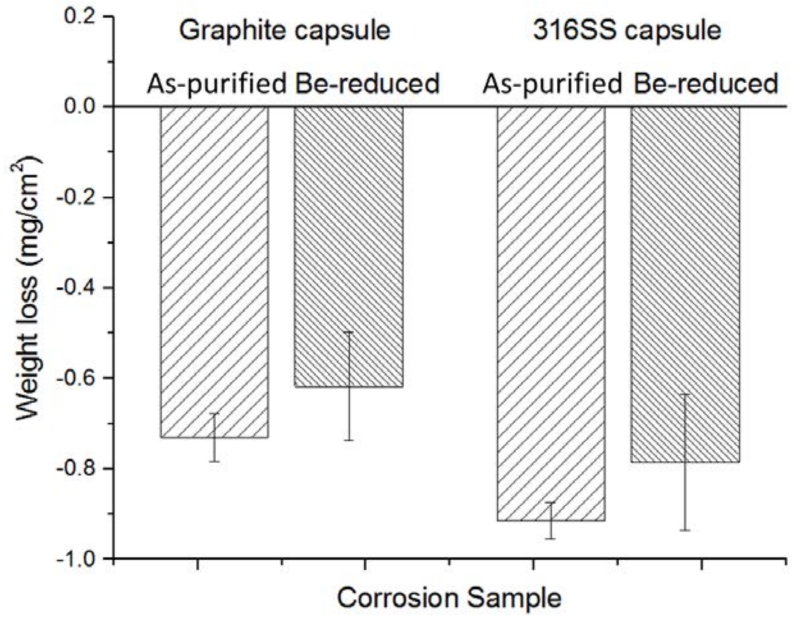

Fig. 43 Weight change results of 316L stainless steel after 2,000 hours in 700°C molten FLiBe in various conditions. Standard deviation of samples in identical conditions are shown with the error bars [5].

Scanning Electron Microscopy (SEM) and Energy Dispersive X-ray Spectroscopy (EDS) were employed to compare the surface morphology and composition of corrosion samples. To aid in corrosion analysis of the surface of metallic samples, a scratch was made prior to testing to mark a region for post-corrosion analysis. Micro hardness indents of various sizes were also made to enable quantification of surface recession. Fig. 44 shows the sample indents and scratch before and after exposure to as-purified molten FLiBe in graphite capsules. Severe grain boundary corrosion results in the rough and bumpy surface. Prominent surface features, such as plowed material on the edge of the scratch, are smoothed over, and the edges of indents were also rounded after corrosion. This type of surface muddling is presumably due to a uniform surface recession [5].

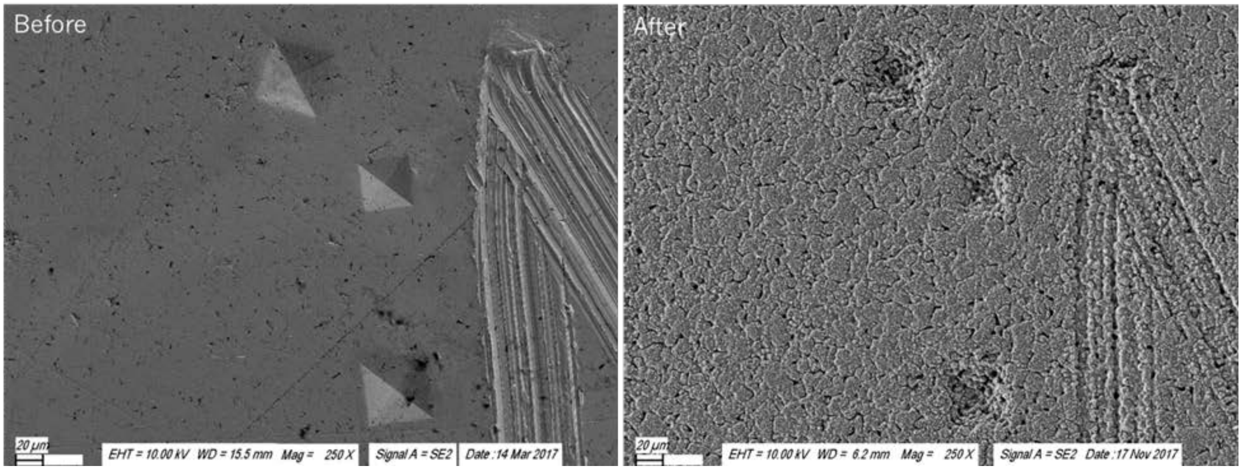

Fig. 44 Surface SEM image of scratch tip and indents on 316SS sample before and after exposure to as-purified molten FLiBe salt in graphite containment at 700°C for 2,000 hours[5].

A surface compositional map of a post-corrosion 316 stainless steel sample for iron, chromium, nickel, molybdenum and carbon is shown in Fig. 45. The molten FLiBe significantly altered the surface of the steel, causing deep cleavage in grain boundaries and the appearance of spherical molybdenum-rich particles protruding from the surface. This is reasonable as molybdenum is more thermodynamically stable than any other constituent in 316 stainless steel, namely chromium and iron, and is likely to remain unaffected in the matrix [5].

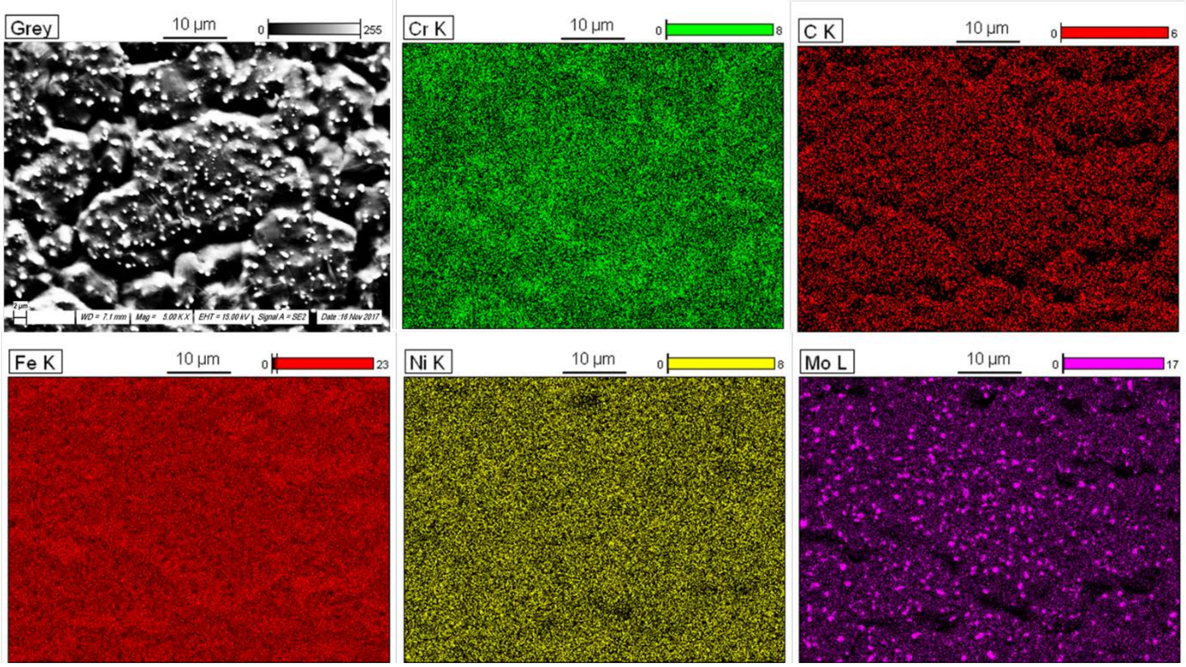

Fig. 45 Plan view SEM and EDS elemental maps of 316 stainless steel exposed to 700°C as-purified FLiBe in a graphite capsule for 2,000 hours [5].

EDS point scans, shown in Fig. 46, compare compositional variations on the surface of 316 stainless steel after corrosion in a graphite capsule. Point 1 is in the center of a bulk surface grain. Point 2 is in the center of a grain boundary. The surface concentration of chromium went down from 16.2% in the reference sample, to 3.7% in the post-corrosion sample. Substantial surface morphology changes such as molybdenum rich particles decorating the surface of the post-corrosion samples. Point 3 is in the center of a protruding Mo rich particle. The molybdenum rich particles show a charging effect from the SEM, indicating they are not conductive and likely a carbide or silicide. Since molybdenum is a strong carbide former, the formation of Mo_2C or other molybdenum carbide is possible [5].

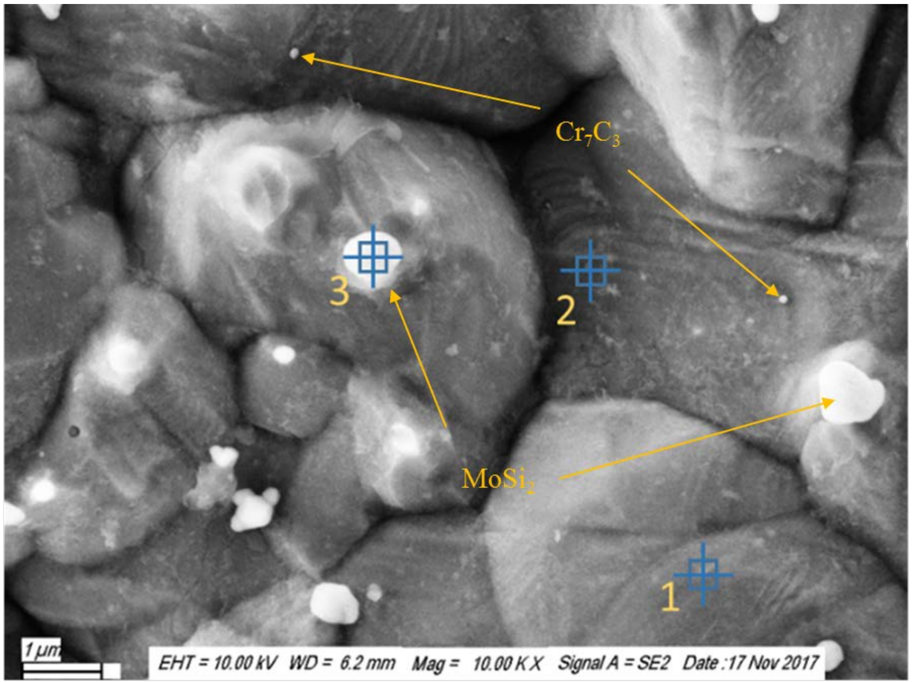

Atom %	C-K	Mg-K	Al-K	Si-K	P-K	Cr-K	Fe-K	Ni-K	Cu-K	Mo-L
Point 1	4.5		0.2	0.4		3.7	77.4	12.0	0.7	1.0
Point 2	3.7	0.1	0.2	0.3		4.1	79.1	11.2	0.5	0.8
Point 3	5.1		0.4	2.0	1.4	2.5	66.3	5.9		16.4

Fig. 46 EDS point scan analysis of post-corrosion 316SS surface after exposure to as-purified molten FLiBe in a graphite capsule. Data is from a 20,000x image and 15kV accelerating voltage [5].

Both the graphite encapsulated, and stainless-steel encapsulated samples showed the same molybdenum particle formation on the surface. This indicates that the segregation of molybdenum and formation of particles is a phenomenon internal to the sample, rather than due to the diffusion of carbon through the salt and deposition on the surface. All samples also show a slight enrichment of iron in grain boundaries relative to other elements.

Cross section SEM and EDS analysis of 316 stainless steel samples reveal the depth of chromium depletion, as well as the formation of intergranular phases in the corrosion samples. Fig. 47(a) and (b) show cross section and line scan of 316 stainless steel before exposure to FLiBe, respectively. Copper was electroplated on the sample surface prior to mounting for edge protection during polishing. Samples are homogenous and the composition immediately jumps to bulk composition values at the surface [5].

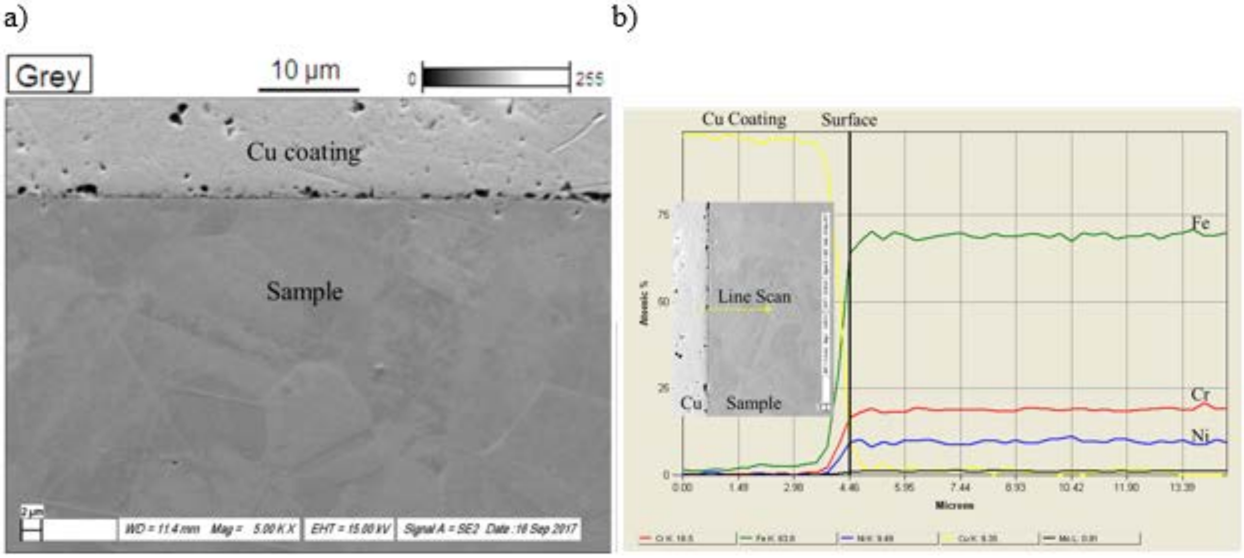

Fig. 47 (a) SEM and EDS maps of 316 stainless steel reference cross section. (b) EDS line scan and SEM image of 316 stainless steel reference cross section at 5,000x [5].

Cross section compositional maps of post-corrosion 316 stainless steel samples for iron, chromium, nickel, molybdenum and copper after various corrosion conditions are shown in Fig. 48 Copper was electroplated on the corrosion sample surface prior to mounting for edge protection during polishing. The depth of chromium depletion was measured from the corrosion surface to the deepest grain boundary depletion region observed. Chromium carbide formation in grain boundaries was more prevalent in graphite encapsulated samples than stainless steel encapsulated samples. In Fig. 48(a) and (b), EDS maps of chromium depict chromium carbide surrounding a sub-surface grain in a stainless steel sample after corrosion in a graphite capsule. Compared to samples encapsulated in stainless steel, Fig. 48 (c) and (d), the graphite encapsulated samples have more inter-granular formation of chromium-rich carbides. Samples encapsulated in stainless steel have more pronounced inter-granular molybdenum carbide formation, shown EDS Mo maps in Fig. 48 (c) and (d). Voids are visible in the bulk center of some surface grains in corrosion sample cross section. This indicates that chromium depletion in the grain boundaries requires enough diffusion of species from the bulk grain to cause void formation [5].

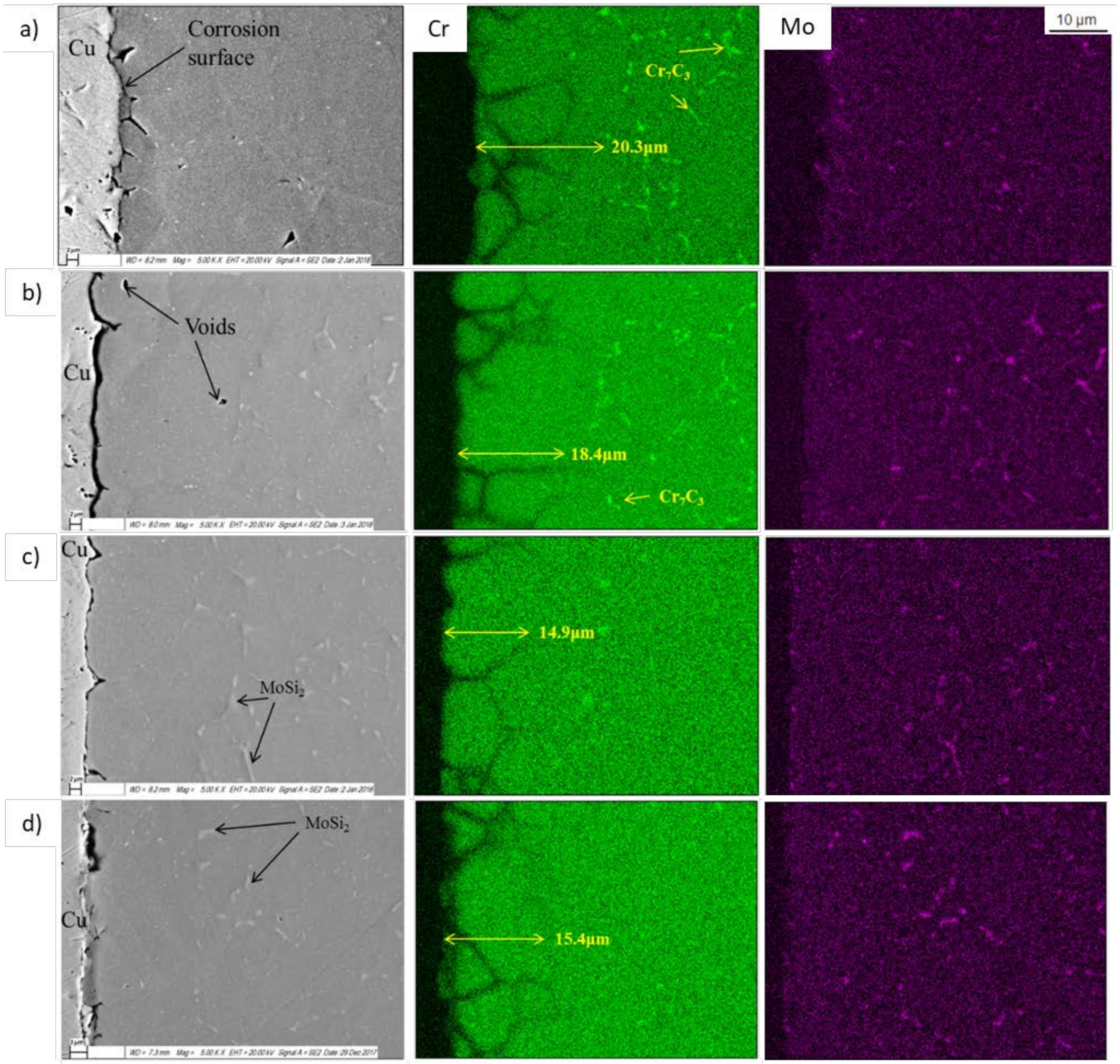

Fig. 48 Cross section SEM and EDS maps of 316 stainless steel exposed to a) as-purified FLiBe in a graphite capsule, b) Be-reduced FLiBe in a graphite capsule, c) as-purified FLiBe in a 316 stainless steel capsule, and d) Be-reduced salt in a 316 stainless steel capsule. Samples were exposed for 2000 hours at 700˚C [5].

Fig. 49(a) shows the line scan for 316 stainless steel exposed to as-purified molten FLiBe in graphite containment, and Fig. 49(b) shows the EDS line scan for 316 stainless steel exposed in 316 stainless steel containment. The chromium depletion layer denoted by red ovals in the surface grains of the graphite-encapsulated sample extends over 6μm into the sample, but less than 3μm in the stainless steel encapsulated sample. In addition, the graphite encapsulated sample shows two chromium-deficient grain boundaries along the line scan at 7μm and 21μm, whereas none are found in the stainless steel encapsulated sample. Cr_7C_3 formation denoted by green ovals is only present in the graphite-encapsulated sample, whereas $MoSi_2$ formation denoted by blue circles is present in both samples. In these regions, corresponding silicon enrichment and iron deficiency is also present [5].

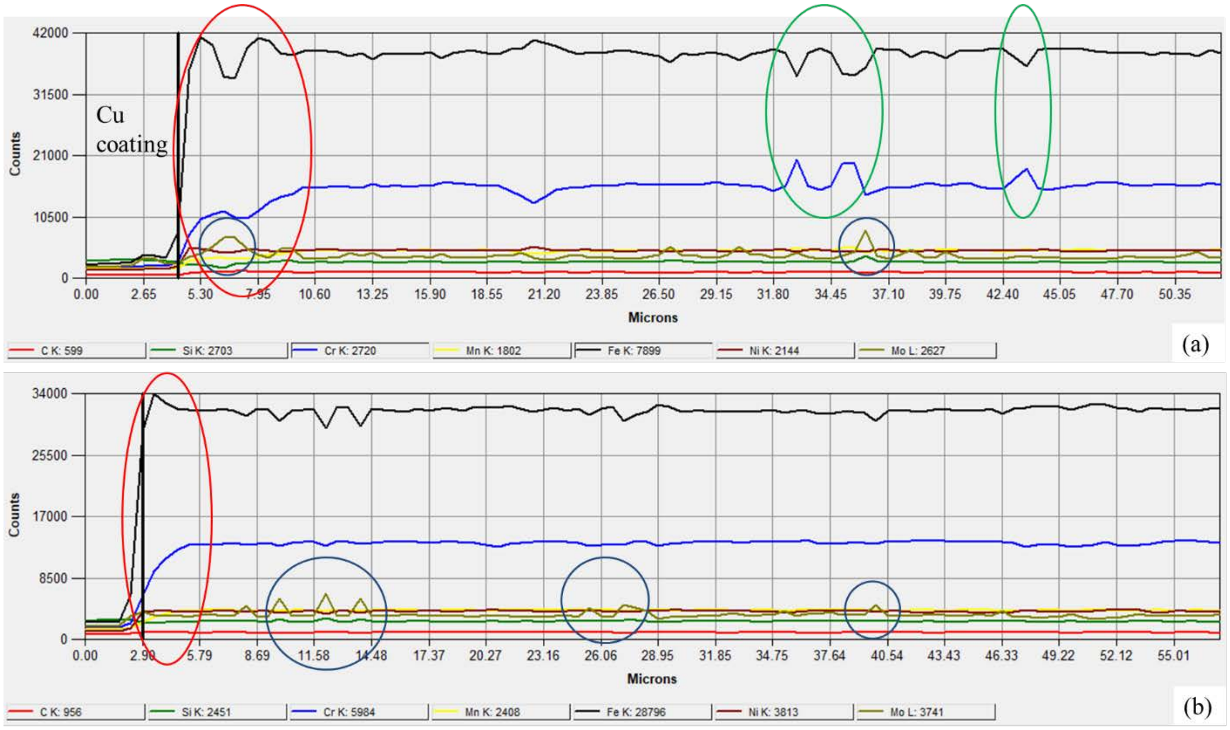

Fig. 49 Post-corrosion EDS line scans of 316 stainless steel tested in (a) a graphite capsule and (b) a 316 stainless steel capsule. Red ovals refer to chromium depletion layer, green ovals refer to Cr_7C_3 particles, and blue circles refer to $MoSi_2$ particles. The corrosion surface is denoted by a black line [5].

It is likely that exposure to FLiBe salt at 700°C could cause a removal of material and a recession of the surface independent of chromium depletion along grain boundaries. The profiles of 300gf Vickers indents on the surface of polished 316 stainless steel before and after 2,000-hour exposure to FLiBe salt were analyzed to observe a possible surface recession. Comparing the diagonal indentation width of indents on the surface of corrosion samples, insight regarding the quantification of surface recession was gained. The profile of the 300gf Vickers indent of the surface of polished 316 stainless steel before and after exposure is shown in Fig. 50. Roughening of the surface means the faces of the indent are not as sharply contrasted with the surface. The FLiBe salt exposure causes surface degradation uniformly across the entire surface and is not preferential to smooth or angled areas. The indentation recessed similarly in both capsules, but indents retained the flat triangular sides better in the stainless steel encapsulated surface. The indent diagonal was approximately 3.5μm wider than the reference indent, growing from 51μm to 54.56μm. The depth was approximately 1μm deeper. This indicates that the surface recession experienced by the sample is essentially uniform along all faces, including areas inside the indent, causing the indent faces to spread outwards relative to the surface face. This surface recession is exasperated at sharp corners and regions, causing a smoothing of edges that appears to increase the indent diagonal. The change in the indentation width was less pronounced for the stainless-steel encapsulated samples than the graphite encapsulated samples, indicating less roughening of the surface [5].

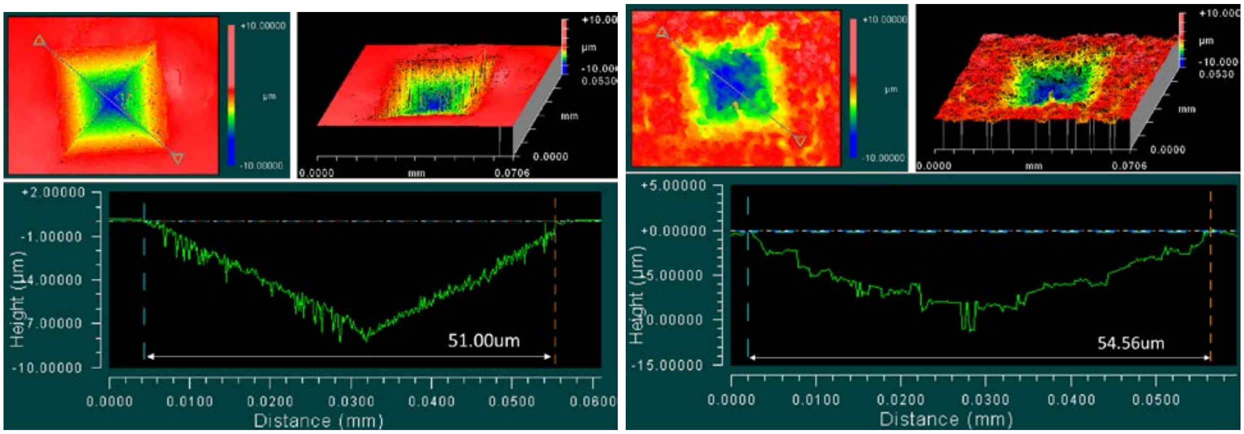

Fig. 50 100x magnification profile of a 300gf indent on polished 316 stainless steel before (above) and after (below) corrosion [5].

The depth of the Vickers indentation before exposure should be exactly 1/7th the diagonal length. By comparing the indent width before and after corrosion, one would theoretically be able to estimate the surface recession. Corrosion of 316 stainless steel was uniform on all surfaces, and in fact, the depth of indents increased after corrosion. This indicates that grain boundary attack dominates compared to surface recession.

Understanding how surface roughness is influenced by salt over time is beneficial for understanding emissivity and heat transfer in nuclear materials. Increasing surface roughness correspondingly increases emissivity at high temperatures due to a greater surface area as a result of ridges and valleys in the surface morphology [46]. Profilometry revealed a drastic roughening of the surface of 316 stainless steel after corrosion in molten FLiBe. Grain boundaries are recessed and exhibit corrosion where chromium depletion was most severe. Fig. 51 shows the roughness profile of samples after corrosion in various conditions and FLiBe salts. Overall roughness RMS went from 0.012µm on the polished 316SS before corrosion (1200-grit mirror finish), to 0.541µm and 0.504µm for the graphite-encapsulated and stainless-steel encapsulated samples exposed to as-purified FLiBe for 2,000 hours, respectively. The roughness of graphite-encapsulated and stainless-steel encapsulated samples exposed to Be-reduced FLiBe are 0.547µm and 0.420µm, respectively. Beryllium reduction of FLiBe reduces the roughening of samples encapsulated in stainless steel by nearly 0.080µm, whereas it has no effect on the roughness of samples encapsulated in graphite [5].

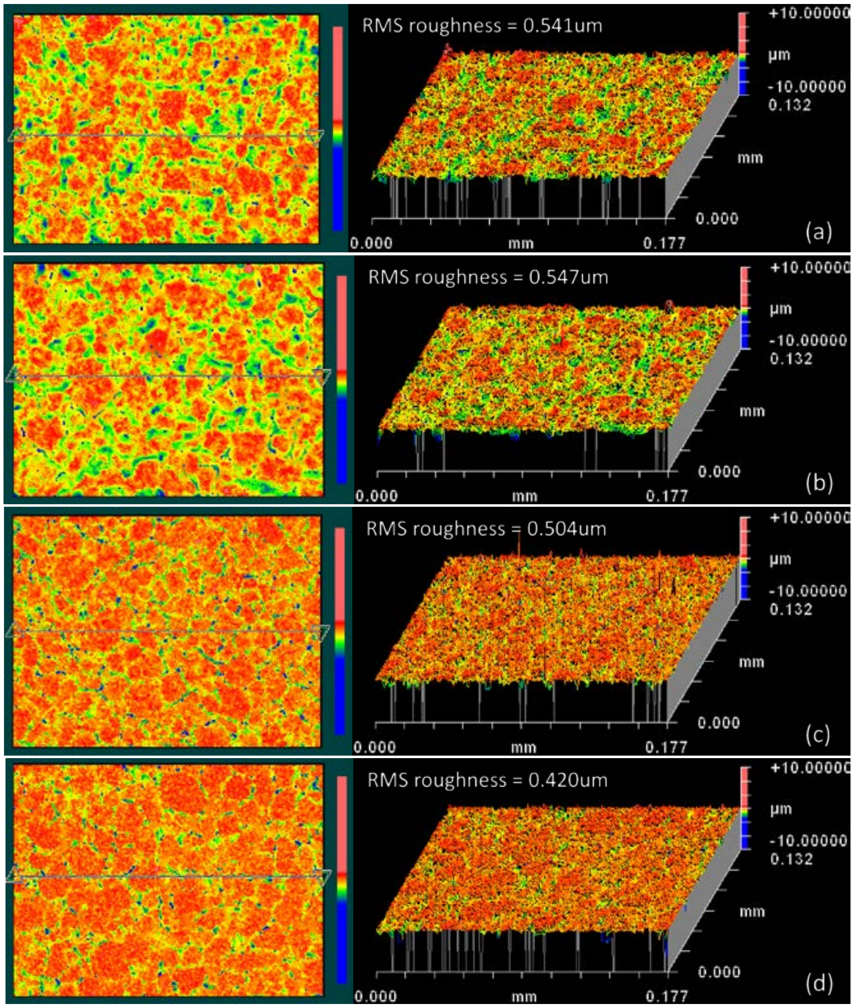

Fig. 51 Roughness analysis of 316 stainless-steel post-corrosion samples. (a) and (b) are graphite-encapsulated samples exposed to as-purified and Be-reduced molten FLiBe. (c) and (d) are stainless-steel encapsulated samples exposed to as-purified and Be-reduced molten FLiBe [5].

<u>Mo-Hf-C</u>

Overall, MoHfC samples showed signs of Hf dissolution into the salt. The samples are shown in Fig. 52. MoHfC samples exposed to as-purified FLiBe look unchanged after corrosion. Samples exposed to Be-reduced FLiBe have a matte surface after corrosion.

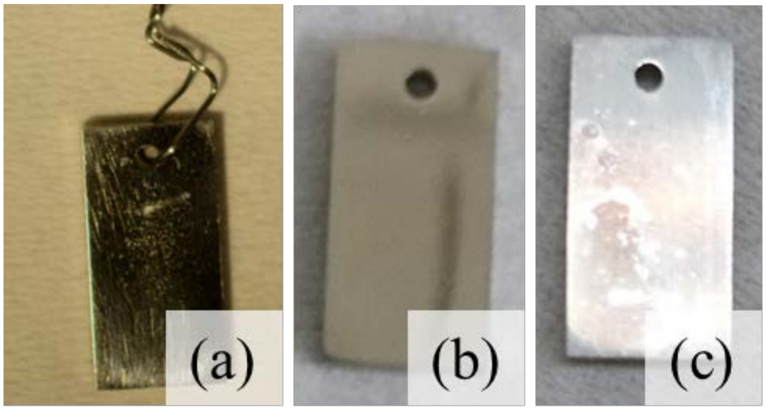

Fig. 52 (a) MoHfC sample set before corrosion, (b) after exposure in as-purified FLiBe salt, and (c) after exposure in Be-reduced FLiBe salt. Individually pictured samples have been ultrasonically cleaned in ethanol and DI water [5].

The weight loss of MoHfC was minimal. Fig. 4 shows a graphical comparison of weight change results for all metallic samples. MoHfC samples exposed to as-purified FLiBe experienced -0.124 mg/cm^2 weight loss, whereas those exposed to Be-reduced FLiBe experienced 0.146 mg/cm^2 weight gain. The standard deviations are 0.021 and 0.10 mg/cm^2, respectively. The mass loss in MoHfC is attributed to the dissolution of dispersed hafnium carbide (HfC) particles at the surface. The mass gain in MoHfC exposed to Be-reduced FLiBe is due to the plating of iron particles on the surface of the samples, resulting in the muddled surface layer observed.

The MoHfC samples exposed to as-purified FLiBe salt do not show significant change after corrosion. The surface maintained a pristine mirror finish with no visible degradation. The samples exposed to Be-reduced salt exhibit the surface formation of iron particles, presumably due to the plate-out of impurity metals occurring on the sample surface during exposure. The surface below the iron coating is still pristine, although the surface is substantially rougher. Fig. 53 shows SEM surface images of the same scratch and Vickers indents on the surface of MoHfC samples before and after exposure to 700°C molten FLiBe salts for 2,000 hours in graphite containment [5].

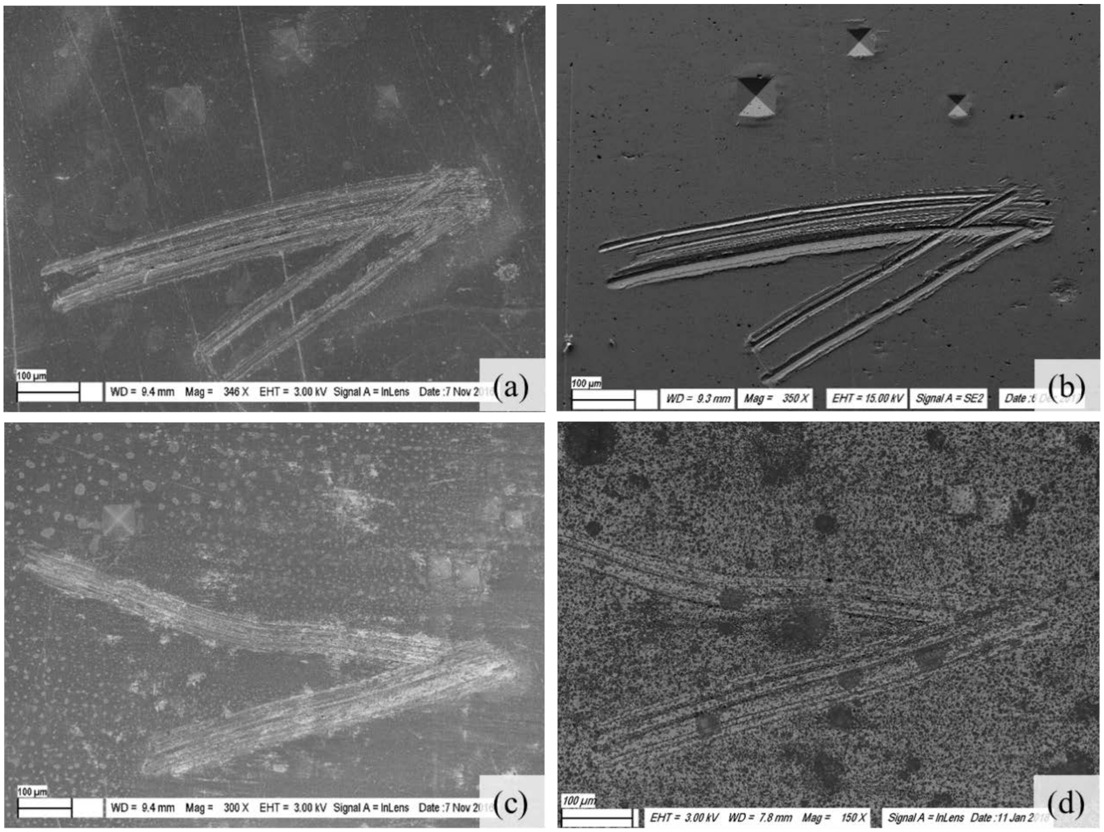

Fig. 53 SEM image comparison of surface marker scratch before (a, c) and after (b, d) corrosion of MoHfC samples. (a) and (b): Sample exposed to as-purified FLiBe. (c) and (d): Sample exposed to Be-reduced and filtered FLiBe [5].

Fig. 54 and Fig. 55 show 500gf Vickers indents before and after exposure to as-purified and Be-reduced FLiBe salts, respectively. Surface SEM images in (a) and (b) were taken using the secondary electron detector to show the topography of the surface. After exposure to as-purified molten FLiBe, the indent did not change shape or morphology, however some pitting was observed where hafnium carbide particles were dispersed in the pre-corrosion sample. EDS analysis below shows the absence of hafnium particles after corrosion.

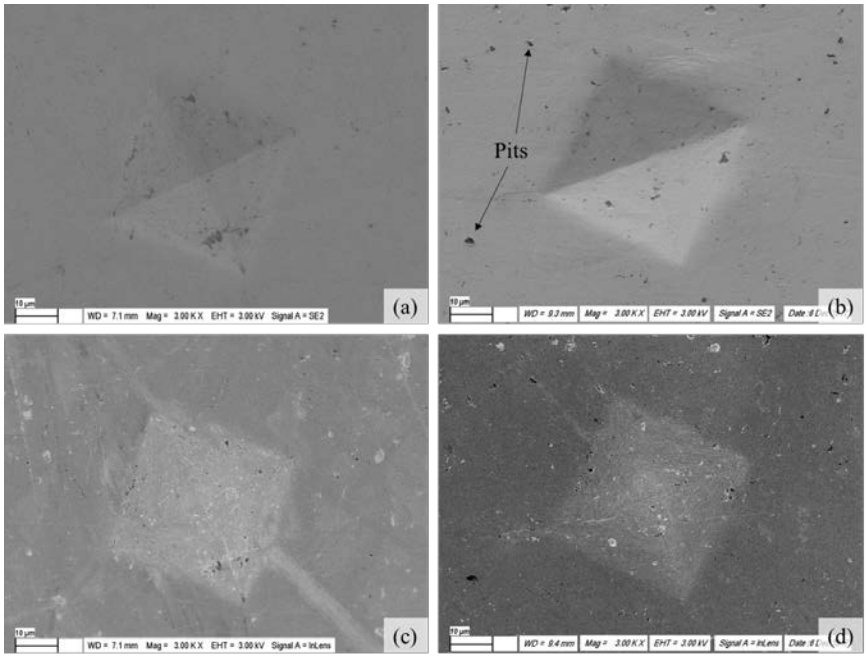

Fig. 54 3,000x magnification SEM images of a 500gf indent on the surface of MoHfC. (a) and (c) are taken before corrosion, and (c) and (d) are taken after corrosion. Two detectors were used to accentuate surface features [5].

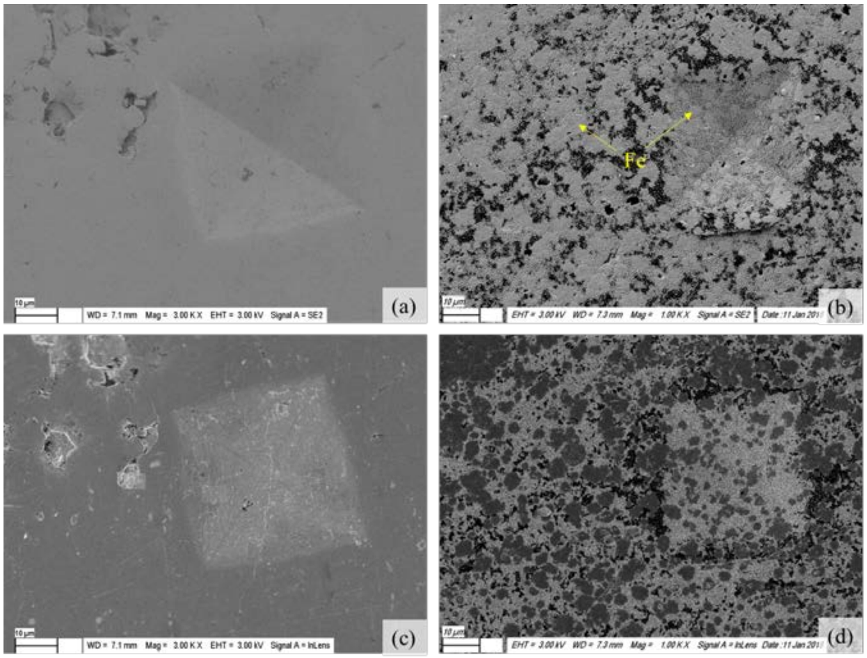

Fig. 55 3,000x magnification SEM images of a 500gf indent on the surface of MoHfC. (a) and (c) are taken before corrosion, and (c) and (d) are taken after corrosion. Two detectors were used to accentuate surface features [5].

The microstructure of MoHfC after corrosion in as-purified FLiBe remains mostly unchanged, except for the disappearance of hafnium. The surface of these samples still had a mirror finish when removing from the salt, whereas all other samples (except SiC) were dull and matte. After exposure to Be-reduced and filtered FLiBe, iron particles are observed decorating the surface of the MoHfC sample. Dark regions in Fig. 56(d) are iron-rich regions on the surface of a pure molybdenum sample. In Fig. 56(b) and (c), MoHfC exposed to both salt chemistries do not depict any hafnium rich regions such as the HfC particles dispersed in the reference sample in Fig. 56(a). The preferential corrosion of Hafnium left behind pits in the molybdenum matrix. Carbon signals in Fig. 56(a) coincide closely with hafnium signals Fig. 56(a). Fig. 56(c) shows that the iron coating is not homogenous on the entire sample surface, with some regions of the MoHfC sample remaining uncoated. Additionally, regions with higher iron concentration show some localization of iron in 3-5 μm sized particles [5].

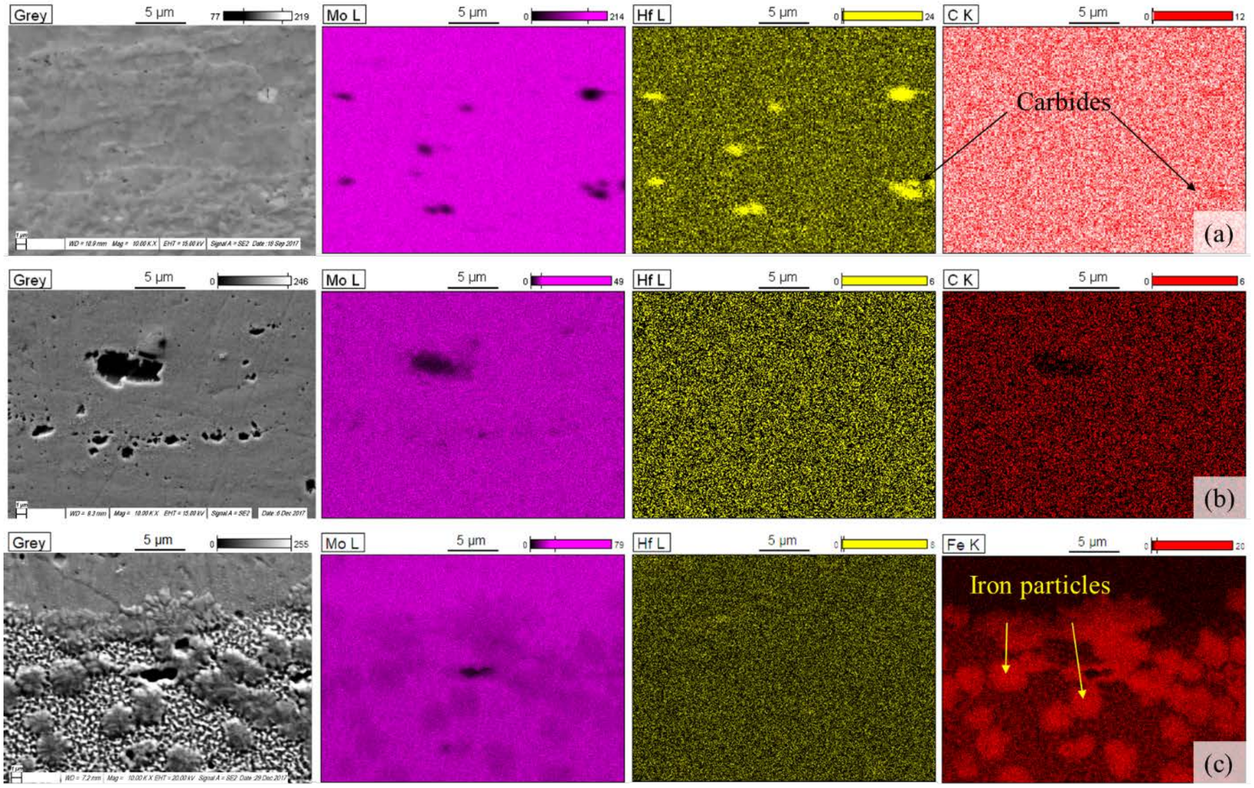

Fig. 56 10,000x magnification SEM and EDS maps of (a) MoHfC reference face, (b) MoHfC face after exposure to as-purified FLiBe, (c) MoHfC face after exposure to Be-reduced FLiBe [5].

After corrosion in Be-reduced molten FLiBe, an interesting phenomenon was exhibited on the surface of MoHfC. A coating of iron and sparsely distributed iron precipitates were observed to form on the surface, as well as some microstructural changes to the underlying molybdenum substrate. High resolution SEM images depicting the exposed molybdenum regions and iron particles are shown in Fig. 57. The exposed Mo substrate shows a slightly ridged but dense surface, whereas the iron coating is more porous and sparse. The formation of the iron coating is possibly due to the incomplete filtration of reduced metals in the Be-reduced FLiBe. Reduction with beryllium causes iron and nickel fluorides to be reduced to metal form. Subsequent filtration with 25um filter should remove precipitated metal particles, but some dissolved metal atoms could remain. After exposure with molybdenum samples, iron diffused through the salt and condensed onto the surface of the molybdenum samples. The iron coating was mainly on the lower two samples in the capsule, which could be explained by gravity concentrating the iron particles to the lower region of the salt [5].

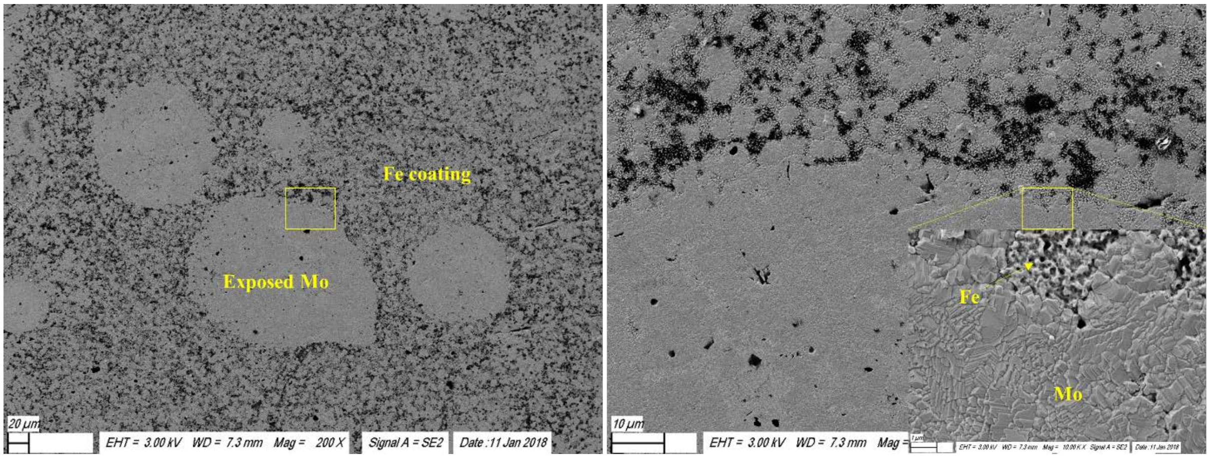

Fig. 57 SEM images of MoHfC sample exposed to Be-reduced and filtered molten FLiBe [5].

W-Zr-C

WZrC samples have a very high mass loss after corrosion. Samples exposed to beryllium reduced salt experienced nearly twice the mass loss that samples in as-purified salt experienced. This is primarily due to zirconium dissolution from the Zr-rich cermet. After exposure for molten FLiBe, WZrC samples look slightly darker. Tungsten mounting wire is extremely brittle after corrosion and snaps easily with any bending.

The WZrC samples showed severe mass loss after corrosion in fluoride salts. The weight change of WZrC to stainless steel and MoHfC is shown in Fig. 58. WZrC exposed to as-purified FLiBe salt at 700°C for 2,000 hours showed a weight loss of -2.80 mg/cm^2, whereas WZrC exposed to Be-reduced FLiBe showed a weight loss of -4.91 mg/cm^2. This is because of the high relative stability of ZrF_4 in fluoride salts, as well as the residual bulk porosity exhibited by the cermet samples. It was found that the Zr-rich phases preferentially dissolved to form ZrF_4, a stable fluoride. Unfortunately, zirconium concentrations were not able to be detected by ICP-OES, so conclusive data showing an increase in zirconium concentrations are not shown. Corrosion was presumably also exasperated due to the porous nature of the WZrC cermet.

The polished surface of material shows small holes/pores because the base material somewhat porous. Fig. 58 shows SEM images of a scratch on WZrC before and after exposure to as-purified FLiBe salt at 700°C for 2,000 hours. Severe corrosion to zirconium rich regions is prevalent throughout the WZrC cermet surface after exposure to molten FLiBe. Bulk porosity of sample causes significant infiltration, exposing zirconium-rich and copper-rich regions to interact with the molten fluoride salt. This increased surface area in turn exasperates corrosion of zirconium. Since zirconium scavenges fluorine and readily forms ZrF_4, the zirconium throughout the sample dissolved, leaving behind large pores and recessions. The tungsten matrix prevails through the corrosion, remaining essentially unchanged [5].

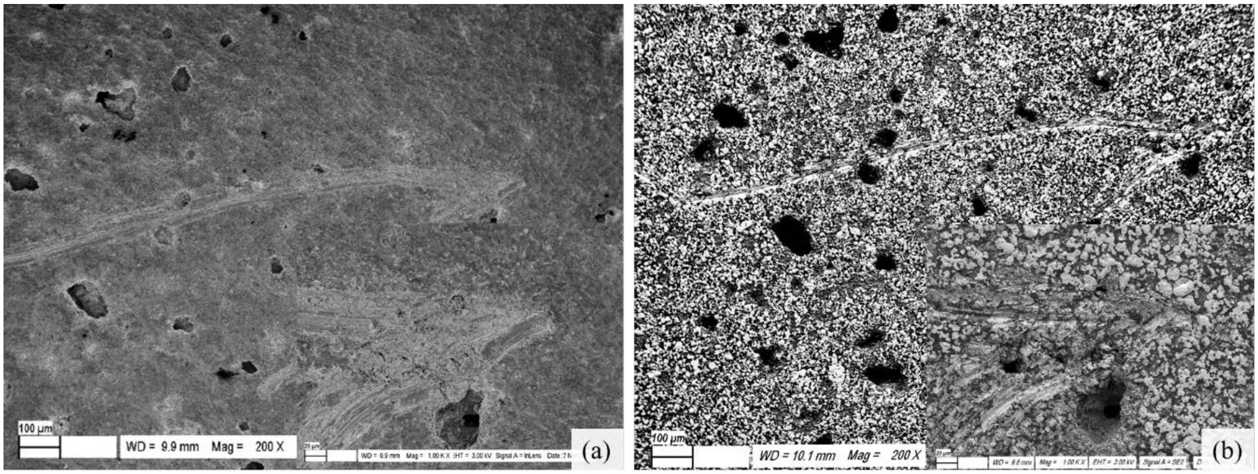

Fig. 58 SEM images of scratch on surface of WZrC (a) before and (b) after corrosion in as-purified molten FLiBe salt [5].

Fig. 59 shows EDS composition maps of a WZrC sample before and after exposure to as-purified molten FLiBe salt. SEM and EDS surface analysis before and after corrosion reveals islands of tungsten and copper grains surrounded by a depleted cermet matrix, originally comprised of zirconium carbide presumably.

The main method of corrosion was the depletion of zirconium from the sample. Prior to exposure, darker regions of the sample were rich in zirconium and carbon, whereas lighter, flat regions are mainly pure tungsten. After corrosion, the tungsten rich regions remained flat and untouched, whereas the zirconium rich dark region surrounding had diminished substantially, leaving the island-like tungsten regions behind. Deep trenches remain where the zirconium-rich material was before corrosion, demonstrating severe corrosion and dissolution of zirconium.

Copper was used as an infiltrating molten metal to densify the cermet. Elemental copper was present in the samples among the zirconium-rich regions surrounding the tungsten islands. After corrosion, the copper regions remained, however much of the region was disrupted due to the high dissolution of zirconium in the same region [5].

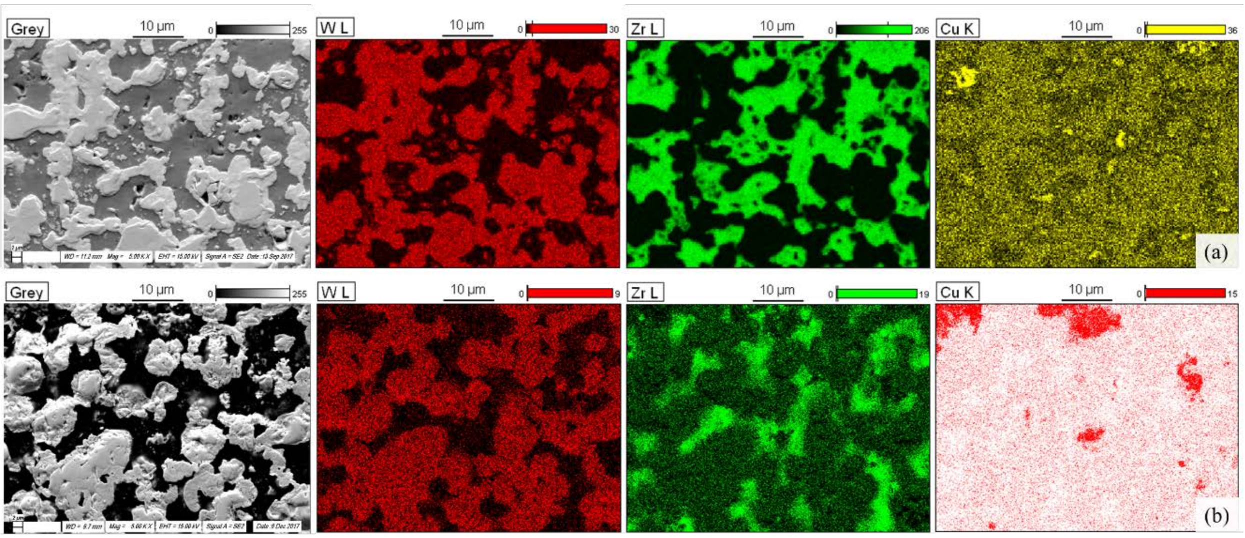

Fig. 59 5,000x SEM images and accompanying EDS composition maps of WZrC before (a) and after (b) exposure to as-purified molten FLiBe salt [5].

Surface roughness images revealed by Zygo profilometry have confirmed the hypothesis that the zirconium species in the material were quickly dissolved by the molten FLiBe salt. Zirconium rich regions show severe attack, and surface roughness values increased substantially. The surface roughness of WZrC increased similarly in the Be-reduced and as-purified variants of FLiBe due to the zirconium dissolution, leaving holes and pits. Deep pits and holes in the post-corrosion samples are seen in Fig. 60. The roughness (RMS) measured by the Zygo Profilometer is shown in Fig. 60. Corrosion was especially severe due to the removal of material from pits. Overall, the roughness of both WZrC samples approximately doubled after exposure to FLiBe salt. Be-reduction and filtration did not affect the surface roughness of the sample as much as it exasperated the corrosion in pitted regions [5].

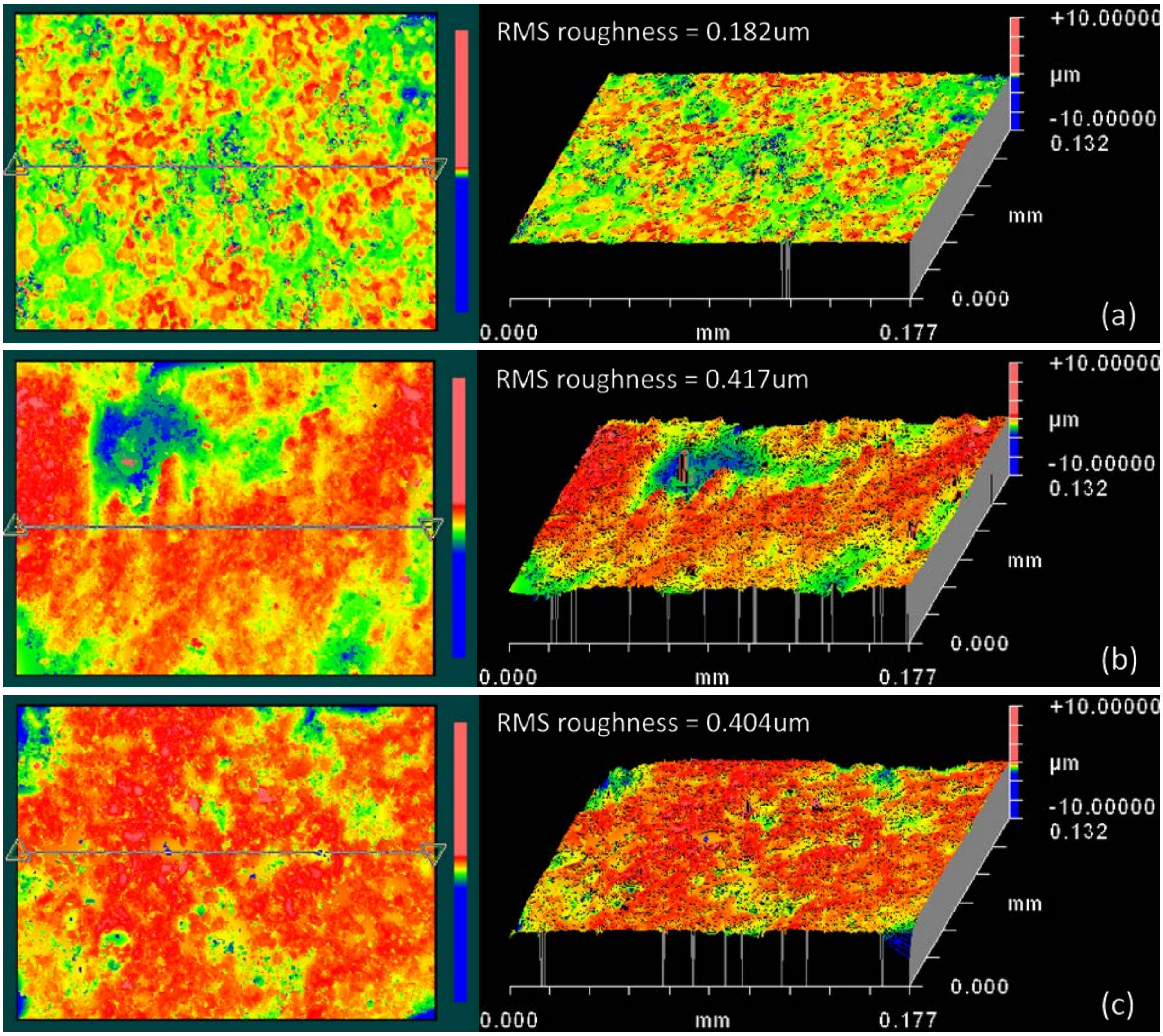

Fig. 60 Surface roughness profile of WZrC samples. (a): Initial conditions before exposure polished to 1200-grit. Bulk porosity results in rough surface. (b): Sample exposed to as-purified FLiBe. (c): Sample exposed to Be-reduced and filtered FLiBe. Roughness measurements were taken on a flat region to avoid pits. Deep pits are visible on both post-corrosion surfaces [5].

XRD analysis of WZrC indicates the formation of iron carbides during exposure to FLiBe salt. The XRD pattern for as-received WZrC cermet is shown in Fig. 61(a). The main phases present are pure tungsten (W) and zirconium carbide (ZrC). Peaks that indicate pure tungsten overlap with a copper tungsten alloy (Cu0.4-W0.6 – PDF card 00-050-1451), however both phases are likely present. After corrosion in as-purified FLiBe, the ZrC peaks disappeared, and signals for W, WC and W_2C peaks are intensified, as seen in Fig. 61(b). Peaks that were weakly present in the reference sample at 2θ = 43.2° and 50.5°, become more pronounced after corrosion. The peaks are characterized as an iron carbide (Fe.94C.06 PDF card 01-074-5520). After corrosion in Be-reduced FLiBe, XRD results shown in Fig. 61(c) indicate the identical phases as the as-purified sample, albeit with different relative concentrations.

Peaks at 2θ = 48.5° and 73° that indicate tungsten carbide (WC) are substantially weaker than in the sampled exposed to as-purified salt. This result could be due to an elevated rate of attack to carbide phases in Be-reduced salt [5].

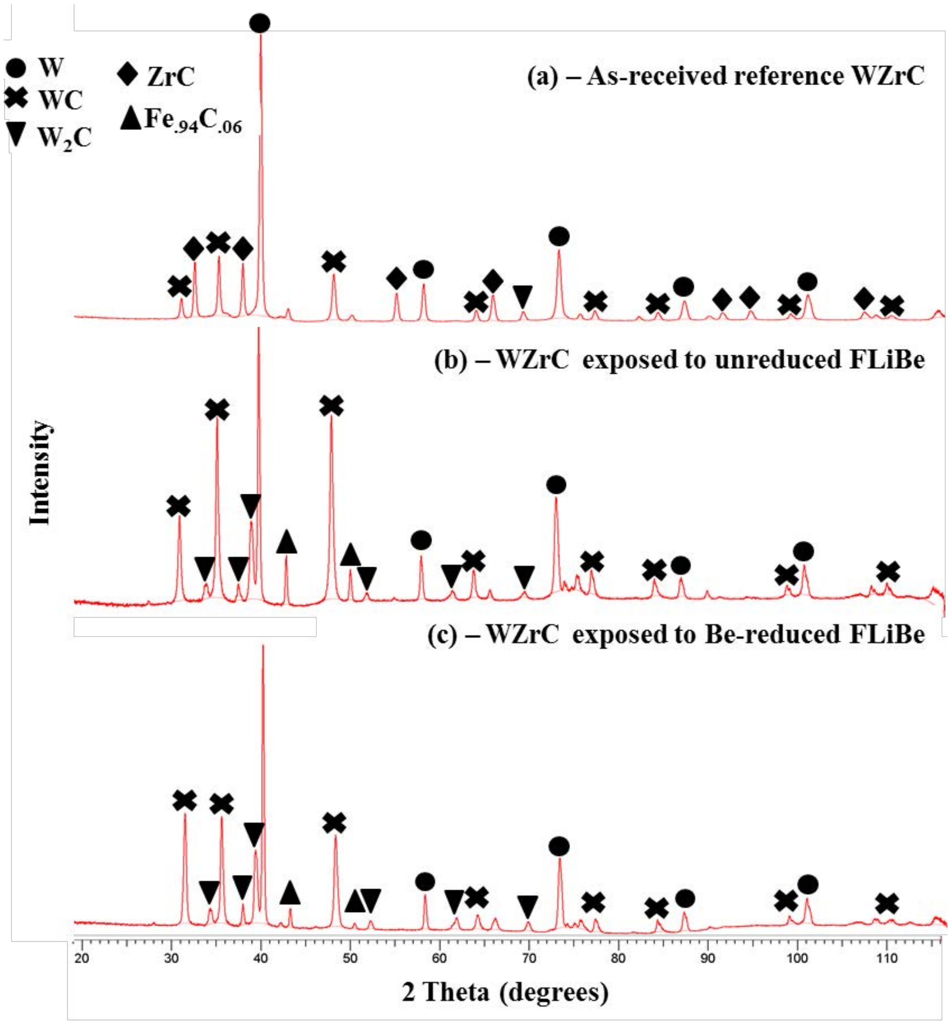

Fig. 61 XRD pattern for (a) reference sample, (b) sample exposed to as-purified FLiBe, (c) sample exposed to Be-reduced FLiBe [5].

Ceramics Exposed to Natural Lithium FLiBe

The weight change results of the ceramic samples are shown in Fig. 62. Weight change of bonded SiC was minimal, with the entirety of the mass lost coming from the dissolution of the bond. The General Atomics coated SiC experienced substantial weight loss after corrosion, despite being the only un-bonded SiC sample. The coating was severely attacked, with a deforestation of SiC pillars comprising the coating observed after corrosion. A3 and IG-110 graphite samples experienced negligible corrosion. The error bars length is a sum of the scale error and standard deviation in the weight change of duplicate graphite samples in each crucible. Two identical graphite samples were placed in respective crucibles for numerical confidence [5].

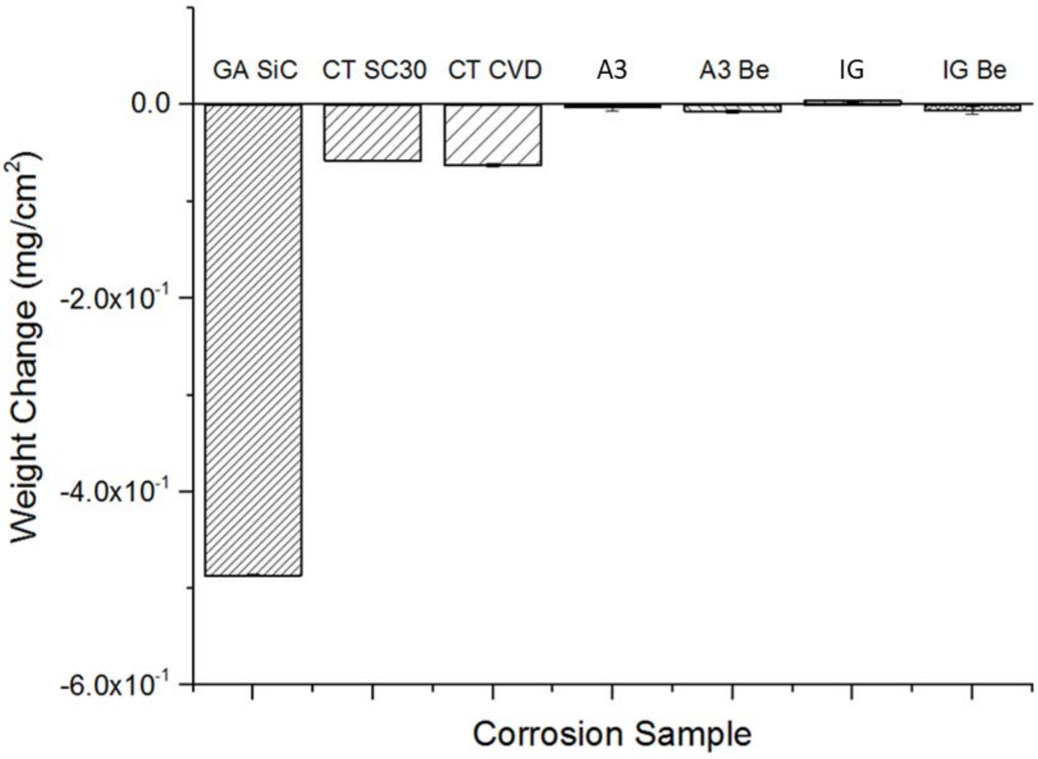

Fig. 62 Weight change results of ceramic samples after exposure for molten FLiBe salt. GA denotes General Atomics, CT denotes CoorsTek. Unless specified the salt used is as-received FLiBe. Be denotes a beryllium reduced salt chemistry [5].

General Atomics SiC coated SiC-SiC

The General Atomics SiC coated SiC-SiC composite sample showed relatively high weight loss of -0.486 mg/cm^2, which is about one order of magnitude higher than other SiC samples as shown in Fig. 62 This is mainly attributed to an observed erosion or delamination of the high surface area PVD coating. SEM images of the surface depicting this phenomenon are shown in the next section.

General Atomics samples are SiC-SiC composite sample that have been coated with a monolithic CVD SiC. Polishing of the composite was done before applying this outer monolithic SiC layer. Fig. 63 shows SEM images at various magnifications of the GA-SiC sample surface before corrosion depicting this morphology. The surface of the General Atomics SiC coated SiC-SiC material shows a unique growth structure and morphology of the applied coating. The uniform SiC coating is comprised of nano-sized SiC rods extending from the surface, forming a tangled network of SiC surrounding the underlying composite. Lower magnification image of a corner of the sample before corrosion portraying the rough SiC web on the surface. Higher magnification images show the PVD SiC coating applied uniformly to the surface, as well as the underlying polished composite. The reference sample shows nearly full coverage of the sample surface with small areas exposing the underlying composite. Additionally, the SiC coating tends to form dispersed clusters that are denoted in an arrow [5].

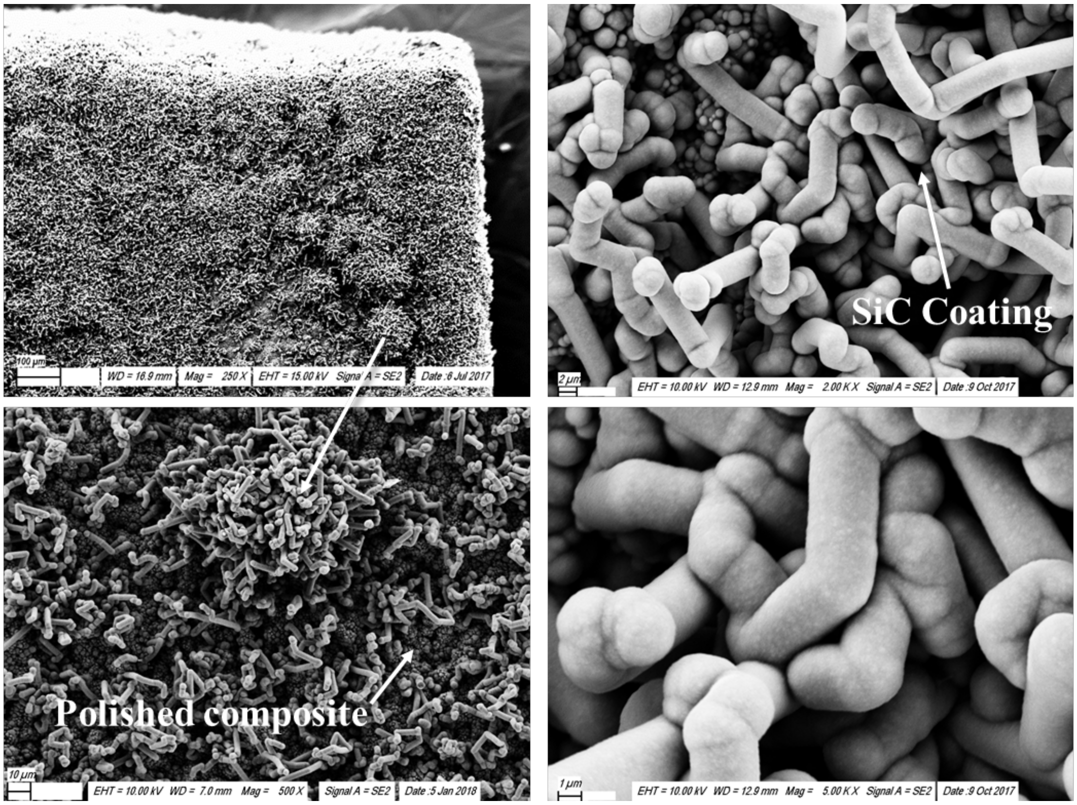

Fig. 63 SEM images of General Atomics SiC coated SiC-SiC before corrosion [5].

After corrosion, the SiC sample shows an erosion and removal of the surface layer of SiC throughout the surface of the sample. SEM images of the polished and coated SiC-SiC sample before and after corrosion are shown in Fig. 64. The monolithic SiC coating was severely attacked by the FLiBe, resulting in exposure of the underlying polished composite. The underlying composite shows little change in morphology after corrosion, and appears unaffected by molten FLiBe [5].

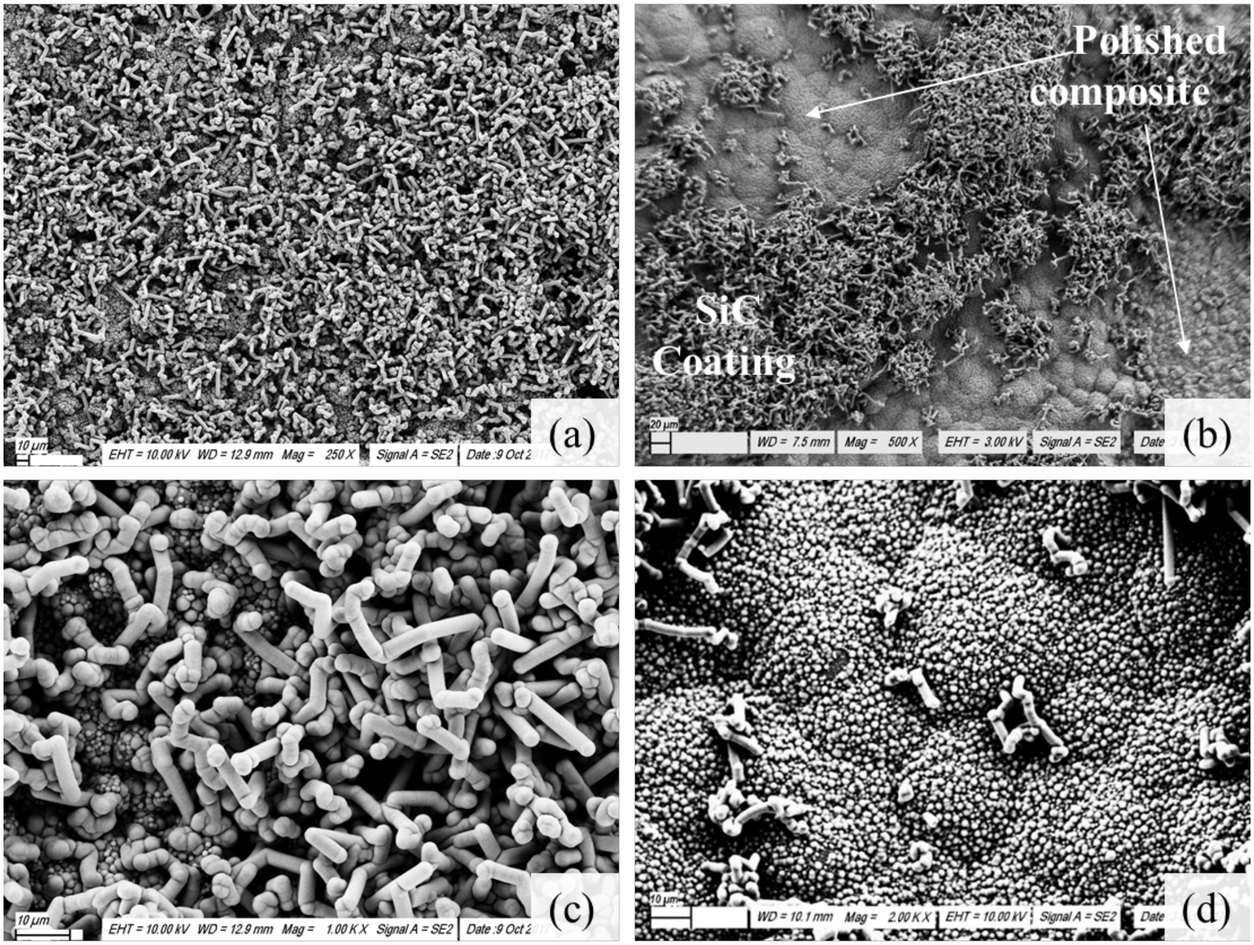

Fig. 64 Various magnification SEM images of the coated GA-SiC sample before and after exposure to molten FLiBe at 700°C for 2,000 hours. (a) and (c) are before exposure, whereas (b) and (d) are after exposure [5].

After corrosion, the thickness of the sample decreased by 0.07mm. Since some parts of the corroded sample were flat and barren compared to the uniform layer on the reference sample, the slight decrease in thickness is reasonable. Overall, the surface of the GA-SiC samples is very rough. The surface area calculations using a caliper area are presumably lower than the actual surface area, which skews weight loss results [5].

CoorsTek CVD bonded SiC

CoorsTek/Ceramatec SiC samples incorporate a solid-state bonded joint that is approximately 5μm thick and primarily composed of aluminum. Fig. 65 shows SEM images of the bulk and bonded region of CVD SiC before corrosion. At some point during exposure the bonded joint fell apart preventing accurate measurement of weight change. While the integrity of the bond proved problematic, the SiC material provided interesting insight into how SiC derives its corrosion resistance [5].

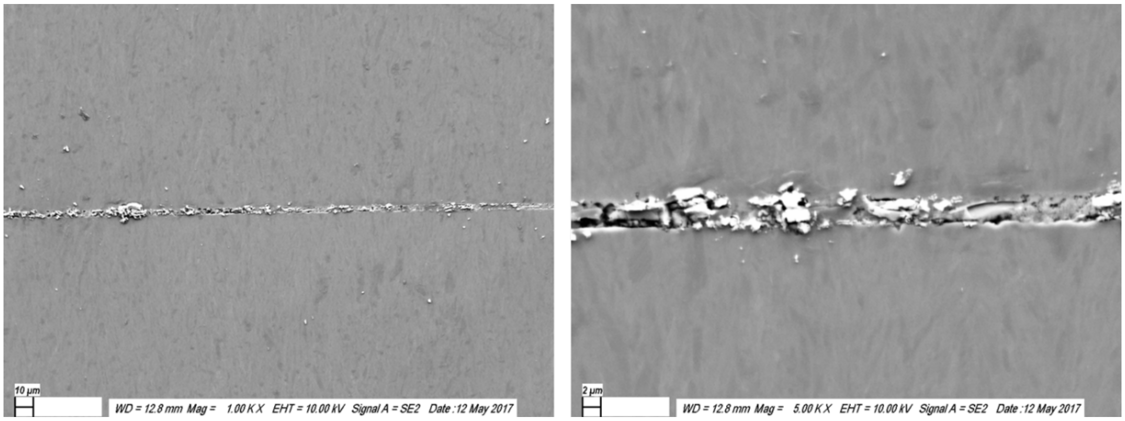

Fig. 65 SEM images of the bonded region of CVD SiC before corrosion [5].

The bond in the CoorsTek CVD SiC sample was investigated with SEM and EDS before corrosion to understand the composition and gain insights as to how the bond was formed. Fig. 66 shows X-ray line-scans of the bonded region of the CVD SiC reference sample in plan-view. The Line scan indicates a sharp interface between the diffusion bonded silicon and aluminum [5].

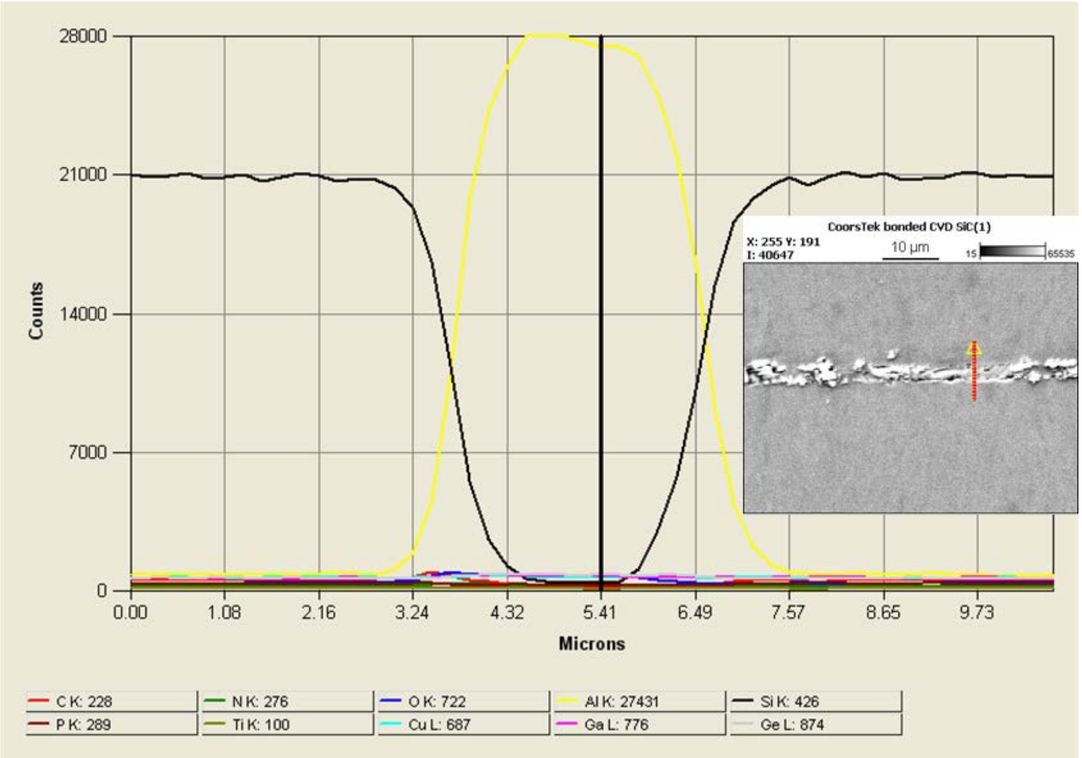

Fig. 66 5000x magnification X-ray line scan across darker, smoother region of bond. Lighter material in center of bond is aluminum, whereas matrix material is CVD SiC [5].

While EDS is not accurate for measuring carbon content, key elements such as Si, Al and O can be measured to reveal information regarding the composition of samples. In all the bonded SiC samples, the bond composition appears to be mostly Al. AlF_3 is a very stable fluoride and a metallic Al would most likely dissolve in FLiBe at the 700°C temperature.

Since SiF_4 is more stable in FLiBe than SiC, it could be possible that the silicon atoms at the surface rapidly diffuse into the salt, leaving behind a thin film of carbon on the surface of the sample. This thin carbon film may act as a protective layer for the underlying SiC, as carbon is very stable in FLiBe. XPS has been employed to investigate the near surface region of the sample. This near-surface technique can detect thin layers of carbon on the surface. By comparing the XPS surface scans of CVD SiC before and after corrosion in molten FLiBe salts, is possible to show in Fig. 67, that a shallow carbon rich layer exists on the SiC surface. The figure shows depth profile and individual scans at various depths in a bulk region of the CoorsTek CVD SiC reference sample and post-corrosion sample surfaces. Approximately 4.2 nm of material is removed between each scan. The surface of CVD SiC after corrosion does not show a carbide peak at 285eV, and the intensity of Si2s and Si2p bonding is greatly diminished relative to the bulk material. These results confirm the suspicion that silicon atoms at the very near surface are removed, resulting in the formation of a carbon-rich layer at the surface. The carbon-rich layer is approximately 10nm thick, and silicon depletion is present until about 40nm into the surface of the CVD SiC. Silicon is very reactive in fluoride salts and forms SiF_4, however carbon has been shown to be inert. Therefore, during exposure in molten fluoride salts, the near surface layers of SiC are altered (Si- bonds broken and Si leached away), and are ultimately left carbon-rich compared to the rest of the material. This thin-film of carbon essentially protects the underlying silicon atoms in the SiC matrix, mitigating further corrosion [5].

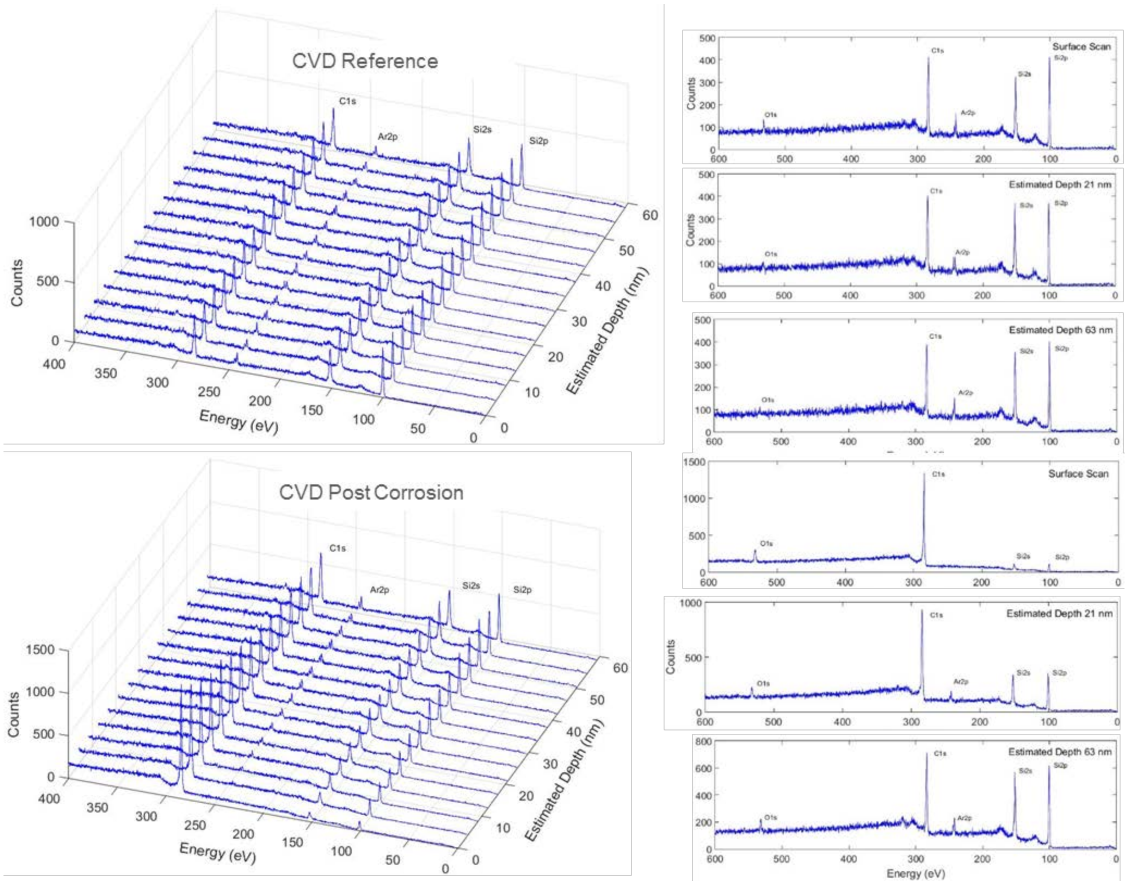

Fig. 67 XPS results of CVD SiC before exposure to as-purified molten FLiBe for 2,000 hours [5].

5. FLiBe Corrosion Flow Loop (UW)

Background

Natural convection (NC) salt loops were first employed at Oak Ridge National Laboratory (ORNL) during the Aircraft Reactor Experiment and the Molten Salt Reactor Experiment (MSRE). These systems were the second of three test beds for studying salt corrosion of various materials. Initially, researchers planned to use these systems only until a reliable molten-salt pump was constructed. However, by 1957 researchers had observed that molten salt corrosion mechanisms are dominated by temperatures rather than flow rate. As a result, use of natural convection loops continued all the way until the end of the Molten Salt Program in 1976. [47]–[50]

Natural convection flow lends itself well to operating over a wide range of conditions. ORNL loops generally operated with a hot wall temperature between 650 C and 815 C (1250 -1500 F) and a temperature drop of anywhere from 20 C to 200 C. The tests often ran for 500 or 1000 hours, with several tests continuing for months or even multiple years. The material data gathered from these systems is instrumental in developing nearly all current theories of molten salt corrosion.

Unfortunately, researchers did not characterize the thermal hydraulic conditions very well. Since flow rates do not have a large impact on corrosion, the flow rate and heat transfer were not critical measurements. Instead, researchers characterized their tests by wall temperatures, measured using thermocouples attached to the outside of tube walls. This makes comparison with modern data challenging, since a wider array of tests are now employed. The ORNL systems had an estimated flow that was quite slow, with quoted speeds ranging from 1 to 4 cm/s for the initial loop designs.[48], [51] Later work, reported in 1977 quoted a more precise 1.7 cm/s, for a FLiBe loop very similar to the UW design.[52]

Flow rates near this order of magnitude are close to those anticipated in the Direct Reactor Auxiliary Cooling System (DRACS) used by the FHR.[53] This makes studies of NC heat transfer characteristics directly applicable to understanding potential DRACS performance. The heat transfer in such a system will require additional verification since it behaves as mixed convection. These flows have both a Reynolds and Grashof number dependence that can inhibit heat transfer below the correlation predictions. ORNL studied heat transfer in forced convection loops, where an extended flow-transition regime also acted to inhibit heat transfer by delaying the onset of turbulence.[54] At the time, this effect was attributed to the strongly temperature dependent viscosity acting to stabilize the flow, an affect that should be observable in the UW loop.

System Overview

The flow loop, modeled in Fig. 68, has a skewed parallelogram flow path, with the top and bottom legs slanted at 10° and 20° off horizontal to aid salt drainage. The two vertical legs will house the hanging sample trains during corrosion testing. Salt flows clockwise, driven by the density difference between the hot salt, located in the bottom and left sides of the loop, and the cold salt, in the top and right sides of the loop. By controlling heat input and removal, the loop operates between 460℃ and 700℃, with a temperature difference up to 120℃ between the hottest and coldest locations. The loop is instrumented with thermocouples and fiber optic temperature measuring cables, plus two electrochemistry probes. The system size is similar to the final iteration of ORNL loops that went into service in the 1970’s. The system dimensions are shown in Fig. 69.

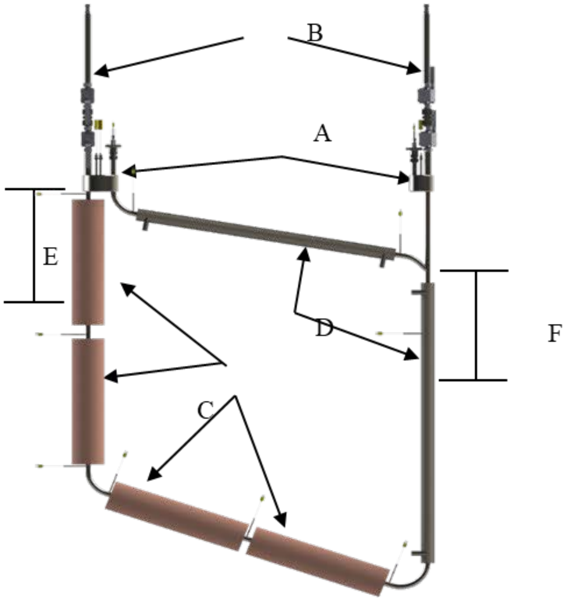

Feature	Value
A	Electrochemistry probes
B	Sample access ports
C	Main heaters
D	Concentric-tube forced-air coolers
E	Location of hot leg sample train
F	Location of cold leg sample train

Fig. 68 Rendering of the UW Flow Loop and its features

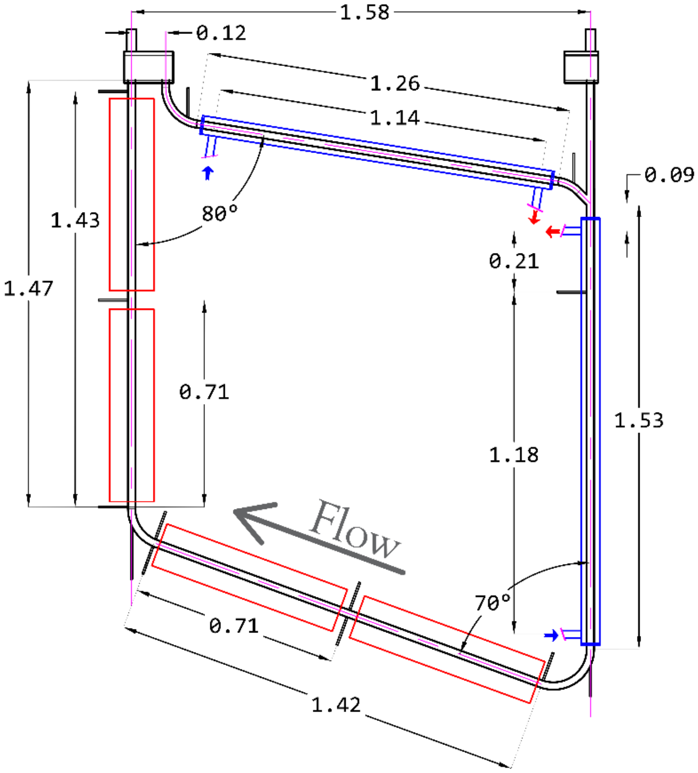

Fig. 69 NC loop dimensions in meters.

Construction of the loop began in spring 2016 and was completed by the years end. Fig. 70 shows the bare piping prior to welding in comparison to the final hefty-looking flow path in the insulated system. The flow path is constructed from seamless type 316 dual-cert stainless-steel tubing, with a 2.54 cm (1 inch) outer diameter and a 1.92 cm (0.76 inch) inner diameter. All bends have a five-inch radius, excepting the upper right corner, where a bending top-cross joins the down-comer at a 45° Y joint. The large expansion tank on top of the riser is a schedule 10 size 6 NPS stainless steel pipe, while the smaller tank above the right side is a size 4 NPS pipe. Both tanks have an internal height of 3.5 inches and have flat tops and bottoms cut out from 6.35 mm (¼ in) stainless steel sheet. During operation, the system contains around 7 kg, approximately 3.3 liters, of salt, filling the tanks to a depth between 4 and 6 cm.

Fig. 70 Flow loop construction, from the bare piping (left) to fully insulated and operational (right).

In addition to expansion space, both tanks provide access for the sample trains through a double ball-valve system, which is designed to prevent oxygen ingress. The lower ball valve is welded to the system, while the upper ball valve and sample chamber can be removed and taken to an inert atmosphere glovebox, where the sample train is loaded or removed. The sample chamber is attached to the loop with a Swagelok fitting and can be purged with dry argon before the valves are opened. A long rod is threaded into the top of the sample train for inserting or removing the samples into the loop. A rotation locking mechanism sits just above the flow path, allowing the rod to twist free and be removed to shut the valves and isolate the gas space for long duration tests.

A smaller double ball valve system is fitted on the large tank to allow insertion of a salt sampling tube or a beryllium rod, to monitor and control salt chemistry. Additionally, the tank is equipped with a three-electrode potentiostat probe for monitoring the electrochemical state of the salt. Beyond this equipment, flow conditions monitored by 52 thermocouples and up to seven fiber optic distributed strain sensors. Ten thermocouples are inserted into the flow, with the rest either tack-welded onto the tube exterior or measuring air-temperatures. The fiber optic sensors use technology from Luna Inc. to measure strain in a standard telecommunications fiber, with a 0.625 [mm] resolution. [55], [56] A thermal-strain correlation converts the readings into high resolution temperature values at the locations shown Fig. 71. Four of the fibers run perpendicular to the flow, at positions A, B, C and D, while three fibers run parallel to the flow in positions E, F, and G, located either in the tube wall or at the flow centerline. Fibers D, F, and G are currently occupying sample corrosion locations and will be removed before the start of corrosion testing. Since it is unlikely they can be reinstalled, all thermal-hydraulic tests must be complete before corrosion testing.

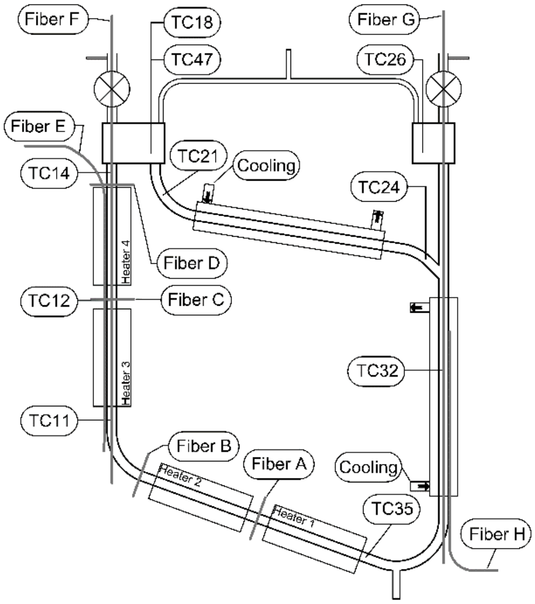

Fig. 71 Positions of thermocouples and distributed fiber optic strain sensors.

Operation History

To date, nearly 2000 hours of flowing salt time have occurred, with temperatures ranging from freezing salt up to 736°C. The loop operation has proven straightforward and the temperatures remain relatively stable under constant power conditions.

The first sets of loop operation took place in the spring of 2017, when the system was filled with a mixture of water and Oakite to remove oil and oxides from the tubes. The mixture was heated to 50 °C and circulated for several days. Afterward, the loop was flushed several times with purified water before a vacuum pump was used to pull a 1 torr vacuum and the system was baked overnight.

The first salt fill took place on June 2nd after the system spent more than 24 hours at temperature waiting for the salt transfer line to melt. The system was successfully filled, but after nearly 10 hours, temperatures around the loop did not indicate flowing salt. After 12 hours, the test was scrapped to drain the loop, except only half the salt could be removed. The cold side of the loop, including the top-cross and down-comer, remained filled salt, held-in by a freeze plug that formed near the bottom of the down-comer cooler. It is assumed the issue was the cooler centering ring, which cannot be heated and is able to conduct heat away quickly. To melt the salt, several layers of insulation were added to the lower right corner, and the cooler annulus was blocked off by stuffing insulation into the air vents. Then the heater zones were turned to maximum power and left overnight. The next morning, additional insulation allowed the plug to finally melt and the system was fully drained and shut-down.

The second flow test began on June 11 and ran until the 12th, without incident. However, none of the fiber optic sensors operated, so the test was kept short. Afterward, a series of improvements to insulation and auxiliary heating were made and the fiber sensors were replaced.

The third test started on August 12 to establish long term operations under constant heater and blower settings. The system states focused on colder temperature operations, particularly looking for indicators of flow freezing. The test was successful, with the loop proving easy to thaw after freezing transients. Velocity pulse tests were also performed during the one-week operation to understand flow conditions. After this test, 2 grams of beryllium metal flakes were added to the dump tank to cause metal impurities in the salt to plate out onto the walls of the dump tank.

On September 2nd salt began melting for Flow Test 4, which began on the afternoon of September 5th when the system was filled to a height of 50 mm above the bottoms of the tanks, as measured by scanning an isolated molybdenum rod vertically while measuring the resistance between it and the loop metal. This test took place over two weeks until September 21st, when it was terminated due to the loss of multiple fiber sensors. Settings during this test focused again on steady state power input and removal over a wider range of conditions, up to a maximum temperature of 736℃.

Flow test 5 ran January 3rd to 31st and expanded the constant power test range as well as attempted work at constant temperature and using oscillating power. The constant temperature operations were unsuccessful due to difficulties tuning the PID controller. The long response times prevented the LabView autotuning VI from successfully determining parameters, and hand-calculated values were not reliable enough for unattended operations. The oscillating power tests were more successful when changing the cooling air flow rate to study the loop’s fundamental frequencies. Input from UC Berkeley was instrumental in designing these curves and analyzing the data.

Flow test 6 began on July 23, 2018 and was completee on September 1, 2018. This test is repeating several previous conditions to study a discrepancy in heat transfer data and to gather more data using fiber sensors at several interesting power levels. Two further oscillation tests are being performed, using an improved curve based on results from the previous of tests. Upon conclusion of this test, the dump tank will be removed for chemical analysis in gloveboxes and the loop will be filled with a fresh batch of purified FLiBe.

System Behavior

Each constant power test begins with the setting the power input and blower speed. The system temperatures undergo a several hour thermal transient, after which the test continues for at least 12 hours at steady state conditions. During the equilibration period, system temperatures approach their new values asymptotically. They often appear to overshoot slightly, with a few degree correction following over the next several hours. This blends seamlessly into the steady state condition that includes a constant temperature oscillation of degree or two on a period that is near 1 day, as shown in Fig. 72. The oscillations appear to result from daily temperature fluctuations in the building, which are less than 1℃. Correlations between the loop and air temperatures shows some degree of correlation ($\rho \approx \pm 0.4$) but the correlation coefficients can be either positive or negative, depending on the test. This indicates there may be an additional effect, such as considering if the temperature change during the approach to steady state is positive or negative.

Luckily, the temperature difference across the loop is more stable, often ± 2℃, and approaches its steady state average faster than loop temperatures. This provides a convenient metric for estimating test start times while operating.

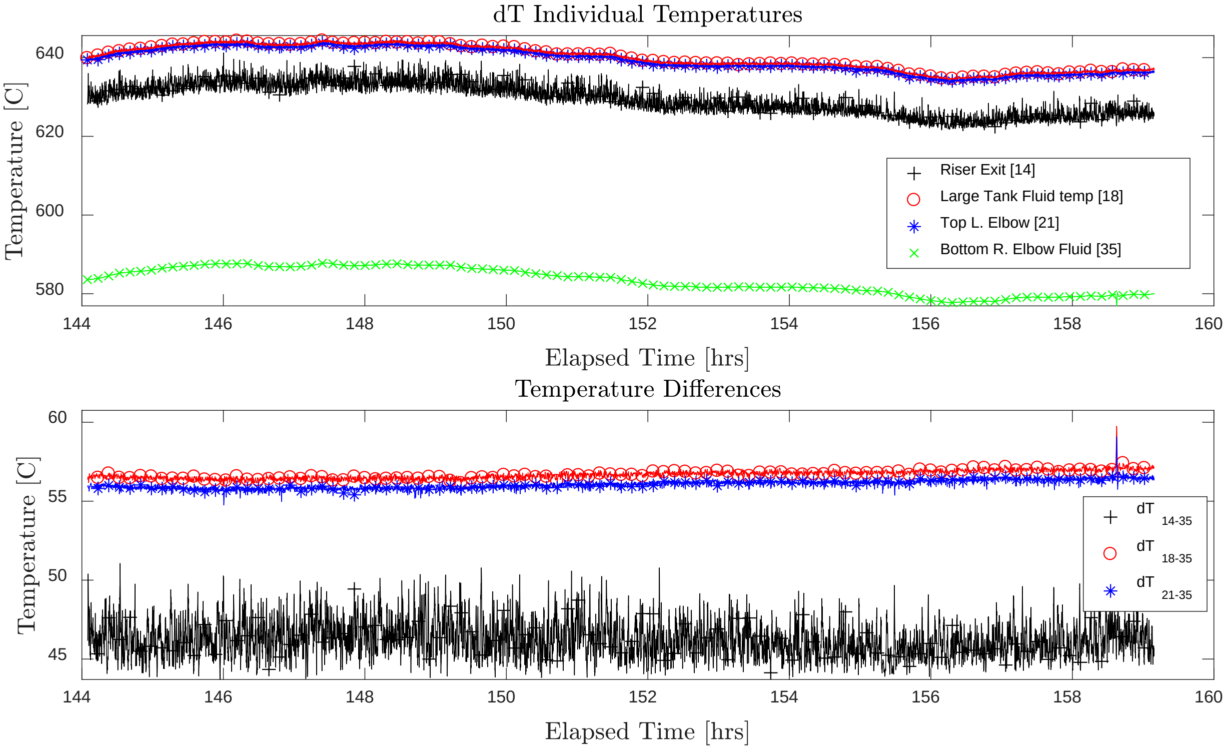

Fig. 72 Temperature readings (top) and the resulting differential temperatures (bottom) during steady operation

The amount of thermal drift varies by heat input and removal, with high power tests showing significantly more oscillations. In addition, high cooling rate tests produce sudden temperature jumps and spikes, such as shown in Fig. 73. These occur over about 5 seconds and can range from $\frac{1}{2}$℃ to 5℃, depending on the cooling rate. Occasionally the jumps will propagate through the heaters and TC11 and TC12 will record a them as well. Another interesting phenomena occurs when the temperature of fluid exiting the top cross cooler (TC24) is colder than the fluid temperature at the lower right elbow (TC35). This results from thermal stratification that causes TC24 to read a cold layer of fluid that mixes with the warmer layers while traveling through the down-comer. This typically occurs during high-cooling rate operation along with the temperature jumps or spikes. It is assumed that both phenomena are related to the frozen salt layer lining the top-cross.

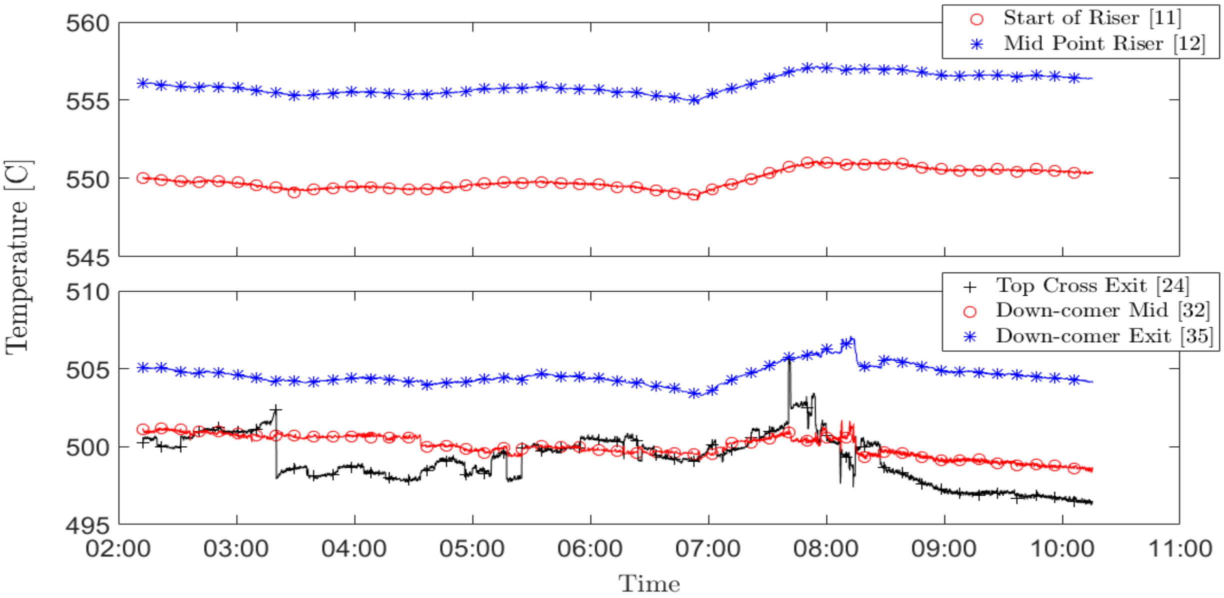

Fig. 73 Temperature transients occurring at the exit of the top cross cooler after 12 hours of constant power conditions. The hot side of the system (top) shows no such jumps or spikes.

Velocity measurements

Measuring flow rates using traditional instruments is not possible due to the high temperatures, corrosive fluid, and small tube diameters. Instead, flow rates are estimated by timing thermal pulses as it passes three thermocouples. The most reliable pulses are generated by momentarily increase the blower power by 15% – 30% for around 10 seconds, followed by turning it off for a similar time before resuming operation. This produces clear pulses, such as are shown in Fig. 74. It is also possible to heat a section of tube directly with a blow-torch. This produces a smaller but sharper hot pulse. It has not been possible to produce thermal pulses with the main heaters, due to their long ramp times, or tape heaters, which do not have a high enough power density.

Once created, a peak search program extracts time stamps, which are used to calculate the time-of-flight between TC24, TC32, and TC35. The three pairs are each used to calculate velocity and then averaged into the test estimate. The different velocity calculation pairs produce slightly different values, depending on how the pulse was performed. But the amount is relatively small and multiple tests performed using different pulse methods tends to reproduce similar velocity estimates.

The exception is low-power operations, where the flow seems almost stagnant and velocity tests produce widely varying results. Under these conditions the flow becomes highly stratified and the location of each thermocouple impacts when the pulse is observed. Most notably, TC24, reads the centerline temperature at the exit of the top cross. At low power operations, thermal pulses produce a cold slug of salt that seems to slip under TC24 to be recorded on TC32 first. The centerline temperature eventually cools, producing a broad pulse that lacks the sharp peak observed on TC32.

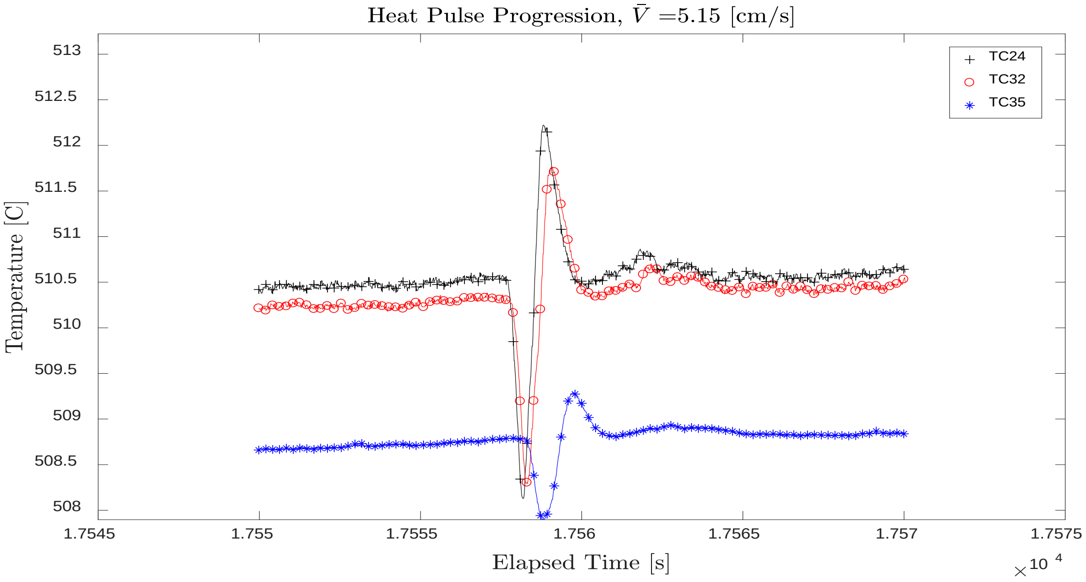

Fig. 74 Example blower pulse used to estimate flow velocity.

During the ANP and MSRE projects, ORNL did not report any changes in velocity that resulted from changing the loop operating conditions. Flow in the UW Loop does change with power input and removal, as shown in Fig. 75.

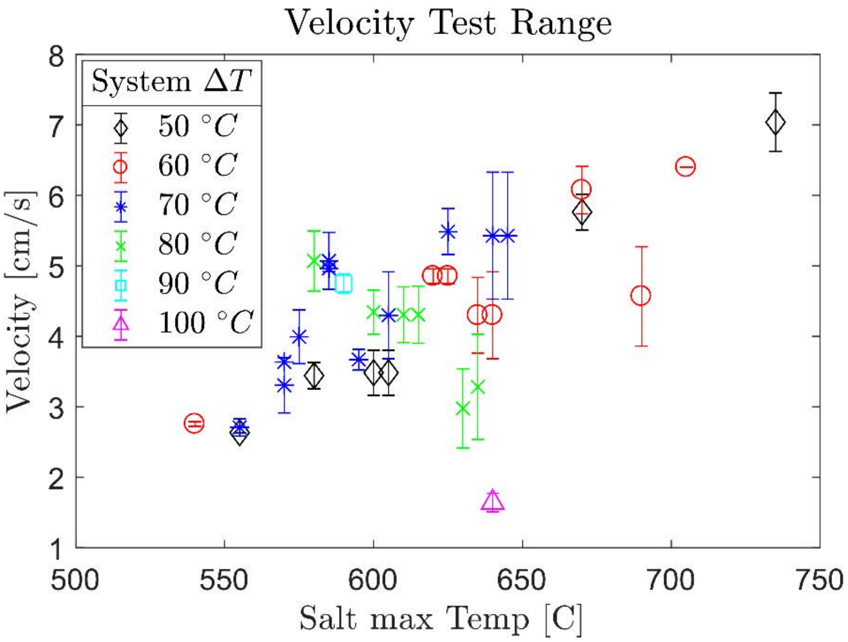

Fig. 75 Velocity estimates and their standard deviations over the full range of operating conditions.

The average velocity is $4.31 \pm 0.65 \frac{cm}{s}$ with a strong dependence on loop temperature. The estimates do not show the anticipated dependence on ΔT, measured between the top-cross inlet (TC21) and the lower-right elbow (TC35). This is likely due in part to a frozen layer of salt insulating the top-cross walls and growing to obstruct flow at high cooling rates.

Distributed Temperature Measurements

The data from fiber optic distributed strain sensors shows thermal stratification within the flow, as seen in Fig. 76. Fibers A and B show remarkably stable profiles, with little to no noise that would indicate secondary flow in the bottom-cross. Fiber C shows a strong externally heated profile, with hot walls and a cold core. The temperature drop between the wall and core is generally $20 - 50\ {}^{\circ}\mathrm{C}/_{cm}$.

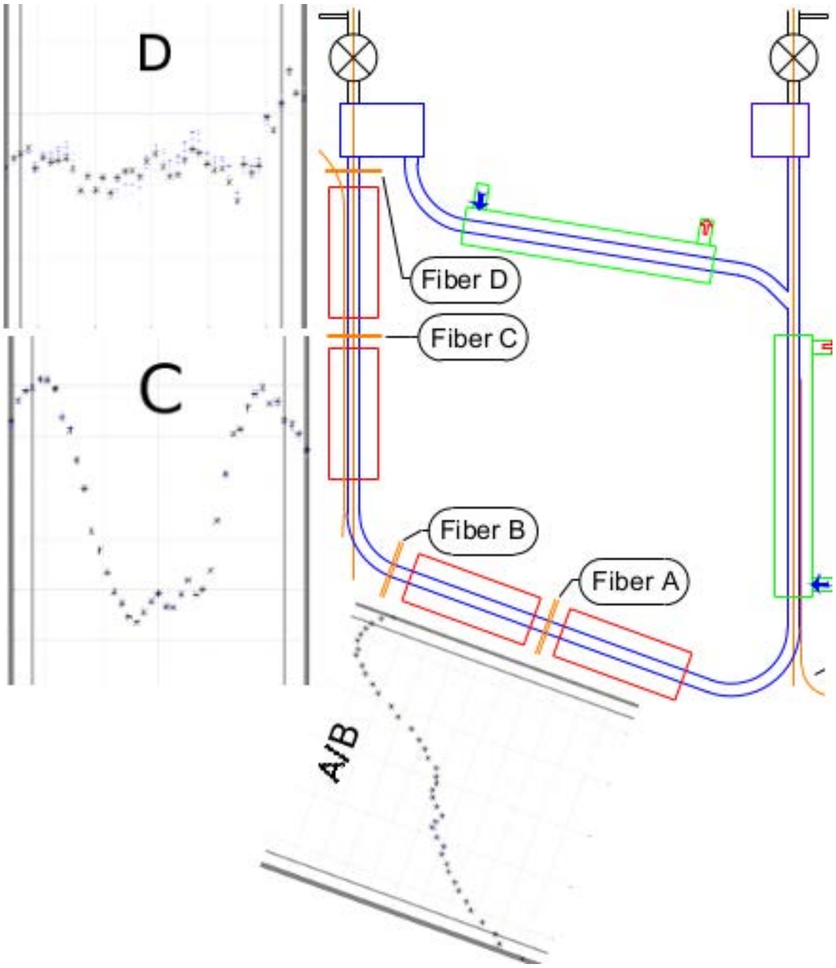

Fig. 76 Still frame images of fiber optic temperature readings at four locations around the system. The temperature axes cover 50°C and the inner tube diameter, marked by light grey lines, is 1.9 [cm].

Fiber D provides a more interesting phenomenon. While it can adopt the cold-core/hot-wall profile observed on fiber C, more often it shows a nearly flat profile with significant fluctuation. The central core constantly oscillates from side to side within the tube, and in some tests will invert, pushing cold salt toward the walls. This seems to result from eddies forming inside Heater 4 due to shear from the strong viscosity gradient that arises due to thermal stratification and the velocity profile, which is peaked near the walls due to the density gradients, which also follow temperature.

The frequency of oscillations on Fiber D are fast, around 5 – 10 Hz, which is recorded at 1 Hz on TC14 as a large amount of measurement noise, shown in Fig. 77.

A similar type of measurement noise is recorded on other thermocouples whenever flow stagnates, such as a during a freezing transient. In this case, the noise results from recirculation cells within the flow path that transfer heat to even the smallest gaps in the insulation. As soon as flow resumes, these cells are damped out and measurement noise drops back to within ±0.5°C.

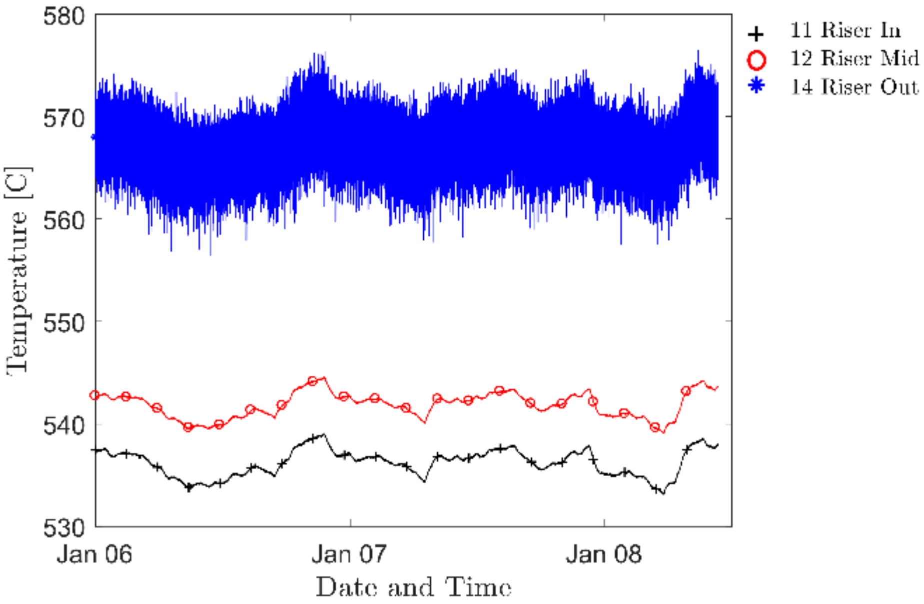

Fig. 77 Comparison of thermocouples measurement noise showing the increased noise at the riser exit due to flow break-down.

Interestingly, over successive tests, Fiber D has shown an increase in flow stability. The most recent Flow Test 6 shows a temperature profile similar to Fiber C, except less sever and it sways from side to side. The temperature profiles do not become flat or invert but are subject to occasional wall-flows of hot salt that create prominent peaks. Fig. 78 shows profiles for several operating conditions during Flow Test 6.

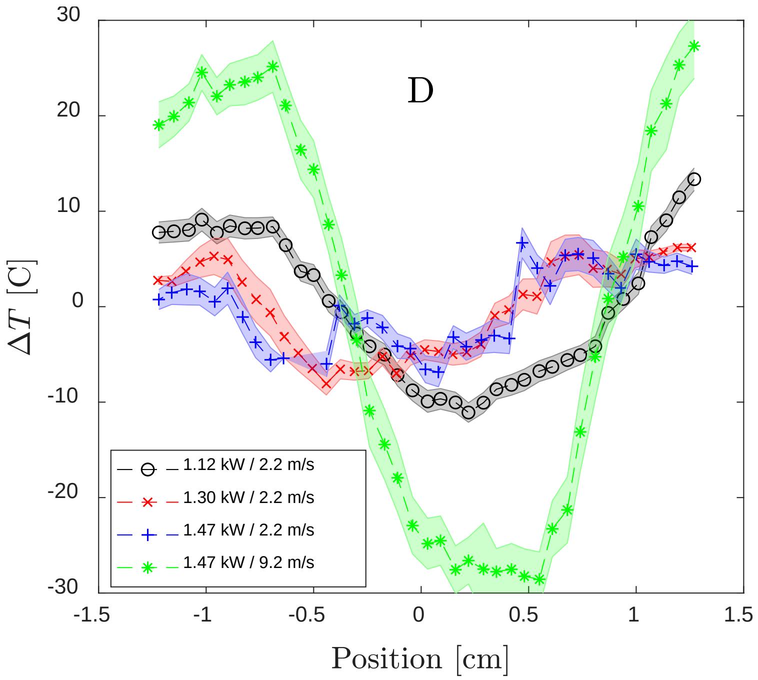

Fig. 78 Fiber D temperature profiles during Flow Test 6 showing increased flow stability.

Heat Transfer

Heat transfer in the loop is expected to behave as mixed convection flow, since $\frac{Gr}{Re^2} \approx 1 - 100$ over the operating range. To examine this, the heat transfer coefficients were calculated from the velocity estimate and temperature measurements and compared against two correlations. A forced convection developing flow correlation:

$$Nu = 3.66 + \frac{\left(0.049 + \frac{0.02}{Pr}\right) Gz^{1.12}}{1 + 0.065\, Gz^{0.7}}$$

Is taken from *Heat Transfer* by G. Nellis [57] and accredited to data from Hornbeck. In this equation, the Graetz number is related to the flow development length as:

$$Gz = \frac{D_h Rd\, Pr}{L}$$

With a small Graetz number indicating flow is fully developed. Also plotted is the laminar Sieder-Tate correlation:

$$Nu = 1.86 \left(Re * \mathrm{Pr}\frac{D}{L}\right)^{\frac{1}{3}} \left(\frac{\mu_{Bulk}}{\mu_{wall}}\right)^{0.14}$$

as recommended by the final ORNL forced-convection molten salt heat-transfer report written by Silverman et. al. [54] This value is calculated at each point to obtain the respective bulk and wall viscosities, whereas the Hornbeck fit is calculated for the range of Pe numbers, independent of the exact flow conditions.

In the top-cross, a heat-balance is calculated between TC21 and TC24 for the salt, and between the air-inlet and air-exit temperatures. From the heat capacitance and velocity of the air flow, the salt tube surface temperature can be calculated and used to determine the thickness of frozen salt inside the top-cross flow path. This is then used to calculate the heat-transfer coefficient for salt. The viscosity of salt near the wall is taken at 460℃ in the Sieder-Tate correlation, due to the freezing layer. Plotting the data and correlations against non-dimensional numbers in Fig. 79, shows that the data sits below the predicted curves and is slightly better predicted by the Peclet number than the Rayleigh.

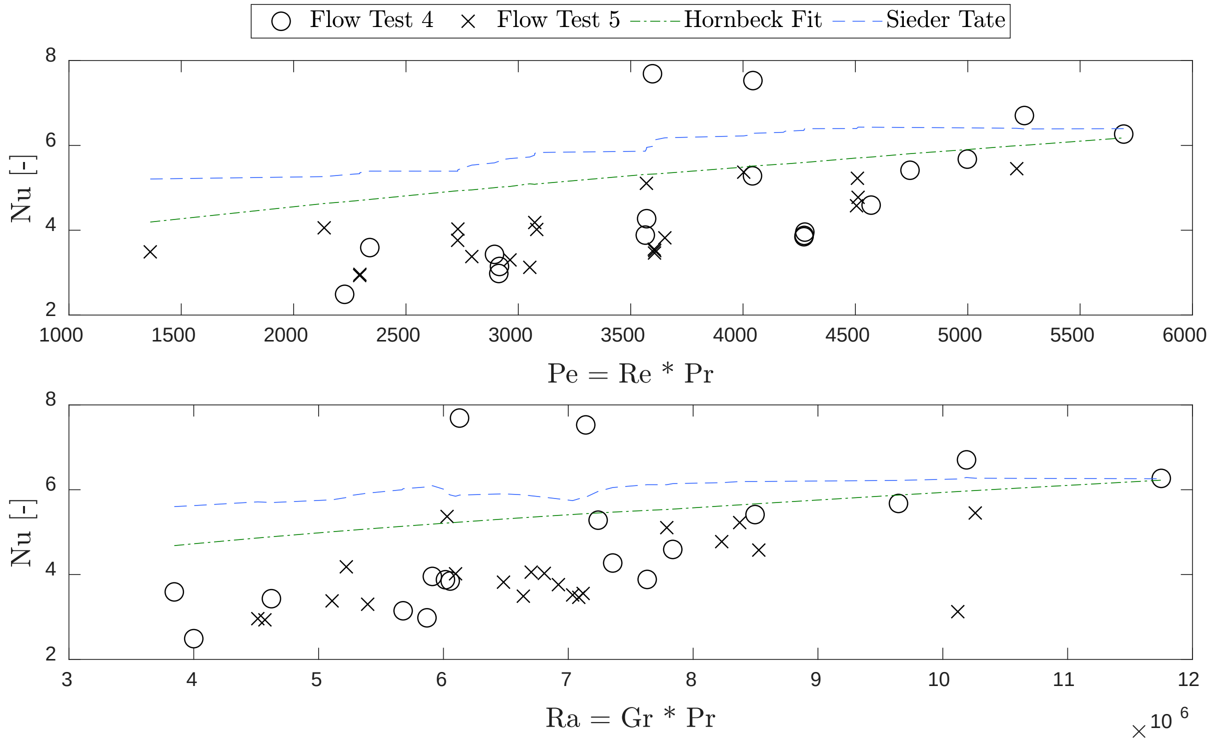

Fig. 79 Heat transfer data and correlations in the top-cross for Flow Test 4 and Flow Test 5.

The more extreme deviation at low Pe and Ra is due to these tests also being low-temperature tests because of the strongly temperature dependent viscosity. It is likely that thicker freezing layers in these tests are not adequately accounted for, causing the deviation. Both Flow Test 4 and Flow Test 5 data agree with each other, although Flow Test 5 appears to have more spread in its data.

On the hot side, the heat transfer correlations are calculated from the temperature difference across each heater and the heater hot-face temperature. The tube wall temperature is measured under Heater 4, and the difference between Heater 4 hot-face and the tube wall is assumed constant for all the heaters, since they operate at the same power levels. This is then used to calculate the wall temperatures and the heat transfer coefficients, plotted in Fig. 80.

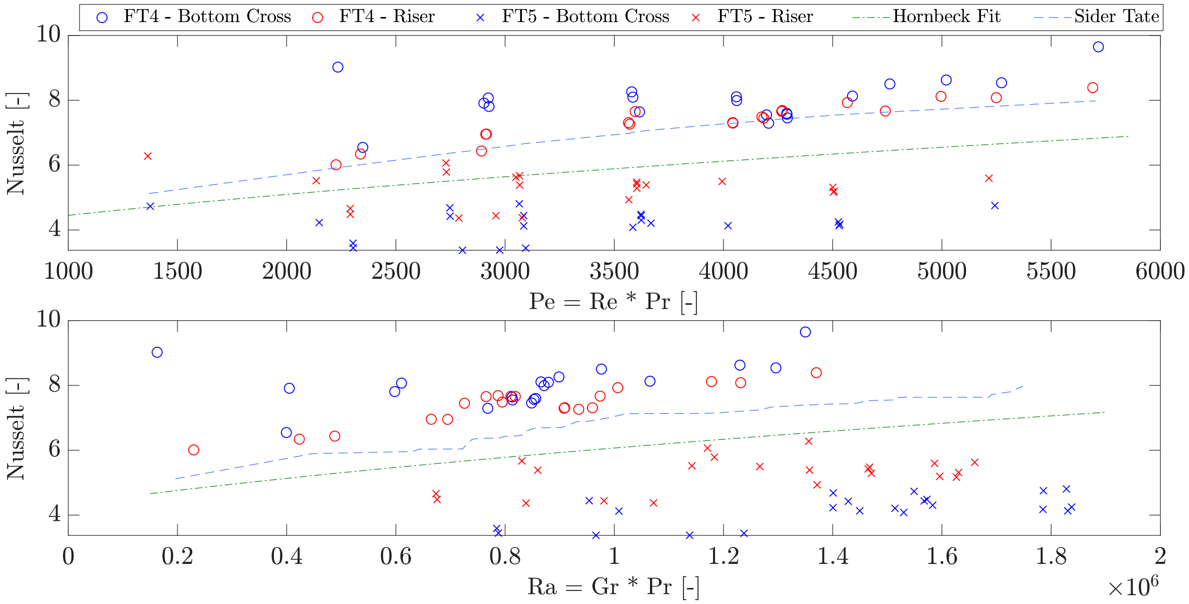

Fig. 80 Heat transfer data and correlations in the bottom-cross and riser for Flow Test 4 and 5.

Here, heat transfer data is better predicted by the Rayleigh number than the Peclet and the Nusselt data shows a striking divide between Flow Test 4 and Flow Test 5. Flow Test 4 data is under-predicted by correlation and the bottom-cross shows the heat transfer enhancement relative to the riser, due to horizontal flow. This spread is particularly noticeable at low Peclet numbers, where the low-flow rates do not suppress recirculation cells within the bottom-cross. Flow Test 5 data is over-predicted by the correlations and the bottom-cross shows reduced heat-transfer relative to the riser. This data also shows dramatic differences in Rayleigh numbers in the bottom-cross and riser for the same operating conditions.

There is no clear explanation for this divide, although the strong impact on heat transfer in the bottom-cross and the previously mentioned increased stability shown on Fiber D, lead to the assumption that the salt viscosity either increased between tests or became at least became less temperature sensitive. A small amount of beryllium metal was added to the dump-tank before Flow Test 4 to reduce corrosion, but the ppm-level addition should not impact the salt properties measurably and should modify both tests relative to Flow Test 3.

One possible factor is an increase in oxygen content in the salt. Between Flow Test 4 and 5, the protective capillary around Fiber G capillary was replaced. To do this, work was performed inside glove-bags, to prevent beryllium release and attempt to maintain an argon atmosphere. However, the negative system pressure would have pulled oxygen in from any leaks in the bags; rather than expel potentially beryllium containing argon. The long capillary took significantly longer to replace than was anticipated, and the argon atmosphere in the glovebags was not monitored closely. Unfortunately, there is insufficient evidence that oxides could cause a viscosity increase. Another possible effect would be a change in the flow path, perhaps from plate-out of metal impurities on the tube walls. This could impact the flow rate and heat-transfer properties. At this time however, there is no clear trend in velocity data to indicate flow-losses have changed in the loop.

Future Work

To examine heat transfer discrepancies, Flow Test 6 is currently underway. This test is rerunning several conditions from previous Flow Tests to provide a direct comparison. A more comprehensive set of velocity pulses is also being gathered for a sensitivity study on the thermal-pulse method. Upon conclusion of Flow Test 6, the salt will be saved for chemical and property analysis while the loop will be filled using a clean batch of FLiBe to rerun several tests.

Additional work includes running several frequency response tests run in collaboration with UC Berkeley based off the results of the current tests. It is hoped that these tests can provide insight to the heat-transfer and flow characteristics, similar to work performed using CIET. A set of salt chemistry tests are also scheduled to run in-situ using the electrochemical probes in the large and small tanks. Analysis of the fresh salt in the loop will provide valuable insight to the corrosion mechanisms that will be studied in the next phase of testing.

Once enough thermal hydraulic data is available for analysis, the material testing campaigns will begin. To perform these tests, several fiber-sensors must be removed and a clean batch of salt produced for the tests. Currently, this test is scheduled to examine corrosion of the high-carbon variant of 316 stainless steel, 316H. The samples have been procured and await polishing and reference analysis.

6. In-Reactor FHR Materials Corrosion Testing (MIT)

In-reactor corrosion tests of 316 stainless steel and Hastelloy N® in molten FLiBe were carried out in the MITR, a 6 MW, light water-cooled, heavy water-reflected tank-type, nuclear research reactor at the MIT Nuclear Reactor Laboratory (MIT-NRL). Materials were exposed to ^{7}Li enriched FLiBe [58]. A specially designed capsule was needed. An S-bend shape titanium thimble and an outer nickel capsule were designed to hold the graphite corrosion capsule [59]. The temperature for corrosion experiments was achieved by utilizing the gamma heating of high-Z materials, which was mainly controlled by reactor power and capsule design. Temperature control (700±3°C) was achieved by adjusting the gas mixture in the gap between nickel capsule and thimble. More details about the in-reactor corrosion tests are described in references [59].

After finishing the 1000-hour test in MIT reactor, the S-shape thimble was transferred into a hot cell, and then the corrosion assembly was disassembled in the hot cell as it cooled down. The cylindrical graphite crucible was transferred into a specially designed glove box for re-melting salt. Alloy samples were pulled out and cleaned in deionized water for 24 hours. Fig. 81 depicts samples tested both in-reactor and out-of-reactor following exposure to ^{7}Li enriched FLiBe salt at 700˚C for 1000 hours. Samples were exposed in both metal-lined crucibles and graphite crucibles. The photos of post-irradiation samples were captured by using a remote-controlled optical microscope due to the high radioactivity from activation products, primarily ^{58}Co and ^{60}Co [58].

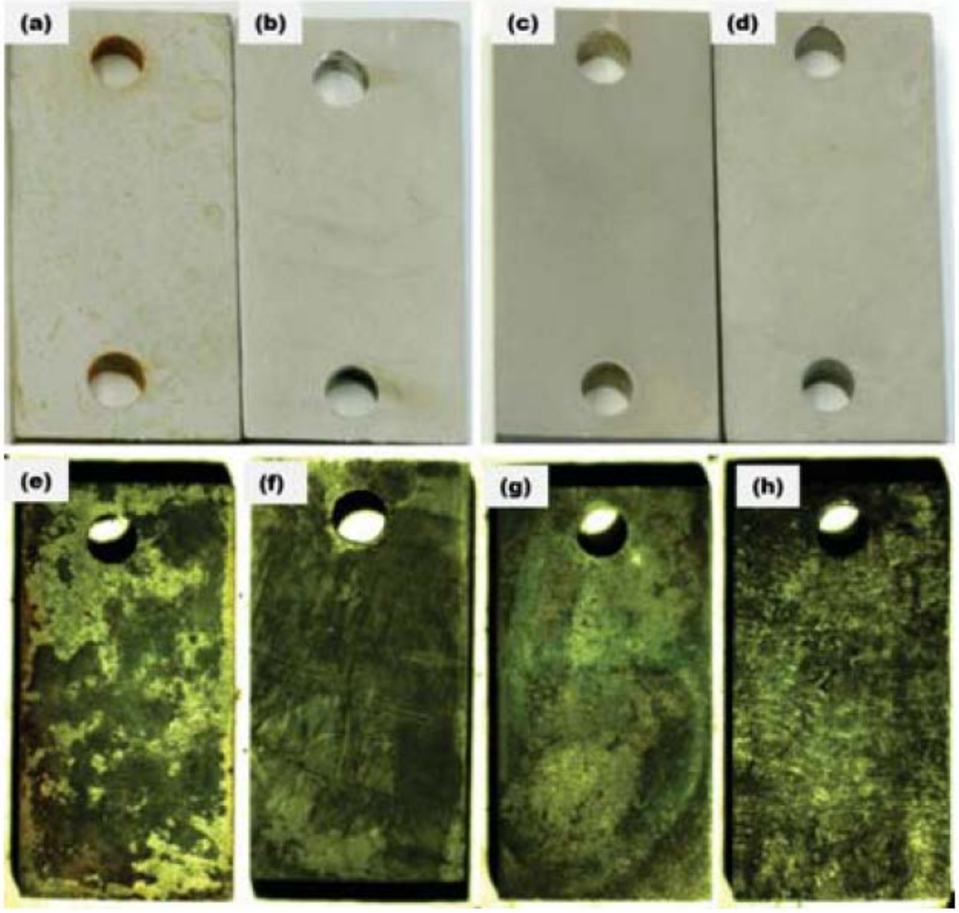

Fig. 81 Out-of-reactor corrosion tested samples: (a) 316L stainless steel in graphite crucible, (b) 316L stainless steel in 316 stainless steel crucible, (c) Hastelloy N® in graphite crucible, and (d) Hastelloy N® in nickel crucible; and in-reactor corrosion tested samples: (e) 316L stainless steel in graphite crucible, (f) 316L stainless steel in 316 stainless steel crucible, (g) Hastelloy N® in graphite crucible, and (h) Hastelloy N® in nickel crucible, in molten FLiBe salt for 1000 hours [58].

The weight change per unit area of the out-of-reactor and in-reactor corrosion tested 316L stainless steel and Hastelloy N® in molten FLiBe at 700°C for 1000 hours is shown in Fig. 82. The samples tested in a graphite crucible lost more weight than ones tested in a metal-lined crucible, and the samples tested in-reactor in the same salt conditions lost more weight than out-of-reactor tested samples. The neutron radiation results in approximately 10 times more weight loss for the 316L stainless steel samples in graphite crucible, and approximately 5 times more weight loss for the samples in 316 stainless steel lined crucible. Radiation also causes about 2 times more weight loss for the Hastelloy N® in nickel lined crucible [58]. The weight gain for the out-of-reactor tested Hastelloy N® in a graphite crucible results of the carbide phase formation due to the infusion of carbon from graphite into the alloy via the molten salt medium [60].

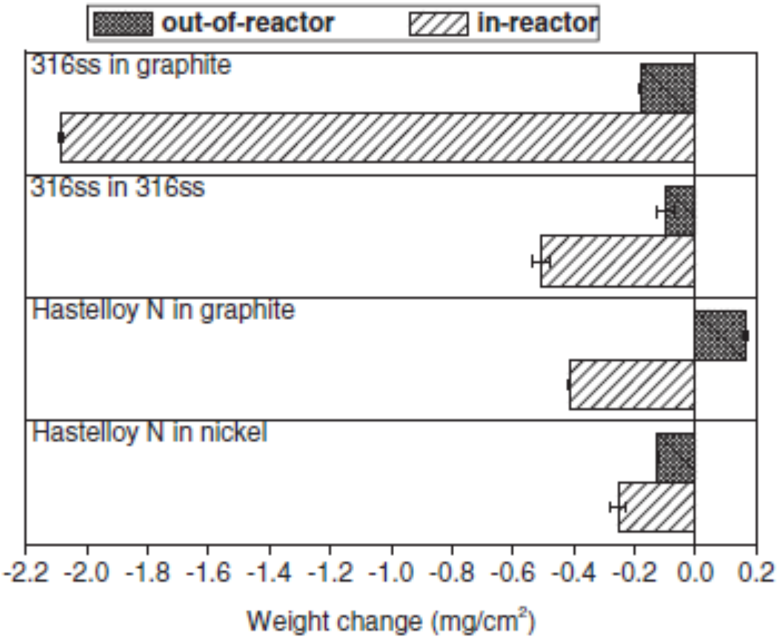

Fig. 82 Weight change of the 316L stainless steel and Hastelloy N® coupons in out-of-reactor and in-reactor corrosion tests in molten FLiBe salt at 700°C for 1000 hours [58].

The surface images of the out-of-reactor corrosion tested samples are shown in Fig. 83. The corrosion attack to these samples is evident by presenting various microstructural features for different alloys in different corrosion crucibles. Fig. 83(a, b) clearly presents the intergranular corrosion in addition to some corrosion attack on the grains. The surface grain boundaries of the 316L stainless steel tested in graphite crucible were attacked deeper than those tested in 316 stainless steel lined crucible. This further suggests the acceleration effect by the presence of graphite in molten salt, consistent with the trends of weight loss measurements shown in Fig. 83. The surface of the Hastelloy N® samples also shows conclusive evidences of corrosion attack. As shown in Fig. 83(c), many carbides particles formed and adhered on the alloy surface, resulting from the chemical reactions of the carbon liberated from graphite with the Cr and Mo in the alloy. These particles were identified as Cr3C2, Cr7C3, Mo2C by XRD analysis [60]. Without graphite in the molten salt, as shown in Fig. 83(d), the initially polished surface exhibited an increase in surface roughness and developed a porous structure layer on surface. The dissolution of alloying elements, most likely Cr, from the alloy into the molten salt resulted in the porous surface. We will conduct the same microstructural observation under SEM for all in-reactor corrosion tested samples to study neutron radiation effects on the corrosion [58].

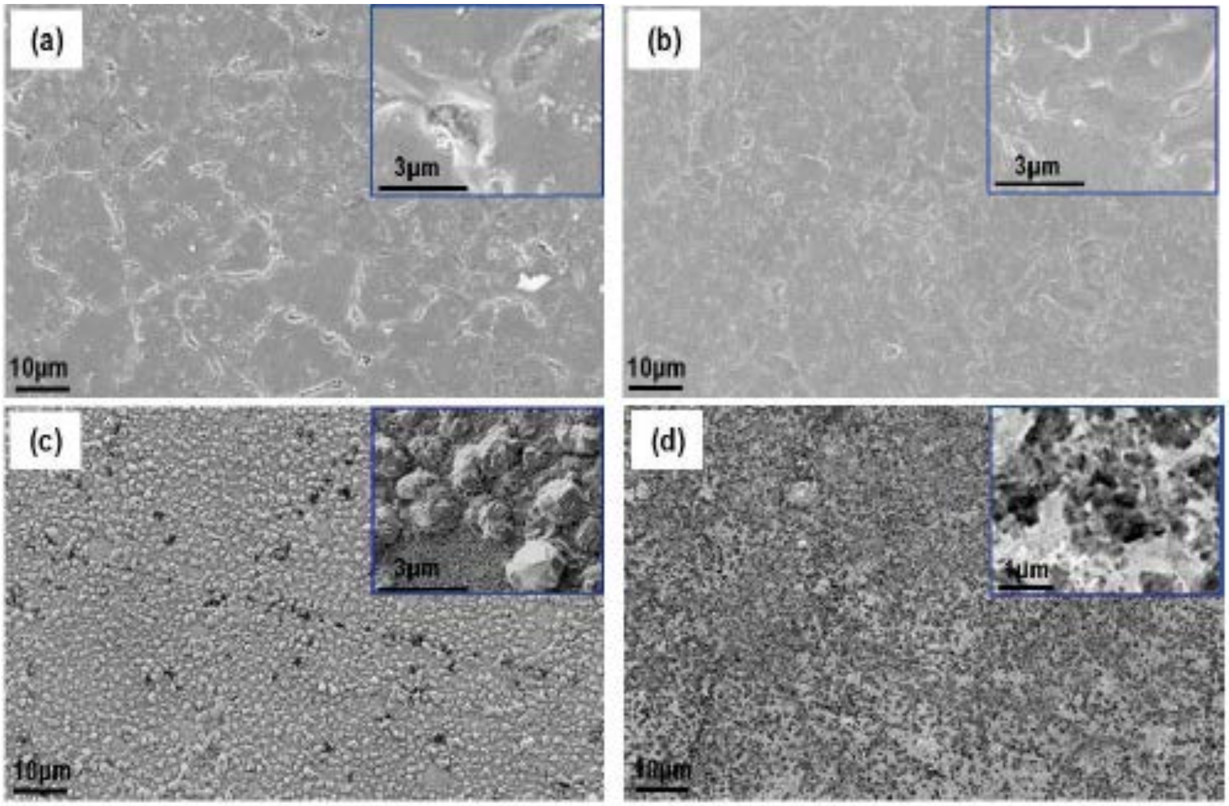

Fig. 83 SEM images of the corrosion surface of (a) 316L stainless steel tested in graphite crucible, (b) 316L stainless steel tested in 316 stainless steel crucible, (c) Hastelloy N® tested in graphite crucible, and (d) Hastelloy N® tested in nickel crucible after out-of-reactor corrosion tests in molten FLiBe for 1000 hours. The inset in each SEM image shows a local microstructure with high magnification [58].

References

[1] J. W. Koger, "Effect of FeF2 Addition on Mass Transfer in a Hastelloy N - LiF-BeF2-UF4 Thermal Convection Loop System," Oak Ridge National Laboratory, Metals and Ceramics Division, ORNL-TM-4188, Dec. 1972.

[2] R. E. Thoma, "Chemical Aspects of MSRE Operations - ORNL - 4658." Oak Ridge National Lab, Tenn, 1971.

[3] B. C. Kelleher, "Purification and Chemical Control of Molten Li2-BeF4 for a Fluoride Salt Cooled Reactor," PhD, University of Wisconsin - Madison, 2015.

[4] G. Zheng, "Corrosion Behavior of Alloys in Molten Fluoride Salts," ProQuest Dissertations Publishing, 2015.

[5] T. Chrobak, "Corrosion of Candidate Materials in Molten FLiBe Salt for Application in Fluoride-salt Cooled Reactors," Thesis, University of Wisconsin - Madison, Madison, WI, 2018.

[6] W. H. Doniger, T. Chrobak, K. Dolan, K. Britsch, A. Couet, and K. Sridharan, "Corrosion and Redox Condition Control of Molten Li2BeF4 Salt for Molten Salt Reactors," *Proc Int. Congr. Adv. Nucl. Power Plants ICAPP*, Apr. 2018.

[7] W. H. Doniger, "Electrochemistry for Corrosion Prevention in Molten Li2BeF4 (FLiBe) Salt for Fluoride Salt-cooled Reactors," Thesis, University of Wisconsin - Madison, 2018.

[8] B. Kelleher, K. Dolan, M. Anderson, and K. Sridharan, “Observed Redox Potential Range of Li 2 BeF 4 Using a Dynamic Reference Electrode,” *Nucl. Technol.*, vol. 195, no. 3, pp. 239–252, 2016.

[9] K. Dolan, “Redox Potential Measurement and Control for the Fluoride-Salt-Cooled High-Temperature Reactor,” MS Thesis, Nuclear Engineering and Engineering Physics, University of Wisconsin - Madison, 2015.

[10] F. Carotti, H. Wu, and R. O. Scarlat, “Characterization of a Thermodynamic Reference Electrode for Molten LiF-BeF2 (FLiBe),” *J. Electrochem. Soc.*, vol. 164, no. 12, pp. H854–H861, Jan. 2017.

[11] B. F. Hitch and C. F. Baes Jr., “An electromotive force study of molten lithium fluoride-beryllium fluoride solutions,” *Inorg. Chem.*, vol. 8, no. 2, pp. 201–207, 1969.

[12] V. K. Afonichkin *et al.*, “Dynamic reference electrode for investigation of fluoride melts containing beryllium difluoride,” *J. Fluor. Chem.*, vol. 130, no. 1, pp. 83–88, 2009.

[13] G. Durán-Klie, D. Rodrigues, and S. Delpech, “Dynamic Reference Electrode development for redox potential measurements in fluoride molten salt at high temperature,” *Electrochimica Acta*, vol. 195, pp. 19–26, Mar. 2016.

[14] C. M. Blood, “Solubility and stability of structural metal difluorides in molten fluoride mixtures - ORNL-TM--760.” Oak Ridge National Lab, TennUSA, 1964.

[15] T. Berzins and P. Delahay, “Oscillographic Polarographic Waves for the Reversible Deposition of Metals on Solid Electrodes,” *J. Am. Chem. Soc.*, vol. 75, no. 3, pp. 555–559, Feb. 1953.

[16] P. Delahay, *New instrumental methods in electrochemistry; theory, instrumentation, and applications to analytical and physical chemistry. With a chapter on high-frequency methods*. New York: Interscience Publishers, 1954.

[17] J.-C. Zhao, M. Larsen, and V. Ravikumar, “Phase precipitation and time-temperature-transformation diagram of Hastelloy X,” *Mater. Sci. Eng. A*, vol. 293, no. 1–2, pp. 112–119, Nov. 2000.

[18] V. Shankar, K. Bhanu Sankara Rao, and S. L. Mannan, “Microstructure and mechanical properties of Inconel 625 superalloy,” *J. Nucl. Mater.*, vol. 288, no. 2–3, pp. 222–232, Feb. 2001.

[19] Y. G. Gogotsi and R. A. Andrievski, *Materials science of carbides, nitrides and borides*. Gogotsi1998, 1998.

[20] A. Paul, J. Lim, K. Choi, and C. Lee, “Effects of deposition parameters on the properties of chromium carbide coatings deposited onto steel by sputtering,” *Mater. Sci. Eng. A*, vol. 332, no. 1–2, pp. 123–128, Jul. 2002.

[21] S. Gomari and S. Sharafi, “Microstructural characterization of nanocrystalline chromium carbides synthesized by high energy ball milling,” *J. Alloys Compd.*, vol. 490, no. 1–2, pp. 26–30, Feb. 2010.

[22] A. Zikin, I. Hussainova, C. Katsich, E. Badisch, and C. Tomastik, “Advanced chromium carbide-based hardfacings,” *Surf. Coat. Technol.*, vol. 206, no. 19–20, pp. 4270–4278, May 2012.

[23] H. Wang, Z. Wang, and S. Chen, “Preparation of molybdenum carbides with multiple morphologies using surfactants as carbon sources,” *J. Solid State Chem.*, vol. 194, pp. 19–22, Oct. 2012.

[24] P. Xiao, Y. Yan, X. Ge, Z. Liu, J.-Y. Wang, and X. Wang, “Investigation of molybdenum carbide nano-rod as an efficient and durable electrocatalyst for hydrogen evolution in acidic and alkaline media,” *Appl. Catal. B Environ.*, vol. 154–155, pp. 232–237, Jul. 2014.

[25] F.-Y. Ouyang, C.-H. Chang, and J.-J. Kai, “Long-term corrosion behaviors of Hastelloy-N and Hastelloy-B3 in moisture-containing molten FLiNaK salt environments,” *J. Nucl. Mater.*, vol. 446, no. 1–3, pp. 81–89, Mar. 2014.

[26] F.-Y. Ouyang, C.-H. Chang, B.-C. You, T.-K. Yeh, and J.-J. Kai, “Effect of moisture on corrosion of Ni-based alloys in molten alkali fluoride FLiNaK salt environments,” *J. Nucl. Mater.*, vol. 437, no. 1–3, pp. 201–207, Jun. 2013.

[27] S. P. Murarka, M. S. Anand, and R. P. Agarwala, “Diffusion of Chromium in Nickel,” *J. Appl. Phys.*, vol. 35, no. 4, p. 1339, 1964.

[28] B. S. Berry, "Diffusion of carbon in nickel," *J. Appl. Phys.*, vol. 44, no. 8, p. 3792, 1973.

[29] J. D. Tucker, R. Najafabadi, T. R. Allen, and D. Morgan, "Ab initio-based diffusion theory and tracer diffusion in Ni–Cr and Ni–Fe alloys," *J. Nucl. Mater.*, vol. 405, no. 3, pp. 216–234, Oct. 2010.

[30] A. F. Smith, "The Diffusion of Chromium in Type 316 Stainless Steel," *Met. Sci.*, vol. 9, no. 1, pp. 375–378, Jan. 1975.

[31] R. Braun and M. Feller-Kniepmeier, "Diffusion of chromium in α-iron," *Phys. Status Solidi A*, vol. 90, no. 2, pp. 553–561, Aug. 1985.

[32] J. R. Keiser, "Compatibility studies of potential molten-salt breeder reactor materials in molten fluoride salts, ORNL-TM-5783," 1977.

[33] L. C. Olson, J. W. Ambrosek, K. Sridharan, M. H. Anderson, and T. R. Allen, "Materials corrosion in molten LiF-NaF-KF salt," *J. Fluor. Chem.*, vol. 130, no. 1, pp. 67–73, Jan. 2009.

[34] A. Das, P. C. Chakraborti, S. Tarafder, and H. K. D. H. Bhadeshia, "Analysis of deformation induced martensitic transformation in stainless steels," *Mater. Sci. Technol.*, vol. 27, no. 1, pp. 366–370, Jan. 2011.

[35] B. R. Kumar, A. K. Singh, B. Mahato, P. K. De, N. R. Bandyopadhyay, and D. K. Bhattacharya, "Deformation-induced transformation textures in metastable austenitic stainless steel," *Mater. Sci. Eng. A*, vol. 429, no. 1–2, pp. 205–211, Aug. 2006.

[36] T. Y. Xing, X. W. Cui, W. X. Chen, and R. S. Yang, "Synthesis of porous chromium carbides by carburization," *Mater. Chem. Phys.*, vol. 128, no. 1–2, pp. 181–186, Jul. 2011.

[37] H. U. Hong, B. S. Rho, and S. W. Nam, "Correlation of the M23C6 precipitation morphology with grain boundary characteristics in austenitic stainless steel," *Mater. Sci. Eng. A*, vol. 318, pp. 285–292, 2001.

[38] H. U. Hong and S. W. Nam, "The occurrence of grain boundary serration and its effect on the M23C6 carbide characteristics in an AISI 316 stainless steel," *Mater. Sci. Eng. A*, vol. 332, pp. 255–261, 2002.

[39] R. Jones, V. Randle, and G. Owen, "Carbide precipitation and grain boundary plane selection in overaged type 316 austenitic stainless steel," *Mater. Sci. Eng. A*, vol. 496, no. 1–2, pp. 256–261, Nov. 2008.

[40] G. Zheng, B. Kelleher, G. Cao, M. Anderson, T. Allen, and K. Sridharan, "Corrosion of 316 Stainless Steel in High Temperature Molten Li2BeF4 (FLiBe) Salt," *J. Nucl. Mater.*, vol. 461, pp. 143–150, 2015.

[41] L. S. Richardson, D. E. Vreeland, and W. D. Manly, "Corrosion by molten fluorides, ORNL-1491," 1953.

[42] J. W. Koger, "Evaluation of Hastelloy N alloys after nine years exposure to both a molten fluoride salt and air at temperatures from 700 to 560C, ORNL-TM-4189," 1972.

[43] P. J. Maziasz, "Overview of microstructural evolution in neutron-irradiated austenitic stainless steels," *J. Nucl. Mater.*, vol. 205, pp. 118–145, 1993.

[44] E. A. Kenik and J. T. Busby, "Radiation-induced degradation of stainless steel light water reactor internals," *Mater. Sci. Eng. R Rep.*, vol. 73, no. 7–8, pp. 67–83, Jul. 2012.

[45] J. R. Keiser, J. H. DeVan, and J. Lawrence, "Compatibility of Molten Salts With Type 316 Stainles Steel and Lithium," *J. Nucl. Mater.*, vol. 85 & 86, pp. 295–298, 1979.

[46] J. L. King, H. Jo, R. Tirawat, K. Blomstrand, and K. Sridharan, "Effects of Surface Roughness, Oxidation, and Temperature on the Emissivity of Reactor Pressure Vessel Alloys," *Nucl. Technol.*, vol. 200, no. 1, 2017.

[47] G. M. Adamson, R. S. Crouse, and W. D. Manly, "Interim Report on Corrosion By Zirconium-Base Fluorides: Work to May 1, 1953," Oak Ridge National Laboratory, Tennessee, ORNL-2337, May 1953.

[48] G. M. Adamson, R. S. Crouse, and W. D. Manly, "Interim Report on Corrosion By Zirconium-Base Fluorides," Oak Ridge National Laboratory, Tennessee, ORNL-2338, Jan. 1961.

[49] J. W. Koger, “Alloy Compatibility with LiF-BeF2 Salts Containing ThF4 and UF4,” Oak Ridge National Laboratory, Oak Ridge National Laboratory, Oak Ridge, Tennessee, ORNL-TM-4286, 1972.

[50] J. R. Keiser, J. H. DeVan, and J. Lawrence, “Compatibility of Molten Salts With Type 316 Stainles Steel and Lithium,” *J. Nucl. Mater.*, vol. 85 & 86, pp. 295–298, 1979.

[51] W. D. Manly, J. W. Allen, J. H. DeVan, W. H. Cook, and D. A. Douglas, “Construction Materials for Molten-Salt Reactors,” in *Fluid Fuel Reactors*, 1st ed., H. G. MacPherson, Ed. Reading, MA: Addison-Wesley Pub. Co., 1958, pp. 595–626.

[52] J. R. Keiser, J. H. DeVan, and D. L. Manning, “Corrosion Resistance of Type 316 Stainless Steel to FLiBe,” Oak Ridge National Laboratory, Oak Ridge, TN, Technical Report ORNL/TM-5782, Apr. 1977.

[53] C. Andreades *et al.*, “Technical Description of the ‘Mark 1’ Pebble-Bed Fluoride-Salt-Cooled High-Temperature Reactor Power Plant,” University of California, Berkeley, Berkeley CA, Technical Report UCBTH-14-002, Sep. 2014.

[54] M. D. Silverman, W. R. Huntley, and H. E. Roberstson, “Heat Transfer measurements in a Forced Convetion Loop with two Molten-Fluoride Salts: LiF-BeF2 - ThF2-UF4 and Eutectic NaBF4-NaF,” Oak Ridge National Laboratory, Oak Ridge, TN, Technical Report ORNL/TM-5335, Oct. 1976.

[55] M. Weathered T. and M. H. Anderson, “Development of Optical Fiber Sensors for use in Sodium Cooled Reactor Instrumentation,” in *Transactions of the American Nuclear Society*, 2014, vol. 111, p. 4.

[56] M. T. Weathered and M. H. Anderson, “On the Development of a Robust Optical Fiber-Based Level Sensor,” *IEEE Sens. J.*, vol. 18, no. 2, pp. 583–588, Jan. 2018.

[57] G. Nellis and S. Klein, *Heat transfer*, 1st ed. New York, NY: Cambridge University Press, 2010.

[58] G. Zheng, D. Carpenter, L.-W. Hu, and K. Sridharan, “High Temperature Corrosion of Structural Alloys in Molten Li2BeF4 (FLiBe) Salt,” in *Advances in Materials Science for Environmental and Energy Technologies V*, Wiley-Blackwell, 2016, pp. 93–101.

[59] D. Carpenter, M. Ames, G. Kohse, Y. Ostrovsky, and L.-W. Hu, “Fluoride salt high-temperature reactor materials irradiation test at the MIT research reactor,” *Proc Int. Congr. Adv. Nucl. Power Plants ICAPP*, vol. 1, pp. 375–384.

[60] G. Zheng *et al.*, “High-Temperature Corrosion of UNS N10003 in Molten Li sub(2)BeF sub(4) (FLiBe) Salt,” *Corros. Houst.*, vol. 71, no. 10, pp. 1257–1266, 2015.

Thesis submitted to UW-Madison

B. C. Kelleher, “Purification and Chemical Control of Molten Li2-BeF4 for a Fluoride Salt Cooled Reactor,” PhD, University of Wisconsin - Madison, 2015.

G. Zheng, “Corrosion Behavior of Alloys in Molten Fluoride Salts,” ProQuest Dissertations Publishing, 2015.

Chrobak, T.J. (2018), Corrosion of Candidate Materials in Molten FLiBe Salt for Application in Fluoride-salt Cooled Reactors (Master’s thesis).

K. Dolan, “Redox Potential Measurement and Control for the Fluoride-Salt-Cooled High-Temperature Reactor,” MS Thesis, Nuclear Engineering and Engineering Physics, University of Wisconsin - Madison, 2015.

W. H. Doniger, “Electrochemistry for Corrosion Prevention in Molten Li2BeF4 (FLiBe) Salt for Fluoride Salt-cooled Reactors,” Thesis, University of Wisconsin - Madison, 2018.

3.2. In-Reactor Corrosion Testing (MIT)[11]

---

[11] D. Carpenter

Summary

The MIT nuclear reactor laboratory (NRL) designed its first three in-core FHR irradiations to duplicate the conditions of the autoclave testing conducted by UW. The graphite holder, salt, and specimens were produced from the same batches of materials to matching dimensions. This is intended to give as direct a comparison as possible to help identify those corrosion effects that are affected by the presence of neutron and gamma irradiation, or how materials' susceptibility to corrosion is changed by accumulated radiation damage. The three MITR in-core irradiations (FS-1, -2, and -3) exposed various graphite, carbon fiber, SS316, Hastelloy, SiC, and SiC composite materials to enriched static flibe at 700°C for 300-1000 hours. After irradiation the specimens were extracted from the salt and analyzed for weight and dimensional changes, as well as microstructural characterization. The unique effects of irradiation (in particular activation/transmutation and generation and adsorption of tritium) added a further complexity to the handling and analysis of these samples. Using facilities at MIT and Idaho National Laboratory, information of the changes to the surface microstructure of the specimens was analyzed. For graphite specimens, frozen salt on samples' surface displays various crystalline shapes, including needle, dendrite, plate, petal, and nuggets. Some hexagonal and snow-like crystals were observed on surfaces cleaned with DI water. These crystals have relatively high concentration of Fe, Ti, Cr, O and F, which are probably associated with the impurities in molten salt. Fractional oxides also formed on the edges of the pores of the cleaned graphite and C/C composite samples. Compared to out-of-reactor specimens, nano-sized carbide particles were not found in the near-surface layer of in-core corrosion samples, possibly due to the presence of tritium. A large number of line dislocation and dislocation loops, evidence of neutron irradiation-induced structural damage, were observed in grains and near to grain boundaries in metal specimens. The precipitates in the alloys probably inhibit the movement of the line dislocations.

Contents

Introduction

The FHR core presents a complex environment encompassing a range of important variables such as neutron and gamma flux, high temperature, and material couplings. The simultaneous interactions of irradiation, temperature, chemistry, and materials microstructure will have important consequences to the design and operation of FHRs. Structure and fuel mechanical and thermal performance, tritium, fission product, and activation product generation and transport, corrosion and radiolysis product generation and transport, and salt uptake by materials may all be affected by these interactions. The MIT NRL designed and conducted a series of integrated irradiation tests to begin the study of these effects and help to identify important contributions of radiation to FHR research and development activities. Because of the lack of modern research in this area (these represent the first irradiations of flibe at high temperature since the MSRE in the 1960s), a series of incremental experiments were conducted to help understand the salt behavior and build best practices for irradiation experiment design and operation. The irradiations in the MITR were also deigned to parallel simultaneous autoclave testing being conducted at the University of Wisconsin in order to isolate irradiation-related effects. The first two in-core irradiations (FS-1 and FS-2) were designed and conducted as part of the first FHR IRP project. In this work, a third experiment, expanding on the capabilities gained from the first two tests, was designed and operated for nearly 1000 hours in the MITR core.

1. Experiment Design

The details of the first two NRL irradiation experiments have been published previously, but are summarized here. In 2013 the first in-reactor irradiation of flibe since the MSRE took place in the MIT Research Reactor's (MITR) inert gas irradiation facility using enriched flibe from the MSRE secondary coolant loop. [1] The MITR is a 6 MW light water-cooled, heavy-water reflected research reactor with in-core positions for flow loops and instrumented experiments. The neutron spectrum in the experiment position is similar to the typical light water reactor, and helium/neon gas control allows nuclear heating to be used to reach the desired temperature. This 1000-hour initial exploratory test at 700°C was followed by a second, larger static capsule irradiation in a purpose-built facility with more than double the volume of flibe. [2]

The goal of these experiments was to develop the engineering knowledge of working with irradiated flibe at the typical FHR temperatures, measure corrosion of possible FHR materials in flibe, and test methods for measuring tritium release during the irradiation. In both experiments the flibe and corrosion specimens were in graphite crucibles with a primary nickel encapsulation (the capsule) and secondary titanium encapsulation (the thimble). Both volumes were swept with a low (100 cc/min) flow of inert gas fed into a tritium detection and capture system (Figure 19). These experiments demonstrated that only a small fraction of the tritium predicted to be generated during irradiation was detectable in the facility off-gas. At the time it was predicted that the balance of the tritium was being adsorbed onto the surfaces within the irradiation capsule and facility tubing, diffused into and trapped within the structures at high temperature, or retained within the flibe itself.

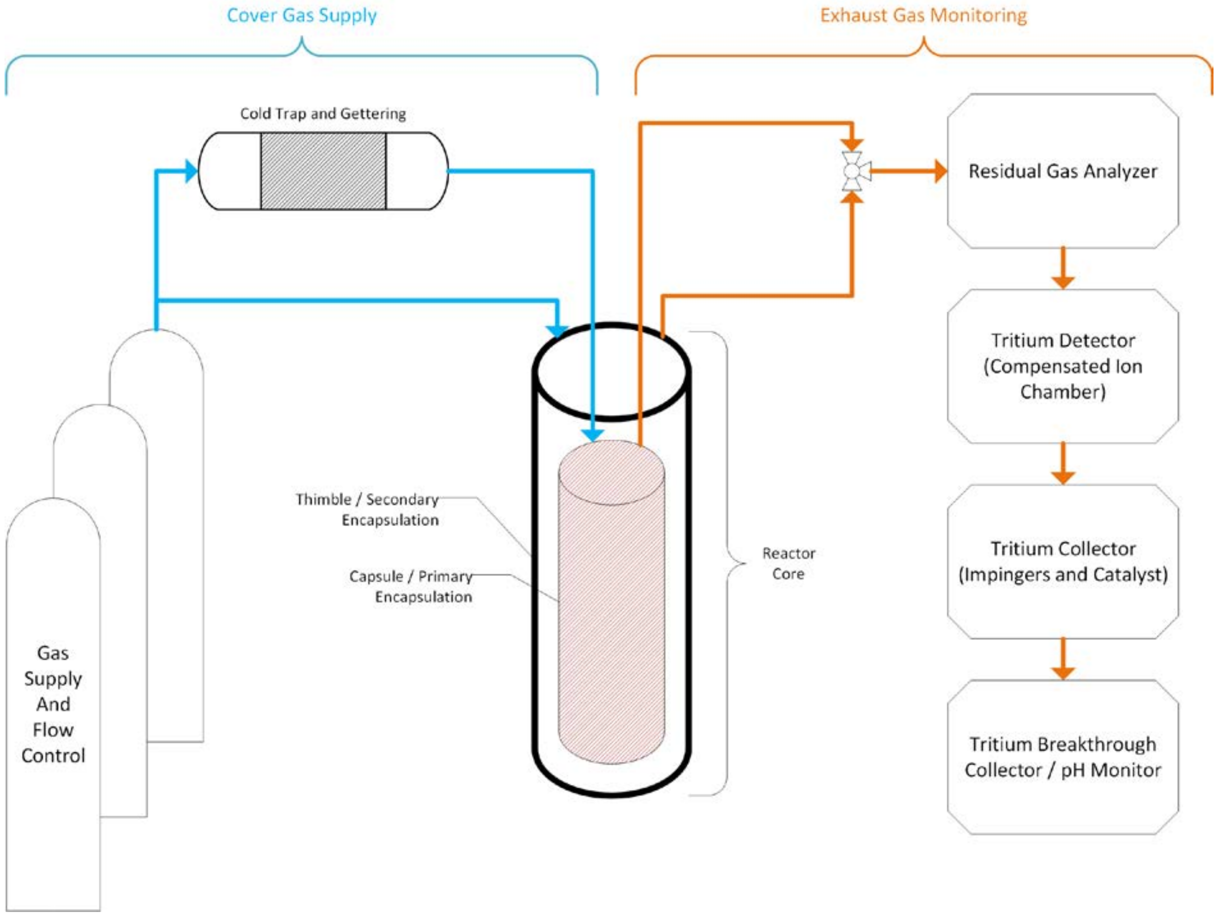

Figure 19. Schematic of irradiation gas flow and tritium capture system for the MITR flibe irradiations.

In-situ Electrical Heating

The FS-3 was designed to include a new in-core electrical heater to provide heat input when reactor power is low. This cartridge-style heater, located along the centerline of the capsule, was intended to maintain a minimum salt temperature above 200°C, suppressing the generation of free fluorine and other fluorides in the capsule gas system, especially while under gamma exposure before reactor startup. Cold frozen salt under irradiation can generate free fluorine. This does not happen at higher temperatures because of the rapid recombination of any free fluorine in the salt at higher temperatures. This guard heater is automatically operated with a PID controller that monitors the capsule temperature. As temperature begins to decrease below the expected set point due to a change in reactor power, first the cover gas mixture is adjusted by adding additional neon. If this is insufficient, then below a certain threshold electrical heating is used to maintain the minimum temperature.

This configuration maintained very low levels of fluoride products in the capsule off-gas, thereby protecting the sensitive downstream components. It should be noted that even though the FS-1 and FS-2 experiments, which operated for 1000 and 300 hours, respectively, did not have such a guard heater system and also operated for extended periods at low temperature, no damage was observed to the inside of the capsule or the gas system metal tubing due to chemical attack. Therefore operation of the experiment in the low temperature regime is still possible if other methods of protecting sensitive out-of-core components are in place.

Fluoride Scrubbing

Two straightforward methods are effective at removing the fluorides from the gas system – a dry catalyst bed (e.g. alumina beads) and sparging through water. Either method can be employed on the gas letdown system ahead of the regulators and sensitive instrumentation in combination with particulate filters (glass and activated charcoal). The downside of a scrubber system is that it would also capture tritiated species that are of interest to the experiment, and so it is desirable to use it only in the event that capsule temperature cannot be maintained above 200°C. This would be accomplished by valves on the letdown system that would optionally direct the gas through the scrubbers.

In practice, such a system would utilize a 3-way solenoid-operated valve. During normal operation the solenoid is energized and gas flows from the in-core capsule directly to the pressure regulators and other instrumentation. If the capsule temperature drops below 200°C, the solenoid is de-energized and gas flow is directed through the fluoride scrubbers. This contingency protects the sensitive instruments, and if the electrical heating and gas mixture systems work as intended, off-gas tritium measurement will not be disrupted. In the event the electrical heating system fails or is not as effective as intended, then the irradiation can safely proceed with reduced tritium measurement performance.

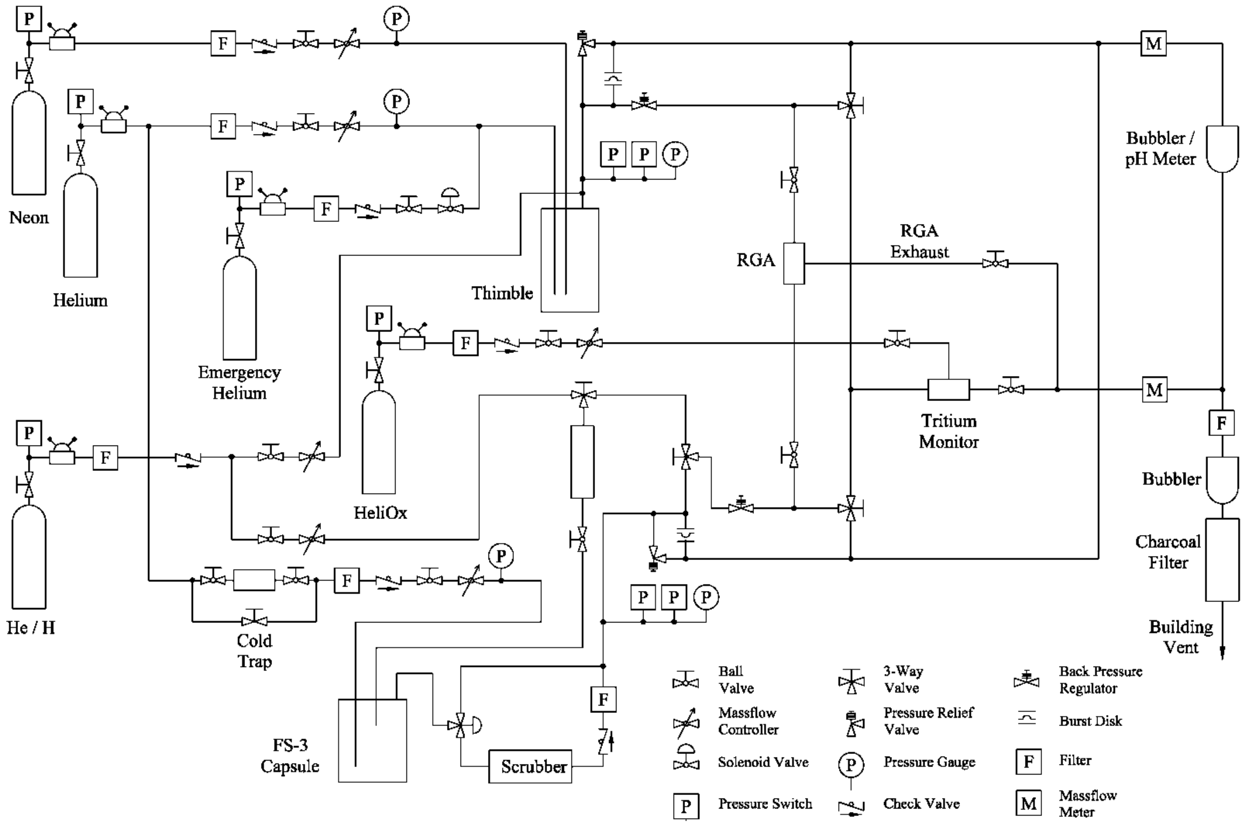

Figure 20. FS-3 gas system diagram.

2. Specimen Test Matrix

As summarized in Table 4, the samples in this investigation are graphitic materials, six different types of nuclear graphite and one type of carbon/carbon (C/C) composite. The geometry includes cylindrical shape (~16mm or ~10mm in height and ~8mm or ~10mm in diameter) and disc shape (~2mm in thickness and ~8mm in diameter). The surface conditions of these samples include polished surface and machined surface. In total, 95 samples including sacrifice samples are tested in three graphite crucibles. Each crucible has five separate compartments/holes. The mass of Li-7 enriched flibe salt in each compartment is listed in Table 4. There is one compartment without molten salt for studying only irradiation effect on the materials. One sample from each type of materials is selected to put in this no-salt compartment for comparing with the same materials tested in molten salt environment.

In addition to A3-3 (matrix) and IG-110U (structural) graphite specimens based on what was exposed in previous FS-1 and FS-2 experiments, additional specimens were supplied by the Chinese Academy of Sciences/Shanghai Institute for Applied Physics (SINAP). These include three different types of graphite manufactured in China, one commercial nuclear-grade graphite (IG-110) manufactured in Japan, and one type of C/C composite fabricated in a Chinese laboratory. Both NG-CT-10 and NG-CT-50 are composed of the same filler and binder source and utilize the same manufacturing processes. These SINAP samples are loaded into upper two graphite capsules; this subset of samples are denoted as FS-S.

Table 4. Sample matrix and the mass of flibe salt in each compartment of graphite crucible for FS-3 in-core experiments.

Flibe mass (g)	ID mark	Material	Surface condition	Thickness/height (mm)	Diameter (mm)	weight (g)
5.2	F71	NG-CT-50	as-cut	2.01	8.02	0.17730
	F77	NG-CT-50	as-cut	2.01	8.02	0.17680
	F72	NG-CT-50	as-cut	2.01	8.01	0.17740
	F78	NG-CT-50	as-cut	2.02	8.01	0.17710
	F83	NG-CT-50	polished	2.04	8.04	0.17244
	F85	NG-CT-50	polished	2.05	8.04	0.17359
	S61	NG-CT-50	as-cut	2.01	8.01	0.17750
5.2	N01	NG-CT-10	as-cut	2.02	8.00	0.18710
	N07	NG-CT-10	as-cut	2.02	8.01	0.18890
	N02	NG-CT-10	as-cut	2.02	8.00	0.18640
	N08	NG-CT-10	as-cut	2.02	8.01	0.19090
	N14	NG-CT-10	polished	2.04	8.04	0.18030
	N15	NG-CT-10	polished	2.04	8.03	0.18385
	S63	NG-CT-10	as-cut	2.02	8.02	0.19000
5.2	V01	TFX-10	as-cut	2.04	8.01	0.17940
	V07	TFX-10	as-cut	2.00	8.03	0.17600
	V02	TFX-10	as-cut	2.21	8.02	0.18810
	V08	TFX-10	as-cut	2.00	8.04	0.17690
	V13	TFX-10	polished	2.03	8.01	0.16519
	V15	TFX-10	polished	2.03	8.01	0.16564
	S65	TFX-10	as-cut	2.03	8.01	0.17460
5.2		IG-110U	as-cut	2.06	7.97	0.17829
	R27	IG-110	as-cut	2.02	8.01	0.17920
	R22	IG-110	as-cut	2.02	8.00	0.17870
	R28	IG-110	as-cut	2.01	8.00	0.17820
	R33	IG-110	polished	2.06	8.00	0.17701
	R35	IG-110	polished	2.06	8.01	0.17806
	S67	IG-110	as-cut	2.00	8.00	0.17570
5.2	X31	C/C	as-cut	2.07	7.96	0.17900
	X32	C/C	as-cut	2.08	7.99	0.18020
	X33	C/C	as-cut	2.06	7.96	0.17650
	X34	C/C	as-cut	2.07	7.96	0.17760
	X41	C/C	polished	2.06	7.99	0.17438
	X42	C/C	polished	2.06	8.04	0.17843
	S69	C/C	as-cut	2.07	7.98	0.17870

10.6	F88	NG-CT-50	as-cut	16.00	8.02	1.42740
	F93	NG-CT-50	as-cut	16.00	8.00	1.42460
	F89	NG-CT-50	as-cut	16.00	7.95	1.41180
	F94	NG-CT-50	as-cut	16.00	8.02	1.42800
	S62	NG-CT-50	as-cut	16.00	7.99	1.41740
10.6	N19	NG-CT-10	as-cut	16.02	8.01	1.49910
	N23	NG-CT-10	as-cut	16.02	8.01	1.50130
	N20	NG-CT-10	as-cut	16.02	8.02	1.49810
	N24	NG-CT-10	as-cut	16.02	8.01	1.52820
	S64	NG-CT-10	as-cut	16.02	8.01	1.51410
10.6	V18	TFX-10	as-cut	16.00	8.01	1.38360
	V23	TFX-10	as-cut	16.00	8.01	1.40360
	V19	TFX-10	as-cut	16.00	8.01	1.38490
	V24	TFX-10	as-cut	16.00	8.01	1.39700
	S66	TFX-10	as-cut	15.99	8.01	1.39900
10.6	R38	IG-110	as-cut	16.02	8.00	1.41280
	R43	IG-110	as-cut	16.00	8.00	1.41930
	R39	IG-110	as-cut	16.02	8.00	1.41340
	R44	IG-110	as-cut	16.01	8.00	1.41230
	S68	IG-110	as-cut	16.02	8.00	1.42010
10.8	X46	C/C	as-cut	10.11	10.03	1.40930
	X47	C/C	as-cut	10.11	10.05	1.41010
	X48	C/C	as-cut	10.11	10.05	1.40750
	X49	C/C	as-cut	10.12	10.02	1.42230
	S70	C/C	as-cut	10.12	10.02	1.41470
5.2	R21	IG-110	as-cut	2.02	8.00	0.17900
		IG-110U	as-cut	2.06	7.99	0.17929
		IG-110U	as-cut	2.07	7.99	0.18010
		IG-110U	as-cut	2.07	7.98	0.17956
		IG-110U	polished	2.07	7.98	0.18387
		IG-110U	polished	2.06	7.98	0.17929
		IG-110U	as-cut	2.07	7.97	0.17875
5.2		A3-3	as-cut	2.06	7.98	0.16170
		A3-3	as-cut	2.06	7.98	0.16271
		A3-3	as-cut	2.07	7.99	0.15901
		A3-3	as-cut	2.07	7.98	0.15808
		A3-3	polished	2.07	7.99	0.17520
		A3-3	polished	2.09	7.99	0.17695
		A3-3	as-cut	2.06	7.98	0.16244
5.2		IG-110U	as-cut	2.06	7.98	0.17896
		IG-110U	as-cut	2.07	7.99	0.17932
		IG-110U	as-cut	2.07	7.98	0.18033
		IG-110U	as-cut	2.07	7.98	0.17928
		IG-110U	polished	2.08	7.98	0.18257
		IG-110U	polished	2.07	7.98	0.18012
		IG-110U	as-cut	2.07	7.98	0.18057
5.2		A3-3	as-cut	2.07	7.97	0.16124
		A3-3	as-cut	2.06	7.97	0.16010

		A3-3	as-cut	2.06	7.97	0.15642
		A3-3	as-cut	2.07	7.98	0.15747
		A3-3	polished	2.03	7.99	0.16067
		A3-3	polished	2.09	7.99	0.17887
		A3-3	as-cut	2.07	7.98	0.15856
0		IG-110U	polished	2.05	7.98	0.17862
		A3-3	polished	2.10	7.99	0.18288
	F86	NG-CT-50	polished	2.05	8.04	0.17411
	N16	NG-CT-10	polished	2.04	8.04	0.18199
	V16	TFX-10	polished	2.04	8.01	0.16662
	R36	IG-110	polished	2.06	8.02	0.17560
	X43	C/C	polished	2.06	8.00	0.17499

The position of each sample listed in Table 4 is shown in Figure 21, with top and cross-section views. The design of the graphite crucibles (Figure 22, Figure 23) is intended to maximize the contact area between the salt and the specimens while maintaining stability given the specimen buoyancy in the liquid salt. The specimen at the top of each chamber may be partially above the salt free surface when the salt is liquid, and is therefore considered a “sacrificial” specimen since the extent of immersion cannon be guaranteed.

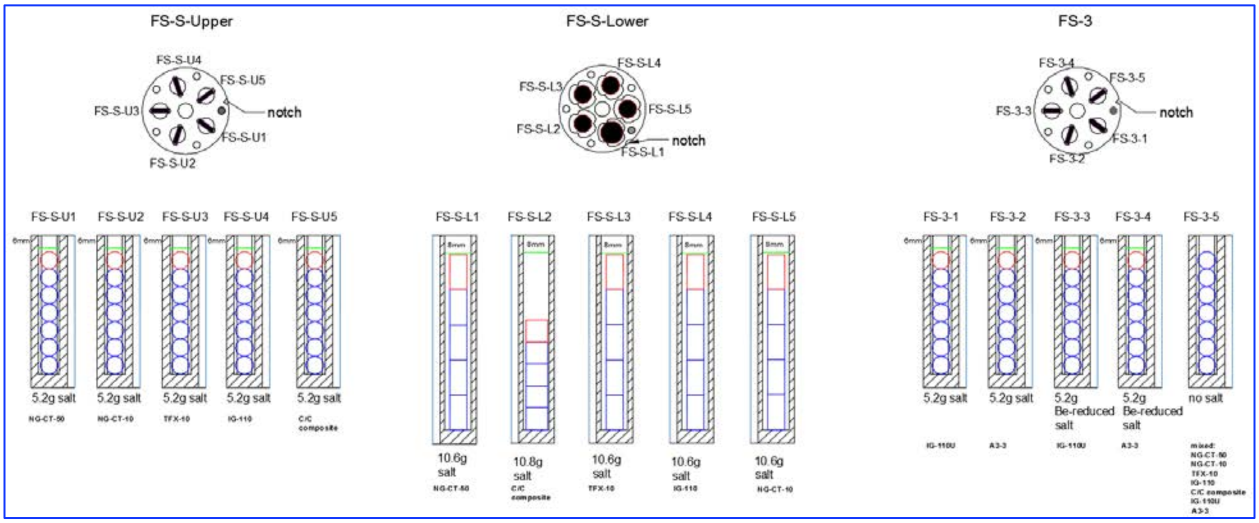

Figure 21. Top view and cross-sectional view of each compartment of graphite crucibles FS-S-upper, FS-S-lower and FS-3 showing the position of each single sample in molten salt. Green line indicates the surface level of molten flibe salt. Red color denotes the “sacrificial” specimens.

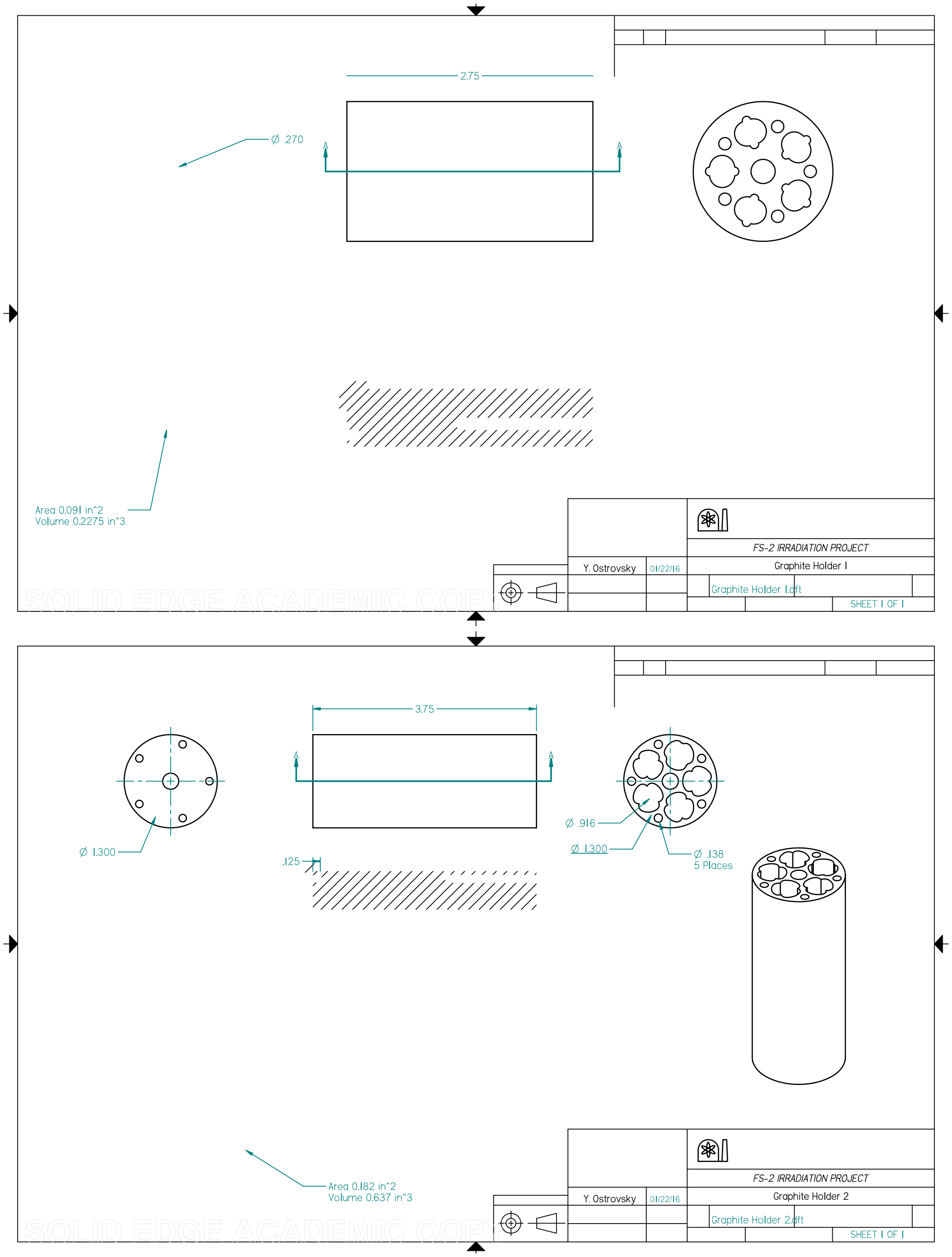

Figure 22. Drawing of FS-3 graphite crucibles for disk specimens (top) and cylindrical specimens (bottom). Seven disk specimens and five cylindrical samples are in the respective chambers.

Figure 23. Photograph of as-fabricated graphite crucibles.

As shown in Figure 24, there is a nuclear heating plate on the top of each graphite capsule and a spacer plate on the bottom. The heating plate both holds the specimens down in the salt and provides additional local heating at the top of each crucible. This creates a small thermal gradient as the reactor power is increased, helping to ensure that as the salt transitions to liquid from the upper free surface down. This prevents damage to the graphite crucible due to volume expansion during the phase change. The bottom spacer helps to reduce axial heat transfer between the crucibles, especially to prevent heating of the bottom of a crucible from the nuclear heating plate in the crucible below.

In the bottom-most crucible there is one compartment without salt, highlighted with a red ring in Figure 24. In this compartment, one of each type of disc-shaped specimen (5 from SINAP and 2 from MIT) are used as control. They are exposed to the same conditions (temperature, irradiation and gases) but without molten salt. These samples will be used as references to investigate the effect of direct contact with molten salt on microstructure and tritium uptake.

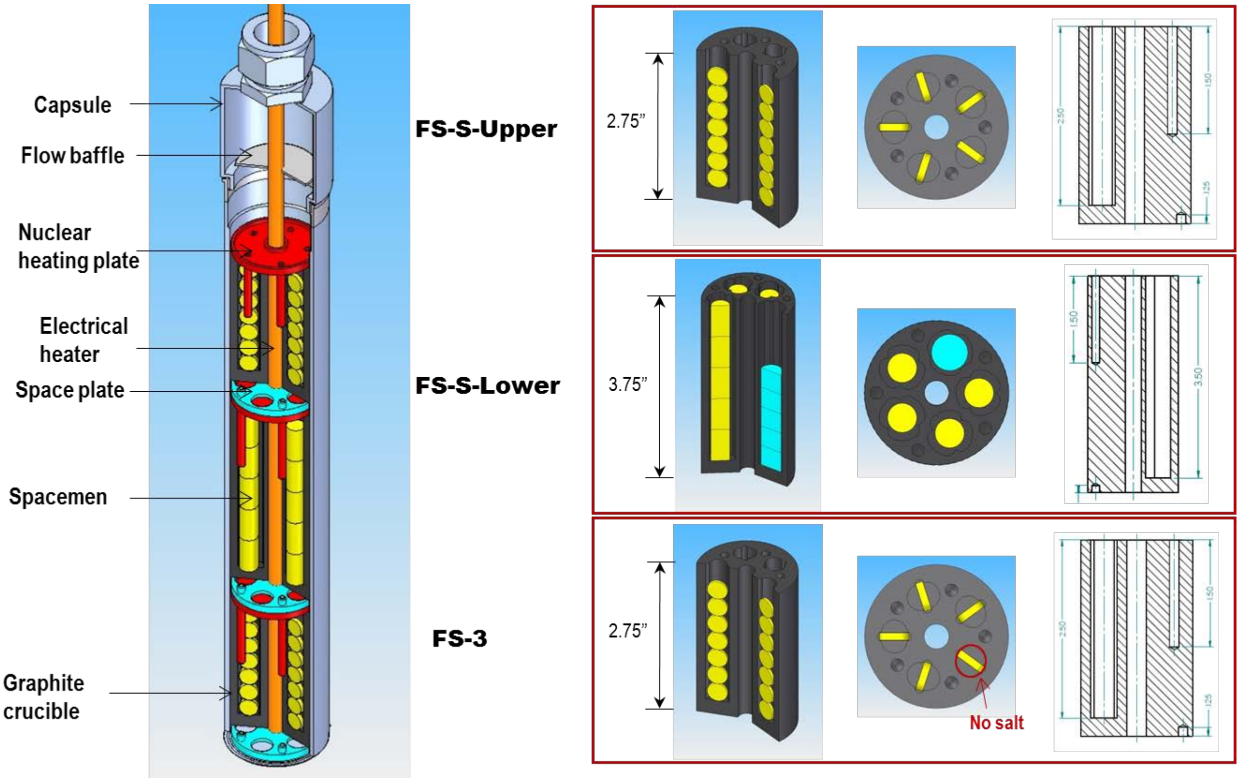

Figure 24. Sectioned view of all FS-3 graphite capsules with specimens loaded (right) and the inner view of assembled capsule (left). Graphite crucible order from top to bottom: FS-S upper for disc specimens, FS-S lower for cylindrical specimens and FS-3 for disc specimens.

3. Neutron Activation Analysis

Trace elements in flibe salt were measured prior to the FS-3 experiment by Neutron Activation Analysis (NAA) at the NRL. The NAA results of the flibe salt used in this irradiation test are shown in Table 5. The concentrations of all of the elements are near or below the levels measured for the standard flibe used in FS-1 and FS-2. Several elements (notably Cr, Fe, Co, and Zn) were found at higher levels in the FS-3 flibe than were found in the reduced-potential flibe used in FS-2. The reduced potential in this flibe was created by the addition of additional beryllium to the molten flibe, which resulted in some elements being reduced from soluble fluoride forms into insoluble elemental forms, which were then filtered from the flibe.

Table 5. Trace elements concentrations in the flibe used to fill the graphite crucibles for the FS-3 experiment. Uncertainties shown are a combination of measurement uncertainties and variability among the different analyses performed. Entries beginning with a "<" symbol were not detected in the sample; the detection limits for that sample and element are given after the "<".

Element	Concentration (ppm)	Uncertainty (ppm)
Na	39	1
Sc	0.126	0.007
Cr	18.9	0.5
Fe	5.95	0.65
Co	0.0093	0.0024
Zn	<1.3	-
Se	<0.25	-
Rb	0.45	0.15
Cs	0.113	0.011
Ba	59	11
Ce	0.186	0.031
Nd	<0.7	-
Eu	0.0066	0.0008
Tb	<0.022	-
Lu	0.009	-
Hf	0.101	0.009
Ta	<0.05	-
Th	0.058	0.006

4. Specimen and Salt Loading

Cleaned samples and crucibles were shipped to the University of Wisconsin-Madison for baking and filling with flibe. This was the same procedure used for the FS-1 and FS-2 in order to achieve the most consistency with the UW autoclave tests.

Prior to loading flibe salt, all three graphite crucibles were baked in 10 vol% H_2 in a ceramic furnace at 850°C for 24 hours. Each graphite crucible was placed in the furnace upside down and a gas tube (stainless steel) was inserted to the bottom of crucible through the central open hole. After the temperature of furnace was above 200°C, the 10 vol% H_2 (balance N_2) gas was slowly fed through the furnace. The furnace temperature was maintained at 850°C for 24 hours for each baking. The main purpose of this baking process was to remove the moisture from the graphite. To consider the influence of baking on the tritium retention in graphite samples, some disk graphite samples with machined and polished surfaces were also baked using the same baking procedures for comparing with non-baked samples. As presented in Table 6, the weight change of the four baked graphite samples was measured.

Among these four samples, A3-3 graphite with machined surfaces lost the most weight, around 0.05mg (0.03 mg/cm^2). The weight loss for other three samples is close or equal to zero. In addition to the weight loss comparison, the microstructure on the surface of these four samples was also compared, and no significant change on their surface microstructure was observed. As shown in Figure 25 the microstructure of the A3-3 sample with a machined surface (highest weight loss) is compared from low to high magnifications. In the high magnification SEM images it is clear that the vein graphite and the microstructural features of typical graphite flakes do not change after the 24-hour baking. This suggests that the baking process does not affect the graphite surface microstructure, and that the influence of baking process on the tritium interaction with graphite is negligible.

Table 6. Comparison of IG-110U and A3-3 graphite before and after baking in 10 vol% H2 environment for 24 hours.

Graphite name	Surface condition	Thickness (mm)	Diameter (mm)	Mass before baking (g)	Mass after baking (g)	Weight lost (mg)
IG-110U	machined	2.0658	7.99	0.18010	0.18010	0.00
IG-110U	polished	2.0717	7.98	0.18387	0.18386	0.01
A3-3	machined	2.0671	7.99	0.15901	0.15896	0.05
A3-3	polished	2.0866	7.99	0.17695	0.17695	0.00

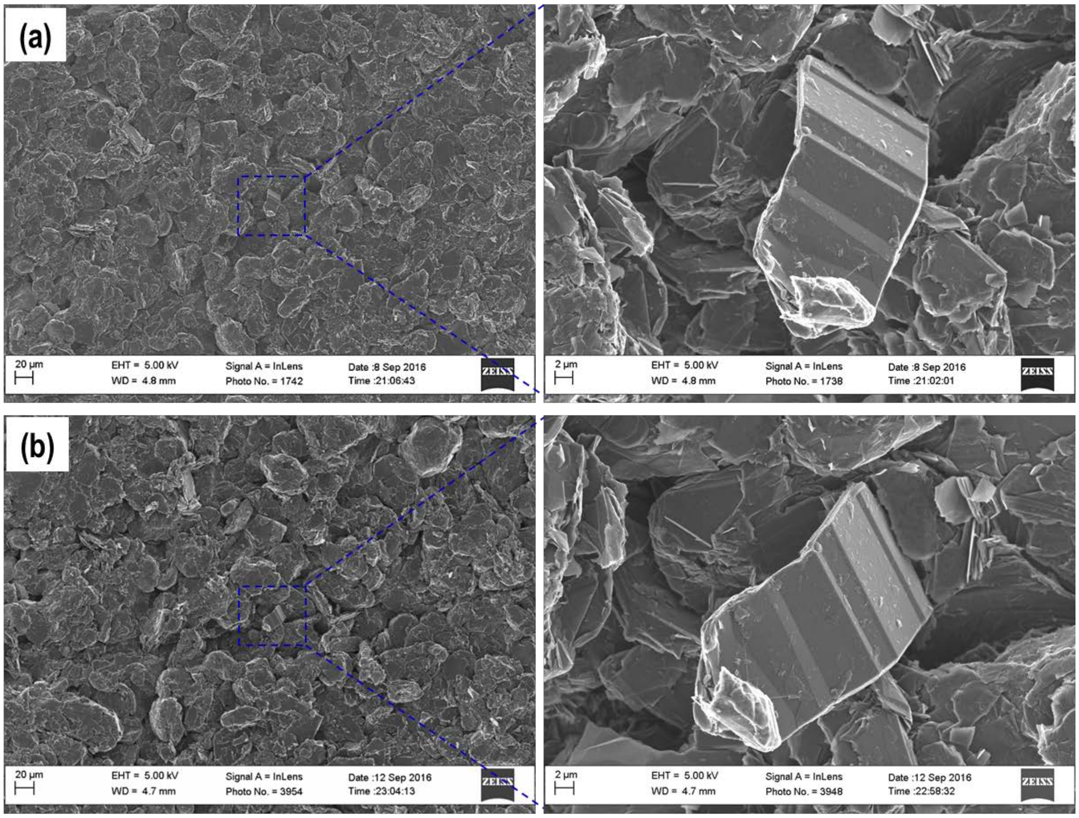

Figure 25. SEM images focused on a specific area machined A3-3 disk samples before (a) and after (b) baking in 10 vol.% H2 environment for 24 hours. Right side SEM images are the zoomed-in area framed in left SEM images.

To avoid salt freezing in compartments during filling salt, a heater was applied. As shown in Figure 26, all graphite samples were first loaded into the crucibles, then the crucibles were placed into the heater. Prior to filling with salt, the crucibles were heated up to ~500°C. Then liquid flibe was smoothly dripped down into each compartment with mass control using a digital scale. As labeled in the lower right photograph in the figure, one compartment of the crucible was not filled salt. After the salt solidified, the loaded crucibles were sealed into a temporary capsule in the glove box for shipping back to the MIT NRL.

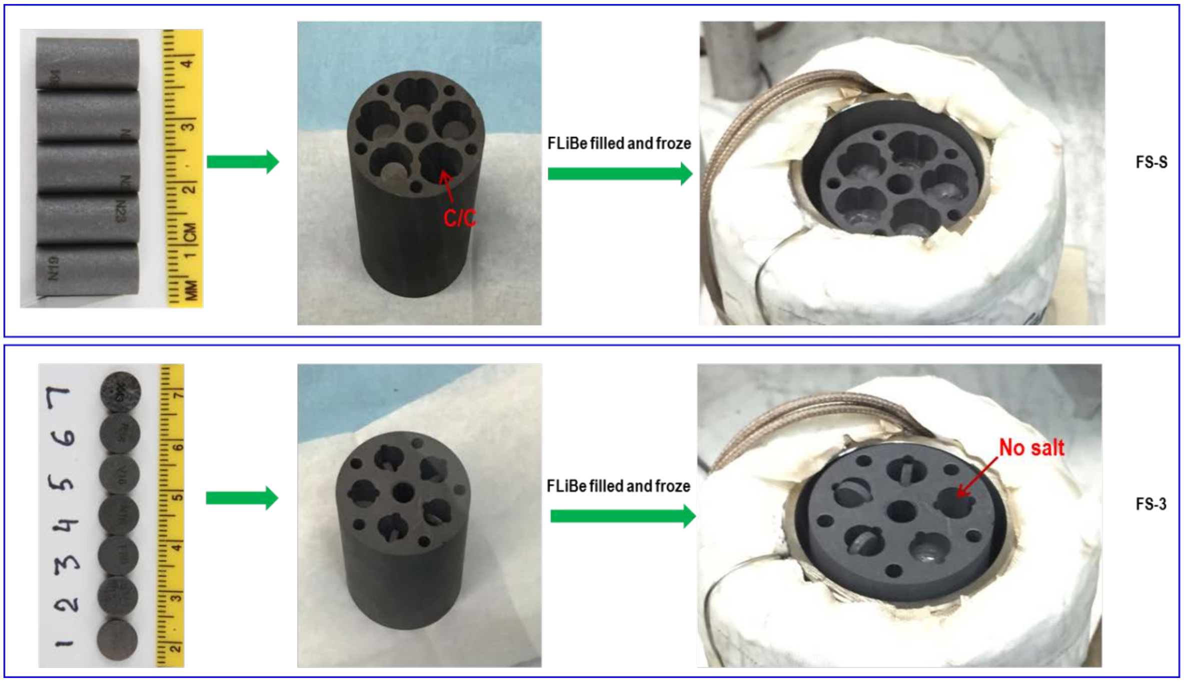

Figure 26. Photographs showing sample loading and flibe salt filling into graphite crucibles.

5. Irradiation

At the NRL the loaded crucibles were inserted into the nickel capsule under helium in a glove bag. The nickel capsule was also purged with helium while being seal-welded. The sealed capsule assembly, maintained under positive helium pressure, was then inserted into the outer titanium thimble. The gas, thermocouple, and heater electrical leads were routed up the instrumentation tube, which was bent into an S-shape to mitigate radiation streaming from the core. The FS-3 assembly (Figure 27) was successfully installed in MITR core on November 8th, 2016.

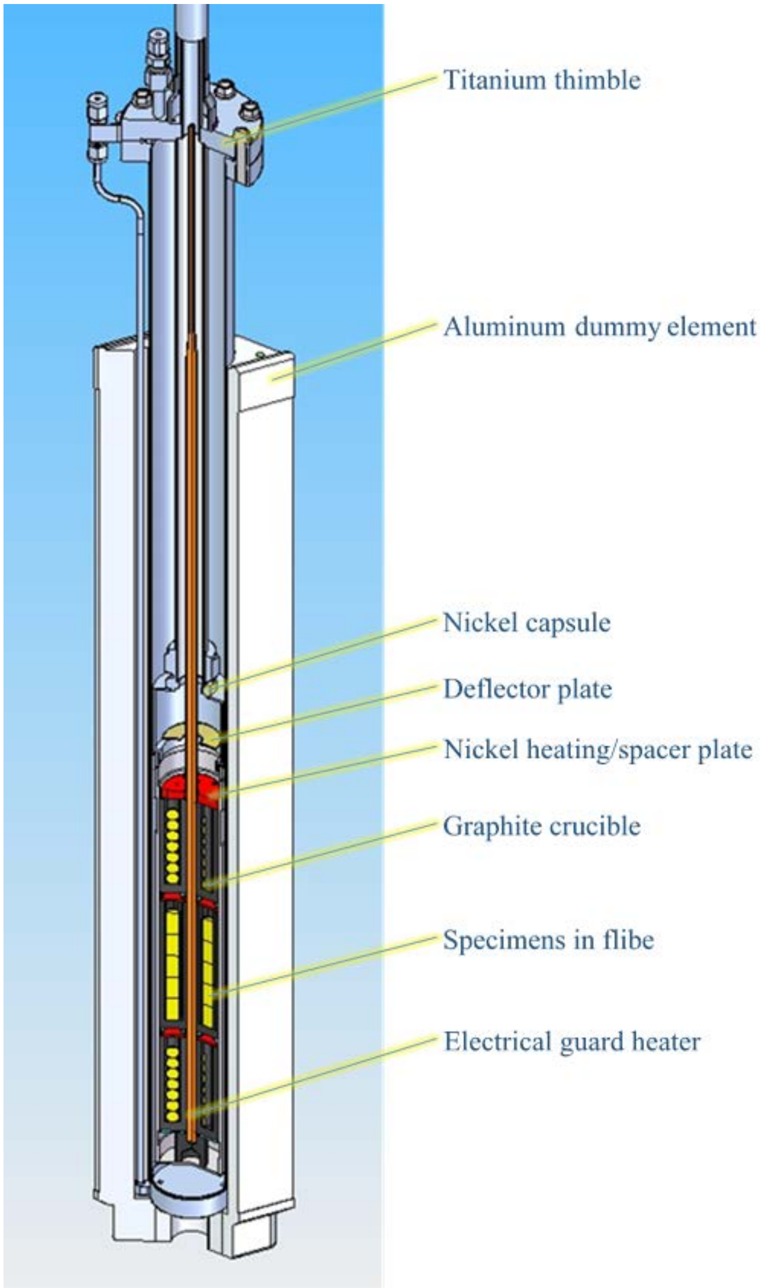

Figure 27. FS-3 experiment assembly MITR in-core section.

Initial Startup

After the assembly was installed and all wires and gas tubing were connected, alarm and control systems were verified. A special procedure was used for the initial experiment startup in order to monitor its behavior and ensure that proper salt melting and thermal stability was achieved. The electrical heater was used to maintain the salt temperature above 200°C. Reactor power was increased slowly from 500 kW to 3.5 MW (capsule is near the melting point of flibe salt at 459°C). While the reactor power was maintained at 3.5 MW, experimenters adjusted the He/Ne gas mixture in the thimble to raise the capsule temperature through salt melting point. Reactor power was then increased power in 0.5 MW steps until the capsule reached desired operating temperature 700°C.

Data Collection

During operation of the experiment, various parameters were monitored and continuously recorded at 2Hz: (1) gas flow rates through the inlet and outlet of the capsule and thimble, (2) pressures at each gas inlet and outlet, (3) radioactivity at different places of gas flowing system, (4) temperature at different locations in capsule (one thermocouple in each graphite crucible), (5) reactor power.

Tritium Collection System

One of the main tasks in the FS-3 experiment is to monitor tritium generation during the irradiation. As shown in Figure 28, an online tritium monitor and tritium bubbler system was implemented to measure tritium generation. One instrument, using a series of compensated ion chambers and low- and high-range detectors, is able to measure tritium activity in real-time. A second bubbler system captured tritium from the gas flow via water bubbling. An initial set of three bubblers captures soluble tritium (TF, THO). The gas then flows through a catalyst furnace and is mixed with oxygen to convert any insoluble (T_2, TH) tritium and then collect it in three additional water vials. These water vials are replaced at least every two days with fresh DI water and clean vials. Each completed set includes six vials of tritiated water and one vial of control that is used as reference of the tritium in the general environment. For counting, the tritiated water in each single vial is diluted and then mixed with a standard scintillation cocktail for a Liquid Scintillation Counter (LSC). The LSC, which generates a calibrated beta energy spectrum, is one of the most sensitive and accurate methods to measure tritium activity.

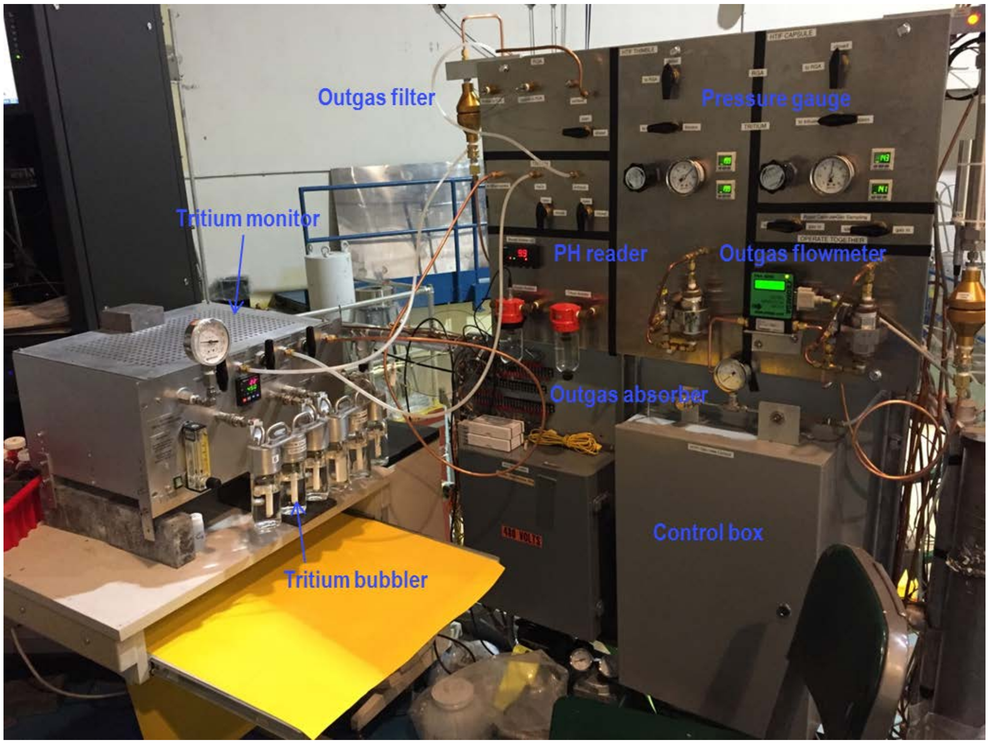

Figure 28. Online tritium monitor and bubbler system, and outlet gas control panel of FS-3 in-reactor experiment.

During irradiation, tritium was monitored from both the capsule cover gas and the thimble sweep gas. Because the outer thimble was maintained at a higher pressure than the capsule and periodically checked for leaks, any tritium collected from thimble outlet gas is a result of tritium permeation through nickel capsule wall during irradiation at 700°C. Since only one bubbler system was available, the tritium sample was only collected from one gas system (either from capsule or from thimble) each time.

Reactor Shutdown and Assembly Removal

At 11:51am, December 18th, 2016, the pressure on the FS-3 outer encapsulation (thimble – 20 psi) suddenly dropped to approximately the same pressure as the inner (capsule – 1 5psi) pressure. This caused an experiment Low Pressure Alarm. This was followed by a slight increase in the experiment temperature, likely due to the decreased thimble pressure creating increased thermal resistance. The increased temperature caused an experiment High Temperature Alert, which did not cause any automatic action. Reactor power was reduced to 5 MW to clear the temperature alarm and investigate the problem. Given the available on the data, it appeared there was a breach between the capsule and thimble encapsulations, leading to all gas flowing into the capsule and out through the normal capsule outlet system. Based on the loss of double encapsulation, it was decided to shut down the reactor. The capsule was maintained >200°C with the electrical heater until the experiment was removed from the core on November 20th, 2016. The assembly was transferred to the NRL hot cells for disassembly. During this time the capsule/thimble was maintained under positive helium pressure.

Operations Data

Figure 29 shows the overall temperature profile (olive green) and reactor power profile (red) during FS-3 in-core irradiation test in molten flibe. TC2 is a thermocouple positioned in the middle graphite crucible. From these two profiles, it is known that the temperature was maintained stably at 700°C while reactor was controlled at around 5.6MW. The electric heater was turned on before increasing reactor power from zero. The heater PID controller reduced its power to zero as the reactor power increased, and brought it on again when reactor was shut down.

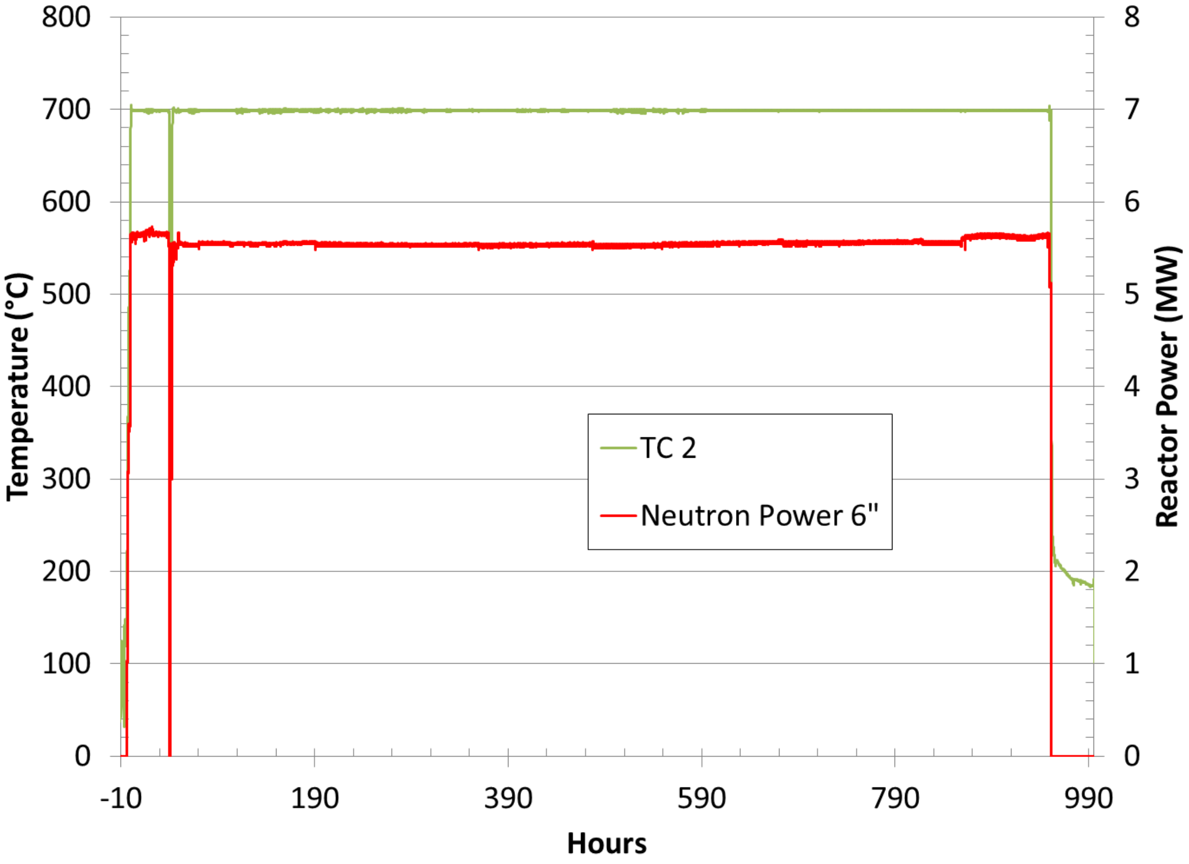

Figure 29. Temperature profile and reactor power profile of FS-3 in-core irradiation experiment.

In order to more closely examine the profiles of reactor power and corresponding temperature on middle graphite crucible, the profiles at initial stage were zoomed in, as shown in Figure 30. From these profiles, it is clear that the reactor power increased step by step until 5.6 MW. The salt passed through its melting point while reactor power was at 3.6 MW. The phenomena of the temperature increasing steps not exactly matching the reactor power increasing steps is because the salt temperature could be modified by changing He/Ne gas mixture and electrical heater power.

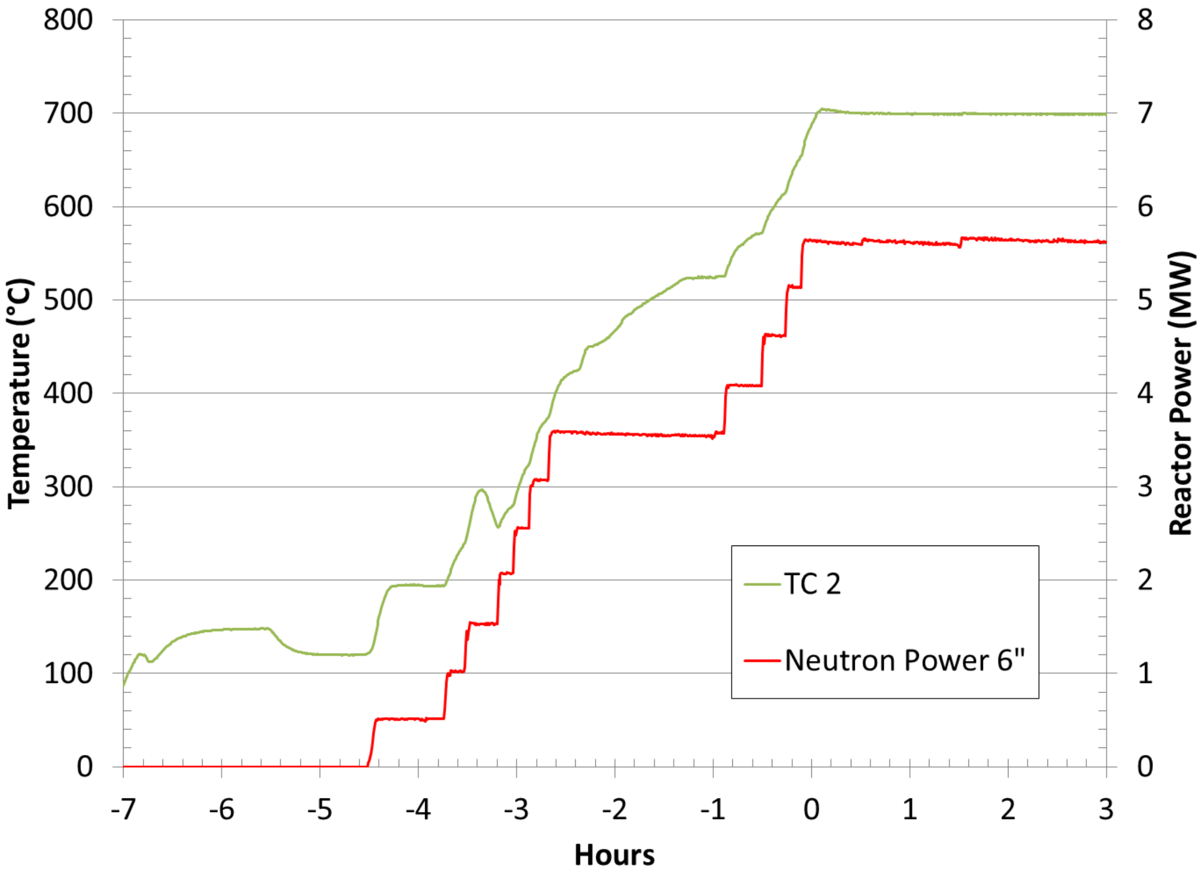

Figure 30. Temperature profile and reactor power profile at initial startup of FS-3 irradiation experiment.

As shown in Figure 31, a scram occurred at around 39.5 hours into the irradiation due to issues unrelated to the experiment. Reactor power decreased to zero in less than one second, causing a rapid cool-down of the FS-3. The control system automatically turned on the electric heater, and the salt temperature dropped down to a minimum of about 240°C until the reactor was restarted.

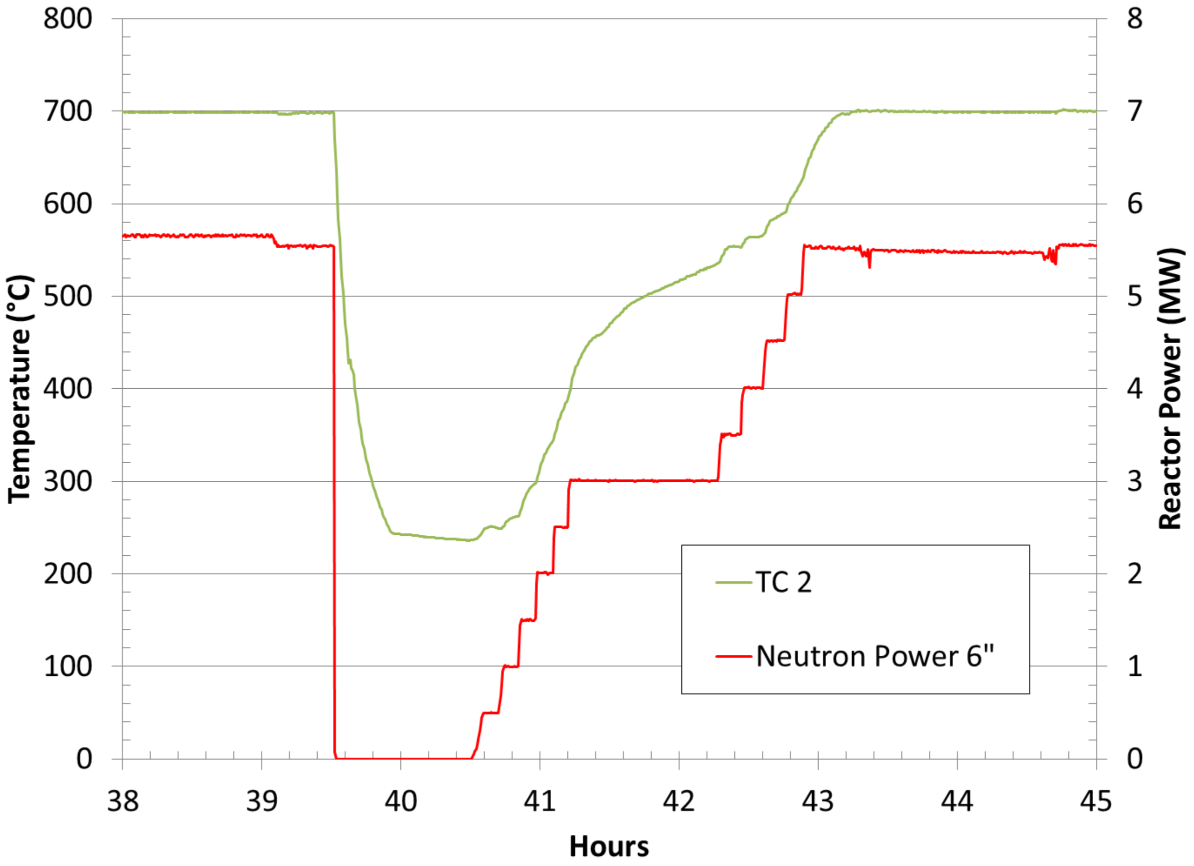

Figure 31. Temperature profile and reactor power profile at a scram that occurred at around 39.5 hours into the irradiation.

As mentioned in previous section, the pressure in outer encapsulation suddenly dropped around 950 hours into the experiment (Figure 32). A breach was formed that allowed gas flow from the capsule to the thimble encapsulation. It was decided to shut down reactor at 951.5 hours. The electric heater was triggered on to maintain the assembly above 200°C until the thimble was removed from reactor core and transferred to the hot cell.

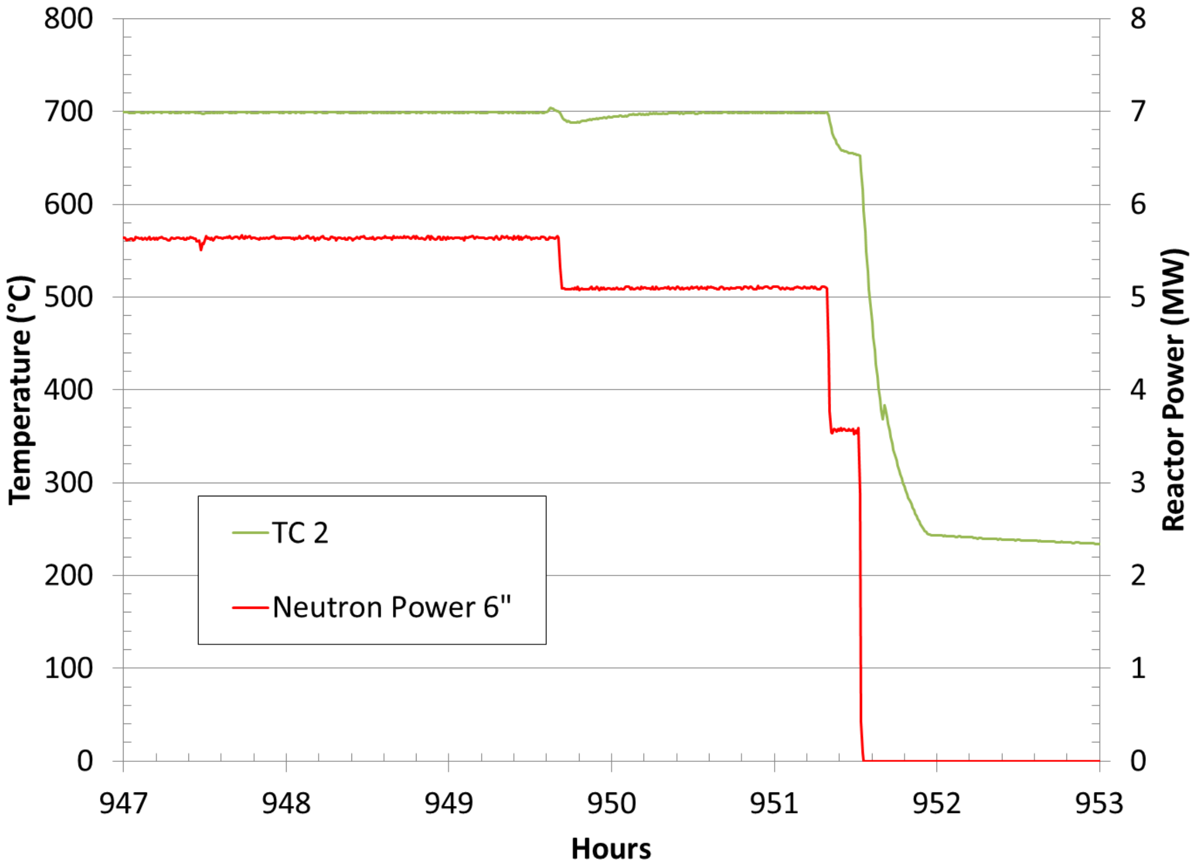

Figure 32. Temperature profile and reactor power profile when reactor was shut down due to a pressure drop in the outer encapsulation.

6. Tritium Measurement Results

Several modifications to the experimental train have improved the quality of tritium data compared to the first two FS irradiations. An important change was the addition of hydrogen to the sweep gas stream, which significantly reduced the rate of parasitic reactions in off-gas tubing prior to the tritium collection system. With a higher yield of collected tritium, the FS-3 release data is a more complete picture of tritium transport and absorption behavior in a fluoride salt system.

The total tritium content in each vial set normalized by the MITR megawatt-days produced during each set interval is shown below in Figure 33. The tritium release data shows some characteristic features which can be explained by absorption into the capsule materials. At the beginning of the experiment, absorption rates into the capsule's fresh graphite crucible and test samples are the highest, and therefore release rates are reduced. As the experiment progresses, absorption sites fill up and release rates begin to increase. Towards the end of the experiment, combined release rates in the capsule and thimble approach the total calculated production rate. Contrary to the tritium coming out from capsule, the tritium coming from the thimble gas line is at a stable rate of 0.5 mCi/MWd from the beginning to the end of experiment. This probably suggests that the tritium permeation rate through capsule wall is constant at 700°C. The tritium concentration within capsule at certain low value at early stage (1-2 days of experiment time) can maintain this constant permeation rate. [3-6]

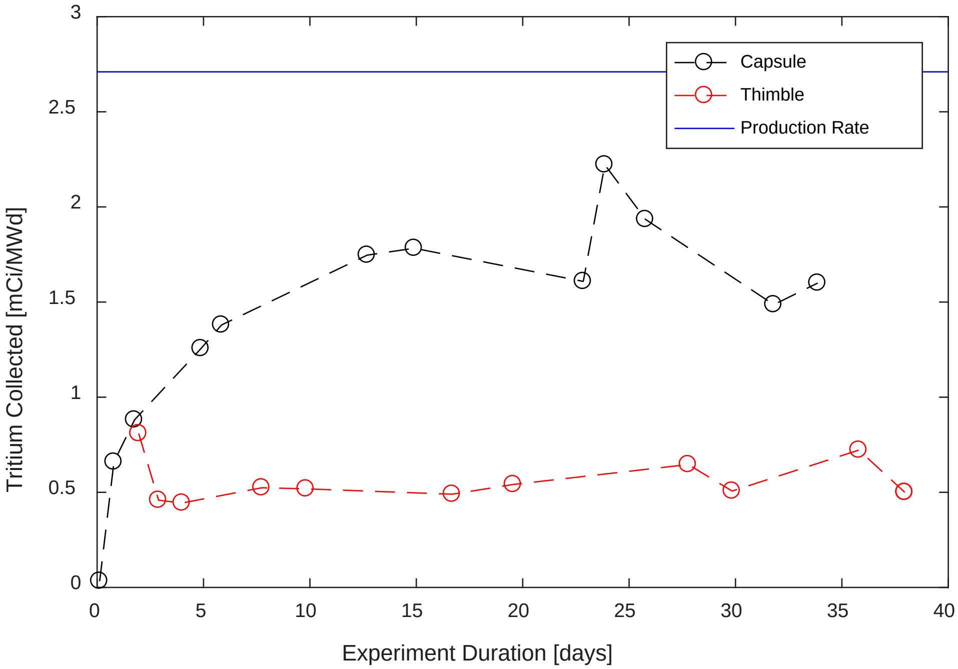

Figure 33. Captured tritium from FS-3 in the Capsule and Thimble region compared to the calculated tritium production rate.

The total collected tritium in FS-3 can be used along with the calculated production rate to estimate the amount of absorbed tritium remaining in the capsule. Because only the capsule or thimble region can be sampled at a time, the data set must be interpolated in order to calculate a comprehensive tritium release rate. Using this methodology, the total calculated release for FS-3 is 457 mCi. Estimation of missing capsule and thimble points as well as scatter in the data set are significant sources of uncertainty in the release calculation. For the production rate calculation, a full-core MCNP MITR model including FS-3 was used. Tritium production from ^{6}Li(n,t), ^{7}Li(n,nc), ^{9}Be(n,t), and ^{19}F(n,t) reactions in each salt region was tallied resulting in a total of 596 mCi produced for the FS-3 run. Therefore, the amount of absorbed tritium in the FS-3 capsule can be estimated as the difference between production and release, or 139 mCi.

Tritium release data from FS-3 supports the hypothesis that significant quantities of tritium were absorbed in the graphite crucible, test samples, and other materials during the in-core irradiation. Work has been accomplished on the development and testing of a thermal desorption furnace for tritium content analysis of these sample materials. A detailed description of the desorption furnace experiments is given in the tritium section of this report.

To study the chemical state of tritium from thimble and capsule, the tritium in first three bubbling vials that absorbs soluble tritium and the tritium in the next three bubbling vials that absorbs insoluble tritium were plotted, as shown in Figure 34. It is apparent that the insoluble tritium from both capsule and thimble is much higher than soluble tritium. Insoluble tritium (T_2, TH) in capsule is approximately 1000 times higher than soluble tritium (TF, THO). Moreover, the soluble tritium from capsule at early stage is higher than later. This might suggests that the limited impurities in molten salt combine with tritium to form soluble tritium. With the exhausting of impurities, the salt becomes more reducing and tritium comes out as T_2 and (or) TH. Another possible reason is that the soluble tritium chemically reacts with metal at high temperature.

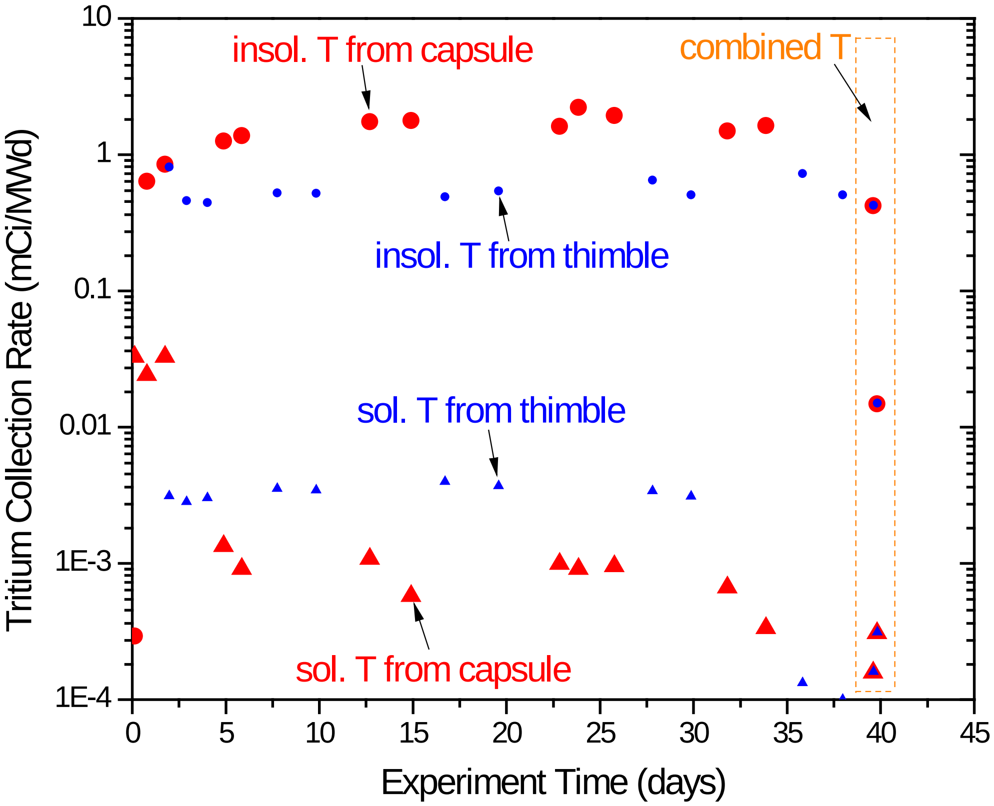

Figure 34. Results of insoluble and soluble tritium collection rate (mCi/MWd) from capsule and thimble gas systems, respectively. The last two data points are the total tritium from both capsule and thimble gas systems by combining both gas outlets and flowing through bubbler.

The both insoluble and soluble tritium collection rates from thimble are at relatively stable level. The insoluble tritium is approximately 100 times higher than soluble tritium from the gas of thimble. Theoretically, soluble tritium (TF, THO) cannot permeate through metallic capsule wall at high temperature. One possible reason to form soluble tritium in thimble is that the insoluble tritium was oxidized by reacting with impurities on inner surface of thimble.

Overall, based on the profiles tritium collection rate vs. experiment time, it is well known that the insoluble tritium is the dominant chemical state in both capsule and thimble during molten flibe salt irradiation experiment in MITR.

7. Post-irradiation Examination

Much of the valuable data from the irradiation experiments must be gathered during post-irradiation examination. This is a particularly complicated process as it is difficult to find high-quality instruments that have authorization for radioactive materials, and preparation and transport of each specimen is significantly more involved. Graphite, SiC, SiC/SiC fiber composite, 316 stainless steel, and Hastelloy N specimens have been cleaned, sectioned, and examined under SEM/EDS, FIB/TEM, and XRD analysis in order to probe salt penetration and changes to the materials microstructure due to irradiation and flibe salt corrosion. This analysis is expanding our understanding of the interactions in these multi-component systems and how modern materials can be best used in different parts of the FHR.

Post-Irradiation Tritium Measurement and Tritium Data Analysis

Multiple methods of measuring the tritium uptake of the materials irradiated in the salt capsules were investigated. Significant gamma and non-tritium beta activity due to neutron activation of components and impurities within the salt, and salt contamination on surfaces (with danger of HF generation and Be toxicity) have complicated the process of tritium measurement and access to equipment. A dedicated facility for thermal desorption of tritium (up to 1100°C) was constructed. In parallel, mapping of tritium activity using beta-sensitive films was attempted using cross-sections cut from the graphite crucible at levels within and above the fill line of the salt chambers.

A chief unknown was how any tritium present within the salt and specimens would be affected by re-heating. At the end of the irradiation the reactor is shut down and flibe cools and solidifies. In order to remove the salt and specimens from the crucibles, the capsule is deconstructed in a hot cell, and the loaded crucible is then transferred to a furnace in a glove box where it is slowly re-heated to drive off moisture. After about an hour at 150°C the crucible is then brought to approximately 500°C to re-melt the salt so that salt grab samples and specimens can be retrieved. During this drying and re-melting the helium atmosphere within the furnace was purged through the tritium counting and collection system. The tritium release to the gas measured during this operation was 30 times lower than that during the in-core operations at similar or higher temperatures, and because it required only several hours the tritium loss during this procedure does not appear to be significant.

Samples of the irradiated graphite crucible (Toyo Tanso IG-110U) and flibe from the initial 2013 MITR irradiation have also been examined with gamma spectroscopy and LSC. The graphite was tested only qualitatively in order to estimate the tritium loading for radiological control purposes. Approximately 1 mg of graphite powder was suspended in scintillation cocktail, resulting in an estimated tritium activity of at least 12 nCi/mg. The actual value is almost certainly higher due to lower counting efficiency – darkening of the solution and geometric losses as some graphite particles visibly plated onto the vial walls. A 20 mg piece of flibe was dissolved in water at room temperature and also scintillated. Some thickening of the scintillation cocktail suggested a possible chemical reaction with the flibe that may have reduced the counting efficiency, and so again the tritium activity of 1.5 nCi/mg should be considered a lower bound. With these caveats in mind, if these concentrations are extrapolated to the total salt and graphite loadings in the irradiation capsule, assuming the tritium is distributed evenly in each, there is expected to be at least 180 µCi of tritium in the salt and 2.4 mCi of tritium in the graphite, compared to 1.5 mCi released into the off-gas over the course of the irradiation, and 620 mCi calculated for total tritium generation based on the neutron fluence, lithium enrichment, and cross sections. In comparison, the second MITR irradiation is estimated to have produced 540 mCi of tritium with only 3 mCi collected in the off-gas.

FS-1 Sample Microscopy

Cleaned FS-1 graphite samples were sectioned into small pieces to reduce the dose rate during sample handling and transfer. Table 7 lists the radioactivity of each of the sectioned samples, including the dose rate on contact surface and at a distance of 30 cm from samples. The main radioactive isotopes in these samples are Mn-54, Co-58, and Co-60, which emit strong gamma rays. The sample name of HN-Ni, HN-G, 316-316 and 316-G in Table 7 corresponds to the Hastelloy N coupons in a nickel-lined crucible, Hastelloy N coupons in a graphite crucible, 316 stainless steel coupons in a 316 stainless steel-lined crucible and 316 stainless steel coupons in a graphite crucible, respectively. These four samples were transferred via special radioactive material shipment to the CAES lab at INL.

Table 7. Radioactivity of sectioned alloy samples.

Sample	Mass (g)	Isotope	Dose rate (mRem/hr)	
			contact	@ 30cm
HN-Ni	0.18557	Mn-54 Co-58 Co-60	600	30
HN-G	0.14782	Mn-54 Co-58 Co-60	380	18
316-316	0.13289	Mn-54 Co-60	1800	40
316-G	0.07820	Mn-54 Co-60	1000	20

The surface of each sample was observed under a scanning electron microscope (SEM) equipped with a focused ion beam (FIB) (Quanta 3D FEG, FEI Company). The cross-section of the near-surface layer was milled using the FIB technique. Transmission electron microscope (TEM, Tecnai TF 30-FEG STwin, FEI

Company) samples were also prepared using the FIB. The main steps of TEM sample preparation is presented in Figure 35.

Figure 35(a) shows the typical corrosion surface of all four in-core corrosion samples. The grain boundaries on the surface were significantly attacked deeper than grains. In addition, a large number of irregular particles were observed on the corrosion surface. Elemental analysis suggests that these particles are Cr-, Ni- and Mo-rich oxides and carbides. The carbide particles formed during corrosion and the oxide particles formed when exposing the cleaned samples to air. The microstructure of the cross-section of the near-surface layer a 316 stainless steel sample is displayed in Figure 35(f). The phenomena of preferential grain boundary attack and precipitation along grain boundaries was clearly observed in this FIB milled and thinned lamella. By comparing with out-of-reactor static corrosion samples, it is found that these phenomena are associated with molten salt corrosion and thermal effects. [10]

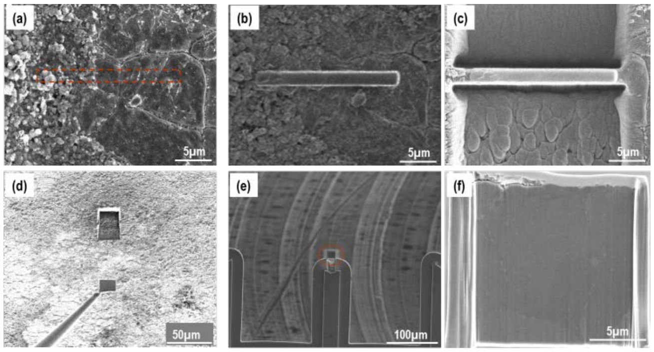

Figure 35. SEM images of 316-G sample illustrating the main steps of the TEM sample preparation by using FIB technique, (a) selecting grain boundary, (b) Pt deposition, (c) FIB milling, (d) lifting out lamella, (e) welding lamella on Cu grid and (d) thinning lamella.

TEM images give more detailed information about the micro features in the samples. All four samples were observed under TEM, but only the results of the Hastelloy N tested in graphite crucible are presented here. As shown in Figure 36, a Mo-rich phase a few microns in diameter is observed in the grain, which exists in the as-received alloy. In addition, the Mo-rich phase was observed in grain boundaries.

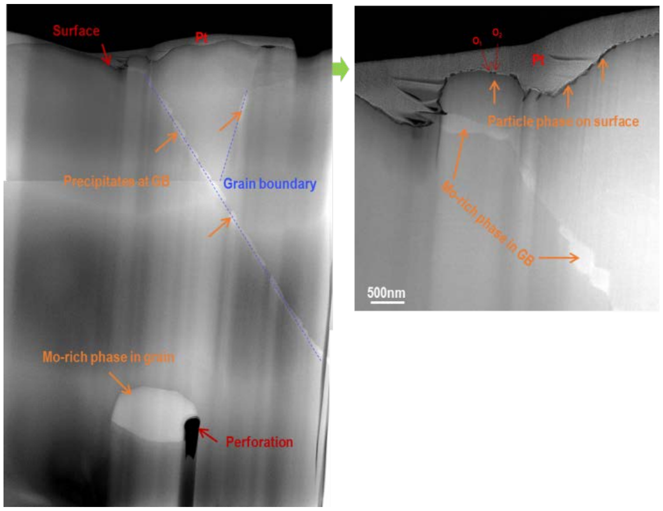

Figure 36. Scanning transmission electron microscopy dark-field images in the near-to-surface layer of in-core molten salt corroded Hastelloy N tested in a graphite crucible

The magnified image on right side in Figure 36 clearly shows the particles phase on corrosion surface. These nano particles were well protected by the Pt deposition during FIB milling and thinning. They were also observed in the out-of-reactor corrosion samples. However, the nano carbide particles that distribute in the near-to-surface layer of out-of-reactor corrosion sample were not found in this in-core corrosion sample. This difference is likely related to the neutron irradiation; one hypothesis is that neutron irradiation induced tritium generation in the molten salt and this tritium reacted with the carbon liberated from the graphite crucible surface. This needs more effort in future work to analyze molten salt chemistry under neutron irradiation. The EDS profiles in Figure 37 suggest the main chemical elements in the particle O_1 and O_2 labeled in Figure 37 are Ni, Cr, Mo, and C as well as O, in addition to Cu (grid), Pt (deposition) and Ga (ion beam source). C signal is usually detected on all samples due to the environmental contamination. This indicates that the round nano particles on the corrosion surface are oxides and possibly carbides, which is consistent with the analysis on corrosion surface.

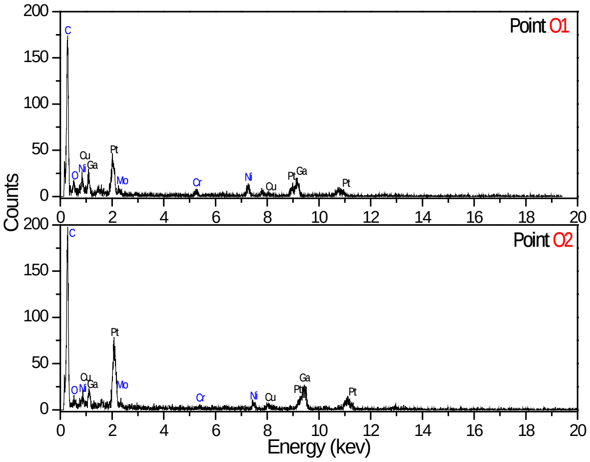

Figure 37. EDS profiles of nano-sized particle O1 and O2 labeled in Figure 36.

The radiation damage dose of tested alloys was calculated to be approximately 0.2 dpa for the 1000-hour neutron irradiation in MITR operating at 5.5 MW. [12] The evidence of neutron irradiation-induced microstructural defects was directly observed under TEM. As shown in Figure 38, a large number of line dislocations and dislocation loops are randomly distributed in the grain and near the grain boundary. The length of line dislocations is in a range from tens to hundreds of nanometers. Since the visibility of this structural damage is dependent on the observation angle of the TEM, the density of radiation-induced dislocations shown in Figure 38 is not representative for whole sample. Additionally, crystallized precipitates hundreds of nanometers in diameter or length were observed in these TEM images. Some line dislocations extend to the end of the precipitates. This suggests that the precipitates inhibit or retard dislocation movement during irradiation at high temperature.

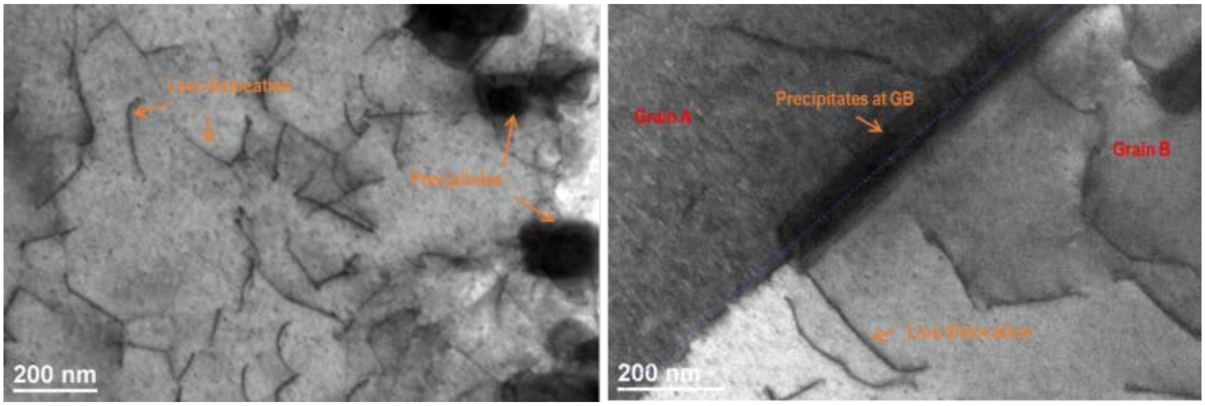

Figure 38. Transmission electron microscopy bright-field images of in-reactor corrosion Hastelloy N tested in nickel-lined crucible showing the neutron irradiation-induced structural damage in grain and near grain boundary.

Combining the microstructural analysis in this study with the weight loss of both in-core corrosion and out-of-reactor corrosion samples[7], neutron irradiation only accelerates the corrosion on alloys' surface due to the molten salt chemistry change. The irradiation-induced structural damage might impact the corrosion of alloys in high-temperature molten salt in the longer term.

Microstructural Analysis of FS-1 Alloys

Four irradiated alloy samples, 316 stainless steel in 316 stainless steel liner (316-316) and in graphite (316-G), Hastelloy N in nickel liner (HN-Ni) and in graphite (HN-G) tested during FS-1 were sectioned and cleaned at MIT, and then transferred to the Center for Advanced Energy Studies (CAES) at INL for microstructural analysis. With the funding support from an awarded NSUF Rapid Turnaround Experiment (RTE) proposal, the phase identification, chemical composition, grain boundary precipitates and newly formed particle phases in grains as well as radiation damage were analyzed by using Rigaku SmartLab x-ray diffractometer, Focused ion beam (FIB) associated with SEM and EDS (Quanta 3D FEG, FEI company), and Transmission Electron Microscope (Tecnai TF 30-FEG STwin STEM, FEI company). Among these analyses, TEM is the most challenge because of the difficulties in TEM sample preparation, especially for the radioactive materials. In addition to the protection facilities for handling radioactive materials, experienced skills are required to efficiently mill and thin TEM samples by using FIB technique.

The SEM images in Figure 39 represent the main steps of TEM sample preparation for all four radioactive alloys by using FIB technique. First, a typical corrosion attacked grain boundary was selected for analyzing the microstructure of the grain and grain boundary in the near-surface layer. Then, a stripe of Pt (~2μm in thickness) was deposited on the selected area to protect the original corrosion surface. The third step was to cut off the materials surrounding selected area including bulk-out and U-cuts. As shown in Figure 39 (c), a slope on the up and down side of the selected area was milled as deep as 20µm, then the sample was tilted and cut in a U shape on the cross-section of the thin piece. Figure 39(d) shows the lift-out process. Under SEM observation, an Omniprobe was inserted and precisely moved to one corner of the selected area. The probe tip was then welded onto the sample by depositing additional Pt. The thin piece was cut through and lifted out by slowly moving the Omniprobe. In Figure 39(e), the lift-out sample was mounted on Cu grid by welding the two bottom corners. Lastly, the FIB lamella was further thinned and cleaned by using the e-beam with different voltages and currents.

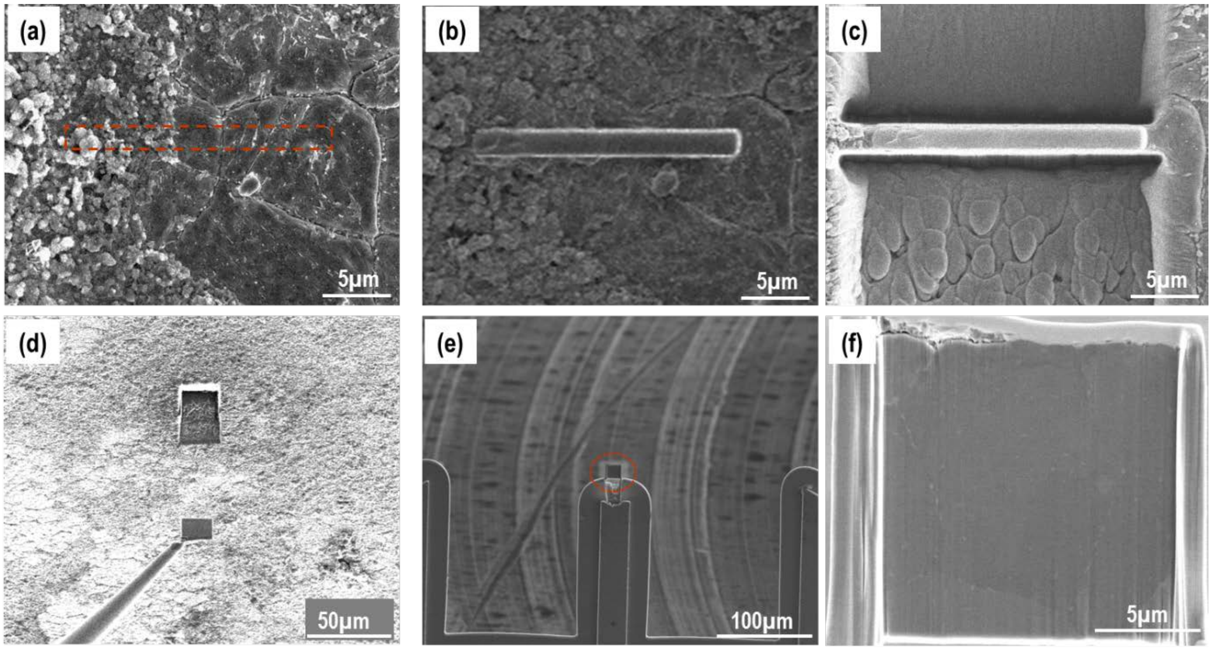

Figure 39. SEM images of 316-G sample illustrating the main steps of TEM sample preparation by using FIB technique, (a) selecting grain boundary, (b) Pt deposition, (c) FIB milling, (d) lifting out lamella, (e) welding lamella on Cu grid and (d) thinning lamella.

Figure 40 shows the FIB lamella of all four alloys. Only one face of these lamellas were thinned for SEM observation and EDS mapping. Although the grain size of Hastelloy N is relatively large, one and more grain boundaries are included in each lamella. From these cross-sectional SEM images, it is observed that the grain boundary and its adjacent area were attacked deeper than other places. Additionally, abundant particle phases and precipitates were observed in the grains and grain boundaries in both 316 stainless steel samples, but Hastelloy N grains were clean except for the typical Mo-rich phase (Figure 40(c)) that exists in as-received Hastelloy N. These Hastelloy N microstructure is different from the out-of-reactor corrosion tested samples, particularly for the Hastelloy N tested in graphite crucible that contains a large number of carbide phases in the grains in near-surface layer. [7] This is probably related to the change of molten salt redox potential caused by the high neutron flux during in-core corrosion experiment.

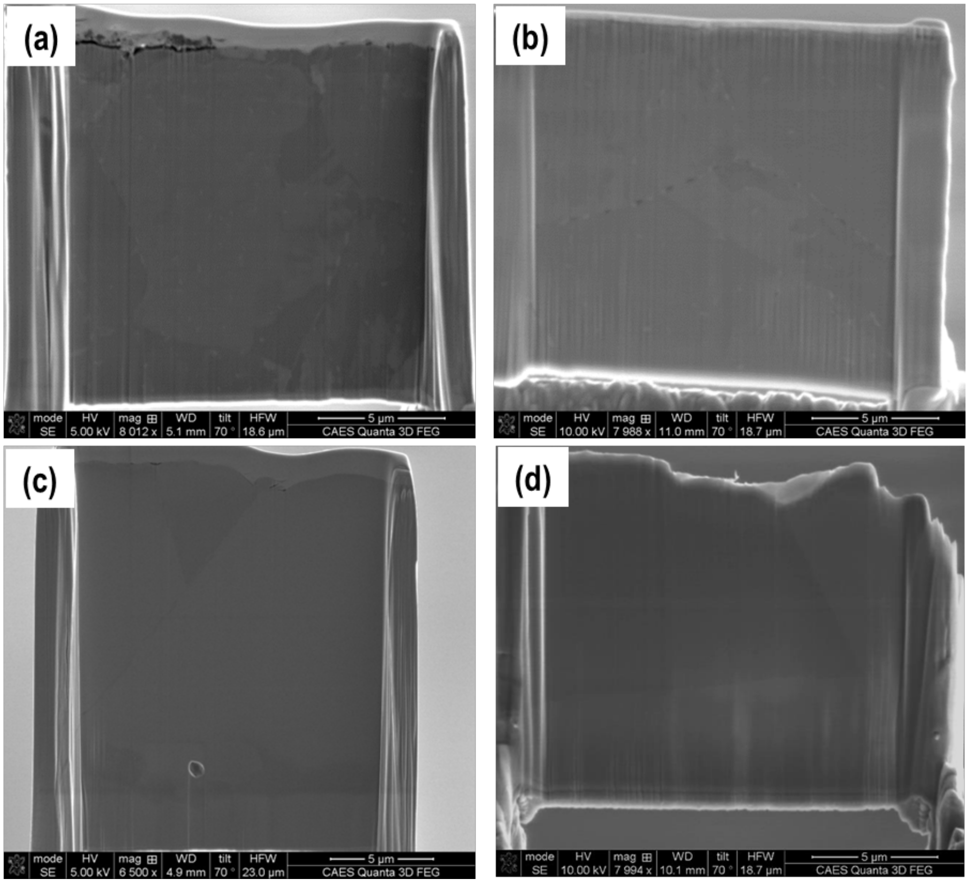

Figure 40. SEM images of FIB lamellas of sample (a) 316-G, (b) 316-316, (c) HN-G and (d) HN-Ni. Only one face was thinned for EDS mapping.

Figure 41 shows the SEM images and EDS maps of main elements Cr, Fe, Ni and Mo in the near-surface layer of HN-G sample. However, the contrast and resolution of each EDS map is too low to identify the interfaces between grains and the Cr concentration gradient underneath corrosion surface because the thickness of FIB lamella is less than 1µm. The relatively high concentration of Mo is still detected along grain boundaries and at Mo-rich phase. The high concentration of Pt on lamella top and two bottom corners is from the Pt deposition and mounting joints. To study the microstructure and chemical compositions of precipitate phase in grains and grain boundary and irradiation-induced structural damage in nanometer level and even atomic level, all four alloy FIB lamellas were further thinned to electron transparent (<100nm in thickness) for TEM analysis. Some STEM images, TEM images and EDS results of four alloys were collected.

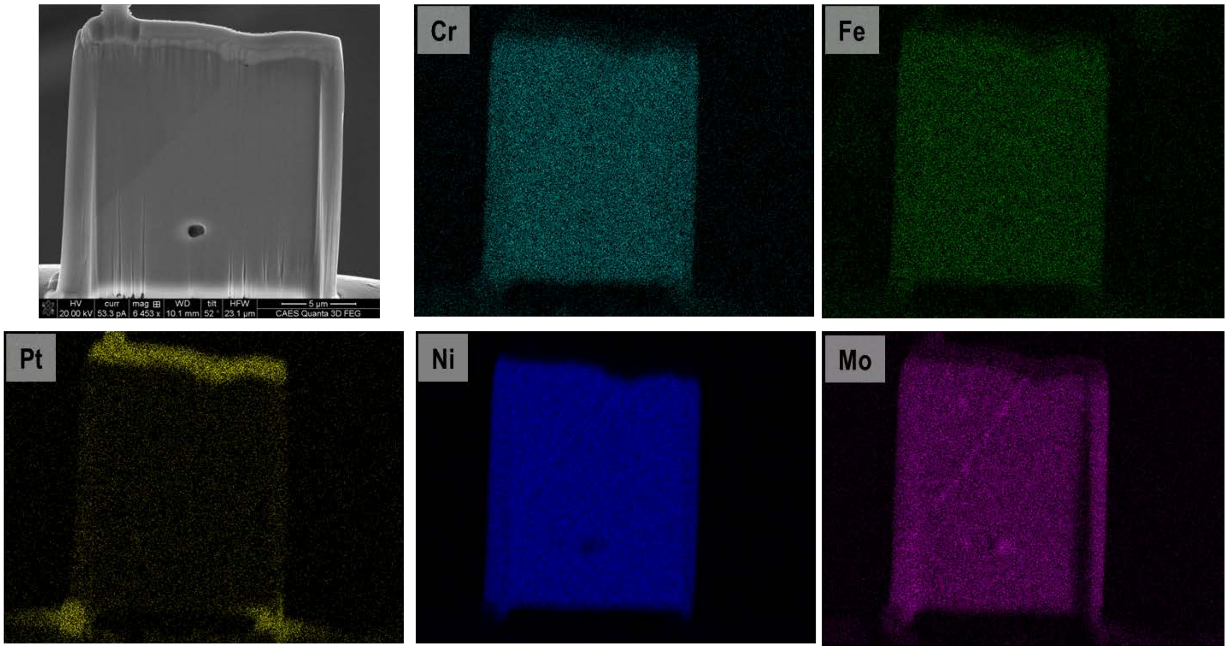

Figure 41. SEM image and EDS maps of Cr, Fe, Mo and Ni in the near-surface layer of HN-G sample, Pt from the surface deposition and mounting joints.

XRD on the Corrosion Surface of FS-1 Alloys

The phase stability of 316 stainless steel and Hastelloy N in high-temperature molten flibe salt under neutron irradiation was analyzed by using the XRD (Rigaku SmartLab) at CAES. Divergent beam mode was selected to scan samples' surface in the range of $2\theta=10\text{-}100^\circ$. Figure 42 shows the XRD patterns on the corrosion surface of 316 stainless steel samples tested in flibe salt in graphite and in 316 stainless steel lined crucibles in MITR. Different from the out-of-reactor corrosion samples [8], the corrosion-induced characteristic peaks of (200) and (211) α-ferrite phase at $2\theta\approx65^\circ$ and $2\theta\approx84^\circ$ almost disappeared in the surface layer of in-reactor tested samples, and only strong (220) peak of γ phase on both samples' surface layer. It should be noted that this γ phase (FeNi) is different from the austenite phase (γ phase) in as-received sample. The depletion of Cr from matrix during corrosion in reactor resulted in the enrichment of Ni and Fe in the surface layer, and then the γ phase (FeNi) formed at high temperature of 700ºC. The massive Cr depletion in the near-to-surface layer of in-reactor tested samples is evidenced by much higher weight loss than out-of-reactor corrosion samples. [9] Therefore, the chemical composition of the γ phase in Figure 42 is different from the austenite γ phase in as-received material. This is very likely associated with the chemistry change of the molten flibe salt under neutron irradiation. Neutron irradiation caused the generation of tritium (T) in salt and also de-bonded fluorine from the salt components of BeF_2 and LiF. Then the T combined with the F forming super corrosive TF dissolved in molten salt. TF attacks most alloying elements on surface and also accelerates Cr depletion from stainless steel. By comparing two XRD patterns in Figure 42, it was found that the graphite crucible promotes the formation of α'-phase (the same as as-received materials). The use of graphite crucible introduced extra carbon source into molten salt then diffused into steel to react with Fe forming the α'-ferrite phase. The main impact of graphite crucible on the corrosion of 316 stainless steel is the formation of lots of carbides on surface, which significantly hastens the corrosion rate.

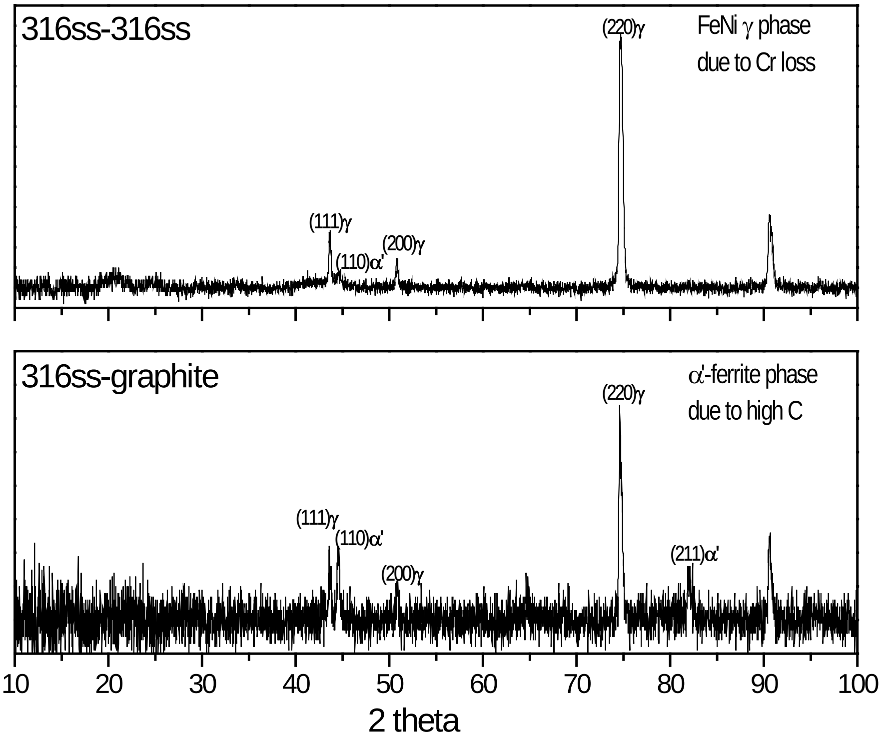

Figure 42: XRD patterns of the 316 stainless steel samples from FS-1 in-reactor molten salt corrosion experiment.

Figure 43 shows the XRD patterns of the Hastelloy N samples tested in molten flibe salt in graphite and nickel-lined crucibles in the MITR for 1000 hours. The main characteristic peaks of FCC nickel matrix and Ni_3Fe enriched phase in surface layer are the same as out-of-reactor corrosion samples. [7] The main peaks of both FCC nickel and Ni_3Fe phases overlapped in the XRD patterns. High-temperature molten salt corrosion depleted Cr from alloys and induced the formation of Ni_3Fe phase in surface layer. However, unlike the out-of-reactor corrosion sample in graphite crucible, no carbide phase was identified on the surface of the in-reactor tested Hastelloy N. This point will be discussed later in the observation of its microstructure. Therefore, no comparable phase change occurred to the Hastelloy N in high-temperature flibe in reactor.

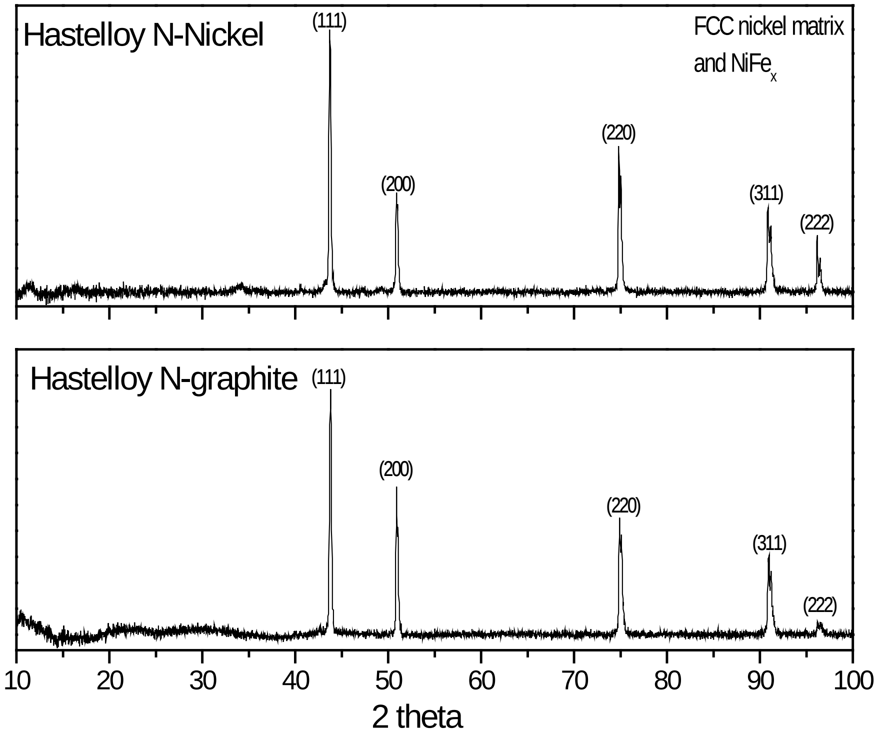

Figure 43: XRD patterns of Hastelloy N samples from FS-1 in-reactor molten salt corrosion experiment.

Microstructure of near-to-surface layer of FS-1 Alloys

As shown in the following four figures, the microstructural features in the near-to-surface layer of four radioactive post-corrosion alloys was analyzed by using Transmission Electron Microscopy (TEM) at INL. The features including precipitates, grain, grain boundary, and particle phases on surface are clearly observed in the scanning transmission electron microscope (STEM) dark-field (DF) images. These features are mainly associated with the thermal effects and corrosion effects in high-temperature molten flibe salt. They are described in details in the following sections.

Figure 44 shows the STEM dark-field image of in-reactor corrosion tested 316 stainless steel sample in 316 stainless steel lined crucible in the reactor. A large number of precipitates with irregular shape formed in grains and at grain boundaries. The size of these precipitates is in the range of 10s of nanometers to 100s of nanometers. The perforation shown in this and other STEM images is resulted from the FIB milling while final thinning lamella to electron transparent thickness. The bright snow-like particles around the perforation is probably damage from the gallium ion beam. The features in two local areas in the left image were observed at higher magnification, shown on right side. Two types of precipitates (dark and bright) formed along the grain boundary and in grains. Chemical composition analysis (not shown here) identified the dark precipitate is Cr-rich and bright precipitate is Mo-rich. In some areas, these two precipitates attach to each other. These precipitates are carbides that formed through a reaction with the carbon in the as-received stainless steel. Therefore, these carbide precipitates are mainly associated with the thermal effects.

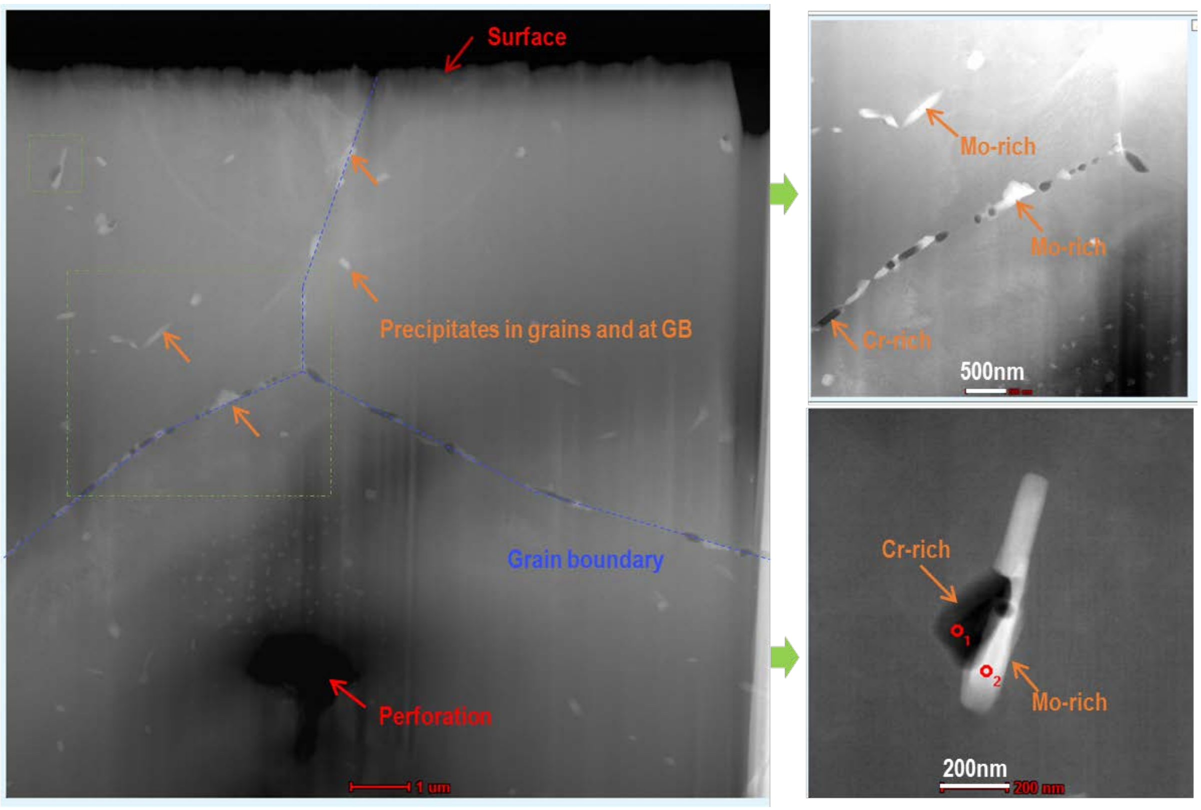

Figure 44: Scanning transmission electron microscope dark-field images focused on the near-to-surface layer of in-reactor corrosion tested 316 stainless steel in a 316 stainless steel lined crucible.

Figure 45 displays the STEM dark-field images of the 316 stainless steel sample tested in graphite crucible. This sample has similar microstructure as the one shown in Figure 44, lots of precipitates with needle, rhombus and strip shapes randomly distributed in the matrix. However, the density of precipitates is relatively higher here than in the sample in the 316 stainless steel-lined crucible. Additionally, more precipitates were observed underneath the corrosion surface. This is probably due to the inward diffusion of carbon from the wall of graphite crucible. The extra carbon reacts with alloying elements in stainless steel and forms more precipitates than the one in the 316 stainless steel-lined crucible. More interestingly, as shown in the lower right image, no precipitate was observed in low angle grain boundaries, which is consistent with the out-of-reactor corrosion samples. [10] Additionally, the cross-sectional STEM images in Figure 44 and Figure 45 suggest that the grain boundary on the alloy surface was attacked deeper than other areas.

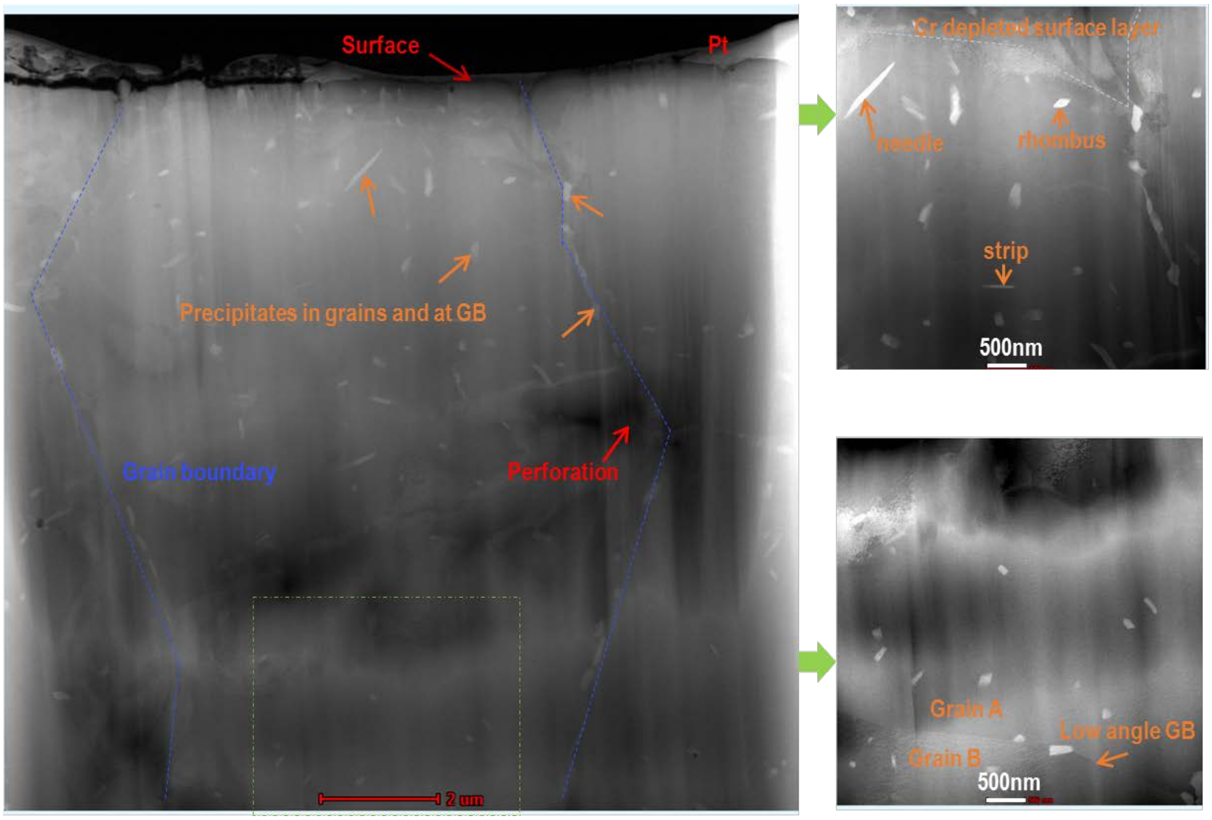

Figure 45: Scanning transmission electron microscope dark-field images focused on the near-to-surface layer of in-reactor corrosion tested 316 stainless steel in a graphite crucible.

Figure 46 shows the STEM images of the near-to-surface layer of Hastelloy N sample tested in molten flibe salt in nickel lined crucible. Different from the 316 stainless steel samples above, the Hastelloy N grains are clean, with no irregular nano-sized precipitates. The uneven surface of Hastelloy N is the evidence of corrosion attack in the molten flibe salt. Many round Mo-rich precipitates aggregate underneath the corrosion surface. The size of these Mo-rich precipitates ranges from a few nanometers to hundreds of nanometers. The high concentration of Mo in as-received Hastelloy N usually moves to surface and grain boundaries at high-temperature. It's reported that the solid solubility of Mo in Hastelloy N is approximately 12%. [11] Moreover, according to the Gibbs free energy of fluoride formation, Mo is resistant to the fluoride salt. On the other hand, with the depleting of Cr from alloy, plus the neutron irradiation accelerated corrosion ($2TF + M (Fe, Cr, Ni) = MF_2 + T_2$), the Mo within the surface layer aggregated and functionally formed a thin barrier layer against molten salt corrosion. Other than the Mo-rich precipitate underneath the surface, some Mo moved to grain boundary and coarsened, forming a discrete Mo precipitate at the grain boundary. The chemical composition analysis of the out-of-reactor tested samples identified that the chemical state of the Mo precipitate is molybdenum silicide.

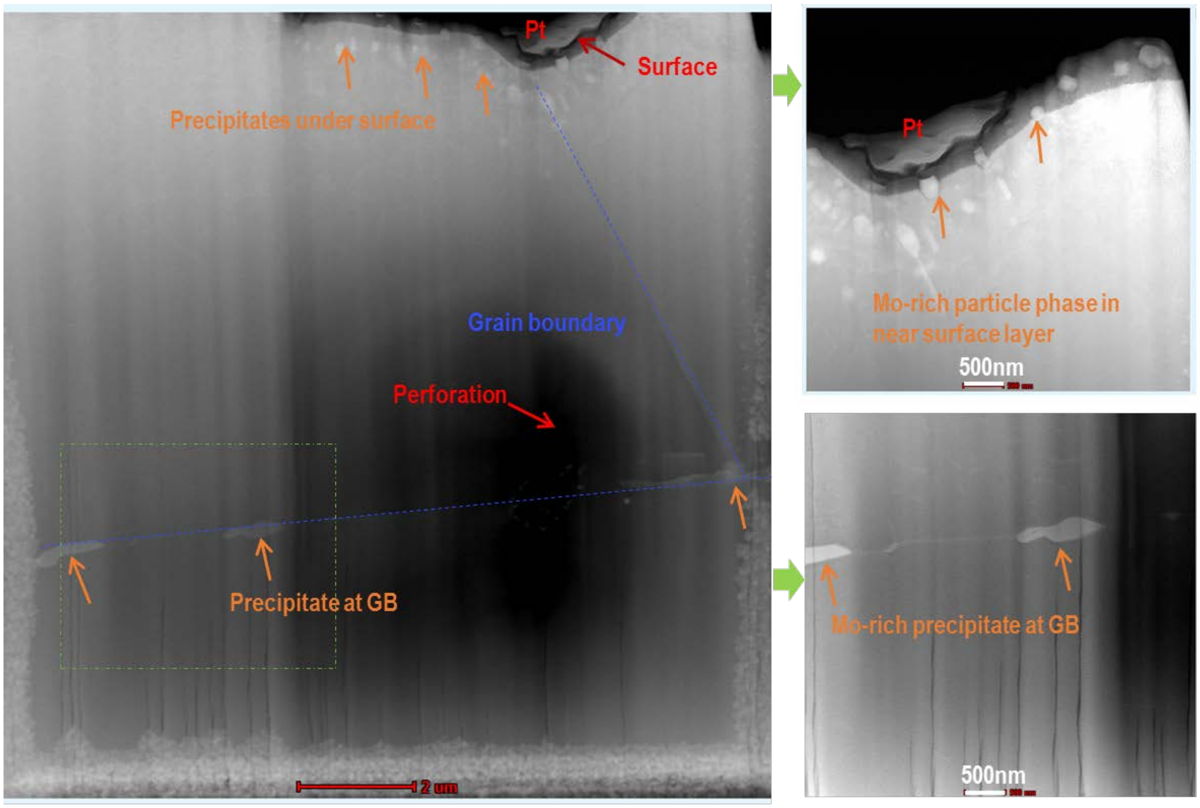

Figure 46: Scanning transmission electron microscope dark-field images focused on the near-to-surface layer of in-reactor corrosion tested Hastelloy N in a nickel-lined crucible.

Figure 47 shows the microstructure of the near-to-surface layer of Hastelloy N tested in a graphite crucible. To present an overview of wider range, two images were stitched together. The inside of this sample displays a similar microstructure as the one tested in a nickel lined crucible, with Mo-rich precipitates in grains and at grain boundaries. Unlike the out-of-reactor corrosion sample, in which a large numbers of new nano-sized carbide phases formed in the near-to-surface layer due to the inward diffusion of carbon, herein the cross-section of the grains is clean except the large Mo phase (several microns in diameter), in good agreement with the XRD analysis. This indicates that the carbon source liberated from the graphite crucible wall reacted with certain components in the molten salt under neutron irradiation, and that these reactions exhausted the carbon from molten salt. Therefore, the available carbon in the molten salt was dramatically reduced. One possible reaction that consumes the carbon is: $C + F^{-} = CF_4$ (gas) +4e. As mentioned above, the neutron irradiation broke the bonding between F^{-} and Be^{2+} and Li^{+} and then accelerated the formation of CF_4. This hypothesis needs further research to prove.

The chemical compositions of the small particles on the corrosion surface were qualitatively analyzed, as shown in Figure 48. The EDS spectra correspond to the two typical particles labeled as O1 and O2 in the upper right image in Figure 47. From the EDS spectra, it is known that the small particles on the corrosion surface might be Cr, Ni and Mo carbides or oxides or a mixture of both. No inward diffusion of these particles was observed, indicating that the particles formed after the corrosion test. The fresh corrosion surface is prone oxidation in the air or water while cleaning samples. Therefore, these surficial nano-sized particles did not impact the corrosion behavior of alloys in molten salt in the reactor.

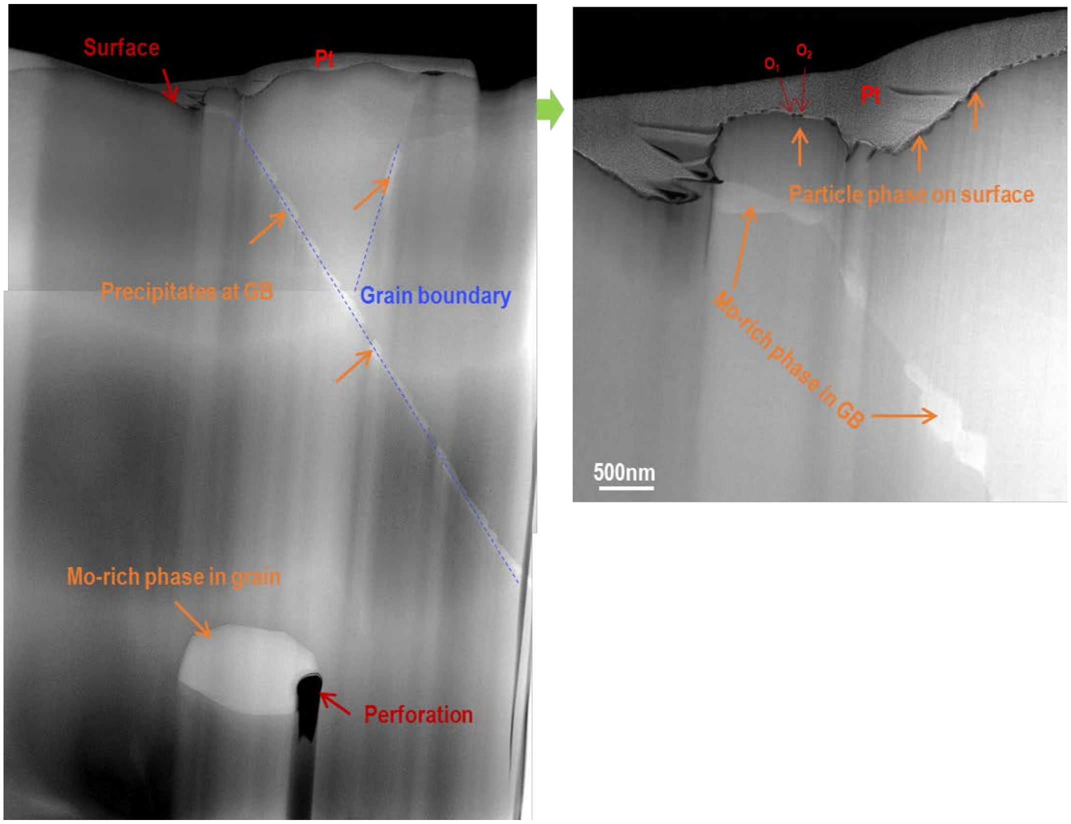

Figure 47: Scanning transmission electron microscope dark-field images focused on the near-to-surface layer of in-reactor corrosion tested Hastelloy N in a graphite crucible

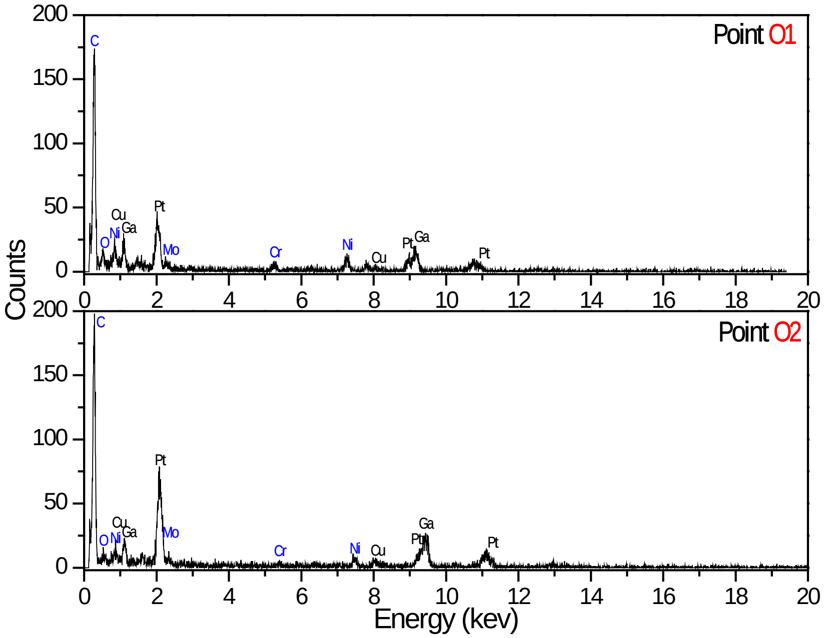

Figure 48: EDS profiles of nano-sized particle O1 and O2 labeled in Figure 47.

Neutron Irradiation Effects on the Corrosion of Hastelloy N in Flibe

In addition to the observation of micro features in the tested alloys, the high in-core neutron flux caused significant structural damage in the evidence of dislocation loops, as shown in the TEM images in Figure 49. The neutron irradiation-induced dislocation loops randomly distribute through entire grain, including the area close to grain boundary. Theoretically, the grain boundary functions as a sink for structural defects; the dislocation loops might move toward grain boundary at high temperatures. These kinds of dislocation loops were found in all of the in-reactor corrosion alloys.

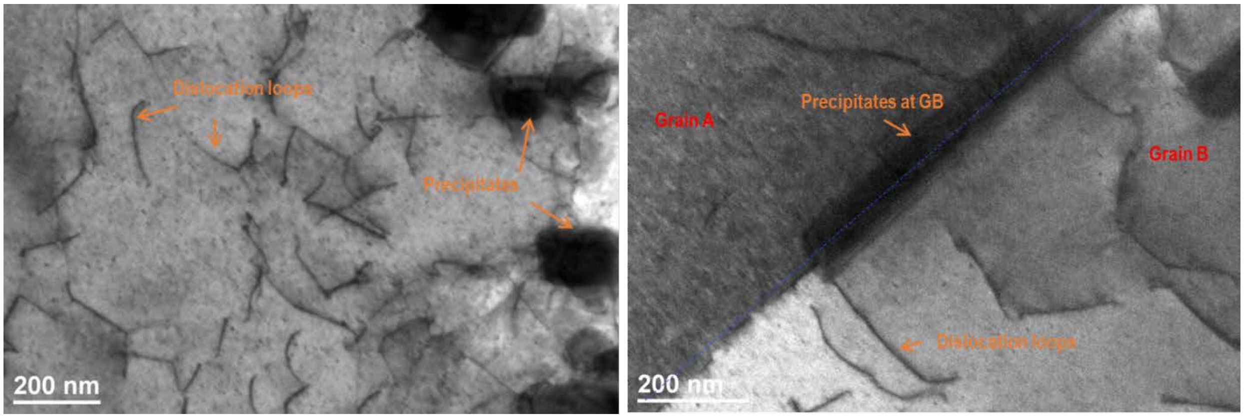

Figure 49: Transmission electron microscopy bright-field images of in-reactor corrosion tested Hastelloy N showing the neutron irradiation-induced structural damage in grain and near the grain boundary.

FS-3 Graphite Analysis

The surface of the FS-3 graphite samples were characterized by using scanning electron microscopy (SEM) and energy dispersive x-ray spectroscopy (EDS) to observe the surface morphology and to identify chemical compositions. Figure 50 shows the SEM images on different locations of the surface of a graphite sample with high degree of graphitization, TFX-10. Lots of frozen salt with various shapes on this sample's surface. This kind of residual salt left on sample's surface is relevant to the surface geometry. As shown in Figure 50 (a), the salt left on the rough edge of engraved letter "B" is more than other area. Some typical salt nuggets and particles on these SEM images are highlighted with blue arrows. This sample surface was fine polished before starting in-core irradiation test in molten salt, smoother than other samples' surface. Therefore, the graphite surface is just partially covered by frozen salt while extracting from molten salt. Most other samples' surface is completely covered by frozen salt.

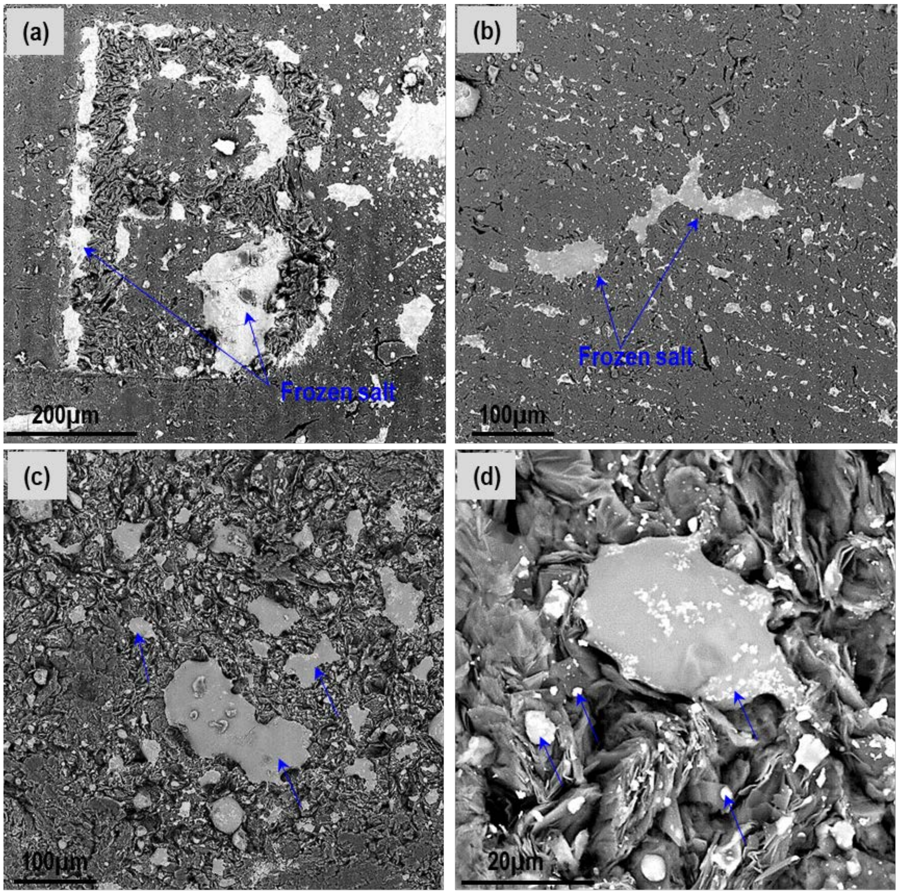

Figure 50: SEM images on the surface of the graphite sample (TFX-10 (V13), provided by SINAP) that was irradiated in molten flibe salt at 700°C in the MITR core (FS-3 in-core experiment) for 960 hours, showing various morphologies of frozen salt on its surface after extracting from crucible. Blue arrows in these SEM images denote the frozen salts.

Figure 51 shows the SEM image, EDS mappings and spectrum on an area of the sample surface shown in Figure 50. The flibe salt components Li and Be are too light to be detected by EDS, but fluorine is clearly identified (Figure 51 (d) and (e)). The detected oxygen peak in EDS spectrum is resulted from the dusts while handling samples in glove box, or the moisture on salt surface while transferring sample to SEM chamber.

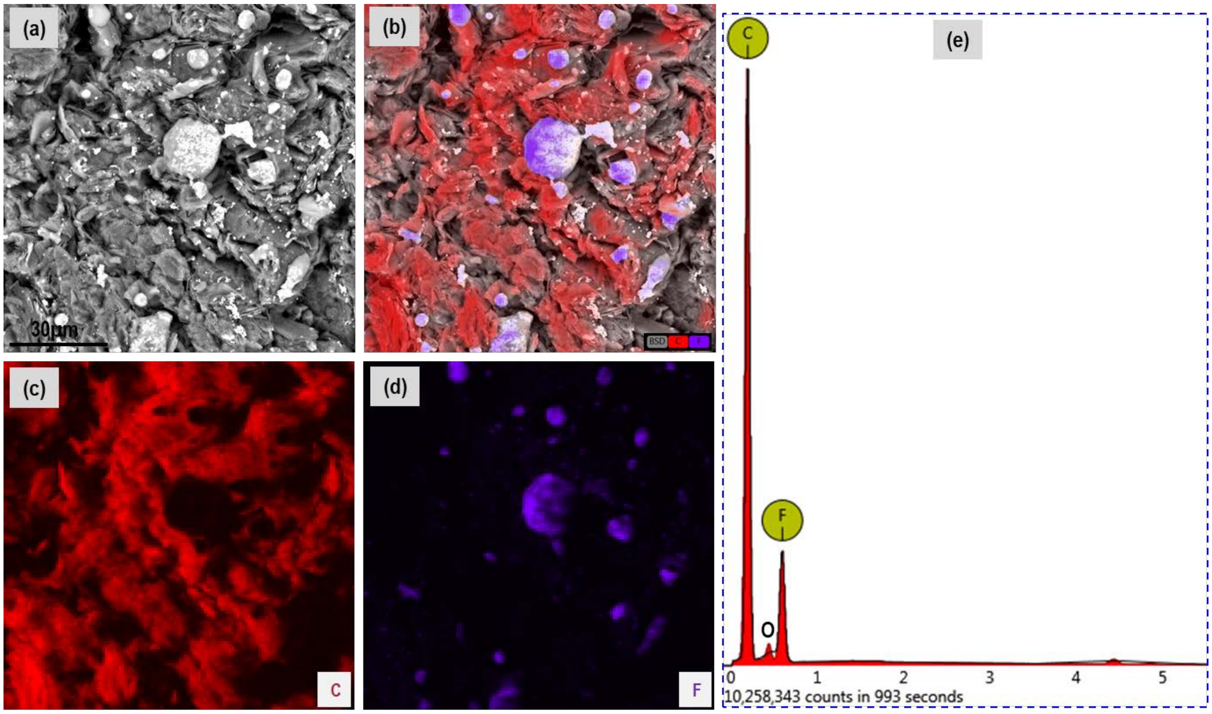

Figure 51: SEM image, EDS mappings and EDS spectrum on an area of in-core molten salt tested graphite's surface shown in Figure 50. (b) is overlapped EDS mappings on SEM image showing the main elemental distribution. (c) and (d) are the EDS mapping of carbon and fluorine, respectively.

8. Conclusions

The FS-3 irradiation has a number of important accomplishments for research into FHR core materials. First is continuously running the high-temperature corrosion tests of 88 graphitic specimens with various shapes in molten flibe salt and 7 disc control samples without salt at 700°C for about 960 hours of irradiation. Second success of this FS-3 in-core experiment is the use of an in-core electric heater to minimize the fluorine generation from solid salt and possible chemical decomposition under neutron irradiation at temperatures lower than 200°C. Third, addition of H_2 in the sweep gas significantly minimized the absorption of tritium on the surface of gas tubing and thimble compared to FS-1 and FS-2. The chemical state of the tritium from both capsule and thimble systems is dominantly insoluble such as T_2 and TH, unlike the previous irradiations. This indicates the reduced adsorption prevented catalysis of further reactions that change the chemical state of the tritium in the sweep gas.

Compared to out-of-reactor molten salt corrosion, neutron irradiation induced tritium generation in molten flibe salt and caused molten salt chemistry changes. Nano carbide particles were not found in the near-surface layer of in-core corrosion samples due to the tritium in molten salt. A large number of line dislocation and dislocation loops, evidence of neutron irradiation-induced structural damage, were observed in grains and near to grain boundaries in all four tested samples. The precipitates in the alloy probably inhibit the movement of the line dislocations. In summary, neutron irradiation accelerated the corrosion only on alloys' surface by changing molten salt chemistry. However, the irradiation- induced structural damage might influence the corrosion resistance of alloys in molten salt in the longer term.

9. References

1. D. CARPENTER, et al., "Fluoride Salt High-Temperature Reactor Materials Irradiation Test at the MIT Research Reactor," *Proceedings of ICAPP*, Charlotte, USA, April 6-9 (2014).
2. D. CARPENTER et al., "Findings of the Second Round of Fluoride Salt High Temperature Reactor Materials Irradiation Tests at the MIT Research Reactor," *Proceedings of the 2015 International Conference on Advances in Nuclear Power Plants: ICAPP 2015*, Nice, France, May 3-6, 2015.
3. H. MORIYAMA, et. al., "Chemical Behaviors of Tritium Formed in a LiF-BeF2 Mixture," *Journal of Nuclear Materials* **148**, (1987) 211-216.
4. M.R. AMES, "Minor and Trace Elements in Flibe after Purification and Corrosion Testing," *Transactions of the American Nuclear Society* **112** (2015).
5. L.H. GEVANTMAN, "Solubility of Selected Gasses in Water," CRC Handbook of Chemistry and Physics 96th ed., Internet Version, http://www.hbcpnetbase.com/ accessed 3/2016.
6. A. SUZUKI, T. TERAI, and S. TANAKA, "Tritium Release Behavior from Li2BeF4 Molten Salt by Permeation Through Structural Materials," *Fusion Engineering and Design* **51–52** (2000).
7. G. Zheng, B. Kelleher, L. He, G. Cao, M. Anderson, T. Allen and K. Sridharan, "High-temperature corrosion of UNS N10003 in molten Li2BeF4 (flibe) salt", *CORROSION* **71**(10) (2015) 1257-1266
8. G. Zheng, B. Kelleher, G. Cao, M. Anderson, K. Sridharan, T. R. Allen, "Corrosion of 316 Stainless Steel in High Temperature Molten Li2BeF4 (flibe) Salt", *Journal of Nuclear Materials* **461**(2015) pp. 143-150
9. G. Zheng, D. Carpenter, L. Hu, K. Sridharan, "High temperature corrosion of structural alloys in molten Li2BeF4 (flibe) salt", *Advances in Materials Science for Environmental and Energy Technologies V: Ceramic Transactions*, September, 2016, **260** pp.93-101
10. G. Zheng, L. He, D. Carpenter, K. Sridharan, "Corrosion-induced microstructural development in 316 stainless steel during exposure to molten Li_2BeF_4 (flibe) salt", *Journal of Nuclear Materials* **482** (2016) pp.147-155
11. R.E. Gehlbach, H.E. McCoy, "Phase Instability in Hastelloy N,"*International Symposium on Structural Stability in Superalloys* (Warrendale, PA: TMS, 1968), p. 346-366
12. A. Mascitti and M. Madariaga, "Method for the Calculation of DPA in the Reactor Pressure Vessel of Atucha II," *Science and Technology of Nuclear Installations* **2011**.

4. Experiments and Modeling for Thermal Hydraulics, Neutronics, and Structural Mechanics

This task involved developing an experimental program and modeling capability for the FHR thermal hydraulics, neutronics, and structural mechanics, including safety modeling of passive decay heat removal systems during accident scenarios. Experimental data was used to validate models where possible. The major effort was led by the University of California at Berkeley with two major activities in thermal hydraulics and neutronics and several smaller activities at the University of New Mexico and MIT. There are five reports on these activities.

- FHR Experiments and Modeling for Thermal Hydraulics (UCB)
- FHR Neutronics Analysis (UCB)
- Experimental and Computational Investigation of Twisted Tube Heat Exchangers (UNM)
- Methodology for Thermal-hydraulic Uncertainty Propagation Licensing Analysis for a FHR Test Reactor – Uncertainty Propagation of Coolant Properties (MIT)
- Effects of Radiative Heat Transfer in High-Temperature Liquids-Salts (MIT/UCB)

4.1. FHR Experiments and Modeling for Thermal Hydraulics (UCB)

FHR Experiments and Modeling for Thermal Hydraulics (UCB)[12]

Summary

This report describes the thermal hydraulics research at the University of California, Berkeley (UCB) related to the understanding and development of fluoride-salt-cooled, high-temperature reactor (FHR) technologies.

A class of heat transfer oils was discovered that in the temperature range of 50°C to 120°C allow simulation of the thermal hydraulics of 700°C liquid salt while matching the Reynolds, Froude, Prandtl, and Grashof numbers. This remarkable good fortune allows low-cost, low-temperature experiments to simulate the thermal hydraulic behavior of high-temperature salts. The CIET (Compact Integral Effects Test) Research Program, using these oils, was originally designed to drastically reduce the time and effort to experimentally simulate the system-level thermal hydraulic phenomena in FHRs. Experimental results would then be used to validate system thermal hydraulic models for modelling and simulation purposes as well as for licensing applications. Since its inception, the CIET Research Program has expanded its reach by building new capabilities that allow the CIET Facility to act as a small-scale reactor simulator. Now, additional areas of research and development related to FHRs and advanced reactors more generally include operation and performance, licensing, system design, human-machine interface, and fault detection. This new research is important for FHR understanding and development not only at UCB but for other organizations as well, such as DOE national laboratories and commercial organizations, such as Kairos Power.

This report is separated into sections to describe the physical enhancements to the CIET Facility including the addition of the Advanced Reactor Control and Operations (ARCO) Facility, experiments and analysis in the CIET Facility, separate effects test (SET) research efforts to support the CIET Facility and other areas of FHR technology development, and thermal hydraulics simulation models and analysis. Major conclusions for this project include:

- *CIET Facility Modifications:* Several physical modifications have been made to the CIET Facility primarily to improve the facility performance and to decrease scaling distortions between the model facility and a prototypical FHR. Physical modifications have led to the operation of the CIET Facility as a small test-scale nuclear reactor rather than a thermal fluids system, including the important addition of the ARCO Facility to allow the study of human-machine interfaces, operator performance, system optimization, and a range of other interesting fields of study such as critical infrastructure cybersecurity. Further research is being performed to identify areas of development possible with advanced integral effects tests, such as the CIET Facility, to establish clear plans of commercial technology development and licensing, such as for digital instrumentation and control systems and control and operation facilities in advanced reactors.
- *Frequency Response Testing:* Over the course of this work, a technique known as frequency response testing was implemented and studied with the CIET Facility. Frequency response testing provides a useful way of extracting information about reactors during operation. Among other things, it can be used for empirical model development, stability analysis, and parameter identification. Possible applications were tested with CIET to better understand the limitations and capabilities of this technique. The heater

---

[12] James Kendrick, Charalamus Andreades, Chris Poresky, Dan deWet, Limin Lin, Per Peterson

power control was then updated with simulated neutronic feedback control. This gives the ability to use a simulated control rod position and temperature feedback coefficients of reactivity with point reactor kinetics to calculate the heater output power. Fuel and coolant feedback coefficients were varied and a large variety of frequency response tests were used to extract information regarding the behavior of the CIET simulated reactor. Frequency response testing was able to show the stability of the reactor, as well as an understanding of the magnitude of temperature feedback.

TABLE OF CONTENTS

DESCRIPTION

This report describes the thermal hydraulics research at the University of California, Berkeley (UCB) related to the understanding and development of fluoride-salt-cooled, high-temperature reactor (FHR) technologies that were supported by an integrated research project (IRP) grant from the Department of Energy, Nuclear Engineering Universities Program (DOE NEUP). The report is separated into sections to describe the physical enhancements to the Compact Integral Effects Test (CIET) Facility including the addition of the Advanced Reactor Control and Operations (ARCO) Facility, experiments and analysis in the CIET Facility, separate effects test (SET) research efforts to support the CIET Facility and other areas of FHR technology development, and thermal hydraulics simulation models and analysis.

1 Introduction

Thermal hydraulic phenomena associated with FHR response to transients significant to reactor safety and performance evolve over short time periods of minutes to days. Therefore, the major constraint on FHR thermal hydraulic experiments is not duration, but instead power and physical scale because of the impracticality of performing thermal hydraulic experiments at the full-power levels of commercial reactors. The ability to use simulant fluids in scaled experiments to replicate molten salt system performance at reduced geometric scale, temperatures, and input powers was a significant development in molten salt thermal hydraulics and allows for the construction of laboratory-scale experiments that produce high quality data valuable for understanding of and technology development for FHRs. UCB has identified a class of heat transfer oils that match the Prandtl (Pr), Reynolds (Re), and Grashof (Gr) numbers of the major molten salts simultaneously, at approximately 50% geometric scale, temperatures between 50-120°C, and heater power under 2% of prototypical conditions. Dowtherm A, a eutectic mixture of two thermally stable compounds (biphenyl ($C_{12}H_{10}$) and diphenyl oxide ($C_{12}H_{10}O$)) can simultaneously reproduce the Re, Fr, Pr, and Gr for the major FHR candidate salts. Scaled systems using Dowtherm A require only a small fraction of the prototype pumping and heating power, which is very attractive in the design and construction of scaled experiments in laboratory settings. Figure 52 shows the close agreement of the Pr for flibe, the prototypical coolant used in FHRs, and Dowtherm A across a common prototypical temperature range of an FHR core. The moderate distortions for Pr at both ends of the temperature range in Figure 52 are due to matching the average Pr through average fluid temperature and Gr through temperature difference in the scaled system.

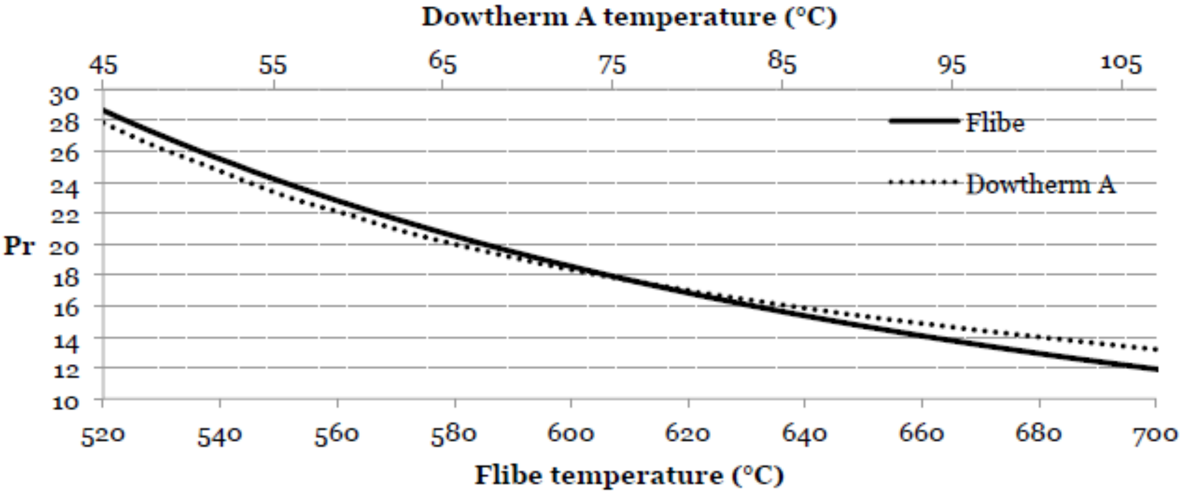

Figure 52. Impact of temperature on Pr in the prototypical and model systems (Zweibaum, 2015).

The use of simulant fluids not only makes experimental molten salt thermal hydraulics tenable in laboratory settings but they drastically reduce the costs of such experiments, dramatically reducing the barrier to entry for experimental molten salt thermal hydraulics. Further, simulant-based experiments use high-quality instrumentation and lab equipment (e.g. heating elements, pumps, heat exchangers, etc.) that allows these experiments to have wide ranges of applications to molten salt thermal hydraulics and molten salt reactor study in general. These very desirable qualities of simulant-based experiments for molten salt thermal hydraulics study directly inspired much of the work at UCB, culminating in the CIET Facility. Finally, we note that because simulant-based experiments are highly effective, relatively inexpensive, and straightforward to build and test with, an experimental strategy of using several simulant-based experiments in parallel or in series could be an effective way to quickly study a large space of phenomena or iterate on potential designs.

The CIET Facility was designed to provide data on the integral transient thermal hydraulic response of FHRs under forced and natural circulation, particularly startup and shutdown transients; loss of forced cooling (LOFC) and loss of heat sink (LOHS) accident transients; and passive, buoyant shutdown rod insertion during transients. CIET has two coupled flow circuits that replicate the primary coolant flow circuit in FHRs including bypass flow and the DRACS flow circuit, a natural-circulation-driven loop designed to passively remove decay heat from the FHR core and reject it to the environment through a thermosyphon-cooled heat exchanger (TCHX). Figure 53 shows a computer aided design (CAD) image of the CIET Facility with the major components identified as well as the front of the facility in real life. Figure 54 is a simplified piping and instrumentation diagram for the facility where major components are identified and the coupled-two-loop structure is clearly shown (in Figure 53 and Figure 54, CTAH is the coiled tube air heater, DHX the DRACS heat exchanger, DRACS the direct reactor auxiliary cooling system, and TCHX the thermosyphon-cooled heat exchanger). As an integral effects test (IET), the driving purpose of CIET was to provide validation data for evaluation models of FHR thermal hydraulic systems, such as RELAP5-3D, so that the evaluation models may be used to provide a licensing basis for advanced FHR designs. The power of IETs to perform this work and aid in the process of reactor design licensing was proven by the APEX-AP1000 facility.

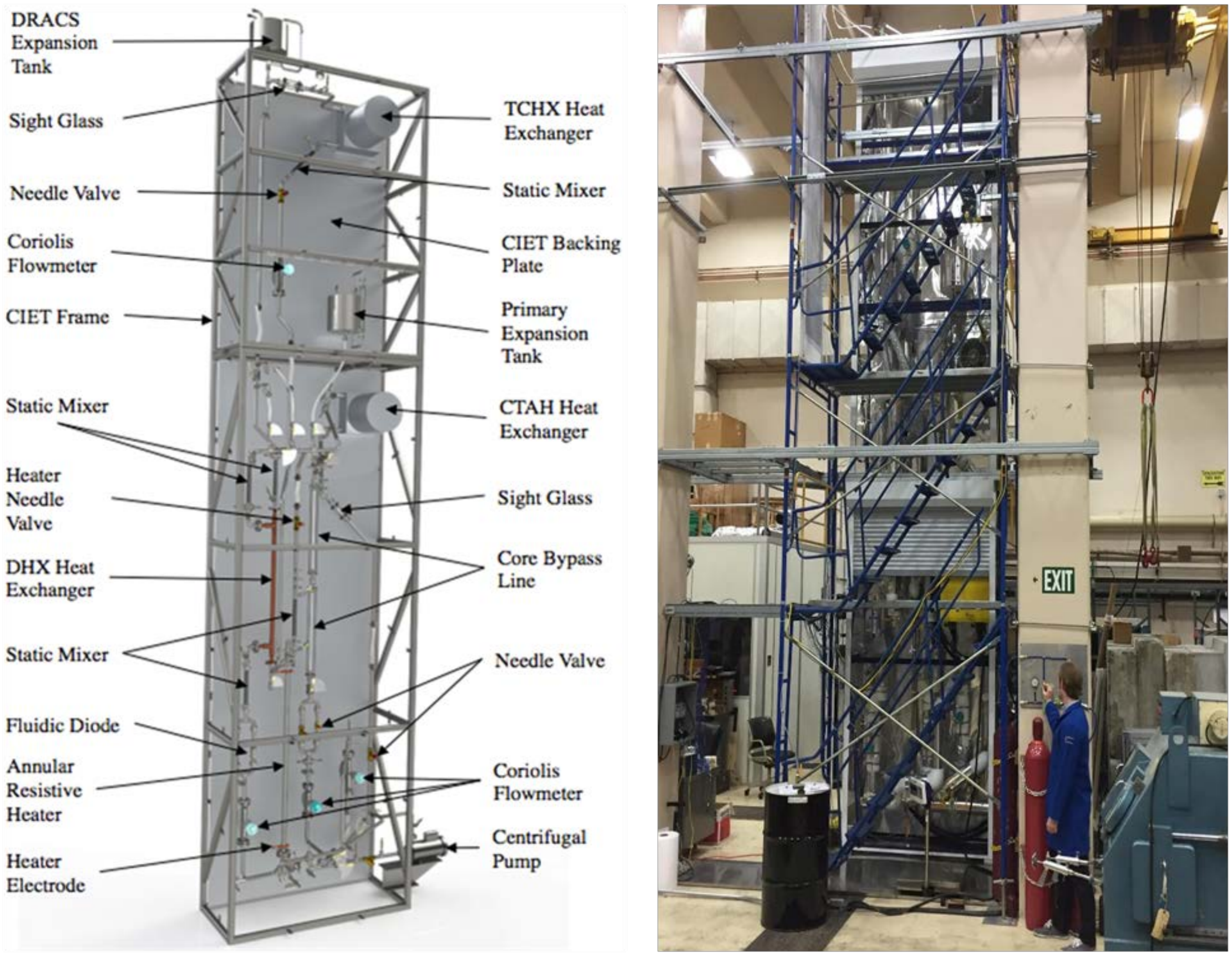

Figure 53. 3-dimensional rendering of CIET with the main components identified (left) and a picture of the facility in reality (right).

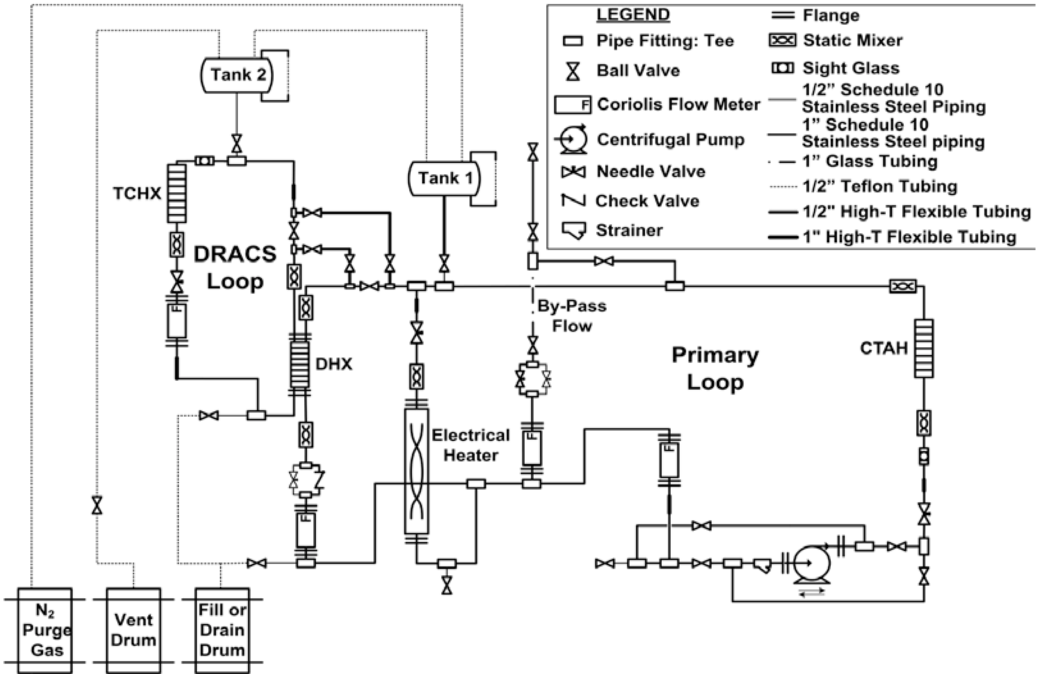

Figure 54. Simplified CIET piping and instrumentation diagram.

Scaling of CIET was based on an earlier PB-FHR commercial design, and therefore does not exactly match the current Mk1 PB-FHR design. Naturally, there will also be distortions between CIET and future FHR commercial prototype reactors resulting from non-matched relative coolant residence times, the use of reduced flow area stainless steel piping with non-scaled thermal inertia, and differences in relative length scaling of key components. However, CIET will act as a proof-of-concept and provide useful validation data for a generic set of FHRs. Given the low cost and time required for construction, final code validation for a future commercial FHR prototype plant would likely include the construction of a CIET-like facility that would closely match the prototypical design.

2 Compact Integral Effect Test Facility Physical Enhancements

The CIET Facility became operational in December of 2014 and was primarily designed and constructed to provide high-quality validation data for thermal hydraulic system analysis models for FHRs. To support this objective and to pursue several additional objectives, many physical modifications to CIET have been made, including the replacement of CIET's heater's inner structure to enhance heat transfer and thus the facility's power rating and the addition of the ARCO Facility.

2.1 Parasitic Heal Loss Evaluation

Parasitic heat loss tests have been performed on the Compact Integral Effects Test (CIET) facility. The goals were:

1. To identify major sources of heat losses between the fluid loop and ambient air, and to reduce these heat losses to a minimum by adding thermal insulation wherever needed and possible, and
2. To develop empirical correlations for overall heat transfer coefficient between the fluid loop and ambient air between pairs of temperature measurement locations.

These goals were achieved during the first quarter of 2015 by measuring fluid flow rates in each branch of the loop and fluid temperatures at many locations along the loop. Figure 55 shows a piping and instrumentation diagram for the loop, indicating the locations of all instrumentation.

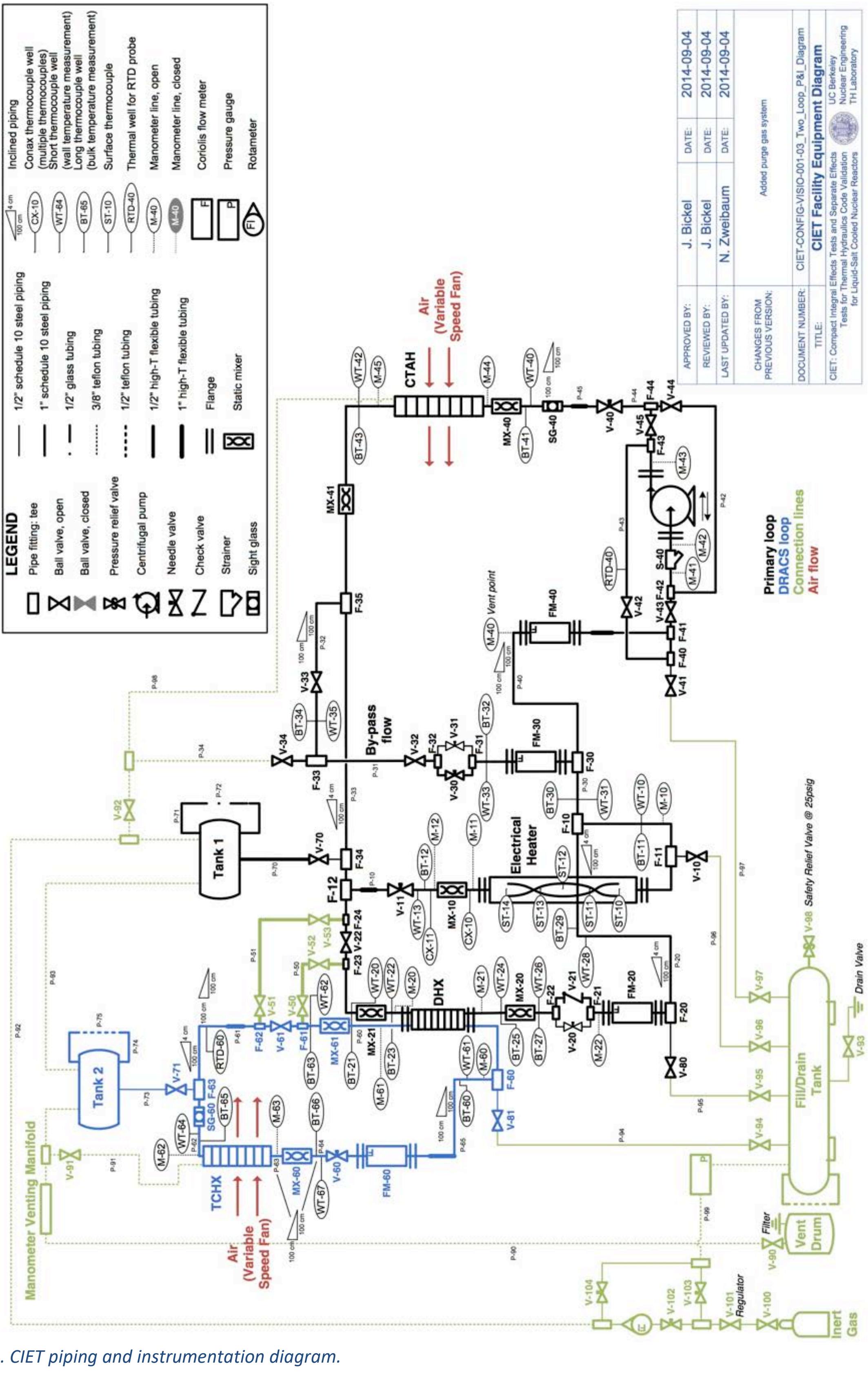

Figure 55. CIET piping and instrumentation diagram.

The tests were divided in several phases:

1. Parasitic heat losses in the primary loop: fluid is flowing through the heater and CTAH branches. The DHX, bypass branches, and DRACS loop, are isolated.
2. Parasitic heat losses in the DHX branch: fluid is flowing through the heater, DHX and CTAH branches. Because of relative friction losses in the heater vs. the DHX branch, about 80% of the flow goes through the heater and is heated while about 20% of the flow goes through the DHX branch. The DRACS loop is isolated.
3. Parasitic heat losses in the DRACS loop: the DRACS loop is connected to the primary loop (similar configuration used for pressure drop measurements in the DRACS loop). Fluid is flowing through the heater, DHX and CTAH branches, and through the DRACS. Because of relative friction losses in the heater vs. the DHX branch and the DRACS, about 90% of the flow goes through the heater and is heated while about 10% of the flow goes through the DHX branch and the DRACS.

An infrared camera (FLIR E4) was used to measure surface temperatures along the primary loop and identify locations where major heat losses occur. As expected and measured, significant heat losses occurred at the CTAH heat exchanger (Figure 56). These do not need to be minimized since it is the role of the CTAH to extract heat from the primary loop. On these pictures, manometer and thermocouple ports also appear as significant heat loss sources. These were subsequently covered with insulation to minimize heat losses.

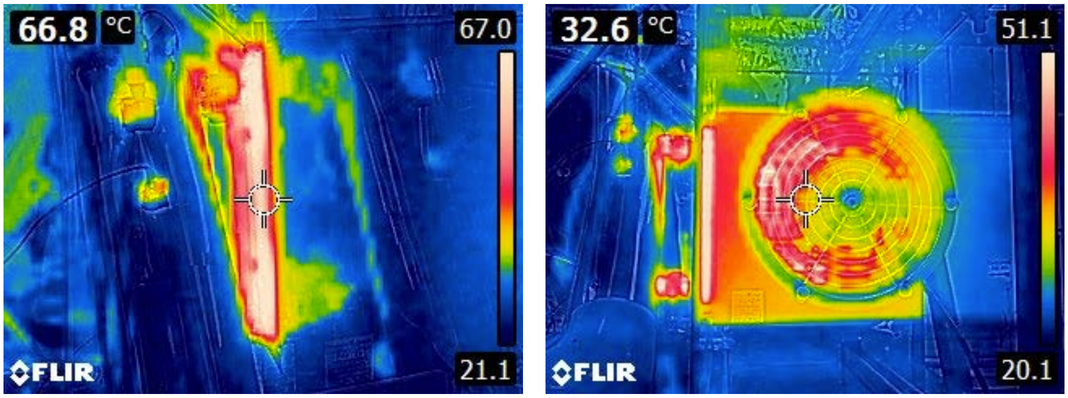

Figure 56. Infrared pictures of the manifold (left) and body (right) of the CTAH fan-cooled heat exchanger.

Non-negligible heat losses occurred at other locations that can be covered with easily removable insulation, such as needle valve knobs and sight glasses (Figure 57).

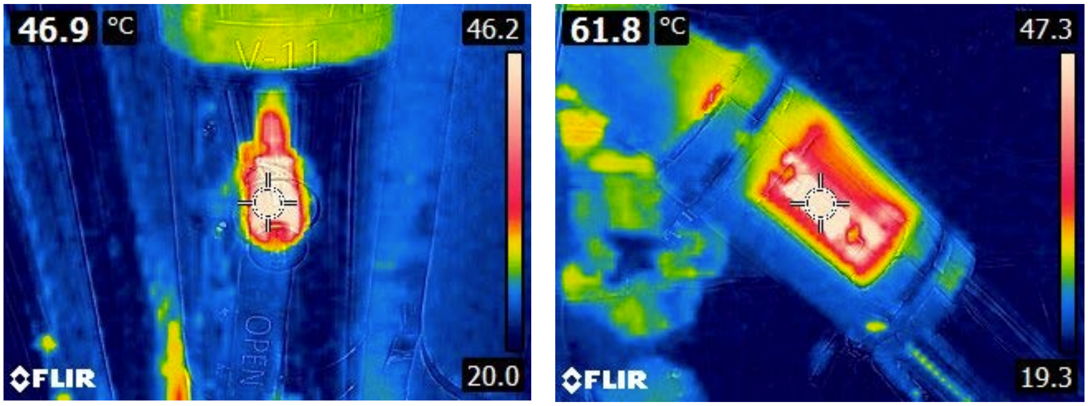

Figure 57. V-11 needle valve knob (left) and S-40 sight glass (right).

Finally, significant heat losses occurred at locations that could be better insulated with permanent insulation, particularly flanges for connections of the pump and electrical heater (Figure 58).

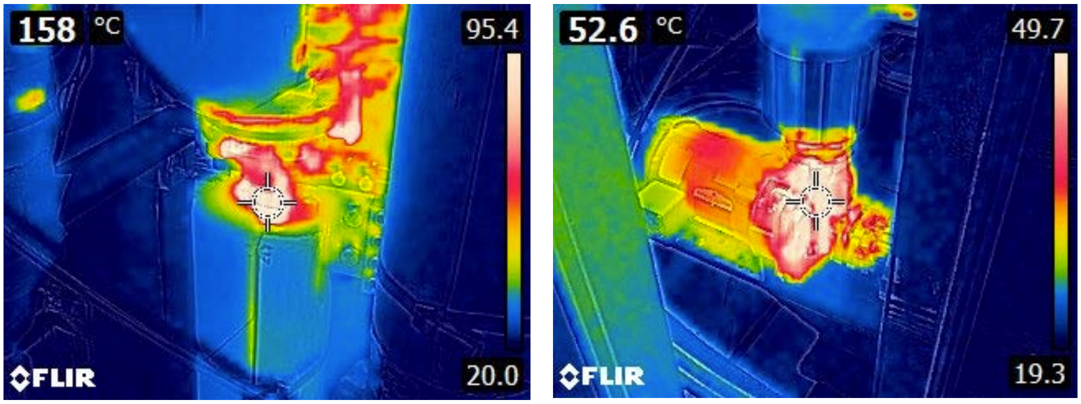

Figure 58. Electrical heater top flange (left) and primary pump (right).

All identified parasitic heat losses are reduced by:

1. Installing additional thermal insulation wherever possible, and
2. Implementing guard heating in the enclosure of the CIET facility, to raise the ambient temperature to be as near to the average temperature of the fluid in the loop as possible.

At locations where only thin, removable insulating pads had been installed have been complemented with flexible fiberglass insulation, as shown in Figure 59.

Figure 59. Installation of flexible fiberglass insulation underneath the removable insulating pads.

2.2 CIET Experimental Program Audit

Over the project lifetime for the CIET Facility, the research program has been conducted according to a quality assurance program designed to comply with the accepted nuclear-grade quality assurance standard used in the U.S. (ASME NQA-1, specifically the 2008 version with the addenda from 2009, which has been endorsed by the U.S. Nuclear Regulatory Agency as satisfying 10 CFR 50 Appendix B requirements). This quality assurance program has been maintained and modified throughout the project lifetime, and as part of these efforts the quality assurance program was audited annually by an expert, external consultant – summaries of these audits are given in this section.

2.2.1 2015 Audit

During the middle part of 2015, the CIET experimental program's quality assurance program was audited. The conclusion from the audit was very positive:

> "The CIET program has taken considerable actions to address the findings and corrective actions from the previous year's audit results. The corrective actions to address the findings were mainly addressed with only a few portions of a couple requirements remaining to be addressed. These few portions are represented by the three findings. This demonstrates a significant improvement over previous year's results."

This was a strong reflection of the CIET Test Program's commitment to quality assurance in its research efforts.

2.2.2 2016 Audit

Daren Jensen, the Quality Assurance Management System Lead at the Idaho National Laboratory, performed the program's annual Quality Assurance Program independent audit in May, 2016, on-site. The overall performance rating is, "Marginally Effective/Meets Some Requirements," which is a decline from previous performance ratings mainly due to staff turnover and limited knowledge transfer and continued training; all personnel involved in the initial building and implementing of the Quality Assurance Program except for Prof. Peterson are no longer part of the UCB community. The audit resulted in 2 noteworthy practices, 10 findings, 2 observations and 4 judgments of need.

The primary conclusion from the audit was that, "documentation is mainly in place, what is lacking is the updating, maintaining and implementation of the programmatic aspects of the QA program." Fortunately, the technical aspects of the quality assurance program that ensure detailed procedures for experiments and data collection were maintained. The path forward for the CIET Quality Assurance Program was primarily programmatic in nature, and significant emphasis must be placed on continual training and indoctrination of students and staff that support the program so that there will not be responsibility gaps as students and staff exit the program. Positively, "although there was little knowledge transfer or training of QA Program requirements for new CIET students/staff, they have taken on learning the QA program and are diligently seeking to understand and implement the QA program. All interviewed understand the importance of the CIET program and the importance of quality assurance in producing the results of the program objectives."

2.2.3 2017 Audit

We are currently drafting a new quality assurance program to use for the continued operation and modification of the CIET Facility. The original quality assurance program has proven difficult to maintain as students have graduated and research priorities have shifted in the lab, although quality assurance has remained an important feature of our research. The new quality assurance program strives to address three primary challenges faced by the old program that are inherent to university research environments:

1. The need for clear personnel roles and responsibilities while being flexible to changing personnel and shifting program goals
2. The need for a simple, clearly organized quality assurance program with a minimal set of procedures

3. The need for regular and rigorous training and education of program personnel to ensure continued and proper use of the quality assurance program

In December 2017, we concluded the first audit of the new quality assurance program. At that point, the new quality assurance program consisted of drafts of a quality assurance plan and a set of implementation documents or procedures that would be used in the research program to satisfy quality assurance requirements. The rating from this audit was, "Marginally Effective/Meets Some Requirements," because the new quality assurance program was still in draft form, did not address all the applicable requirements from NQA-1, and had not been implemented in the CIET Research Program. These are all correct findings and are as expected.

Moving forward, the findings and judgments of need from this audit will be the first list of items to be addressed in the revised draft of the new quality assurance program for the CIET Research Program. After sufficient review, the new quality assurance program will be implemented in the CIET Research Program for a significant duration before undergoing a second quality assurance program audit. At that point the goal is for the new quality assurance program to be judged, "Effective/Meets All Requirements." This future work is also planned to be published in detail to allow for the transparency and detail needed for other nuclear engineering research laboratories at other universities to replicate our efforts.

2.3 CIET Heater Flow Instability and Enhancement

During the initial heated testing of CIET, including steady-state and transient operation, oscillations in coolant temperature were observed at the heating element outlet, as shown in Figure 60. The fluctuating fluid temperature at the CIET heating element outlet was not expected, but provided insights on the dynamic response of the CIET loop and its heat structures. As Figure 60 shows, a clear phase lag exists between oscillations at the heating element outlet, and oscillations at the inlet to the coiled tube air heater (CTAH), simulated by an oil-to-air cooler with a variable speed fan, immediately downstream. The phase lag and amplitude reduction occurs due to a combination of the advection time for the coolant from the heating element outlet to the CTAH inlet (8.5 seconds for 0.18 kg/s mass flow), and heat transfer to and from solid heat structures between the heating element and CTAH.

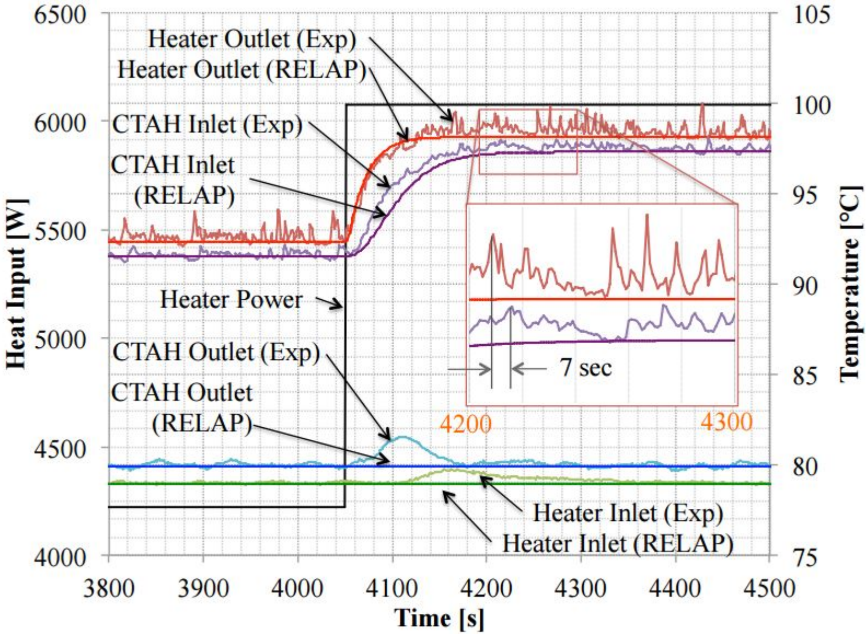

Figure 60. Oscillating coolant temperatures observed during CIET forced-circulation test 2015-04-28_Power_Step_Change_Transient_Test, involving a step change in heating element power from 4220 W to 6070 W at 4050 seconds.

By the time the fluid exits the CTAH the fluctuations damp greatly. However, it is that the proportional–integral–derivative control of the CTAH fan speed is imperfect in maintaining a constant CTAH outlet temperature immediately after the power step change, resulting in a temperature anomaly at the outlet. The time delay and amplitude reduction for this temperature anomaly to arrive back at the heating element inlet is also readily apparent and agrees closely to the predicted delay due to the 28.8 second fluid transit time from the CTAH outlet to the heating element inlet. CIET 1.0 was modeled in RELAP5-3D (Version 4.0.3ie) providing excellent prediction for the time averaged fluid temperatures, but this model was not capable of simulating the high-frequency fluid temperature oscillations.

Figure 60 depicts power step changes under forced cooling operation with a fixed mass flow rate that were performed primarily for validating the RELAP5-3D model for thermal inertia of the system’s solid structures and fluid inventory, which affects its response time to such transients. In particular, because the thermal capacity of the solid structures in the loop is of the same order of magnitude as the thermal capacity of the oil (approximately 50 kJ/K and 20 kJ/K, respectively), it is important to account for the fact that some heat structures are more tightly coupled to the system’s fluid inventory to accurately predict the system’s transient behavior. During model optimization, closer agreement between code results and experimental data is obtained by separating the weakly coupled thermal masses (e.g. flanges, valves) and the strongly coupled thermal masses (e.g. pipe walls) into separate heat structures in the RELAP5-3D model, based upon measured values for weights of individual components and the fact that weakly coupled thermal masses account for roughly 20% of the total weight of the system’s solid structures.

While the unexpected oscillations of the heating element outlet temperature led to a number of insights about the dynamic behavior of the CIET experiment, these oscillations are undesirable because they degrade the quality of the transient data collected in CIET for use in code validation. Likewise, such instabilities would be undesirable in an actual FHR, because they have the potential to drive heated surfaces to excessively high local temperatures and to generate fluctuating thermal stresses (i.e. thermal striping) that could lead to high-cycle fatigue and failure of structures. For this reason, additional experiments were performed to identify the cause of the instabilities in the annular heating element.

In the heated experiments, the flow rate of the coolant in the loop was measured with a Siemens SITRANS FC430 Coriolis mass flow meter. No fluctuation of the mass flow rate was observed, indicating that the instability occurs with a constant average mass flow rate. This observation implicated local buoyancy and/or viscosity induced flow instabilities as the likely cause of the temperature oscillations as temperature is observed to fluctuate independent of the bulk mass flow rate. Temperature oscillations were measured by two thermocouples in-line with the fluid at the exit of the heating element after a flow mixer. One thermocouple is close to the wall of the pipe and the other is closer to the center of the pipe. The average temperature measurement difference between these thermocouples during the most recent test (2015-10-22_Power_Step_Change_Transient_Test) was 0.63°C with a standard deviation of 0.13°C, indicating good agreement within the expected combined uncertainty of both thermocouples of +/-1.0°C. Therefore the temperature measurement of the fluid at the heating element outlet correctly reflects the fluid’s bulk temperature.

To identify the cause of the temperature oscillations, the outside surface of the heating element was instrumented with multiple thermocouples at elevations of 0.75 m (ST-12) and 1.52 m (ST-14) above the bottom of the 1.62 m long heated section.

These experiments showed that the CIET heating element has substantial azimuthal temperature non-uniformity around its circumference caused by flow instability. Figure 61 shows azimuthal temperatures at the vertical center (ST-12) and vertical top (ST-14) of the heating element during a low power step change test with power changing from 1500 W to 5000 W in 500 W steps; azimuthal positions are labeled based on their cardinal direction on the outer tube surface. Temperature distributions in the azimuthal direction at varying vertical locations are the most convincing evidence that flow instability does occur within the heating element. Figure 61 not only shows distinct azimuthal temperature distributions at the vertical center and vertical top of the heating element, but shows that the relative positions of the hottest and coldest azimuthal temperatures change throughout the test, a clear indication of flow instability within the annular heating element.

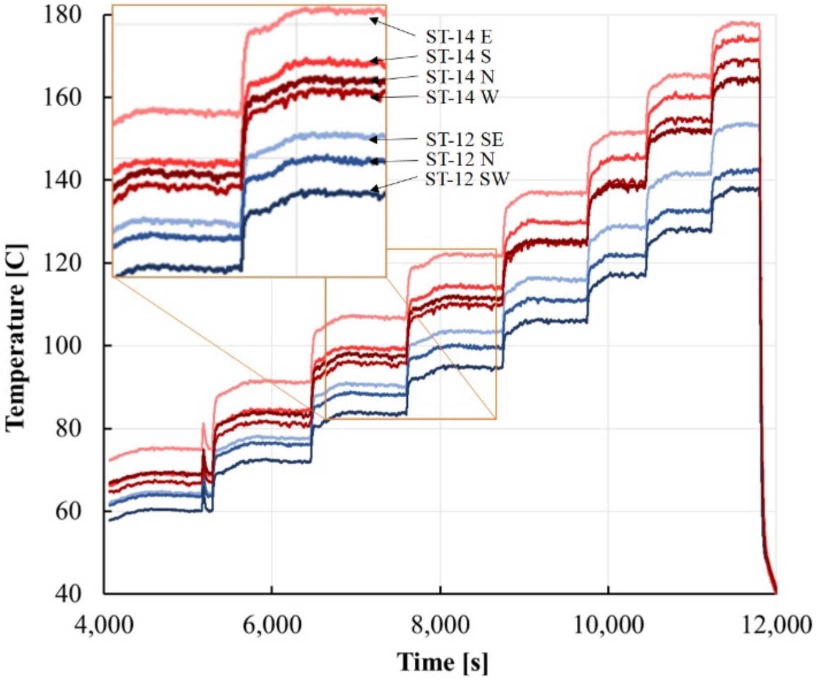

Figure 61. Azimuthal temperature distribution at the vertical center (ST-12, 3 blue lines) and vertical top (ST-14, 4 red lines) of the annular heating element during a low power step change test 2015-10-22_Power_Step_Change_Transient_Test.

To further investigate the cause of this flow instability, ultrasonic thickness gage testing, using the Olympus 38DL Plus ultrasonic thickness gage, was performed to measure the oil gap thickness between the inner and outer tubes of the CIET annular heating element. Three azimuthal positions were used as measurement points, as Figure 62 shows.

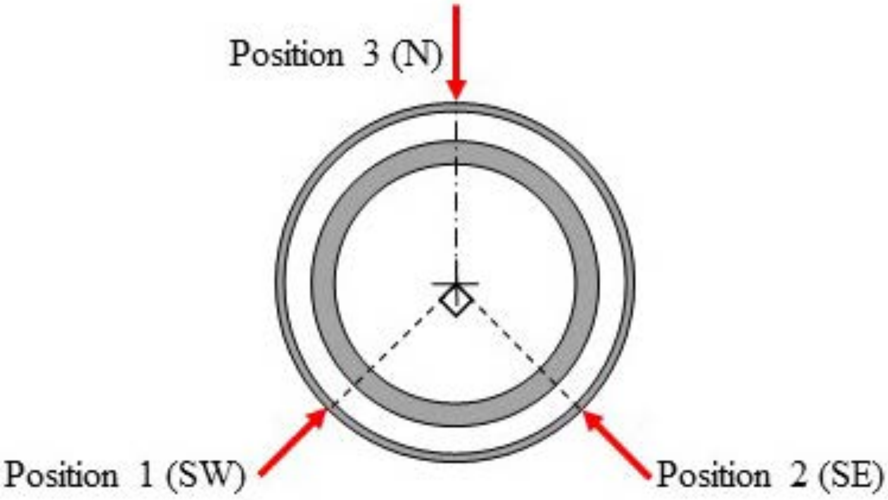

Figure 62. Azimuthal measurement locations of oil gap thickness measurements.

Geometry calculations were done to compare the measured oil gap thickness at each test position to generate the true center of the inner tube compared to the outer tube. Figure 63 shows that the three test positions (rotated to simplify the geometry calculations) and the three virtual circles created using the measurement data to find the true center, indicated in Figure 63 by the star at the center of the figure.

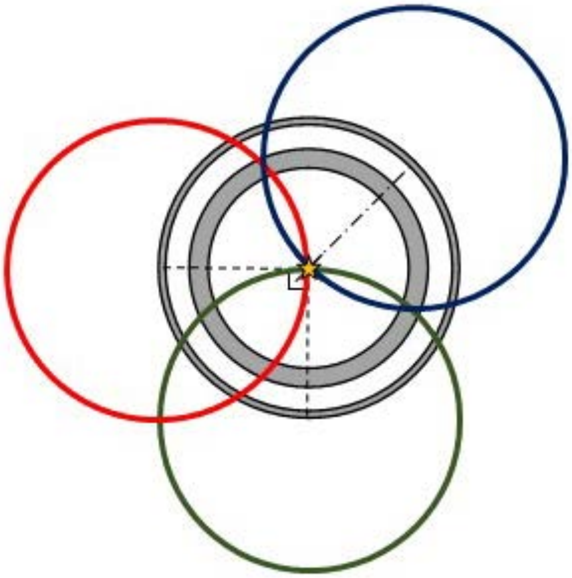

Figure 63. Virtual circles overlaid on the rotated heater assembly cross-section with the intersection and thus true center starred.

In theory, this data analysis technique should give a very precise and over-constrained measurement of the true center of the inner tube as compared to the outer tube. However, significant accuracy challenges come from accurately measuring the test positions on the outside of the outer heater tube, primarily azimuthally. Preliminary results confirm the misalignment and non-concentricity of the two tubes in the heating assembly, but the precise location of the inner tube relative to the outer tube is not known due to measurement error considerations. If deemed necessary, more precise results can be obtained by carefully locating test positions on the surface of the outer tube as well as several more redundant test locations, perhaps even eight azimuthal test positions. Figure 64 shows the approximate distortion of the inner tube from the desired position. The uncertainty, which primarily comes from the uncertainty of the testing position on the surface of the heater assembly rather than from the instrument itself, masks the true location of the inner tube but does support conclusively the suspected off-normal geometry.

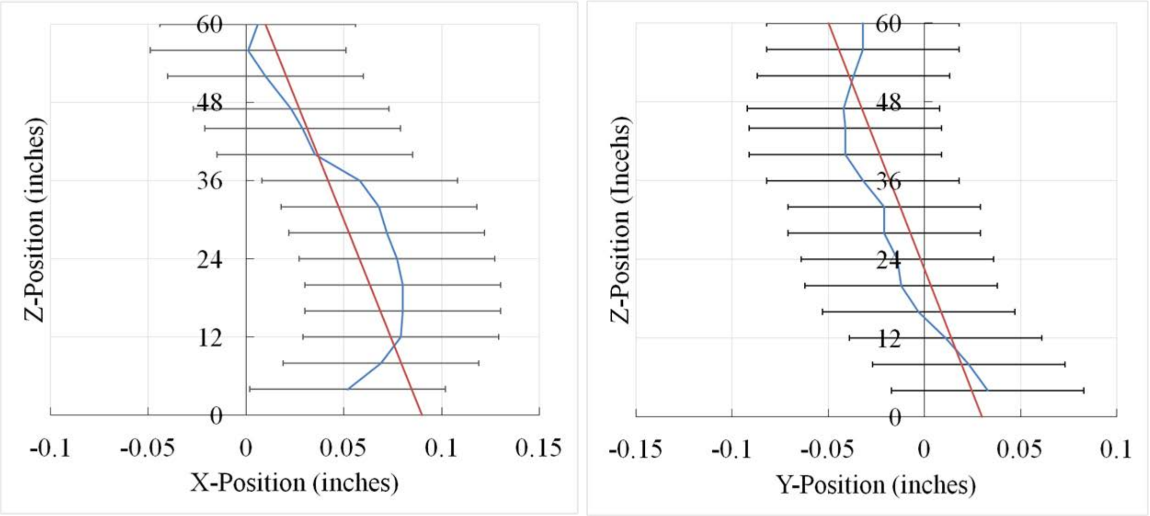

Figure 64. Displacement of CIET heater inner tube.

Rather than work to adjust the current heater configuration to be closer to the desired geometry, the replacement of the inner tube with a geometry that includes features to enhance the heat transfer within the heater was performed. An increase in the heat transfer capacity of the heater is effectively a power uprate for the CIET facility.

Undergraduate researcher Raleigh Lukas designed and commissioned replacement inserts for the heating element in the CIET Facility. Previously, the heating element was an annular configuration of two tubes with the outer tube being electrically heated and oil (Dowtherm A) flowing through the gap. A new insert was designed; the new heater inner assembly consists of a perforated tube with end caps and a twisted tape inside the perforated tube along its length. Two iterations of this new insert design were fabricated: one insert with 23% open surface of the perforated tube and one with 51% open surface.

Figure 65 shows the new heater insert design in more detail. The CAD drawings are idealized to show the perforations of the tube across the entire electrified length of the outer tube. However, due to the fabrication method of the perforated tubes, there is a spiral weld seem that is present across the perforated length of the tube. This spiral weld seam is seen in Figure 65 and in more detail in Figure 66. Figure 66 shows small segments of the perforated tubes before surface grinding with the twisted tapes. The different perforation open surface amounts can also be seen in Figure 66. More information is found in Table 8.

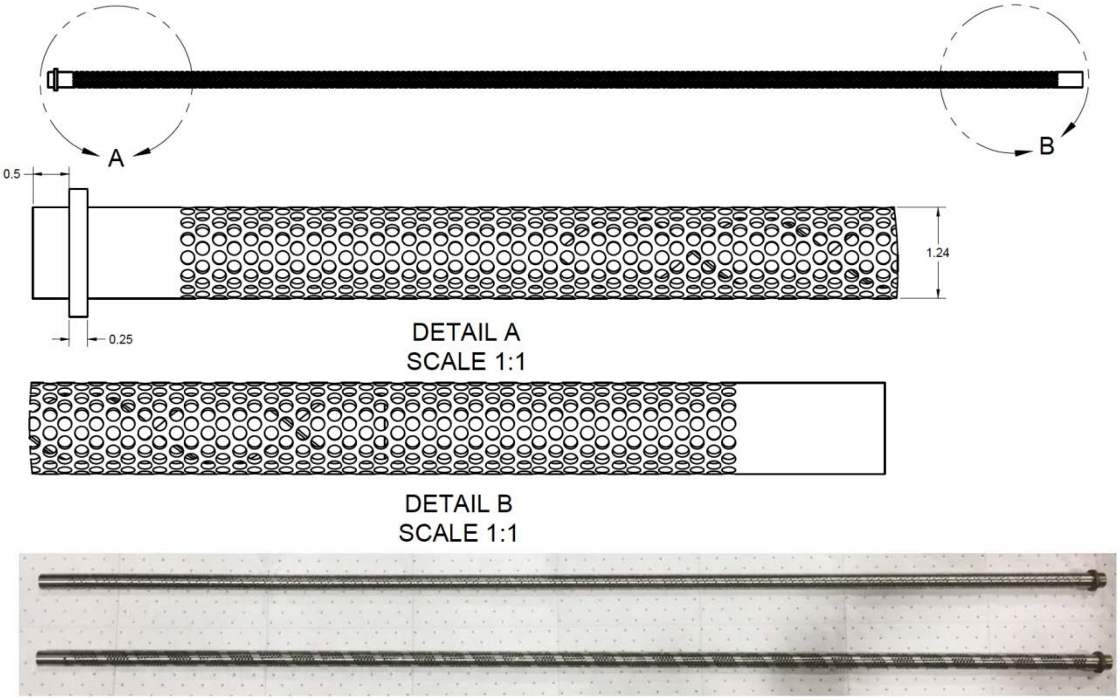

Figure 65. Idealized CIET modified heater CAD drawing (above, units in inches, NOT AS BUILT) and photograph (below, AS BUILT).

Figure 66. Detailed view of segments of the perforated tubes with the Teflon spacers (left) and twisted tapes (right); note the spiral weld seems.

Table 8. Dimensional data for the new heater inner tube inserts.

	51% Open Tube	23% Open Tube
Assembly mass (kg)	3.120	3.800

Length (cm)	216	216
Tape length (cm)	180.	180.
Tape diameter (cm)	2.54	2.54
Hole diameter (cm)	0.476	0.318
Hole pitch (cm)	0.635	0.635
Tube outer diameter (cm)	3.175	3.175
Tube inner diameter (cm)	2.725	2.725

To construct the new heater inserts, 304 stainless steel perforated tubes with 1.313" OD (3.34 cm) were first ordered and constructed by Perforated Tubes, Inc. (Figure 67, left). 304 stainless steel twisted tapes were made by Fuel Efficiency, LLC to be inserted within the perforated tubes (Figure 67, center). Finally, a 1.313" OD (3.34 cm), 304 stainless steel rod from McMaster-Carr was purchased to be used to machine the end pieces for the heater assembly in UC Berkeley's machine shop (Figure 67, right). These pieces were taken to a welder in Berkeley who used TIG welding to secure the tapes within the tubes and to attach the end pieces (Figure 68, left). These assemblies were then taken to General Grinding in Oakland, where they were centerless ground to 1.25"± 0.001" (3.175±0.003 cm) OD. Stainless steel collars were cut from a 0.25" (0.635 cm) thick stainless-steel plate with a water jet then welded to the tube assemblies to provide support for the inner tubes within the CIET facility's heater assembly (Figure 68, right). PTFE spacers were machined from a PTFE rod from McMaster-Carr in the UC Berkeley machine shop to prevent the inner assembly from contacting the walls of the outer tube and to ensure a uniform annular gap between the walls of the inner perforated tube and outer tube (can be seen in Figure 66, left). The final heater inner assembly is shown in front of the CIET Facility in Figure 69.

Figure 67. Components of the new inner assembly for the CIET heater: perforated tubes (left), twisted tapes (center), and end caps (right).

Figure 68. Finished heater assembly before centerless grinding and the addition of the support collar (left) and after (right).

Figure 69. Finished heater inner assembly in front of the CIET Facility.

The new heater inner assembly design was intended to increase the heat transfer between the oil and the electrified outer tube of the heater. Nusselt number correlations for twisted tapes indicate the effective heat transfer coefficient of the new configuration should be 93% of the current annular configuration, though these correlations can only serve to inform estimates because there is no literature on twisted tapes in combination with perforated tubes. Twisted tape correlations also indicate the modified heater will have only 24% of the pressure drop of the current configuration. Relevant results from CIET tests with the new perforated tube inserts for the heater and the previous plain tube insert are given below with corresponding analysis.

2.3.1 Nusselt Number

The Nusselt number correlation for the plain inner tube is given in Eq. (1). This correlation predicts all of the data within ±5% and standard deviation S = 0.4 at a heater power of 5 kW. The data were taken over the range 1773 < Re < 3955 and 14.3 < Pr < 15.3. The Nusselt number correlation for the 23% open tube with twisted tape is given in Eq. (2). This correlation predicts 95% of data within ±17% and S = 6.7. These data were taken over the range 1765 < Re < 7622 and 14.2 < Pr < 28.9. Finally, the Nusselt number correlation for the 51% open tube with twisted tape is given in Eq. (3). This correlation predicts 95% of data within ±6% and S = 3.4. These data were taken over the range 2160 < Re < 8690 and 14.0 < Pr < 29.5.

$$Nu = (2.65 \times 10^{-9})\Re^3 - (1.82 \times 10^{-5})\Re^2 + (4.18 \times 10^{-2})\Re - 22.1 \tag{1}$$

$$Nu = 0.0839 \times Re^{0.709} \times Pr^{0.201} \tag{2}$$

$$Nu = 0.0391 \times Re^{0.812} \times Pr^{0.408} \tag{3}$$

2.3.2 Friction Factor

The pressure drop data for the plain inner tube is correlated by Eq. (4). This correlation predicts all of the data within ±6% and S = 45.1 Pa at a heater power of 5 kW. These data were taken over the range 1773 < Re < 3955. The friction factor correlation for the 23% open tube with twisted tape is given in Eq. (5). This correlation predicts all of the data within ±4% and S = 0.03. These data were taken over the range 1769 < Re < 9015. Finally, the friction factor correlation for the 51% open tube with twisted tape is given in Eq. (6). This correlation predicts 95% of data within ±4% and S = 0.03. These data were taken over the range 1243 < Re < 9030.

$$\Delta P(Pa) = (3.50 \times 10^{-4})Re^2 - (1.13)\Re + 1550 \tag{4}$$

$$f = 70.6 \times Re^{-0.53} \tag{5}$$

$$f = 17.9 \times Re^{-0.34} \tag{6}$$

From equations Eqs. (2) and (3) we see that over the range of Reynolds and Prandtl numbers tested, the 51% open tube's Nusselt number is a much stronger function of Prandtl number than that of the 23% open tube (Prandtl number exponent of 0.408 vs. 0.201) and a slightly stronger function of Reynolds number (Reynolds number exponent of 0.812 vs 0.709). From Eqs. (5) and (6), we see that the 23% open tube's friction factor is a much stronger function of Reynolds number than that of the 51% open tube (Reynolds number exponent of -0.53 vs. -0.34). Table 9 below illustrates some observed values of the Nusselt number and heat transfer coefficient at prototypical conditions and compares them to literature values.

Table 9. Heat transfer properties of modified inner tubes: literature correlations and measurements.*

	Re	Nu (lit.)	h) (Lit.)	Nu (Obs.)	h) (Obs.)
23% open tube	6697	147	492	68.9	232
51% open tube	6312	141	473	139	469
Plain tube	3163	12.8	257	12.4	249

* at m=0.18 kg/s, P=5kW

Finally, graphs of the observed heat transfer coefficient and pressure drop as functions of mass flow rate at a heater power of 5kW are shown in Figure 70 and Figure 71. The observed data are also compared to literature data.

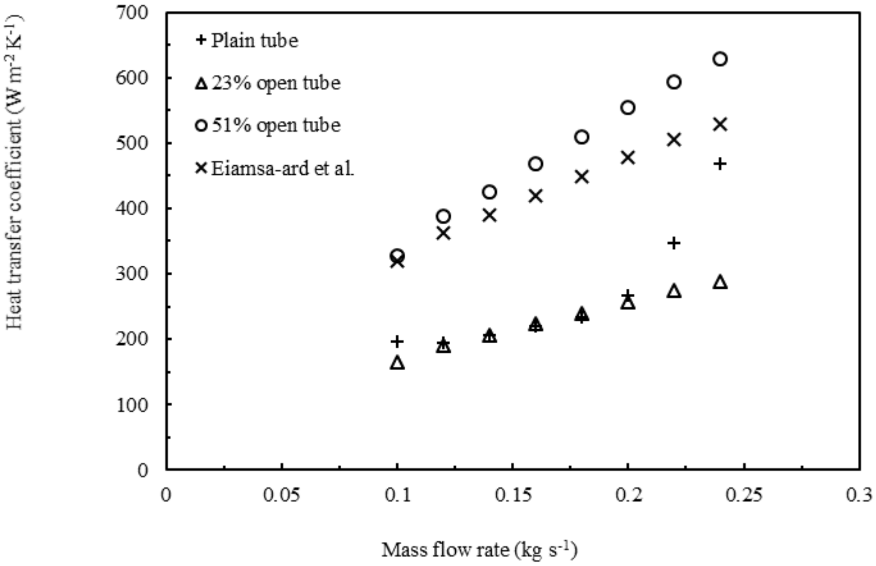

Figure 70. Heat transfer coefficient as a function of mass flow rate at P = 5kW for the various tube inserts; plain tube data from experiment, perforated tube data from Nusselt number correlations above.

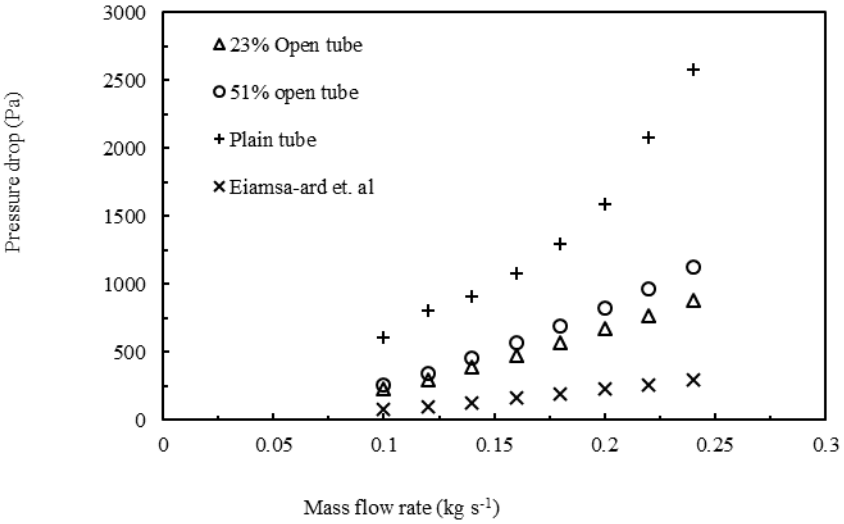

Figure 71. Pressure drop across heater as a function of mass flow rates at P = 5kW for the various tube inserts; plain tube data from experiment, perforated tube data from friction factor correlations above.

Other important observations and effects of the new tubes include:

- An increase of residence time in the heater by 157% for the 51% perforated tube, compared to the plain tube. The heater core now makes up 8.1% of the total system volume, compared to 3.3% previously.

- Turbulence is achieved at lower flow rates and temperatures. This helps reduce radial temperature differences at the heater outlet, as observed by the parallel thermocouples there.
- Much lower average and maximum surface temperatures, which drove the increased heat transfer coefficients observed. In addition, the maximum surface temperature is closer to the average with the new insert. This will enable a significant power uprate to the CIET facility, because the heater tube temperature is the primary limiting factor on heater power.
- The size of the perforations in the tubes was found to have a significant effect on the heat transfer properties of the tubes, and a minor effect on the pressure drop properties. The heat transfer coefficient of the 51% open tube over the range of prototypical conditions was about twice as high as that of the 23% open tube.
- Maximum achievable heater power with the 51% open tube is now 10kW or more; maximum power is dictated by maximum surface temperature.

2.4 Advanced Control and Data Acquisition System for CIET

The need for an advanced control and data acquisition system for CIET was identified. Major requirements include greatly increased data collection rates, greatly increased control signal rates, overall increase in response time of user interface, modern user interface that is more flexible for experiment control and has a flexible system architecture to meet future needs, and a user interface that is more prototypical of an advanced reactor using a digital control system. The control and data acquisition system is undergoing hardware, software, and software engineering upgrades to achieve these expanded and more demanding goals of the overall CIET Program.

Hardware

- NI PXI System: advanced hardware that has dedicated timing and synchronization components for system control and data acquisition; this hardware has its own CPU that will independently and reliably handle dedicated control and data acquisition processes
- Host computer: the computer that interfaces with the PXI System is being upgraded to use modern hardware and software to aid user interface and enhance the user capabilities of the overall system
- Control station: Large monitor screens (approximately 50 inches, three screens total) are being identified to be able to integrate as one seamless control interface with touch interface capabilities to simulate a modern advanced reactor control interface to maximize the effectiveness of a digital control system

Software

- NI LabVIEW 2015 with Real Time Module: advanced software that is designed to interface with the PXI System to allow for precise timing and synchronization; LabVIEW is a comprehensive software package that will allow for complete system control and data acquisition without the need for other software packages from third parties
- Others: other software suites are being determined that may aid in user interface and interactions, seamless control of the composite system, and advanced data analysis

Software Engineering

- Modern code architecture: significant effort is being placed in learning best practices for building a flexible, adaptable code architecture to achieve the stated goals as well as allow for expansion for future goals; this effort will lead into the design and implementation of a digital reactor control system for advanced reactors that will be a significant focus of the research in the CIET Program

Employing standard software development methodologies: to effectively interface with the quality assurance requirements dictated by NQA-1 as well as effectively organize the design and implementation of a digital control system for CIET and effectively for advanced reactors such as FHRs, this effort will employ a standard software development method. The best method for this application has yet to be determined, as this is still a nascent effort in the CIET Program

The architecture and code for the control system is currently under development, with a strong emphasis on best practices, as specified above. We're working with two professors in the Mechanical Engineering department at UCB to ensure the development of a modern, real-time control system architecture that serves our needs now and is able to be expanded well into the future. In parallel, the CIET Program's quality assurance plan is being reworked to be more flexible for transient staffing inherent in the university research environment. Emphasis is being placed on transparency and ease-of-use, while still striving to adhere to the high standards laid out in ASME's NQA-1.

A new control system architecture has been developed by dividing the system's functions into discrete tasks, and further separating these tasks into individual states that are performed in series. The new control system has been used in several new experiments that it has enabled, which have also highlighted future needs and capabilities for the control system as well. Research continues to improve the architecture further to be clearer and more flexible for expansion in the future.

Current work has been focused on connecting the primary control computer (the "Supervisor") to the other computers in the Advanced Reactor Control and Operations (ARCO) Facility (the "Reactor" and "Power Conversion" computers) to allow for communication of data and command signals from all positions. This will allow a distribution of responsibilities and enable plant operation and operator studies.

2.5 Advanced Reactor Control Interface

Critical to simulating the operation of an FHR is the operator interface. Driven by this philosophy, we are developing a modern control room layout and interface with which to conduct experiments using the plant simulation. While many experimental interfaces are designed with utility as the sole priority, a lack of consideration for human factors can often result in suboptimal control efficiency. We are therefore incorporating human factors engineering lessons from the nuclear and other industries to design and implement a unique control room theory of operations and set of human-machine interfaces. These human-machine interfaces will be instrumental for conducting plant operation simulations and incorporating scenarios related to cybersecurity and model-based fault detection. Thus far, the advanced reactor control and operations (ARCO) facility has been constructed and we are beginning the specification of capabilities and controls for each control console.

In service of expanding the control of CIET to include a simulated power conversion system and plant-wide operations, we have been continuing our work to develop the advanced reactor control and operations (ARCO) facility. After we completed construction at the end of 2017, we began the process of adding capabilities to simulate an entire FHR power plant. A key feature of ARCO distinguishing it from a traditional integral effects test control interface is that it seeks to emulate FHR control room concepts of operations. The configuration, which will enable the iterative development of unique roles and responsibilities for FHR operators, consists of digital interfaces for only three staff members (one supervisor and two operators) and two overview displays. In order to realize an advanced operations philosophy, we are planning a set of capabilities for online fault detection and prognostic health monitoring that will become intrinsic to experimental scenarios.

A Master of Engineering team has worked on simulating the FHR power conversion system and formulating models suitable for online fault detection. They have functionally implemented their system via new human-machine interfaces (HMIs) for operating CIET via ARCO. As of Q1 2018, these interfaces primarily allow control utility and have incorporated basic user-centered design principles. The team has used a schematic piping and instrumentation diagram on which they “mount” their indications and therefore reinforce an operator’s mental model of the system. They began testing their new interface to control their power conversion simulation from the operator stations and have identified some bugs in network communication that would allow simulations and CIET experiments to be run simultaneously with two-way feedback.

With an eye toward the future, we have begun wire framing and iterating individual display concepts to be used by each member of the control room staff and to coordinate the entire control room at the overview displays. Right now, these are hand-drawn diagrams to organize general size, shape, and placement of modules and applications such as digital communication tools, on-line data analysis, interactive procedures, health monitoring. We have built a 3D model of ARCO in the popular SketchUp software and will move on to detailed HMI design using this software. This practice will also facilitate design documentation and the establishment of a style guide to inform the design of future interface elements. Work beyond this point has been supported by a grant from the Center for Long-Term Cybersecurity and the Nuclear Energy University Program (NEUP) office within the U.S. DOE.

The current configuration of ARCO is shown below in Figure 72. ARCO has the workstations for a control room supervisor, a reactor operator, and a turbine operator, as well as two overview displays and an observer stool. Right now, CIET is operated from the control room supervisor workstation alone, with reactor and turbine simulations being run on each of the operator workstations independently. Once we successfully implement the networking capabilities, however, operation of CIET and the simulations will be connected, and control will be distributed across the three workstations.

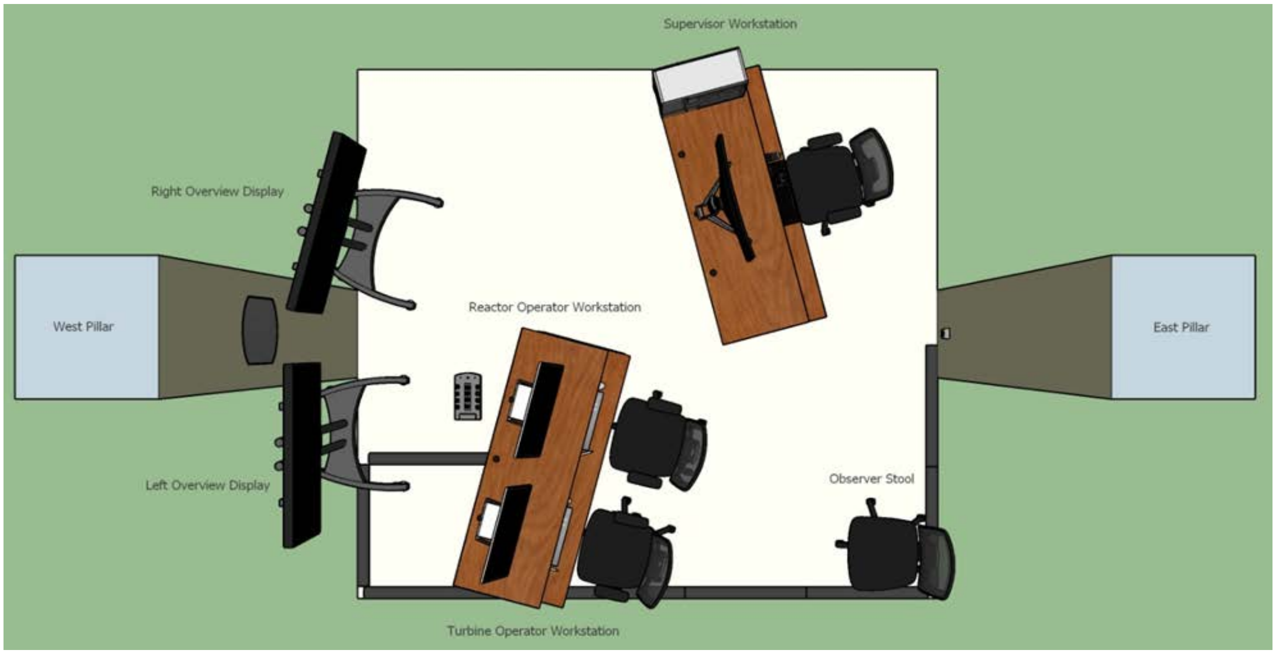

Figure 72. SketchUp overhead view of ARCO facility as-built showing operator workstations, overview displays, and observer stool.

There are still some significant infrastructural tasks to complete before ARCO is a fully-functioning distributed advanced reactor control room test bed, but the potential for future research is vast. By iteratively designing operation of an FHR while also running CIET experiments, we can derive higher-density data from experiments and more efficiently develop prototypical design insights. We can test fault detection and mitigation strategies. We can continuously verify and validate models in real-time alongside facility operation. We can simulate the impact of grid integration to research the load-following potential of FHRs. We can test and design startup and shutdown procedures. ARCO can serve as the foundation for many new research directions supporting the design of FHRs.

3 Compact Integral Effect Test Facility Experiments and Analysis

Many experiments have been conducted using the CIET Facility. The two major classes of experiments (LOFC transients and frequency response testing) are described in this section, with additional information in section 5.

3.1 Loss of Forced Circulation (LOFC) Transient Testing

Loss of forced circulation (LOFC) transient testing has been used for the CIET facility. LOFC transient tests were being performed to understand the performance capabilities of the DRACS system to remove decay heat in CIET, and subsequently in FHRs. Results, analysis and discussion are included in section 5.1.3.

3.2 Frequency Response Testing

As the next generation of reactors are being designed, it is important that techniques be developed to extract information and provide insight into the reactors during operation. Frequency response testing was used extensively for things like empirical model development, stability analysis, and parameter identification with advanced reactor designs of the past. Since the last frequency response tests with nuclear reactors, the field of system identification has grown considerably. This work attempts to bring modern advancements in system identification techniques to frequency response testing of nuclear reactors. The different capabilities and applications of frequency response testing are being studied using the CIET facility.

Frequency response testing started as one of the first data-based model identification techniques, quickly becoming a powerful tool in the early days of automation. Since then, it has only become more powerful in a world driven by big data. Used properly, it should be able to provide insight into the stability of reactors during operation, identify leaks and clogs in heat exchangers, provide an on-line system identification tool, as well as optimize the reactor control systems.

Initial frequency response tests with the CIET facility simply tested the dynamic heating capability of the heater, as shown in Figure 73. Sinusoids of varying frequencies were used as inputs for the power of the heating element. Although the heaters are well suited for controlling the heater power with sinusoidal inputs, it can be rather cumbersome using sinusoids to get frequency response function of a system. The system must be at steady state before the test can commence. The heater is then perturbed using a sinusoid of a given sequence. The system must then reach steady state again before a new frequency can be tested. To get the whole frequency response function at a range of frequencies can take a very long time.

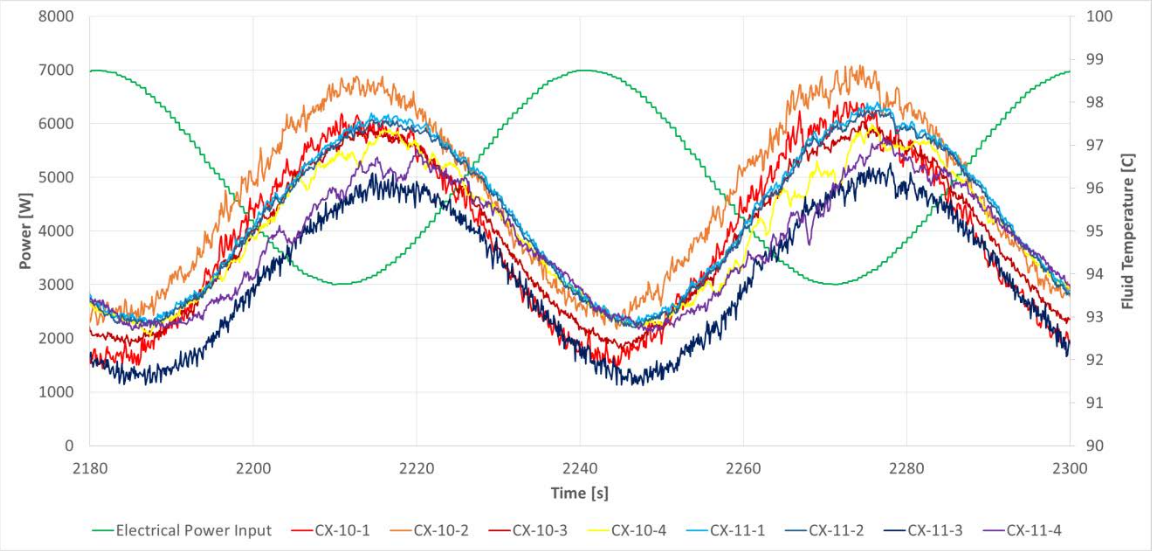

Figure 73. CIET input power oscillations experiment close-up: 4kW amplitude, 0.017 Hz frequency.

For that reason, different inputs were studied that are broadband signals, in that they contain signal power at a variety of frequencies during a single input. These were studied for the different parameters of interest. Some are able to discriminate against slight nonlinearities; others can be customized to probe a range of specific frequencies in a single period of the sequence. Tests were generated with different amplitudes, lengths, and bit-sizes to better understand how the various parameters affected the quality of the results. The frequency range of these tests are governed by choosing the length and bit-size appropriately. The amplitude should be high enough so as to be distinguishable from noise, but not so high that it excites nonlinearities in the system. During actual testing of a nuclear reactor, tests must be conducted on-line without disturbing normal operation. This requires the amplitude of the signals to be as low as possible. These tests tested that boundary to better understand how to maximize the signal-to-noise ratio.

The different types of broadband input signals were studied to learn their benefits and challenges, and how to design them to obtain good frequency response functions. The main type of sequence used for testing was the Maximal-length Pseudorandom Binary Sequence (PRBS). Other types of sequences such as Hall Binary Sequences (HAB), Quadratic Residue Binary Sequences (QRBS), and Twin Prime Binary Sequences (TPBS) were equally as capable as PRBS, while sequences like the Pseudo-random Ternary Sequence and the Pseudorandom Quinary Sequence performed poorly and showed no advantage over variations of the other sequences. Examples of the signals are given in Figure 74.

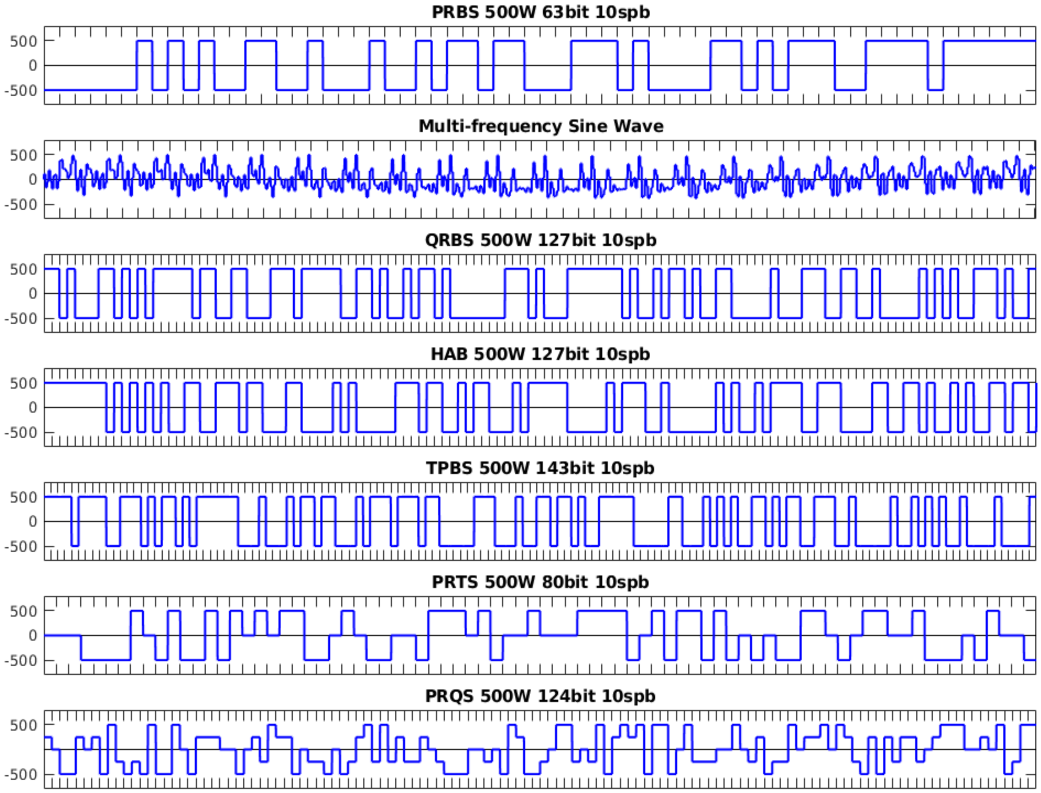

Figure 74. Example broadband input signals.

The bit-width of the sequence needed to be chosen appropriately to obtain good results. The maximum frequency with signal power is determined by the bit-width. This should be chosen as to probe the frequencies of interest without having significant signal power above half of the sampling frequency to prevent aliasing. Additionally, the controller must be able to change power to meet the desired power, before the bit value changes. For CIET, digitally controlled tests with a bit-size of 2 seconds gave poor results while a bit-size of 10 seconds gave good results.

Amplitudes of 200, 500, 1000, and 2000 Watts were used during testing. The frequency response functions for all were rather close with the proper selection of the other parameters. The results become less accurate as the amplitude decreases, but none of the amplitudes tested thus far have been too low to obtain meaningful results. Given proper period averaging, low amplitude tests can be implemented in a reactor during operation to obtain the frequency response function without disturbing operation.

The sequence lengths determined the minimum frequency and the fundamental harmonic of the test. The longer the sequence, the more frequencies contain signal power. This can be good for probing many frequencies, but can reduce the amplitude of the signal power at any given frequency enough to give poor results.

The figures below show the examples of the relationship between an input signal to the heater and the output signal in the bulk fluid (Figure 75) and Bode plots for the frequency response functions for all tests (Figure 76) and successful tests (Figure 77) to make the representative behavior clearer.

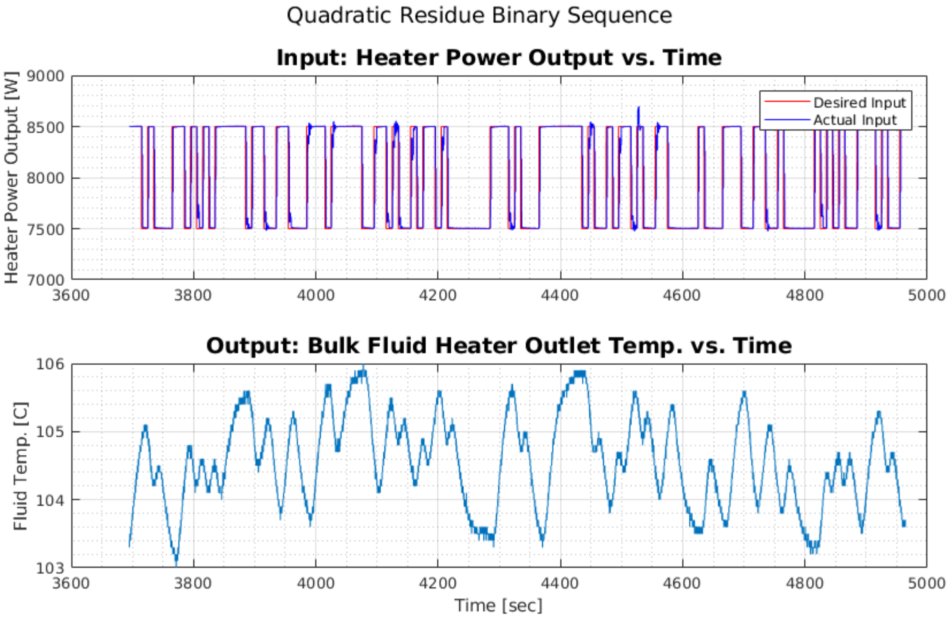

Figure 75. Example of input/output relationship with perturbed heater power as the input and the bulk fluid temperature as the output.

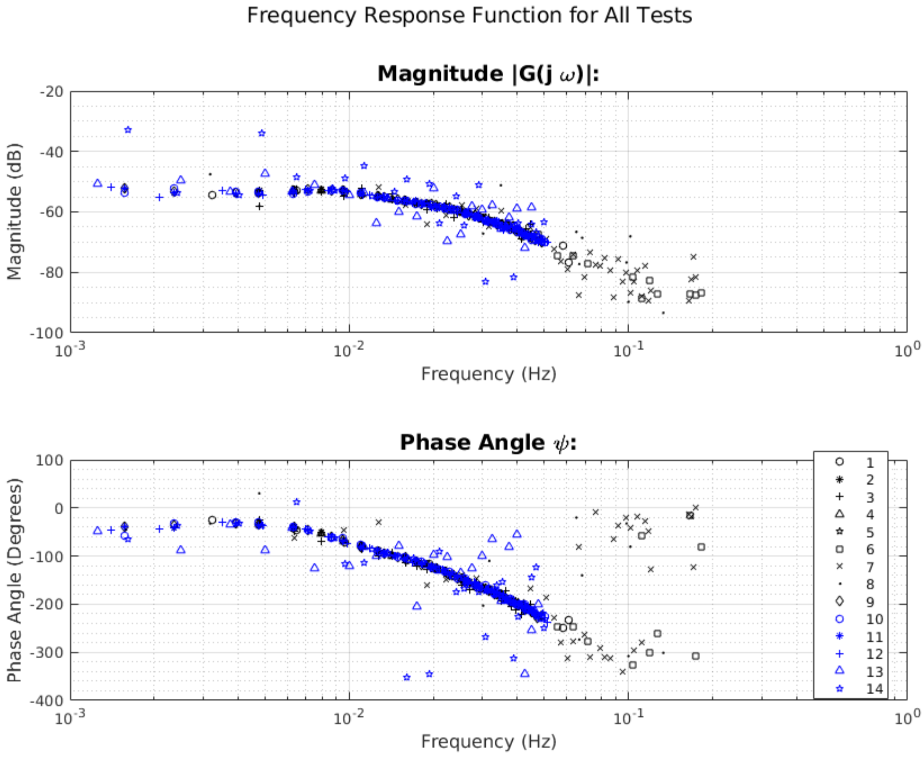

Figure 76. Frequency response function of all tests using the relationship between the heater power and the bulk fluid temperature at the heater outlet.

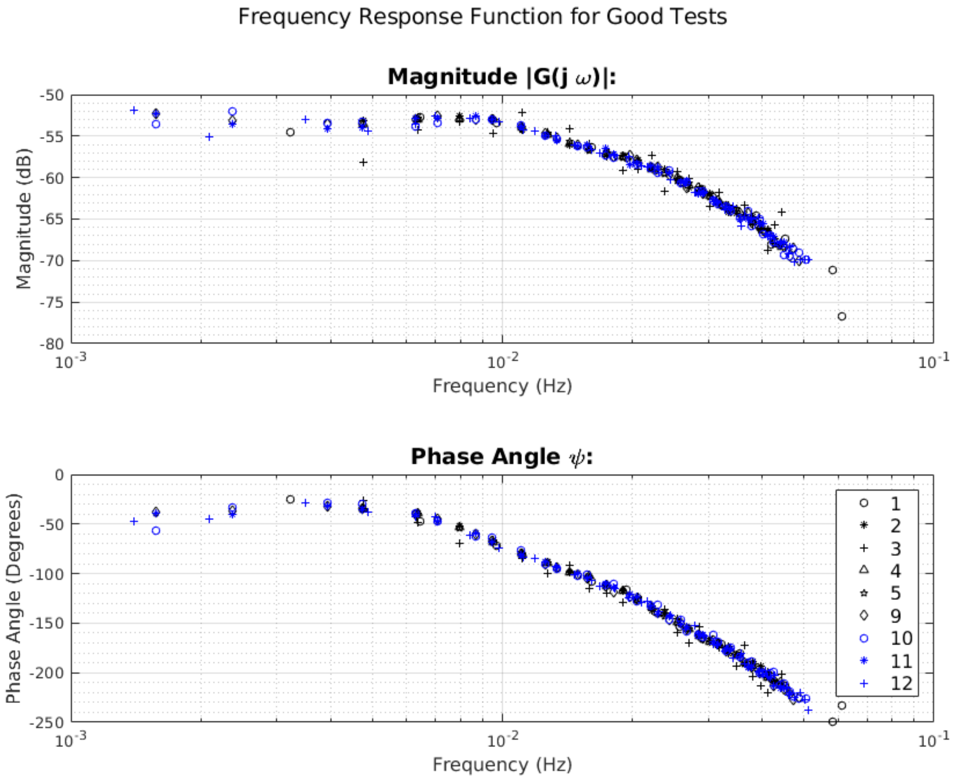

Figure 77. Frequency response function between the perturbed heater power and the measured bulk fluid temperature at the heater outlet of successful tests (Tests 1-5, 9-12).

After the technique of frequency response testing was developed, and the intricacies of designing good input sequences was understood, it was time to start applying it to extract useful information from CIET. One application of frequency response testing in nuclear reactors is determining the fuel and coolant reactivity feedback coefficients. The heater of CIET was updated to operate under simulated neutronic feedback. This used the reactivity of a simulated control rod with the reactivity feedbacks from the fuel (heater) temperature and the bulk fluid temperature to calculate the CIET power using a one-group point reactor kinetics model. The simulated neutronic feedback (SNF) tests used frequency response testing to understand how changing the feedback coefficients can affect the dynamics of a reactor. Baseline feedback coefficients for the fuel and coolant were calculated using a SERPENT model of an FHR. These were input into the SNF controller as the standard feedback coefficients. Frequency response tests were then conducted ½, 1, 1.5, 2, and 3 times the standard coefficients. Figure 78 shows the input (control rod position) and output (heater power) relationship used to measure the frequency response function for simulated neutronic feedback and Figure 79 shows the Bode plot of the frequency response function for high, medium, and low temperature feedback coefficients (combined fuel and coolant temperature feedback coefficients).

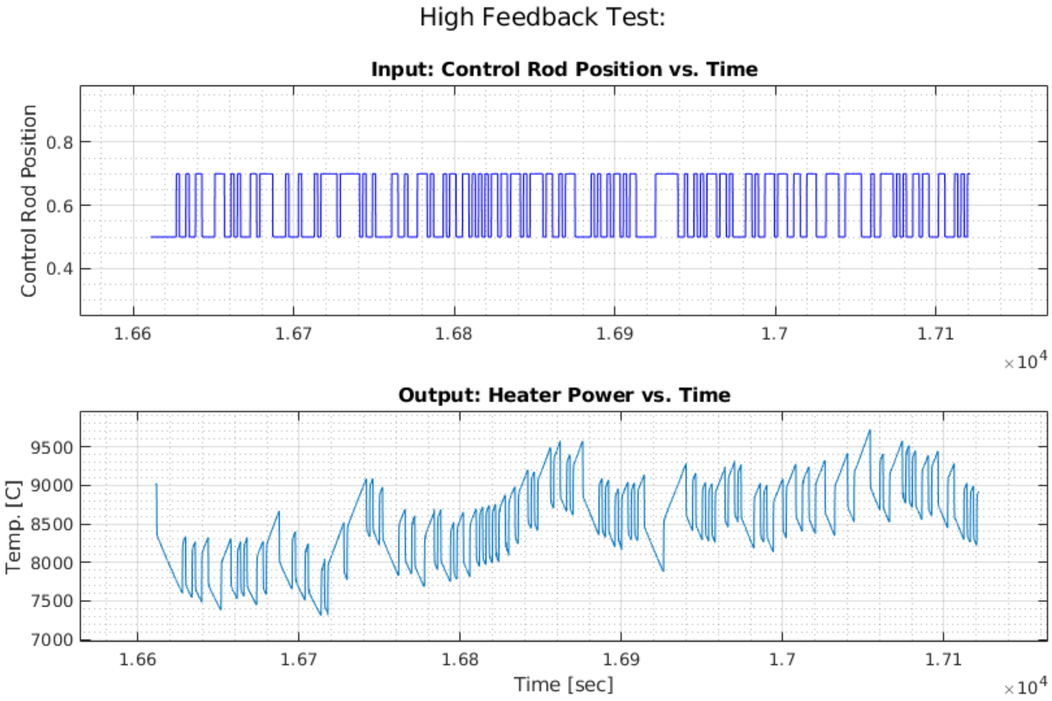

Figure 78. Input and output used for measuring frequency response function of simulated neutronic feedback testing.

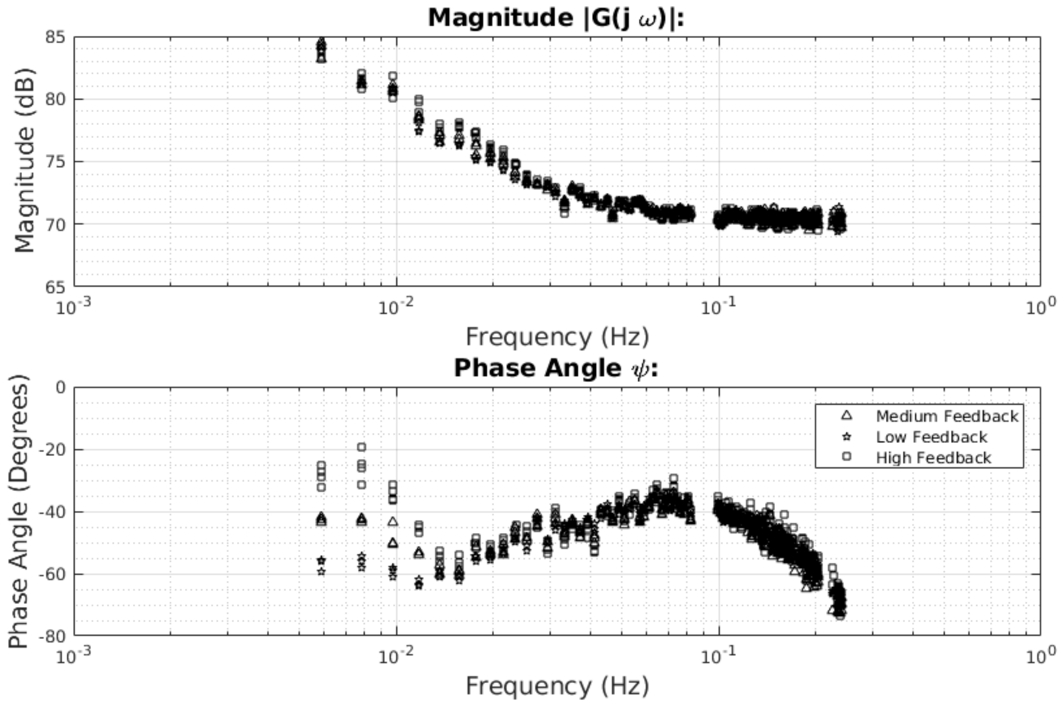

Figure 79. Frequency response function between simulated control rod position and heater power for tests with different temperature feedback coefficients.

Clear differences were observed in the frequency response functions of the reactor operating with different feedback coefficients. The zero power reactor had a lower phase angle response at the lower frequencies compared to the tests with high feedback. The magnitude response was similar for all tests regardless of the feedback coefficients.

After this, new tests were conducted with a wider frequency range, as well as different reactivity feedback coefficients. Results are still pending, but will likely feature similar behavior. Once the frequency response functions are obtained, they can be compared to the analytical transfer functions. The feedback coefficients in the analytical model can be varied until it matches the experimental results. Once the two models match, the parameters of the analytical model are essentially those of the experimental model. These will be compared to the feedback coefficients that were used as inputs in the power calculation to determine if frequency response testing was able to properly extract the coefficients.

4 Separate Effects Test (SET) Program

During the IRP, there were two primary separate effects tests supporting our research: the Pebble-Bed Heat Transfer Experiment and the Cartridge Heater Experiment.

4.1 Pebble-Bed Heat Transfer Experiment (PBHTX)

The Pebble-Bed Heat Transfer Experiment (PBHTX) is a scaled facility designed to measure heat transfer coefficients within a pebble-bed test section for the conditions applicable to the Pebble-Bed Fluoride-Salt-Cooled High Temperature Reactor (PB-FHR). A simulant oil called Dowtherm A is used as the heat transfer fluid, which matches the Prandtl number of flibe at temperatures lower than the PB-FHR conditions. A dimpled test section 0.0889m long is filled with randomly packed 0.00635m diameter copper pebbles, some of which are instrumented with thermocouples to measure temperature. The inlet and outlet fluid temperatures are also recorded. A Coriolis flowmeter is used to measure the mass flow rate of the oil within the loop. A power supply is used to vary the heater power sinusoidally, and in this way the frequency response of the test section can be measured to a high accuracy. The facility is designed so that the range of Reynolds and Prandtl numbers are matched with the prototypical conditions. The loop has been built using flexible stainless-steel piping and tri-clamp fittings. It is built in a modular fashion, implying that the pebble-bed test section could be replaced for future tests. Preliminary data is in the process of being collected, and heat transfer data will be collected in early 2016.

The primary objective of PBHTX is:

To measure the interfacial heat transfer coefficient in a pebble bed geometry for a range of Reynolds and Prandtl number that encompass the PB-FHR operating conditions, and compare to correlations in the literature, especially Wakao's correlation.

This primary objective has been done for two heat transfer fluids: Drakesol 260AT and Dowtherm A. The secondary objectives are:

1. Measure the friction head loss in the test section geometry
2. Measure permeability of the test section and compare to the analytical Carman-Kozeny relationship
3. Gain experience designing and developing modular scaled Dowtherm A loops that allow for flexibility in testing
4. Use sinusoidal oscillations to extract thermal inertia information from the collected data

There are several advantages to using sinusoidal oscillations to measure heat transfer coefficients as opposed to step change responses:

1. Accurate measurements of thermal inertia of the test section can be made with frequency response data.
2. In the data reduction procedure, the interfacial heat transfer coefficient is a function of the derivative of the pebble temperature. With a sinusoidal temperature variation in the pebble temperatures, the derivative can be easily obtained to a higher accuracy than could be done for the step change responses.
3. More data can be collected over a longer interval of time when periodic steady state conditions are achieved. This would help reduce any potential distortions due to transient effects.

With PBHTX we can exercise more control over the minimum and maximum temperatures of the fluid. This is because a larger power to the heater can be achieved. A larger temperature difference between the pebbles and oil can be obtained than was possible during the step change response tests. In this way data can be collected for a larger variety of non-dimensional numbers.

The PBHTX facility was fully constructed on October 31st, 2015. Preliminary testing of key components was completed to check that they function as intended. This was done for the heater, heat exchanger, power supply and instrumentation. Head loss data was also collected in the test section and the heat exchanger. Figure 80 shows two pictures of the facility from different directions with callouts indicating major components.

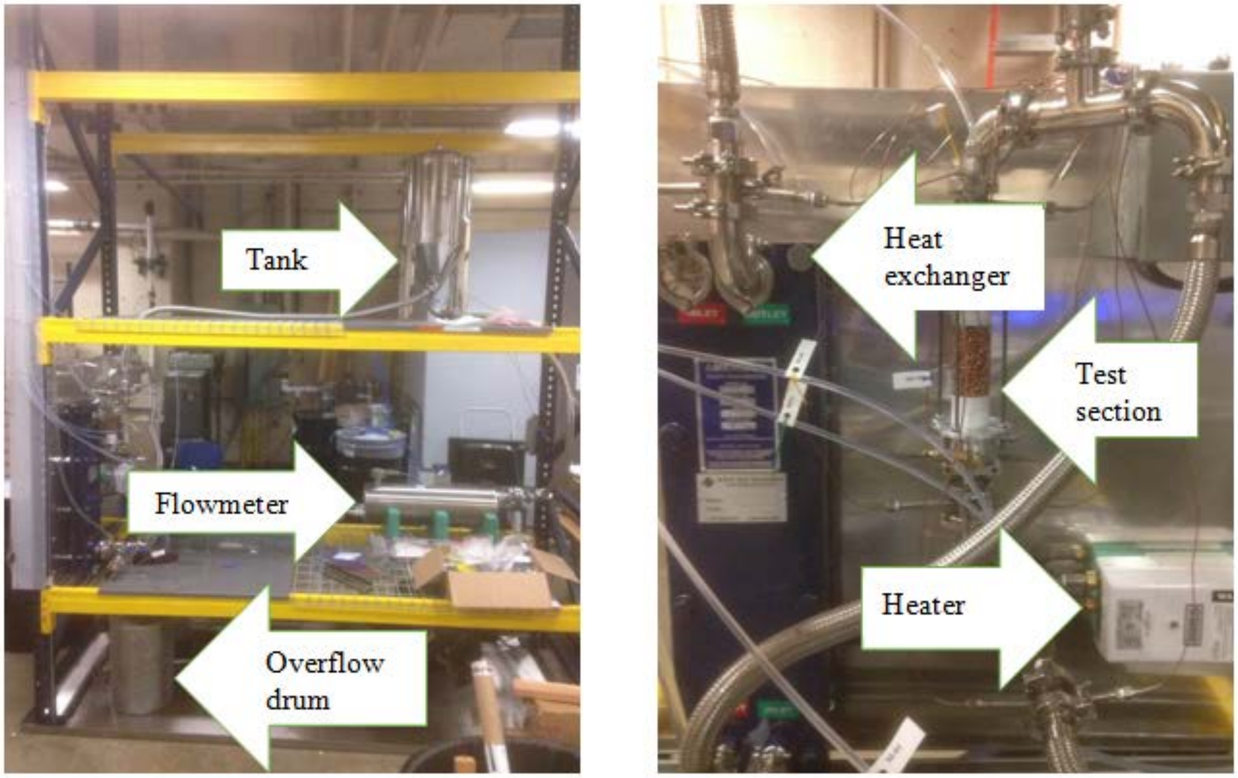

Figure 80. PBHTX view from the North showing the tank, flowmeter and overflow drum (left) and View from the West showing the heater, test section and heat exchanger (right).

The pebble-bed core can be regarded as a porous medium and thus porous media governing equations can be used to develop models for the PB-FHR core. The interfacial heat transfer coefficient is a parameter that is determined either from predictive correlations or from experimental data. The Prandtl number of Drakesol 260AT and flibe can be matched with a distortion within 5%, as shown in Figure 81.

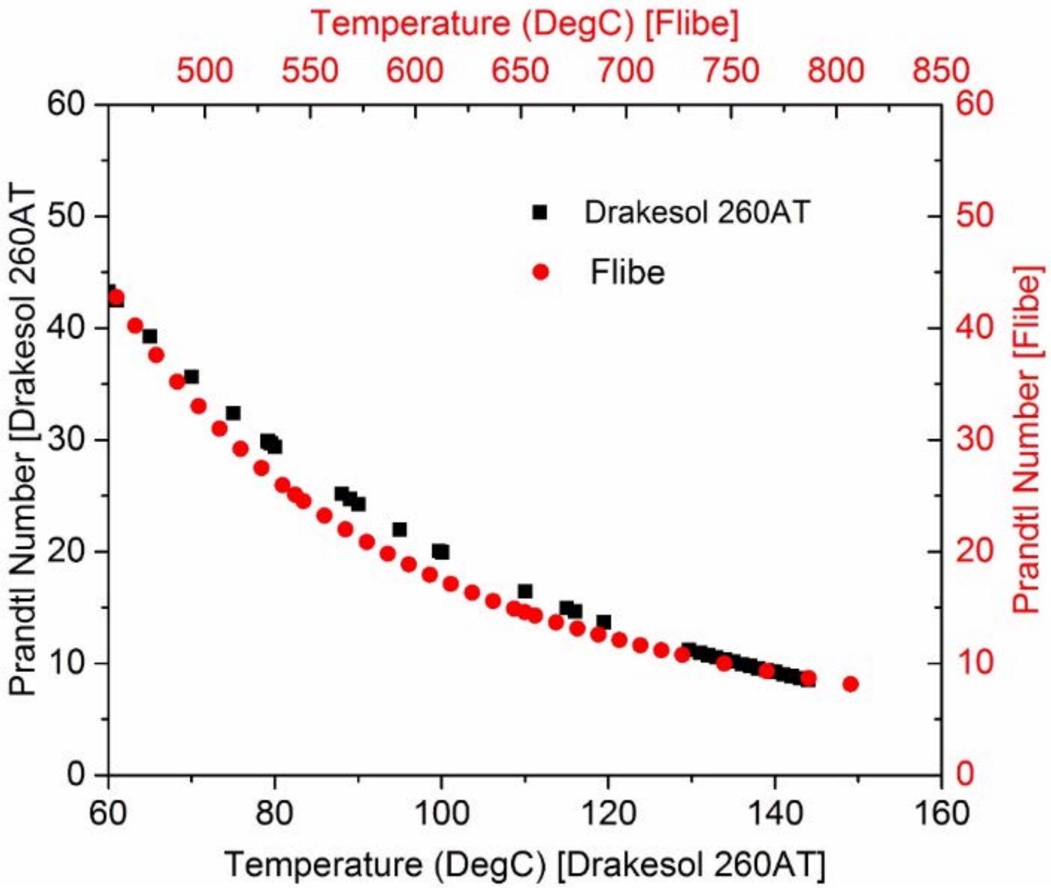

Figure 81. Prandtl number match between Drakesol 260AT and flibe.

The heater power is being oscillated and that directly affects the oil temperature at the inlet of the test section. Figure 82 shows the temperatures in the test section. Table 10 shows the location of the instrumentation.

Table 10. Instrumentation location description.

Thermocouple Name	**Location in the Test Section**
T02I	Fluid bulk temperature at the outlet (top)
T03P	Pebble temperature at inlet
T05P	Pebble temperature in the middle
T08P	Pebble temperature at outlet
T11I	Fluid bulk temperature at the inlet (bottom)

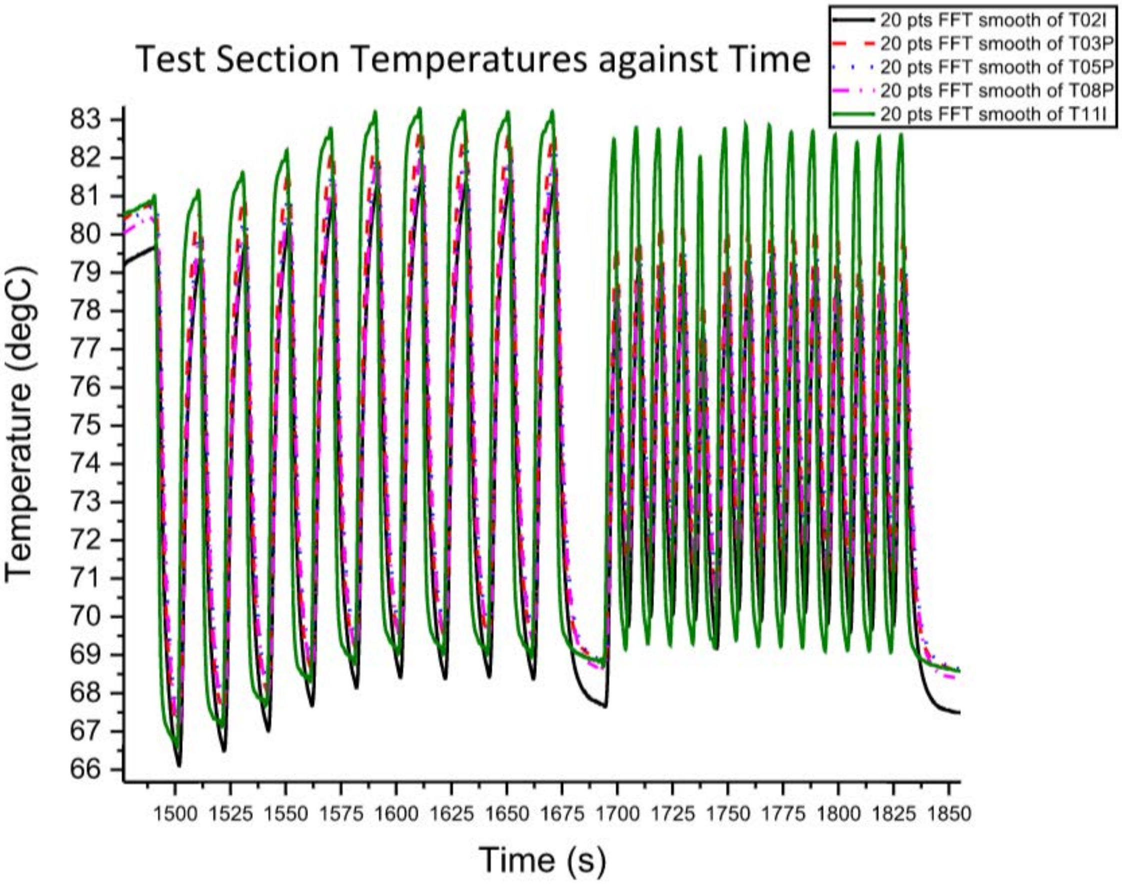

Figure 82. Thermocouple measurements throughout the oscillatory transient.

These frequency response tests allow us to get large temperature differences between the pebbles and the oil.

During the second quarter of 2016, a test of the PB-HTX was performed when the oil was discolored and the flow in the loop was disturbed. Upon further investigation, we found that the instantaneous water heater was the source of this problem. The Drakesol 260AT oil had eaten away at the plastic in the heater which eventually caused the heater to clog and for plastic residue to be seen throughout the loop. Figure 83 depicts the outlet of the heater after it was cut open. One can see that there are layers of plastic residue on the walls of the pipe and the other parts of the outlet. Figure 84 shows the stopper in the pipe that was removed and cleaned with a sonic cleaner. The ridges were formed by the Drakesol 260AT eating away at the plastic and this plastic would then flow throughout the loop as a residue.

Figure 83. Heater outlet internals after degradation in contact with oil.

Figure 84. Close-up of material degradation from contact with medium-temperature oil.

Modifications to the facility after this event included: rebuilding the test section to rid it of plastic residue contamination and to fix leaks, installation of a new flowmeter, updates to the sinusoidal power LabVIEW code and data acquisition code, replacement of manometer lines due to contamination from the plastic residue, and measurement of the Drakesol 260AT viscosity for a more exact value. Further ambient-temperature tests were run to verify that there were no leaks and the experiment in general was running properly.

After the repairs of the heater to the PB-HTX loop were finished, ambient tests were completed and proved to be successful in some respects. There was no longer leftover residue from the thermally degraded plastic materials in the heater being deposited around the loop; however, the flowmeter proved to be more degraded than previously thought. The Coriolis flow transmitter was replaced but that proved to not be the source of the problem. This prompted the lab to upgrade to a newer Coriolis flowmeter, the Siemens FC430 Coriolis mass flow meter design which is used also in CIET. It was concluded that the Drakesol 260AT oil should be drained out of the loop after every experimental run to avoid prolonged contact with the plastic materials in the heater element.

4.2 Cartridge Heater Experiment (CHEX)

The Cartridge Heater Experiment (CHEX) was designed to test similitude between Dowtherm A and fluoride salt for natural convection heat transfer from a vertical cylinder. Experiments were conducted in Dowtherm A and were compared to results from Oak Ridge National Laboratory (ORNL) using flinak. Both laminar, transition and turbulent conditions were investigated. Data collection and data processing is complete, and simulation work is underway to complement the experimental results. Figure 85 shows the CHEX experimental setup and Figure 86 shows experimental results demonstrating Dowtherm A and flinak similitude.

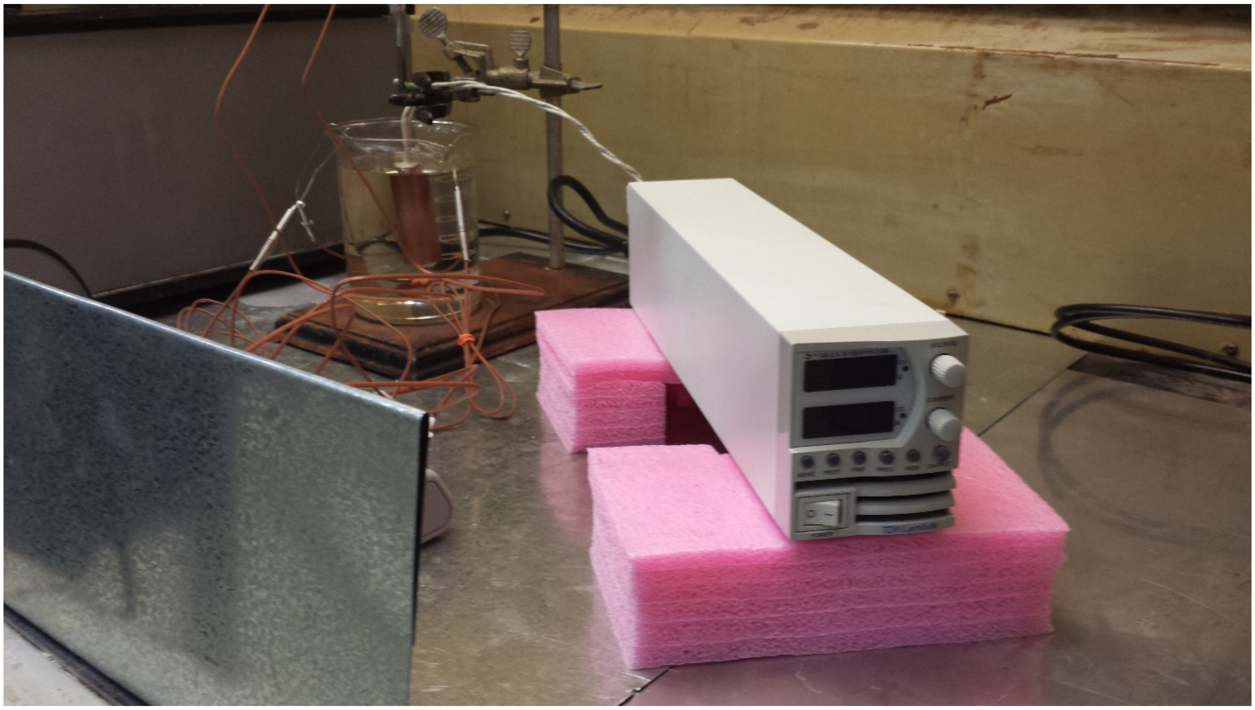

Figure 85. CHEX experimental setup with a DC power supply to control the power to the cartridge heater located within a copper sleeve.

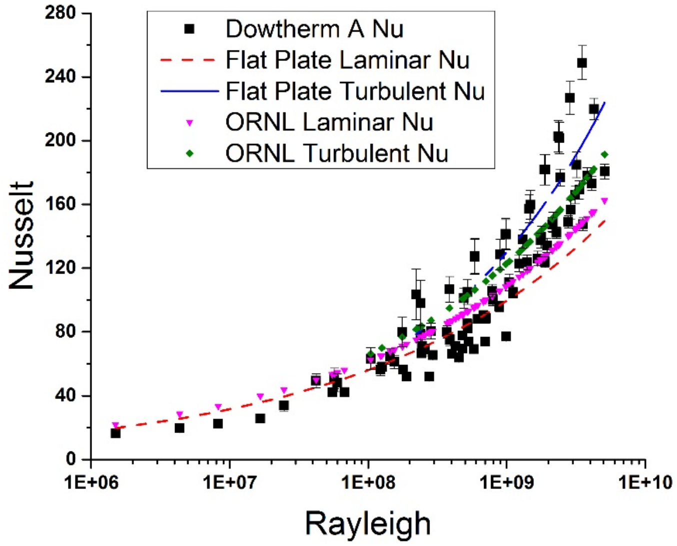

Figure 86. Experimental results showing comparisons between Dowtherm A and ORNL flinak data.

5 Thermal Hydraulic Simulation Models and Analysis

In coordination with CIET Facility experiments and analysis, much research has been performed with computational models and simulations. A strong focus at UCB is the coordination of experimentation and simulation, and the CIET Research Program is no exception. Simulation models have been used to simulate initial CIET steady-state and transient experiments, LOFC experiments, and recent frequency response testing.

5.1 Verification and Validation in the CIET Facility

Verification and validation is the process of confirming that the simulation code behaves according to physical laws and phenomena (verification) and can replicate the specific behavior and phenomena relevant in systems of interest (validation). The primary system codes that were verified and validated by experimental data from CIET are RELAP5-3D and FANCY (FHR advanced natural circulation analysis).

5.1.1 Initial Verification and Validation Efforts

An early activity with CIET during this project was the verification and validation of RELAP5-3D and FANCY models of coupled natural circulation. The RELAP5 and FANCY models of CIET 1.0 reproduce its geometry (i.e. components lengths, elevations, hydraulic diameters and flow areas), pressure and temperature boundary conditions, and working fluid thermophysical properties. Material properties for the stainless steel and copper tubing, as well as the fiberglass insulation, are manually implemented in the models. In particular, thermal mass of the system has an impact on transient modeling and validation. Therefore, masses of individual components were measured and recorded throughout the assembly process of CIET 1.0, and these individual masses were added to heat structures in the RELAP5 and FANCY models when transient model validation is performed. Figure 87 shows a labeled 3-dimensional model of CIET 1.0 and the corresponding nodalization diagram for the RELAP5 and FANCY models. On the diagram, the primary loop (heater and DHX) and the DRACS loop are highlighted in green.

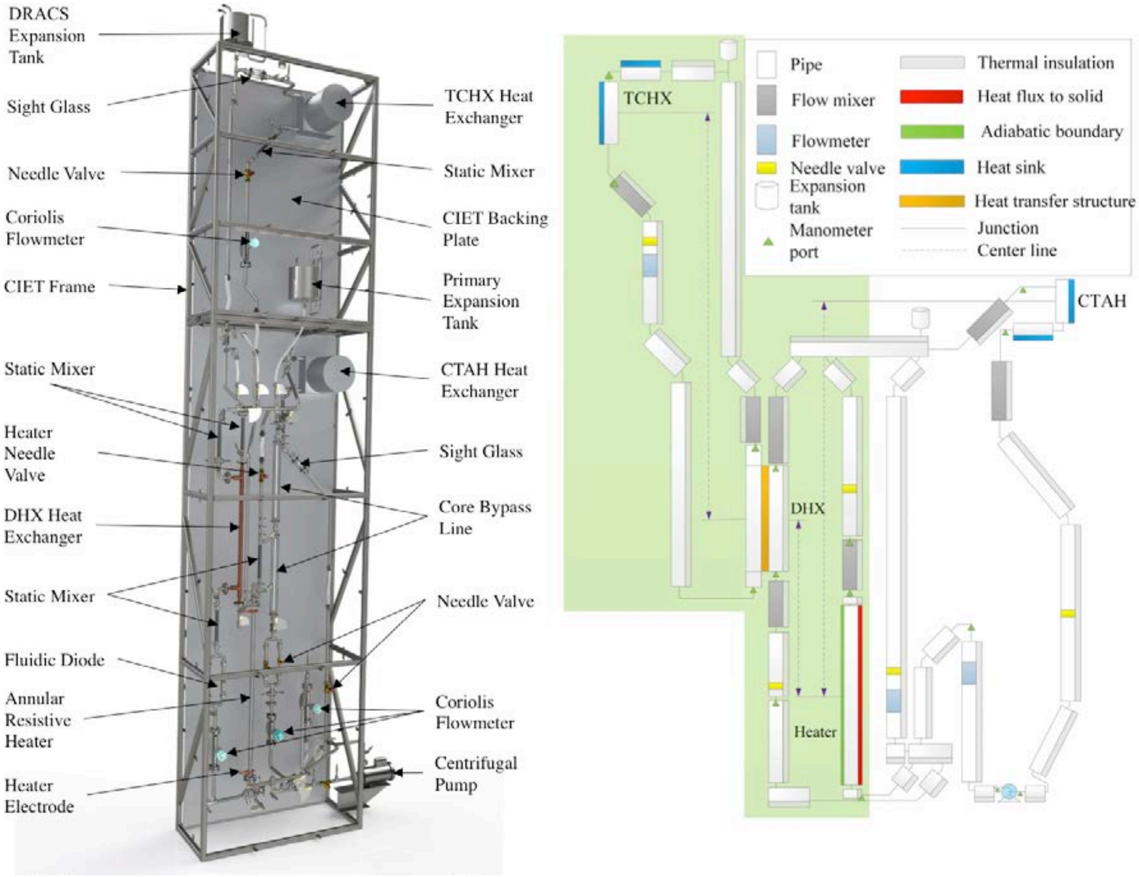

Figure 87. CIET 3-dimensional model, not showing insulation (left) and corresponding nodalization diagram for the RELAP5 and FANCY models (right).

Prior to the V&V effort, pressure drops were measured at various flow rates in each branch of the CIET 1.0 loop at room temperature. The flow rate ranges selected for this series of tests covered Reynolds numbers (Re) up to 1,600 in each branch, corresponding to expected regimes during forced and natural circulation operation of CIET. The goal of these tests was to generate CIET-specific component-scale friction number correlations in the following non-dimensional form, which were subsequently implemented in RELAP5 and FANCY:

$$K + f\frac{L}{D} = A + B\Re^{-C}$$

where K is the sum of form losses, f the friction factor, L the component length, D the component hydraulic diameter, and A, B and C empirically-derived coefficients. This series of tests validated the analytical correlation for laminar flow friction factor in straight, cylindrical pipes (f=64⁄Re) and its applicability to the CIET 1.0 annular heater, with an agreement within 10% between experimental data and the analytical correlation. Moreover, CIET-specific correlations were derived for static mixers, Coriolis flowmeters and fan-cooled heat exchangers, as listed in Table 11. These correlations yield higher friction numbers than vendor-provided charts over the range of Re of interest, therefore confirming the value of performing such tests prior to any V&V effort.

Table 11. CIET-specific friction number correlations for static mixers, Coriolis flowmeters and fan-cooled heat exchangers.

Component	**Friction Number**
Static Mixer	$K + f\frac{L}{D} = 21 + \frac{4{,}000}{\Re}$
Coriolis Flowmeter	$K + f\frac{L}{D} = 18 + \frac{93{,}000}{\Re^{1.35}}$
Fan-Cooled Heat Exchanger	$K + f\frac{L}{D} = 400 + \frac{52{,}000}{\Re}$

For this study, all calculations were run with RELAP5-3D/Ver. 4.0.3 and FANCY/Ver. 2.0 in transient mode until steady-state conditions are reached for fluid temperatures and mass flow rates in each loop.

For code verification, the following tests were performed at steady-state:

1. Is the heat input to the fluid equal to the sum of the heat removed through the TCHX and parasitic heat losses along the loop?
2. Is the mass flow rate uniform in each loop?
3. Is energy and mass conservation verified in each loop?

The code results have passed these tests, hence partly verifying proper solving of the fundamental conservation equations.

For single natural circulation loops, at all power input levels and TCHX outlet temperatures tested, the agreement between RELAP5 and experimental data for the loop mass flow is within 1% and the agreement between FANCY and experimental data is within 3%. For coupled natural circulation between the primary loop and the DRACS loop, the agreement between RELAP5 and experimental data remains within 8% and the agreement between FANCY and experimental data remains within 13% in both loops. The comparison between best estimate code solutions and experimental data in the non-dimensional space shows an excellent agreement between both code calculations and experimental data in the coupled loops, where flow is in the fully laminar regime. The results also show remarkable agreement with the correlation proposed by Vijayan for steady flow in a fully laminar natural circulation loop, which is the case here. Figure 88 supports these conclusions. For further information on model V&V for CIET performed at UCB a more detailed discussion is included in the references (Zweibaum et al., 2016).

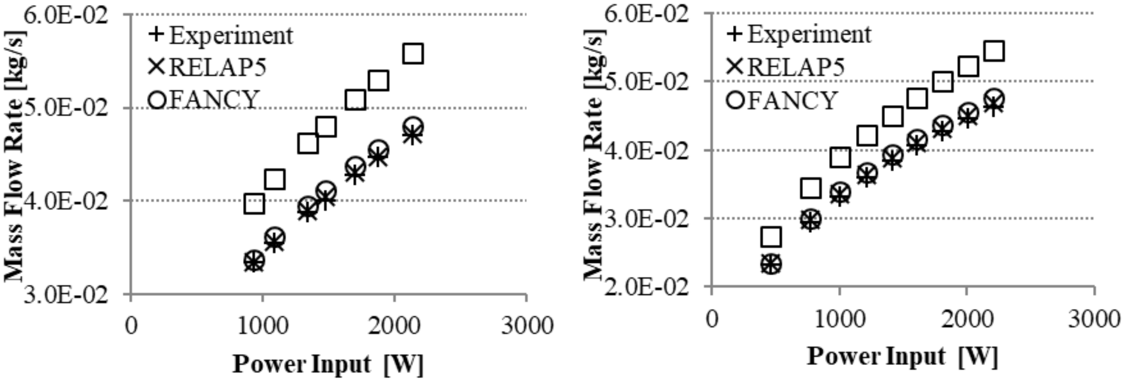

Figure 88. Comparison of experimental, RELAP5, FANCY, and analytical natural circulation mass flow rates for various heat inputs and TCHX outlet temperatures of 46°C (left) and 35°C (right).

5.1.2 Forced Cooling and Power Step Change Model Validation

Experimental data has been collected for transient, forced cooling model validation using heat input step changes, a fixed coolant mass flow rate of 0.18 kg/s in the CTAH loop and a controlled CTAH outlet temperature of 80°C. Corresponding boundary conditions have been reproduced in RELAP5-3D. The only discrepancy between the model and the experiment is that RELAP5-3D uses a fixed CTAH outlet temperature boundary condition of 80°C instead of the more complex real evolution resulting from the CTAH controller on CIET, because of the lack of a detailed model for the CTAH at the time of this study. Power step changes under forced cooling operation with a fixed mass flow rate are aimed at validating the model for thermal inertia of the system's solid structures and fluid, which affects its response time to such transients.

Thermal capacities for each heat structure are documented in the RELAP5-3D input deck provided in Nicolas Zweibaum's PhD dissertation (Zweibaum, 2015). In particular, because the thermal capacity of the solid structures in the loop – ~50 kJ/K – is of the same order of magnitude as the thermal capacity of the oil – ~20 kJ/K –, it is important to account for both types of heat structures to accurately predict the system's transient behavior.

Figure 89 shows a comparison of RELAP5-3D results and experimental data for an entire test, and Figure 90 shows details of this comparison for a selection of power step changes up and down. Throughout the test, the agreement between RELAP5-3D results and experimental data is within 2°C. More specifically, the agreement is within instrumentation accuracy (±0.5°C) for the heater outlet temperature and there is a delay of ~100 s in the response of the CTAH inlet temperature to power step changes compared to experimental data. The agreement between code results and experimental data for the CTAH outlet and heater inlet temperatures is within instrumentation accuracy, except for the short periods during which the code uses an idealized CTAH outlet temperature boundary condition of 80°C instead of the more complex controller implemented on CIET 1.0.

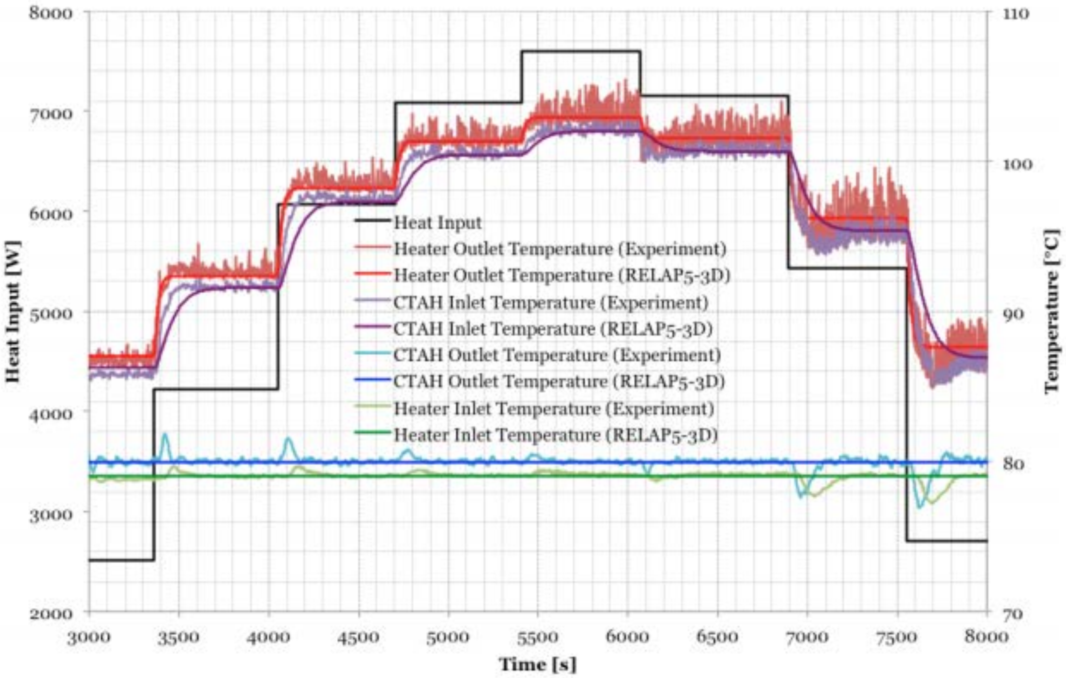

Figure 89. Experimental data and RELAP5-3D results for transient forced cooling in CTAH loop.

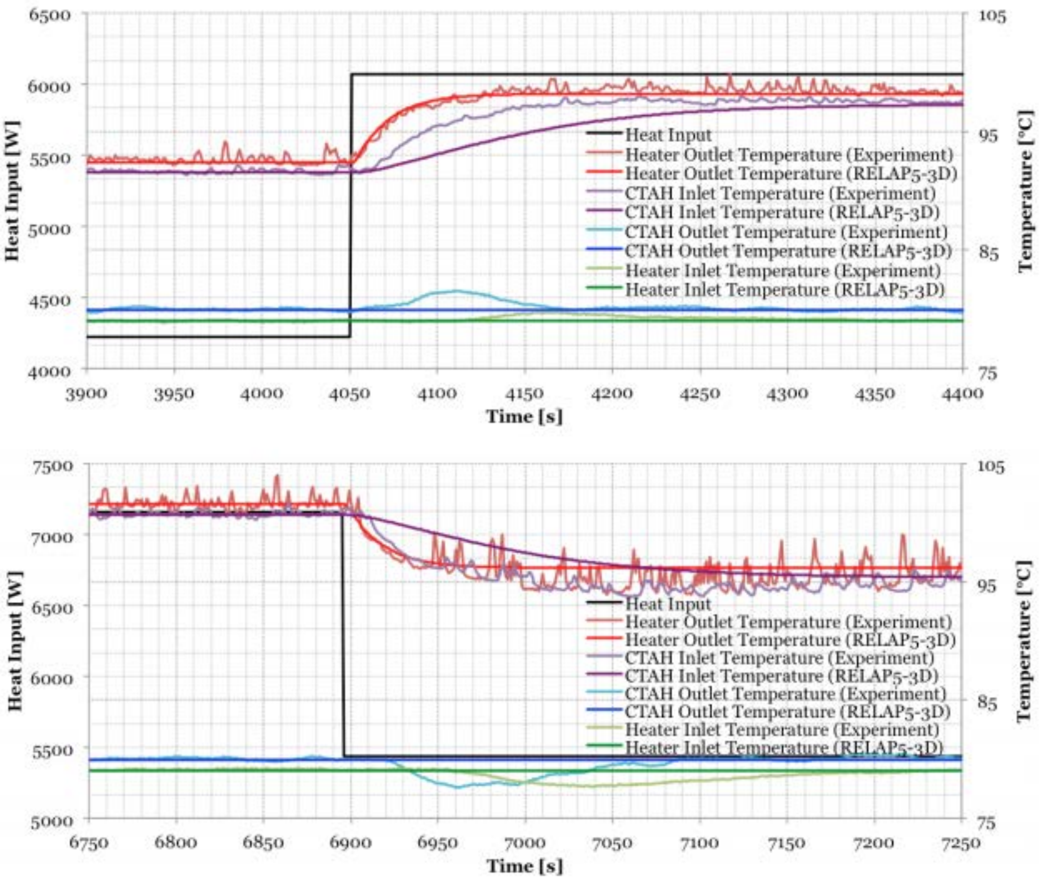

Figure 90. Experimental data and RELAP5-3D results for transient forced cooling in CTAH loop (details).

The fact that RELAP5-3D accurately predicts the transient increase of the heater outlet temperature indicates that the model has the correct thermal capacity for the heater element. Conversely, the thermal capacity between the heater outlet and the CTAH inlet does not appear to be modeled perfectly, since RELAP5-3D predicts a slower response of the CTAH inlet temperature than CIET produces. Because accurate data for the masses of the CIET thermal structures, and therefore for their thermal capacities, was measured during fabrication of the CIET 1.0 facility and implemented in the code, this disagreement may be due to the approach to modeling these structures, and the fact that some of the thermal structures (e.g. pipe walls), which have a large surface area compared to their thermal inertia, are more tightly coupled to the fluid than components with small surface areas compared to their thermal inertia (e.g. flanges, valves). As shown in Figure 91, closer agreement between code results and experimental data is indeed obtained by separating the weakly and the strongly coupled thermal masses into separate heat structures in the RELAP5-3D model, based upon measured values for weights of individual components and the fact that weakly coupled thermal masses account for ~20% of the total weight of the system's solid structures.

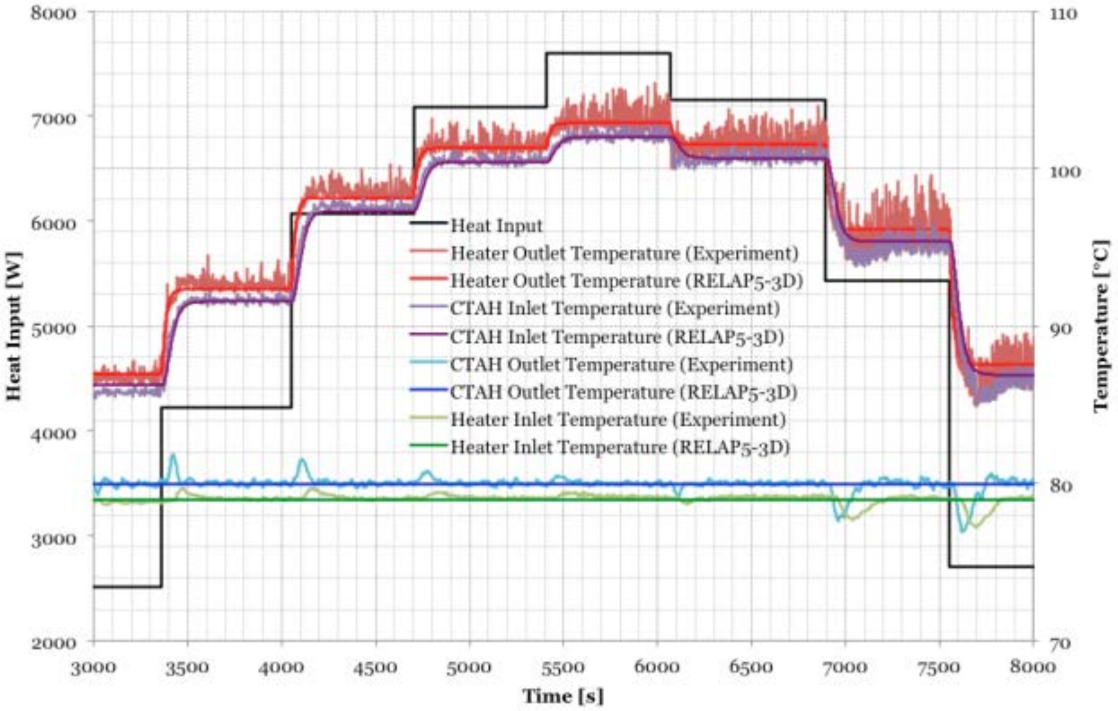

Figure 91. Experimental data and RELAP5-3D results for transient forced cooling in the CTAH loop using decoupled heat structures.

5.1.3 Loss of Forced Circulation (LOFC) Transient Model Validation

The next step in transient model V&V is validation of the RELAP5-3D model's ability to predict system behavior in the case of design basis accidents. The first experiment designed and conducted for this purpose using CIET 1.0 is the LOFC. The LOFC event is performed experimentally using CIET 1.0 by following the modified LOFC experimental procedure document (CIET-TEST-PLAN-012M-00_LOFCM_Test_Procedure) updated on 7/24/2015. This is a later iteration of the experimental procedure which includes improved clarity in its description of steps. There are two aspects to implementing the LOFC in the RELAP model. The first is the inclusion of appropriate steady-state conditions prior to the LOFC event and the second is the implementation of the specific procedures needed to reproduce the LOFC event. The steady-state conditions defined by the experimental procedure are listed below:

1. CTAH Outlet Temp: 80°C
2. TCHX Outlet Temp: 46°C
3. DHX flowrate: 0.018 kg/s
4. CTAH flowrate: 0.18 kg/s

The temperature and flow initial conditions are implemented by setting hydrodynamic component, junction, and branch initial conditions. Additionally, the flowrate in the CTAH is enforced by setting the time-dependent junction which represents the pump to supply a flowrate of 0.18 kg/s. An additional initial condition that was determined from CIET 1.0 steady-state experimental data is the definition of the temperature in the hot leg (where the CTAH outlet is the temperature in the cold leg) of the primary loop. This is estimated from the experimental results as 95°C. The RELAP simulation then finds its own steady-state condition but this process is expedited by using a reasonable value for the first guess.

After steady-state conditions are reached in the CIET facility, the LOFC transient steps can be performed. The experimental procedure for the LOFC transient is listed here:

1. Turn the pump feedback off.
2. Set the pump frequency to 0.
3. Set the “Desired Power” to 2kW.
4. Turn the CTAH fan feedback off.
5. Set the CTAH fan frequency to 0.
6. Close valve V-40 to eliminate flow through the CTAH branch, representing an insurmountable pressure head through the CTAH branch during natural circulation decay heat removal in the primary loop. Because this valve does not have a counterpart in a prototypical system, the experimental procedure may need to be updated in future experiments.

Because CIET 1.0 is configured with automated controls which can respond to system conditions in order to try to maintain target values, feedback controls need to be shut off in the simulation of equipment failure. The question of how to implement these procedures in RELAP has been explored in our preliminary study and the individual events are listed here:

1. The pump is set to a frequency of 0 by setting the time-dependent junction that acts as a pump to coast down to a flowrate of 0.
2. The insurmountable pressure head through the CTAH branch during natural circulation operation is simulated by using a trip valve which closes at a specific time step.
3. The heater power is changed from 6 kW to 2 kW using a heater power table which consists of time values and corresponding heater values.
4. The CTAH unit in CIET 1.0 is a fan but is represented in the RELAP model as a heat structure that removes heat. The CTAH fan frequency is set to 0 by changing its heat transfer coefficient to 0 at the desired time.

In order to assess the capability of these events implemented in the RELAP model as accurate predictors of CIET 1.0 behavior, we have conducted a preliminary simulation of the LOFC event using the RELAP model. The data from this study is presented along with experimental data for the LOFC experiment in CIET 1.0 in Figure 92 and Figure 93. The time period in focus for the transient is the 100-second interval which begins at steady-state, experiences flow reversal as the trips occur, and ends as the DRACS loop begins to remove decay heat. For this preliminary study, we compare two sets of data: temperatures and flowrate across components. The temperatures we examine are the inlet and outlet for both the heater and the DHX which are shown in Figure 92. We also examine the flowrate across the heater, the CTAH, and the DHX in Figure 93.

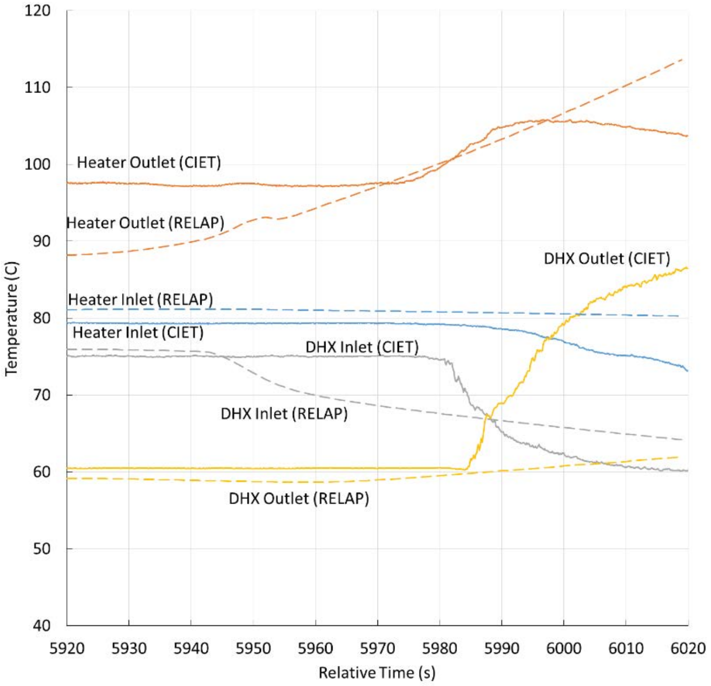

Figure 92. Temperature comparison of heater and DHX inlet and outlet for CIET 1.0 experimental results and RELAP simulation results.

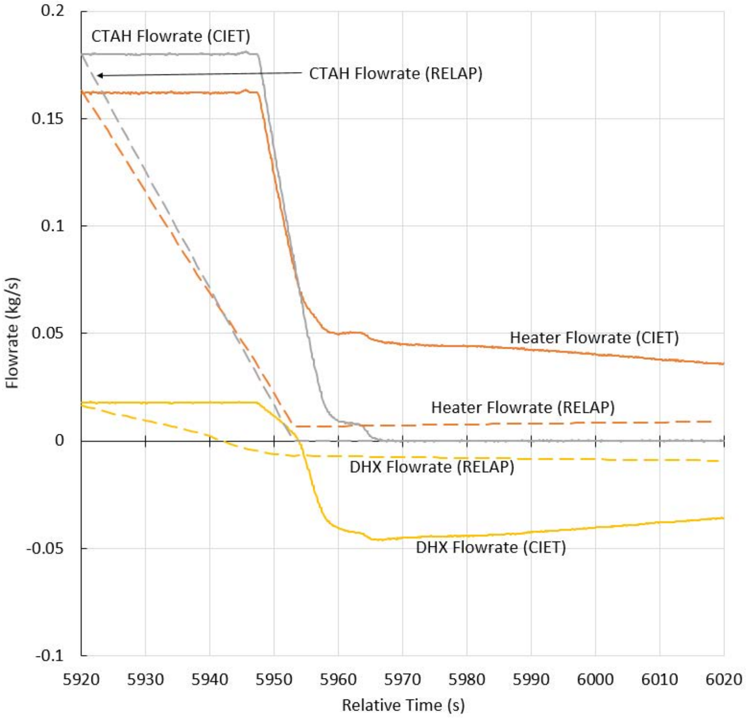

Figure 93. Flowrate comparison of heater, DHX, and CTAH for CIET 1.0 experimental results and RELAP simulation results.

We will first compare the temperature results from the RELAP LOFC simulation with the experimental results from the CIET 1.0 facility. Each component temperature in focus is color-coded with dashed lines representing RELAP simulation results and solid lines representing experimental results. It is first important to note that the temperatures initially increase and decrease in accordance with response to the LOFC event, which supports the RELAP model's capability of producing physically consistent behavior. However, it is clear that the RELAP simulation does not predict the CIET 1.0's temperature change to the accuracy desired. More specifically, the concavity of the RELAP-predicted temperature curves do not match the more sudden changes exhibited in the physical system. The RELAP results show a heater outlet temperature that continues to increase while the CIET 1.0 data shows a peak. In all temperature profiles, the RELAP results do not capture the response of the system to the loss of heat transfer to the CTAH and increased heat transfer to the DHX. This may indicate that these preliminary results do not accurately replicate the performance of the DRACS loop in removing increased amounts of heat. This is supported by the convergence of the DHX inlet and outlet temperatures in the RELAP results, representing minimal heat removal, while the DHX inlet and outlet temperatures diverge in the experimental results. Another apparent source of inconsistency is the difference in the steady-state conditions reached by the RELAP model versus CIET 1.0, which may have a significant impact on simulated response. These inconsistencies, however, will be further explored and understood in future work with a focus on better modeling the heat transfer to the DRACS loop.

We will next compare the flowrate results from the RELAP simulation with the experimental results from the CIET 1.0 facility. Like the temperature data, the flowrate data is color-coded and differentiated by line type. The flowrate results from RELAP seem to trend alongside the experimental results. The flowrate in the RELAP simulation across the heater and the DHX after the initial component trips, however, has a much lower magnitude than the flowrate in the experimental results. The RELAP simulation also seems to predict a much more stable response from the system while there is some fluctuation immediately following the LOFC event in CIET which may be attributable to the time delay between experimental procedures. One possible reason for the difference in magnitude may be the improperly modeled flow losses during the LOFC event or missing information in the inertia of the DRACS loop. Discovering the source of this flowrate inconsistency will be a primary goal in the further development of the LOFC model.

However, it is promising to see that each of the flowrate trends studied does follow the same trend as in the experimental system. Most importantly, flow reversal is demonstrated in the DHX, flow stoppage is demonstrated in the CTAH, and flow reduction is demonstrated in the heater as the pump shuts off and forced circulation is lost in the CTAH branch of the primary loop. One possible influential factor on the discrepancy in the magnitude of flowrate predictions in the RELAP simulation is that flowrate changes, as shown in Figure 5, are much more gradual than in the experimental configuration of the LOFC event. This may be due to some lack of fidelity in modeling the pump coast down and heater power drop and will be a first step in improving the model.

For transient, forced cooling in the CTAH loop using step changes to heater power input, agreement between RELAP results and experimental data is within 1°C for a fixed coolant mass flow rate and controlled CTAH outlet temperature. This agreement was also accomplished by decoupling heat structures with small surface areas compared to their thermal inertia. This study both validated the use of RELAP models to predict system behavior in the case of power step changes under forced circulation, and provided insight into the modeling of heat structures using RELAP.

Our preliminary study of the LOFC transient event modeled in RELAP has yielded useful results in the improvement of models for prediction of the CIET 1.0 facility's response in design basis scenarios. It demonstrates prediction of initial trends in temperature changes as well as flow reversal and flow distribution in the reactor loops. Transition of flow from the CTAH branch of the primary loop to the DHX branch is also demonstrated. Because there are significant inconsistencies between the RELAP results and the experimental results for the flowrate across facility components in particular, there is study needed before further conclusions can be drawn in the validation effort.

Further work in verification and validation of complex transients like LOFC events include more detailed solution verification with supporting sensitivity analyses, model calibration to more accurately represent the experimental configuration including the system's thermal inertia, and uncertainty quantification for both experimental results and model prediction.

More information on progress in this area can be found in a paper presented at ICAPP 2016, which is included in the references for this report. These results demonstrated that the model accurately predicted both values and rates of change in flow for the CTAH, Heater, and DHX during the transient. However, the temperature data, while matching within 3°C for starting and ending conditions, had a significant time lag between simulation and experimental results. The temperature changes occurred almost simultaneously with flow rate changes in the simulation while the temperatures took about 20 seconds to change in the experimental data.

Subsequent efforts have been focused on discerning the reason for this discrepancy. One hypothesis that has recently been tested was to better match measurement locations in the RELAP5-3D model to the physical thermocouple positions on CIET. This was a reasonable candidate for the cause of the inconsistency because the flow rate of Dowtherm A after LOFC is only 0.05 kg/s, meaning that the time for heat to propagate through the system may render small distances between temperature measurement locations significant for time distortion. However, after carefully measuring the locations of thermocouples on CIET and modifying the RELAP5-3D simulation to read temperatures at the corresponding nodes in the model, the results showed no significant improvement.

Next steps to address the temperature data time lag include assessment of the model nodalization, convective heat transfer boundary conditions for the axial direction of the nodes, and the coupling of heat structures and hydrodynamic volumes. Because this work helps demonstrate the suitability of RELAP5-3D for building best-estimate thermal hydraulic models of FHRs, the consistency and reliability of results will be contingent on the ability of the software to predict phenomena in pebble-bed salt-cooled reactors.

The nodalization of RELAP5-3D models of the CIET facility were compared with system design specifications. The models were then used to confirm results for previous tests presented in the Ph.D. dissertation of Nicolas Zweibaum. By comparing the dynamic results from RELAP5-3D with the experimental data obtained from CIET, it became clear that the modeling of heat structures needed to be improved through finer discretization and a more thorough understanding of the heat capacity of structural elements. A new license was issued for the software and installed on a server for future modeling.

RELAP5-3D is still in use at UCB for the development and understanding of FHRs, and more information can be found in the following section.

5.2 Frequency Response Testing Application to Verification and Validation

One useful product of frequency response testing is a set of identified system parameters that can be incorporated into system models and used for validation and verification efforts. This may prove invaluable in identifying discrepancies in capturing subtle components of transient behavior, further supporting the credibility of our verification and validation program. Furthermore, system parameters such as time constants and overall heat transfer coefficients will allow us to build simplified system models that represent the CIET facility with a smaller number of control volumes and simplified equations so that we can assess their loss of fidelity. Simplified models can provide not only benchmarking data, but also prove useful in situations where computation resources are scarce, such as in on-line system monitoring.

Using data from a CIET facility capability test on August 17, 2015 and a heater power oscillation test on February 28, 2017, we have developed a code in MATLAB that automates data processing, allowing us to quickly calculate frequency domain values and visualize results to aid our qualitative analysis of raw data. Preliminary results and data analysis for this work are described in a paper that was presented at the 17th International Topical Meeting on Nuclear Reactor Thermal Hydraulics, titled “Preliminary Experimental Results for Frequency Response Testing in FHRs and MSRs Using the Compact Integral Effects Test”.

Furthermore, we have developed a methodology for using the results of frequency response testing to validate simple system models in CIET and to simplify the process of determining system parameters. We derive simple models of CIET and show early results and examples of analysis in the University of California, Berkeley Thermal Hydraulics Lab Report UCBTH-17-002, titled “Frequency Response Testing in the CIET Facility”.

To generalize the strategy, each amplitude-phase-frequency set represents a single data point in the definition of a system’s frequency response. We can then visualize this frequency response across the frequency domain using graphs such as Bode gain plots, in which we plot the gain, or input-output magnitude ratio in decibels, against frequency. These plots follow a set of rules and contain characteristics such as break frequencies where we can isolate simple relationships between known and unknown variables and system parameters in order to formulate solvable algebraic equations. We identify these equations through theoretically modeling our system using first principles and manipulating our model into a set of input-output disturbance ratios in the frequency domain. By following this process, we obtain an empirical basis for validating very simple frequency-domain models that can be used to better understand system behavior, determine parameters, and confirm the robustness of modeling assumptions. A similar technique was applied to the Oconee nuclear plant during operation.

Following the basic development of frequency response testing as a testing method to drive validation in TH simulation benchmarking exercises, development of frequency response testing methods has continued to continue to improve system and conjugate heat transfer understanding. More information is found in (de Wet, 2018).

REFERENCES

C. Andreades, “Nuclear Air-Brayton Combined Cycle Power Conversion Design, Physical Performance Estimation and Economic Assessment,” Ph.D. Dissertation, Department of Nuclear Engineering, University of California, Berkeley (2015).

D. de Wet, "Designing frequency response tests for system identification of advanced nuclear reactors," M.S. Thesis, Department of Nuclear Engineering, University of California, Berkeley (2018).

C. Forsberg and P. F. Peterson, “Basis for Fluoride-Salt-Cooled High-Temperature Reactors with Nuclear Air-Brayton Combined Cycles (NACC) and Firebrick Resistance-Heated Energy Storage (FIRES),” *Nuclear Technology,* Vol 196, pp. 13–33, October 2016.

Z. Guo *et al.*, “Development of the FHR advanced natural circulation analysis (FANCY) code,” presented at NURETH-16, Chicago, IL, 2015.

N. Haneklaus *et al.*, “Thermal hydraulic benchmarking exercises to support fluoride-salt-cooled, high-temperature reactor (FHR) licensing,” presented at NURETH-16, Chicago, IL, 2015.

L. Huddar *et al.*, “Experimental strategy for the determination of heat transfer coefficients in pebble-beds cooled by fluoride salts,” presented at NURETH-16, Chicago, IL, 2015.

L. Huddar, "Heat Transfer in Pebble-Bed Nuclear Reactor Cores Cooled by Fluoride Salts," Ph.D. dissertation, Dept. Nucl. Eng., Univ. Cal. Berkeley, Berkeley, CA, 2016.

L. Huddar, A.J. Albaaj, J. Bickel, C. Lee, and P.F. Peterson, “The use of frequency response techniques for the measurement of heat transfer coefficients in pebble-beds cooled by fluoride salts using simulant fluids,” in *International Congress on Advances in Nuclear Power Plants (ICAPP)*, San Francisco, CA, 2016.

J. C. Kendrick and P. F. Peterson, “Nuclear quality assurance for universities,” presented at ANS Annual Meeting, Philadelphia, PA, 2018.

J.C. Kendrick A.J. Novak, C.M. Poresky, N. Zweibaum, and P.F. Peterson, “Observations of flow instability in a heated narrow vertical slot in the UCB CIET facility,” in *International Congress on Advances in Nuclear Power Plants (ICAPP),* San Francisco, CA, 2016.

J.C. Kendrick and P.F. Peterson, “Simulant fluids for use in molten salt thermal hydraulics experiments,” in *Specialist Workshop on Advanced Instrumentation and Measurement Techniques for Nuclear Reactor Thermal Hydraulics (SWINTH),* Livorno, Italy, 2016.

R. Lukas, J. C. Kendrick, and P. F. Peterson, “Improved heat transfer and volume scaling through novel heater design,” in *2017 Annual ANS Meeting*, San Francisco, CA, June, 2017.

A.J. Novak, N. Zweibaum, J. Anderson, and P.F. Peterson, "Dynamical system scaling of integral natural circulation experiments for fluoride-salt-cooled reactors," in *International Congress on Advances in Nuclear Power Plants (ICAPP)*, San Francisco, CA, 2016.

C. M. Poresky, “Frequency Response Testing in the CIET Facility,” *Department of Nuclear Engineering, U.C. Berkeley,* **Report UCBTH-17-002** (May 2017).

C. M. Poresky and P. F. Peterson, “On-line monitoring-prognostics and health management for nuclear power plants,” presented at ANS Annual Meeting, Philadelphia, PA, 2018.

C. Poresky, J. C. Kendrick, and P. F. Peterson, “Preliminary Experimental Results for Frequency Response Testing in FHRs and MSRs Using the Compact Integral Effects Test”, in *17th International Topical Meeting on Nuclear Reactor Thermal Hydraulics,* Xi’an, China, September 2017

C. Poresky, J. Kendrick, N. Zweibaum, and P.F. Peterson, “Preliminary model validation for thermal hydraulic integral transient behavior in fluoride-salt-cooled high-temperature reactors”, in *International Congress on the Advances in Nuclear Power Plants (ICAPP)*, San Francisco, CA, 2016.

N. Zweibaum, Z. Guo, J. C. Kendrick, and P. F. Peterson, “Design of the compact integral effects test facility and validation of best-estimate models for fluoride-salt-cooled high-temperature reactors,” *Nucl. Tech*., vol. 196, no. 3, Dec. 2016.

N. Zweibaum, "Experimental Validation of Passive Safety System Models: Application to Design and Optimization of Fluoride-Salt-Cooled, High-Temperature Reactors," Ph.D. Dissertation, Department of Nuclear Engineering, University of California, Berkeley (2015).

4.2. FHR Neutronics Analysis (UCB)

FHR Neutronics Report (UCB)[13]

Summary

The Integrated Research Project (IRP) is to address major challenges in the development of commercial Fluoride-salt-cooled High-temperature Reactor (FHR), which uses graphite-matrix coated-particle fuel with a pebble bed geometry and a liquid salt coolant flibe. In the scope of the IRP, efforts on understanding and modeling the core neutronics for FHRs spans in various areas, including code-to-code benchmark to verify the credibility of neutronics codes in modeling reactors with TRISO particle type fuel, development of numerical models for FHR cores, uncertainty and sensitivity study of Monte Carlo models due to nuclear data, and analyzing the activation process and gamma radiation shielding of the FHR coolant.

The major projects are:

- ***Code-to-code benchmark:*** To date, no fueled experiments using pebbles immersed in salt have been conducted. Early-stage benchmarking of FHRs must rely heavily on code-to-code comparisons. The design of test cases for the IRP FHR neutronics benchmark starts with a simple, infinite cell containing pebbles and is examined with varying levels of homogenization. And the second scenario includes a graphite reflector and black boundaries to simulate a simplified reactor geometry, allowing for leakage and reflector effects.

- ***Multiphysics modeling for FHR cores:*** This project developed dedicated models for FHRs with different levels of spatial and energy resolution for the broad need in reactor design and analysis, including coupled heat diffusion and point kinetics unit cell models, Monte Carlo neutronics models, and coupled multi-group neutron diffusion and multi-scale porous media model. The methodology was applied to the TMSR SF-1 and Mk1 design to simulate both steady state and transient scenarios.

- ***Investigation of uncertainties in Monte Carlo models due to nuclear data***: Sensitivity and uncertainty analyses for effective multiplication factor and coolant density reactivity coefficient due to nuclear data are performed for the Mark-1 pebble-bed fluoride-salt-cooled high-temperature reactor (Mk1 PB-FHR).

- ***Salt activation and shielding analysis:*** This project aims to analyze the shielding property of the Mark-1 PB-FHR reactor design, in three steps: burnup calculation, shielding calculation and flux to dose conversion. The calculation can serve as a primitive analysis on the shielding properties of the materials used in Mark-1 PB-FHR.

---

[13] Xin Wang, Dan Shen, Jun Shi, Manuele Aufiero, Quicang Shen, Massimiliano Fratoni

TABLE OF CONTENTS

1 Introduction

The Integrated Research Project (IRP) is to address major challenges in the development of commercial Fluoride-salt-cooled High-temperature Reactor (FHR), which uses graphite-matrix coated-particle fuel with a pebble bed geometry and a liquid salt coolant flibe. In the scope of the IRP project, efforts on understanding and modeling the core neutronics for FHRs spans in various areas, including:

- Code-to-code benchmark

- Numerical modeling methodologies for FHR core neutronics and thermal-hydraulics

- Investigation of uncertainties in Monte Carlo models due to nuclear data

- Salt activation and shielding analysis

2 Code-to-code benchmark

Fluoride-salt-cooled high-temperature Reactors (FHRs) are a relatively new reactor concept. The fuel form of these salt-cooled reactors is a solid fuel employing the same tri-isotropic (TRISO) coated particles used in many high temperature gas-coolant reactors (HTGRs). There are a few different designs for fuel assemblies or elements, including pebbles, plates and prismatic blocks; this IRP focuses on a pebble-bed core design. To date, no fueled experiments using pebbles immersed in salt have been conducted. This is further complicated by the effectively inability to set up a simple experiment to obtain data about the neutronics behavior of such a system. Without validation capability, early-stage benchmarking must rely heavily on code-to-code comparisons. Fortunately, as the pebble fuel has been used in critical facilities and reactor before, albeit not using a salt coolant, there are some measurement data available that capture some of the phenomena associated with the pebbles themselves, such as the so-called “double-heterogeneity” of the particle/pebble geometry. Reports from the International Atomic Energy Agency (IAEA) Collaborative Research Projects (CRPs) such as IAEA-TECDOC-1382 and IAEA-TECDOC-1694 contain a great deal of information and benchmark data from various HTGR facilities and verification scenarios. Of particular interest to the IRP at this stage is the Pebble-Bed Modular Reactor (PBMR) “Pebble Box” benchmark in IAEA-TECDOC-1694, which defines a number of test cases for the purposes of a code capabilities check. The design of test cases for the IRP FHR neutronics benchmark are very similar to the Pebble Box benchmark, both of which start with a simple, infinite cell containing pebbles and is examined with varying levels of homogenization. This allows some quantification of the resonance self-shielding and neutron streaming effects. The second scenario includes a graphite reflector and black boundaries to simulate a simplified reactor geometry, allowing for leakage and reflector effects.

2.1 Unit cell benchmark specification

This benchmark focuses on the neutronics physics behavior of a Face-Centered Cubic (FCC) unit cell system. The main concern of the study is to test code capabilities and make a code-to-code comparison. The unit cell benchmark consists of three cases:

Case 1: Homogenous mixture

Description: cube unit cell filled with a single material that is a mixture of coolant and pebble components.

Geometry: cube of side length 9.2575 cm, reflective boundary conditions on all sides.

Material:

Material	Density g/cm^3	Temperature K	Isotope	Mass fraction
Mixture	1.872	900	O-16	2.53927E-03
			U-235	3.22769E-03
			U-238	1.56268E-02
			C-nature	5.20535E-01
			Si-nature	4.82195E-03
			B-10	4.63687E-08
			B-11	2.06506E-07
			Li-6	5.50568E-06
			Li-7	6.42115E-02
			Be-9	4.12446E-02
			F-19	3.47787E-01

Table 12: Material information for Case 1

Cross sections: any library, optional graphite scattering kernel for carbon.

Case 2: Single level heterogeneity

Description: cube unit cell filled with pebbles and coolant. The pebbles are comprised of homogeneous inner fuel region and shell.

Geometry: cube of side length 9.2575 cm, reflective boundary conditions on all sides. As shown in Figure 1, there are eight 1/8 pebbles in the vertex, six 1/2 pebbles in the face center of the cube. The radius of pebble is 3 cm and the radius of its inner fuel region is 2.5 cm. The space among pebbles is filled with FLiBe coolant.

Material:

Material	Density g/cm^3	Temperature K	Isotope	Mass fraction (relative)	Atom fraction (relative)
Fuel	1.842	900	O-16	7.81961E-03	
			U-235	9.93958E-03	
			U-238	4.81225E-02	
			C-nature	9.19269E-01	
			Si-nature	1.48491E-02	
			B-10	8.01063E-08	
			B-11	3.56758E-07	
Matrix (shell)	1.73	900	C-nature		8.77414E-02
			B-10		9.64977E-09
			B-11		3.90864E-08
FLiBe	1.9740	900	Li-6		0.0002
			Li-7		1.9998
			Be-9		1.0000
			F-19		4.0000

Table 13: Material information for Case 2

Cross sections: any library, optional graphite scattering kernel for carbon.

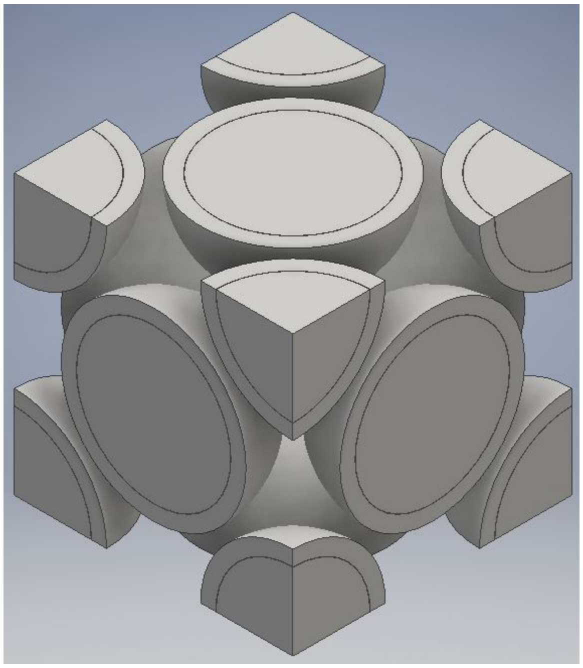

Figure 94: Case 2 configuration.

Packing fraction	57.02%
Radius of the pebble	3cm
Radius of inner fuel region	2.5cm
Thickness of shell	0.5cm

Table 14: Case 2 geometry information

Case 3: Double heterogeneity

Description: cube unit cell filled with pebbles and coolant. The pebbles are comprised of inner fuel region and shell. The inner fuel region of pebble is comprised of 11558 fuel particles and graphite matrix. The packing factor of fuel particles is 6.97%.

Geometry: cube of side length 9.2575 cm, reflective boundary conditions on all sides. Case 3 keeps everything the same as case 2 except that the inner fuel region of pebble is filled with particles and graphite matrix as shown in Figure 95. The radius of fuel particle is 0.0455 cm. For the ordered particles, the side length of particle FCC lattice is 0.2828 cm.

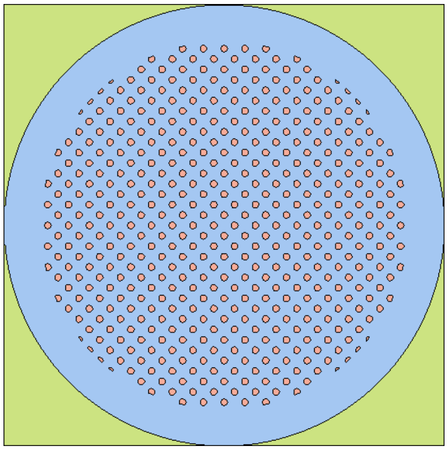

Figure 95: Pebble in Case 3.

Centre fuel kernel radius	0.025 cm
Buffer layer thickness	0.009 cm
Inner PyC layer thickness	0.004 cm
SiC layer thickness	0.0035 cm
Outer PyC layer thickness	0.004 cm
Particle radius	0.0455 cm

Table 15: Case 3 TRISO geometry information

Material:

Material	Density, g/cm^3	Temperature, K	Isotope	Atom fraction (relative)
Fuel	10.5	900	O-16	2.0
			U-235	0.173
			U-238	0.827
Buffer	1.05	900	C-nature	1
PyC	1.90	900	C-nature	1
SiC	3.18	900	Si-nature	4.77240E-02
			C-nature	4.77240E-02
Matrix (shell)	1.73	900	C-nature	8.77414E-02
			B-10	9.64977E-09
			B-11	3.90864E-08
FLiBe	1.9740	900	Li-6	0.0002
			Li-7	1.9998
			Be-9	1.0000
			F-19	4.0000

Table 16: Material information for Case 3

Cross sections: any library, optional graphite scattering kernel for carbon.

Results of interest

- *Keff*
- Effective delayed neutron fraction
- Effective generation time & life-time
- Neutron spectrum
- Cross section:

Li-6	(n, t)
Li-7	Capture
F	Capture
U-238	Capture
U-235	Fission
U-235	Capture
FLiBe	Elastic scattering

Table 17: Expected cross section

Reference result

- Software used

  Serpent 2 – 3D Monte Carlo code

- Case 1&2&3 using thermal scattering cross sections for carbon

	case1		case2		case3(ordered TRISO)		case3(random TRISO)	
k-eff	1.30504E+00	3.4E-05	1.34638E+00	3.5E-05	1.42187E+00	3.7E-05	1.42516E+00	3.7E-05
beta_eff	6.51083E-03	0.00089	6.50994E-03	0.00087	6.48759E-03	0.00083	6.50227E-03	0.00083
gen_time	2.88459E-04	0.00011	2.83159E-04	0.00011	2.74491E-04	0.00011	2.74415E-04	0.00011
lifetime	3.76446E-04	7.4E-05	3.81189E-04	7.3E-05	3.90265E-04	6.8E-05	3.91036E-04	7.0E-05

Table 18: Summarized results using thermal scattering library

- Case 1&2&3 not using thermal scattering cross sections for carbon

	case1		case2		case3(ordered)	
k-eff	1.30685E+00	3.4E-05	1.34900E+00	3.5E-05	1.42435E+00	3.7E-05
beta_eff	6.51428E-03	0.00087	6.55570E-03	0.00088	6.52010E-03	0.00084
gen_time	2.87402E-04	0.00012	2.81364E-04	0.00011	2.73186E-04	0.00011
lifetime	3.75592E-04	7.5E-05	3.79505E-04	7.1E-05	3.89049E-04	7.1E-05

Table 19: Summarized results not using thermal scattering library

- Neutron spectrum

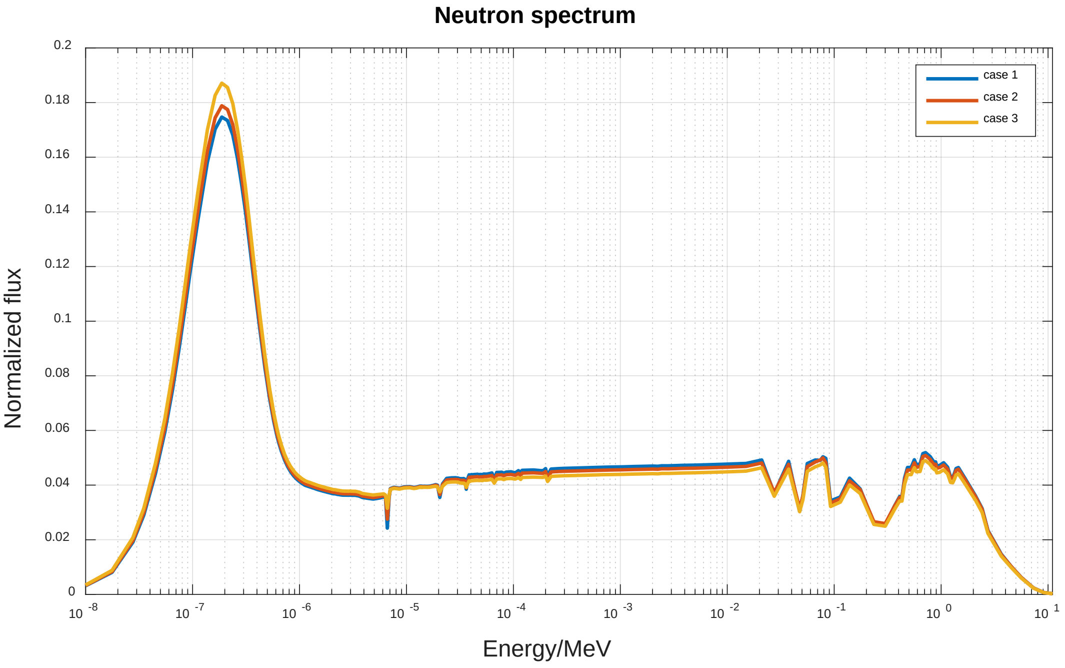

Figure 96: Average neutron spectrum in Scale238 energy grid.

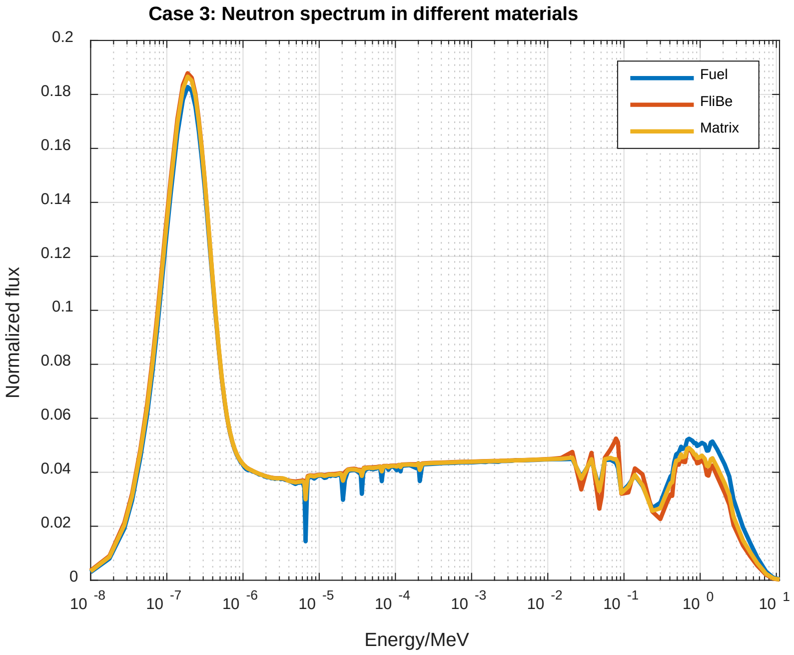

Figure 97: Case 3: Neutron spectrum in different materials.

- Selected cross section

In certain energy group, microscopic cross section can be expressed as:

$$\sigma = \frac{\Sigma[\mathrm{cm}^{-1}]}{N[\mathrm{cm}^{-1}\cdot \mathrm{b}^{-1}]} = \frac{1}{N}\frac{\int_{E_{i+1}}^{E_i} \Sigma(\mathrm{r},\mathrm{E})\phi(\mathrm{r},\mathrm{E})\,\mathrm{d}^3 r dE}{\int_{E_{i+1}}^{E_i} \phi(\mathrm{r},\mathrm{E})\,\mathrm{d}^3 r dE}$$

Energy group, MeV	Microscopic cross section, b					
	Li-6(n, t)	Li-7(n, γ)	F(n, γ)	U-238(n, γ)	U-235(n, f)	U-235(n, γ)
[1.00000E-11, 6.25000E-07]	4.22843E+02	2.03609E-02	4.29247E-03	1.21090E+00	2.31901E+02	4.23222E+01
[6.25000E-07, 5.53000E-03]	4.09470E+01	1.97733E-03	4.20312E-04	1.14476E+01	2.66002E+01	1.39338E+01
[5.53000E-03, 8.21000E-01]	1.03750E+00	4.74510E-05	1.03526E-03	3.57175E-01	1.93451E+00	5.82802E-01
[8.21000E-01, 1.00000E+01]	2.06658E-01	4.83508E-06	1.00440E-04	6.52802E-02	1.21795E+00	6.89562E-02

Table 20: 4-group microscopic cross section

Energy group, MeV	Macroscopic cross section, cm^{-1}
[1.00000E-11, 6.25000E-07]	2.79699E-01
[6.25000E-07, 5.53000E-03]	2.74905E-01
[5.53000E-03, 8.21000E-01]	3.22302E-01
[8.21000E-01, 1.00000E+01]	1.73396E-01

Table 21: FLiBe elastic scattering macroscopic cross section

2.2 3D full core benchmark specification

The second stage of this benchmark specification is a simplified model of the TMSR-SF1 core. The core in this benchmark is a solid fuel molten salt cooled high-temperature reactor. It uses 6.0cm-diamter spherical fuel elements, which contains 17.12wt% uranium. The coolant of primary loop is 2LiF-BeF_2 molten salt. The temperature is set to 900 K.

Core layout

The cylinder core includes a middle cylinder active region, top reflector, bottom reflector and radial reflector as shown in Figure 98 and detailed parameters can be found in Table 22. Top and bottom reflector are mixture of grap

hite and coolant. For the top reflector, the volume ratio of FLiBe and graphite is 1:3.69936 and for the bottom reflector, the volume ratio of FLiBe and graphite is 1:3.08061. The active region consists of a fuel region and a pure coolant region. Fuel pebbles are distributed randomly in the fuel region, which is the upper section of active core. The gap among pebbles and the bottom section of active core are filled by coolant.

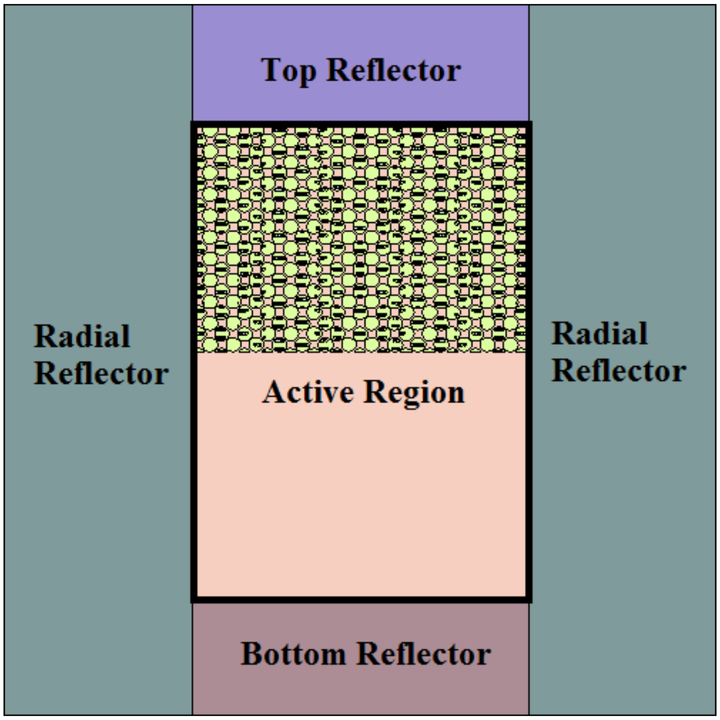

Figure 98: Layout of the core.

Active region	
The diameter/height of the active region	135cm/205.7cm
The height of fuel region	99.3223 cm
The packing factor of fuel region	57.02%
Temperature	900K
Reflector layer	
The diameter/height of the top reflector	135cm/50.35cm

The diameter/height of the bottom reflector	135cm/50.35cm
The outer shape of radial reflector	Cylinder, diameter: 285.0cm, height: 306.4cm

Table 22: Parameter of core design

The model includes 7168 pebbles, the number required to achieve criticality using a random packing with a fresh core and no control elements. Rather than using explicitly defined pebble locations, a regular lattice of the FCC arrangement was used. Due to the regular lattice, the pebbles on the periphery of the core were cut and the exact fuel volume was not known. The pitch of the particle lattice was first tweaked so that the effective particle packing factor was maintained. Following that, the pitch of the pebble lattice was iterated to preserve the nominal pebble packing factor. As such, it should be noted that the lattice used in the unit cell and the simplified core model are very similar, but not identical.

Fuel elements

The core uses 6.0 cm-diameter spherical pebble fuel elements. Each pebble contains 11558 TRISO particles. Graphite is used to fill the gap among fuel particles and to compose the cladding of pebble. The design parameter of pebbles is shown in Table 23.

Radius of the pebble	3cm
Radius of inner fuel region	2.5cm
Thickness of shell	0.5cm

Table 23: Design parameter of fuel pebble element

The design parameter of TRISO is as follows:

Centre fuel kernel radius	0.025 cm
Buffer layer thickness	0.009 cm
Inner PyC layer thickness	0.004 cm
SiC layer thickness	0.0035 cm
Outer PyC layer thickness	0.004 cm
Particle radius	0.0455 cm

Table 24: Design parameter of TRISO

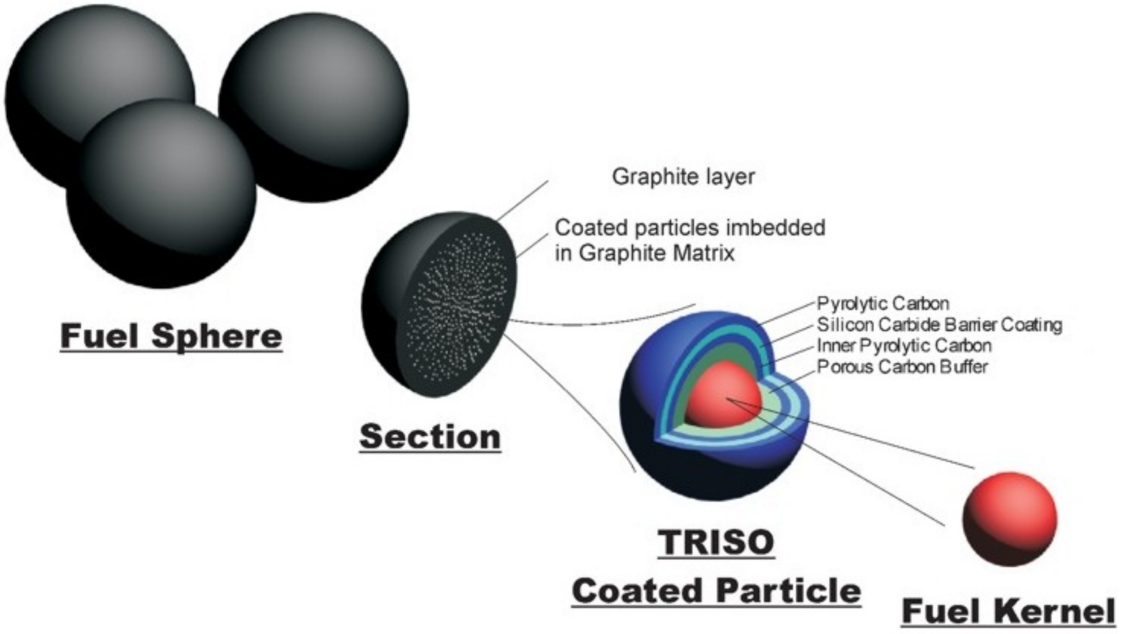

Figure 99: Fuel element.

Material

The material data for fuel elements can be found in Table 25. The density of FLiBe is calculated by the following formula where the unit of temperature T is C:

$$\rho = 2279.92 - 0.488 \cdot T(kg/m^3)$$

Fuel region in TRISO	Total mass density = 10.5 g/cm^3
Isotope	Relative atom density
O-16	2.0
U-235	0.173
U-238	0.827
Buffer layer	Total mass density = 1.05 g/cm^3
C	1
PyC layer	Total mass density = 1.90 g/cm^3
C	1
SiC layer	Total mass density = 3.18 g/cm^3
Isotope	Relative atom density
Si	4.77240E-02
C	4.77240E-02
Matrix (shell) of pebble	Total mass density = 1.73 g/cm^3
Isotope	Relative atom density
C	8.77414E-02

B-10	9.64977E-09
B-11	3.90864E-08

Table 25: Fuel element material

Table 26 and Table 27 list the material data for coolant FLiBe and graphite reflector.

FLiBe	Total mass density = 1.9740 g/cm^3
Isotope	Relative atom density
Li-6	0.0002
Li-7	1.9998
Be-9	1.0000
F-19	4.0000

Table 26: Coolant material

Radial reflector	Total mass density = 1.75 g/cm^3
Isotope	Relative atom density
C	8.77414E-02
B-10	9.64977E-09
B-11	3.90864E-08
Upper reflector	Total mass density = 1.7977 g/cm^3
Isotope	Relative mass density
C	1.3776
B-10	1.2630E-07
B-11	5.6251E-07
Li-6	5.1025E-06
Li-7	5.9509E-02
Be-9	3.8224E-02
F-19	3.2232E-01
Bottom reflector	Total mass density = 1.8049 g/cm^3
Isotope	Relative mass density
C	1.32114
B-10	1.21128E-07
B-11	5.3945E-07
Li-6	5.8762E-06
Li-7	6.8533E-02
Be-9	4.4020E-02
F-19	3.7119E-01

Table 27: Graphite reflector material

Results of interest

- K_{eff}
- Neutron spectrum (average in the fuel region of kernel)
- Radial Leakage and axial leakage
- Peaking factor (axial peaking factor & radial peaking factor)

- Several locations: power flux spectrum (scale238)
- Prompt lifetime
- Effective generation time ADJ
- Beta effective (effective delayed neutron fraction)
- Reactivity coefficients
- With/without alpha beta to see the k-eff and spectrum

2.3 Reference result

- Face-Centered Cubic lattice design

For FCC ordered pebbles and particles, we need to decide the pitch of FCC lattice. From Table 28, we can find that the optimal pitch length for TRISO and pebble lattice are 0.2828 cm and 9.25 cm.

Pitch of TRISO lattice (cm)	packing factor	Designed packing factor: 6.9678%
0.2829	6.95%	
0.2828	6.97%	
Pitch of pebble lattice (cm)	packing factor	Designed packing factor: 57.02%
9.24	57.21%	
9.25	57.03%	
9.2575	56.90%	
9.26	56.85%	

Table 28: FCC lattice design

The center of pebble FCC lattice is located in the center of fuel region.

- Software used

Serpent – 3D Monte Carlo code

- Summarized results

	Ordered pebbles and particles				Random pebbles and particles	
	Using thermal scattering libraries		Not using thermal scattering libraries			
Keff	9.93376E-01	8.3E-05	9.98900E-01	8.4E-05	1.00065E+00	8.4E-05
Generation time	6.66765E-04	0.00019	6.70006E-04	0.00019	6.39128E-04	0.00019
Lifetime	6.66980E-04	0.00028	6.74203E-04	0.00029	6.44081E-04	0.00029
Prompt lifetime	6.67134E-04	0.00028	6.74359E-04	0.00029	6.44243E-04	0.00029
Beta effective	6.77814E-03	0.00111	6.77636E-03	0.00109	6.76688E-03	0.00108

Table 29: Summarized results (1)

Leakage from the outer cylinder	Radial leakage	11.46%
	Upper leakage	5.64%
	Bottom leakage	0.16%
Axial peaking factor		1.1556
Radial peaking factor		1.1497

Table 30: Summarized results (2)

Doppler coefficient	900K		1200K		$\Delta\rho$(pcm)	$\triangle\rho/\triangle T$
	Keff=0.993376	8.3E-05	Keff=0.986853	8.3E-05	-665.40±11.74	-2.2180±0.0391
Coolant temperature coefficient	900K (ρ=1.9740g/cm3)		1200K (ρ=1.8276g/cm3)		$\Delta\rho$(pcm)	$\triangle\rho/\triangle T$
	Keff=0.993376	8.3E-05	Keff=0.988471	8.3E-05	-499.53±11.74	-1.6651±0.0391
Void reactivity coefficient	Void fraction = 0%		Void fraction = 5% (ρ=1.8753g/cm3)		$\Delta\rho$(pcm)	$\triangle\rho/\triangle$void fraction
	Keff=0.993376	8.3E-05	Keff=0.992830	8.3E-05	-55.36±11.74	-11.07±2.35

Table 31: Summarized results (3)

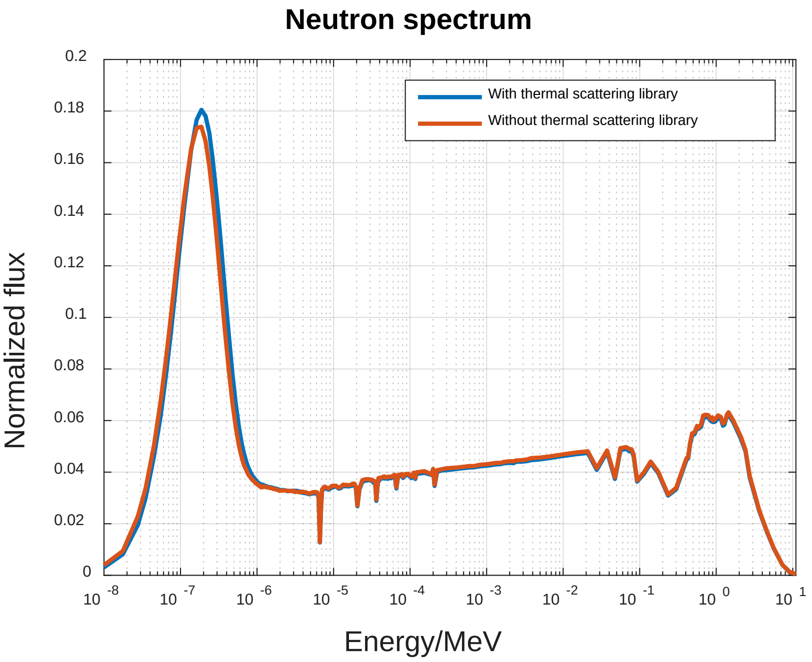

Figure 100: Neutron spectrum in fuel region of kernel.

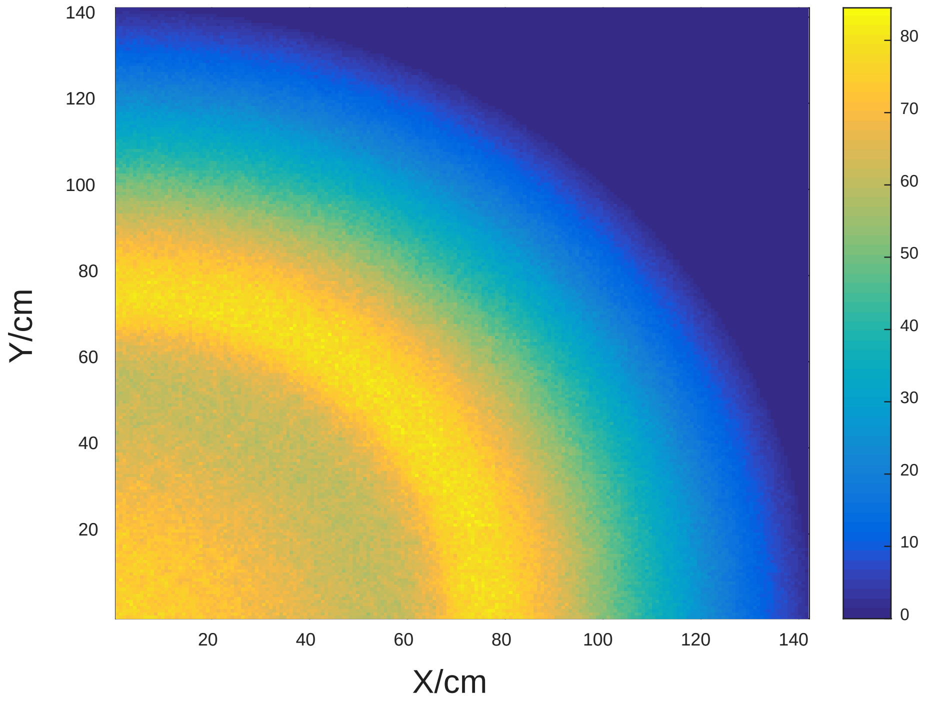

Figure 101 Thermal flux in X-Y plane.

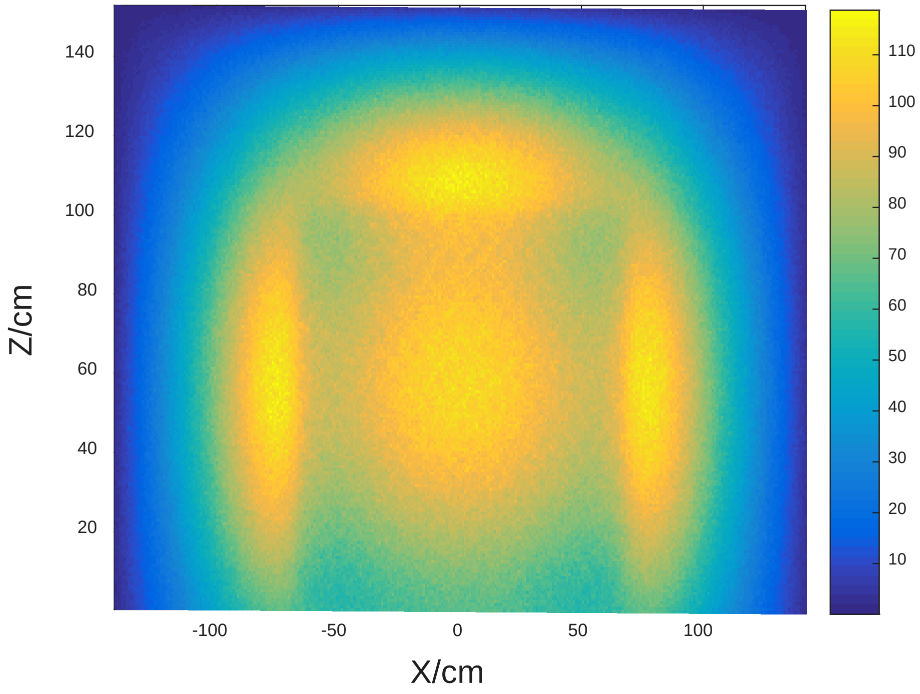

Figure 102: Thermal flux in X-Z plane.

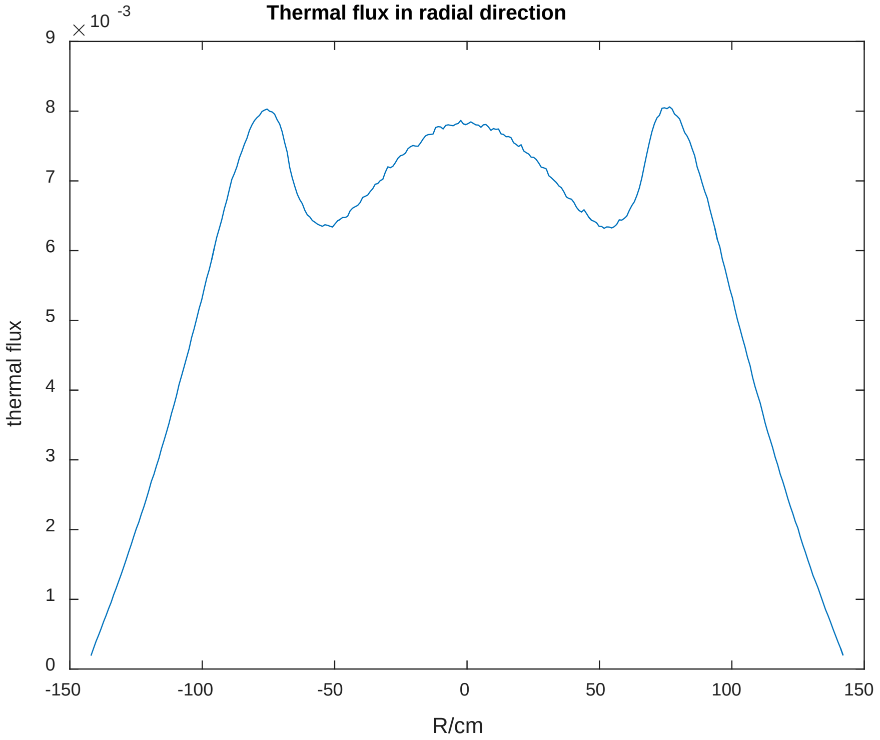

Figure 103: Radial thermal flux integrated from Z=3.5277 to Z=102.85cm.

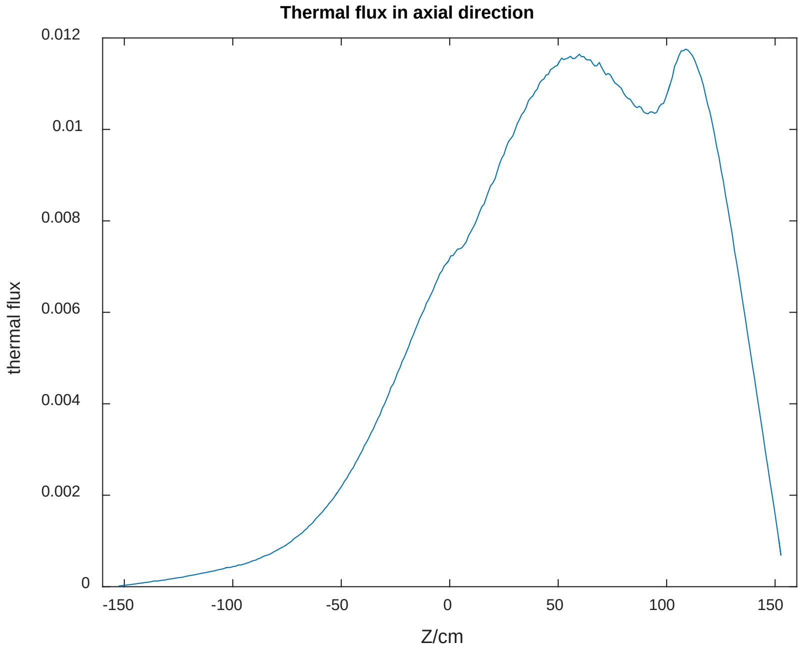

Figure 104: Axial thermal flux integrated from X=-67.5 to X=67.5cm.

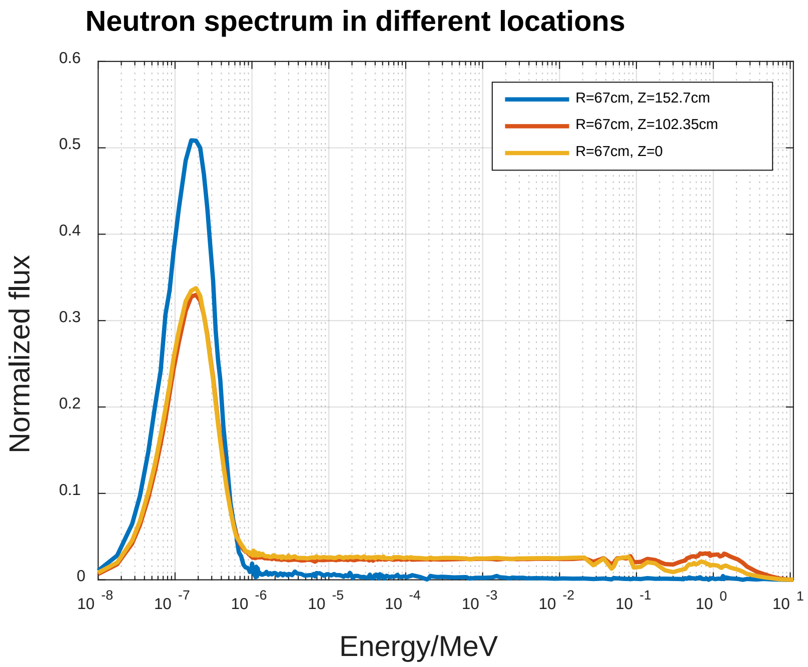

Figure 105: Neutron spectrum in different locations.

2.4 Code-to-code comparison results

Identification of modeling issues and other simulation phenomena is important in developing a robust benchmark specification. The is important to code effects from the methodological effects; it is important that the specification describes a system that does not leave a great deal of ambiguity in its details that can lead to errors in simulations results separate to differences in calculated values arising from different codes. The latter is one of the key outcomes of this benchmark, while the former serves only to add unnecessary error in the comparison.

Codes Used in Baseline Comparison

There are a number of neutronics codes available to perform criticality simulations, calculate fluxes, generate cross-sections, perform sensitivity analyses, burnup and generate point-kinetic parameters. There are two primary methodological approaches to solving these problems: deterministic and stochastic. While the deterministic approach is more mature and even preferred by many to perform neutronics calculations, the stochastic approach offers a higher-fidelity simulation by avoiding a number of approximations necessary to perform the necessary calculations. This benchmarking exercise not only provides the opportunity to use both and compare results but may uncover certain issues that arise from using either methodology; it is thought that Monte Carlo codes, the principle stochastic approach, is better suited to TRISO/pebble fuels, owing to the high-fidelity between the geometry definition in a model and the physical reality of a system. However, it lacks the historical confidence that deterministic codes now enjoy as well as suffering from an increased computational demand.

This work within this report shows the preliminary work done using the following codes and methodologies:

- Serpent 2, a 3D criticality/burnup Monte Carlo code from VTT, Finland.
- MCNP6, 3D general-purpose Monte Carlo transport code from LANL, US.
- SCALE6.1, a simulation suite designed for nuclear safety analysis with dozens of purpose-built modules for various applications, developed at ORNL, US. The transport modules within SCALE6.1 used are:
- T-XSDRN, a 1D discrete ordinates code used in the TRITON sequence.
- KENO-VI, a 3D Monte Carlo code.

Unit cell benchmark code-to-code comparison results

Three cases were examined in the unit cell model:

- Full volume-averaged homogenization. All geometry is collapsed into a single region and all materials blended into a single mixture. The mass fraction of each isotope is derived from the total mass of the isotope in the fully heterogeneous case divided by the total mass.
- Single level heterogeneity. The fuel zone (TRISO particles and graphite matrix) is homogenized while the pebble shell and FLiBe geometry is retained.
- Double heterogeneity. All geometry is preserved.

The figures of merit (FOM) identified for the unit cell stage of the benchmark are:

- K_{inf} – infinite multiplication factor
- β_{eff} – delayed neutron fraction
- L – prompt neutron lifetime
- Flux spectrum averaged across the whole cell (Case 3 only)
- Selected few-group cross sections (Case 3 only)

Case 1 – Full Homogenization

This case represents the simplest form of code-to-code validation. The model features no discrete geometry; it's essentially a point reactor model consisting of only fuel and pebbles. Table 32 contains the k_{inf} and point kinetics parameters calculated from the 5 different transport sequences used:

Transport Code	K_{inf}	**Uncertainty**	**Vs. Serpent [pcm]**	β_{eff} **[pcm]**	**L [µs]**
Serpent 2 (MC-CE)	1.30535	± 0.00004	-	654	319
MCNP6 (MC-CE)	1.30536	± 0.00007	1	656	290
KENO-VI (MC-CE)	1.30537	± 0.00024	2	-	99.1
KENO-VI (MC-MG)	1.30802	± 0.00018	267	-	99.3/245
T-XSDRN (DO-MG)	1.30788	-	253	-	-

Table 32: K_{inf}, β_{eff} and L for Case 1

The k_{inf} results generally agree with each other. The one stark contrast observable is the clustering of CE and MG results. Within each of these groups, the values are very close, but a 250-300pcm difference exists between the two of them.

The delayed neutron fraction is only available in Serpent 2 and MCNP6, though here the results are also in good agreement. Also, the prompt neutron lifetime results from Serpent 2 and MCNP are within about 10% of each other. The KENO-VI results show a much lower value, though this result is not particularly meaningful as the calculation for L did not use the adjoint flux. The KENO-VI MG result does feature an adjoint-weighted flux calculated lifetime, though this value is about 15-25% lower than the Serpent and MCNP. T-XSDRN does not feature capability to calculate either the delayed neutron fraction or prompt lifetime.

Case 2 – Single Heterogeneity

This case is a stepping stone case between the simplest unit cell and the complex DH pebble cell. As mentioned previously, the fuel region of each pebble is blended together by volume-average homogenization, but the pebble "macro" geometry is intact. This does introduce new phenomenon into the model, such as neutron streaming between pebbles and spatial discretization of some materials, notably Li-6, a strong neutron poison. The model doesn't, however, exclude the phenomena associated with the TRISO particles; the DH is a complex structure to deal with in deterministic methodologies and it was the intention for this case to provide an additional calibration scenario for participants' results. Table 33 contains the k_{inf} and point kinetics parameters calculated from the 5 different transport sequences used:

Transport Code	K_{inf}	**Uncertainty**	**Vs. Serpent [pcm]**	β_{eff} **[pcm]**	**L [µs]**
Serpent 2 (MC-CE)	1.34662	± 0.00004	-	656	303
MCNP6 (MC-CE)	1.34678	± 0.00007	16	647	305
KENO-VI (MC-CE)	1.34738	± 0.00019	76	-	251
KENO-VI (MC-MG)	1.34933	± 0.00020	271	-	251
T-XSDRN (DO-MG)	1.34928	-	266	-	-

Table 33: K_{inf}, β_{eff} and L for Case 2

The k_{inf} is larger in this case when compared to the fully homogenized case, though the results relative to each to other within this case are consistent with the first case. The increased k_{inf} is likely attributed to increased neutron streaming and moderation through the graphite shells and salt.

Case 3 – Double Heterogeneity

The final case is a unit cell with fully defined pebbles, including all the TRISO particles. In the CE codes, these particles are all modeled explicitly. In the MG codes, a treatment is used to modify the cross-sections of the fuel zone materials, then the content of that fueled region is homogenized into a single mixture (DH cell treatment in SCALE6.1). This scenario serves as the basic simulation "building block" that closely mimics an actual salt-pebble system, albeit with the infinite pebble bed assumption. In addition to the parameters observed in the previous two cases, the flux spectrum averaged over the whole cell and selected cross sections have also been computed. Table 34 contains the k_{inf} and point kinetics parameters calculated from the 5 different transport sequences used:

Transport Code	K_{inf}	**Uncertainty**	**Vs. Serpent [pcm]**	β_{eff} **[pcm]**	**L [µs]**
Serpent 2 (MC-CE)	1.42214	± 0.00004	-	652	277
MCNP6 (MC-CE)	1.42153	± 0.00007	-61	656	340
KENO-VI (MC-CE)	1.42163	± 0.00020	-51	-	244
KENO-VI (MC-MG)	1.42284	± 0.00017	70	-	257
T-XSDRN (DO-MG)	1.42178	-	-36	-	-

Table 34: K_{inf}, β_{eff} and L for Case 3

The initial comparison of k_{inf} results here looks very favorable, with the range of values about 130 pcm wide and no result deviating greater than 100 pcm from the reference Serpent result. However, this does not square with the results from the two previous cases between CE and MG simulations. This implies a cancellation of errors and likely a false agreement between the different codes. Furthermore, the values obtained from Serpent and MCNP start to deviate, an unexpected result. This could be attributed to different thermal scattering data used between the two codes; although the ENDF/B-VII.0 cross section data and TSL was used in all simulations within this exercise, the specific instances packages with, at least, Serpent and MCNP may be different.

Figure 106 shows the scalar flux spectrum, divided into 238 energy groups (SCALE-238 group structure) for each of the codes in the DH case. Between each of the Monte Carlo codes there is good agreement in the spectral data, upon visual inspection. There is a small artifact between the two KENO data and the others: a short, broad peak in the epithermal region, for example. After some discussion, no consensus was arrived at for this aberration, though a recheck of the energy group definition would be done. The one serious discrepancy is the MCNP vs. the other Maxwellian peak, which is higher than the rest. This also could be a result of inconsistent TSL data used for graphite between each code.

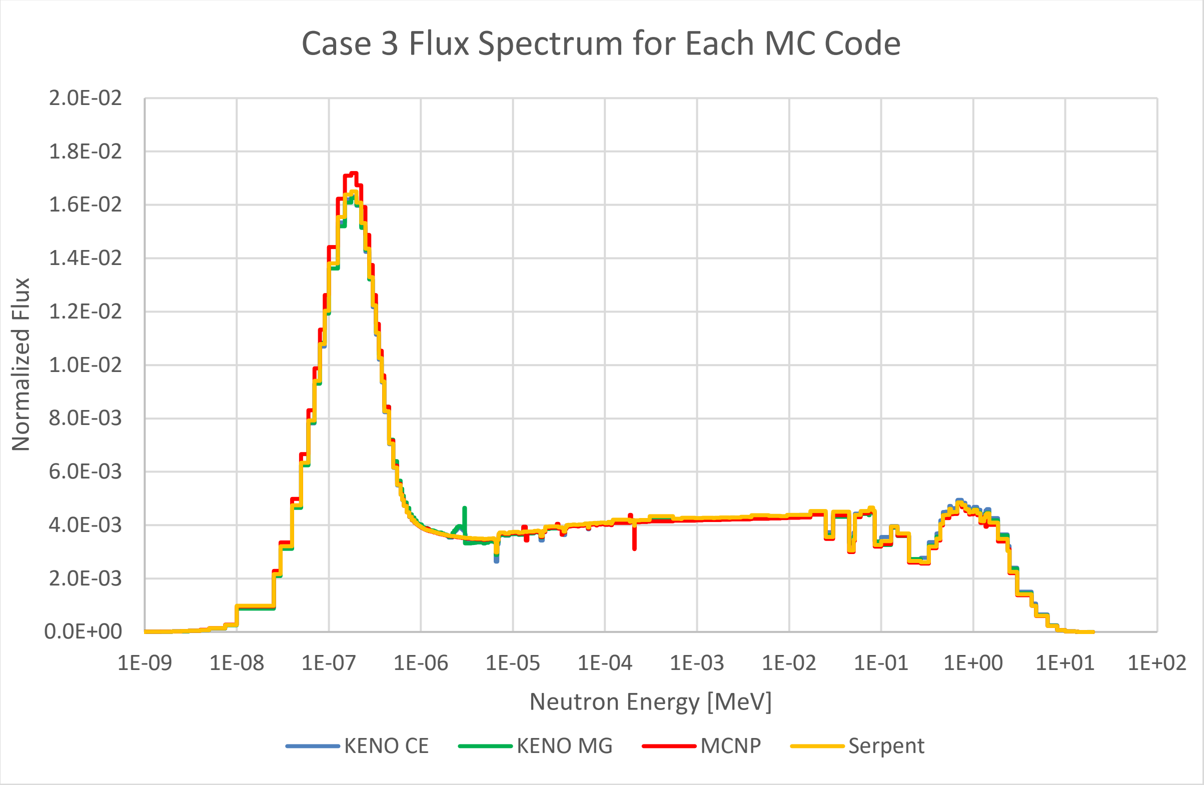

Figure 106: Neutron flux per lethargy as a function of neutron energy for Serpent 2, MCNP6 and KENO-VI.

2.5 3D full core benchmark code-to-code comparison results

Unlike the unit cell case, which was an infinite lattice of pebbles, this scenario has finite bounds. The outer boundaries of the reflector regions are all subject to black boundary conditions. This also introduces a non-zero leakage into the system. At present, work as only been carried out on this stage of the benchmark using MC codes. Table 35 contains the k_{eff} and point kinetics parameters calculated from the 4 different transport sequences used:

Transport Code	**K_{eff}**	**Uncertainty**	**Vs. Serpent [pcm]**	**β_{eff} [pcm]**	**L [µs]**
Serpent 2 (MC-CE)	0.99338	± 0.00008	-	679	667
MCNP6 (MC-CE)	0.98945	± 0.00008	-393	670	672
KENO-VI (MC-CE)	0.99047	± 0.00020	-291	-	622
KENO-VI (MC-MG)	0.99889	± 0.00023	551	-	702

Table 35: K_{eff}, β_{eff} and L for 3D full core benchmark

The difference between MCNP6 and KENO-VI CE is about 100 pcm, but the difference between these codes and Serpent is about 400 pcm. At this stage, the source of such discrepancy is unknown. The MG evaluation is ~1,000 pcm higher.

One interesting feature of such a compact reactor with a large portion of moderating facility located in a reflector is the two distinct "humps" in the radial thermal flux profile. At the center of the core, where the power density is high, there is a maximum in the thermal neutron flux. Around 10cm into the radial reflector from the inner diameter is a second, narrower hump in the flux. Obviously capturing this result in a code is important and was considered to be a suitable FOM for participants to obtain. Figure 107 shows the radial neutron flux profile as calculated by Serpent 2 and MCNP6.

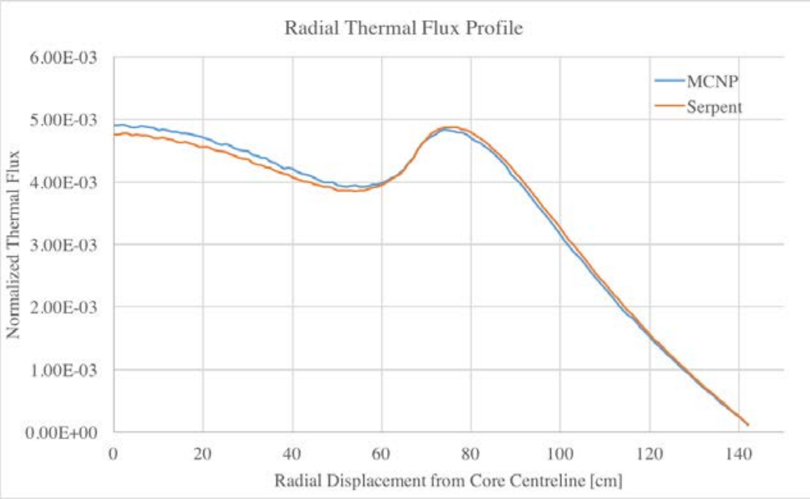

Figure 107: Radial thermal neutron flux of the Stage 2 model. Flux is sampled at 0.5cm intervals radially. Each interval averages the flux axially over the whole height of the fuel zone.

A similar double peak of thermal flux is observed axially through the centerline of the core. The first peak is seen near the center of the fueled zone and the second just inside the top reflector. It should be noted that the top reflector region in the model is not accurately representative of the actual geometry of TMSR-SF1, but is nevertheless a useful system feature to try and capture for the purposes of verification. Figure 108 shows the axial thermal neutron flux profile of the core as simulated by Serpent 2 and MCNP6.

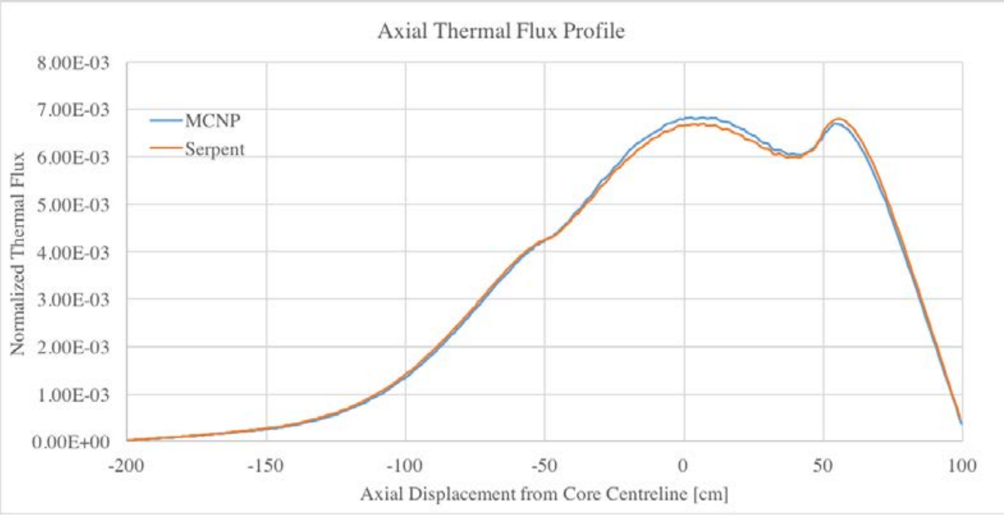

Figure 108: Axial thermal neutron flux of the Stage 2 model. Flux is sampled at 0.5cm intervals axially. Each interval averages the flux radially over the whole of the fuel zone.

Some discussion was given to determining power peaking factors. Contrary to a typical light-water reactor (LWR), which is largely axially prismatic, the TMSR-SF1 is highly heterogeneous in fuel geometry. As a result, the axial and radial power peaking factors are disjunct and a traditional approach might not be as useful. Table 36 contains the results from this traditional approach calculated using Serpent 2 and MCNP6.

Code	Axial Peaking Factor	Radial Peaking Factor
Serpent 2	1.1479	1.1106
MCNP6	1.1314	1.1236

Table 36: Power Peaking Factors in the Simplified Core

The final FOM considered for the simplified core model are selected reactivity coefficients (RC): coolant, void and fuel Doppler coefficients. The coolant RC is the temperature dependence of the salt reactivity contribution. Both the cross-section temperature and corresponding density variation is included in the calculation. The void coefficient was calculated by changing the density of the salt alone. The Doppler RC was calculated by varying the cross-section temperature of the uranium cross sections. The temperature-dependent RCs were determined using 50K intervals over a 300K range of 900K to 1200K. The void RC was determined using 2% void intervals between 0 and 10% reduction of salt density. Table 37 contains the specified RCs calculated using Serpent 2, MCNP6 and KENO-VI.

Code	Coolant	Void	Doppler
Serpent 2 (MC-CE)	-1.630 ± 0.033	-13.73 ± 0.99	-2.160 ± 0.033
MCNP6 (MC-CE)	-1.680 ± 0.039	-11.30 ± 1.13	-2.160 ± 0.038
KENO-VI (MC-CE)	-1.557 ± 0.092	-8.70 ± 2.90	-2.083 ± 0.094
KENO-VI (MC-MG)	-1.763 ± 0.108	-15.00 ± 3.25	-

Table 37: Reactivity Coefficients

A comparison of these values shows that Serpent and MCNP6 are in good agreement with each other, but the KENO-VI results varying significantly. It should be noted that there is greater uncertainty associated with the KENO RCs and the results were obtained from non-adjoint-weighted calculations.

The leakage values were obtained by creating neutron flux surfaces tallies at the outer boundary of the top, bottom and radial reflectors.

Code	Neutron Leakage		
	Top	Bottom	Radial
Serpent 2	-11.46%	-0.16%	-5.68%
MCNP6	-11.60%	-0.16%	-5.71%

Table 38: Neutron leakage from simplified core

3 Multiphysics modeling for FHR core

3.1 Coupled neutron diffusion and porous media CFD for PB-FHRs

Multi-group neutron diffusion models were developed for design optimization and safety analysis, because they are compatible with current computation resources in nuclear industry, with which simulations can be carried out on stand-alone workstations or small computation clusters within a reasonable time. For areas where diffusion assumption is limited, e.g. in vicinity of control rods, the simplified spherical harmonics equations were implemented to improve the accuracy of diffusion equation by relaxing the isotropic assumption in neutron transport. The neutronics model is coupled to a porous media CFD module with multiscale treatment that computes conductive heat transfer inside TRISO particles and fuel pebbles, as well as convective heat transfer between fuel pebbles and coolant. More details about the governing equations and implementation of the models can be found in [3].

3.1.1 Multiphysics modeling for TMSR SF-1

The TMSR research center was founded in 2011 at Shanghai Institute of Nuclear Applied Physics (SINAP) with the aim of studying, designing and commercially deploying molten salt based re- actors as a part of China’s next generation nuclear reactor fleet in the context of the rapid growing demand in energy and exacerbating air pollution from fossil fuel combustion. As a first step of a multistage commercialization plan, the TMSR Solid Fuel-1 (SF-1) reactor is a research reactor that would serve the objectives of demonstrating the capability in molten salt based re- actor design and construction, gaining hand-on experiences in novel reactor development, and providing experimental data for model validation in related fields, namely thermal-hydraulics, neutronics, material, etc. To minimize risk in such an innovative project, the design team takes a conservative approach by making use of existing technology that has been tested in other types of reactors whenever possible and simple design that might not be the most economical choice for large scale commercial deployment but relatively easy to implement in the first FHR in the world. Its simplicity and representativeness of the FHR technology makes it a good choice as our model development and verification baseline design.

3.1.1.1 TMSR SF-1 design overview

TMSR SF-1 is a 10 MW thermal nuclear reactor that combines the technology of liquid flibe coolant and TRISO particle fuel. The geometry of the design is shown in figure 16. The active region of the core consists of two opposite truncated cones with base diameter of 136 cm and aperture of 60 degree, connected by a 180 cm high cylinder with the same diameter. The cones are both cut at 30.3 cm in height with the minimum diameter of 30.0 cm.

TMSR SF-1 uses the same 6.0 cm fuel pebbles as those in the helium gas cooled high-temperature reactor (HTR), that contain a 5.0 mm thick graphite shell and the enclosed TRISO particles in a graphite matrix, as shown in figure 17.

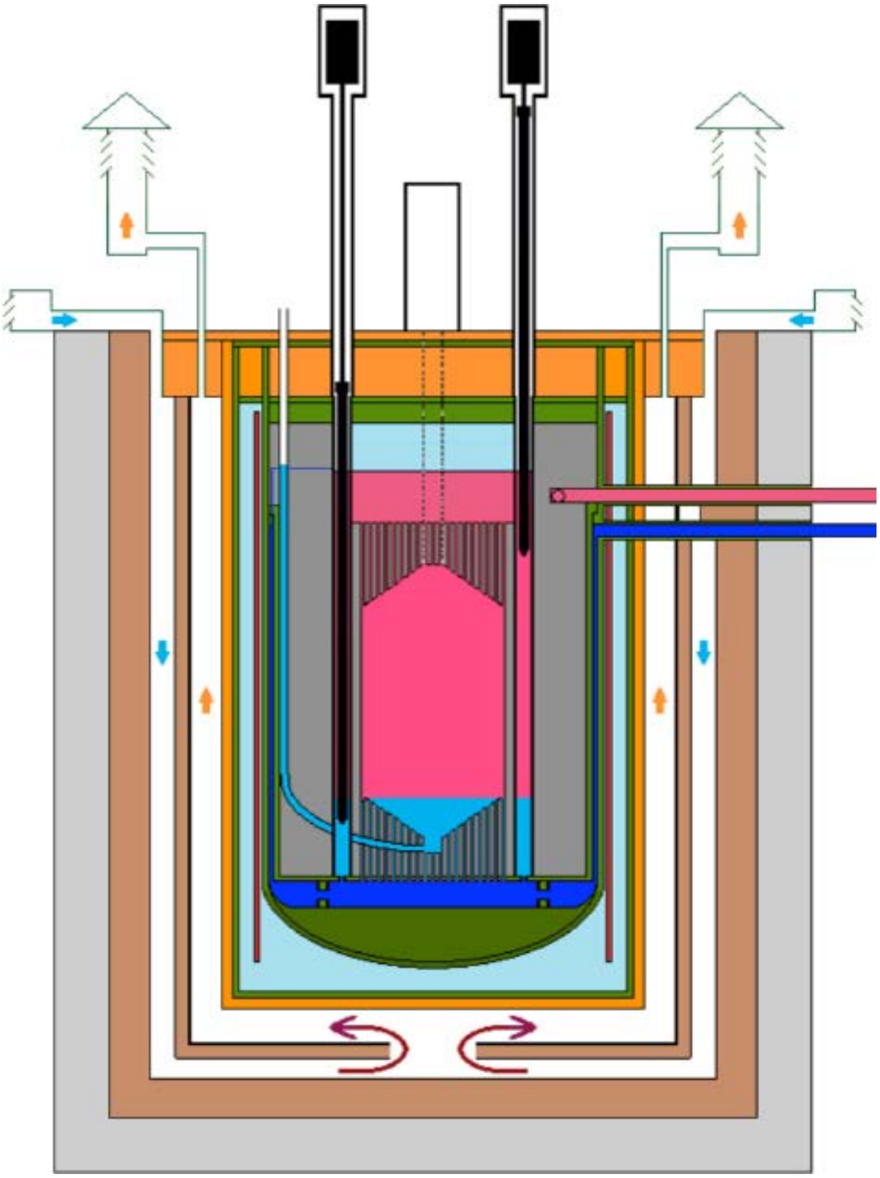

Figure 109: *Schematic of the TMSR core design*

TMSR SF-1 adopts a once-through fuel cycle, which although may not be the most economical approach comparing to online refueling, it is less demanding on the pebble handling system and is easier for predicting fuel composition in the core. At the start of a fuel cycle, the pebbles are loaded individually from the bottom of the core into the flibe salt until the core reaches criticality, with about 11,000 fresh fuel pebbles. Fuel pebbles are buoyant in the salt and fills the upper region. The bottom of the fuel pebble bed has a cone shape with an angle depending on the pebble/fluid interaction. The lower region of the core is left with flibe salt.

The primary coolant (enriched liquid flibe) enters the core from the bottom at a nominal inlet temperature of 672◦C and flows upward across the pebble region with a nominal outlet temperature of coolant of 700◦C. The heat is then transported to the secondary loop through a heat exchanger for electricity production.

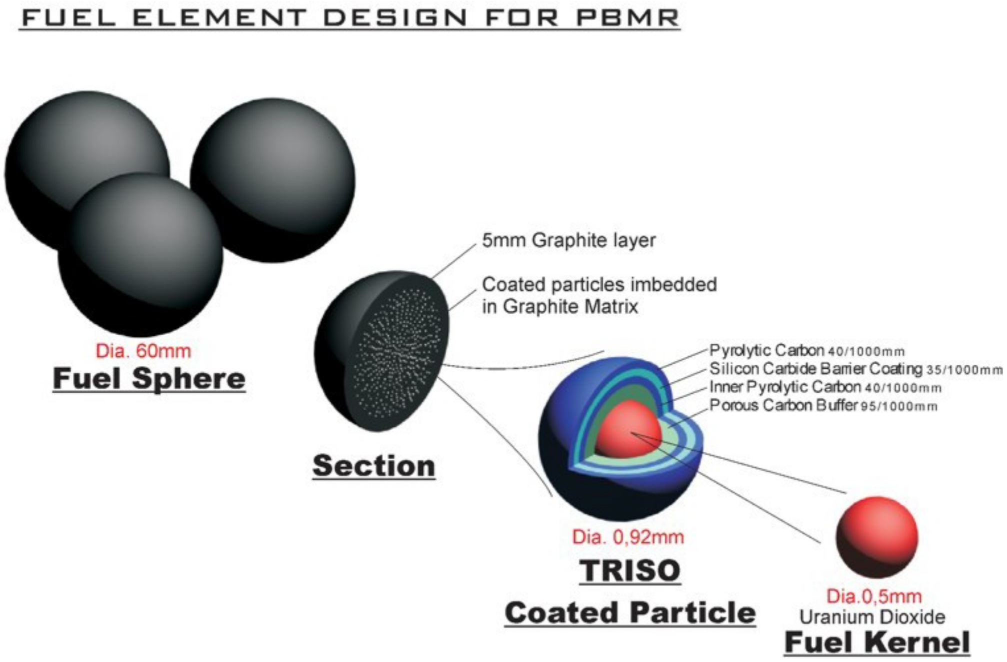

Figure 110: Schematic of fuel pebbles and TRISO particles in TMSR SF-1

An outer graphite reflector, which provides neutron moderation and reflection that flattens the radial power distribution and improves neutron economy surround the TMSR SF-1 core. It also hosts various channels for neutron sources, salt and pebble loading and instrumentation, as well as the 16 control rods for reactivity control.

3.1.1.2 Multi-physics modeling for TMSR SF-1

As shown in Figure 18, the multi-physics reactor core model is composed by three regions: an upper porous region that represents a fuel pebble and flibe salt porous mixture, a lower region with only flibe salt and an outer graphite reflector region. Coupled heat transfer and neutron diffusion equations are solved with homogenized material properties for each region.

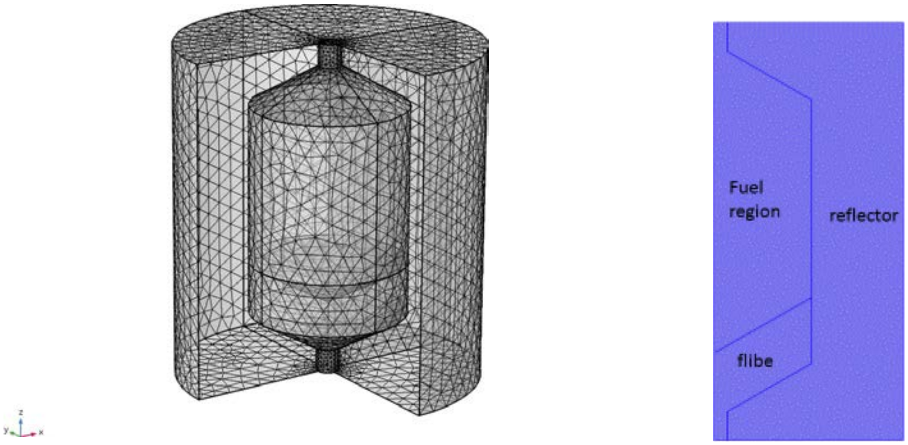

Figure 111: Schematic of three dimensional and two dimensional TMSR SF-1 core model geometry

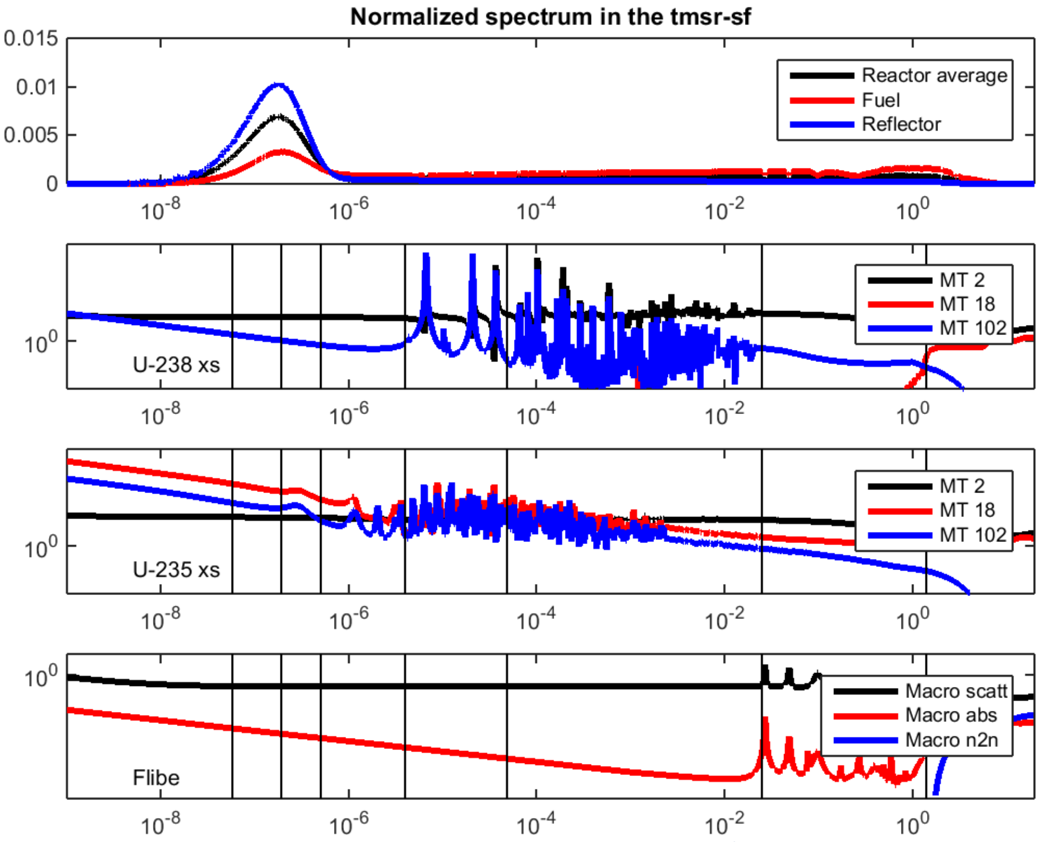

Figure 112: Macroscopic cross-sections of major isotopes in the core (vertical bars are energy group bounds, MT2=scattering, MT18=fission, MT102=absorption)

Multigroup neutron diffusion equations are implemented into COMSOL as user defined PDEs, with the homogenized group constants for each regions defined as input. Furthermore, SPN treatment can be used in regions where the diffusion assumption is questioned, such as in the vicinity of the control rods. The group constants that are used by the diffusion and SPN models are generated from a Serpent model for the TMSR SF-1 core with explicit representation of randomly packed TRISO particles and fuel pebbles, using the nuclear data library ENDF/B-VII.0.

Group #	Lower Energy Boundary (MeV)
1	1.4E+00
2	2.5E-02
3	4.8E-05
4	4.0E-06
5	5.0E-07
6	1.9E-07
7	5.8E-08
8	0.0E+00

Table 39: Energy group structure adopted in the multi-group neutron diffusion model

In order to automate the process and to ensure reproducibility of the results, a MATLAB code is developed to read data from Serpent output files, fit the parameters to the respective functions of reactor conditions, and input the group constants into COMSOL. The code is set up for any user defined group structures and the one that is used in the current models is shown in table 28. The eight-group energy structure is chosen to capture the cross section features of the major isotopes: U-235, U-238, and those in flibe. Figure 19 shows the normalized spectrum in different reactor zones and the scattering, fission, absorption and (n, 2n) cross sections of the major isotopes, in superposition of the currently used group structure.

The thermal-hydraulics model is implemented in COMSOL as well, so that the multiphysics equation system can be solved in a fully coupled fashion. To model the flow field and heat transfer in the pebble bed, porous media approach computes a liquid temperature and a fuel temperature at each point in the region and connect the two phases through convective heat transfer. The fuel temperature is of prime importance in FHR transient response because of the large Doppler temperature reactivity feedback. Therefore, multiscale temperature treatment is implemented for a more realistic representation of the feedback from fuel temperature changes. Temperature inside fuel pebbles are computed in three subdivided fuel layers, and likewise the fuel kernel in the TRISO particles are divided into three sub-layers, for which temperatures are tracked during a transient and are used to compute fuel region macroscopic cross-sections.

3.1.1.3 Code-to-code verification

Code-to-code comparison is crucial for code verification when experimental data is lacking. Code verification has been done in this work by comparing both steady state and time dependent results to a reference code under various conditions. The reference model [4] couples the neutron transport code Serpent and CFD code OpenFOAM internally for best computation performance. Serpent solves the neutron transport equation with Monte Carlo method using continuous energy nuclear data with full geometry details. OpenFOAM simulates heat transfer phenomena and computes temperature distribution in the coolant and fuel. To model the reactor core as realistic as possible, the random packing of TRISO particles and fuel pebbles are also simulated, using the discrete element method (DEM).

3.1.1.3.1 Power distribution comparison

Isothermal condition, whereby the core is maintained at uniform temperature by external heat source, is a good starting point for code-to-code comparison for the neutronic modules, as they do not require coupling with thermal-hydraulics. In order to verify the reliability of the neutronic modules, the power density distribution is computed.

Figure 20 shows the steady state power distribution on a 2.0 cm x 2.0 cm mesh, the result from the COMSOL model on the left and that from the reference model on the right, both normalized such that the full core integration is unity. Satisfying similarity has been found between the results. The diffusion-based model captures the boundary effect of the reflector adequately despite the fundamental flaw of the diffusion assumption in vicinity of the boundaries. However, because the individual pebbles are not explicitly modeled, the diffusion model cannot represent the local variation in power due to the discrete packing of fuel pebbles. As a result, the power profile seems smoother in the COMSOL model. In a randomly packed pebble bed, the porosity is slightly higher at the center and lower at the wall because of the ordering effect. Near the walls, the Monte Carlo result shows a drop in power density due to ordered pattern of pebbles, but this can not be captured by the COMSOL model because it uses homogenized cross sections in the fuel region. The variation can be better reflected in the COMSOL model if the core is divided into multiple radial zones, with different set of cross-sections generated for each zone. Furthermore, the interface between the fuel pebble region and the flibe region is approximated by a straight line in the COMSOL model. This is different from the randomly packed fuel region in the reference model but can be calibrated for a better match.

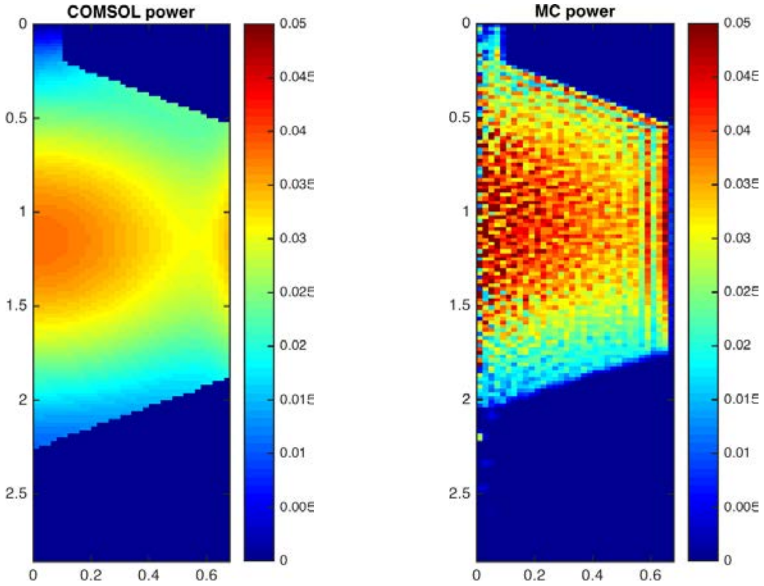

Figure 113: Steady state power profile computed from the COMSOL model and the Monte Carlo reference model

3.1.1.3.2 Multiplication factor comparison

The first global parameter that is compared under isothermal conditions is the multiplication factor, which is the most important global parameter in nuclear reactor modeling and control. At the same nominal conditions (flibe density at 1.9 g /cm3 and fuel temperature at 900 K), the multiplication factor value from COMSOL and reference model is shown in table 3.7. The difference between the COMSOL model and the reference model is larger than two times of the Monte Carlo statistical error, indicating that the difference is statistically significant. This shows that diffusion based models are inadequate in computing the neutron multiplication factor.

Parameter	value
COMSOL k_{eff}	1.03029
Reference k_{eff}	1.08416 ± 0.00012
Δk_{eff}	0.05397

Table 40: Comparison of multiplication factor

However, for transient analysis, which we are most interested in, the changes in the multiplication factor when the operation conditions deviates from the nominal ones is more important than the absolute values.

3.1.1.3.3 Time constant comparison

The time constant of the system is compared via zero power reactivity insertion transient simulations. External reactivity is inserted into the core at nominal zero power conditions and without temperature reactivity feedback that would stablize the power at a certain level, the reactor power increases exponentially due to excess external reactivity and the speed in which the power ramps up is a direct characteristic of the reactor time scale in the model.

Figure 21 shows the power excursion within 0.1 second following a reactivity insertion. As we can see, the results from the COMSOL model match closely to those from the Serpent model, as well as the analytical prediction, for a large range of inserted reactivities, from 26 pcm to 3599 pcm.

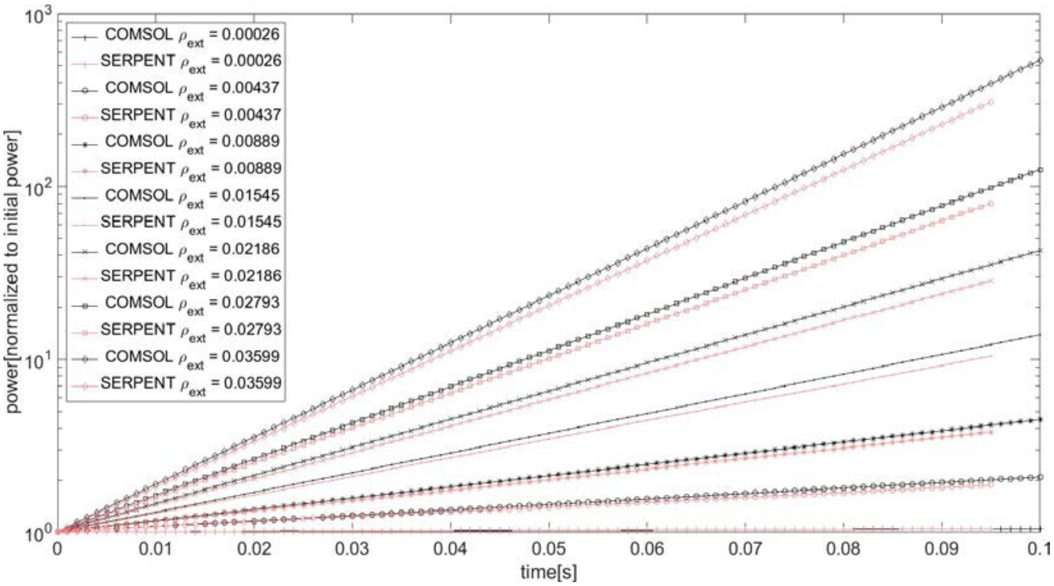

Figure 114: Comparison between the diffusion based model and the Monte Carlo based model for zero power reactivity insertion transients

3.1.1.3.4 Temperature feedback comparison

The ability of accurately capturing the temperature reactivity feedback coefficients is crucial for a coupled neutronics and thermal-hydraulics model because these parameters are the macroscopic manifestation of the coupling between thermal hydraulics and neutronics. They embody the effects of temperature change on core neutronics. The two major ones in FHR, the fuel Doppler feedback and the coolant temperature feedback coefficients, are computed from both models and are compared in Figure 22. The same y-axis range is used in the two plots for a visual comparison of the order of magnitude of these two feedback mechanisms. The fuel Doppler feedback is obviously the dominant effect in TMSR SF-1 cores.

The fuel temperature feedback curves agree well. The relative error in flibe reactivity feedback is larger but the absolute error is small due to the small magnitude of flibe feedback. And the discrepancy between flibe feedbacks is within statistical errors of the Monte Carlo computation.

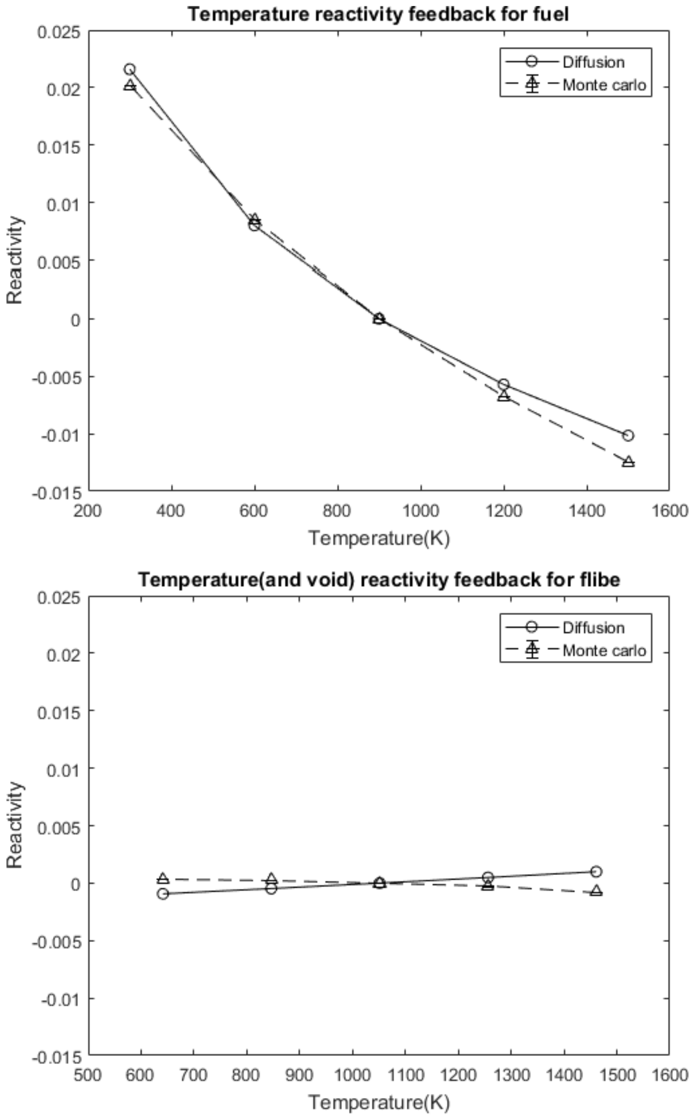

Figure 115: Comparison between the diffusion based model and the Monte Carlo based model for fuel and flibe temperature (and void) feedback effect. Error bar shows statistical error in Monte Carlo results.

3.1.1.4 TMSR SF-1 steady state results

After careful code-to-code verification for the multi-physics model, parameters such as power, flibe and fuel temperatures. Uniform temperature and uniform upward velocity are imposed as the inlet boundary condition. Vacuum boundary condition for neutron diffusion is used outside of the reflector.

The neutron flux distribution in the core is plotted in figure 23. An eight-group energy structure is used in the neutron diffusion equations but the neutron flux values are regrouped into thermal ([0.00E+00, 5.00E-07] MeV) and fast ([5.00E-07, 1.40E+00] MeV) regions for plotting purpose. As confirmed by the plots, fast neutrons are generated exclusively from nuclear reac- tions in the fuel region and are then scattered by the matters in the core as they get thermalized. The moderation effect of the coolant is dwarfed by that of the graphite reflector in TMSR. As a result, a large portion of thermal neutrons is found inside the reflector, besides the center of the core.

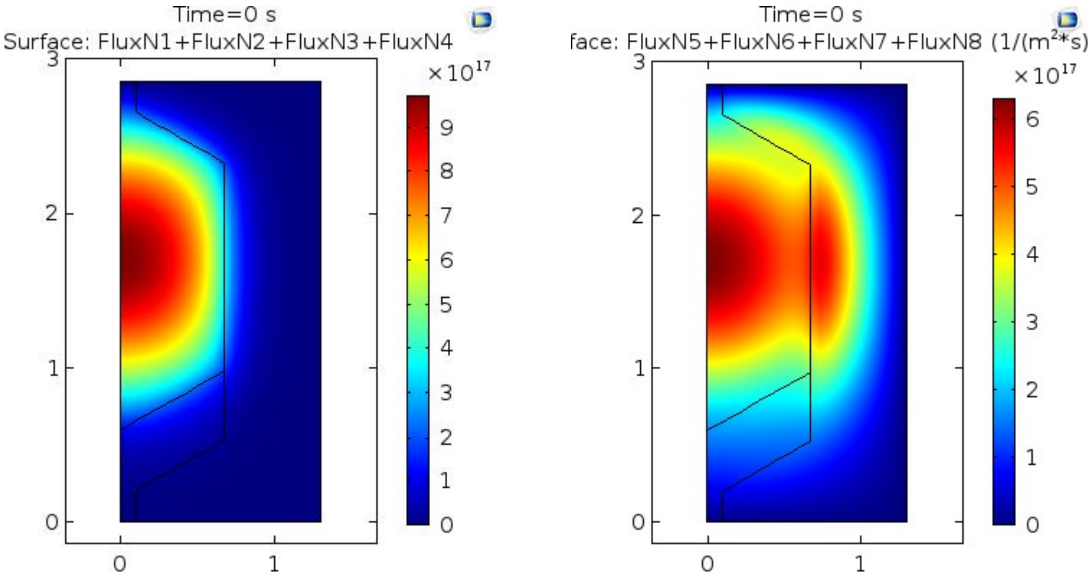

(a) Fast neutron flux ([5.00E-07, 1.40] MeV) **(b)** Thermal neutron flux ([0.00, 5.00E-07] MeV)

Figure 116: Steady state neutron flux

The thermal neutrons that travel back from the reflector to the fuel region cause a peak in power density near the border as they trigger nuclear reactions. As shown in figure 24, the power peaks at the center of the fuel region, decreases outward and increases again next to the reflector boundaries due to the moderation effect of the graphite reflector. This confirms that the neutron diffusion based model captures the boundary effect adequately. The radial power peaking in TMSR SF-1 is 1.24 at nominal conditions with fresh fuel.

Because of the large volumetric heat capacity of flibe, the coolant is a very efficient heat carrier in FHRs. The coolant enters the bottom of the TMSR SF-1 core at 672◦C, as imposed by the inlet boundary condition, and gradually heats up to, on average, 705◦C as it flows through the fuel region.

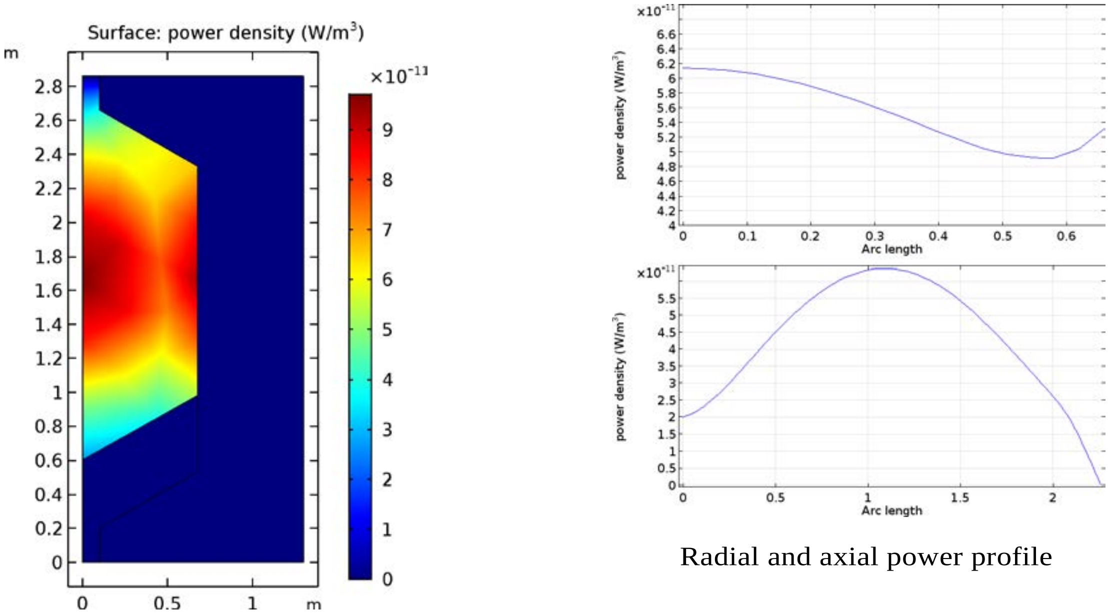

Radial and axial power profile

Figure 117: Power distribution in TMSR SF-1

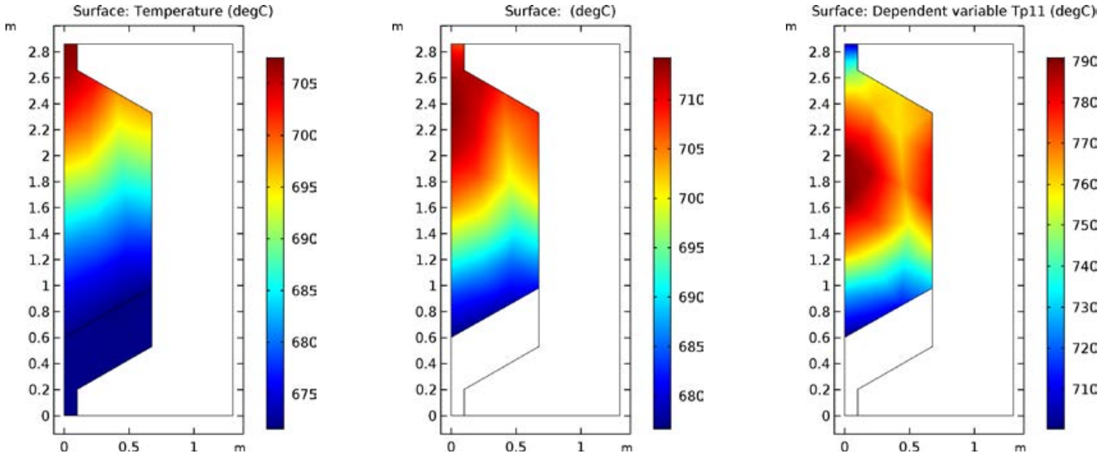

(a) Flibe **(b)** Fuel surface **(c)** Inner TRISO fuel layer

Figure 118: Steady state temperatures of coolant and selected locations in fuel element in TMSR SF-1 core, with multiscale treatment

Among all the temperatures computed in the solid fuel elements, only the coldest (in the pebble shell) and the hottest (in the center layer of TRISO particles) temperature in a pebble are shown in figure 3.15 as the upper and lower bound of the solid phase temperatures. The temperature distribution in the center of the TRISO particles resembles the power profile: hottest in the center of the core and coldest at the two axial extremities, within a range between 710 and 790 ◦C. The surface temperature is, on the other hand, affected both by the nuclear power and by the coolant flowing upward across the core and shifting the peak temperature upward. The hottest fuel surface temperature is attained at the top of the core, where the coolant is the hottest.

Overall, both the coolant and the fuel are far below their respective safety limits at steady state. The large thermal margins make the TMSR SF-1 core very robust to transient scenarios.

3.1.1.5 TMSR SF-1 transient analysis

To demonstrate the model's capability in simulating transient behavior and to understand the implication of the multiscale treatment on safety parameters, such as power, coolant temperature and temperature in the solid fuel elements, reactivity insertion and overcooling transients are simulated and the results are discussed in this section.

3.1.1.5.1 Reactivity insertion transients

Starting from steady state under nominal conditions and with the same boundary conditions described in the previous section, 1$ is inserted into the core at time 0. Although an insertion of 1$ is highly unlikely due to the designed limit of the control rod, it is useful to test the model's ability to handle a large amount of reactivity insertion and to understand the core behaviour in this case as a bounding example. At the onset of the reactivity insertion transient, nuclear power rate increases due to excess of reactivity. Following the power excursion is the temperature rise in the core, first in the fuel, due to the direct deposit of the nuclear energy, and then in the coolant as the energy diffuses out of the fuel pebbles. By design, both elements provide negative temperature reactivity feedback that at the end re-stabilizes the core.

Temperature reactivity feedback is the most important natural safety mechanism in the core during a reactivity insertion without SCRAM. In FHRs, the feedback from the Doppler broadening of the fuel resonance absorption cross-sections, i.e. the Doppler feedback, is much more prominent than the coolant void feedback. And it reacts promptly, because the Doppler feed back is directly initiated by the changes in the fuel temperature. As a result, the timescale of a reactivity insertion transient is short, shorter than the circulation time of the primary coolant, so the inlet coolant condition remains constant during the simulation.

Figure 26 shows the power and temperature evolution during a 1$ or 0.5$ reactivity insertion. During the 1$ prompt insertion transient, the core maximum fuel temperature is 1500◦C, below the safety limit (1600◦C). Coolant temperature is raised by only 100◦C at the peak.

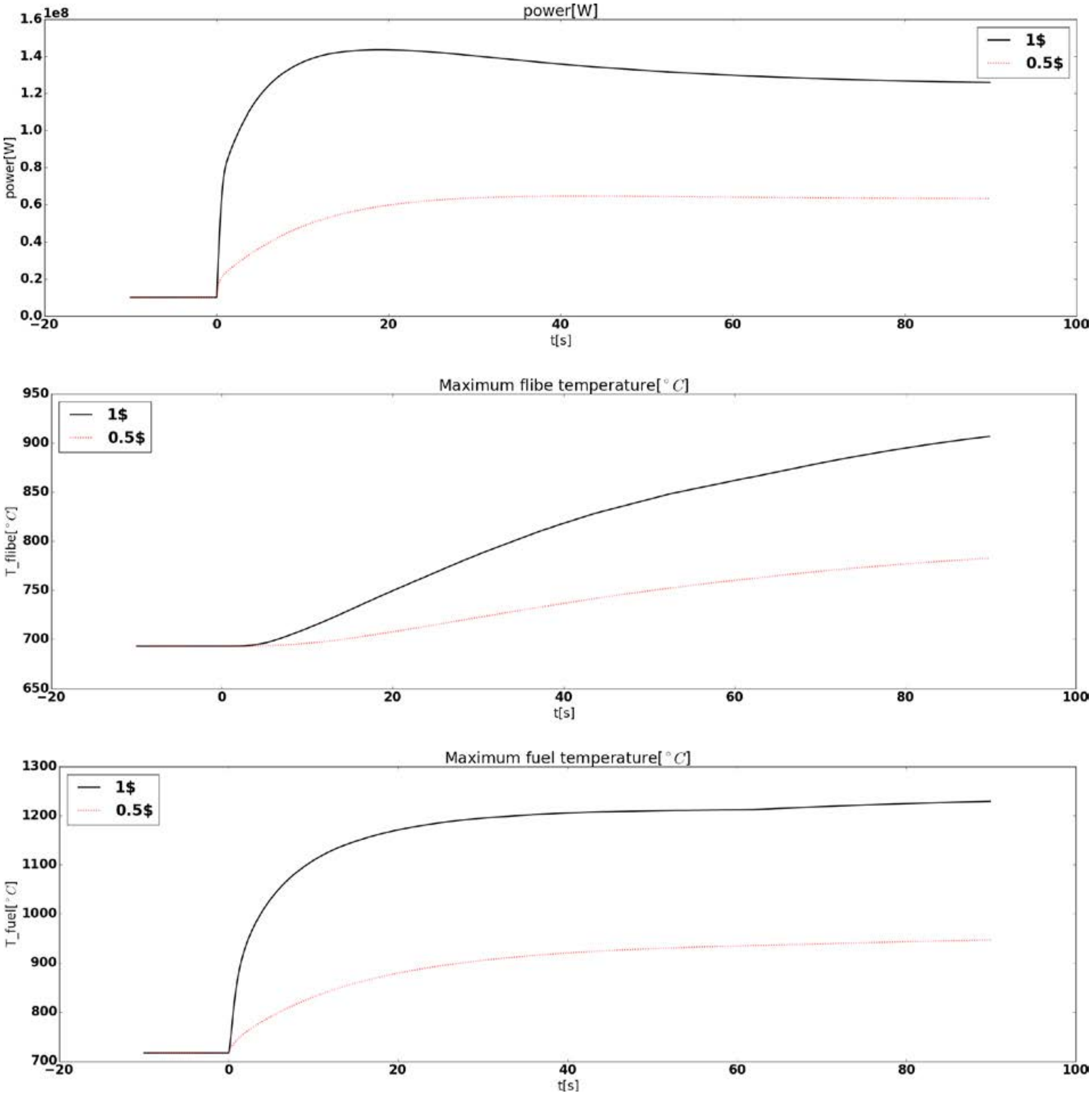

Figure 119: RI transients results

Figure 27 shows the effect of the timescale of the reactivity insertion on the safety parameters. Without SCRAM, the reactor reaches the same end state due to reactivity feedback mechanisms. However, safety measures can take in place to mitigate the consequence if the transient is slow.

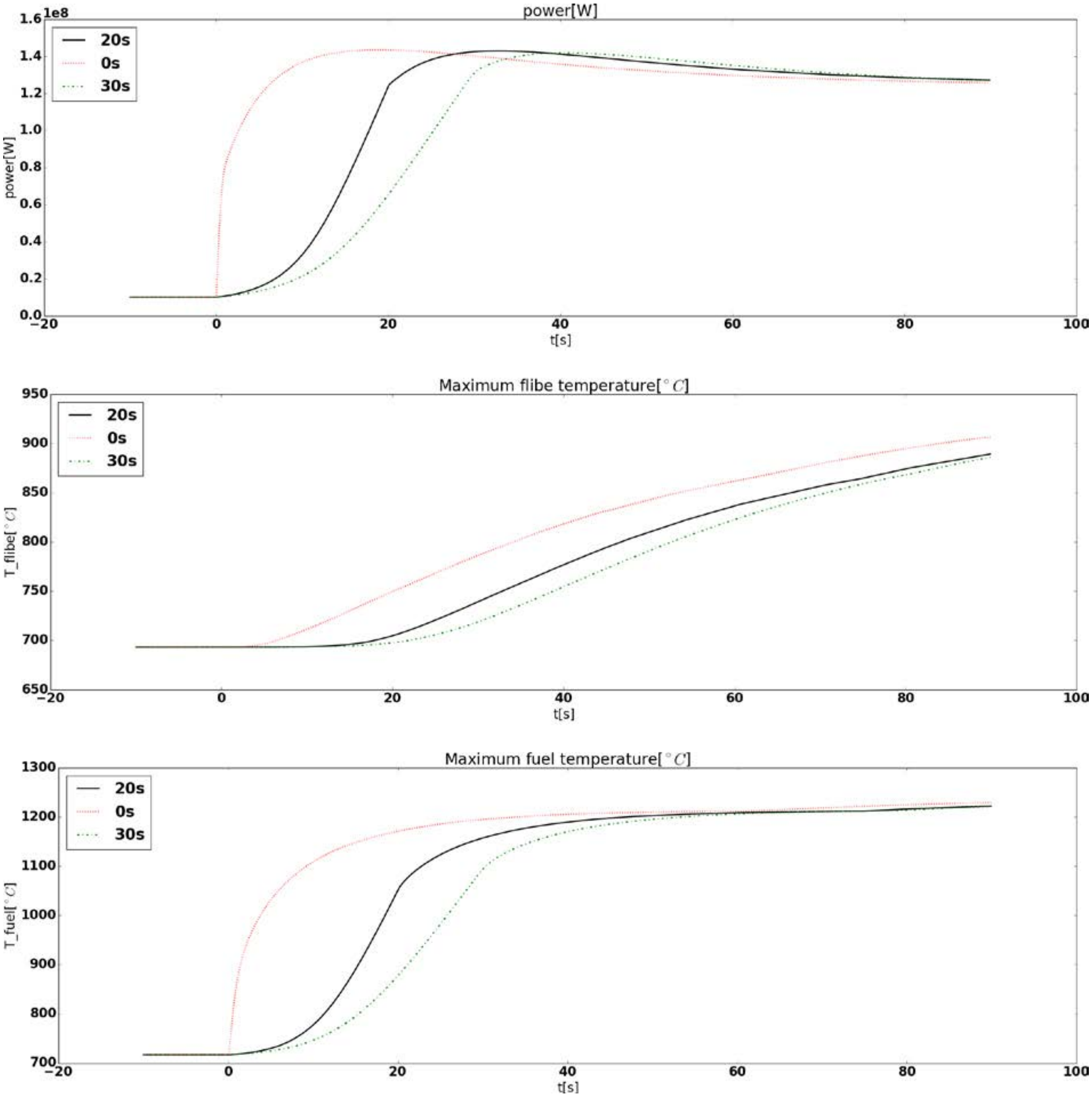

Figure 120: RI transients results

3.1.1.5.2 Overcooling transients

Figure 121: Full core power during overcooling transient

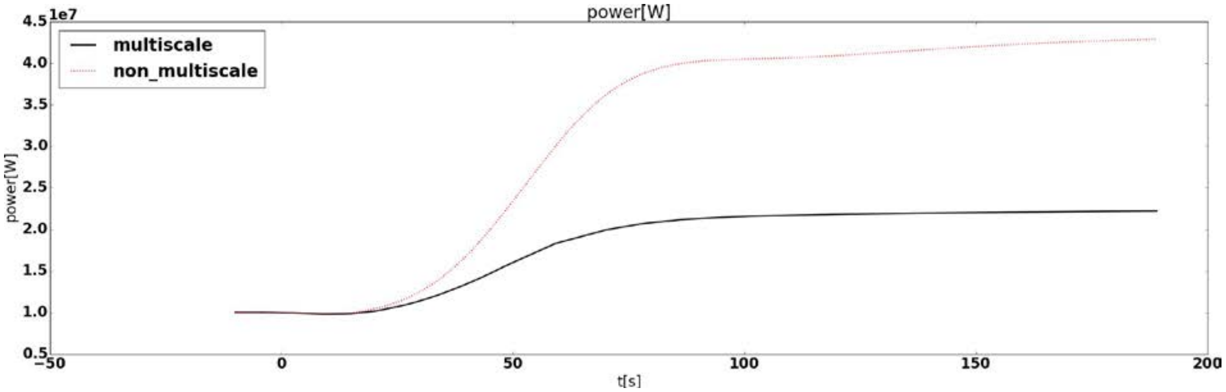

Starting from the steady state conditions, the inlet coolant temperature is decreased by 100◦C in 10 seconds and remains at the lower level during the simulated overcooling transient. Within the short timescale of the simulation, it is reasonable to assume that the other inlet conditions (e.g. coolant mass flow rate) and the reactor control parameters (e.g. control rod positions) remain unchanged.

The colder coolant introduces positive reactivity insertion due to negative flibe temperature reactivity feedback, which causes a power increase, as shown in figure 28. The increase is slow at the beginning because the temperature reactivity feedback is mainly from the coolant, weaker then the Doppler feedback from the fuel, which comes into effect after about 10 seconds when the cooling reaches the fuel materials. Because the transient is initiated in the coolant, the multiscale power increases less than that in the model with uniform fuel temperature, because it can capture the feedback from fuel while the fuel material gets cooled gradually from the shell to the center kernel. The change in temperature in turn results in negative reactivity feedback that stabilize the power at a higher level than the initial rate.

Figure 29 shows that both the average and maximum coolant temperature drops at first due to the colder inlet and increase later due to the increased power. The average coolant temperature drops immediately due to the decreased inlet temperature. On the other hand, the maximum coolant temperature, which is also the outlet temperature, is not affected until the colder coolant arrives at the top of the core. This parameter is directly related to the hot-leg temperature and determines the reactor safety margin. However, this is not a safety concern for over-cooling transients where the coolant temperature is below the steady state condition.

Figure 30 shows the variation of both the maximum and the average fuel temperature during the transient, with two different models. The average fuel temperature drops with the coolant, heats up from the reactivity feedback and in the end stabilizes at a lower level than the steady state temperature. The location where the fuel temperature peaks changes from the center of the core to the top as the coolant flows through the core. At the end of the transient, the peak fuel temperature is higher than the steady state temperature despite the colder coolant that flows through the core, but is still well below the safety limit. Both the average and the maximum fuel temperature in the core is higher with the multiscale treatment, because it captures the feedback from the fuel correctly.

Overall, the end state of the fuel temperature is lower while the coolant temperature is higher in the non-multiscale model because it overestimates the contribution to the negative reactivity feedback from the coolant. In fact, the estimated maximum flibe temperature in this case is much higher than in the multiscale case, even higher than the steady state value. This may lead to over conservatism in the design.

If we take a closer look at the temperature profile inside the fuel pebbles during the transient, figure 3.25 shows the temperature in each solid layer at each time stamp. It takes a few seconds for the drop in the inlet coolant temperature to affect the solid temperature. The core-wise average temperatures in the fuel elements decrease at first as the cold coolant flows upward in the core. At around 50 second, the temperatures increase due to the surge in power. The temperatures finally stabilize after about 150 seconds. The surface temperature is much lower than the steady state temperature because the coolant temperature is much lower. The temperatures gradient inside a fuel pebble is higher after the transient because the power is at a higher level. The difference between the hottest layer and the shell changed from 60 K to 130 K after the transient. As a result, the inner most layer has a slightly higher temperature after the transients, although the safety margin to fuel damage is still very large.

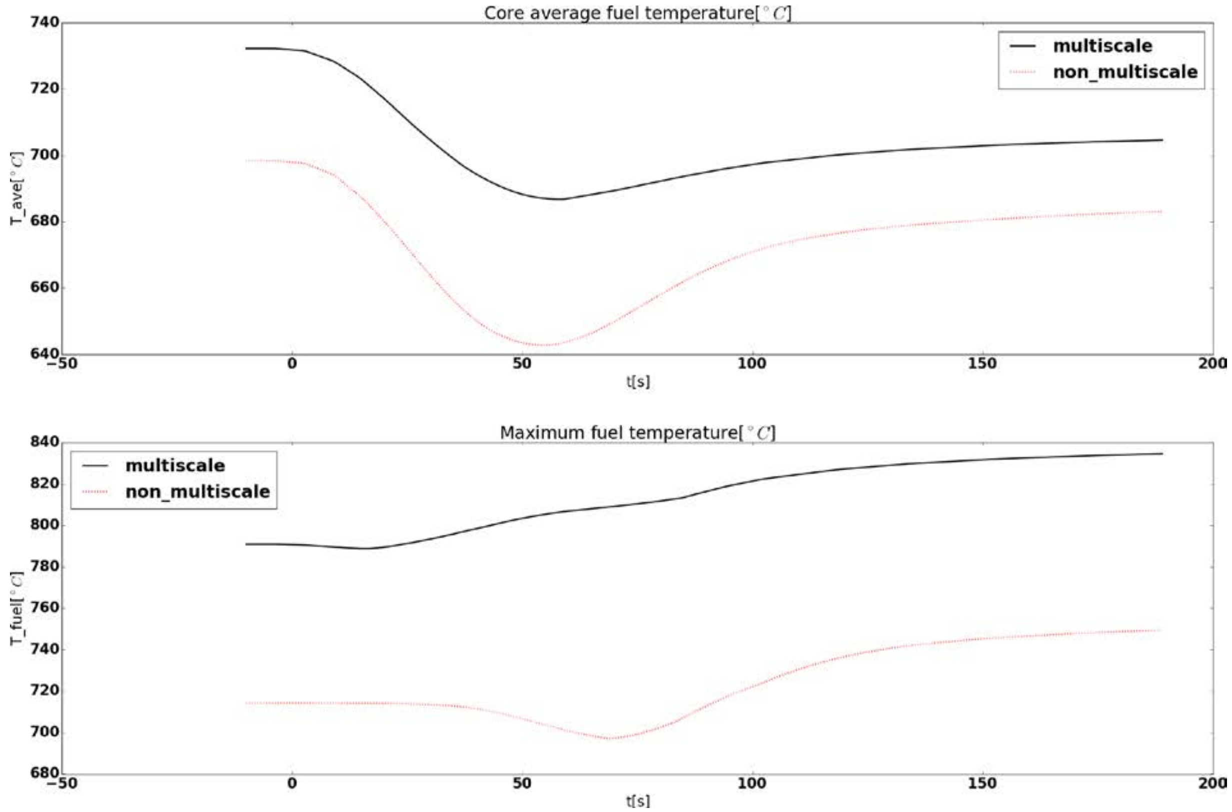

Figure 122: Core average and maximum fuel temperature during overcooling transient

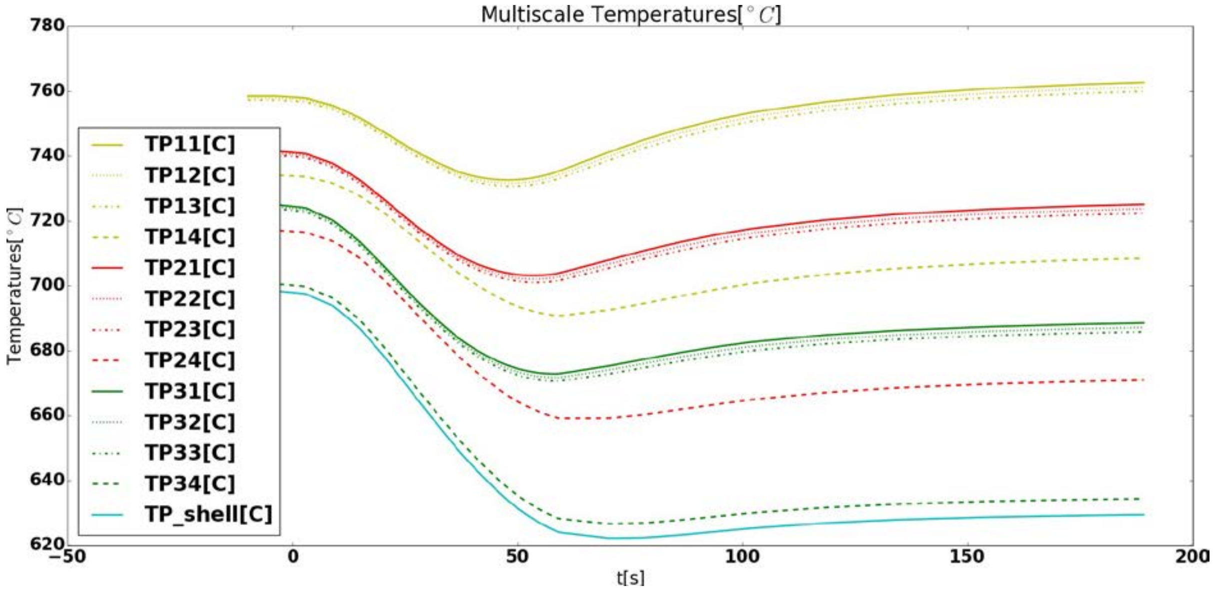

Figure 123: Core average of temperatures inside fuel pebbles during overcooling transient for TMSR SF-1. Notation for temperatures: TP_{ij} represents the ith TRISO layer in the jth pebble layer. TP_{shelll} is the temperature in the graphite shell of the pebble.

3.1.2 Multiphysics modeling for Mk1

A coupled thermal-hydraulics and neutronics model is implemented for Mk1 for transient analysis. The model solves multi-group diffusion equations for neutronics, where the cross-sections are generated for each component using the Serpent model discussed in the previous section.

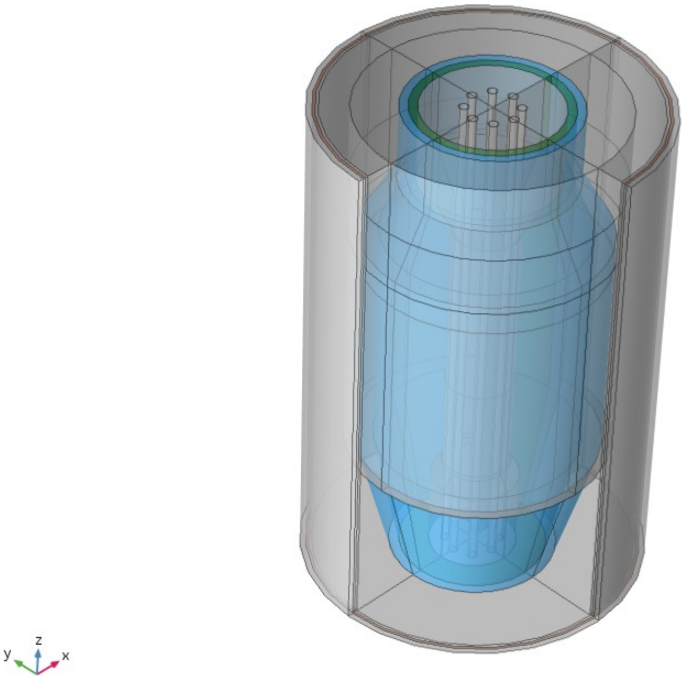

Figure 124: Schematic of the Mk1 multiphysics model geometry. Green region is the fuel pebble region and blue region is the blanket pebble region.

The porous media formulation is used to model the pebble-bed flow field and heat transfer in Mk1. The convective heat transfer between the fuel surface and the coolant is modeled using the Wakao correlation and the Ergun correlation is used for pressure loss computation. Pressure boundary conditions are imposed on outlet surfaces. A velocity profile or an overall flow rate is specified for inlet surfaces.

The fuel region is divided radially and axially into 6 zones, based on the different neutron spectrum characteristics, and in each zone a different set of cross-sections is generated as a multi-variable linear function of the flibe density and logarithm of fuel temperatures. The fuel kernel in each TRISO particle is divided into three layers with equal volume, i.e. same amount of fuel, and the temperature in each layer is computed at each time step using the multi-scale heat transfer mode.

Region	Density [g/cc]	Conductivity [W/m.K]	Specific heat [J/kg/K]

Kernel	10.5	3.5	400
Buffer	1.0	0.5	2000
IPyC	1.9	4.0	2000
SiC	3.2	30	1300
OPyC	1.9	4.0	2000
Coating *	1.89	0.76	1736

*Table 41: Nominal material properties of Mk1 fuel element used in the models. *Coating com- bines all the non-power-generating layers in a TRISO particle.*

Region	Density [g/cc]	Conductivity [W/m.K]	Specific heat [J/kg/K]
Kernel	1.74	193	684
Fuel	1.81	15	1744
Shell	1.96	193	684
Pebble *	1.85	17	1700

*Table 42: Nominal material properties of Mk1 fuel pebble used in the models. *Pebble: pebble-wise material properties*

3.1.2.1 Steady state Mk1 core analysis and design optimization

Steady state power, thermal and fast neutron flux distribution is shown in figure 32. As shown in the figure, the thermal flux peaks in the center reflector, in the graphite blanket pebble area and the outer reflector. As a result, the power peaks in the vicinity of the reflectors when the thermal neutrons enters the fuel area and initiates nuclear reactions. The annular design of the Mk1 core results in a power peak in the center reflector, where most of the thermal flux aggregates.

The fast flux is generated in the fuel region and is transported into the nearby area while the neutrons get thermalized. The blanket pebbles, between the fuel pebble region and the outer reflector, gets higher irradiation damage from the fast neutrons, serving as a disposable reflector.

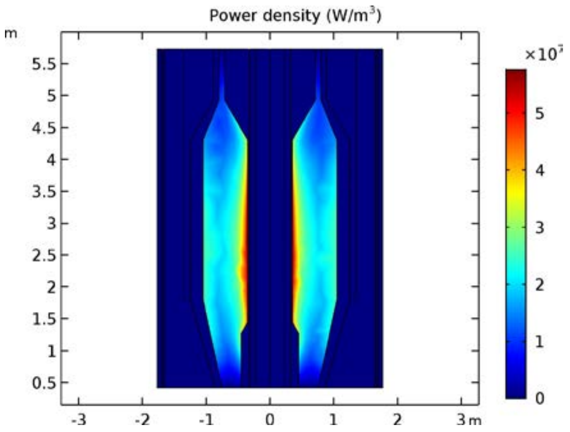

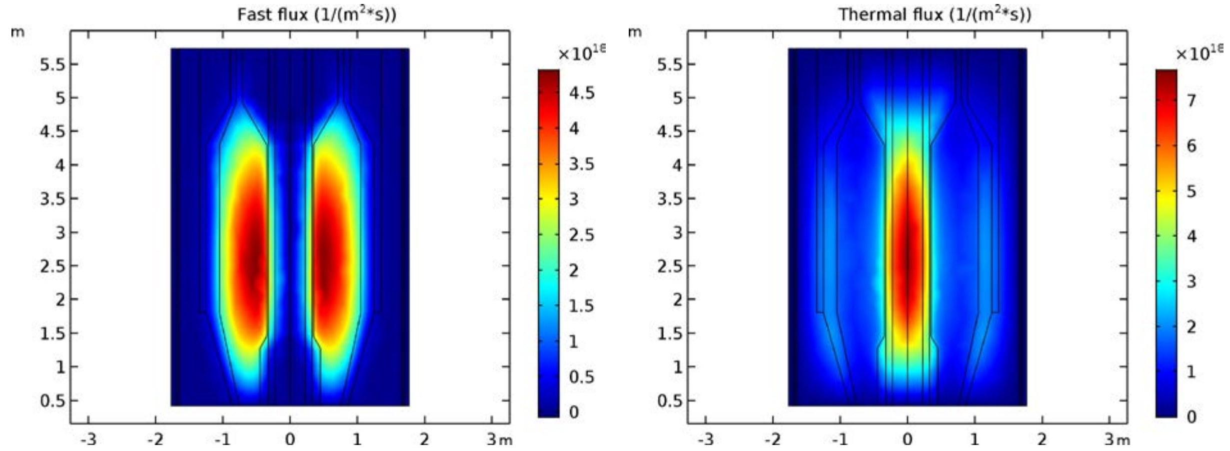

Figure 125: Steady state power and neutron flux distribution at operating conditions

Figure 33 shows the temperature of the coolant and the TRISO kernel temperature distribution in the core. The coolant can efficiently cover all the areas in the core and provide sufficient cooling to the fuel. Although the power peaks at the center, the fuel and the coolant temperatures are low in the center because of the inlet coolant along the center reflector. The peak temperature for both phases is found near the outlet.

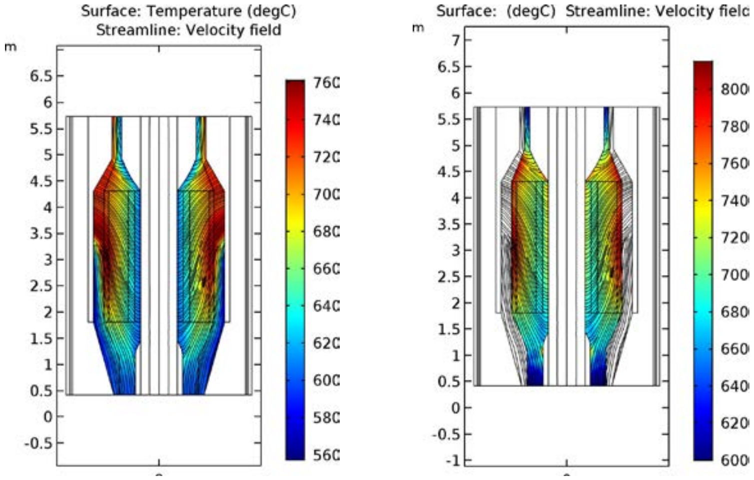

Figure 126: Coolant and fuel temperature distribution in the core

3.1.2.2 Overcooling transients

An over-cooling transient happens when colder coolant introduces positive reactivity to the core via temperature reactivity feedback and causes power to increase (shown in figure 34). In this study, a 100◦C drop in coolant inlet temperature in 10 seconds in a core with fresh fuel and without inserted control rods is simulated as an example case.

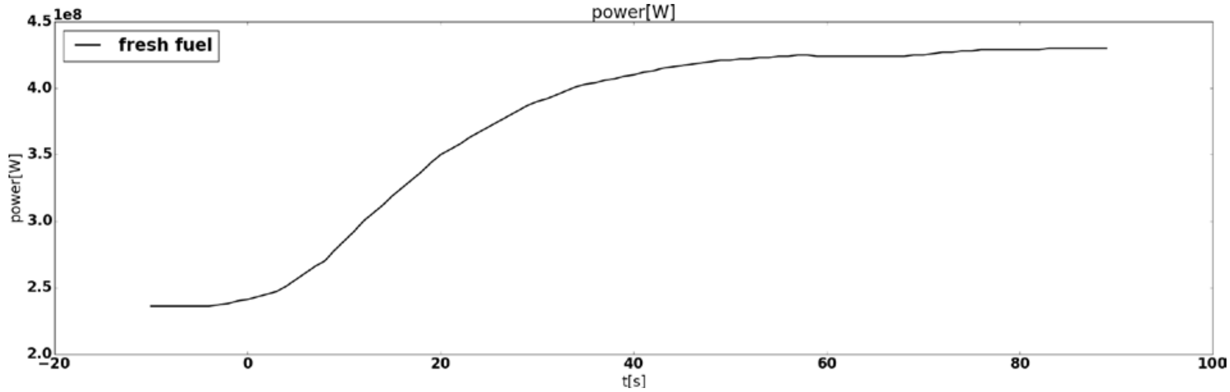

Figure 127: Full core power level during an overcooling transient

The change in fuel temperature is determined by local power level, which is increased, and coolant temperature, which might increase due to the higher power level or decrease due to the colder inlet. Figure 35 shows the core-wise peak fuel temperature. It decreases slightly at the begining and increase to almost 1150 ◦C .

The coolant outlet temperature is shown in figure 36. It remains constant until the changes propagate through the core. It increases at first due to the raised power rates and thus the increased heat flux transferred from the fuel, and decreases when the cold coolant arrives at the outlet.

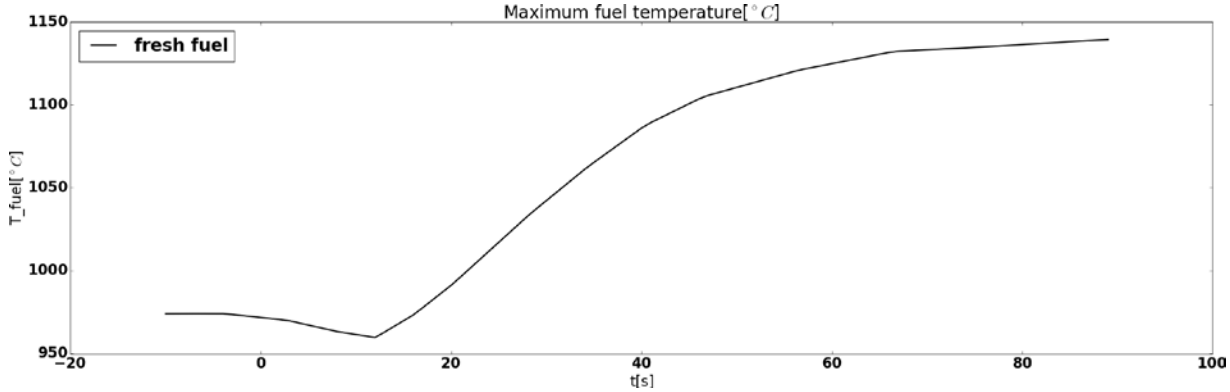

Figure 128: Maximum fuel temperature during an overcooling transient

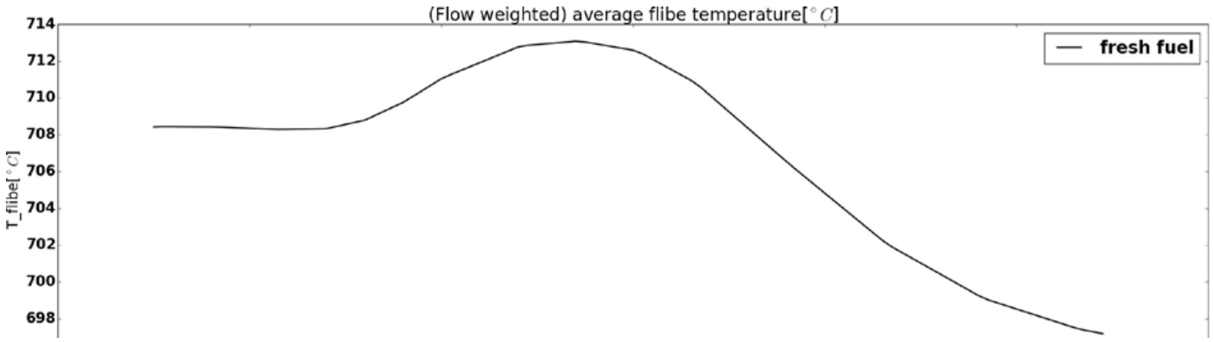

Figure 129: Flibe temperature during an overcooling transient

3.2 Monte Carlo – CFD Coupling for PB-FHRs

Pebble-bed fluoride-cooled high-temperature reactors (FHR) require innovative multi-physics tools in order to perform coupled neutronics-thermal/hydraulics simulation. For this reason a new tool was developed by internally coupling OpenFOAM porous-media CFD solvers and the Monte Carlo neutron transport code Serpent. Differently from previous coupled solvers, this tool accounts for the full dimensionality of the neutron transport problem, with explicit description of the pebbles random packing in the core, and the random distribution of the TRISO fuel particles inside the pebbles. The newly developed tool is applied to model various operational conditions of the TMSR- SF. The discrete element modeling (DEM) capabilities of OpenFOAM are adopted to simulate the initial fuel core loading and to study the reactor approach to criticality. The detailed pebble power distribution, the coolant temperature field and the effect of asymmetric control rod insertion in the TMSR-SF are also presented as examples of the capabilities of the new tools.

3.2.1 SERPENT-OpenFOAM coupling

The developed multi-physics tools are based on the coupling the Monte Carlo code Serpent [version 2.1.24 3] for neutron transport and the CFD code OpenFOAM [version 2.4 4, 5] for thermal- hydraulics, including pebble motion. In standard neutronics-CFD coupling, the main quantity to be exchanged from the neutronics solution to the CFD solver is the volumetric power density distribution. In the available Serpent–OpenFOAM coupling schemes, at each neutron collision, an implicit estimate of the local fission energy deposition is computed via standard Serpent collisional estimators and scored in the Finite-Volume cell containing the collision point. On the other hand, the OpenFOAM mesh and field information are passed to Serpent neutron tracking routines, in order to update the material, temperature and density information at collision points. These pre-existing flexible Serpent– OpenFOAM coupling capabilities for steady-state and transient reactor analysis via both external- and internal-coupling mode [7, 8] were adapted to PB-FHRs. Extensions to these capabilities were developed to allow the exchange of information involving pebbles position, power distribution, and temperature profile. In addition, the discrete element method (DEM) capabilities of the multi-physics toolkit OpenFOAM were integrated in the coupling scheme.

DEM [9] is a numerical simulation technique that allows modeling of assemblies of spheres via the explicit solution of the equation of motion for each element. Previous models of pebble bed reactors solved the neutron transport problem via deterministic [10] or Monte Carlo [3] codes assuming a ordinate lattice pebble distribution. The newly developed scheme, which includes the DEM capabilities, allows to accurately predict and model random bed configurations.

Accurate and detailed models of fluid flow in pebble-bed reactors were developed in the past [11, 12]. These models, based on Large Eddy Simulation (LES) or Direct Numerical Simulation (DNS) techniques, have been adopted for modeling relatively small domains, consisting of a few or a few tens of pebbles, and are still considered too computationally expensive for full core reactor analysis. For this reason, an OpenFOAM incompressible solver with porous-media approximation of the pebble-bed region was adopted to model flibe flow and temperature in the reactor core. This approach consists in the homogenization of the heat transfer and fluid flow governing equations over a coarse, “macroscopic” scale which is larger than the characteristic length of the problem (i.e., the fuel pebble size). The homogenized temperature distributions can be obtained at a relatively low computational cost and offer a reliable description of the reactor behavior at core level.

The suitability of this approach for the sake of neutronics-thermal/hydraulics studies is further sup- ported by the fact that neutron migration lengths in PB-FHRs are several times larger that the “macroscopic” scale adopted for the porous-media homogenization of the fluid flow and heat transfer problem.

A detailed description of previously developed OpenFOAM porous-media solvers for simplified nuclear reactor modeling can be found e.g., in [13], along with the main homogenized equations for transient problems.

The OpenFOAM C++ library is featured by automatic matrix construction and solution capabilities for scalar and vector equations, adopting several possible differencing and interpolation schemes. For this reason, its adoption is particularly suitable for the modeling of complex coupled phenomena. In addition to the ease of implementing the constitutive equations of different physical phenomena, Open- FOAM is provided by different pre-implemented models and solvers for the simulation of fluid flows, also considering the porous media formulation. For this reason, the specific OpenFOAM development efforts were mainly devoted to Serpent coupling capabilities, benefiting from available fluid flow and heat transfer solvers. In particular, the PIMPLE algorithm (a merged PISO-SIMPLE algorithm) for incompressible flow was adopted, with Boussinesq approximation to include buoyancy effects. The spatial discretization makes use of second order schemes and the available OpenFOAM *GAMG* Multi- Grid solvers for linear systems. Non-linear solution is achieved via simple, Picard iterations.

The neutronics model takes advantage of the Serpent transport features developed for HTGRs [14], namely the tracking capabilities with explicit treatment of both TRISO particles dispersion inside the pebbles and pebbles position in the reactors with fully resolved double heterogeneity. The specific Serpent code features introduced for the internal OpenFOAM coupling scheme and the advantage of the peculiar Serpent Delta tracking capabilities can be found in [7, 8]

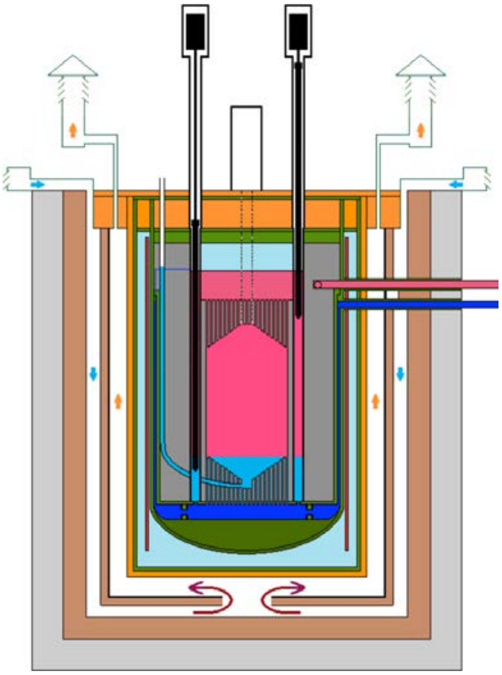

Figure 130: Schematic illustration of the TMSR-SF design [from 15].

3.2.2 TMSR-SF modeling

The advanced multi-physics modeling capabilities developed so far for PB-FHRs were applied to the simulation of the TMSR-SF reactor core [15]. This is a 10 MW demonstrator test reactor developed by the Shanghai Institute of Applied Physics and Chinese Academy of Sciences to be deployed in the next 5 to 10 years. In this design, 6 cm–diameter fuel pebbles fill a cylindrical cavity and are cooled by a $2LiF\text{-}BeF_2$ mixture (flibe) that operates between 672 ˚C and 700 ˚C. Thick graphite reflectors surround radially and axially the core cavity, as shown in Figure 16 and Figure 17 [from 15]. Fuel pebbles are loaded from the bottom of the reactor cavity and float in flibe, settling in the top part of the core. A total of around 14,000 pebbles can be loaded in the reactor and criticality is expected to be achieved when about 11,000 fresh pebbles are loaded. In the DEM model the time-dependent sphere-to-sphere and sphere-to-wall contact forces need to be resolved along with the drag forces related to the relative flow of the fluid in which the elements are immersed.

The initial fuel loading and the approach to criticality of the TMSR-SF were studied, taking into account the peculiar cone-shaped fuel assembly structure that forms as pebbles are loaded from the center of the bottom graphite reflector. The detailed pebble power distribution, the coolant temperature field and the effect of asymmetric control rod insertion were presented as useful results that can be more easily achieved with the present approach, with respect to simplified 2D or neutron diffusion-based solver.

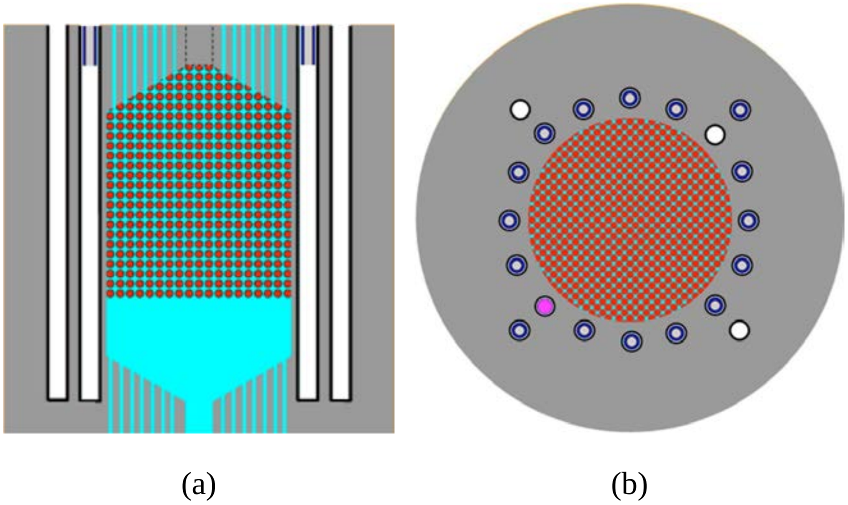

Figure 131: Details of the TMSR-SF reactor core [from 15]. X-Z (a) and X-Y (b) sections. Gray: graphite reflectors. Light blue: flibe salt. Red: fuel pebbles. Control rod channels surround the active region.

3.2.2.1 Fuel pebbles initial loading

Figure 18 shows vertical cross sections of the OpenFOAM results for the fuel elements distribution in the TMSR-SF core at different phases of the initial fuel loading (the reflector is not shown for clarity). The pebbles are injected from the central part of the bottom cone and accumulate in the top due to both the buoyancy effects and the drag forces. The 3D OpenFOAM DEM simulations in the considered conditions predict that the bed forms a cone-shaped bottom. Mock-up pebble injection experiments [16] show that the flow pattern at the bottom of the bed determines the bottom shape and it could vary from convex to concave. Preliminary analysis has been carried out, to establish the impact of the bed bottom shape on the neutronics of the system. Although small, the effect on reactivity and power distribution is noticeable leading to about 50 pcm difference on the effective multiplication factor, between a convex and a concave shape.

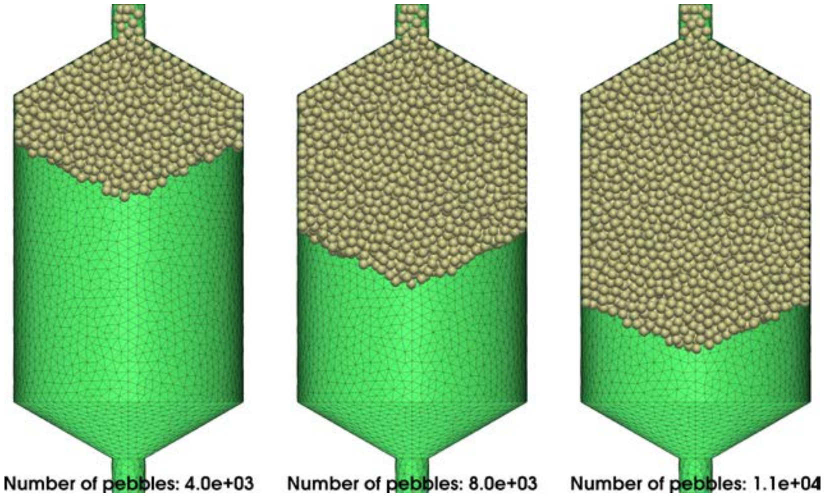

Figure 132: Cross sections from the DEM OpenFOAM results of the simplified TMSR-SF fuel loading.

The developed multi-physics model has been adopted to simulate the approach to criticality during the fuel pebble loading in the TMSR-SF reactor core. The explicit DEM modeling allows taking into account the space-dependent packing fraction and assembly shape of the pebble bed resulting from the random sphere settling in the considered conditions. Figure 19 shows Serpent–OpenFOAM coupling results for the effective multiplication factor during reactor loading. The calculations were performed on a 20 cores Intel(R) Xeon(R) CPU E5-2670 v2 @ 2.50GHz machine. The DEM simulation adopted the standard domain decomposition approach to parallel computing, while neutron transport benefited from the hybrid OMP/MPI Serpent capabilities. The results presented in Figure 19 required a total of 5.5 hours of simulations (wall-clock time), with each criticality source calculation having a statistical uncertainty of approximately 16 *to* 18 *pcm*.

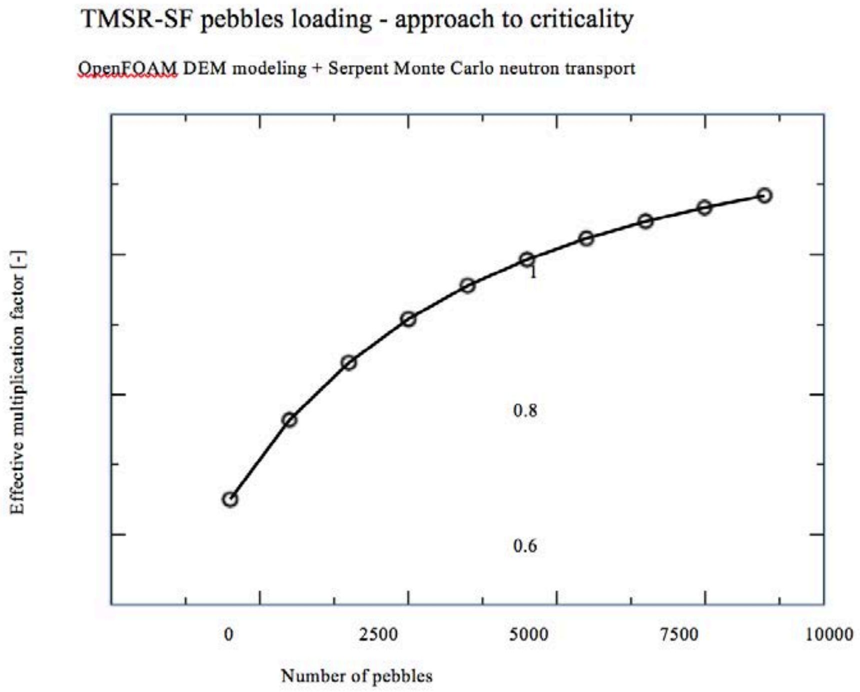

Figure 133: Effective multiplication factor as a function of the TMSR-SF pebble loading.

3.2.2.2 Coupled simulation at full power

In Figure 20, the Serpent-OpenFOAM results for the TMSR-SF operation at full power are presented. The specific TMSR-SF design allows simple boundary conditions to be applied at core boundaries. In particular, due to the presence of several salt injection channels in the bottom graphite reflector, a uniform velocity has been prescribed at the lower limits of the spatial domain. Moreover, as far as the heat transfer model is concerned, Dirichlet condition is imposed at the core inlet, with a uniform inlet temperature of 670 $^{\circ}C$. In the present model, due to the lack of information on the graphite cooling channels, the CFD solution domain is limited to the core cavity. Thus, insulation boundary conditions are applied at the interface between the active region and the radial reflector. As expected, the flibe temperature rises smoothly in the active region, with a temperature interval of approximately 30 $^{\circ}C$. As a further modeling assumption, an uniform average effective heat transfer coefficient between the flowing flibe salt and the fuel pebbles has been adopted with a value of 6 $\mathrm{kW\,m^{-2}\,K^{-1}}$, based on previous investigations.

The power distribution is peaked in the core center. Nonetheless, the moderator effect of the graphite is clearly visible, inducing an increased fission rate in the outermost layer of pebbles close to the reflector. This has a beneficial effect, partially flattening the radial power profile, with a noticeable impact on the pebble power distribution. Due to the relatively small dimensions of the core cavity, a large fraction of neutrons reaches the graphite reflector, gets thermalized and returns to the active region. In the present study, the 20 channels present in the reflector were considered empty (i.e., filled by flibe salt), with control rods fully withdrawn. On the other hand, the salt region without pebbles at the bottom of the core shows very poor moderating properties with respect to graphite. This fact, related to the adopted ^{6}Li content in the flibe, implies a rather large difference between the fission power deposition in the pebbles at the top and the bottom of the active region. These two effect combined lead to a global pebble power peaking factor of about 1.3 and to the peculiar power distribution presented in Figure 21.

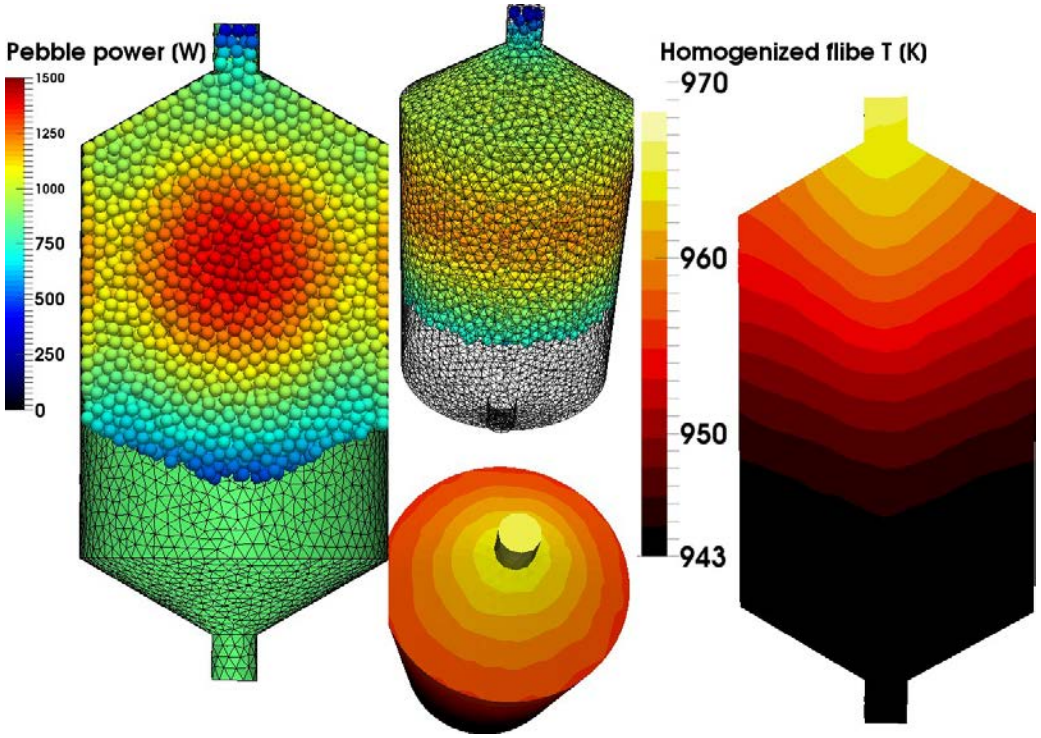

Figure 134: Serpent–OpenFOAM results at full power. Spatial power distribution: X-Z cross section (left) and lateral view (top). Homogenized flibe temperature top view (bottom) and X-Z cross section (right).

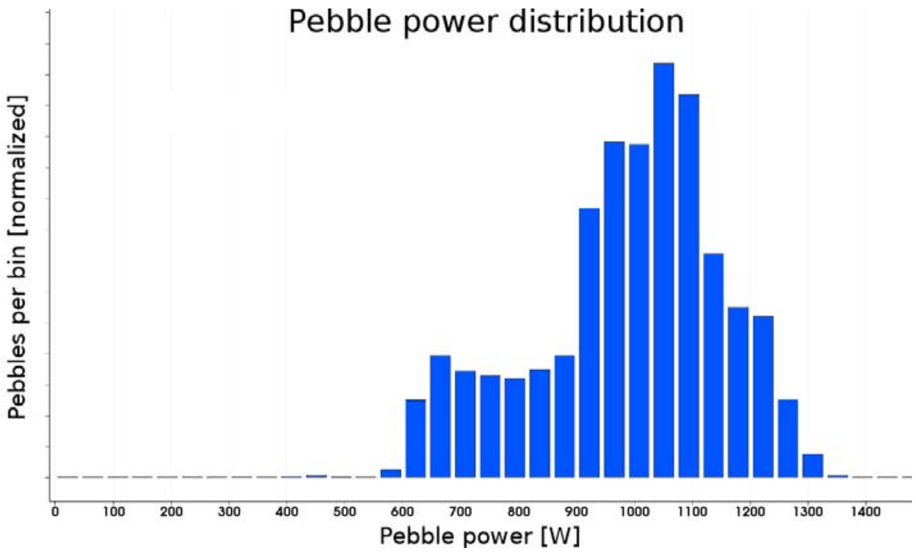

Figure 135: Power distribution in the fuel pebbles.

3.2.2.3 Control rod insertion

The strong effect of the radial reflector is further highlighted by the study of the effect of control rods insertion on the power distribution. In Figure 22, the effect of asymmetric control rods insertion s presented. For this Serpent–OpenFOAM simulation, two adjacent control rods have been fully inserted in the channels. No detailed geometrical information about the control rods design were openly available at the moment of this study. For this reason, their effect has been investigated by modeling a homogeneous mixture of flibe and boron carbide in two reflector channels. The control rods insertion on one side of the core induces a large deformation of the pebble power distribution, leading to a shift of the peak toward the opposite direction.

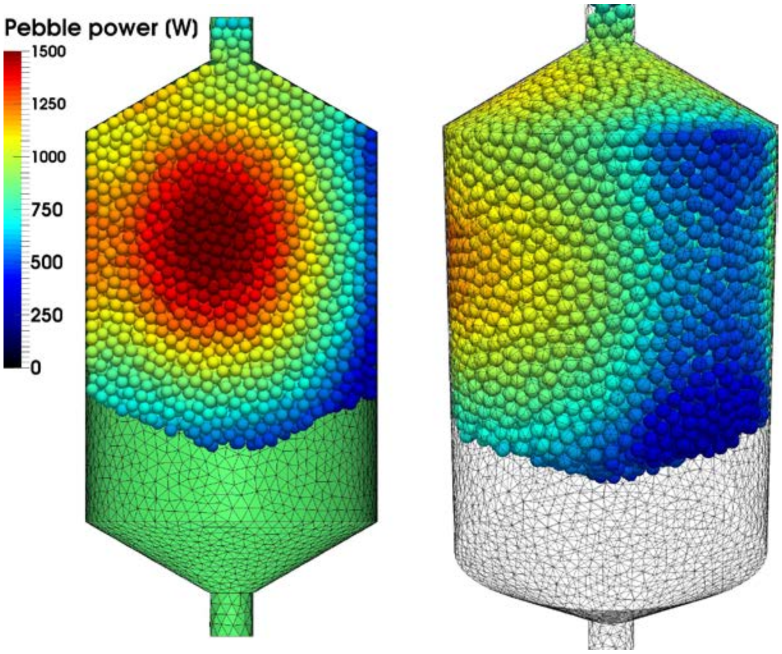

Figure 136: Effect of asymmetric control rods insertion on the core power distribution. X-Z cross section view (left) and lateral core view (right).

4 Sensitivity and uncertainty analysis of the PB-FHR

The objective of this work is to analyze the sensitivities and uncertainties due to nuclear data for the effective multiplication factor (k_{eff}) and coolant density reactivity coefficient (α_{cool}) in the PB-FHR. As reference core design this study uses the one of the Mk1 PB-FHRs with fresh UO_2 fuel with enriched at 4.8 wt.% (as necessary to obtain a critical core). The core design specifications are summarized in Table 43 and the model is reproduced in **Figure 137**. A complete description of the reactor design is available in [2]. The latest Serpent version 2.1.29 is used for sensitivity calculations, and two different covariance matrices (SCALE 44- and 56-energy group) are applied and compared for uncertainty propagations.

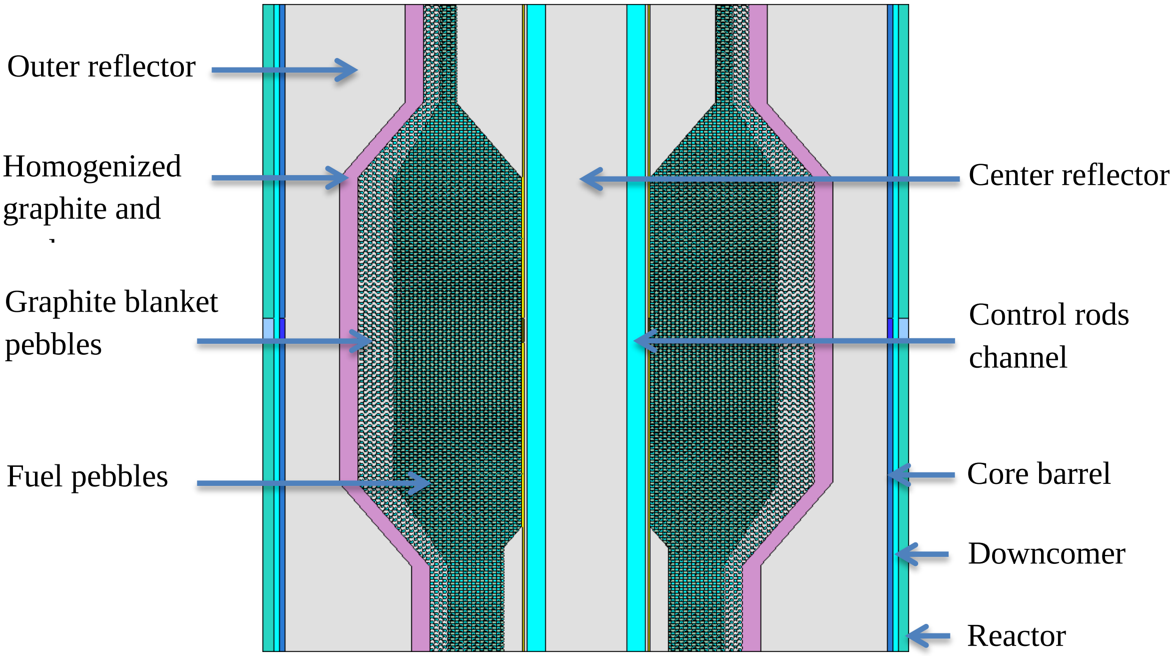

Figure 137: Mk1 PB-FHR model vertical cross section.

CORE DESIGN	
Core inlet temperature	600°C
Core bulk-average outlet temperature	700°C
Average pebble bed void fraction	40.0%
Inner reflector radius	0.35 m
Outer radius of fuel pebble region	1.05 m
Outer radius of graphite pebble region	1.25 m
Average power density in active fuel region (fuel pebbles in entrance-, active- and converging regions)	23.0 MW/m^3
Number of fuel pebbles in core and defueling chute	470,000

Number of graphite pebbles in core and defueling chute	218,000
FUEL PEBBLE DESIGN	
Pebble diameter	30.0 mm
Graphite coating thickness	1.0 mm
Inner graphite core diameter	25.0 mm
Uranium enrichment	4.8 wt.%
Number of coated particles per pebble	4730
Coated particle packing fraction in fuel layer	40%
FUEL KERNEL DESIGN	
Fuel kernel diameter	400 µm
Buffer layer thickness	100 µm
PyC inner layer thickness	35 µm
SiC layer thickness	35 µm
PyC outer layer thickness	35 µm
MATERIALS DENSITY	
UO_2 (fuel kernel)	10.97 g/cm^3
Porous graphite (buffer layer)	1.05 g/cm^3
Pyro graphite (PyC inner and outer layer)	1.87 g/cm^3
SiC (SiC layer)	3.18 g/cm^3
Graphite (reflector)	1.74 g/cm^3
SS-316 steel (core barrel and reactor vessel)	8.00 g/cm^3
Flibe at 650°C (coolant)	1.96 g/cm^3

Table 43: Mk1 PB-FHR core design specifications [1].

4.1 Calculation methodology

4.1.1 Reactivity and Coolant Density Reactivity Coefficient

The Mk1 PB-FHR core is modeled using Serpent version 2.1.29 (a three-dimensional continuous-energy Monte Carlo reactor physics burnup calculation code) with ENDF/B-VII.0 nuclear data library. The fuel kernel composition is assumed to be fresh UO_2 with 4.8 wt.% enriched uranium, and core calculations are done at an average operating temperature of 650°C with all rods out in a 3-D model. Enough histories are used to limit the statistical error on k_{eff} to 5 pcm or less. The coolant density reactivity coefficient is calculated and compared using two different approaches: (1) generalized perturbation theory [18][19], and (2) direct perturbation calculation. The following equation represents the GPT approach:

$$\alpha_{cool} = \frac{\frac{dk_{eff}}{k_{eff}}}{\frac{dN}{N}} = \frac{\frac{dk_{eff}}{k_{eff}}}{\frac{d\Sigma_{t,cool}}{\Sigma_{t,cool}}} = E\left[{}^{(-\gamma)}ACC_{cool} - {}^{(-\gamma)}REJ_{cool}\right], \qquad (1)$$

where

k_{eff} = effective multiplication factor,

N = coolant material density,

$\Sigma_{t,tool}$ = coolant material total macroscopic cross section,

$E(X)$ = expected value over the whole neutron population of the quantity X associated to each particle,

${}^{(-\gamma)}ACC_{cool}$ = accepted events related to coolant density in the history of particles for generation $-\gamma$,

and ${}^{(-\gamma)}REJ_{cool}$ = rejected events related to coolant density in the history of particles for generation $-\gamma$,

This equation, indeed, has the same definition as the total sensitivity of k_{eff} due to the coolant material flibe, $S_{\Sigma_{t,cool}}^{k_{eff}}$, which can be extracted directly from the Serpent 2.1.29 sensitivity output.

In the direct perturbation method, two additional k_{eff} calculations are performed at −5% and +5% coolant density while preserving all other parameters. Eq. (2) below is derived to calculate the coolant density reactivity coefficient:

$$\boldsymbol{\alpha_{cool.}} = \frac{\Delta\rho}{\frac{\Delta N}{N}} = \frac{\rho_2-\rho_1}{5\%-(-5\%)} = \frac{\left(1-\frac{1}{k_2}\right)-\left(1-\frac{1}{k_1}\right)}{0.1} = \frac{\frac{1}{k_1}-\frac{1}{k_2}}{0.1}, \qquad (2)$$

where

ρ = reactivity,

N = coolant material density,

ρ_1 = reactivity at −5% coolant density,

ρ_2 = reactivity at +5% coolant density,

k_1 = k_{eff} at −5% coolant density,

and k_2 = k_{eff} at +5% coolant density.

4.1.2 Sensitivity Calculation

Serpent version 2.1.29 provides a function for sensitivity/perturbation calculation based on a collision history approach. It allows the calculation of the effects of nuclear data perturbation on several response functions: the effective multiplication factor, reaction rate ratios and bilinear ratios (e.g., effective kinetic parameters and coolant density reactivity coefficient). A sensitivity analysis associated with 44- and 56-energy group is performed using the Serpent code. A very brief description of the method is summarized here, and a detailed explanation can be found in [18].

In linear perturbation analysis, the effect of a perturbation of a parameter x on the response R can be expressed as:

$$\boldsymbol{S_x^R = \frac{dR/R}{dx/x}}, \qquad (3)$$

where

S_x^R = relative sensitivity coefficient of R with respect to x.

For the k_{eff} sensitivity coefficient ($S_x^{k_{eff}}$) for a generic parameter x (e.g., cross-sections, $\bar{\nu}_t, \chi$ data and scattering distributions) by applying the first order perturbation of particle weights,

$$S_x^{k_{eff}} = \frac{<\phi^+, \frac{1}{k_{eff}} \frac{\partial \boldsymbol{F}}{\partial x/x} \phi> - <\phi^+, \frac{\partial \boldsymbol{L}}{\partial x/x} \phi> + <\phi^+, \frac{\partial \boldsymbol{S}}{\partial x/x} \phi>}{<\phi^+, \frac{1}{k_{eff}} \boldsymbol{F} \phi>}$$

$$= \boldsymbol{E}\left[{}^{-\gamma}\boldsymbol{ACC}_x - {}^{-\gamma}\boldsymbol{REJ}_x\right], \qquad (4)$$

where

$\phi+$ = adjoint neutron flux,

ϕ = forward neutron flux,

$\boldsymbol{F}$ = neutron fission production integral operator,

$\boldsymbol{L}$ = neutron loss integral operator,

$\boldsymbol{S}$ = neutron scattering integral operator,

${}^{(-\gamma)}ACC_x$ = accepted events related to parameter x in the history of particles for generation $-\gamma$,

and ${}^{(-\gamma)}REJ_x$ = rejected events related to parameter x in the history of particles for generation $-\gamma$.

For the sensitivity of coolant density reactivity coefficient ($S_x^{\alpha_{cool}}$), generalized perturbation theory is applied in our study, as well as equivalent generalized perturbation theory (EGPT, [20]) for comparison. From the classical perturbation theory, the coolant density reactivity coefficient is defined as:

$$\boldsymbol{\alpha_{cool} = \frac{<\phi^{+},\Sigma_{t,cool}\phi>}{<\phi^{+},\frac{1}{k_{eff}}F\phi>} = \frac{<\phi^{+},\Sigma_{t,cool}\phi>}{<\phi^{+},\frac{1}{k_{eff}}\chi_t\bar{v}_t\Sigma_f\phi>},} \qquad (5)$$

where

$\chi_t\bar{v}_t\Sigma_f$ = total fission neutron production operator.

Let $\Sigma_1 = \Sigma_{t,cool}$ and $\Sigma_2 = \frac{1}{k_{eff}}\chi_t\bar{v}_t\Sigma_f$. In the GPT approach, the reference response R and perturbed response R' are defined as:

$$\boldsymbol{R = \alpha_{cool} = \frac{<\phi^{+},\Sigma_1\phi>}{<\phi^{+},\Sigma_2\phi>},} \qquad (6)$$

$$\boldsymbol{R' = \alpha'_{cool} = \frac{<\phi^{+}+\Delta\phi^{+},(\Sigma_1+\Delta\Sigma_1)(\phi+\Delta\phi)>}{<\phi^{+}+\Delta\phi^{+},(\Sigma_2+\Delta\Sigma_2)(\phi+\Delta\phi)>},} \qquad (7)$$

By applying the first order expansion of Eq. (7):

$$\boldsymbol{\frac{dR}{R} = \frac{<\phi^{+},d\Sigma_1\phi>}{<\phi^{+},\Sigma_1\phi>} - \frac{<\phi^{+},d\Sigma_2\phi>}{<\phi^{+},\Sigma_2\phi>} + \frac{<\phi^{+},\Sigma_1 d\phi>}{<\phi^{+},\Sigma_1\phi>} - \frac{<\phi^{+},\Sigma_2 d\phi>}{<\phi^{+},\Sigma_2\phi>} + \frac{<d\phi^{+},\Sigma_1\phi>}{<\phi^{+},\Sigma_1\phi>} - \frac{<d\phi^{+},\Sigma_2\phi>}{<\phi^{+},\Sigma_2\phi>},} \qquad (8)$$

Then the relative sensitivity of the response R (i.e., coolant density reactivity coefficient) to parameter x can be expressed as:

$$\boldsymbol{S_x^R = \frac{<\phi^{+},\frac{\partial\Sigma_1}{\partial x/x}\phi>}{<\phi^{+},\Sigma_1\phi>} - \frac{<\phi^{+},\frac{\partial\Sigma_2}{\partial x/x}\phi>}{<\phi^{+},\Sigma_2\phi>} + \frac{<\phi^{+},\Sigma_1\frac{\partial\phi}{\partial x/x}>}{<\phi^{+},\Sigma_1\phi>} - \frac{<\phi^{+},\Sigma_2\frac{\partial\phi}{\partial x/x}>}{<\phi^{+},\Sigma_2\phi>} + \frac{<\frac{\partial\phi^{+}}{\partial x/x},\Sigma_1\phi>}{<\phi^{+},\Sigma_1\phi>} - \frac{<\frac{\partial\phi^{+}}{\partial x/x},\Sigma_2\phi>}{<\phi^{+},\Sigma_2\phi>},} \qquad (9)$$

The first two terms in Eq. (9) are the direct effect of the perturbation of x on R, and the other four terms are the indirect terms. The indirect terms results are automatically provided by Serpent 2.1.29. However, Serpent does not provide the direct terms results, so a post-processing calculation is needed. In the case of coolant material flibe, $\frac{\partial\Sigma_2}{\partial x/x} = \frac{\partial(\frac{1}{k_{eff}}\chi_t\bar{v}_t\Sigma_f)}{\partial x/x} = 0$, thus, the direct term of S_x^R is:

$$(S_x^R)_{direct} = \frac{<\phi^+,\frac{\partial \Sigma_1}{\partial x/x}\phi>}{<\phi^+,\Sigma_1\phi>} - \frac{<\phi^+,\frac{\partial \Sigma_2}{\partial x/x}\phi>}{<\phi^+,\Sigma_2\phi>} = \frac{<\phi^+,\frac{\partial \Sigma_1}{\partial x/x}\phi>}{<\phi^+,\Sigma_1\phi>} = \frac{<\phi^+,\frac{\partial \Sigma_1}{\partial x/x}\phi>/<\phi^+,\Sigma_2\phi>}{<\phi^+,\Sigma_1\phi>/<\phi^+,\Sigma_2\phi>} = \frac{S_x^{k_{eff}}}{\alpha_{cool.}} = \frac{S_x^{k_{eff}}}{S_{\Sigma_{t,cool}}^{k_{eff}}}. \quad (10)$$

Both *k_{eff}*

Both k_{eff} sensitivity due to parameter *x* ($S_x^{k_{eff}}$) and total k_{eff} sensitivity due to the coolant material flibe ($S_{\Sigma_{t,cool}}^{k_{eff}}$) are calculated by Serpent. Finally, the sensitivity of coolant density reactivity coefficient to parameter *x*, $S_x^R = S_x^{\alpha_{cool}}$, is obtained by adding the direct and indirect terms in the GPT method.

In the EGPT method, two additional k_{eff} sensitivity calculations are performed at −5% and +5% coolant density while preserving all other parameters. The $S_x^{\alpha_{cool}}$ calculation is derived below:

$$S_x^{\alpha_{cool}} = \frac{\partial \alpha_{cool}/\alpha_{cool}}{\partial x/x} = \frac{\partial\left(\frac{\partial k_{eff}/k_{eff}}{\partial N/N}\right)}{\frac{\partial k_{eff}/k_{eff}}{\partial N/N}} \Bigg/ \frac{\partial x}{x} = \frac{\partial\left(\frac{\partial k_{eff}/k_{eff}}{\partial N/N}\right)}{\partial x/x} \cdot \frac{\partial N/N}{\partial k_{eff}/k_{eff}} = \frac{\partial\left(\frac{\partial k_{eff}/k_{eff}}{\partial x/x}\right)}{\partial N/N} \cdot \frac{\partial N/N}{\partial k_{eff}/k_{eff}}$$

$$= \frac{\partial S_x^{k_{eff}}}{\partial k_{eff}/k_{eff}} \cong \frac{S_x^{k'_{eff}} - S_x^{k_{eff}}}{\frac{k'_{eff} - k_{eff}}{k_{eff}}}, \qquad (11)$$

where

k_{eff} = effective multiplication factor at −5% coolant density,

k'_{eff} = effective multiplication factor at +5% coolant density,

$S_x^{k_{eff}}$ = k_{eff} sensitivity due to parameter *x* at −5% coolant density,

and $S_x^{k'_{eff}}$ = k_{eff} sensitivity due to parameter *x* at +5% coolant density.

1.3. Uncertainty Calculation

The nuclear data uncertainties as well as the correlations that exist between them associated with the ENDF/B-VII.0 libraries are provided in 44- and 56-energy group with covariance matrices SCALE 44 and SCALE 56, respectively.

The relative uncertainty of effective multiplication factor and coolant density reactivity coefficient due to each isotope *i*, reaction *x*, and energy group *j* are obtained by applying the sandwich rule:

$$\left(\frac{\Delta k_{eff}}{k_{eff}}\right)^2 = \left(\boldsymbol{S}_{i,x}^{k_{eff}}\right)^T \boldsymbol{COV}(\boldsymbol{i},\boldsymbol{x};\boldsymbol{i},\boldsymbol{x})\, \boldsymbol{S}_{i,x}^{k_{eff}}\,, \qquad (12)$$

$$\left(\frac{\Delta\alpha_{cool}}{\alpha_{cool}}\right)^2 = \left(\boldsymbol{S}_{i,x}^{\alpha_{cool}}\right)^T \boldsymbol{COV}(i,x;i,x)\, \boldsymbol{S}_{i,x}^{\alpha_{cool}}\,, \qquad (13)$$

where

$$\boldsymbol{S}_{i,x}^{k_{eff}} = \begin{bmatrix} \dfrac{\partial k_{eff}/k_{eff}}{\partial x_{i,x,1}/x_{i,x,1}} \\ \dfrac{\partial k_{eff}/k_{eff}}{\partial x_{i,x,2}/x_{i,x,2}} \\ \vdots \\ \vdots \\ \dfrac{\partial k_{eff}/k_{eff}}{\partial x_{i,x,j}/x_{i,x,j}} \end{bmatrix}$$

is the relative k_{eff} sensitivity vector due to isotope i, reaction x, and energy j,

$$\boldsymbol{S}_{i,x}^{\alpha_{cool.}} = \begin{bmatrix} \dfrac{\partial \alpha_{cool}/\alpha_{cool}}{\partial x_{i,x,1}/x_{i,x,1}} \\ \dfrac{\partial \alpha_{cool}/\alpha_{cool}}{\partial x_{i,x,2}/x_{i,x,2}} \\ \vdots \\ \vdots \\ \dfrac{\partial \alpha_{cool}/\alpha_{cool}}{\partial x_{i,x,j}/x_{i,x,j}} \end{bmatrix}$$

is the relative α_{cool} sensitivity vector due to isotope i, reaction x, and energy j,

and $\boldsymbol{COV}(i, x; i, x)$ = relative covariance matrix of isotope i and reaction x.

4.2 Results and discussions

4.2.1 Relative Uncertainty of keff

The total and relative k_{eff} uncertainties due to nuclear data (≥ 0.1%) with covariance matrices SCALE 44 and SCALE 56 are listed and compared in Table 44. Both cases show almost same uncertainties except ^{235}U $\bar{\nu}_t$ and ^{238}U capture. The relative k_{eff} sensitivities due to these two exceptions with 44- and 56-energy group are almost same, so the discrepancy of uncertainty is from the different standard deviations in two covariance matrices. Total relative k_{eff} uncertainty due to nuclear data is ~1.38%, and ^{7}Li (n, γ) is the largest uncertainty contributor of ~1.24%. Only SCALE 56-energy group covariance matrices are used in the rest of the study.

Reaction	44-energy group uncertainty, pcm	56-energy group uncertainty, pcm	Difference, %
Total	1,370	1,380	0.7
^{7}Li capture	1,250	1,240	0.8
^{235}U $\bar{\nu}_t$	302	379	20.3
^{238}U capture	241	214	12.6
^{19}F capture	172	172	0
^{235}U capture	158	157	0.6
^{235}U fission	149	148	0.7
^{12}C capture	139	138	0.7
^{235}U fission x capture	138	138	0
^{12}C elastic	122	121	0.8
Others	< 100	< 100	-

Table 44: Contributions to k_{eff} uncertainty from different reactions.

4.2.2 Coolant Density Reactivity Coefficient

The coolant density reactivity coefficient is calculated using both the GPT capabilities available in Serpent and the direct perturbation method. For the latter method k_{eff} calculations are performed at −5% and +5% coolant density compared to the reference value. The coolant density reactivity coefficient is found to be 32.3 ± 0.5 pcm per 1% void increase using direct perturbation and 36.0 ± 5.0 pcm per 1% void increase using GPT. Serpent GPT approach generates a larger statistical error of ~14% on α_{cool}. This is due to the fact that the GPT estimators require a very long simulation time to achieve lower statistical errors as the sensitivity coefficient is so close to 0, especially for reactions involving scattering.

4.2.3 Relative Sensitivity of Coolant Density Reactivity Coefficient

The relative sensitivities of coolant density reactivity coefficient due to nuclear data (≥ 0.1) calculated using GPT (Eq. (10)) and EGPT (Eq. (11)) methods are compared in Table 45. Note that only the direct effects (i.e., explicit derivative of α_{cool} with respect to cross sections) are present in this section because they are the major uncertainty contributors to α_{cool}, and for a full core modeling in Serpent GPT approach they require a reasonable amount of computing time for acceptable statistical errors. Serpent GPT method gives constant statistical errors of ~14%, which is mainly from the statistical error of ~14% in calculating α_{cool}. For the EGPT method, sensitivities due to elastic scattering (^{19}F elastic, ^{9}Be elastic and ^{7}Li elastic) have large associated statistical uncertainties (> 30%), resulting in the deviation from GPT results. If needed, such statistical uncertainty can be reduced by increasing the number of cycles at the expenses of significantly longer computational time. A large discrepancy is also found in ^{9}Be (n, xn), but the result in this case is within two-standard deviation. In general, sensitivity results are consistent within two-standard deviation, thus, are considered acceptable.

Reaction	Serpent GPT	EGPT	Difference, %
^{7}Li capture	2.09 ± 0.30	1.99 ± 0.04	5
^{19}F elastic	−1.36 ± 0.21	−2.14 ± 0.80	57
^{19}F capture	0.93 ± 0.13	0.87 ± 0.02	7
^{9}Be elastic	−0.89 ± 0.13	−0.87 ± 0.46	2
^{6}Li (n, t)	0.43 ± 0.06	0.43 ± 0.01	2
^{7}Li elastic	−0.38 ± 0.06	−0.30 ± 0.33	22
^{9}Be (n, xn)	−0.25 ± 0.04	−0.14 ± 0.02	42
^{9}Be capture	0.20 ± 0.03	0.18 ± 0.01	8
Others	< 0.1	< 0.1	-

Table 45: Relative sensitivity of α_{cool} with 1-σ in coolant material.

4.2.4 Relative Uncertainty of Coolant Density Reactivity Coefficient

The relative uncertainties of coolant density reactivity coefficient due to nuclear data (≥ 0.1%) in coolant material (direct effects due to the change of cross section when the coolant density is perturbed) are summarized in Table 46. These values are obtained using sensitivities from Serpent GPT method and covariance data from the 56-group SCALE library. The uncertainty contributors in non-coolant materials (i.e., indirect effect due to the changed flux when the coolant density is perturbed) are not calculated here because they are usually small and require long simulation time to lower the statistical errors of $S_x^{\alpha_{cool}}$.

Reaction	Relative uncertainty, %
^{7}Li capture	31.30
^{19}F capture	4.33
	2.10
^{7}Li elastic	1.67
^{9}Be capture	0.99
^{19}F (n, α)	0.82
^{9}Be (n, xn)	0.80
^{19}F inelastic	0.78
^{19}F inelastic x elastic	-0.65*
^{9}Be (n, α)	0.51

^{9}Be elastic	0.47
^{19}F (n, α) x elastic	0.12
^{19}F capture x elastic	0.10
Others	< 0.1

Table 46: Relative uncertainty of α_{cool} in coolant material.

*Negative sign is due to the negative correlations between different reactions in covariance matrices (e.g., ^{19}F inelastic and elastic).

It is obvious that ^{7}Li (n, γ) contributes the most uncertainty to coolant density reactivity coefficient. This value of 31.30% is coming from the known large uncertainty in ^{7}Li radiative capture nuclear data. In addition, ^{19}F (n, γ), ^{19}F elastic and ^{7}Li elastic are also considerable contributors to α_{cool} uncertainty (> 1%).

5 Salt activation analysis

In the design of a reactor, the analysis on shielding is a significant step, both for the safety of humans and materials. Among all kinds of radiations, gamma radiation is of great importance and accounts for the most part of the dose outside of the reactor. Therefore, this project aims at analyzing gamma radiation shielding requirements for salt of the Mark-1 PB-FHR design. We have first determined the source of gamma radiation from the activation analysis of the coolant, and then calculated the energy spectrum behind the shielding material and finally arrive at the dose outside of the Mark-1 PB-FHR.

The project can be split into three steps:

(1) determine the activation of flibe and the gamma radiation source from the activation of flibe salt;

(2) calculate the shielding property of the material used in Mark-1 PB-FHR;

(3) determine the dose outside of the reactor shielding material.

5.1 Burnup Calculation and Analysis

Figure 45 shows a model of the Mark-1 PB-FHR vessel. In the core, there are totally 470,000 pebbles randomly distributed and floating in flibe. The region of pebbles and flibe is painted as light green in Figure 45[1].

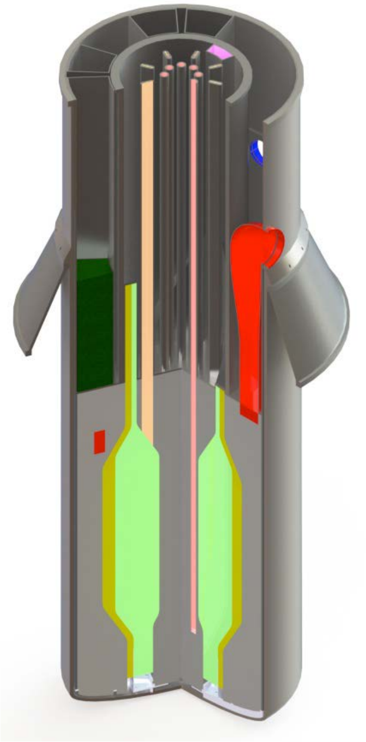

Figure 138: *The Mark-1 PB-FHR reactor vessel.*

5.1.1 Geometry

The pebbles in the core are randomly distributed. In Serpent, there are two methods specially designed to deal with High Temperature Gas-cooled Reactors (HTGR), named implicit particle fuel model and explicit particle / pebble bed fuel model. The former mixes the nuclides together and sample new TRISO particles on the neutron flight path and the latter one reads the positions of the particles from a separated file. The latter can also be applied to specify the pebble-bed geometry.

In the activation calculation, we focus on the behavior on the flibe and used a simplified model consisting of a unit cell model. The boundary conditions are all set as reflective type, indicating that the unit cell model is repeated infinitely in three directions.

The unit cell model is briefly shown in Figure 46 below. This figure is a screenshot from a SolidWorks (R) 3D model.

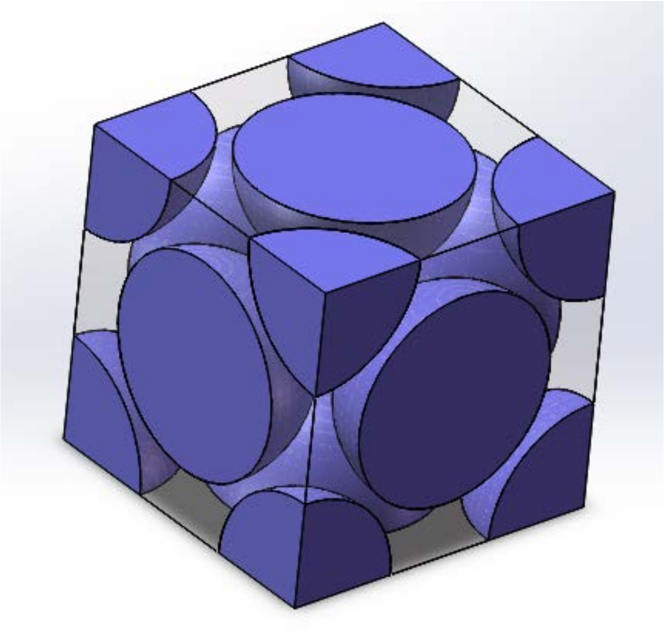

Figure 139: The SolidWorks (R) model of the unit cell.

A face-centered cube (FCC) model is used. The pebbles do not touch their neighbors in the model and the pitch of the cube is determined to get the actual coolant fraction 40.0%.

If we assume the pitch is *a*, then *a* must satisfy the following equation:

$$(1-40.0\%)a^3=\left(8\times\frac{1}{8}+6\times\frac{1}{2}\right)(\frac{4}{3}\pi r^3)$$

"r" in the equation represents the radius of the pebbles. According to the design, the radius of the pebbles is 15.0mm, thus we can induce the pitch of the cube a is 45.50828mm.

5.1.2 Material

To simulate the refueling process, the compositions of the pebbles are different. In Figure 46, the four 1/8 spheres in the lower four corners of the model shares the same composition, so as the four at the upper four corners of the model. The compositions of the six pebbles at the center of the faces differ from each other.

In the pebbles, the TRISO particles are of a cube infinite 3D lattice geometry and the coat of the fuel particles are not modeled, but mixed with the graphite filled in the gap between particles.

Flibe is mainly composed with lithium, beryllium and fluorine, just as the name "f-li-be" indicates. In most analysis, this composition is enough but for activation and shielding calculation, we have to take impurities and activation products into account. The composition of flibe including the impurities is listed as follows:

Analyte	**Result / $(\mathrm{mg} \cdot \mathrm{kg}^{-1})$**	**Analyte**	**Result / $(\mathrm{mg} \cdot \mathrm{kg}^{-1})$**
Lithium	135000	Chromium	53.3
Beryllium	88200	Aluminum	28
Potassium	544	Nickel	10.7
Sodium	469	Thallium	10.6
Magnesium	139	Barium	9.51
Calcium	132	Strontium	3.7

Table 47: The composition of raw materials FLiBe measured using ICP-OES and ICP-MS.

Note that the rest part of flibe is fluorine and it is not listed in the table. And the composition of each element listed in Table 34 is natural except lithium. The abundance of each isotope of the element is obtained from the Nuclear Wallet Cards published by Brookhaven National Laboratory in October, 2011.

The temperature of the material is set according to the design report of Mark-1 PB-FHR, which is listed in Table 35 below.

Material	Temperature (K)
flibe	928
fuel	1073
Graphite in the pebble shell	963
Graphite in the pebble central core	1023
Mixture*	1023

*Table 48: Temperature of the materials in Mark-1 PB-FHR. * Mixture here represents the mixture of graphite between the particles and silicon in the coat of particles*

5.1.3 Burnup Steps and Total Power

The burnup steps setting is as follows:

First, 10 steps at 5 days, full power

Then, 10 steps at 10 days, full power

Followed by 10 steps at 30 days, full power

Followed by 1 step at 50 days, full power

Followed by 5 steps at 100 days, full power

The total power of the unit cell is calculated from the power density of the reactor core. The power density is $23.0\mathrm{MW/m^3}$, therefore, the total power is:

$$P = 23.0 \times 10^6 W/m^3 \times (0.044550828\mathrm{m})^3 \approx 2167.70W$$

5.1.4 Calculation Conditions

The calculation conditions are as below:

- The version of Serpent used in this step is Serpent 2.1.29 compiled by gnu gcc compiler.
- The nuclear data library is ENDF B/VII.0 and gre7.20 (thermal scattering cross section library)
- The population of neutrons per cycle is set as 10000 and number of inactive cycles as 500, number of active cycles 1000.

5.1.5 Result Analysis

After calculating on Savio HPC Cluster, a burnup output file is produced. With the help of MATLAB 2016a (R), analysis on the results is performed.

The focus of the analysis is on the composition evolution and especially the variation of gamma radiation sources. The atom density and activity evolution are both analyzed and plotted. Moreover, the nuclides whose atom density or activity is of top 4 or top 6 are paid more attention to. Some animation gif's are created to show the accounts that those top nuclides take.

Lithium, beryllium, fluorine are three main elements in flibe, therefore, the figures on the evolution of the atom density of the main nuclides ^{6}Li, ^{7}Li, ^{9}Be, ^{19}F are specially plotted. To conveniently get the evolution pattern of the four nuclides, the atom density after each burnup step is divided by the initial atom density of the corresponding nuclide (listed in Table 36 below). However, the evolution pattern of ^{6}Li is apparently different from the others, so the figure of ^{6}Li is separated from the other three nuclides'.

Nuclide	**Atom density ($\mathbf{10^{24}/cm^3}$)**
^6Li	3.000E-07
^7Li	2.298E-02
^9Be	1.156E-02
^{19}F	4.822E-02

Table 49: Initial atom density of lithium, beryllium, and fluorine in flibe

The evolutions of atom density of those four nuclides are demonstrated as follows and the detailed analysis on ^{6}Li will be discussed later.

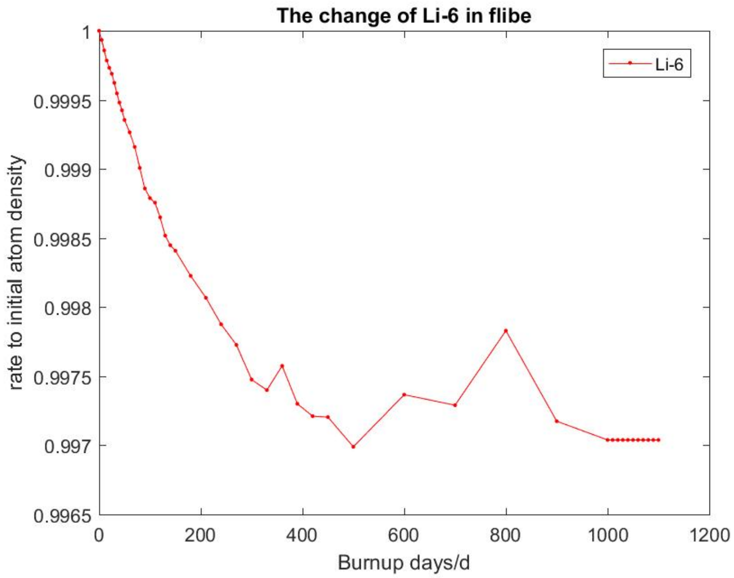

Figure 140: Relative atom density evolution of ^{6}Li in flibe.

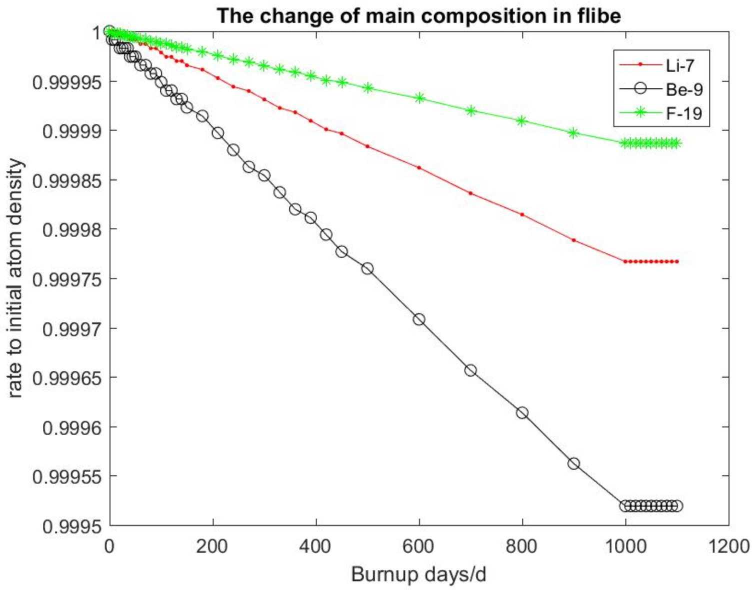

Figure 141: Relative atom density evolution of ^{7}Li, ^{9}Be, ^{19}F in flibe.

The four figures below showing the absolute atom density evolution of ^{6}Li with different initial ^{6}Li atom density. The initial atom density of each case is listed in Table 39.

Directions	**Atom density ($10^{24}/cm^{3}$)**
Up left	3.163E-07
Up right	1.149E-07
Down left	1.149E-06

Down right	3.000E-07

Table 50: *Different initial atom density of* ^{6}*Li*

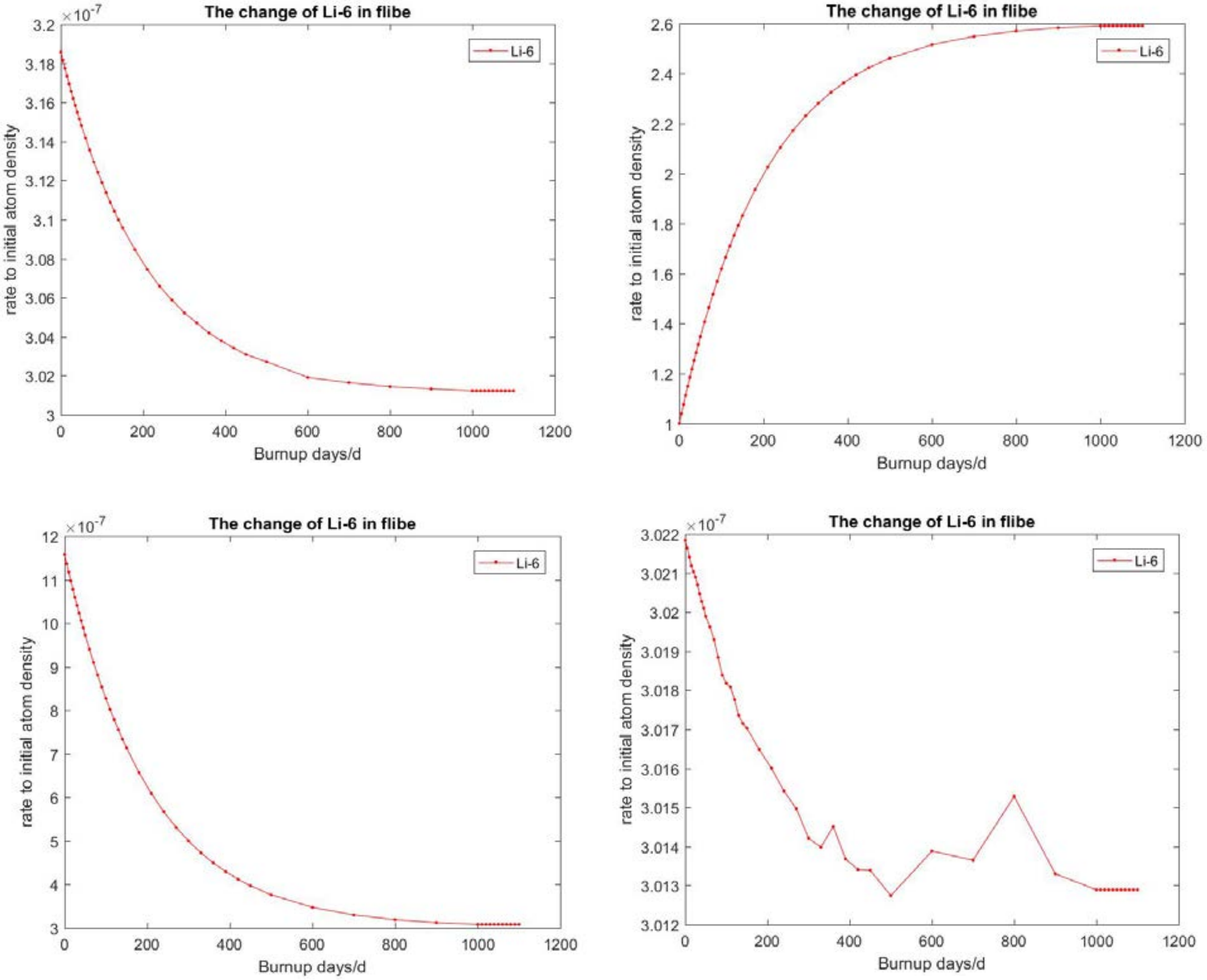

Figure 142: The absolute atom density evolution curves of ^{6}*Li*

As we can see from Figure 49 above, the absolute atom density of ^{6}Li is coming to a convergence value of approximately 3E-07 (unit: 1E+24/cm^{3}). Another three calculations with different initial atom density of ^{6}Li are performed and confirm the trend of convergence.

This convergence pattern can be derived analitically, just as follows:

The source of ^{6}Li is mainly from the beta minus decay of ^{6}He, and its disappearance is mainly the ^{6}Li (n, t)α (sometimes written as ^{6}Li (n, α) t) reaction. So the atom density of ^{6}Li to time should obey the differential equation as below:

$$\frac{\mathrm{d}N(^6Li)}{\mathrm{d}t} = \lambda N(^6He) - \sigma_{(n,t)} N(^6Li)\phi$$

In the equation, λ is the decay constant of ^{6}He, $\sigma_{(n,t)}$ is the micro cross section of (n, t) reaction of ^{6}Li, and ϕ is the scalar neutron flux.

Therefore, the atom density of ^{6}Li should be

$$N(^6Li) = \frac{\lambda N(^6He)}{\sigma_{(n,t)}^{^6Li}\phi} + [N_0(^6Li) - \frac{\lambda N(^6He)}{\sigma_{(n,t)}^{^6Li}\phi}]e^{-\sigma_{(n,t)}^{^6Li}\phi t}$$

So after a long time, the atom density of ^{6}Li will arrive at a convergence value.

$$\lim_{t\to\infty} N(^6Li) = \frac{\lambda N(^6He)}{\sigma_{(n,t)}^{^6Li}\phi}$$

From the detectors set in the Serpent model, those values slightly depend on time, so we can substitute those values by constants. Those constants are the average value of corresponding detector output during the burnup process.

$$\lambda \approx 0.859238 s^{-1}$$

$$N(^6He) \approx 1.93 \times 10^{10} cm^{-3}$$

$$\sigma_{(n,t)}^{^6Li}\phi \approx 99.7b \times 5.7 \times 10^{14} cm^{-2}s^{-1} \approx 5.68 \times 10^{-12} s^{-1}$$

If we insert those value into the limit of the solution, we will get the convergence value of ^{6}Li’s atom density as approximately $3 \times 10^{17} cm^{-3}$, that is, 13.05ppm. This value agrees with the trend indicated in Figure 50, especially in the fourth figure, the trend of vibration around $3 \times 10^{17} cm^{-3}$ is very obvious and convincing.

Then comes to the analysis on activity and activation products. First is the evolution of the share of impurity and the total activity in the flibe. From Figure 50, we can draw a conclusion that the share of impurities is gradually increasing during the full power operation. And the increasing pattern is almost linear. That is because during the burnup process, the main components of flibe, such as ^{6}Li, ^{7}Li, ^{9}Be, ^{19}F may experience many neutron-induced reactions and produce a lot of new nuclides, which are regarded as impurities.

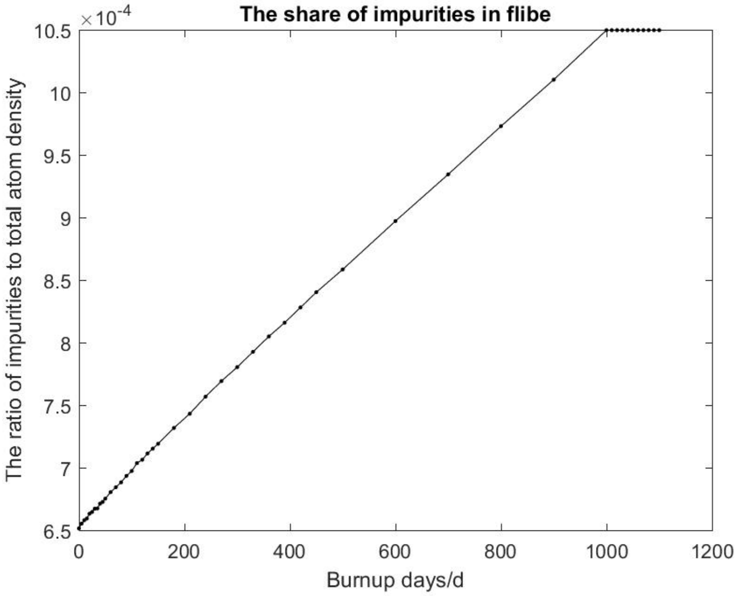

Figure 143: The evolution of the share of impurities in flibe

Then to confirm the tendency of impurities' increase with time, a long-term simulation is performed to observe the variation of impurities' share in flibe in 10 years' time. The evolution of the share of impurities in flibe in 10 years is illustrated in Figure 51 below.

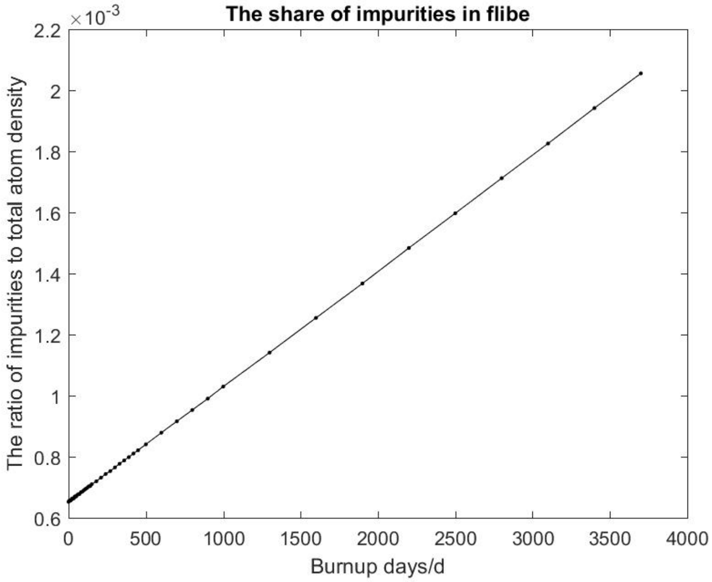

Figure 144: The evolution of the share of impurities in flibe in 10 years.

As is indicated in Figure 52, the account of impurities in flibe continues to increase in 10 years' activation process.

Figure 145: The share of impurities in flibe during the whole lifetime of the reactor

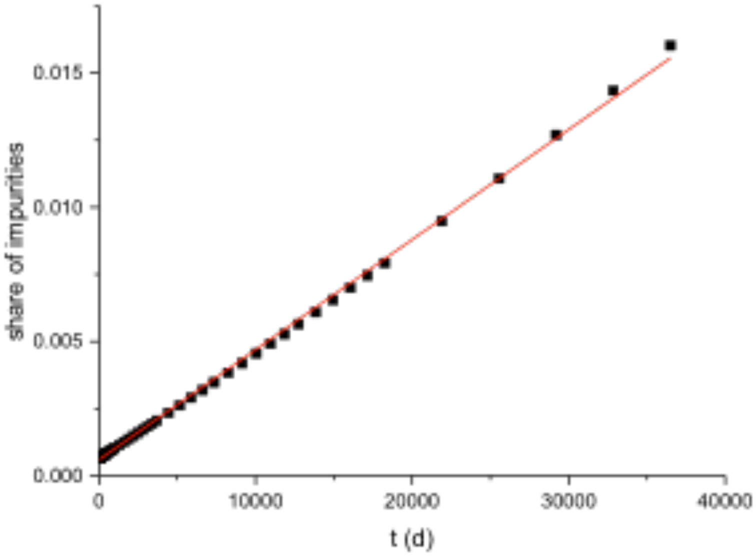

Then to determine the evolution pattern of the whole service life of the reactor, a 100 years' activation calculation is performed and as is shown in Figure 52 above, the share of impurities is still increasing linearly. The linear fit function is as follows:

$$y = 5.953 \times 10^{-4} + 4.099 \times 10^{-7} t$$

$$R^2 \approx 0.99900$$

Therefore, we can conclude that the share of impurities will increase continuously during full power operation of the reactor, along the whole service life of the reactor.

The change of activity in flibe is shown in Figure 53 below:

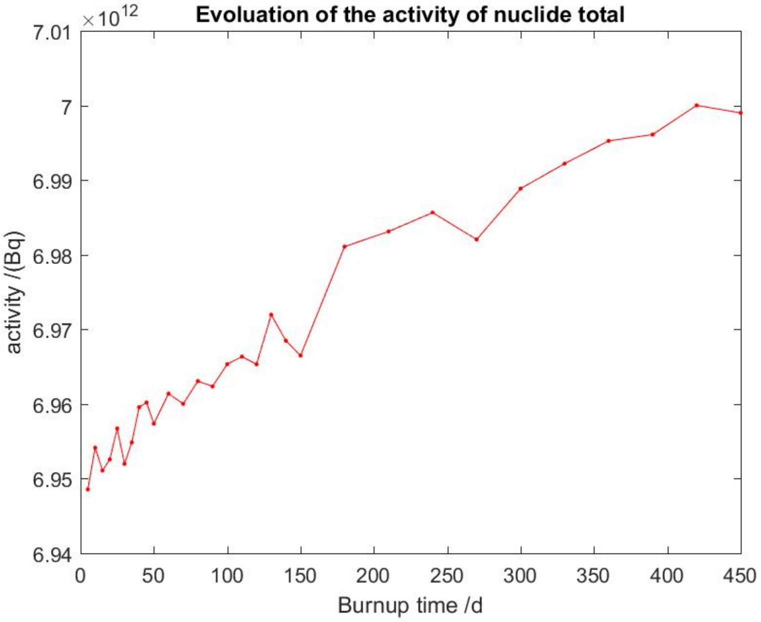

Figure 146: Evolution of the activity in flibe.

The initial point of activity is eliminated because the value is too small. Otherwise the curve describing the activity change in full power status will become a nearly horizontal line.

From the curve, we can see the activity in flibe is rising too but with some fluctuation. That is because the activation product is gradually accumulated. The fluctuation may result from the calculation uncertainty and the slight fluctuation of some activation products.

Sorted by the activity contribution, the top 7 nuclides are ^{8}Li, ^{8}Be, ^{20}F, ^{16}N, ^{6}He, ^{19}O, ^{24}Na, which account for more than 98.2% of the total activity. The evolution of those nuclides are plotted as Figure 54 below.

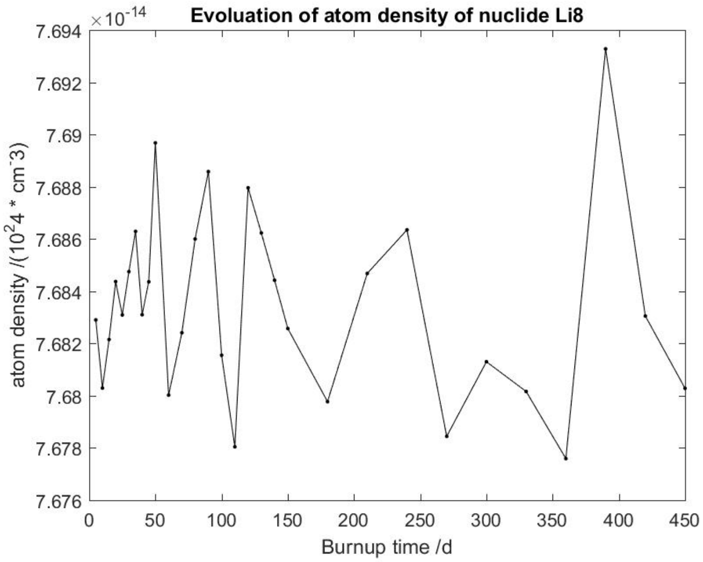
Evoluation of atom density of nuclide Li8
×10^-14
7.694
7.692
7.69
7.688
7.686
7.684
7.682
7.68
7.678
7.676
atom density /(10^24 * cm^-3)
0
50
100
150
200
250
300
350
400
450
Burnup time /d

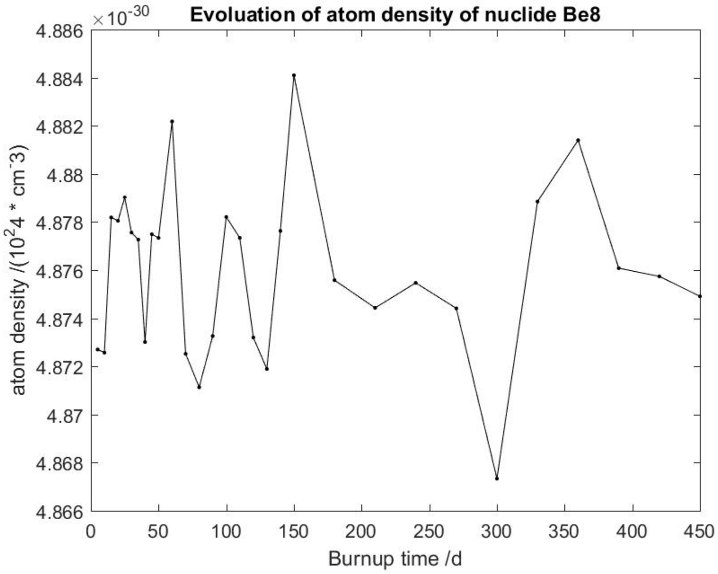
Evoluation of atom density of nuclide Be8
×10^-30
4.886
4.884
4.882
4.88
4.878
4.876
4.874
4.872
4.87
4.868
4.866
atom density /(10^24 * cm^-3)
0
50
100
150
200
250
300
350
400
450
Burnup time /d

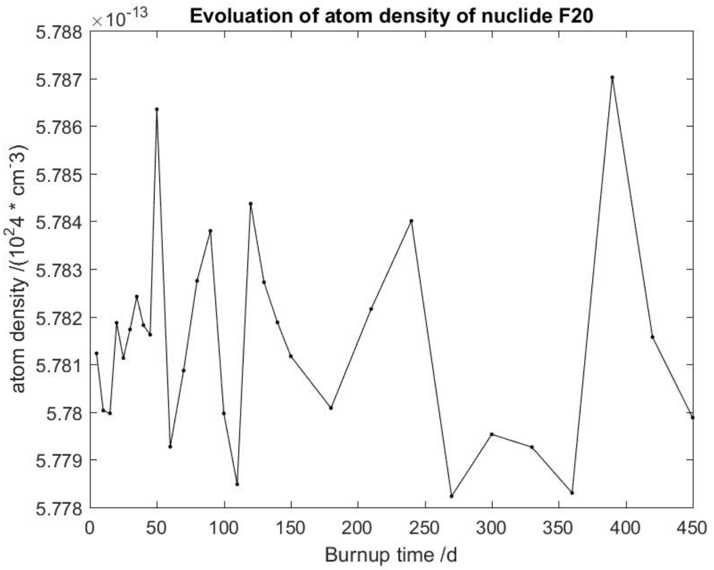
Evoluation of atom density of nuclide F20
×10^-13
5.788
5.787
5.786
5.785
5.784
5.783
5.782
5.781
5.78
5.779
5.778
atom density /(10^24 * cm^-3)
0
50
100
150
200
250
300
350
400
450
Burnup time /d

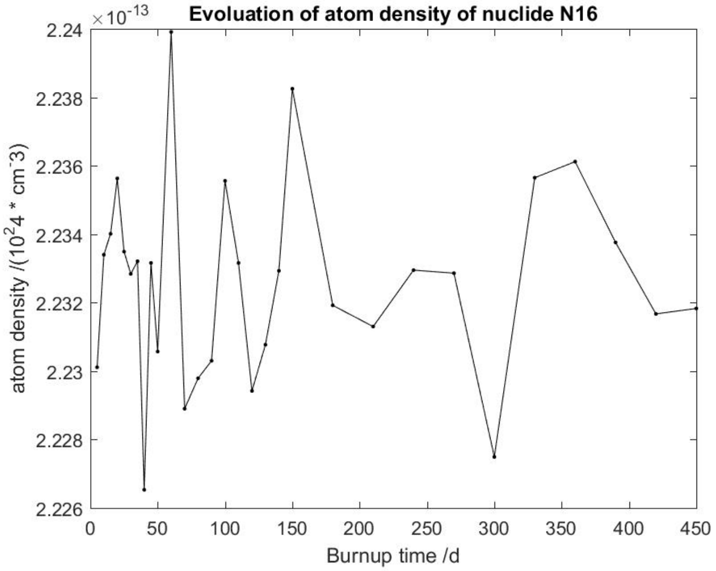
Evoluation of atom density of nuclide N16
×10^-13
2.24
2.238
2.236
2.234
2.232
2.23
2.228
2.226
atom density /(10^24 * cm^-3)
0
50
100
150
200
250
300
350
400
450
Burnup time /d

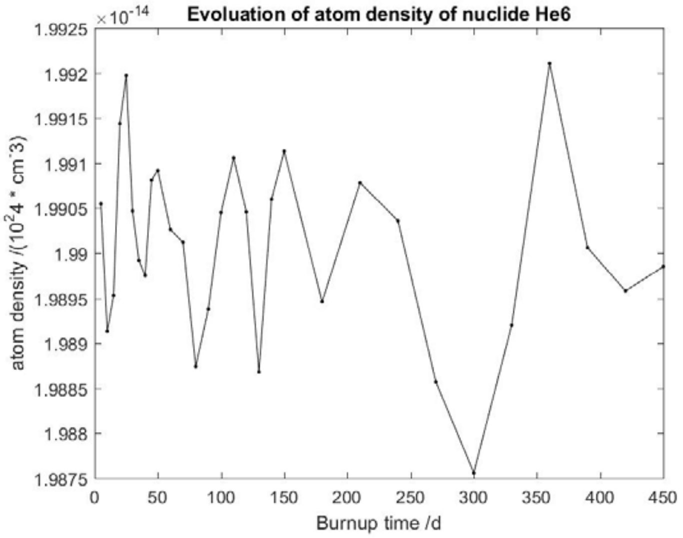
Evoluation of atom density of nuclide He6
×10^-14
1.9925
1.992
1.9915
1.991
1.9905
1.99
1.9895
1.989
1.9885
1.988
1.9875
atom density /(10^24 * cm^-3)
0
50
100
150
200
250
300
350
400
450
Burnup time /d

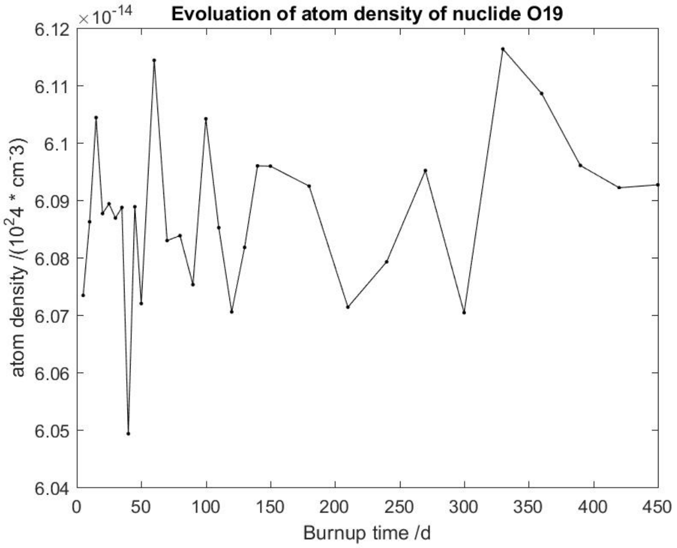
Evoluation of atom density of nuclide O19
×10^-14
6.12
6.11
6.1
6.09
6.08
6.07
6.06
6.05
6.04
atom density /(10^24 * cm^-3)
0
50
100
150
200
250
300
350
400
450
Burnup time /d

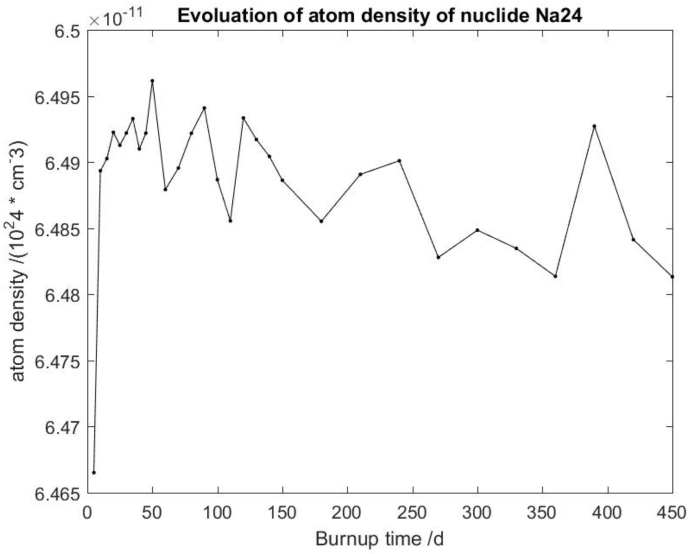
Evoluation of atom density of nuclide Na24
×10^-11
6.5
6.495
6.49
6.485
6.48
6.475
6.47
6.465
atom density /(10^24 * cm^-3)
0
50
100
150
200
250
300
350
400
450
Burnup time /d

Figure 147: Evolution of atom density of ^{8}Li, ^{8}Be, ^{20}F, ^{16}N, ^{6}He, ^{19}O and ^{24}Na.

Among all the sources of activity, some nuclides emit beta particles while others emit gamma rays and some emit both. So to determine the gamma sources, those activation products have to be identified and classified, especially the seven nuclides mentioned above.

After careful check of the nuclides decay mode and the data from ENDF/B-VII.1 MF8 [23], the main source nuclides of gamma radiation are ^{20}F, ^{16}N, ^{6}He, ^{19}O, ^{24}Na. However, each nuclide can give several discrete lines of gamma rays, and the branch ratio varies a lot. Here, those discrete lines accounting for more than 0.1% of the total emission of the nuclide will be considered.

Below is the gamma source and the discrete lines' energy and their branch ratios:

Nuclide	Energy/MeV	Relative Intensity	Nuclide	Energy/MeV	Relative Intensity
F20	1.633600E+00	6.454304E-01	O19	1.971400E-01	2.681884E-02
N16	1.754900E+00	4.677639E-04	O19	1.356800E+00	1.409457E-02
N16	2.741500E+00	3.169970E-03	O19	1.444100E+00	7.382870E-04
N16	2.822200E+00	5.025560E-04	O19	1.554000E+00	3.887193E-04
N16	6.128600E+00	2.590097E-01	Na24	1.368600E+00	1.487358E-02
N16	7.115200E+00	1.894250E-02	Na24	2.754000E+00	1.485276E-02
O19	1.098900E-01	7.103218E-04			

Table 51: Gamma source spectrum from the activation products in flibe.

The relative intensity of each discrete line is calculated from the total activity of the nuclide and the branch ratio of the discrete line. This gamma source spectrum can be used in the shielding calculation and analysis, which is the next step of the project.

5.2 Shielding Calculation and Analysis

The shielding calculation will try to determine the shielding requirements for materials used in Mark-1 PB-FHR. In this step, a brief literature review is performed and then a simplified model is used to analyze the materials' shielding property.

5.2.1 A Brief Literature Review

Shielding is a widely discussed issue about reactors and there are many papers about that, many on neutron shielding but also a lot on gamma shielding.

For neutron shielding, we usually first determine the real neutron flux in the inner and outer wall of the system and then develop an optimized shielding strategy to keep the flux below expected limit values. In more accurate calculation, the salt's thermal hydraulic behavior has to be closely coupled to its neutronic behavior, because the salt's circulating time is of the same order of magnitude as the lifetime of the precursors of delayed neutrons.

For gamma shielding, there are two types of gamma radiation, one is the primary gamma ray directly from fuel region and the other is the secondary gamma ray from the interaction between the primary neutron from the fuel region and the shielding material. When the shielding material's thickness is greater than a specific value, the secondary gamma ray may dominate the dose rate. Hence, it is necessary to use coupled neutron and gamma ray transport calculation for deep penetration problems. In addition, similar to the neutron shielding calculation, the gamma shielding calculation can also be split into two steps, first determine the neutron and gamma flux on the walls of the system and second deal with the deep penetration problem.

Drawn from the review, to determine the dose rate outside of the Mark-1 PB-FHR, we also need to finish the two steps. First, perform a full core calculation of the reactor and get the neutron flux and gamma flux on the outer wall of the core, and then perform deep penetration calculation to get the gamma flux on the outer wall of the vessel, then we can use the flux to dose conversion coefficients to determine the dose rate at the place of interest.

5.2.2 Simplified Calculation Model

In the actual analysis of the Mark-1 PB-FHR reactor, the model is largely simplified and the aim of this step is just estimating what is the thickness of a certain material necessary to reduce the gamma intensity by a factor of 10/100/1000/1E+06. A 1-D model is established to determine the necessary thicknesses.

The 1-D model is shown in Figure 55 below:

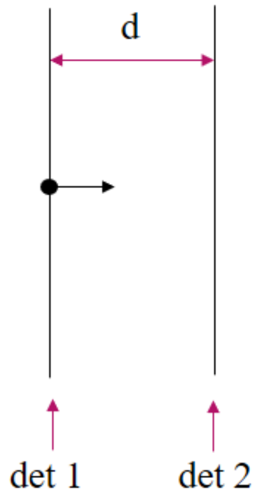

Figure 148: The 1-D model for shielding calculation.

As is illustrated in Figure 55, the gamma rays are emitted from a point close to the left infinite plane. The directions of the rays are all the same and vertical to the plane. Two gamma current detectors are set on the two parallel infinite planes, and the detector 1 will be eliminated after setting the source-emitting rate. The middle part of the two planes is filled with the experiment material and the width between the two planes can be changed by a Python script. The calculation is performed with Serpent 2.1.29 compiled by gnu gcc compiler and the photon xsdata file is obtained from the ac_nuclear directory on savio HPC Cluster. Materials we have to calculate are flibe, graphite and metallic structure (316 stainless steel). The metallic structure is not considered before, and it is in fact the 316 stainless steel.

United Performance Metals (UPM), is a global distributor of high-performance metals, on the product introduction website of this company, there is the composition of the 316 stainless steel. Reference [28] is a detailed study of 316 stainless steel, including the composition, the creep property, etc. On that paper, the principle structure metal is a modified grade of 316 stainless steel, which contains less Sulphur, Phosphorous and Silicon. Compared to the composition on the product page of UPM, those two set of values agree with each other, except less impurities.

The composition of 316 stainless steel from *UPM [28]* is listed in Table 3.6 below:

Element	**Percent by Weight Maximum Unless Range is Specified**
Carbon	0.08
Manganese	2.00
Silicon	0.75
Chromium	16.00 18.00
Nickel	10.00 14.00
Molybdenum	2.00 3.00
Phosphorus	0.045
Sulfur	0.030
Nitrogen	0.10
Iron	Bal.

Table 52: *The Composition of 316 stainless steel.*

Then I use a Python script to control the process of setting thickness, submitting jobs, checking the completeness of the job, extracting detector output, changing the thickness. At each thickness point, three calculations are performed to reduce the stochastic error.

After an attempt to determine the range of the calculation, it can be inferred that the shielding power of 316 stainless steel is the best of the three materials. And the shielding power of flibe and graphite is similar. This pattern can be theoretically induced from the average atom mass of the three materials. 316 stainless steel contains a lot of Iron atoms, which is much heavier than Fluorine or Carbon atoms in flibe or graphite, so the gamma reaction cross section of 316 stainless steel is much larger. In the meantime, the average atom mass of flibe and graphite is close thus the shielding power of the two materials is similar.

Another problem is that the thicker the shielding material is, the larger the stochastic error will be. Therefore, different number of simulated particles ("nps" in Serpent) should be specified to different thickness of shielding material. The "nps" set in Serpent is tabled below:

Material	Thickness/cm	nps
Flibe	0~90	1.0E+07
	100~190	5.0E+07
	200~290	1.0E+09
Flibe	300~370	5.0E+09
Graphite	0~90	1.0E+07
	100~190	5.0E+07
	200~290	1.0E+09
	300~390	5.0E+09
Metallic Structure (316 stainless steel)	0~69 (each step increased by 3)	1.0E+09

Table 53: *Number of simulated particles setting in Serpent.*

Different "nps" setting is also realized by the Python script. For flibe and graphite, the interval between two thickness point is 10 cm, while for 316 stainless steel, it is 3cm. The stochastic error of each calculation is reduced to less than 8%, and the lowest is less than 0.59%. Taking three times' calculation each point into account, the stochastic error can be lower than 5%.

According to the shielding theory, ideally, the attenuation should be an exponential reduce process, so the remaining intensity curve should be nearly an exponential function to the thickness of the shielding material. Therefore, a normal scale figure and a semi-log scale figure are plotted for each of the material.

5.2.3 Shielding Analysis of Flibe

Below is the attenuation curve of flibe. In the semi-log scale figure, a linear fit and a quadratic fit are performed and the R^2's are displayed in the figures. The figures are all plotted by Origin 9 (R).

Figure 3.12-1: Relative intensity behind the shielding flibe

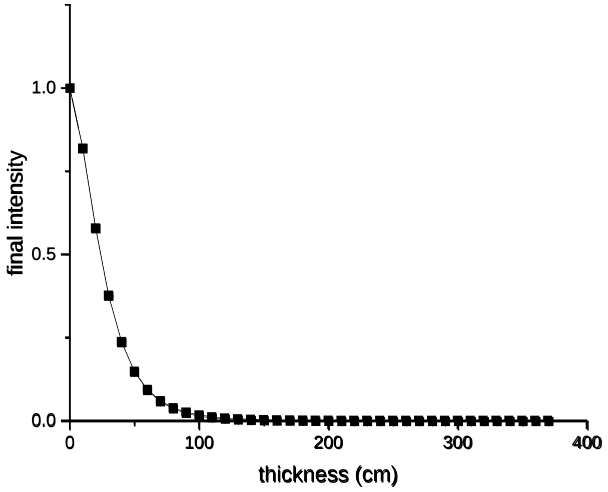

Figure 3.12-2: Relative intensity behind the shielding flibe (semilog scale)

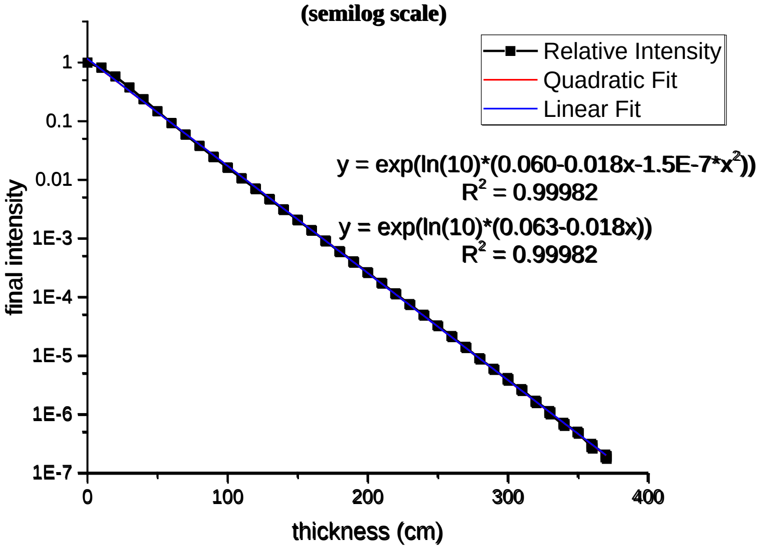

Figure 149: Relative intensity behind the shielding flibe.

The curve in the semi-log figure is almost a straight line, and it can be concluded from the quadratic fit function and the linear fit function.

The linear fit function is:

$$\lg y = 0.063 - 0.018x$$

While the quadratic fit function is:

$$\lg y = 0.060 - 0.018x - 1.5 \times 10^{-7}x^2$$

The quadratic coefficient is very small, indicating that the curve is very close to a straight line. Also, the R^2's are very close to 1, so the fitting is rather reasonable.

Then the thicknesses of flibe needed to reduce the intensity of gamma rays by 1/10, 1/100, 1/1000, 1E-6 are listed in the following table.

Remaining intensity ratio	Thickness/cm			
	B-spline	**Linear Fit**	**Quadratic Fit**	**Result**
1E-01	58.7	58.2	58.2	58.4
1E-02	111.8	113.0	113.0	112.6
1E-03	168.0	167.7	167.8	167.8
1E-04	223.6	222.5	222.5	222.9
1E-05	277.7	277.3	277.2	277.4
1E-06	330.7	332.0	331.9	331.5

Table 54: Thickness needed to reduce the intensity of gamma radiation by a certain ratio for flibe.

5.2.4 Shielding Analysis of Graphite

The attenuation curve of graphite is shown in Figure 57 below. In the semi-log scale figure, a linear fit and a quadratic fit are performed and the R^2's are displayed in the figures.

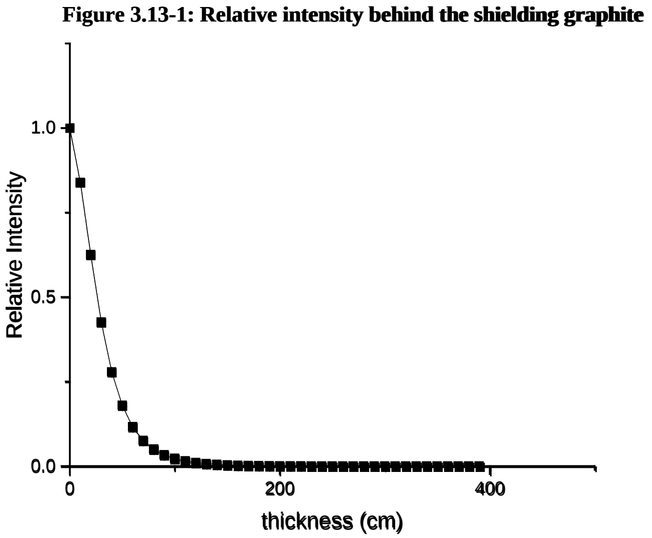

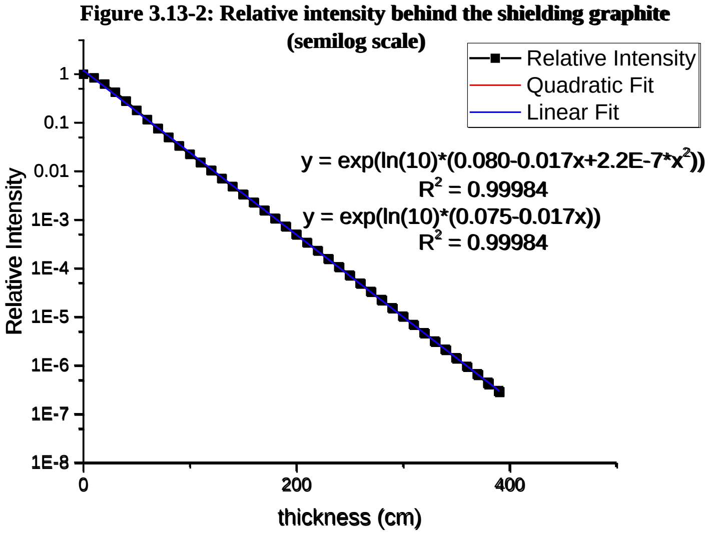

Figure 150: Relative intensity behind the shielding graphite.

The curve in the semi-log figure is almost a straight line, too.

The linear fit function is:

$$\lg y = 0.075 - 0.017x$$

While the quadratic fit function is:

$$\lg y = 0.080 - 0.017x + 2.2 \times 10^{-7}x^2$$

The quadratic coefficient is very small, indicating that the curve is very close to a straight line. Also, the two R^2's are both very close to 1, so the fitting is rather reasonable.

Then the thicknesses of graphite needed to reduce the intensity of gamma rays by 1/10, 1/100, 1/1000, 1E-6 are listed in the following table.

Remaining intensity ratio	**Thickness/cm**			
	B-spline	**Linear Fit**	**Quadratic Fit**	**Result**
1E-01	64.0	63.58	63.6	63.7
1E-02	121.2	122.7	122.6	122.2
1E-03	182.0	181.9	181.6	181.8
1E-04	241.9	241.0	240.8	241.2
1E-05	300.8	300.1	300.0	300.3
1E-06	359.0	359.3	359.3	359.2

Table 55: Thickness needed to reduce the intensity of gamma radiation by a certain ratio for graphite.

5.2.5 Shielding Analysis of 316 Stainless Steel

Figure 58 below is the attenuation curve of 316 stainless steel. In the semi-log scale figure, a linear fit and a quadratic fit are performed and the R^2's are displayed in the figures.

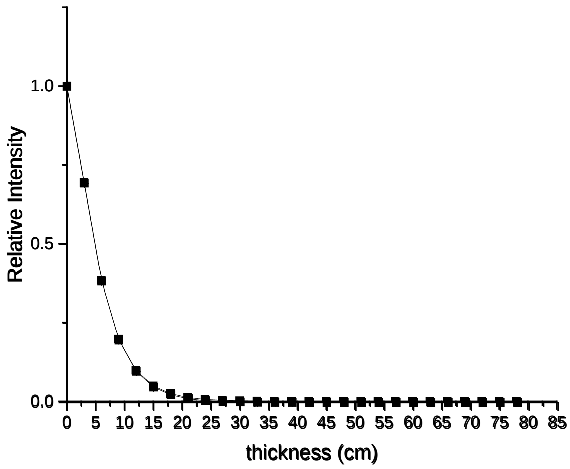

Figure 3.14-1: Relative intensity behind the shielding steel

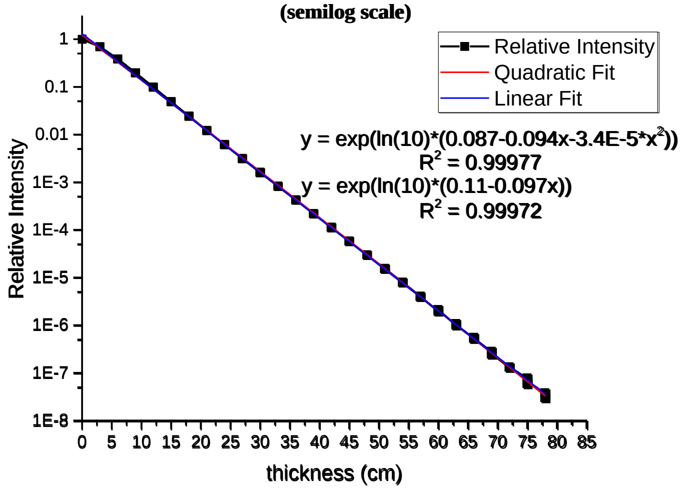

Figure 3.14-2: Relative intensity behind the shielding steel (semilog scale)

Figure 151: Relative intensity behind the shielding 316 stainless steel.

The curve in the semi-log figure is almost a line, but may not be that straight as the two materials above. The detailed values are as follows:

The linear fit function is:

$$\lg y = 0.11 - 0.097x$$

While the quadratic fit function is:

$$\lg y = 0.087 - 0.094x - 3.4 \times 10^{-5}x^2$$

The quadratic coefficient is small, indicating that the curve is close to a straight line. However, the quadratic coefficient of 316 stainless steel is larger than that of flibe or graphite, so this curve is not that close to a straight line than the curve of flibe or graphite does. In addition, the two R^2's are both very close to 1, so the fitting is rather reasonable.

Then the thicknesses of 316 stainless steel needed to reduce the intensity of gamma rays by 1/10, 1/100, 1/1000, 1E-6 are listed in the following table.

Remaining intensity ratio ra	**Thickness/cm**			
	B-spline	**Linear Fit**	**Quadratic Fit**	**Result**
1E-01	11.96	11.50	11.47	11.64
1E-02	22.1	21.82	21.95	21.96
1E-03	32.33	32.15	32.35	32.28
1E-04	42.71	42.47	42.67	42.62
1E-05	53.19	52.80	52.92	52.97
1E-06	63.15	63.12	63.10	63.12

Table 56: Thickness needed to reduce the intensity of gamma radiation by a certain ratio for 316 stainless steel.

5.3 Dose Calculation and Analysis

During the shielding calculation in the second step, a log scale energy grid is set to the detector 2 and therefore obtained the energy spectrum of the photons that penetrate the shielding material. Then the dose can be calculated with the flux to dose coefficients.

The flux to dose coefficients are from ICRP Publication 116 [29]. Linear interpolation is processed to the coefficient table and the energy bins of the log scale energy grid are represented by the center of each bin.

In ICRP Publication 116's "Photons: effective dose per fluence" table, data for particles incident in six geometries are listed. Therefore, the calculation below is also performed for those six situations.

There are totally 8 types of projections, that is, anteroposterior (AP), posteroanterior (PA), right lateral (RLAT), left lateral (LLAT), right anterior-posterior oblique (RAO), left anterior-posterior oblique (LAO), right posterior-anterior oblique (RPO), and left posterior-anterior oblique (LPO)], abdomen (in the two projections of AP and PA), and pelvis (in the two projections of AP and PA). In the ICRP Publication 116, data for AP, PA, LLAT, RLAT are tabulated, with another two types – ROT for rotation, and ISO for isotropic projection. In the following calculation, those six situations are calculated separately.

The calculation result of flibe is listed in the Table below. Because all the calculation of shielding assume the source emitting rate as 1, the figures in Table 46 is in fact the dose rate to source rate ratio.

Remaining intensity ratio	Thickness /cm	AP	PA	RLAT	LLAT	RAO	LAO
1E-01	58.4	7.023E-01	6.697E-01	5.999E-01	5.800E-01	6.457E-01	5.936E-01
1E-02	112.6	7.370E-02	7.060E-02	6.350E-02	6.150E-02	6.810E-02	6.280E-02
1E-03	167.8	7.600E-03	7.300E-03	6.500E-03	6.300E-03	7.000E-03	6.500E-03
1E-04	222.9	7.601E-04	7.238E-04	6.503E-04	6.287E-04	6.986E-04	6.425E-04
1E-05	277.4	7.422E-05	7.053E-05	6.332E-05	6.119E-05	6.808E-05	6.257E-05
1E-06	331.5	7.330E-06	6.945E-06	6.232E-06	6.018E-06	6.706E-06	6.157E-06

Table 57: Dose rate outside of shielding material flibe

(unit: pSv/source particle).

As is indicated in Table 46, the dose rates of different thickness of shielding material are almost the same except the order magnitude. And the orders are the same as those remaining intensity ratio. This pattern indicates that the energy spectrum after different thickness of shielding is similar. That is, the dependence of flibe's absorption cross-section dependence on the gamma energy is not that strong.

The usage of the data in Table 46 should be like this: if the source rate is 10^{12}/s, and the thickness of the flibe is 222.9 cm, then the AP dose rate outside should be

$$7.601 \times 10^{-4} \times 10^{12} pSv/s = 0.7601 mSv/s$$

Remaining intensity ratio	Thickness /cm	AP	PA	RLAT	LLAT	RAO	LAO
1E-01	63.7	6.784E-01	6.476E-01	5.808E-01	5.617E-01	6.245E-01	5.746E-01
1E-02	122.2	7.160E-02	6.860E-02	6.180E-02	5.980E-02	6.620E-02	6.100E-02
1E-03	181.8	7.400E-03	7.000E-03	6.300E-03	6.100E-03	6.800E-03	6.300E-03
1E-04	241.2	7.354E-04	7.005E-04	6.299E-04	6.090E-04	6.763E-04	6.222E-04

1E-05	300.3	7.181E-05	6.828E-05	6.135E-05	5.930E-05	6.593E-05	6.062E-05
1E-06	359.2	6.934E-06	6.585E-06	5.915E-06	5.716E-06	6.359E-06	5.845E-06

Table 58: *Dose rate outside of shielding material graphite (unit: pSv/s).*

Then comes the dose rate calculation results for graphite. Similarly, the data is tabulated in Table 48.

Similar pattern is obtained from the results of graphite, that is, the values from different thickness of graphite are similar regardless of the orders, which means that the dependence of graphite’s absorption cross section on gamma energy is also weak.

Finally, the same calculation and analysis process is performed on 316 stainless steel, and the results are as follows:

Remaining intensity ratio	Thickness /cm	AP	PA	RLAT	LLAT	RAO	LAO
1E-01	11.64	7.299E-01	6.825E-01	6.054E-01	5.826E-01	6.587E-01	6.005E-01
1E-02	21.96	7.150E-02	6.720E-02	5.990E-02	5.770E-02	6.490E-02	5.930E-02
1E-03	32.28	7.200E-03	6.800E-03	6.100E-03	5.800E-03	6.600E-03	6.000E-03
1E-04	42.62	7.208E-04	6.759E-04	6.027E-04	5.805E-04	6.529E-04	5.965E-04
1E-05	52.97	7.348E-05	6.868E-05	6.119E-05	5.890E-05	6.637E-05	6.057E-05
1E-06	63.12	6.996E-06	6.522E-06	5.805E-06	5.585E-06	6.304E-06	5.748E-06

Table 59: *Dose rate outside of shielding material 316 stainless steel (unit: pSv/s).*

The usage of the values for graphite and 316 stainless steel is the same as that of flibe mentioned above.

REFERENCES

[1] Kai Wang et al., “Application of RELAP5 / MOD4 . 0 Code in a Fluoride Salt-Cooled High- Temperature Test Reactor”. In: *Advances in thermal hydraulics*. Reno, 2014, pp. 1–11.

[2] C.H. Andreades et al., “Technical Description of the “Mark 1” Pebble-Bed Fluoride-Salt-Cooled High-Temperature Reactor (PB-FHR) Power Plant,” Department of Nuclear Engineering, University of California, Berkeley (2014).

[3] Xin Wang, ‘Coupled neutronics and thermal-hydraulics modeling for pebble-bed Fluoride-Salt-Cooled, High-Temperature Reactor (FHR)’, PhD thesis, 2018

[4] H. G. Weller *et al.* “A tensorial approach to computational continuum mechanics using object- oriented techniques.” *Computers in Physics*, **12**: pp. 620 – 631 (1998).

[5] H. Jasak, A. Jemcov, and Z. Tukovic. “OpenFOAM: A C++ library for complex physics sim- ulations.” In: *International Workshop on Coupled Methods in Numerical Dynamics*. IUC, Dubrovnik, Croatia, September 19-21, 2007 (2007).

[6] “PSG2 / Serpent Monte Carlo Reactor Physics Burnup Calculation Code.” URL http://montecarlo.vtt.fi (2011).

[7] J. Leppänen *et al.* “Unstructured mesh based multi-physics interface for cfd code coupling in the serpent 2 monte carlo code.” In: *PHYSOR 2014, Kyoto, Japan, Sep. 28 - Oct. 3, 2014* (2014).

[8] M. Aufiero *et al.* “Serpent–openfoam coupling in transient mode: simulation of a godiva prompt critical burst.” In: *Joint International Conference on Mathematics and Computation, Supercom- puting in Nuclear Applications and the Monte Carlo Method (M&C+ SNA+ MC2015).*

[9] P. A. Cundall and O. D. Strack. “A discrete numerical model for granular assemblies.” *Geotech- nique*, **29(1)**: pp. 47–65 (1979).

[10] Clifford and K. Ivanov. “PBMR 400MW benchmark calculations using the simplified P_3 ap- proach.” In: *Proceedings of HTR2010, Prague, Czech Republic, October 18-20, 2010* (2010).

[11] Y. A. Hassan. “Large eddy simulation in pebble bed gas cooled core reactors.” *Nuclear Engi- neering and Design*, **238(3)**: pp. 530 – 537 (2008).

[12] Shams *et al.* “Quasi-direct numerical simulation of a pebble bed configuration. part i: Flow (velocity) field analysis.” *Nuclear Engineering and Design*, **263**: pp. 473–489 (2013).

[13] C. Fiorina *et al.* “Gen-foam: a novel openfoam based multi-physics solver for 2d/3d transient analysis of nuclear reactors.” *Nuclear Engineering and Design*, **294**: pp. 24 – 37 (2015).

[14] J. Leppänen and M. DeHart. “Htgr reactor physics and burnup calculations using the serpent monte carlo code.” *Trans. Am. Nucl. Soc*, **101**: pp. 782–784 (2009).

[15] X. YU and G. LIU. *Overview of TMSR-SF1 & SF0. Technical Report* –, TMSR Center, SINAP, CAS (–).

[16] P. Bardet *et al.* “The pebble recirculation experiment (prex) for the ahtr.” *Proceedings of Global 2007*, (pp. 9–13) (2007).

[17] A.T. Cisneros, “Pebble Bed Reactors Design Optimization Methods and their Application to the Pebble Bed Fluoride Salt Cooled High Temperature Reactor (PB-FHR),” Ph.D. thesis, Department of Nuclear Engineering, University of California, Berkeley (2013).

[18] Gandini, “A Generalized Perturbation Method for Bi-linear Functions of the Real and Adjoint Neutron Fluxes,” *Journal of Nuclear Energy* **21**, pp. 755-765 (1967).

[19] M. Aufiero et al., “A Collision History-based Approach to Sensitivity/Perturbation Calculations in the Continuous Energy Monte Carlo Code SERPENT,” *Annals of Nuclear Energy* **85**, pp. 245-258 (2015).

[20] Gandini, G. Palmiotti and M. Salvatores, “Equivalent Generalized Perturbation Theory (EGPT),” *Annals of Nuclear Energy* **13**(3), pp. 109-114 (1986).

[21] Leppänen J. Serpent_manual[R].2015

[22] Tuli J K. NUCLEAR WALLET CARDS[R].National Nuclear Data Center, Brookhaven National Laboratory, 2011

[23] Chadwick M B, Herman M, Obložinský P, et al. ENDF/B-VII.1 Nuclear Data for Science and Technology: Cross Sections, Covariances, Fission Product Yields and Decay Data[J]. Nuclear Data Sheets, 2011,112(12):2887-2996.

[24] Merk B, Konheiser J. Neutron shielding studies on an advanced molten salt fast reactor design[J]. Annals of Nuclear Energy, 2014,64:441-448.

[25] Mohammadi A, Hassanzadeh M, Gharib M. Shielding calculation and criticality safety analysis of spent fuel transportation cask in research reactors[J]. Applied Radiation and Isotopes, 2016,108:129-132.

[26] Alizadeh A, Shirani A S, Kashi S. Neutron and gamma-ray deep penetration calculation through biological concrete shield of VVER-1000 reactor by a new technique based on variance reduction[J]. Annals of Nuclear Energy, 2013,60:86-92.

[27] Metals U P. 316 Stainless Steel Sheet, Coil & Plate[EB/OL]. https://www.upmet.com/products/stainless-steel/316316l.

[28] Mathew M D, Sasikala G, Mannan S L, et al. A comparative study of the creep rupture properties of type 316 stainless steel base and weld metals[J]. Journal of engineering materials and technology, 1993,115(2):163-170.

[29] Petoussi-Henss N, Bolch W E, Eckerman K F, et al. Conversion coefficients for radiological protection quantities for external radiation exposures[J]. Annals of the ICRP, 2010,40(2-5):1-257

4.3. Experimental and Computational Investigation of Twisted Tube Heat Exchangers (UNM)

Experimental and Computational Investigation of Twisted Elliptical Tube Heat Exchangers (UNM)[1]

Executive Summary

Liquid salts as heat transfer fluids compared to other reactor coolants have greater volumetric heat capacities, have higher Prandtl numbers and are expensive coolants. While total pumping power is low because of the high heat capacity, there is relatively poor heat transfer compared to other coolants for the same pumping power. These characteristics may result in decay heat cooling systems operating in the transitional flow regime. Under such operational conditions, alternative heat exchanger designs may provide better performance at lower costs. The use of twisted-elliptical-tube versus straight-tube heat exchangers were experimentally evaluated in a test loop using Dowtherm A to simulate flibe salt coolants. Parallel computational investigations were conducted.

Twisted Elliptical and Plain Wall Heat Exchangers Tested in Heat Transfer Facility (Photo Credit: Hipex PTY. Ltd.)

The twisted elliptical tubes were found to have significant performance advantages in both the experimental and computational studies for use in FHR decay heat cooling systems. The results of the experimental work included: (1) date for heat transfer performance in twisted elliptical tubes under buoyancy-affected flow regimes, not previously published in the public domain, (2) Nusselt number correlations developed using this data and (3) comparison of twisted elliptical tube and unbaffled plain tube bundle performance for buoyancy-affected and low forced-convection flow regimes, showing up to 55% heat transfer coefficient enhancement on the shell side for natural circulation flow and greater than 250% heat transfer coefficient enhancement on the shell side for transitional forced convection flow. Results from the computational analysis showed that twisted elliptical heat exchangers can provide a 23% to 51% cost savings compared to a standard shell-and-tube heat exchanger for the intermediate heat exchanger used in a commercial FHR.

---

[1] J. Hughes (jhughes7@unm.edu or hughes.joel.thomas@gmail.com) and E. Blandford (edb@unm.edu)

Contents

1 Introduction

For the University of New Mexico, the Integrated Research Project fell into two major themes in support of Fluoride-salt-cooled High-temperature Reactor (FHR) development: heat transfer work and mass transfer work. These two major themes helped to explore potential limitations of the FHR technology: economic and performance penalties associated with high viscosity and expensive coolants and the use of twisted elliptical tubes as a potential solution, and the use of acoustically-enhanced inert gas sparging to reduce tritium concentration in the circulating flibe coolant, which has economic, safety, and licensing implications. The major findings from the heat transfer effort are detailed below, with the mass transfer work being summarized in a sister report.

Heat transfer work for this Integrated Research Project also fell into two areas: experimental work (which was the primary focus and use of the fund) and computational work, which was a supporting work performed to better understand the potential of the twisted elliptical tube technology and the set the stage for post-processing the data collected at the Heat Transfer Facility (HTF). Twisted elliptical tubes were tested in the facility and were found to have significant performance advantages in both experimental and computational studies.

The following report is a summary of the project progression, work description, infrastructure development, and data analysis, and results from the two studies. Only the high level aspects are covered, as much more detail can be found in the sources described in the annotated bibliography provided in the References and Further Reading section. Finally, suggested subjects of future work and research in the area are presented.

2 Timeline of Project

The two works were not staged separately, but were performed concurrently. Work on the HTF was begun in 2013. It started as a simple natural circulation loop with bi-directional forced-flow capability. This early loop was run with deionized water and featured a single Joule heated tube on the vertical leg as the heat source and a simple concentric tube heat exchanger on the cold leg as a heat rejection heat exchanger. This early version was not insulated and was used for two purposes: (1) obtaining practice with heat transport loop design and operation and (2) collecting natural circulation data, which was subsequently used to as a validation tool against a single-phase, natural circulation predictive code adopted from the lead-fast reactor community for application to FHRs.

During this phase of the work, progress was being made in better understanding the types of heat exchangers that would be applicable to FHR decay heat removal systems and potential enhancement mechanisms. Twisted elliptical tubes were identified as an important potential enabling technology for Direct Reactor Auxiliary Cooling System (DRACS) heat exchangers due to the inherent heat transfer enhancement and the greater predictability of the technology when operating in laminar to transitional flow regimes. Potential vendors for the twisted elliptical tube technology were identified, and Hipex Pty. Ltd. was selected as the supplier. Four bundles were ordered, but the ones used for this project were a single-wall, bayonet-style twisted elliptical tube heat exchanger and single-wall, bayonet-style plain unbaffled tube heat exchanger for comparison.

The HTF was heavily modified to account for the new test sections. A secondary, intermediate loop was added between the primary heated loop and the house chilled water supply to provide for inlet temperature control and data collection on the secondary side of the test section. Both loops were made to be run with Dowtherm A, a mineral oil with good scaling properties to the flibe working fluid of FHRs. About this time, Farris Engineering Center, the building in which the project was housed, was slated for renovation and the facility was broken down and moved to a nearby building, Centennial Engineering Center. It was rebuilt over the course of a couple of months in a newly finished laboratory. The insulation and finishing touches were finalized in January, 2017, and testing on the twisted elliptical tube bundle commenced immediately following leak and other shakedown and debugging tests. This testing proceeded for approximately 300 hours or so to provide enough data to build the heat transfer performance maps for the heat exchanger necessary to resolve the inertial and buoyancy effects at a correlation development level.

Once data collection was complete on the twisted elliptical tube bundle, the HTF was again heavily modified. This third iteration saw the following changes: replacement of the twisted elliptical tube bundle with the plain tube bundle, the addition of a bypass line on the secondary loop to provide for testing for double-walled heat exchanger concepts (a project funded by a separate, but related, Nuclear Energy University Program award), and other supporting infrastructure for this double-walled work. The data from the single-walled, plain bundle was collected in Summer and Fall of 2017 and post-processed during this time.

2.1 Heat Transfer Facility Experimental Work

The data collected from the Heat Transfer Facility for this project was for single-walled heat exchangers with twisted elliptical tubes and plain tubes. In both cases, low Reynolds numbers were investigated so the effect of buoyancy on the heat transfer could be determined. Pressure drop data was not collected because of the rather complex bundle geometry and because the expected pressure drop at the low flow rates investigated was not found to be within the range easily measured with off-the-shelf pressure transducers (a side effect of the drastically reduced pumping power when using Dowtherm A as a simulant fluid for molten salts) [1].

Heat transfer coefficients were found to be very effectively enhanced by the twisted geometry of the twisted elliptical tubes. Enhancement of up to 200% over unbaffled plain tube performance was observed for the same Reynolds number. Due to the high cost of flibe used in FHRs and the typically high volumetric value of nuclear grade systems, a factor of roughly

1.5-2 fold reduction in heat exchanger size is very significant. Heat transfer enhancement over plain tubes was observed to generally increase as a function of Reynolds number for the range measured (up to $Re \sim 1300$ on the shell side) [2]. In addition, it was also noticed that the predictability of the heat transfer performance was enhanced when using the twisted elliptical tube bundle compared to the plain tube bundle. This can be understood because the operating regime was in the laminar to transitional regime, which is well known to have a high level of unpredictability in heat transfer coefficient for smooth geometries, but for certain enhanced geometries (such as the twisted elliptical tubes), has a smooth transition.

In summary, the results of the experimental work included the following:

- Data for heat transfer performance in twisted elliptical tubes under buoyancy-affected flow regimes, not previously published in the public domain
- Nusselt number correlations for this data
- Comparison of twisted elliptical tube and unbaffled plain tube bundle performance for buoyancy-affected and low forced-convection flow regimes, showing up to $\sim 55\%$ heat transfer coefficient enhancement on the shell side for natural convection flow and greater than $\sim 250\%$ heat transfer coefficient enhancement on the shell side for transitional forced convection flow

2.2 Computational Work

In conjunction with the experimental work that was ongoing with the Heat Transfer Facility, a separate computational study on heat exchanger optimization was performed using the Python programming language. While the experimental work focused primarily on buoyancy effects on the heat transfer and was intended to aid in design of safety systems for the FHR (such as in a Direct Reactor Auxiliary Cooling System (DRACS) Heat Exchanger (DHX), which could be relied upon during design basis events for emergency system cooling), the computational study focused on larger scale, intermediate heat exchangers used to transfer the bulk of the reactor power to the power conversion cycle [1].

The study compared standard segmented baffle shell-and-tube and twisted elliptical tube heat exchanger designs for a variety of fouling and manufacturing cost assumptions utilizing two recently developed metaheuristic algorithms for optimization: cuckoo search algorithm and firefly algorithm. Both algorithms had been utilized in the past for optimization of shell-and-tube heat exchangers, but were applied to the FHR intermediate heat exchanger specifically to compare shell-and-tube and twisted elliptical tube for the FHR application. Results heavily favored the twisted elliptical tube from several aspects, with the major one being cost. At $\$375/kg$ flibe specific cost, the twisted elliptical tube design was estimated to save up to $\sim 23 - 48\%$ compared to the shell-and-tube design. In addition, the overall packaging of the twisted elliptical tube design was much smaller and less complex than that of the shell-and-tube design. In summary, the computational study strongly confirmed the cost savings potential of twisted elliptical tubes in FHRs.

In summary, the results of the computational work included the following:

- Twisted elliptical tube heat exchangers can provide up to $\sim 23-51\%$ cost savings over the lifetime of the equipment over standard shell-and-tube heat exchanger technology for intermediate heat exchanger use in a commercial FHR

3 Description of Work

3.1 Heat Transfer Facility

The following description of work is an abbreviated summary of the methodology and findings of the single-wall, twisted and plain tube bundle experimental performance. More detail can be readily obtained from Hughes [1] and Wallace [2]. Journal publications resulting from the work are currently being written up.

Photographs of the Heat Transfer Facility are provided in Figures 1 and 2. These photographs were taken prior to the insulation of the loops, so that the components could more easily be seen. The Heat Transfer Facility is composed of several circuits: the "primary" loop, in which the heat source is provided and from which heat is rejected through the test section, the "secondary" loop, which is used to control the tube-side boundary condition inside the test section and from which heat is rejected to the house chilled water supply, which is the final circuit and is integrated with the university's utilities.

The Heat Transfer Facility is capable of providing $\sim 5-7$ kW of heat input into either Dowtherm A or water working fluid, which is circulated throughout the primary loop. The primary loop circulation motive force is provided by either a pump (for forced circulation) or natural circulation, as the test section is located vertically above the heater to aid in providing the driving pressure for buoyancy-driven runs. The primary loop is capable of bi-directional forced flow and unidirectional natural circulation flow. The secondary loop accepts heat from the primary loop via the test section, which is the heat exchanger being tested. The secondary loop is simpler than the primary loop and is designed only for unidirectional forced flow. It rejects its heat through a heat rejection heat exchanger to the building chilled water supply, which was plumbed to the shell side of the heat rejection heat exchanger. The overall setup, combined with a programmable power supply for the heat input, allowed control of boundary conditions of the test section to a rather precise degree, with the only perturbations coming from changes in chilled water supply flow rate and temperature. In general, such changes were slow, and simple to compensate for because the usual solution would be to simply wait for the transient to reach a new steady state. The major components in the system are illustrated and labeled in Figure 3.

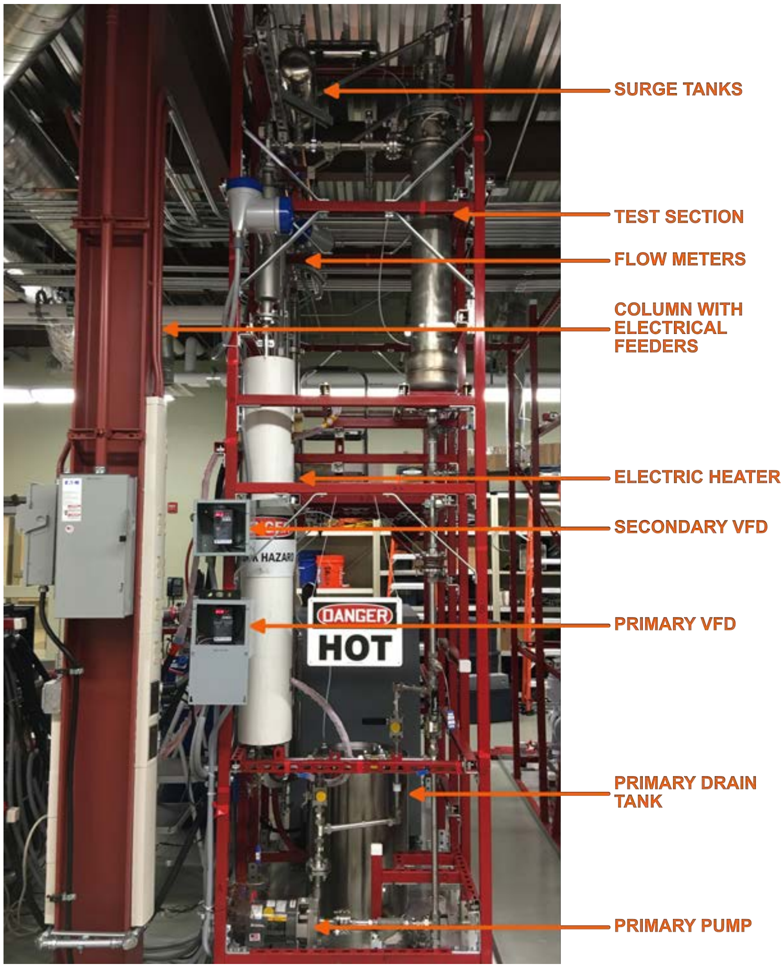

Figure 1: Photograph of the as-built heat transfer facility, prior to insulation, with the primary loop visible on the near side of the structure.

Conventional instrumentation and control is one of the primary motivations for performing scoping and validation type experiments utilizing simulant fluids such as Dowtherm A instead of molten salts directly. This was true in the Heat Transfer Facility, where standard T-type, ungrounded thermocouples were utilized for measuring bulk temperatures around the loops. Because of the improved response time, low loop velocities, and sensitivity of natural circulation flow rate to pressure drop, the thermocouples were not placed in thermowells but instead were swaged directly into the loop, with the tip insertion in the center of the 1 in fittings. High quality flowmeters were procured from Krohne: a high accuracy Coriolis flowmeter was placed on the primary loop, where natural circulation flow rates are outside the range of good accuracy for many flowmeter technologies, and a 3-beam ultrasonic flowmeter was placed on the secondary loop. The instrumentation of the Heat Transfer Facility is illustrated and labeled in Figure 4.

In addition, a number of T-type surface thermocouples were installed in the loop. Many of these were placed on the electric heater to provide tube-wall surface temperature measurements (to avoid wall superheat that might lead to Dowtherm A boiling) and several were

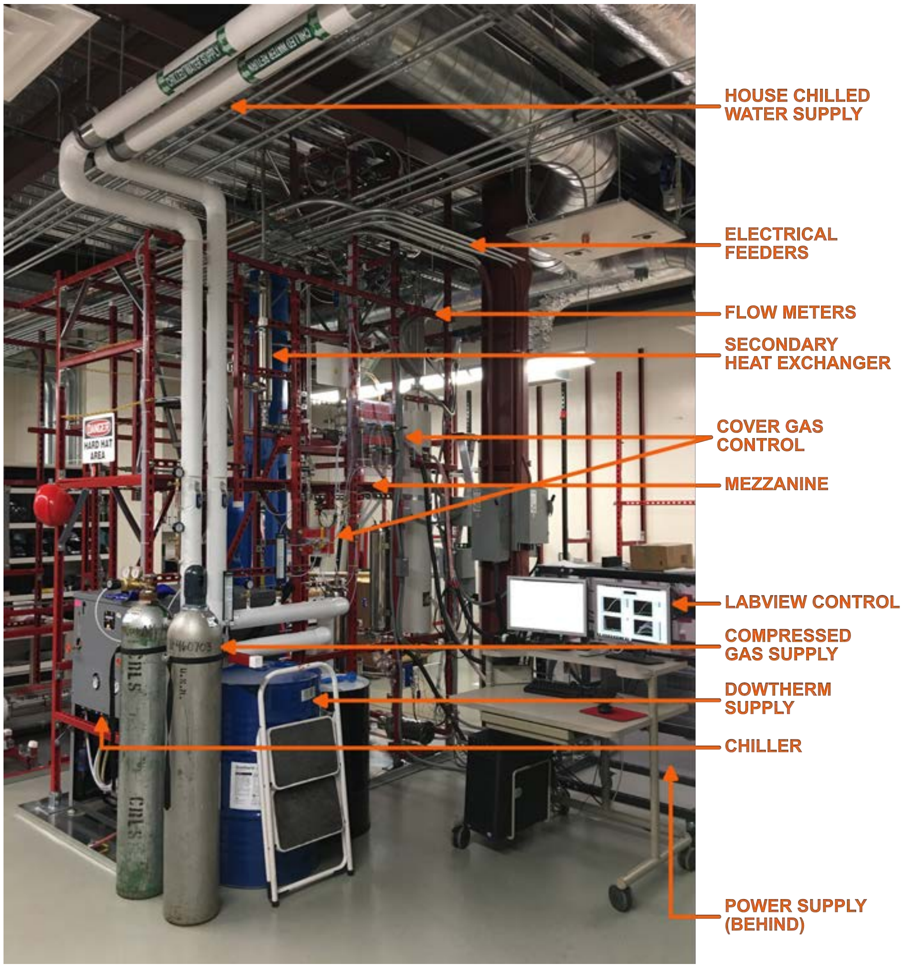

Figure 2: Photograph of the as-built heat transfer facility, prior to insulation, with the secondary loop visible on the near side of the structure and some of the cover gas system and auxiliary systems visible in the foreground.

placed at various locations on the test section shell surface and insulation surface, so that heat losses through the insulation could be estimated. This latter point was important, as the heat duty in the test section was determined by $\dot{m}C_p\Delta T$ balance, averaged from the primary and secondary loop measurements. In cases of low flow rates, since the heat exchanger effectiveness is high and uncertainty in heat transfer coefficient determination was also high, relatively "small" heat losses through the insulation could become very significant in the heat transfer coefficient calculation. To reduce inaccuracies associated with this effect, the loop was run at various temperatures and flow rates with the secondary side drained, so that heat losses in the test section could be accounted for by calibrating the thermocouples readings to read consistently.

On additional aspect to the Heat Transfer Facility was the cover gas system that was installed to manage level control, Dowtherm A exposure to oxygen, and odors. Because the fluid is organic, at elevated temperatures it can become oxidized in a oxygen containing environment. To reduce this potential, a nitrogen cover gas was utilized. The cover gas

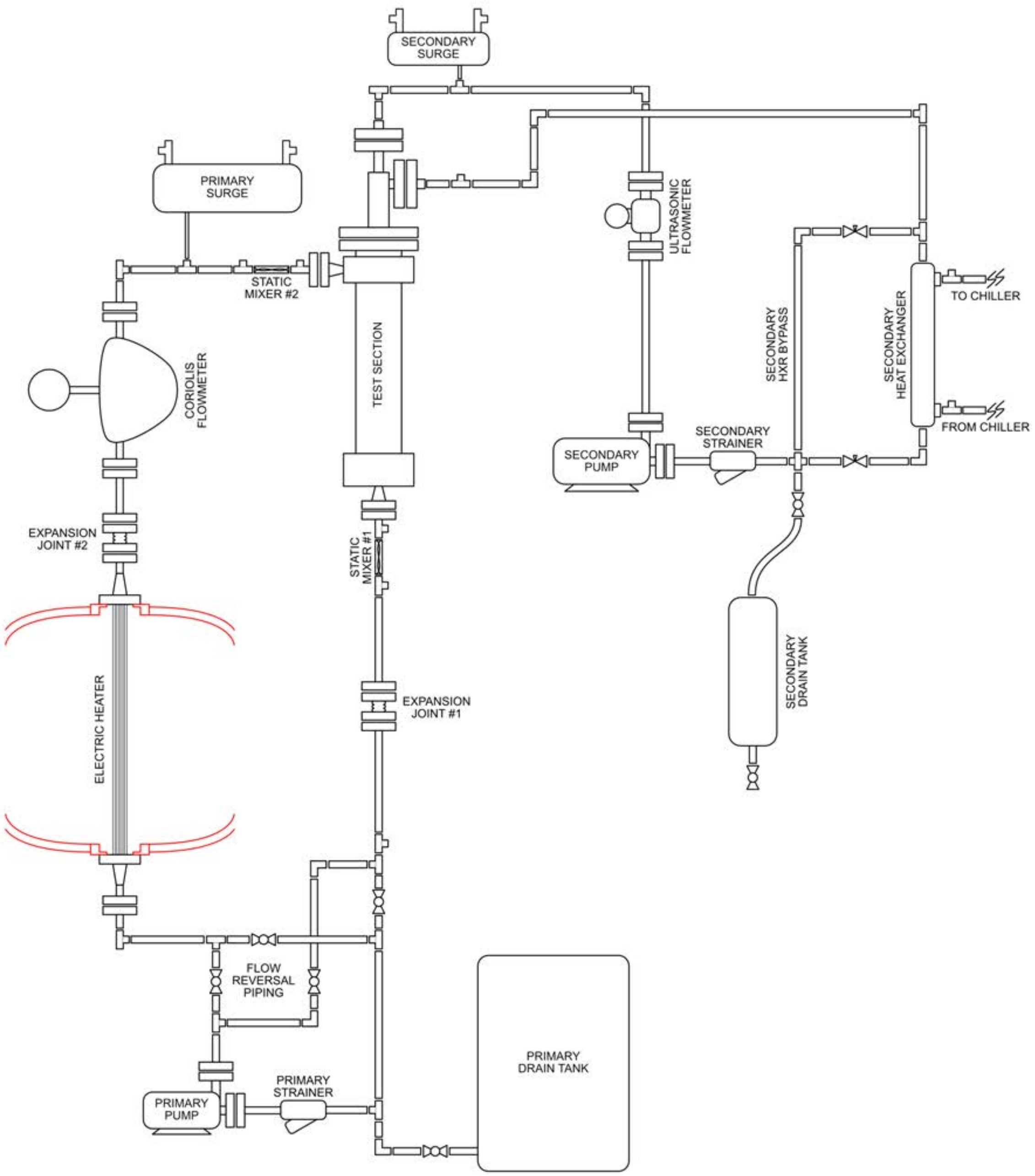

Figure 3: Diagram showing the three loops of the Heat Transfer Facility, with the major components labeled.

system is illustrated in Figure 5 and consisted of a gas supply subsystem and an exhaust subsystem. The supply subsystem routed the nitrogen to the drain tanks, the test section, and the surge tanks. Routing to the surge tanks was simply so that the residual air in the tanks upon loop fill could be subsequently purged. The gas was used as a “air piston” to push the Dowtherm A from the drain tanks up into the loops. Finally, exhausted gas was sent through an odor-reducing filter and to a laboratory snorkel, to reduce odors in the

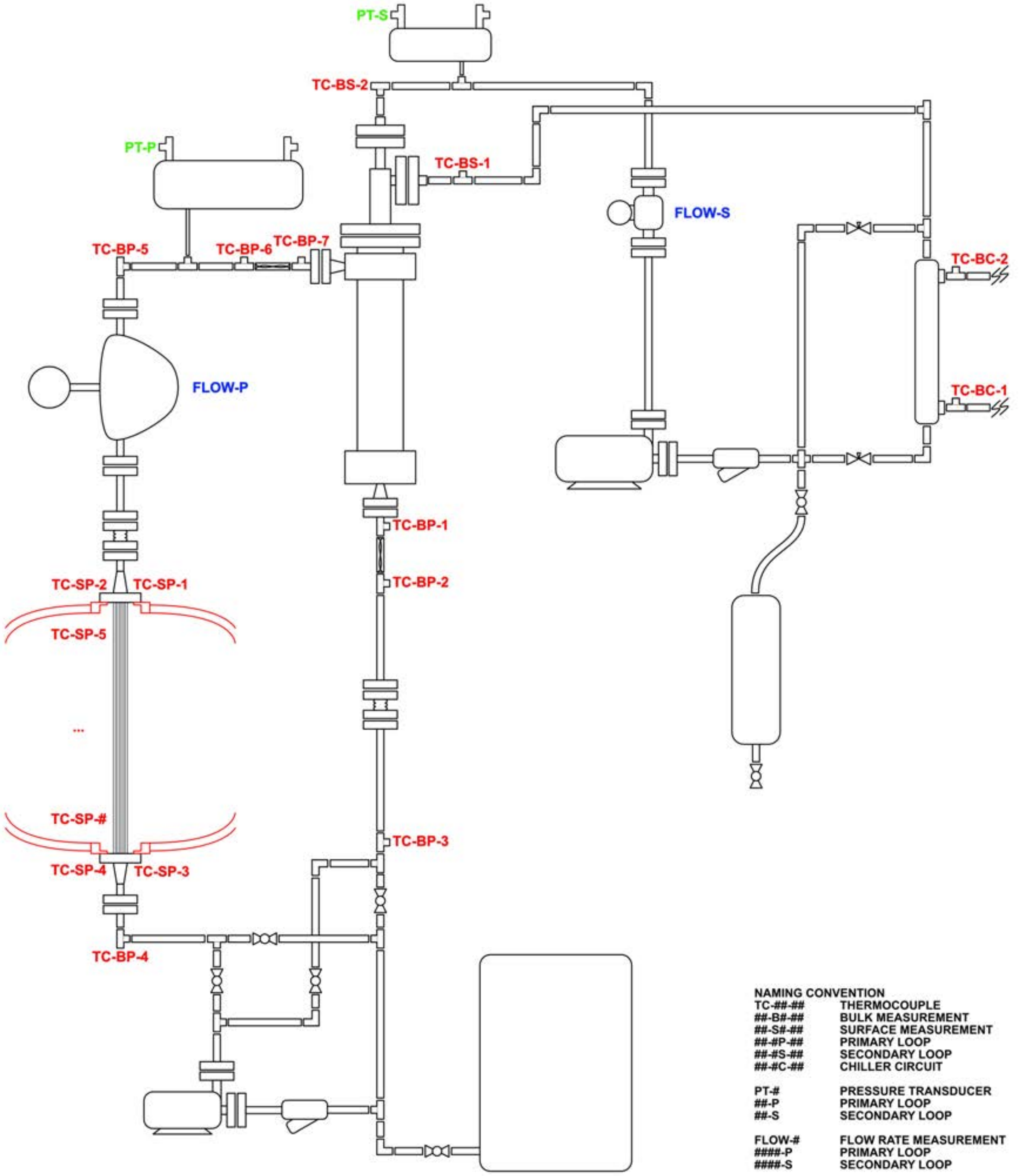

Figure 4: Diagram showing the three loops of the Heat Transfer Facility, with the measurement locations and types.

laboratory (Dowtherm A has a rather strong aromatic scent).

The test section consisted of a set of sister dip-type heat exchangers: one with twisted elliptical tubes and one with plain tubes (and unbaffled for low pressure drop) that were supplied by Hipex Pty. Ltd., a company that specializes in enhanced heat exchanger design and fabrication for the food processing industry. A photograph of the bundles are provided

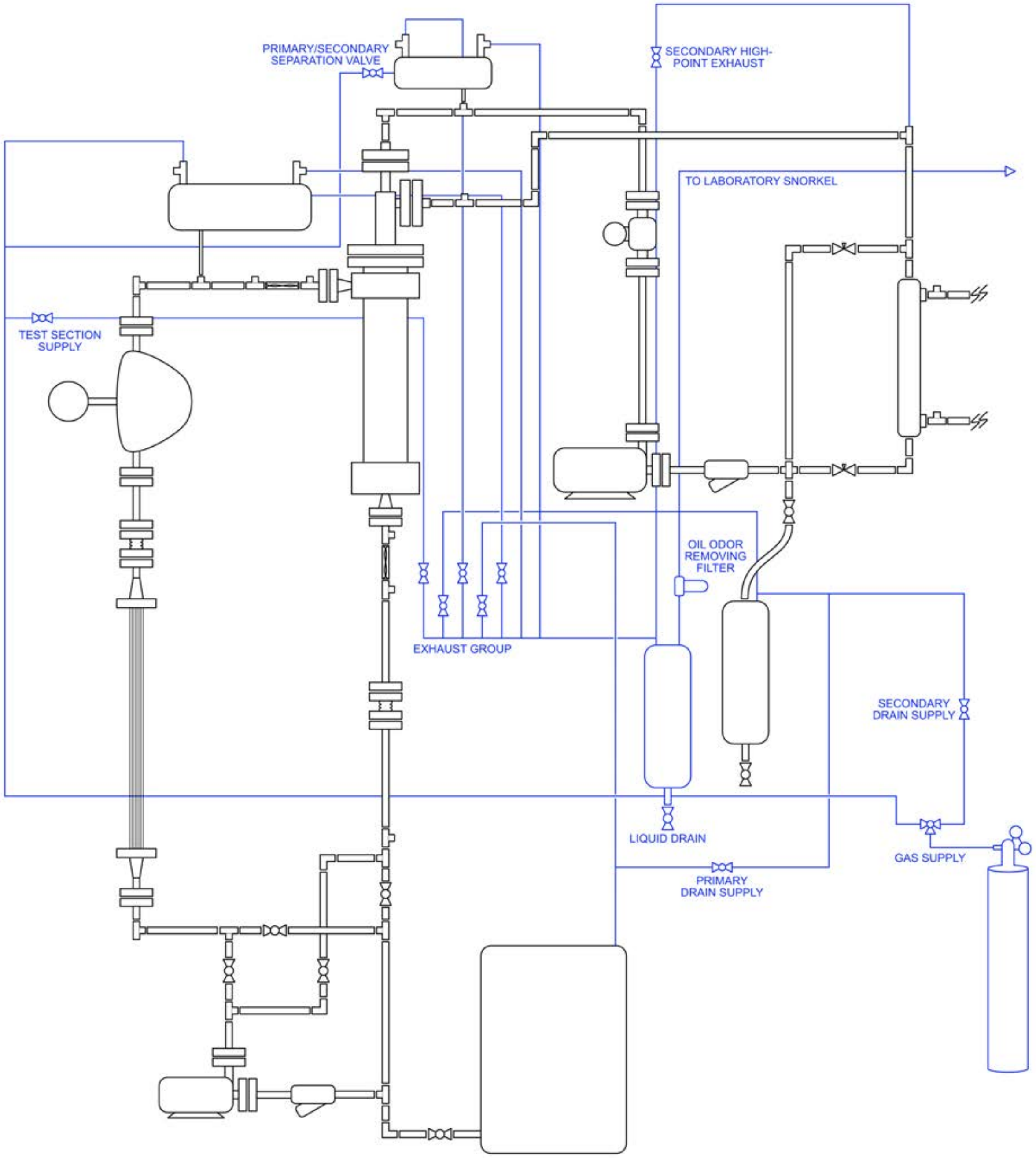

Figure 5: Diagram showing the three loops of the Heat Transfer Facility, with the cover gas system.

in Figure 6. A custom shell was fabricated in Albuquerque to fit the heat exchanger set, and they were tested one at a time in the Heat Transfer Facility. The heat exchangers were roughly a meter long, with just over two dozen tubes arranged in a circular pattern and an aggressive twist pitch to enable the maximum heat transfer enhancement for low flow rates. The tube pattern layout as circular was rather different than most of the twisted elliptical tube designs provided in literature, since in this case the tubes did not touch and were not

Figure 6: Single wall plain and twisted elliptical tube heat exchangers tested in the HTF, masked for clarity (photo credit: Hipex Pty. Ltd.).

self supporting. The circular layout was often used by the vendor and had the advantage of very low pressure drop and flow over the full surface of each heat exchanger tube (no small dead zones at tube contact points, which could presumably lead to localized fouling). It should be noted that for larger bundles with longer and more numerous tubes, it may be more advantageous to use the typical triangular packing with tube-to-tube contact points.

To develop Nusselt number correlations from the experimental data, it was first necessary to determine heat transfer coefficients. A much more detailed explanation can be found in Hughes [1], but the basic process was as follows: (1) data was read in from the experimental log files produced from LabVIEW, (2) in parallel, the geometric information about the heat exchanger bundle was assigned, (3) ancillary data was read in (flow direction, working fluid type, etc.), (4) parasitic heat losses through the test section insulation were estimated and the shell-side outlet temperatures were corrected for these losses by utilizing the mass flow rate and thermophysical properties of the fluid, (5) heat duty through the test section was estimated from the average of the $\dot{m}C_p\Delta T$ relation for both fluids, (6) a set of outer iterations on predicted heat duty and inner iterations on predicted overall heat transfer coefficient were performed to converge on those parameters given the input flow rates and temperature from the experimental data file, and (7) post-processing of the data, including calculating metrics of probability distribution function central value (e.g. mean or median) and central tendency

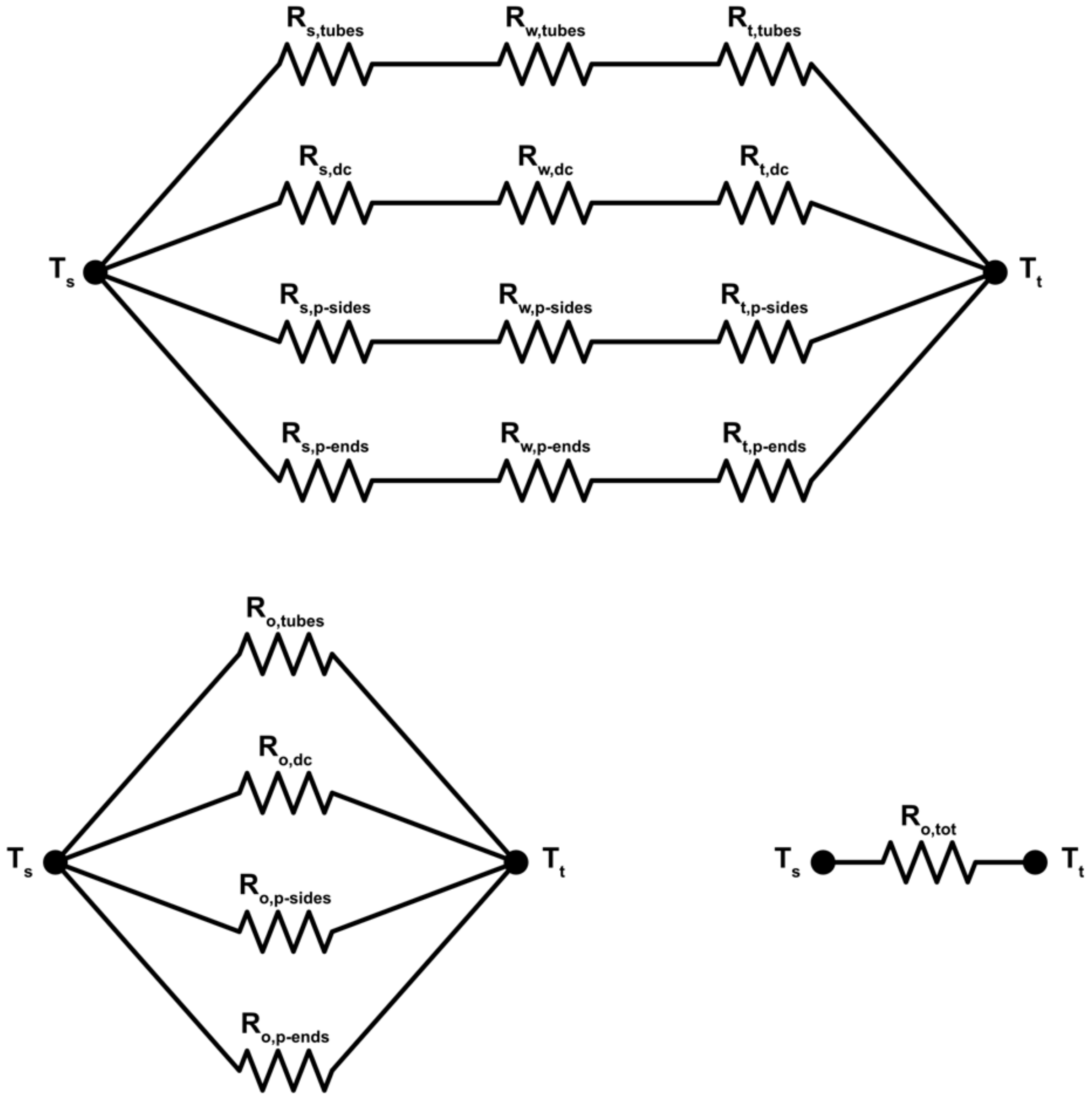

Figure 7: The thermal circuit for the dip-type heat exchanger bundles, in various forms.

(e.g. standard deviation or median absolute deviation about the median).

It is worth noting that the data reduction was complicated somewhat by the non-trivial geometry of the heat exchanger. The dip-type heat exchanger bundles features a central downcomer and upper and lower collection plena. These additional heat exchanger surfaces contributed to the overall heat exchange in the system, but where not the primary measurement objective. As such, their heat transfer performance was predicted and taken into account when determining the "target" heat transfer coefficient (e.g. shell-side or tube-side heat transfer coefficient relative to the tubes). Since the data reduction was performed for quasi-steady state conditions, the thermal circuit concept was employed according to Figure 7, where $R_{w,tubes}$ and $R_{t,tubes}$ were the target thermal resistances for measurement. A final slight complication was due to the effect of the downcomer on the thermal profile of the heat exchanger. Depending on whether the shell-side (primary loop) flow was upflow or downflow, the test section acted closely either to a parallel-flow (for upflow) or countercurrent-flow (for downflow) heat exchanger. However, the downcomer flow was opposite to the tube bundle, so the thermal profile had an element of two-tube-side pass heat exchangers (conceptually similar to a U-tube bundle). For accuracy in all testing conditions, it was considered necessary to account for this effect, even though the downcomer represented a minor part of the overall heat transfer area. This general problem, termed "unbalanced heat exchangers" was solved by Roetzel and Spang [3], and the governing equations are shown below. These equations were used to back out the logarithmic mean temperature difference correction factor (typically called F in heat exchanger nomenclature), so that the correct mean temperature difference could be determined. The true mean temperature difference in this case is lower than the logarithmic mean temperature difference, which resulted in an effective increase in the measured overall heat transfer coefficient. Typically, the calculated effect was small, as one might intuit from the relative surface area difference between the downcomer and the tube bundle.

$$\frac{\Delta T_m}{T_{s,in} - T_{t,in}} = \frac{V}{\ln\left(\frac{2-(\Phi_s+\Phi_t)+V}{2-(\Phi_s+\Phi_t)-V}\right)} \tag{1}$$

$$V = \sqrt{(\Phi_s^2 + \Phi_t^2) + 2\,(2\epsilon - 1)\,\Phi_s\Phi_t} \tag{2}$$

$$\epsilon = \frac{NTU_{t,cocurrent}}{NTU_{t,total}} = \frac{(US)_{cocurrent}}{US} \tag{3}$$

$$\Phi_s = \frac{T_{s,in} - T_{s,out}}{T_{s,in} - T_{t,in}} \tag{4}$$

$$\Phi_t = \frac{T_{t,out} - T_{t,in}}{T_{s,in} - T_{t,in}} \tag{5}$$

One of the main drivers for collecting experimental data on the buoyancy-affected regimes for the twisted elliptical tube bundles was that it simply did not satisfactorily exist in the open literature, as far as the researchers were aware. This is illustrated in Figure 8, where the Reynolds number ranges for the data collected in the Heat Transfer Facility resided is compared to available literature correlations. It is also clear from the figure that significant deviations between literature correlations is seen in this Reynolds regime, especially considering the tight twist pitch in the bundle (signified by the low $s/d_{max,in}$ ratio tested), as desired for good low Reynolds performance. The aggressive twist pitch is illustrated in Figure 9, which shows the available literature correlations as a function of modified Froude number and twist pitch ratio at two Reynolds numbers of interest as well as how the tested bundle compares.

A summary of the twisted elliptical tube bundle experimental results follows. The first step before correlation development was to compare the predicted overall heat transfer co-

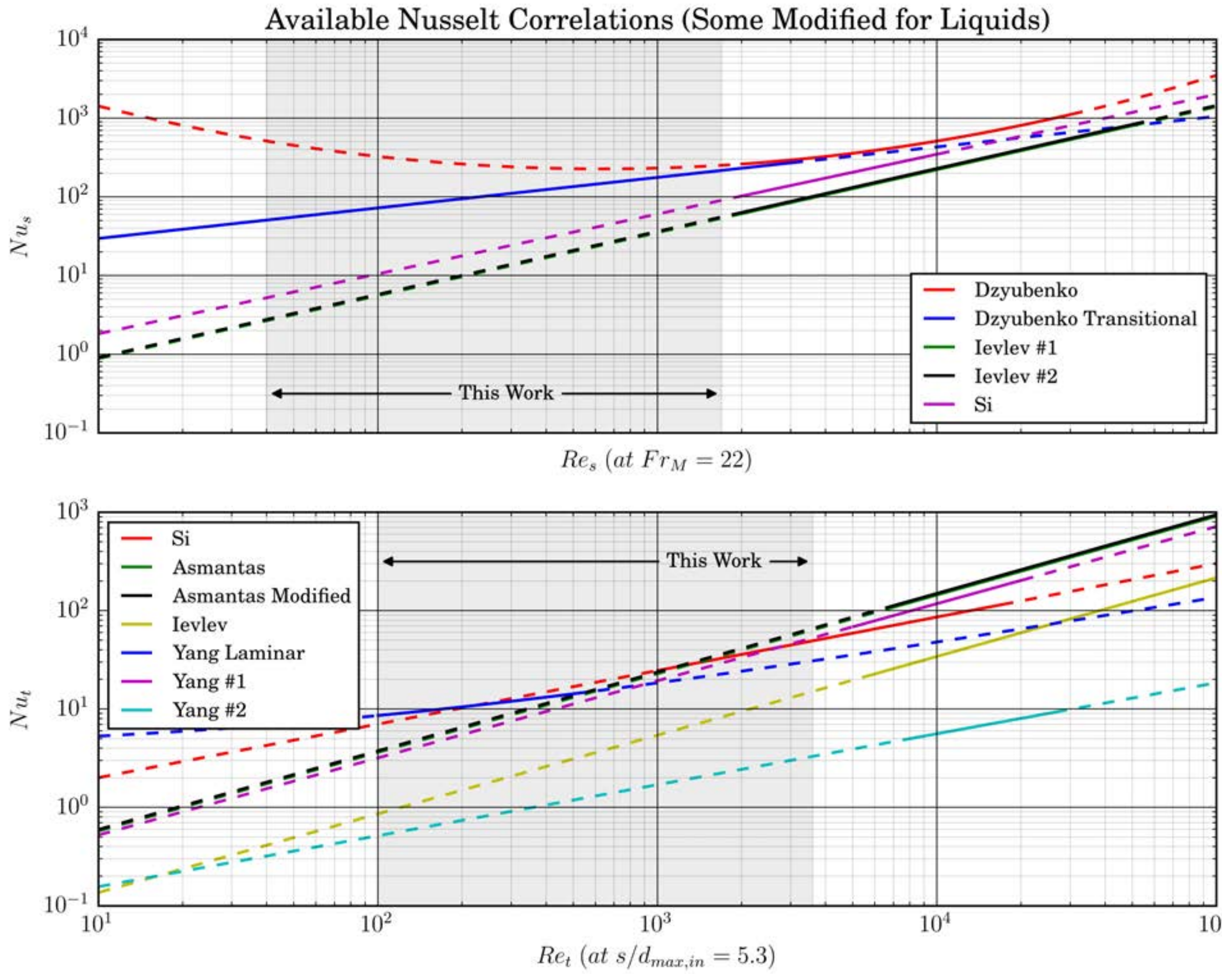

Figure 8: Comparison of available Nusselt number correlations as a function of Reynolds numbers.

efficient $U_{predict}$ with the measured overall heat transfer coefficient U for all of the data collected, for both upflow and downflow, and for buoyancy-affected and buoyancy-unaffected flow regimes. The validation metrics used were the mean absolute relative error, or "MARE," as defined in Equation 6 [4] and the maximum absolute relative error, or "MaxRE," as defined in Equation 7 [5]. In addition, for the results plots presented below, the error bars were based on the median absolute deviation around the median, which is a robust metric of central tendency [6], and is presented in Equation 8.

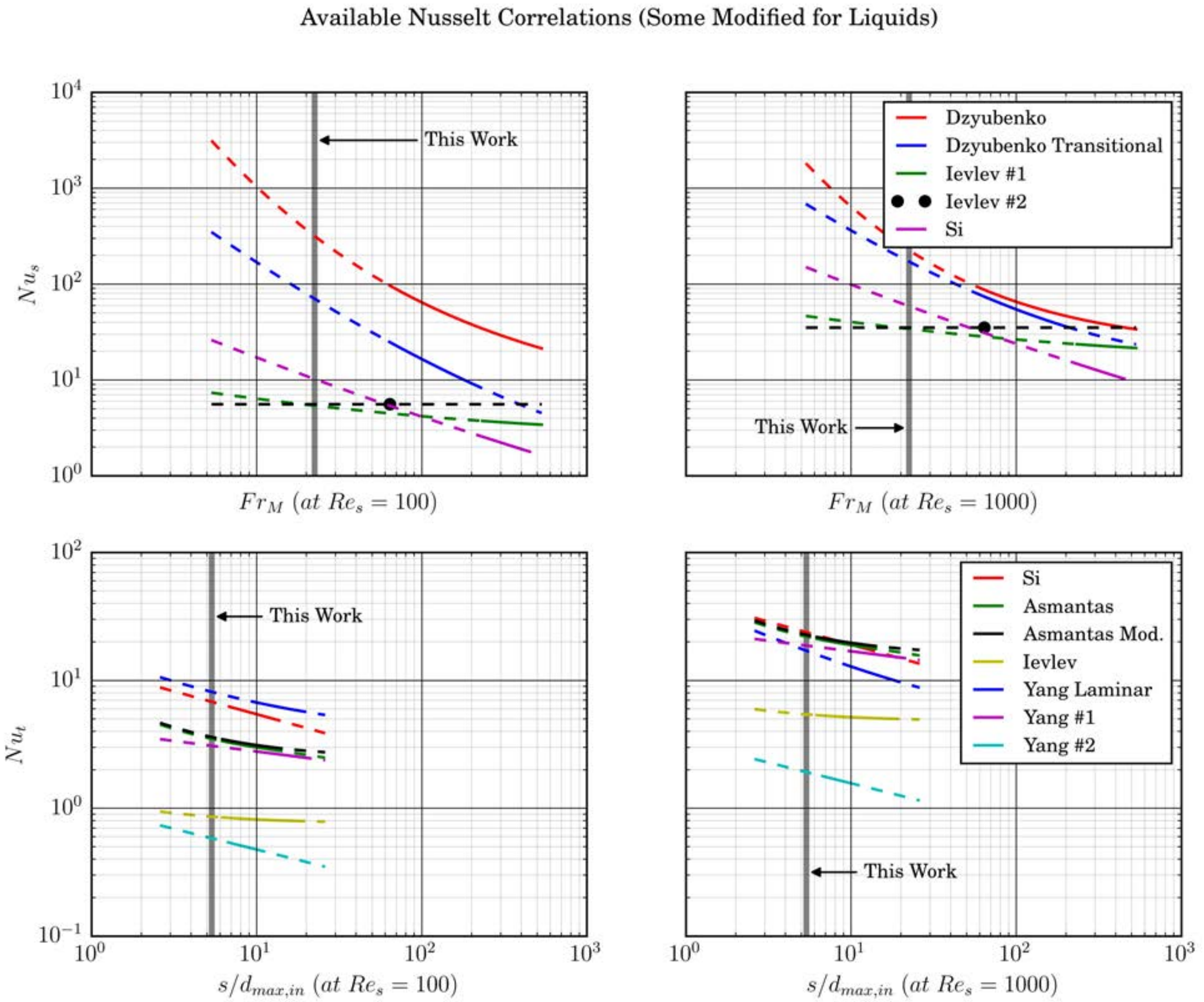

Figure 9: Comparison of available Nusselt number correlations as a function of twist pitch characteristics.

$$MARE = \frac{1}{N}\sum_{i=1}^{N}\left|\frac{y_{predict} - y_{measured}}{y_{measured}}\right| \tag{6}$$

$$MaxRE = \max\left|\frac{y_{predict} - y_{measured}}{y_{measured}}\right| \tag{7}$$

$$MAD = \left(\frac{1}{c}\right) M_i \left|x_i - M_j\left(x_j\right)\right| \tag{8}$$

The results are presented in Table 1. As might be anticipated, the literature correlations, in general, do not match very closely to the experimental results. The reasons for this are somewhat multifaceted, but are anticipated to be related to the following factors: (1) circular tube layout likely to have different performance than triangular tube layout (although the

Table 1: Tube-side and downflow shell-side forced circulation agreement for heat transfer / overall heat transfer coefficient (evaluated as MARE / MaxRE and measured U evaluated by way of predicted MTD) with available correlations.

Shell-side Correlation/ Tube-side Correlation	Dzyubenko Transitional	Ievlev #1	Ievlev #2	Si
Si	14.35% 41.67%	38.85% 59.52%	37.78% 58.57%	21.15% 40.15%
Asmantas	19.58% 46.73%	40.37% 61.71%	39.31% 61.30%	22.41% 55.34%
Asmantas Modified	19.92% 41.35%	39.82% 59.63%	38.74% 59.15%	21.56% 52.05%
Ievlev	37.47% 76.73%	62.17% 81.38%	61.66% 81.26%	53.83% 79.52%
Yang Laminar	7.73% 34.61%	42.53% 59.45%	41.58% 58.50%	26.63% 41.01%
Yang #1	16.03% 48.90%	42.74% 63.09%	41.76% 62.70%	26.04% 57.08%
Yang #2	62.25% 83.44%	78.07% 87.56%	77.84% 87.46%	74.18% 86.06%

fundamental physics of the problem are likely the same, the correlation fitting constants are anticipated to be different), (2) the effect of buoyancy on the heat transfer results is striking, and is well illustrated by Figure 10, which will be discussed below, and (3) it is possible that different assumptions about which parameters to include in the wetted perimeter in the hydraulic diameter calculation between researchers led to some disagreement in the predicted Nusselt numbers. One set of correlations actually did a fairly acceptable job of predicting overall heat transfer coefficient: the Dzyubenko transitional correlation [7] and the Yang laminar correlation [8], with a calculated MARE of $< 8\%$ and a MaxRE of $< 35\%$.

Since most of the literature correlations did not produce an extremely satisfactory fit to the data and did not include any parameter for assessing buoyancy impact, it was considered useful to produce new correlations that would include the additional physics in the buoyancy-affected case. The methodology is summarized: (1) the "best" tube-side correlation for the high-Reynolds tube-side data range was selected and used to determine shell-side correlations using the high-Reynolds tube-side data, (2) the shell-side Nusselt correlations were fit, iterating on Reynolds and Richardson number limits as required to perform a good fit to the data, and (3) the new shell-side correlations were used to fit the low Reynolds number data for the tube-side. Finally, the purely-predicted overall heat transfer coefficients were compared against measurement.

Figure 10 plots the shell-side data collected for the twisted elliptical tube bundle. The data shows bifurcated heat transfer performance below Reynolds of about 700, with higher Nusselt numbers measured for assisted (downflow) flow, when the buoyancy force vector

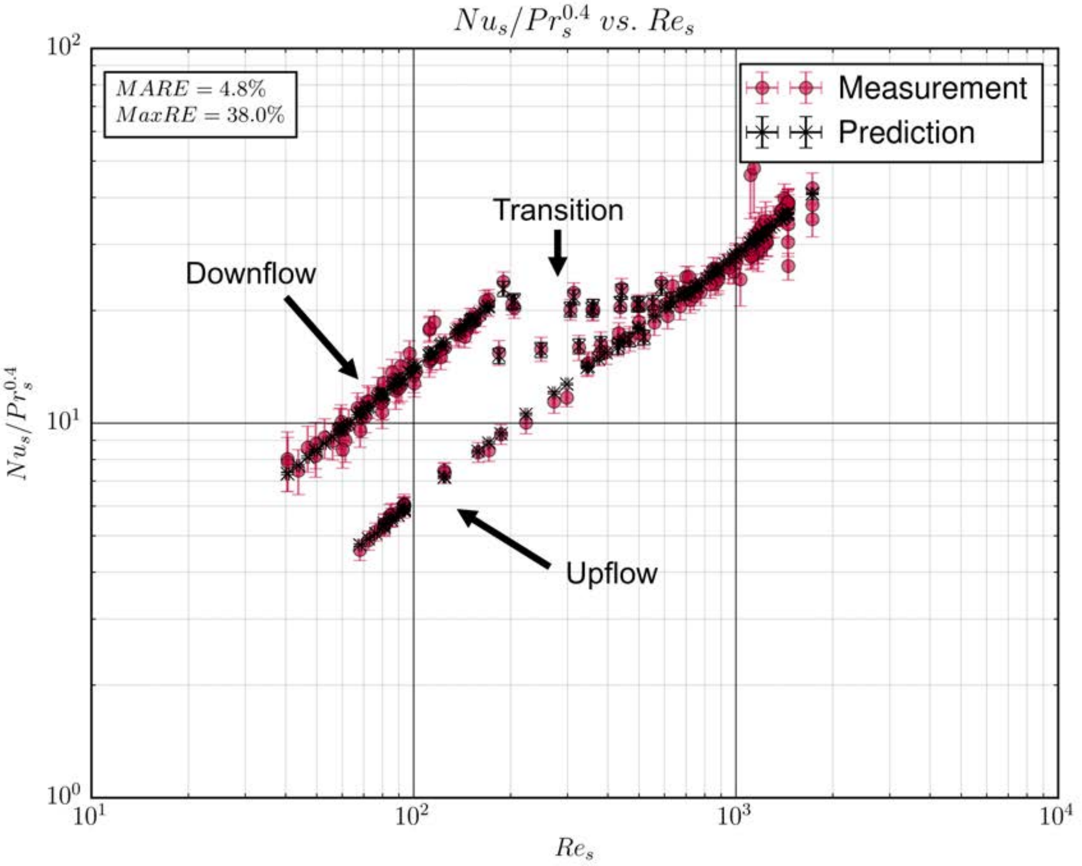

Figure 10: Comparison of experimental results and predictions for shell-side convection in the twisted elliptical tube bundle using the new correlations and using the Si correlation for tube-side $Re_t > 1000$. The level of agreement (evaluated as MARE) between predicted and measured Nu_s was $\sim 5\%$ and MaxRE was $\sim 38\%$.

aligned with the bulk flow direction and lower performance when for opposed (upflow) flow, when the buoyancy and bulk flow directions were opposite each other. In the range of Reynolds between $\sim 70 - 200$, the enhancement in shell-side Nusselt number for assisted compared to opposed flow was roughly a factor of 2x, which would nominally result in a reduction of heat exchanger size of about 25%, assuming no enhancement on the tube-side and minimal wall thermal resistance. Since there will be tube-side enhancement due to the swirl flow inside the tubes, the actual required size of the heat exchanger would likely be greater than 25%, although reality would depend upon significance of wall thermal resistance and fouling considerations.

In the range of $Re =\sim 700 - 1000$, the assisted and opposed flow heat transfer begins to converge. This was expected to be the case at some point, since for forced flow conditions, the momentum boundary layer at the wall is a function only of the pressure boundary conditions at the inlet and outlet of the heat exchanger, and not impacted by the local

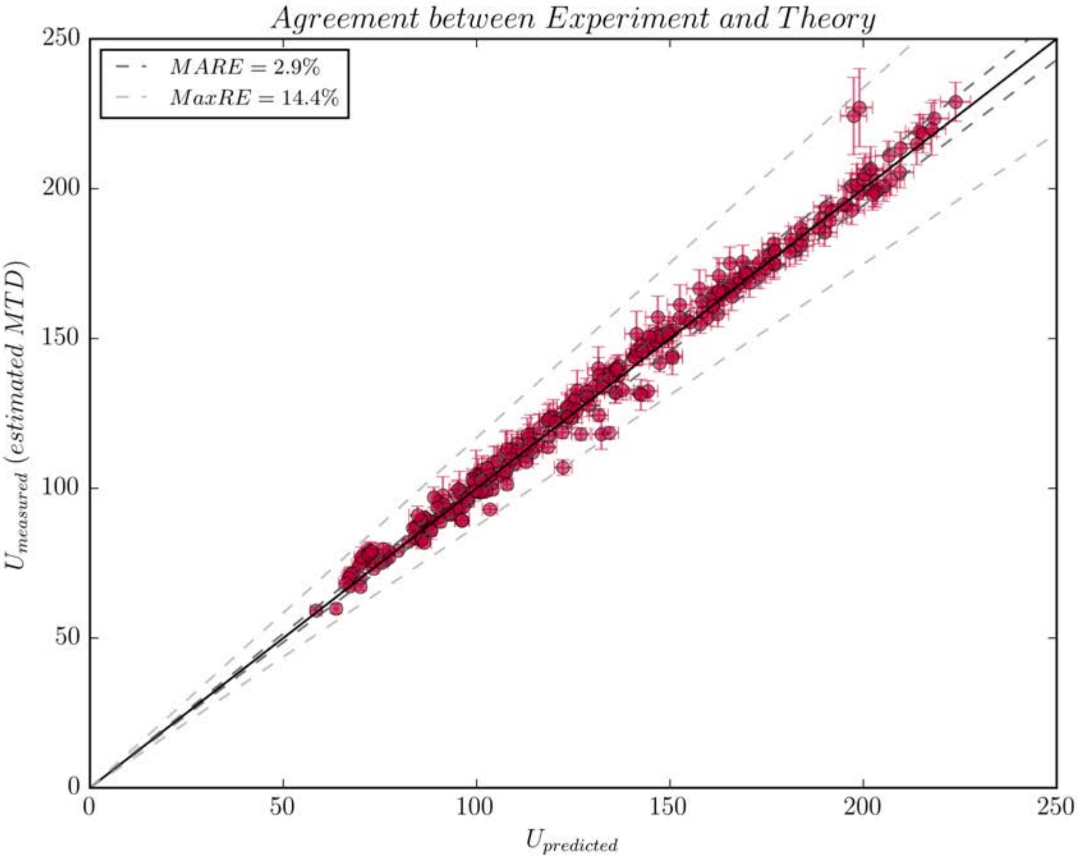

Figure 11: Comparison of experimental results and predictions for overall heat transfer coefficient in the twisted elliptical tube bundle using the new correlations and using the Si correlation for tube-side $Re_t > 600$. The level of agreement (evaluated as MARE) between predicted and measured Nu_s was $\sim 3\%$ and MaxRE was $\sim 14\%$. For the methodology used to determine the "measured" U, this level of agreement is the same as between measured and predicted Q.

momentum contributions of the buoyancy term in the Navier-Stokes equations. Figure 11 shows the predicted versus measured overall heat transfer coefficients for the data collected across all flow modes and Reynolds ranges. The MARE is calculated to be much better than the literature correlations, although there are a 5-10 outliers out of the greater than 250 data points collected.

Experimental measurements of the plain tube bundle reveal substantial performance enhancement of the twisted elliptical tubes over plain tubes. For natural circulation conditions, the performance improvement on the shell side peaked at roughly 55% around $Re \sim 125$, as shown in Figure 12. In addition, forced flow in the opposing flow configuration (upflow) received even greater enhancement, achieving performance improvements of up to 250% over plain tube results. Upflow performance improvements are presented in Figure 13. Additional

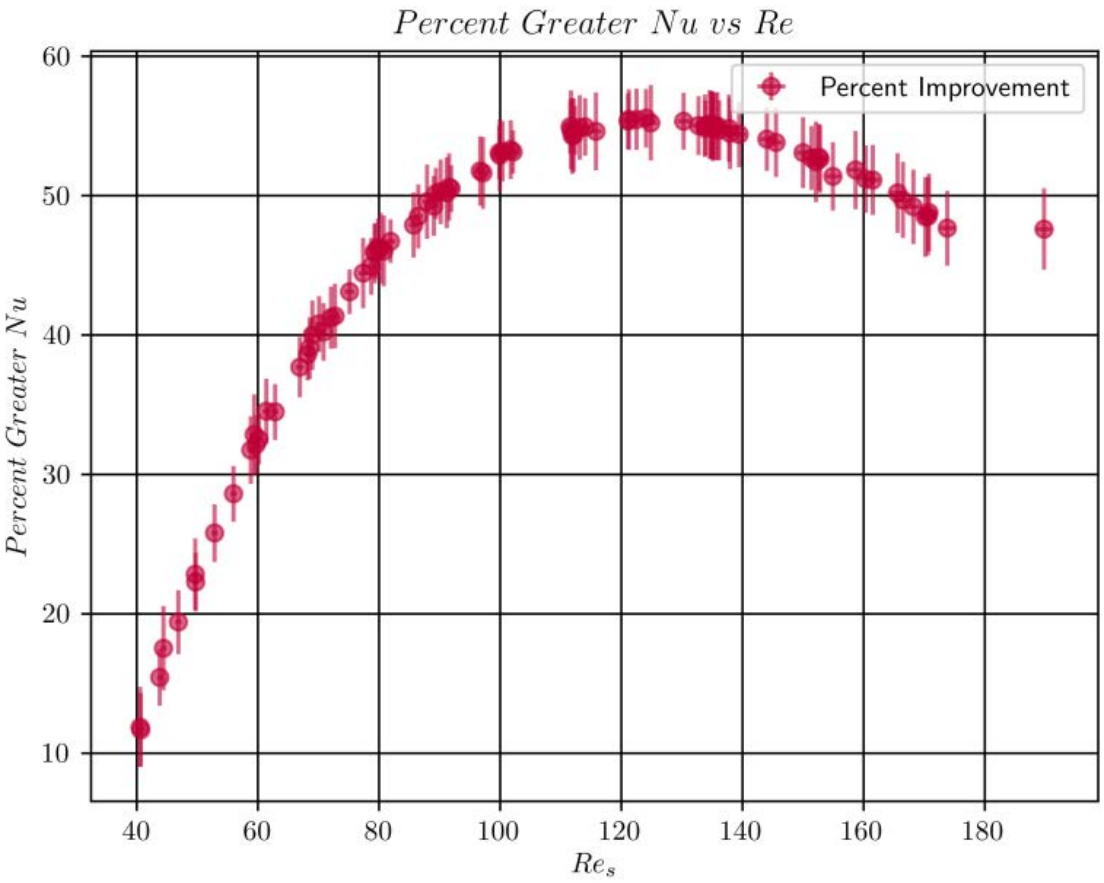

Figure 12: Enhancement of the twisted elliptical tubes over the plain tubes for natural circulation.

information on the plain tube performance and its comparison to twisted elliptical tubes can be found in Wallace [2].

3.2 Computational Work

The following description of work is an abbreviated summary of the methodology and findings of the intermediate heat exchanger optimization study. More detail can be readily obtained from Hughes [1]. A journal publication resulting from the work is currently being written up.

The high cost flibe coolant utilized in FHRs combined with the coolant's relatively high viscosity and Prandtl number present some interesting constraints on heat transfer in the FHR. While low circulating powers are needed in the system due to the high volumetric heat capacity of flibe, the reduced Reynolds numbers resulting from the elevated viscosity lead to rather poor heat transfer coefficients compared to other coolants for the same pumping

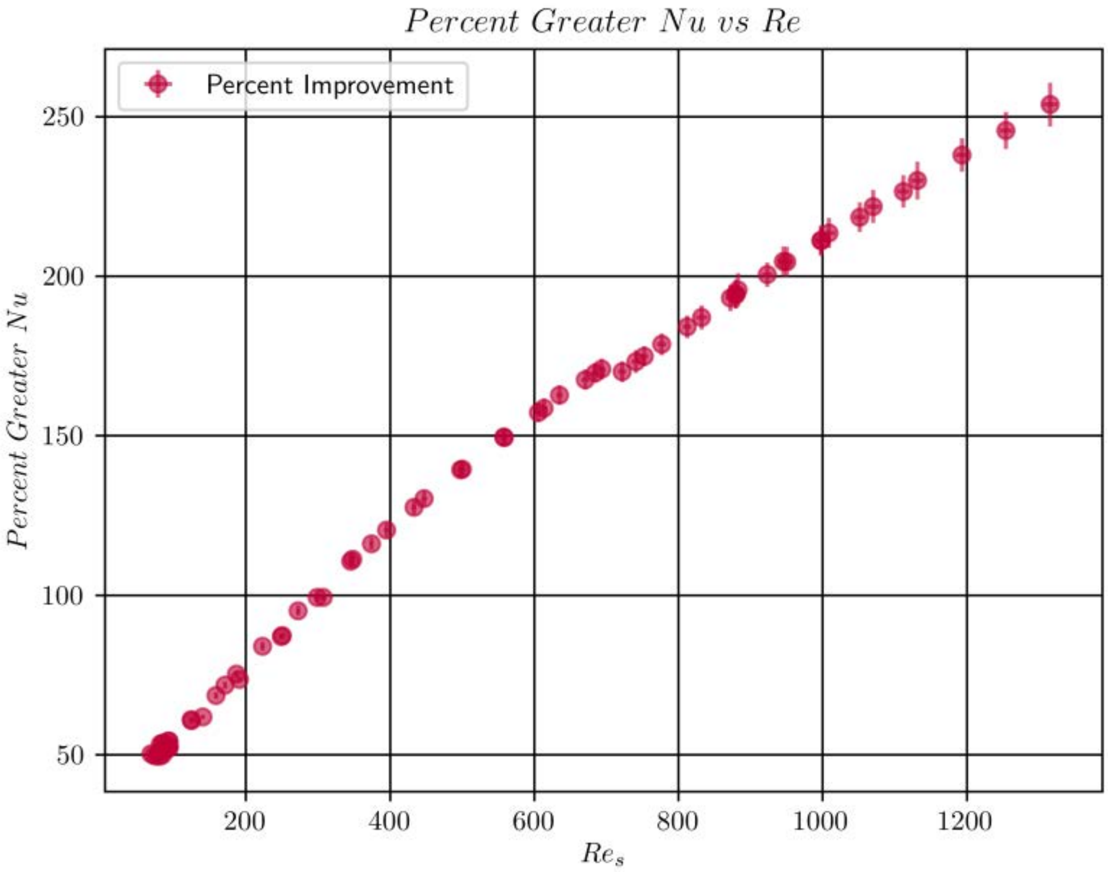

Figure 13: Enhancement of the twisted elliptical tubes over the plain tubes for forced circulation in opposed flow configuration (upflow).

Table 2: Design parameters utilized in this study, loosely based on values found in [10] and [11].

Parameter	Value
FHR baseline thermal duty	236 MW_{th}
IHX thermal duty	118 MW_{th}
Tube-side flow rate	423 kg/s
Shell-side flow rate	489 kg/s
Tube-side inlet temperature	545 $°C$
Shell-side inlet temperature	700 $°C$
Shell-side outlet temperature	600 $°C$

power. In addition, for most "reasonable" allowable pressure drops, the Reynolds numbers in the system are low enough to be in the transitional regime, which is problematic to design to for many typical geometries due to its time variant heat transfer behavior (which leads to poor predictability and may increase potential for thermal fatigue).

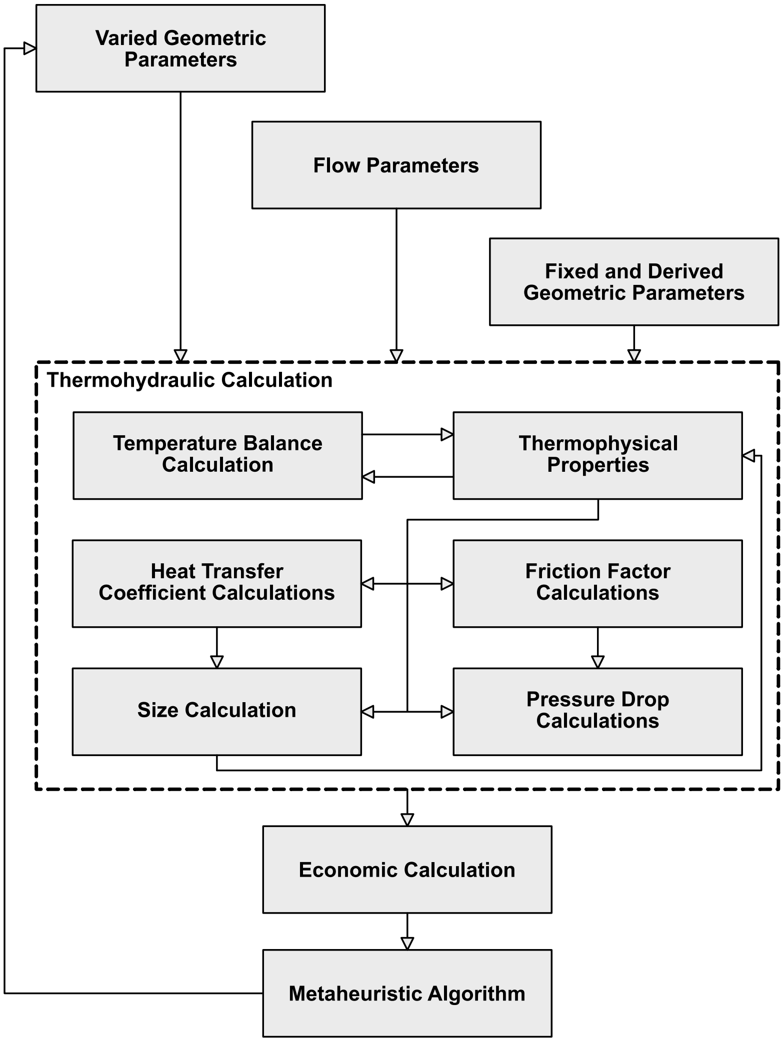

Figure 14: Illustration of the methodology used in the optimization, based on [9].

To aid in understanding the potential for twisted elliptical tube technology in the intermediate heat exchanger, this study was performed. In it, two different metaheuristic optimization algorithms were applied to design shell-and-tube and twisted elliptical tube heat exchangers. Although the details of the algorithms will not be discussed here, a flowchart for the design calculations is shown in Figure 14. A range of available geometric parameters were provided to the program in conjunction with the process parameters shown in Table 2. From these, the optimization algorithm sampled from the available geometric parameters to build a "population" of potential heat exchangers.

For each member of the population, a heat exchanger sizing calculation is performed to determine the length of heat exchanger required to meet the process duty requirements. In addition, pressure drop and pumping power requirements are also determined and an estimate is made of the heat exchanger capital cost using cost correlations available in the literature. Finally, the optimization algorithm evaluates the resulting population of solutions, and if maximum iterations has not been exceeded, proceeds to produce a new solution based

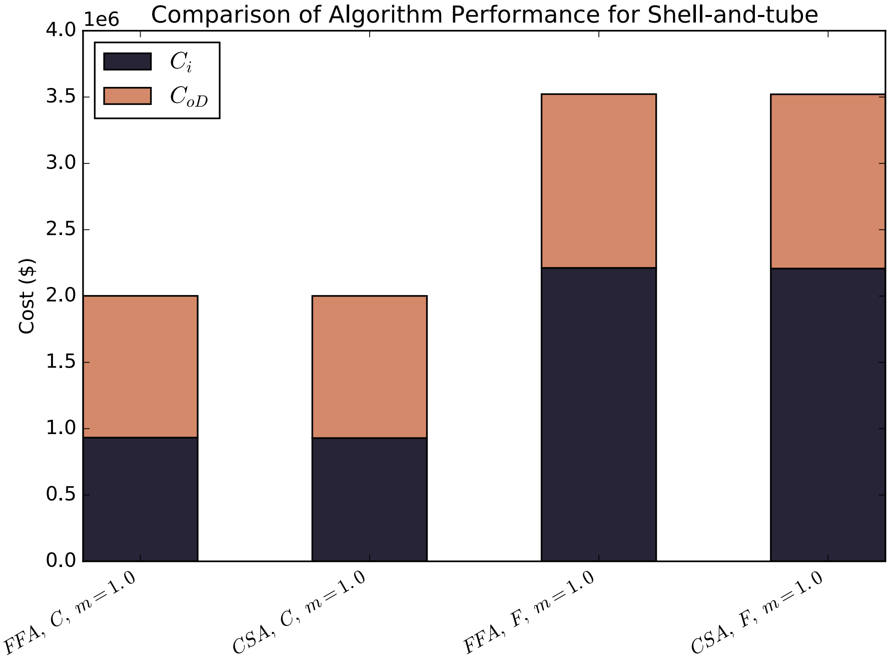

Figure 15: Performance of FFA and CSA for shell-and-tube heat exchangers, where C = clean ($F_{foul[t,s]} = 0.00000\ (m^2\ {}^\circ C)/W$), F = fouled ($F_{foul[t,s]} = 0.00025\ (m^2\ {}^\circ C)/W$), and m = capital cost multiplication factor.

on the details of the algorithm. This basic methodology has been applied many times with varying algorithms to shell-and-tube heat exchangers, but had not been applied to twisted elliptical tubes, and appeared a logical methodology to apply to better understand the limits between the technologies.

The performance of the two algorithms is compared in Figures 15 and 16. It was found that the two metaheuristic algorithms used, Firefly Algorithm (FFA) and Cuckoo-Search Algorithm (CSA) performed essentially identically to each other given the search parameters used (see Hughes [1] for more information on these parameters). As such, FFA was used for the continuation of the study since it performed faster. For twisted elliptical tubes, a manufacturing multiplier of $m = 1.0$ or $m = 1.3$ was applied to the capital cost to investigate sensitivity of the total cost to the manufacturing overhead associated with twisting the tubes.

Figure 17 illustrates the cost differential between the twisted elliptical tube and shell-and-tube heat exchanger designs, for both clean and fouled design conditions. The twisted elliptical tube heat exchanger was found to be much cheaper, regardless of fouling level design point for the base electricity cost assumption of $\$0.12/kWh$. The cost advantage to the twisted elliptical tube design increases or decreases according to the cost of electricity. As the required heat exchanger volume of the shell-and-tube design is much higher than its counterpart, the optimal pressure drop is also increased in an attempt to offset the extra flibe volume. However, the result is that, while flibe volume is decreased, the greatly increased pressure drop results in greatly increased present cost of the electricity used to run the molten

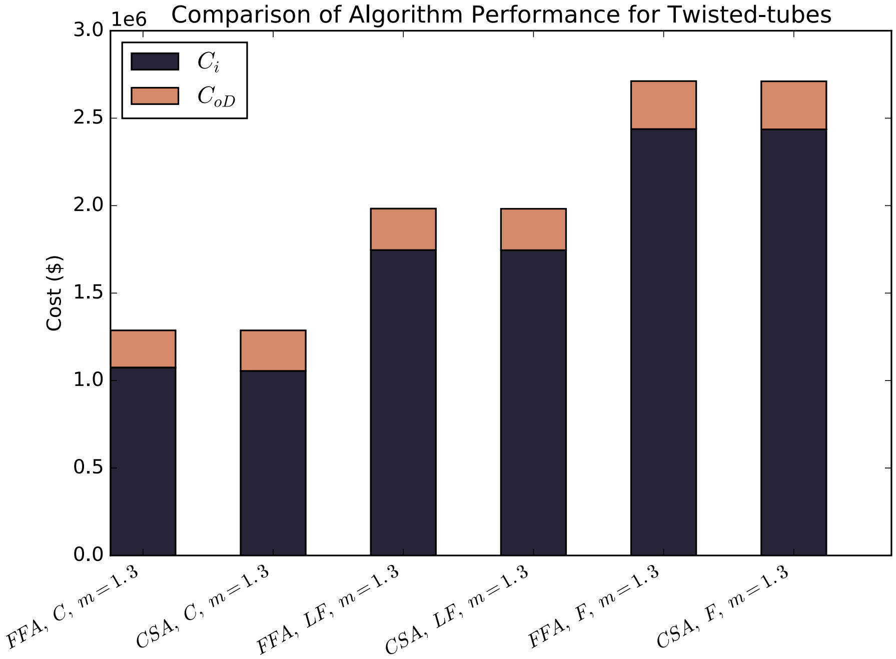

Figure 16: Performance of FFA and CSA for twisted-elliptical-tube heat exchangers, where C = clean ($F_{foul[t,s]} = 0.00000\ (m^2\ ^{\circ}C)/W$), F = fouled ($F_{foul[t,s]} = 0.00025\ (m^2\ ^{\circ}C)/W$), LF = less fouled ($F_{foul[t,s]} = 0.000125\ (m^2\ ^{\circ}C)/W$), and m = capital cost multiplication factor.

salt pumps over the lifetime of the equipment.

Finally, the thermal resistance distribution between the different heat exchanger options was investigated, and is shown in Figure 7. Interestingly, for both shell-and-tube and twisted elliptical tube heat exchangers, the tube-side convective film resistance was found to be the most important, despite allowing conventionally tube diameters in the parameter space. This indicates that better cost performance could potentially be achieved by going to even smaller tube diameters, although other constraints would come into play. The fouling assumptions were found to be a very significant portion of the thermal resistance of the optimized bundles. In summary, it was found that twisted elliptical tube heat exchangers could enable a total present cost savings of $\sim 23-51\%$, depending upon design fouling level, electricity cost, and manufacturing overhead for constructing twisted elliptical tube heat exchangers.

4 Suggested Future Work

There are a number of topics that could provide strong value to the FHR research community if researched further. Two of these future studies are underway to varying degrees. The third is a suggested future study that has not yet been started.

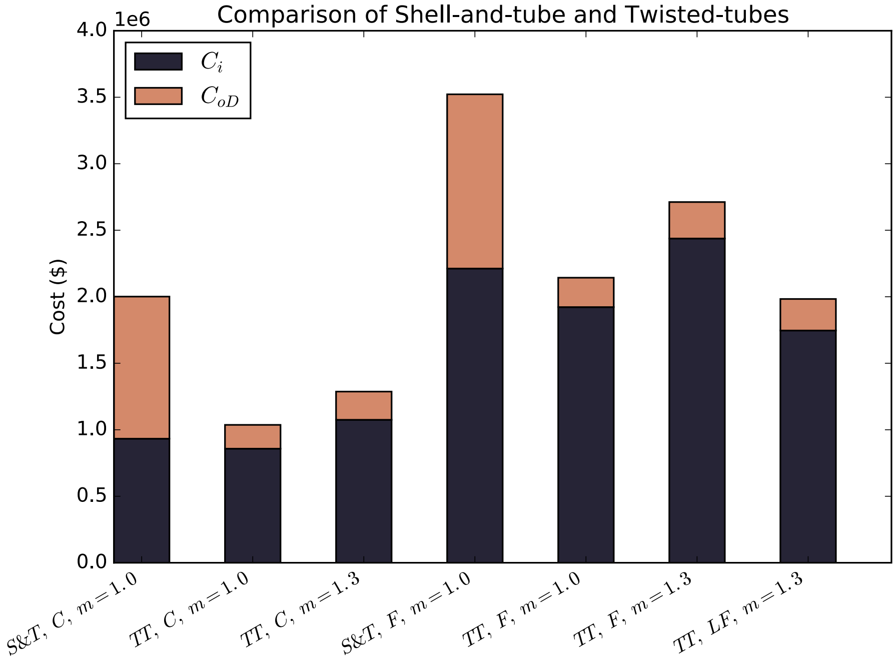

Figure 17: A comparison of shell-and-tube and twisted-elliptical-tube heat exchanger costs, as determined by FFA, where S&T = shell-and-tube, TT = twisted-elliptical-tube, C = clean ($F_{foul[t,s]} = 0.00000\ (m^2\ °C)/W$), F = fouled ($F_{foul[t,s]} = 0.00025\ (m^2\ °C)/W$), LF = less fouled ($F_{foul[t,s]} = 0.000125\ (m^2\ °C)/W$), and m = capital cost multiplication factor.

4.1 Computational Fluid Dynamics Validation

Validation of computational fluid dynamics modeling approaches are one important area of opportunity that the data presents. Argonne National Laboratory has performed some early modeling of twisted elliptical tubes in relevant Reynolds ranges using Nek5000, a spectral methods large eddy simulation tool [12]. This work is likely to continue and results are anticipated to be published concurrently in archival form in a sister journal article to the experimental results. There are many challenges associated with the phenomena of the system, which include the complex twisted geometry (with its implied similarities to rotational systems) and the effect of buoyancy.

4.2 Scaling work

In concert with the computational fluid dynamics validation work, work is also underway to perform a more formal non-dimensionalization of the governing equations for the system to better understand the physics behind the correlations developed thus far and to potentially provide improved correlations, if better correlating parameters are discovered. Such an approach was taken by Ievlev et al. [13] and resulted in the modified Froude number, a purely

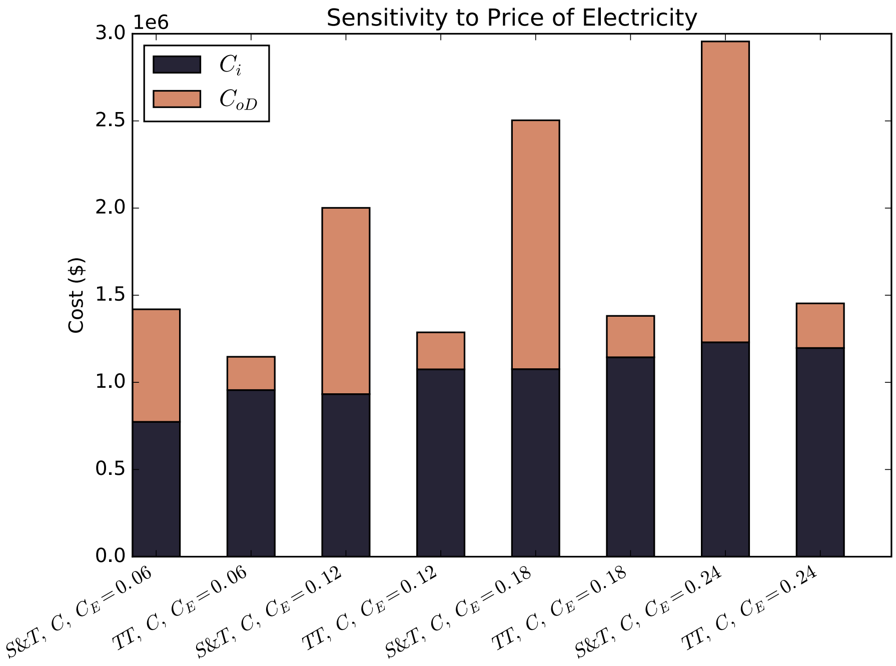

Figure 18: A comparison of shell-and-tube and twisted-elliptical-tube heat exchanger costs, as determined by FFA, where S&T = shell-and-tube, TT = twisted-elliptical-tube, C = clean ($F_{foul[t,s]} = 0.00000\ (m^2\ °C)/W$), m = 1.0 for shell-and-tube exchangers and 1.3 for twisted-elliptical-tube exchangers, and C_E is the cost of electricity in $\$/kWh$.

geometrical parameter that results from a solid body rotation approximation to the governing equations. This parameter was used successfully in the form of logarithmic polynomials to correlate data for twisted elliptical tube bundles in forced convection, but it is not clear at this time whether it is sufficient for correlation of buoyancy-affected flows. The goal of this study will be supporting to the experimental and computational work to resolve this question.

4.3 Application of Experimental Data to DHX Design Studies

A final study or set of studies that have not begun but would be considered a logical extension of the work would be to leverage the experimental, computational, and scaling work discussed above and perform design studies for application to FHRs. This work could take many forms, but a sensible approach might be to perform integrated system optimization (perhaps techno-economic) of a DHX in a DRACS decay heat removal system and compare to plain or shell-and-tube options. A slightly different approach could be to investigate flow stability and predictability improvements in the system by utilizing the twisted design. In either case, there is ample opportunity to apply the research results to design challenges.

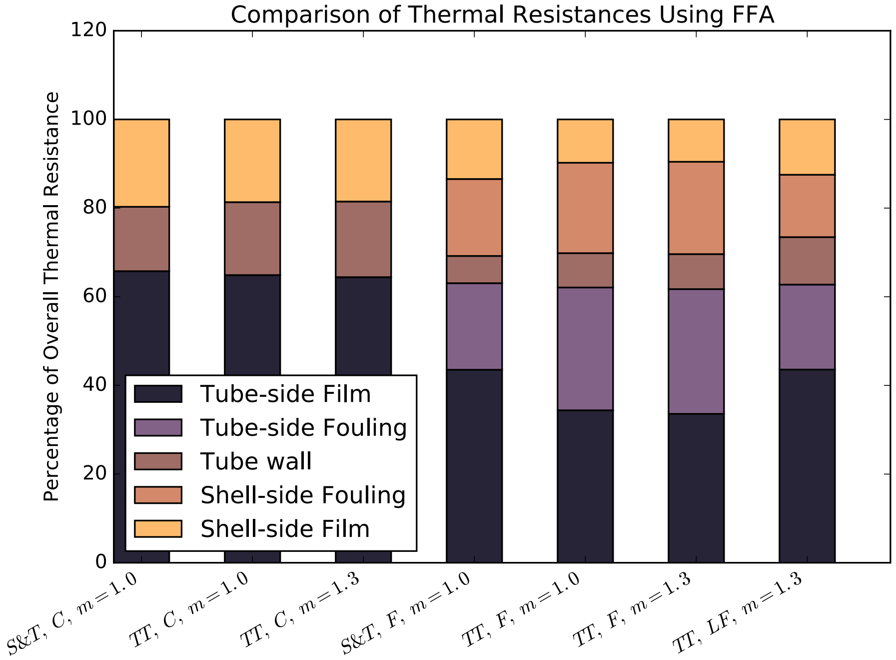

Figure 19: A comparison of shell-and-tube and twisted-elliptical-tube thermal resistances, as determined by FFA, where S&T = shell-and-tube, TT = twisted-elliptical-tube, C = clean ($F_{foul[t,s]} = 0.00000\ (m^2\ ^\circ C)/W$), F = fouled ($F_{foul[t,s]} = 0.00025\ (m^2\ ^\circ C)/W$), LF = less fouled ($F_{foul[t,s]} = 0.000125\ (m^2\ ^\circ C)/W$), and m = capital cost multiplication factor.

5 References and Further Reading

Joel T. Hughes et al. “Directional DRACS Heat Exchanger Concepts for the FHR”. In: Transactions of the American Nuclear Society. Washington, D.C.: American Nuclear Society, 2013. [14]

Early paper exploring concepts for a “directional” decay heat removal heat exchanger.

Joel T. Hughes and Edward D. Blandford. “Compact Double-wall Twisted-tube Heat Exchanger for the Fluoride Salt-cooled High-temperature Reactor (FHR) with Implications for In-service Inspection”. In: Transactions of the American Nuclear Society. Anaheim, CA: American Nuclear Society, 2014, pp. 1064–1067. [15]

Paper exploring concept for combining twisted elliptical tubes with plain tubes in a double-wall configuration for addressing tritium permeation challenges in the FHR. This work was a precursor for the NEUP further investigating this concept that was subsequently awarded to UNM, and which also utilized the Heat Transfer Facility for obtaining experimental data.

Joel T. Hughes and Edward D. Blandford. “Experimental Investigation of a Direction-

ally Enhanced DHX Concept for High Temperature Direct Reactor Auxiliary Cooling Systems". In: Nuclear Engineering and Design 303 (2016), pp. 132–152. issn: 00295493. doi: 10.1016/j.nucengdes.2016.03.030. url: http://dx.doi.org/10.1016/j.nucengdes.2016.03.030. [16]

Follow-on paper with experimental results for a "directional" decay heat removal heat exchanger. This experiment utilized water as a hydrodynamic simulant fluid and tested different fluidic diode integrations into the shell of the heat exchanger. Several of the concepts tested appeared to perform well. These concepts would appear to pair well with the twisted elliptical tube designs tested under the IRP, which would be a logical next experimental step if the directional DHX concept were to be studied further.

Joel Hughes et al. "On the Question of Decay Heat Removal System Redundancy for Fluoride Salt-cooled High-temperature Reactors (FHR)". In: International Congress on Advances in Nuclear Power Plants. San Francisco, CA: American Nuclear Society, 2016, pp. 1973–1985. isbn:9781510825949. [17]

A study investigating redundancy of DRACS for the FHR. It employed response surfaces to speed up the Monte Carlo uncertainty propagation while using RELAP5-3D as a systems modeling tool. The basic methodology of the paper could be combined with uncertainty data from twisted elliptical and plain tube bundles to better understand the impact of heat transfer coefficient uncertainty and stability on safety systems' performance.

J. T. Hughes. "Experimental and Computational Investigations of Heat Transfer Systems in Fluoride Salt-cooled High-temperature Reactors". PhD dissertation. University of New Mexico, 2017. [1]

One of several thesis and dissertations that came out of work supported or partially supported by the IRP. This dissertation covers most of the heat transfer work described in this report, and additionally several studies not described in detail here, including the directional decay heat removal heat exchanger study and the DRACS redundancy study.

B. Wallace. "Analysis of Double-Wall and Twisted-Tube Heat Exchanger Concepts for use in Fluoride Salt-Cooled High-Temperature Reactors". Master's thesis. University of New Mexico, 2017. [2]

A master's thesis focused on twisted elliptical tube, double wall heat exchanger concepts. This thesis also gathered the plain tube heat exchanger data, which allowed a comparison to be made to the twisted elliptical tubes. In addition, concepts involving plain double-walled heat exchangers and hybrid twisted-elliptical and plain, double-wall heat exchangers are explored experimentally using a three fluid heat transfer setup added to the Heat Transfer Facility.

M. Liu et al. "Conceptual design of a freeze-tolerant Direct Reactor Auxiliary Cooling System for Fluoride-salt-cooled High-temperature Reactors". In: Nuclear Engineering and Design 335 (2018), pp. 54–70. [18]

A computational study investigating freeze-tolerant concepts for DRACS for the FHR. Somewhat not intuitively, overcooling and the accompanying freezing of salt is a failure mechanism for passive decay heat removal systems in the FHR that has the potential to not only cause failure of the containing vessels through plastic deformation, but could also disable the heat removal pathway and potentially lead to overheating. This study explores different design options for mitigating against overcooling, while not compromising the heat removal capability of the system.

Nomenclature

C_p	fluid heat capacity ($J/(kg\ {}^\circ C)$ or $kJ/(kg\ {}^\circ C)$)
N	number of measurement points
S	heat transfer area (m^2)
T	temperature (${}^\circ C$)
U	overall heat transfer coefficient based on outside tube surface ($W/m^2\ {}^\circ C$)
V	intermediate parameter
c	normalization constant
y	measurement value or prediction

Greek symbols

ϵ	effectiveness or NTU fraction of co-current pass
Φ	dimensionless temperature change

Non-dimensional numbers

NTU	number of transfer units

Other subscripts

s	shell side
t	tube side

References

[1] J. T. Hughes. "Experimental and Computational Investigations of Heat Transfer Systems in Fluoride Salt-cooled High-temperature Reactors". PhD dissertation. University of New Mexico, 2017.

[2] B. Wallace. "Analysis of Double-Wall and Twisted-Tube Heat Exchanger Concepts for use in Fluoride Salt-Cooled High-Temperature Reactors". Master's thesis. University of New Mexico, 2017.

[3] W. Roetzel and B. Spang. "Thermal Calculation of Multipass Shell and Tube Heat Exchangers". In: *Chemical Engineering Research and Design* 67 (1989), pp. 115–120.

[4] Rahman Abdulmohsin. "Gas Dynamics and Heat Transfer in a Packed Pebble-bed Reactor for the 4th Generation Nuclear Energy". PhD dissertation. Missouri University of Science and Technology, 2013.

[5] William L. Oberkampf and Matthew F. Barone. "Measures of Agreement Between Computation and Experiment: Validation Metrics". In: *Journal of Computational Physics* 217.1 (Sept. 2006), pp. 5–36. ISSN: 00219991. DOI: `10.1016/j.jcp.2006.03.037`. URL: `http://www.sciencedirect.com/science/article/pii/S0021999106001860`.

[6] Christophe Leys et al. "Detecting Outliers: Do Not Use Standard Deviation around the Mean, Use Absolute Deviation around the Median". In: *Journal of Experimental Social Psychology* 49.4 (2013), pp. 764–766. ISSN: 00221031. DOI: `10.1016/j.jesp.2013.03.013`. URL: `http://dx.doi.org/10.1016/j.jesp.2013.03.013`.

[7] B. V. Dzyubenko and V. M. Ievlev. "Heat Transfer and Hydraulic Resistance in an Intertubular Space of a Heat Exchanger with Flow Twisting". In: *Izvestia Akademii Nauk SSSR, Energetika i Transport* 5 (1980), pp. 117–125.

[8] Li Yang and Zhi-xin Li. "Numerical Analysis of Laminar Flow and Heat Transfer in Twisted Elliptical Tubes". In: *China Academic Journal Electronic Publishing House* 20.5 (2003).

[9] Antonio C. Caputo, Pacifico M. Pelagagge, and Paolo Salini. "Heat Exchanger Design Based on Economic Optimisation". In: *Applied Thermal Engineering* 28.10 (2008), pp. 1151–1159. ISSN: 13594311. DOI: `10.1016/j.applthermaleng.2007.08.010`.

[10] Hyun Jin Lim and Per F. Peterson. *Conceptual Design of the Intermediate Heat Exchanger (IHX) for the PB-AHTR.* Tech. rep. UCBTH-09-005. Berkeley, CA: University of California, 2009.

[11] Charalampos Andreades et al. *Technical Description of the "Mark 1" Pebble-Bed Fluoride-Salt-Cooled High-Temperature Reactor (PB-FHR) Power Plant.* Tech. rep. UCBTH-14-002. Berkeley, CA: Department of Nuclear Engineering, University of California, Berkeley, 2014, pp. 1–153.

[12] D. Shaver et al. "Calculation of Friction Factors and Nusselt Numbers for Twisted Elliptical Tube Heat Exchangers using Nek5000". In: *Transactions of the American Society of Mechanical Engineers 5th Joint US-European Fluids Engineering Summer Conference* (2018).

[13] V M Ievlev et al. *Analysis and Design of Swirl-Augmented Heat Exchangers*. New York, New York: Hemisphere Publishing Corporation, 1990. ISBN: 0891167013.

[14] Joel T. Hughes et al. “Directional DRACS Heat Exchanger Concepts for the FHR”. In: *Transactions of the American Nuclear Society*. Washington, D.C.: American Nuclear Society, 2013.

[15] Joel T. Hughes and Edward D. Blandford. “Compact Double-wall Twisted-tube Heat Exchanger for the Fluoride Salt-cooled High-temperature Reactor (FHR) with Implications for In-service Inspection”. In: *Transactions of the American Nuclear Society*. Anaheim, CA: American Nuclear Society, 2014, pp. 1064–1067.

[16] Joel T. Hughes and Edward D. Blandford. “Experimental Investigation of a Directionally Enhanced DHX Concept for High Temperature Direct Reactor Auxiliary Cooling Systems”. In: *Nuclear Engineering and Design* 303 (2016), pp. 132–152. ISSN: 00295493. DOI: `10.1016/j.nucengdes.2016.03.030`. URL: `http://dx.doi.org/10.1016/j.nucengdes.2016.03.030`.

[17] Joel Hughes et al. “On the Question of Decay Heat Removal System Redundancy for Fluoride Salt-cooled High-temperature Reactors (FHR)”. In: *International Congress on Advances in Nuclear Power Plants*. San Francisco, CA: American Nuclear Society, 2016, pp. 1973–1985. ISBN: 9781510825949.

[18] M. Liu et al. “Conceptual design of a freeze-tolerant Direct Reactor Auxiliary Cooling System for Fluoride-salt-cooled High-temperature Reactors”. In: *Nuclear Engineering and Design* 335 (2018), pp. 54–70.

4.4. Methodology for Thermal-hydraulic Uncertainty Propagation Licensing Analysis for a FHR Test Reactor – Uncertainty Propagation of Coolant Properties (MIT)

Methodology for Thermal-hydraulic Uncertainty Propagation Licensing Analysis for a FHR Test Reactor – Uncertainty Propagation of Coolant Properties (MIT)[14]

Summary

An important Fluoride-salt-cooled High-temperature Reactor (FHR) development step is to design, build, and operate a test reactor. Through a literature review, liquid-salt coolant thermophysical properties have been recommended along with their uncertainties of 2-20%. This study tackles determining the effects of these high uncertainties by proposing a newly developed methodology to incorporate uncertainty propagation in a thermal-hydraulic safety analysis for test reactor licensing. A hot channel model, Monte Carlo statistical sampling uncertainty propagation, and limiting safety systems settings (LSSS) approach are uniquely combined to ensure sufficient margin to fuel and material thermal limits during steady-state operation and to incorporate margin for high uncertainty inputs. The method calculates LSSS parameters to define safe operation. The methodology has been applied to two test reactors currently considered, the Chinese TMSR-SF1 pebble bed design and MIT's Transportable FHR prismatic core design; two candidate coolants, flibe ($LiF\text{-}BeF_2$) and nafzirf ($NaF\text{-}ZrF_4$); and forced flow and natural circulation conditions to compare operating regions and LSSS power (maximum power not exceeding any thermal limits). The calculated operating region accounts for uncertainty (2σ) with LSSS power (MW) for forced flow of 25.37±0.72, 22.56±1.15, 21.28±1.48, and 11.32±1.35 for pebble flibe, pebble nafzirf, prismatic flibe, and prismatic nafzirf, respectively. The pebble bed has superior heat transfer with an operating region reduced 10% less when switching coolants and 50% smaller uncertainty than the prismatic. The maximum fuel temperature constrains the pebble bed while the maximum coolant temperature constrains the prismatic due to different dominant heat transfer modes. Sensitivity analysis revealed 1) thermal conductivity and thus conductive heat transfer dominates in the prismatic design while convection is superior in the pebble bed, and 2) the impact of thermophysical property uncertainties are ranked and should be considered for experimental measurements in the following order: thermal conductivity, heat capacity, density, and lastly viscosity. Broadly, the methodology developed incorporates uncertainty propagation that can be used to evaluate parametric uncertainties to satisfy guidelines for non-power reactor licensing applications, and method application shows the pebble bed is more attractive for thermal-hydraulic safety. Although the method was developed and evaluated for coolant property uncertainties, it is readily applicable for any parameters of interest.

---

[14] R. Romatoski (romatoskirebecca@sau.edu)

Problem Statement

To enable the commercial deployment of FHR technology, test reactor design, construction, and operation is crucial to gain insight into the design and operational parameters associated with this novel technology. A FHR test reactor (FHTR) will demonstrate feasibility, provide a licensing basis for FHRs, and support testing capabilities for materials, components, and systems. A method to incorporate uncertainty propagation in a thermal-hydraulic licensing analysis is developed and applied to two test reactor designs under consideration.

Research and test reactors are non-power reactors that primarily function for training and research. They do not produce electricity and thus are licensed differently. Test reactors, like the FHTR, aim to test fuel and materials in realistic reactor environments in order to advance high temperature reactor development. The safety analysis and licensing of test reactors follow different regulatory guidelines than power reactors. Test reactor power levels are generally orders of magnitude below a power reactor, hence the fission product inventory is also several orders of magnitude less. Therefore, a different set of regulatory requirements are developed for non-power reactors.[1]

The FHTR is a unique design compared to water reactors and has unique safety features that must be met. Thermal-hydraulic licensing of a test reactor requires analysis of safety limits and limiting safety systems settings (LSSS) as defined by the Nuclear Regulatory Commission (NRC) in NUREG-1537. The safety limits protect the integrity of the physical barriers, which guard against uncontrolled releases of radioactivity. The LSSS impose requirements on settings for automatic protective devices related to those variables having significant safety functions. The LSSS setting will ensure that automatic protective action will correct the abnormal situation before a safety limit is exceeded.[2] Essentially, the LSSS defines the operating region of the test reactor. The operating region is given by specifying the power, mass flow rate, and temperatures associated with maintaining the reactor within the LSSS. Essentially, safe operation of the test reactor requires the reactor primary coolant to remain in the liquid phase and ensure the integrity of the reactor vessel and fuel. The thermal limits, which arise from the thermal limits of the materials, used are listed in Table 3.5.1 for the FHTR.

---

[1] NRC, 1996, “Guidelines for Preparing and Reviewing Applications for the Licensing of Non-Power Reactors,” No. NUREG-1537, Office of Nuclear Reactor Regulations, Nuclear Regulatory Commission (1996).

[2] ANS, 2007, “The Development of Technical Specifications for Research Reactors,” No. ANSI/ANS-15.1-2007, American Nuclear Society (2007).

Table 3.5.1: LSSS Criteria

Thermal Limit	Flibe	Nafzirf
Minimum inlet temperature, T_{in}	505°C	550°C
Maximum bulk outlet temperature, T_{out}	704°C	704°C
Maximum coolant temperature, $T_{c,M}$	1200°C	1200°C
Maximum fuel temperature, $T_{f,M}$	1300°C	1300°C

Because the two candidate coolants, $LiF\text{-}BeF_2$ (flibe) and $NaF\text{-}ZrF_4$ (nafzirf), are not well studied and their properties have high uncertainty ranging up to 20%, the challenge is understanding the effects of the uncertainty of the coolant thermophysical properties on a thermal-hydraulic LSSS analysis. Table 3.5.2 lists the recommended thermophysical properties and their uncertainties for the two bounding candidate salt coolants.

Monte Carlo uncertainty propagation is used to obtain statistics for the effect of the property uncertainties on LSSS power. The LSSS operating limits are calculated and compared for two FHTR designs taking into account property uncertainties, namely the solid fueled thorium molten salt reactor design TMSR-SF1 of Shanghai Institute of Applied Physics (SINAP) which uses pebble bed fuel and the Transportable FHR (TFHR) design of MIT which uses prismatic fuel assembly blocks.

A thermal-hydraulic analysis code was developed to model a prismatic and a pebble bed FHR called Thermal-hydraulic Uncertainty Propagation Licensing Analysis (TUPLA-FHR). The goal of uncertainty propagation is to explore how possible errors in input data impact the results of an analysis. The code combines methods that take into account uncertainties due to design tolerances and correlation uncertainties using a hot channel model and uncertainties due to the thermophysical properties using Monte Carlo uncertainty propagation with a LSSS licensing analysis approach to defining an operating region for reactor power and temperature. The method is applied to study the effects of thermophysical property uncertainties and can be extended for other parameters of interest.

Table 3.5.2: Coolant Properties[3]

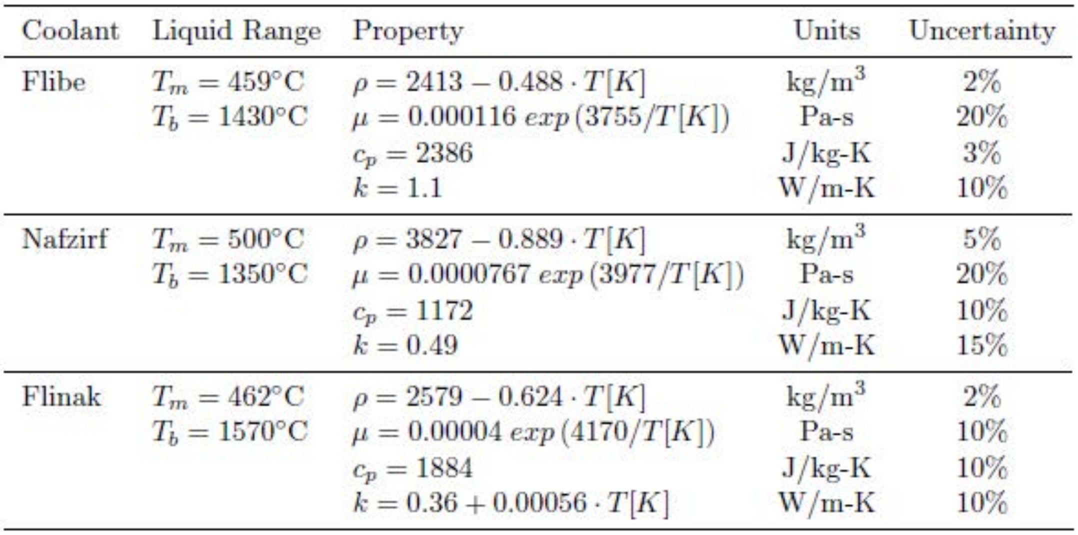

Coolant	Liquid Range	Property	Units	Uncertainty
Flibe	$T_m = 459°\text{C}$	$\rho = 2413 - 0.488 \cdot T[K]$	kg/m^3	2%
	$T_b = 1430°\text{C}$	$\mu = 0.000116\, exp\,(3755/T[K])$	Pa-s	20%
		$c_p = 2386$	J/kg-K	3%
		$k = 1.1$	W/m-K	10%
Nafzirf	$T_m = 500°\text{C}$	$\rho = 3827 - 0.889 \cdot T[K]$	kg/m^3	5%
	$T_b = 1350°\text{C}$	$\mu = 0.0000767\, exp\,(3977/T[K])$	Pa-s	20%
		$c_p = 1172$	J/kg-K	10%
		$k = 0.49$	W/m-K	15%
Flinak	$T_m = 462°\text{C}$	$\rho = 2579 - 0.624 \cdot T[K]$	kg/m^3	2%
	$T_b = 1570°\text{C}$	$\mu = 0.00004\, exp\,(4170/T[K])$	Pa-s	10%
		$c_p = 1884$	J/kg-K	10%
		$k = 0.36 + 0.00056 \cdot T[K]$	W/m-K	10%

Results

A steady-state operating region is defined for a pebble bed and prismatic core design for two candidate primary coolants and both forced and natural circulation flow (eight combinations). Presented results include a single LSSS analysis, sensitivity study, and thermophysical coolant property uncertainty quantification.

The results for the single LSSS analysis without uncertainty are shown in the LSSS diagrams in Figures 3.5.1 and 3.5.2. The region that does not exceed any of the thermal hydraulic limits is the operating region, which is the area shaded in gray on the LSSS diagrams. The LSSS power is the most liming power level for reactor operation that does not exceed any of the thermal limits. The inlet, outlet, coolant, and fuel lines in the LSSS diagrams mark the thermal hydraulic limits from Table 3.5.1 which outlines the safe operating region.

The resulting LSSS diagrams for forced flow are shown in Fig. 3.5.1 and for natural circulation flow are shown in Fig. 3.5.2 for both the pebble bed and prismatic designs and for both flibe and nafzirf coolants. Hot channel axial nodal temperature distributions for forced flow are shown in Fig. 3.5.3.

---

[3] Romatoski, R. R., & Hu, L. W. (2017). Fluoride salt coolant properties for nuclear reactor applications: A review. Annals of Nuclear Energy, 109, 635–647. https://doi.org/10.1016/j.anucene.2017.05.036

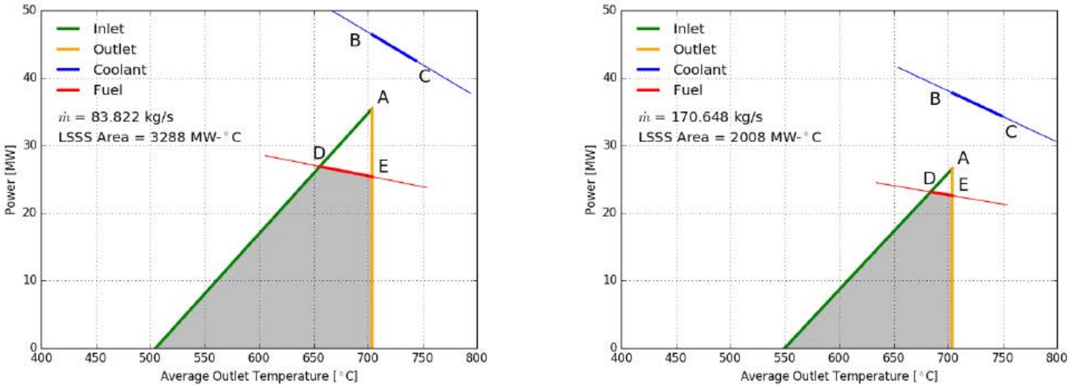

(a) Flibe Pebble Bed Core

(b) Nafzirf Pebble Bed Core

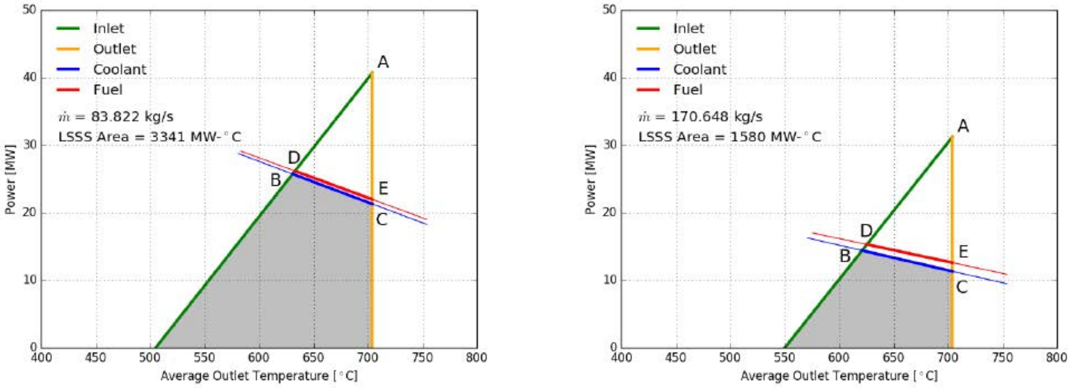

(c) Flibe Prismatic Core

(d) Nafzirf Prismatic Core

Figure 3.5.1: Forced Flow LSSS Results

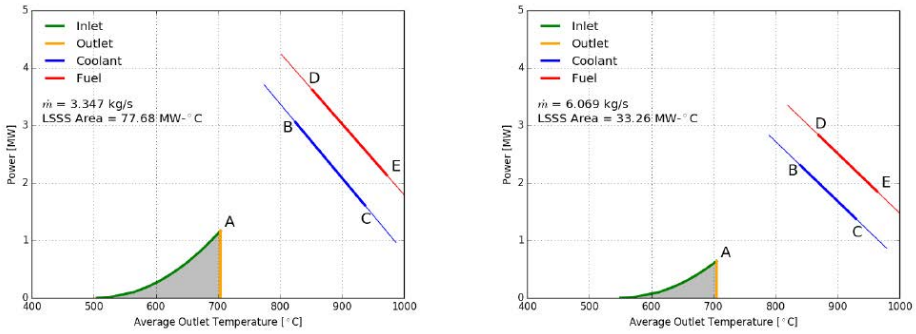

(a) Flibe Pebble Bed Core

(b) Nafzirf Pebble Bed Core

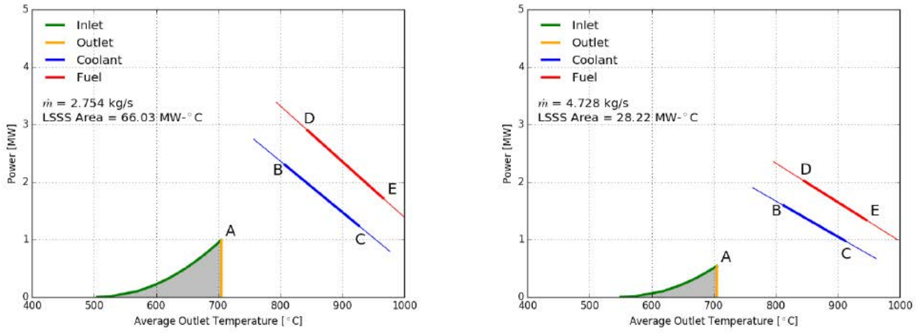

(c) Flibe Prismatic Core

(d) Nafzirf Prismatic Core

Figure 3.5.2: Natural Circulation Flow LSSS Results

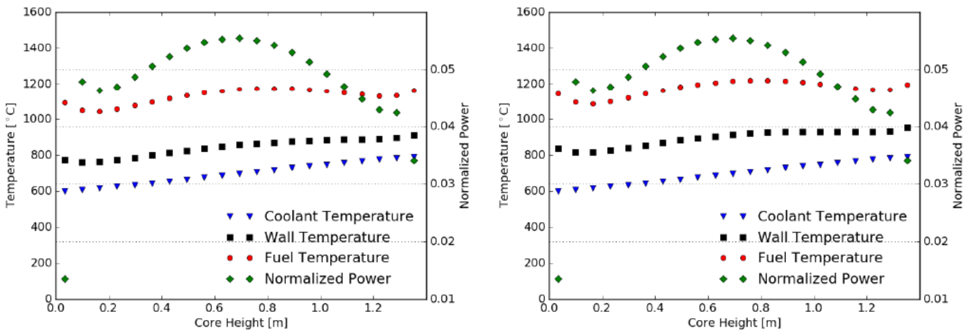

(a) Flibe Pebble Bed Hot Channel

(b) Nafzirf Pebble Bed Hot Channel

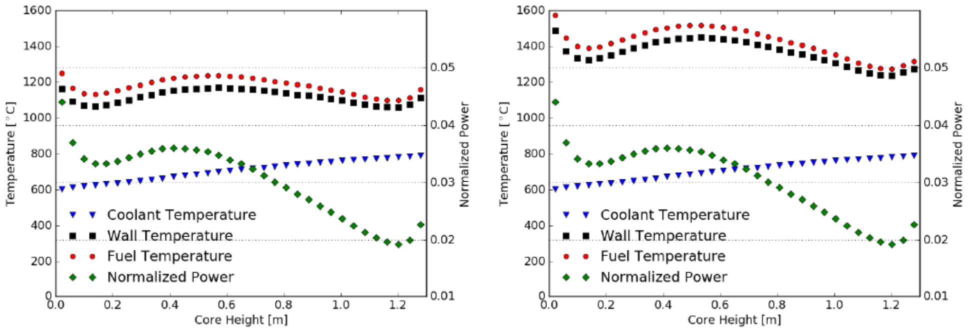

(c) Flibe Prismatic Hot Channel

(d) Nafzirf Prismatic Hot Channel

Figure 3.5.3: Forced Flow Hot Channel Axial Nodal Temperatures

A sensitivity study allows each thermophysical property to determine the effects of its individual uncertainty on LSSS operating region. The sensitivity of LSSS power to each thermophysical property is graphed in Figure 3.5.4 for forced flow and Figure 3.5.5 for natural circulation flow. The figures show a sensitivity study for all four thermophysical properties for 2%, 20%, 3%, and 10% for density, viscosity, heat capacity and thermal conductivity, respectively, for flibe and 5%, 20%, 10%, and 15% for nafzirf, respectively.

The statistical LSSS power with 95/95 tolerance limits (two times the sample standard deviation) are summarized in Table 3.5.3. The lower limit of the 95/95 tolerance limit determines the LSSS power that incorporates the thermophysical property uncertainty. Using the lower limit will reduce the LSSS operating region to define a safe operating region that accounts for the uncertainty.

Table 3.5.1: LSSS Power Thermophysical Property Uncertainty 95/95 Tolerance Limits

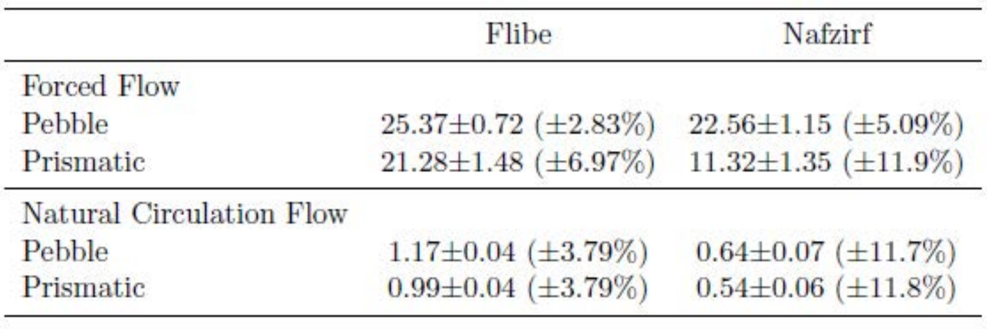

	Flibe	Nafzirf
Forced Flow		
Pebble	25.37±0.72 (±2.83%)	22.56±1.15 (±5.09%)
Prismatic	21.28±1.48 (±6.97%)	11.32±1.35 (±11.9%)
Natural Circulation Flow		
Pebble	1.17±0.04 (±3.79%)	0.64±0.07 (±11.7%)
Prismatic	0.99±0.04 (±3.79%)	0.54±0.06 (±11.8%)

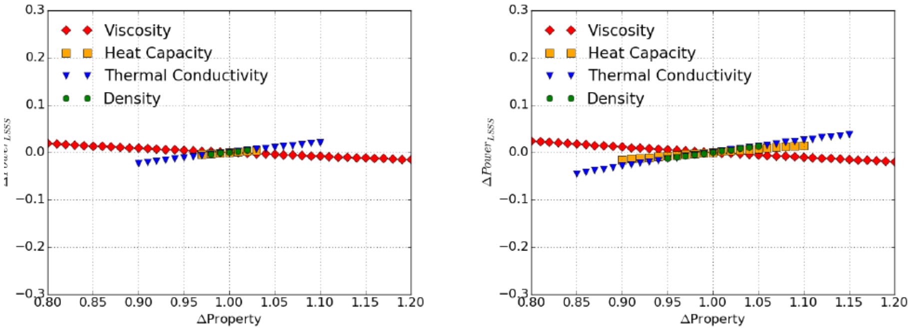

(a) Flibe Pebble Bed Core (b) Nafzirf Pebble Bed Core

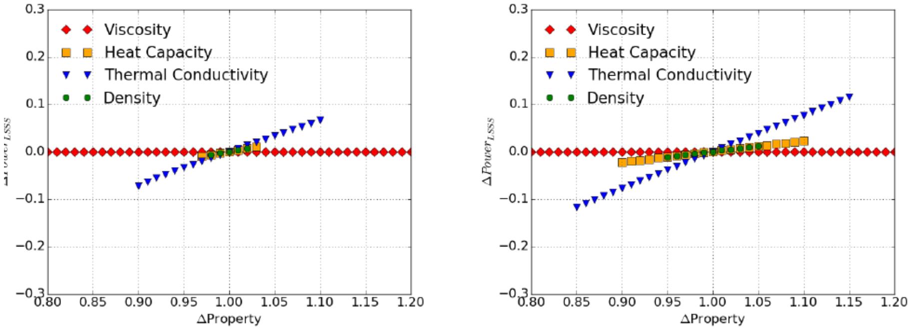

(c) Flibe Prismatic Core (d) Nafzirf Prismatic Core

Figure 3.5.4: Forced Flow Sensitivity Study

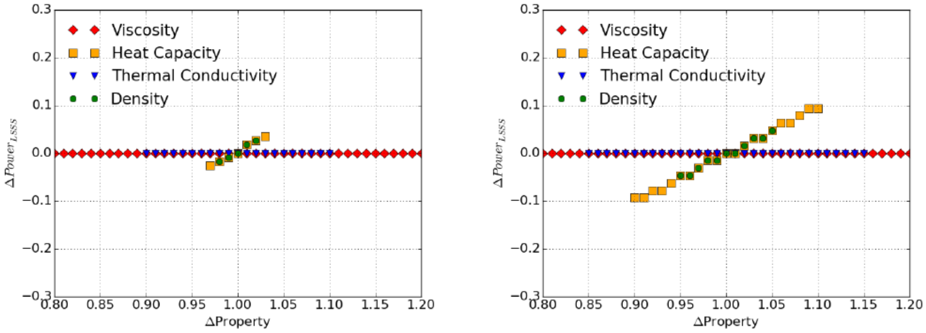

(a) Flibe Pebble Bed Core (b) Nafzirf Pebble Bed Core

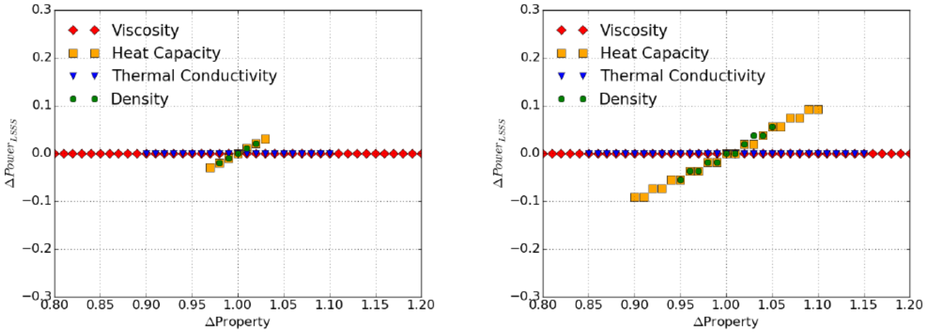

(c) Flibe Prismatic Core (d) Nafzirf Prismatic Core

Figure 3.5.5: Natural Circulation Flow Sensitivity Study

Conclusions

For licensing an FHTR, the developed method for defining a safe steady-state operating region incorporates coolant thermophysical property uncertainties and applies LSSS. The results demonstrate the method for test reactor safety licensing analysis and elicit design considerations for an FHR. The sensitivity analysis results show that 1) thermal conductivity and thus conductive heat transfer dominates in the prismatic design while convection is superior in the pebble bed as confirmed by comparing the axial temperature distributions of the wall and coolant, and 2) the impact of thermophysical property uncertainties are ranked and should be considered for experimental measurements in the following order: thermal conductivity, heat capacity, density, and lastly viscosity.

Given the larger contribution of conductive heat transfer for the prismatic design for forced flow, the larger uncertainty of thermal conductivity contributes to a larger LSSS power uncertainty and is shown as the largest contribution to uncertainty for the prismatic design by a sensitivity study. Naturally, the uncertainty increases when switching from flibe to nafzirf as nafzirf properties have higher uncertainties. For natural circulation, heat capacity and density, which are the driving forces of natural circulation, are the largest contributions to LSSS power uncertainty.

The pebble bed design is more attractive from a thermal-hydraulic safety standpoint. It is more resilient to salt coolant selection, has a higher LSSS power, is constrained by the maximum fuel not coolant temperature limit, and has lower LSSS thermophysical property uncertainty.

The most limiting constraint is the maximum average outlet temperature limit dictated by Hastelloy N ASME code temperature. If further study can increase this structural material temperature limit, the pebble bed operating area will expand more than the prismatic.

The two test reactor designs demonstrate the method and different or updated designs can be implemented to conduct an LSSS analysis with uncertainty quantification. This study examined thermophysical property uncertainties; however, the methodology can be used to quantify the uncertainty of other quantities of interest. The analysis focused on steady-state operation; thus, future work is needed to look at transient and accident scenarios.

References Published:

Romatoski, R. R. (2017). *Fluoride-Salt-Cooled High-Temperature Test Reactor Thermal-Hydraulic Licensing and Uncertainty Propagation Analysis* (Doctoral Dissertation). Massachusetts Institute of Technology, Cambridge, MA.

Romatoski, R. R., & Hu, L. W. (2017). Fluoride salt coolant properties for nuclear reactor applications: A review. *Annals of Nuclear Energy*, *109*, 635–647. https://doi.org/10.1016/j.anucene.2017.05.036

References Submitted for Publication:

Romatoski, R.R., & Hu, L.W. (TBD). Fluoride-Salt-Cooled High-Temperature Test Reactor Thermal-Hydraulic Licensing and Uncertainty Propagation Analysis. *TBD*.

4.5. Effects of Radiative Heat Transfer in High-Temperature Liquids-Salts (MIT/UCB)

Effects of Radiative Heat Transfer in High-Temperature Liquids-Salts (MIT)[18]

Summary

New FHR designs utilize high-temperature fluoride salts that may experience the effects of participating media radiative heat transfer. While radiative heat transfer has not been extensively studied for LWRs, its effects become significant at temperatures over 600-700°C due to its dependence on the absolute temperature to the fourth power [T^4] in liquid salts. This effect is not seen in high-temperature helium that is transparent. Radiative absorption and emission can increase energy transfer and increase temperature uniformity within the liquid-salt, which has large implications in accident scenarios where better heat transfer can reduce peak temperatures. MIT is creating a methodology to understand the effects of radiative heat transfer in high-temperature liquid-salts by: (1) performing extensive opacity measurements on a variety of halide (fluoride and chloride) salts between 600-1000°C and (2) performing detailed modeling and simulation of the complex phenomena of radiative heat transfer in halide salts for key, representative flow geometries and structure surface emissivities. Figure S.1 shows the black body emission spectrum at 800°C where the adsorption coefficients are at the wavelengths to begin to make radiative heat transfer important.

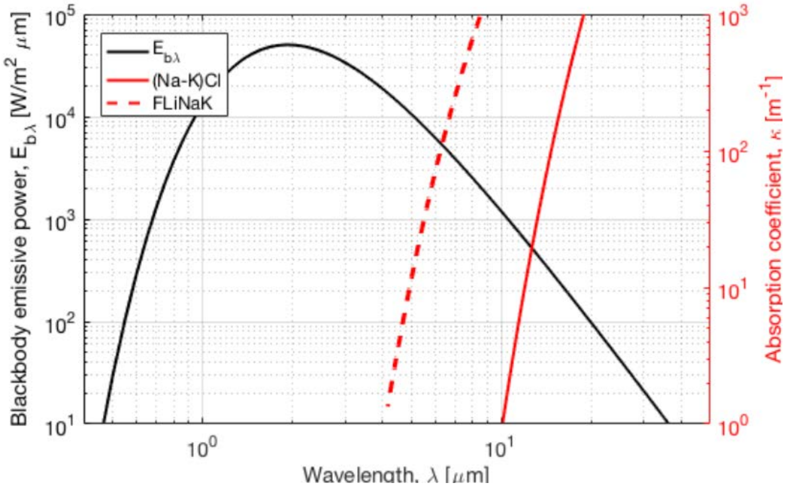

Figure S.1. Black body emission spectrum at 800C for index of refraction, n=1.4 and theoretical, pure (Na-K)Cl and FLiNaK absorption coefficients.

---

[18] Carolyn Coyle, Emilio Baglietto, and Charles Forsberg (cforsber@mit.edu)

Introduction

New FHR designs utilize high-temperature fluoride salts that may experience the effects of participating media radiative heat transfer. While radiative heat transfer has not been extensively studied for LWRs, its effects become significant at temperatures over 600-700°C due to its T^4 dependence [1]. Radiative absorption and emission can increase energy transfer and temperature uniformity within the liquid-salt, which has large implications in accident scenarios. MIT is creating a methodology to understand the effects of radiative heat transfer in high-temperature liquid-salts by: (1) performing extensive opacity measurements on a variety of halide (fluoride and chloride) salts between 600-1000°C and (2) performing detailed modeling and simulation of the complex phenomena of radiative heat transfer in halide salts for key, representative flow geometries and structure surface emissivities.

(1) Initial upgrades have been made to the FTIR spectroscopy facility to allow for the measurement of fluoride and chloride salt absorption coefficients in the near to mid IR wavelength range. These upgrades include new FTIR sources and detectors, improved optics, and an innovative Inconel 600 cuvette design.

(2) STAR-CCM+ participating media models have been validated using numeric solutions for coupled conduction and convection cases. Spectral banding methods have also been investigated for accuracy and convergence. Preliminary pool simulations have shown that radiative heat transfer can reduce wall temperatures while increasing temperature uniformity in some cases.

By performing experiments with liquid-salts to measure salt IR absorption properties and quantify radiative heat transfer for key geometries and operating conditions, this work addresses unanswered thermal hydraulic and heat transfer performance questions.

Description

Radiation exchange in participating media, such as liquid-salts, depends on the temperature-dependent properties of the fluid. This radiation may be transmitted, attenuated, or emitted. This leads to the following radiative heat transfer equation[1] [2]:

$$\frac{dI_\eta}{ds} = -\kappa_\eta I_\eta + \kappa_\eta I_{b\eta}$$

---

[1] For a participating, non-scatting medium

where κ_η is the absorption coefficient and I_η and $I_{b\eta}$ are the incoming and blackbody intensities, respectively. However, to solve this equation, the optical properties in regions of significant emissive power must be well characterized.

The first set of experiments will measure the fundamental absorption coefficients of candidate liquid-salts over the temperature range of interest (between 600-1000°C) between 2-12 micron wavelengths. Fluoride and chloride salts are generally believed to be fairly transparent in this region, but Fig. 1 shows that there is still emissive power in LiF-NaF-KF (FLiNaK) and NaCl-KCl salts in the near to mid IR wavelength bands. Additionally, FHR salts can contain impurities that can greatly increase the average absorptivity in the visible and near IR regions. The test apparatus shown in Fig. 2 will be used to measure the spectral absorption coefficient using Fourier Transform Infrared (FTIR) spectroscopy.

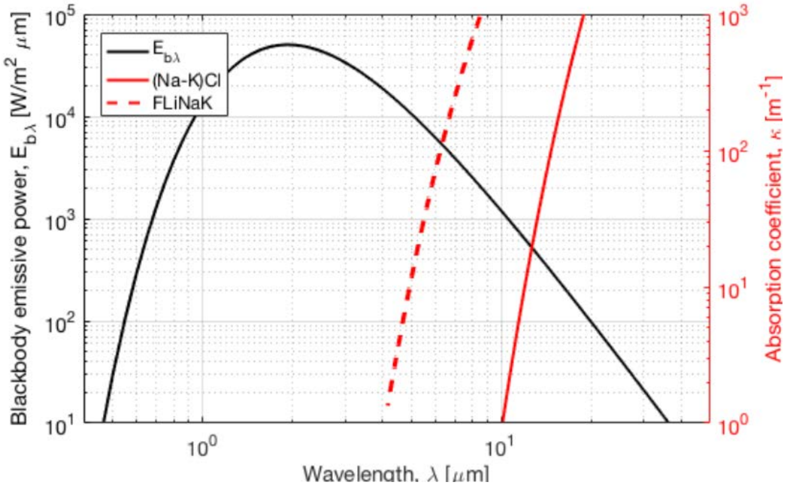

Fig 1. Black body emission spectrum at 800C for index of refraction, n=1.4 and theoretical, pure (Na-K)Cl and FLiNaK absorption coefficients.

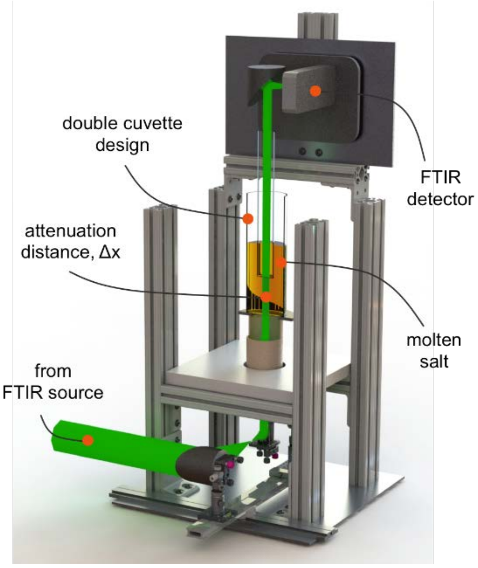

Fig 2. Optical measurement apparatus model.

The FTIR apparatus is composed of two, concentric Inconel 600 cuvettes, a light source, and light detector. Liquid-salt is placed inside the outer cuvette while the position of the inner cuvette is changed to achieve different fluid thicknesses. Inconel 600 perforated plates are used as windows with holes that allow light to pass through the salt, but contain the fluid by surface tension. Given a known salt sample thickness, initial light intensity, I_0, and final light intensity, I_i, the attenuation coefficient can be calculated at individual wavelengths according to the following equation:

$$\kappa(T,\lambda) = \frac{-1}{\Delta x_j - \Delta x_i} ln\left(\frac{I_j(T,\lambda)}{I_i(T,\lambda)}\right)$$

A prior version of this apparatus concept without the upgrades defined above was successfully used by *Tetreault-Friend* to measure the attenuation coefficients of binary nitrate and binary chloride salts at 400°C and 800°C, respectively, in a wavelength range of 500nm to 2500nm [3].

Using the measured spectral absorption data, computational fluid dynamics (CFD) simulations will be run quantify the impact of thermal radiation to the overall heat transfer. High-fidelity 3D CFD simulations are conducted using STAR-CCM+, a vetted commercial code. These simulations are run at high temperatures with participating media multiband thermal radiation models that have been validated against participating media coupled with conduction and convection test cases with known numerical solutions. The modeling of wavelength-dependent radiative heat transfer in participating media is complex, and thus far for halide salts has only been solved carefully for relatively simple flows in cylindrical channels [4]. This work will expand upon previous studies by moving to spectrally banded absorption coefficients that are capable of capturing the order of magnitude change in absorption coefficient over relevant wavelengths. Spectral band values are defined by the following equation:

$$\bar{\kappa} = \frac{\int_{\lambda 1}^{\lambda 2} \kappa_\lambda E_{b\lambda} d\lambda}{\int_{\lambda 1}^{\lambda 2} E_{b\lambda} d\lambda}$$

The bands are divided so that each band has an equal percentage of blackbody emissive power. Figure 3 shows the values of the spectrally banded FLiNaK absorption coefficient for 1-4 bands.

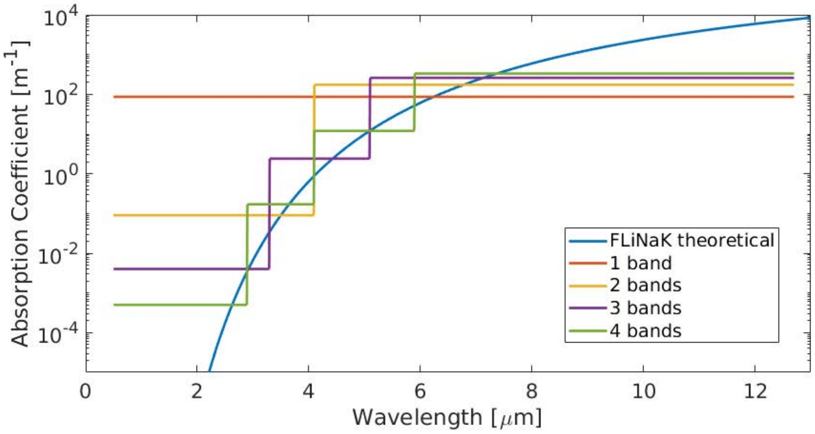

Fig 3. FLiNaK spectrally banded absorption coefficients for 700°C.

After solving for the absorption coefficient values as a function of the number of bands, the integral power densities (P), defined by the equation below, were compared for temperatures between 500-900°C. This was used to look at the accuracy of the spectral banding method as temperatures vary across the fluid.

$$P = \sum_{i=1}^{N} \int_{\lambda 1i}^{\lambda 2i} \bar{\kappa}_i E_{b\lambda} d\lambda$$

As can be seen in Figure 4, there is a significant jump when moving from 1 to 2 bands, showing that, at a minimum, 2 bands should be used for simulations. As you increase the number of bands, the solutions start to converge to the exact values.

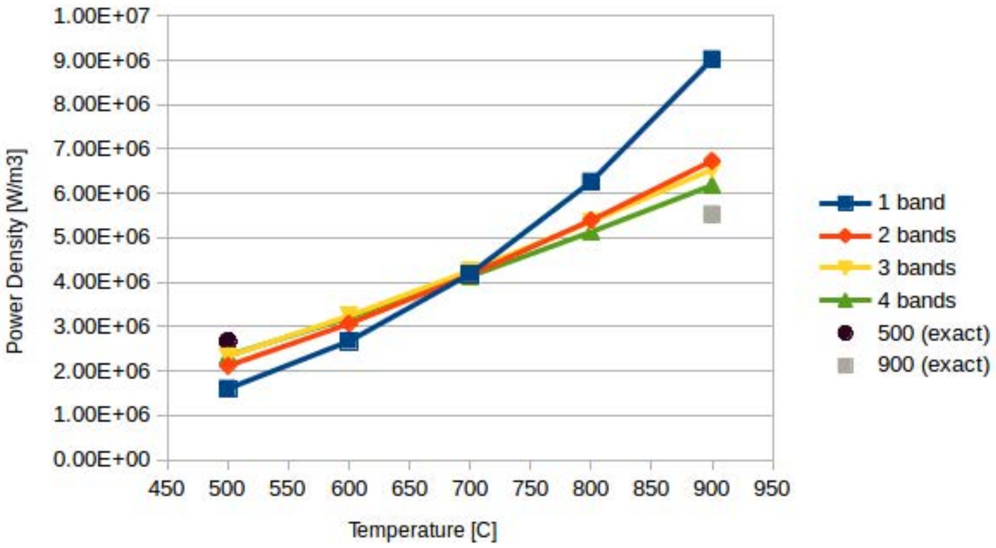

Fig 4. Integral power density as a function of temperature and number of spectral bands. Results demonstrate the importance of having at least 2 bands.

Finally, initial 3D, transient CFD simulations were conducted to gain insight into the effects of radiative heat transfer on proposed experiment designs. This simulation models FLiNaK with 3 spectral bands in a 0.5m diameter, 0.5m tall tank with a 0.03m diameter rod heater producing a heat flux of 1.2MW/m^2. The top and bottom surfaces are adiabatic while 1kW/m^2 is lost on the outer wall. Results (Figure 5) show that radiative heat transfer does have a significant effect on the heated wall temperatures as well as the temperature uniformity.

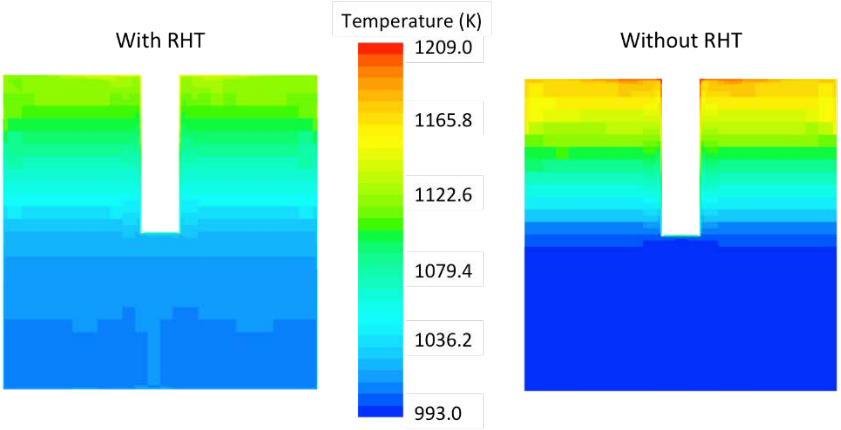

Fig 5. Transient, heated pool simulation results. A 3-banded spectral model was used with theoretical FLiNaK absorption coefficients and run for 10 minutes of physical time.

Next steps will include validating the accuracy of CFD methodology with high-temperature liquid-salt experiments as well as low-temperature scaled experiments using a simulant fluid such as Dowtherm A [5] to isolate and confirm the contributions of radiative heat transfer. By demonstrating that CFD can capture the correct physics, complex geometries with new salts can be analyzed for use in various heat transfer applications.

References

1. C. FORSBERG, D. WHYTE, “Converging Fission and Fusion Systems Toward High-Temperature Liquid-Salt Coolants: Implications for Research and Development and Strategies,” *Trans, ICCAP*, San Francisco, CA (2016).
2. M. F. MODEST, *Radiative Heat Transfer*. Elsevier Inc., 3rd edition, 2013.
3. M. TETREAULT-FRIEND ET AL., “Optical Properties of High Temperature Molten Salt Mixtures for Volumetrically Absorbing Solar Thermal Receiver Applications,” *Solar Energy*, 153 (2017) 238-248.
4. E. CHALEFF ET AL., “Radiation Heat Transfer in Molten Salt FLiNaK,” *Nuclear Technology*, 196 (2016).
5. THERMAL HYDRAULICS WORKING GROUP, “Fluoride-Salt-Cooled High-Temperature Reactor Benchmarking White Paper,” University of California, Berkeley, (2016).

5. Evaluation Model Benchmarking and Validation Workshops (UCB)

This task involved conducting joint workshops with IRP member universities, advisory committee members, and relevant experts to review current progress, help direct further efforts, and assure that the most critical issues of FHR technology development were addressed by the IRP. Many of these activities were joint activities with the Georgia Tech IRP.

FHR Phenomenology and Benchmark Exercise Workshops

Summary

A series of workshops throughout the duration of this IRP were held that included IRP members (faculty, staff, and students) and external experts from other academic institutions, national laboratories, and commercial companies in the U.S. and abroad. The goal of the workshops was to coordinate a broad benchmarking campaign to provide input for the development of advanced modeling and simulation tools for FHR development and analysis. Further description is provided below.

- *Workshop 1:* The primary results are the formation of technical area working groups (neutronics, thermal hydraulics, and materials corrosion, activation, tritium and transport (MATT)), the close collaboration with the second FHR IRP led by the Georgia Institute of Technology, and the establishment of a path forward for the benchmarking campaign including future workshop planning. White paper available on UCB's FHR website as UCBTH-15-006 (http://fhr.nuc.berkeley.edu/references/fhr-white-papers/).
- *Workshop 2:* The benchmarking workshop resulted in a variety of plans for moving forward, with a common theme being the need for delineating collaboration options between IRP members and identifying specific benchmarking needs. White papers from each working group have been compiled on the actual discussions, conclusions, and paths forward for each working group within the IRP. The Thermal Hydraulics Working Group's white paper has been finalized and is available from the UCB FHR website (http://fhr.nuc.berkeley.edu/references/fhr-white-papers/).
- *Workshop 3:* Development of modern, powerful modeling and simulation toolsets are underway at many levels, paving the way for future design and development of nuclear reactors and systems without heavy reliance on expensive and relatively limited experiments. However, a significant, cross-cutting need that was identified (and all-too-often set aside) is the need for high-quality validation data for these new tool sets. Until these two ends are reconciled, work will continue to move forward on improving existing and new modeling and simulation toolsets as much as possible while pursuing experimental programs at national and international levels that can address multiple gaps/needs at once. A white paper summarizing the workshop presentations and discussions has been released with input from the MIT-led IRP and is available from the Georgia Institute of Technology: https://smartech.gatech.edu/handle/1853/58808. The MATT working group concluded that

there was a need for a review paper on methods to control redox (and thus corrosion) in high-temperature fluoride salts that assembled what was currently known to help focus future work going forward. The review paper “Redox Potential Control in Molten Salt Systems for Corrosion Mitigation,” authored by J. Zhang et al was prepared and published in *Corrosion Science*. https://doi.org/10.1016/j.corsci.2018.08.035.

- *Workshop 4:* The last workshop with be a joint FHR IRP Workshop in Washington D.C. with Georgia Tech on December 12-13, 2018. We expect participation from several external collaborators and contributors such as U.S. and international national laboratories, the U.S. Department of Energy, Southern Nuclear, Kairos Power, etc. The workshop theme is "FHR to Megawatts," with discussions focused on future efforts in support of FHR commercialization, identifying knowledge gaps that university research can aim to fill, and other mechanisms to support advanced reactor development and deployment.

Description

Joint workshops were conducted with participation from IRP member universities, advisory committee members, and relevant experts to review current progress, help direct further efforts, and assure that the most critical issues of FHR technology development are addressed by the IRP. This is a brief summary of the activities in and results from each workshop in this IRP.

1st IRP-2 Workshop on FHR Phenomenology and Benchmark Exercise Definition

From March 11th to March 13th, UCB organized a workshop including all IRP-2 universities (UCB, MIT, UW and UNM); members from a second FHR IRP (Georgia Institute of Technology, The Ohio State University, and Texas A&M University); national experts from Idaho National Laboratory (INL) and Oak Ridge National Laboratory (ORNL); as well as international experts from the Australian Nuclear Science and Technology Organisation (ANSTO) in Sydney, the Shanghai Institute of Applied Physics (SINAP) in China, and the Ulsan National Institute of Science and Technology (UNIST) in South Korea. In total, roughly 30 experts supported by an equally large group of students from the listed universities discussed the path forward for FHR phenomenology and benchmarking.

The conclusions from this workshop were mainly regarding the structure of the IRP, initial benchmarking efforts, and future workshops. There were three clear technical areas that resulted from the discussions during the workshop: Neutronics; Thermal Hydraulics; and Materials Corrosion, Activation and Mass Transport. Working groups based on these technical areas were formed and were led by IRP members, and were advised by an advisory group expert on the specific technical area. This breakdown of IRP members into working groups, advised by experts in the different technical areas, helped facilitate productive progress on code benchmarking exercises throughout the three years of the IRP. Members of this IRP and the Georgia Tech IRP collaborated reasonably closely on the benchmarking efforts in the three technical areas to maximize the resources dedicated to FHR advancement at the university level.

Initial benchmarking exercises and high-level paths forward were discussed during the workshop for each technical area. The lessons learned from previous benchmarking efforts in the nuclear energy sphere were to begin with simple problems to practice the effort of benchmarking with a large group of participants, then move to more complex and realistic benchmarking exercises as the working groups become familiar with the benchmarking process. Specific initial benchmarking exercises and general paths forward can be found in the associated white paper, available on UCB's FHR website as UCBTH-15-006 (http://fhr.nuc.berkeley.edu/references/fhr-white-papers/).

Each working group in this effort consisted of students and professors from FHR IRP partner universities with related interests in the technical area of the working group as well as universities and organizations that fall outside the formal IRP organization. Additionally, each working group had its own advisory committee consisting of professors, national laboratory scientists, and other technical area experts to help guide research efforts. Beyond guiding the efforts within this new IRP, the oversight of an expert advisory committee helped facilitate collaboration and mentorship between established experts within the Nuclear Engineering field and students in Nuclear Engineering, ensuring a high degree of knowledge transfer and continuation of FHR development capability. The flexibility of having the efforts divided among three working groups also allowed for more contact and collaboration through video-conferencing and side meetings at conferences related to the working groups' technical area. The IRP partner universities, including the GT-led IRP, were divided into working groups as follows:[1]

- Neutronics: UCB, GT, MIT
- Thermal Hydraulics: UCB, OSU, UNM, UW
- MATT: UW, MIT

Each working group identified two lead faculty members who co-chaired the group. The responsibilities of the lead faculty included: developing a working group charter, communication and coordination within the working group as well as with the other working groups, organization of working group resources, prioritization of benchmarking efforts, coordination and integration of the working group advisory committee, and other managerial duties.

During the beginning of the combined IRP efforts, the working groups primarily worked separately as their technical areas were relatively disparate. However, sharing individual experiences with benchmarking efforts with the other working groups was critical in further development of benchmarking best practices and creating positive communication practices. Also, as the understanding of FHR phenomena advanced during the IRPs, the more complex phenomena required coupled development between working groups, e.g. thermal hydraulics – neutronics coupling to understand complex FHR transient behaviors that will be important for licensing efforts.

2nd IRP-2 Workshop on FHR Benchmark Progress

The second IRP-2 workshop on FHR benchmark progress was held April 13-15, 2016 on the UCB campus and consisted of approximately forty experts and thirty students. The majority of the discussions were broken into three working groups: Materials Activation, Tritium, and Transport (MATT); Thermal Hydraulics; and Neutronics. Discussions with the entire workshop were also held to discuss cross-cutting issues, progress in international research programs, and future planning for this IRP.

---

[1] Texas A&M University (TAMU) has an established and impressive expertise in instrumentation and control, and as such does not readily fall into the working group structure. TAMU's role in this benchmarking campaign was never established, instead they contributed to FHR technology development and understanding in other, equally important ways.

Overall, the workshop was determined to be a success and all participants were satisfied with the discussions. The benchmarking workshop resulted in a variety of plans for moving forward, with a common theme being the need for delineating collaboration options between IRP members and identifying specific benchmarking needs.

White papers from each working group have been compiled which are very informative on the actual discussions, conclusions, and paths forward for each working group within the IRP. The Thermal Hydraulics Working Group's white paper has been finalized and is available from the UCB FHR website (http://fhr.nuc.berkeley.edu/references/fhr-white-papers/). The benchmarking workshop resulted in a variety of plans for moving forward, with a common theme being the need for delineating collaboration options between IRP members and identifying specific benchmarking needs.

3rd IRP-2 Workshop on FHR Benchmark Progress

The third FHR workshop for this IRP was organized and hosted by the Georgia Institute of Technology from March 8 through March 9 on the Georgia Tech campus in support of their FHR IRP. This MIT-led IRP had significant presence at the workshop and contributed greatly.

The workshop objective was to: "review the capabilities of the current modeling and simulation (M&S) tools for multi physics analysis of the FHRs and to identify the gaps and needs for the development, extension, and or V&V of existing tools necessary to support the licensing of the FHRs." The first day of the workshop consisted of presentations from community experts on modeling and simulation tools they're familiar with, including the NEAMS Workbench, the Moose framework, SAM, the TRACE/PARCS toolset, as well as several university-developed tools from the member universities of both FHR IRPs. The second day consisted of breakout sessions for the three research communities (neutronics, thermal fluids/hydraulics, and materials) to discuss research progress, presentations from the previous day, and gaps and needs identification for the development and/or extension of modeling and simulation tools and verification and validation (V&V), important parts of benchmarking exercises.

The UCB team presented the tools developed for modeling FHR at the coordinated workshop. Two sets of tools were presented: (1) a high-fidelity, computationally demanding tool that couples Serpent for neutronics (Monte Carlo) and the multiphysics toolkit OpenFOAM for thermal-hydraulics and structural analysis, including discrete element modeling to simulate pebbles motion; and (2) a lower fidelity model based on COMSOL (for which a diffusion solver was developed) for scoping analysis. Both tools are capable of modeling steady-state and transient scenarios. The workshop highlighted that, although many have potentials, tools with capabilities necessary to model FHR (e.g., double heterogeneity, salt properties, etc.) remain scarce and the tools developed within this IRP project are at the cutting-edge.

Overall, the workshop was successful and encouraging. Development of modern, powerful modeling and simulation toolsets are underway at many levels, paving the way for future design and development of nuclear reactors and systems without heavy reliance on expensive and relatively limited experiments. However, a significant, cross-cutting need that was identified (and all-too-often set aside) is the need for high-quality validation data for these new tool sets. Until these two ends are reconciled, work will continue to move forward on improving existing and new modeling and simulation toolsets as much as possible while pursuing experimental programs at national and international levels that can address multiple gaps/needs at once.

In line with workshop conclusions, the MATT working group came to the major conclusion that there was a need to assemble a review paper on methods to control redox (and thus corrosion) in high-temperature fluoride salts that assembled what was currently known and defined known redox options. The review paper would provide a bridge between different groups examining different methods for redox control and accelerate work going forward. The review paper “Redox Potential Control in Molten Salt Systems for Corrosion Mitigation,” authored by J. Zhang et al was prepared and published in *Corrosion Science*. https://doi.org/10.1016/j.corsci.2018.08.035 The authors include J. Zhang (Virginia Tech.; corresponding author: zjinsuo@vt.edu), C. W. Forsberg (MIT), M. F. Simpson (Univ. Utah), S. Guo (Virginia Tech.), S. T. Lam (MIT), R. O. Scarlat (U. of Wisconsin), F. Carotti (Univ. Wisconsin-Madison), K. Chan, P. Singh (Georgia Tech.), W. Doniger, K. Sridharan (Univ. Wisconsin-Madison), and J. R. Keiser (ORNL). The abstract for this review paper is:

> In a molten salt nuclear reactor system, the redox potential must be controlled for mitigating corrosion of structural materials. The paper presented a critical review on the available knowledge of redox potential control in molten fluoride salt systems. The major potential contaminants that affect the redox potential and material corrosion are TF, oxides, hydroxides, and various metal fluorides. Redox potential control methodologies include gas sparging, contacting the salt with a reducing metal, and adding soluble salt redox buffers to the salt. Redox potential measurement technologies include electrochemical

sensors and optical spectroscopy. The paper also analyzed the current technology issues and recommended near future studies.

A white paper summarizing the workshop presentations and discussions has been released with input from the MIT-led IRP and is available from the Georgia Institute of Technology here: https://smartech.gatech.edu/handle/1853/58808.

4th IRP-2 Workshop on FHR Benchmark Progress

We will hold a joint FHR IRP Workshop in Washington D.C. on December 12-13, 2018. We expect participation from several external collaborators and contributors such as U.S. and international national laboratories, the U.S. Department of Energy, Southern Nuclear, Kairos Power, etc.

There will be panel discussion in all the areas of project activities (materials activation and transport, thermal hydraulics, neutronics, tritium generation and transport, and instrumentation and control) with short presentations by the co-leads of each technical area followed by in-depth discussion. Presentations will focus on issues, methods used to address the issues, results, and impacts. There will also be an opportunity for students involved in FHR research within the IRPs to give poster presentations to interested participants.

The theme for the workshop will be, "FHR to Megawatts," and serious discussion will be focused on future efforts in support of FHR commercialization, identifying knowledge gaps that university research can aim to fill, and other mechanisms to support advanced reactor development and deployment. The primary goal of the workshop will be to develop a roadmap for future directions with input from participants from industry, national laboratories, and the U.S. DOE. Further questions should be directed to the IRP PIs.

6. Subcritical Driven Facility (MIT)[21]

Summary

There are multiple technical strategies to develop an FHR. One option is a subcritical facility where a research or test reactor is used to provide a flux of neutrons to drive a subcritical facility that represents part the reactor core—fuel, 700°C flowing salt, pumps, salt cleanup systems, tritium generation and other reactor characteristics. We examined the option of using the MIT reactor for this purpose where an FHR subcritical facility power density generated by fission would be about 30% of the commercial reactor. At such a power level, the subcritical facility can be used to provide an integrated nuclear systems test before building a full reactor. The attraction of such a facility is that it can be built in several years at a small fraction of the cost of reactor to provide experimental and operating information on an FHR. That is because the research or test reactor provides an existing source of neutrons, the safety envelop for the subcritical facility and an existing licensing basis for such a test. The MIT reactor was designed and licensed with a subcritical facility and in the past operated the subcritical facility for other types of experiments. The work indicates such a facility could be built within the licensing bases of the MIT reactor.

---

[21] K. Sun

1. Introduction

The subcritical driven facility is capable of combining significant nuclear fluence and flexible testing space. More importantly, it is designated to be built aside of a licensed reactor, so that capital cost is reduced by sharing infrastructure, operating personnel, and administrative management expenses. The subcritical driven facility will be licensed as an experimental facility rather than going through the longer path of licensing an advanced reactor concept. This is due to the reactor safety systems that are used to assure many safety functions — a design feature of such research reactors.

The MIT Nuclear Reactor Laboratory (NRL) has designed, licensed, constructed, operated, and de-fueled such a facility. A neutron capture therapy (NCT) section at the MITR [1] had a fission converter-based epithermal neutron irradiation facility that was licensed to operate by the U.S. Nuclear Regulatory Commission (NRC). An isometric view of the entire facility at the MITR is shown in Fig. 1. Eleven MITR fuel elements were placed between the graphite columns and concrete biological shield. Fission was initialized by the source neutrons from the MITR core and transporting through the gas window adjacent to the heavy-water reflector. The operation of the subcritical facility replies on the driven neutrons as the source term and it is not able to maintain the chain reactions alone. Thirteen years after the initial operation commenced in 2000, the fission converter was de-fueled in 2013.

In the current study, a MITR driven subcritical facility has been proposed for demonstrating the FHR technologies. The room and the shielding of the de-fueled fission converter provide the needed space. The system would operate at 700°C with local power densities up to 30% of a demonstration FHR. The scale of the system allows early integrated testing with significant neutron fluxes, to reduce technical risks in designing and licensing of a full-scale test reactor. Unlike a reactor test loop, it enables integrated tests that includes prototypical control rods, instrumentation, and cleanup systems. One specific FHR variant was used to allow a realistic evaluation of subcritical facility requirements. Overall, such a novel concept is considered as a cost-effective path for code validation, operation, maintenance, instrumentations, and system testing. Table 1 summarizes the integrated test facility options for different the FHR technology domains.

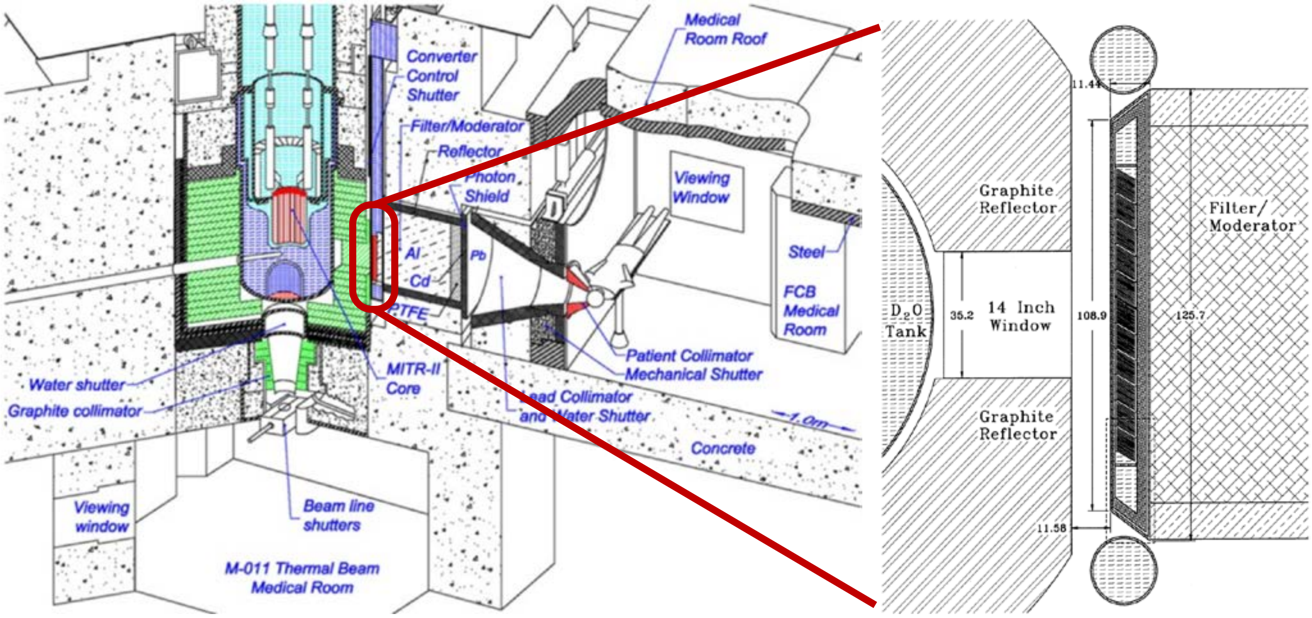

Fig. 1. Isometric view of the fission converter-based neutron irradiation facility constructed at MITR

Table 1. Summary of integrated test facility options for demonstrating the FHR technologies
Score being made from 1 (poor) to 5 (excellent)

Options / Parameters	In-core Test Loop	Zero-power Critical Facility	Subcritical Driven Facility	Full-scale Test Reactor
Neutron Flux	5	1	4	5
Power Density	3	1	4	5
Test Volume / Space	1	5	5	5
Neutronics	1	5	5	5
Fuel Cycle	1	1	4	5
Thermal-hydraulics	4	1	5	5
Material Testing	5	1	4	5
Chemistry Control	5	1	5	5
Reactor System	1	4	5	5
Instrumentations	4	3	5	5
Integrated Level	3	2	5	5
Technical Risk	5	5	4	1
Licensing Effort	5	5	4	1
Capital Cost	5	4	4	1

2. Design of MITR Driven Subcritical Facility

The MITR uses rhomboid-shaped fuel elements. The 27 in-core positions for fuel elements and/or irradiation experiments are illustrated in Fig. 2. These positions are divided into three concentric rings with 3, 9 and 15 rhomboid-shaped areas, respectively. The edge-to-edge distances of the three concentric hexagons of the fuel region are 12.4 cm, 25.5 cm, and 38.4 cm. Each fuel element contains 15 fuel plates, which consist of ~ 93% enriched uranium sandwiched between sides of aluminum cladding. The surrounding core tank has a cylindrical shape, 52 cm in diameter and 73 cm in height. There is a heavy water reflector surrounding it from the sides and the bottom. In addition, a three-meter high light-water plenum, which is capable of effective neutron shielding, sits above the core tank. As mentioned previously, a fission converter, driven by the MITR, was operated as a subcritical facility within the biological shield.

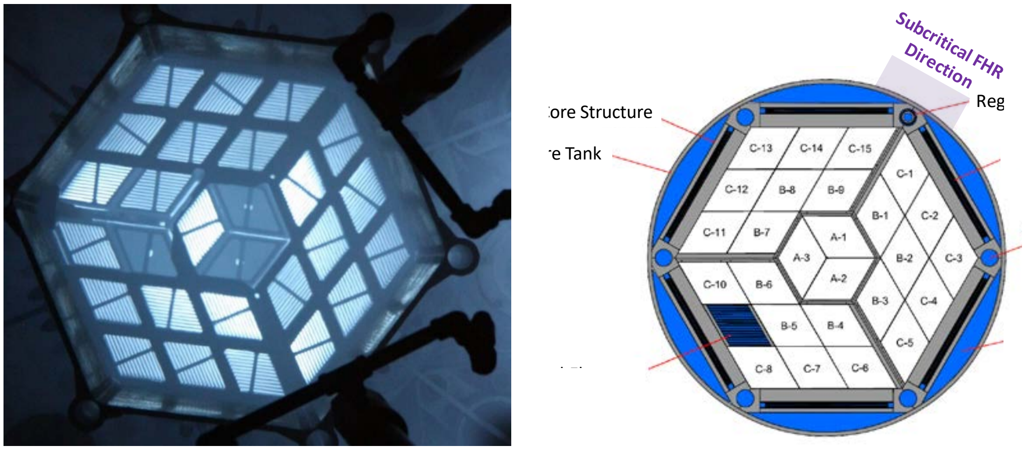

Fig. 2. Top view of the MITR core (left) and horizontal cross-section with indications (right)

The general design features of the MITR driven subcritical facility inherits from a Transportable FHR (TFHR) concept proposed by MIT [2]. Prismatic graphite based fuel blocks, originally developed for General Atomics for Gas-Turbine-Modular Helium Reactor (GT-MHR) [3], are adopted. The detailed fuel block design, including the TRISO layout, packing fraction, coolant channel distribution, and etc., can be found in Ref [2]. The only change is that burnable poison is not implemented for the subcritical facility, since fuel cycle is not its primary focus. However, the poisoned fuel blocks could be potentially accommodated and tested at a later stage. A six-block arrangement (see Fig. 3 left) is proposed for minimize the geometrical buckling, so that an optimal neutron economy could be achieved. The proposed fuel block height in this facility is 60 cm. This is determined by the subcritical multiplicity. The active zone is surrounded by coolant plenum and graphite reflector. It should be noted that the system design of the subcritical facility is an ongoing effort. The present neutronic analysis aims to reveal the theoretical feasibility. The active region of the attached FHR system will be located next to the 14-inch window of the MITR, where the thermalized neutrons could come through. The vertical and horizontal cross-sections of the combination are shown in Fig. 3.

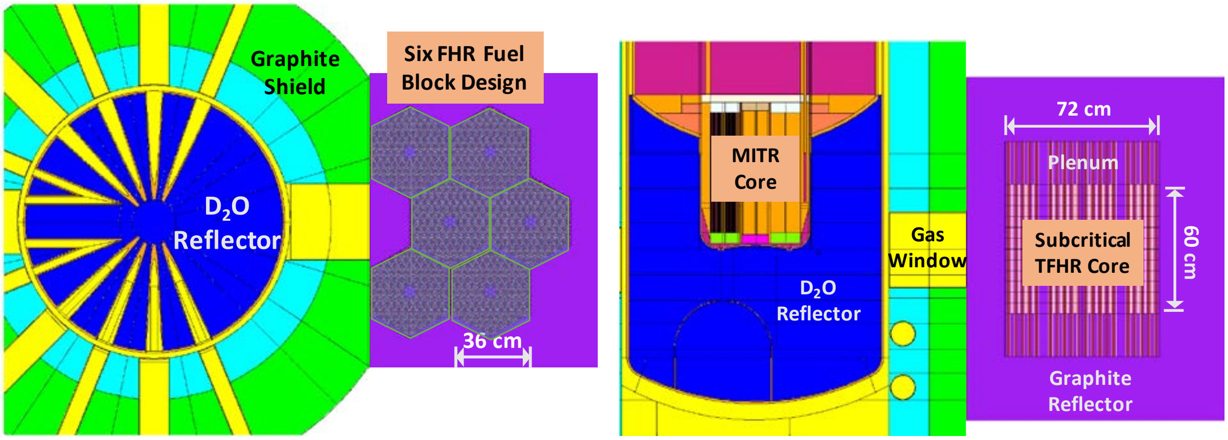

Fig. 3. Horizontal (left) and vertical (right) cross-sections of the MITR driven subcritical facility

3. Deriving Subcritical Multiplication using Surface Source Method

The goal of the subcritical test facility is a major systems test of a reactor core design that includes neutronics, thermal-hydraulics, materials, and systems designs. The ability to accomplish that is driven by neutronics thus it is the starting point for design of such systems.

The methods for evaluating the subcritical multiplication from literatures, such as Refs [3, 4, 5, 6], are mostly applied to the accelerator driven system (ADS), which adopts an intense high-power proton beam and a spallation target as the driver mechanism. Such a neutron source could be easily defined and further used for quantifying the subcritical multiplication of the ADS. However, the currently proposed subcritical facility is driven by an actual nuclear reactor, i.e., the MITR. Determining the source neutrons, that coming from the MITR core and transporting through the gas window adjacent to the heavy-water reflector, require significant efforts. Furthermore, the entire system (including both the MITR and the attached FHR system) is operating at a critical mode as a whole. This brings additional challenges for quantifying the subcritical multiplication of the attached FHR system alone. In this section, the authors propose a step-wise method, using surface source writing and reading capability in MCNP, for deriving the subcritical multiplication.

Step 1: Fully Isolated Subcritical Facility

The calculation model at the first step includes an "inactive" MITR core and an "active" attached FHR system. It is to obtain an effective multiplication factor (k_{eff}) of the latter being completed isolated, i.e., no neutron comes from the MITR side. This step also helps in confirming that the attached FHR system is not able to maintain chain reactions on its own.

Step 2: Joint MITR Driven Critical System

Both the MITR core and the attached FHR system are "active" in the calculation model at the second step. An MCNP "surface source" is created at the MITR side of the 14-inch gas window, which is the primary path for the source neutrons traveling to the attached FHR system. The "surface source" records all neutron tracks that cross the given surface (in the defined direction towards the attached FHR system for this particular case) and enter the neighboring cells. This joint model also contains detailed power tallies. They will be used for the later verifications. It should be noted that the joint system will operate at a critical mode, where the chain reactions are maintained at the MITR side.

Step 3: Surface Source Driven Subcritical Facility

The calculation model at the last step again includes an "inactive" MITR core and an "active" attached FHR system. Differently, the created MCNP "surface source", which was created in the previous step, will be applied. The interactions between the two sides will be simulated by this artificial neutron source. In this context, the multiplicity of the attached FHR system due to an external source, i.e., the MITR for this particular case, could be defined as k_{src}. Obviously, the k_{src} values depend on the multiplicity of the system itself (i.e., k_{eff}) and the characteristics of the external source. The effect due to the introduction of the external source is determined by the "source importance" parameter φ^*:

$$\varphi^* = \frac{1-k_{\text{eff}}}{k_{\text{eff}}} \cdot \frac{k_{\text{src}}}{1-k_{\text{src}}} \quad \text{from Ref [6-4]} \tag{6-1}$$

Verification of Surface Source Method

The credibility of the surface source method is essential for the investigating the neutronic features of the subcritical facility. It is verified by comparing the fission power distributions within the driven system between the joint model (from Step 2) and the surface source model (from Step 3). The results (in terms of overall percentage) are presented in Fig. 4. Very good agreements between the two sets of numbers can be found. The surface source model slightly underestimates the power in the fuel blocks adjacent to the concrete shield, so that the flux shape is moderately shifted to the remote end. This is because created surface source focuses on the neutron track within the gas window and does not take into account those inside the concreate shield. However, the observed discrepancies are insignificant (less than 0.7% for any fuel blocks). It can be concluded that the surface source method for deriving the subcritical multiplication is sound.

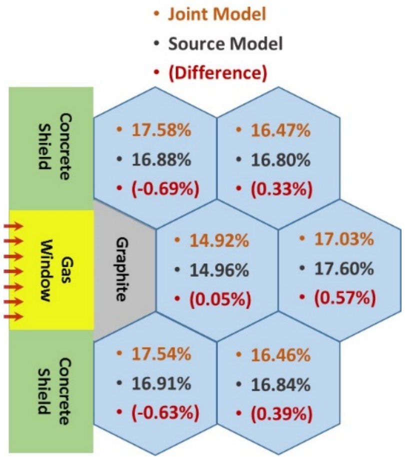

Fig. 4. Fission power distribution comparisons between joint and surface source models

4. Results of Key Neutronics Features

Multiplication Factor and Fission Power

The multiplication factor and the resulting fission power have been investigated by artificially changing U-235 enrichment in fuel. The primary purpose is to establish the link between the neutron multiplicity and the system fission power level. The results are presented in Table 2. As seen, with the low enriched uranium upper limit of 20 wt %, the proposed six-block design facility is capable of maintaining chain reactions on its own and this is obviously beyond the subcritical basis. With 1% lower enrichment, the six-block design becomes subcritical with and without the source neutrons, i.e., those from the operating MITR core. However, the margin to criticality is only several hundreds of pcm (1 pcm = 10^{-5}), which is considered insufficient for taking into account uncertainties from various source terms. For example, the shutdown margin is 1000 pcm at the MITR. The target operating power is 1 MW, which corresponds to ~ 16 wt % U-235 enrichment. For this particular case, the margin to criticality becomes sufficient (~ 1800 pcm). This observation does not necessarily imply that the subcritical facility design should adopt 16 wt % enriched uranium fuel. The useful take-away is that for a subcritical system with a k_{eff} of 0.97 or a k_{src} of 0.98, the fission power generated during actual operation is approximately 1 MW. This finding will guide the future design optimization works. It should be mentioned that the average power density of the subcritical facility is 2.5 W/cc, when the operating power is 1 MW. Comparing to the TFHR average power density of 7.6 W/cc, more than 30% of the reference level could be achieved. Last but not least, one can find in Table 2 that the source importance (φ*) stays at a constant level as long as the system multiplicity is higher than 0.90.

Table 2. Multiplication factor and fission power of the MITR driven subcritical facility

Enrichment (wt %)	k_{eff} [1]	k_{src} [1]	φ^*	Maximum Power [1] (MW)	Operating Power [2] (MW)
20.0	1.00200	-	-	-	-
19.0	0.99469	0.99692	1.729	2.75	-
16.0	**0.96934**	**0.98241**	1.766	**1.44**	**1.01**
15.0	0.95886	0.97666	1.795	1.18	0.87
13.0	0.93584	0.96251	1.760	0.84	0.66
10.0	0.88976	0.93304	1.726	0.50	0.43
6.0	0.78608	0.85851	1.651	0.24	0.22
2.0	0.51166	0.61239	1.508	0.07	-

[1] Assuming all components at room temperature, subcritical multiplication is maximized.

[2] As temperature rises up to operating condition, subcritical multiplication is reduced.

Neutronic Effects on Absorber Rods

The subcritical facility is designed to be able to significantly reduce the generated fission power without shutting down the MITR. Considering the subcritical facility has a relatively large volume, it is not practical to design a complete neutron shield. The most efficient way is to create a neutron barrier on the path of the 14-inch gas window. The preliminary plan is to introduce four absorber rods at the dummy "half-block" between the window and the subcritical facility (see the scheme in Fig. 5). The four rods will be divided into two groups, each pair being able to operate independently. The neutronic effect due to the absorber rods is shown in Fig. 5. With one pair being inserted, k_{src} is decreased from 0.98 to 0.90. As a results, the fission power is reduced by a factor 4. With one additional pair being inserted, k_{src} is further decreased to 0.80. Accordingly, the fission power is lowered by another half.

The power distribution will be affected by inserting the absorber rods. The corresponding change is also demonstrated in Fig. 5. With the absorber rods in, the fission events are shifted towards the two fuel blocks adjacent to the concrete shield. It is because the implemented neutron barrier is not effective to the scattering event inside the concrete shield, which in turn becomes a more distinct path for neutron transportations.

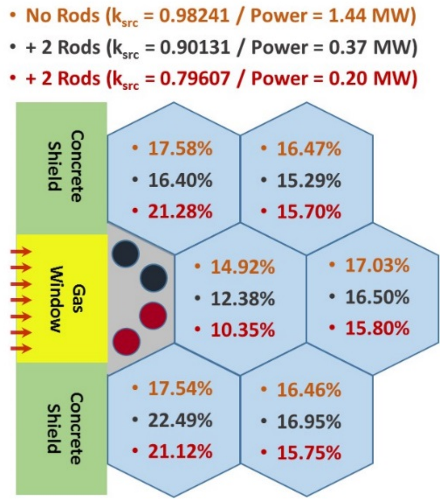

Fig. 5. Fission power distribution shift due to designed absorber rods insertion

It is worthwhile to mention that the effectiveness of the absorber rods in terms of system fission power is about a factor of 8. Considering the normal operating condition of the subcritical facility has a 30% average power density of the TFHR, the absorber rods could reduce this ratio to ~ 4%. This is a representative TFHR decay power level and it creates a useful platform to test the decay heat removal without forced flow, i.e., under natural convection. Thermal-hydraulic system design for the subcritical facility is currently under way at MIT.

Neutronic Impact on MITR Operation

The neutronic impact of the subcritical facility on the MITR operation is expected to be insignificant. This has been confirmed by the results shown in Table 3.

The power distribution in the C-ring (i.e., the outermost ring of the MITR), which shall be influenced the most in the core, has been examined. As can be seen, the fission power is slightly increased (by less than 1%) at C-1 and C-15 Positions, which are on the near end of the subcritical facility; whereas the minor reduction (also by less than 1%) is found at C-8 Position, which is on the far end (see the MITR core configuration in Fig. 3). It indicates negligible power deformation at the fuel element level. More pronounced effect is expected at a more localized level, but no safety related concern is foreseen at this conceptual design stage. In addition, the absorber rod insertion is found sufficiently enough to restore the original power distribution.

Another important finding is that implementing the subcritical system will introduce positive reactivity by 0.174% Δk/k. Given the limit of a “Movable” Category in-core experiment at the MITR is 0.2% Δk/k [8], the reactivity effect caused by operating the subcritical system is fairly mild. The results in Table III also indicate the absorber rods can effectively decouple the two fission systems. Minor reactivity change can be observed, when the four absorber rods are fully inserted.

Table 3. MITR power deformation and reactivity effect due to the subcritical system

Power (MW)	**MITR (alone)**	**Joint System**	**4 Absorb Rods In**
C-1 Position	**0.204**	**0.205**	**0.204**
C-2 Position	0.217	0.218	0.218
C-3 Position	0.212	0.213	0.212
C-4 Position	0.214	0.214	0.214
C-5 Position	0.213	0.213	0.213
C-6 Position	0.228	0.228	0.228
C-7 Position	0.217	0.217	0.217
C-8 Position	**0.197**	**0.196**	**0.197**
C-9 Position	0.210	0.210	0.210
C-10 Position	0.212	0.211	0.211
C-11 Position	0.229	0.229	0.230
C-12 Position	0.229	0.229	0.229
C-13 Position	0.221	0.221	0.222
C-14 Position	0.199	0.200	0.199
C-15 Position	**0.207**	**0.208**	**0.207**
Reactivity Effect ($\Delta k/k$)	-	***+ 0.174%***	***+ 0.019%***

5. Summary of Subcritical Driven Facility Study

This study [9] proposed an MIT Reactor (MITR) driven subcritical facility with 700 °C salt circulating through multiple full-width partial-height fuel assemblies operating with a power density up to 30% of a reference Fluoride-salt-cooled High temperature Reactor (FHR). Since the subcritical facility is designated to be built aside of a licensed reactor, its capital cost is reduced by sharing infrastructure, operating personnel, and administrative management expenses. Furthermore, such a system will be licensed as an experimental facility rather than going through the longer and risky path of licensing an advanced reactor concept.

The goal of this subcritical test facility is to explore the integrated effect of an advanced reactor core design that includes neutronics, thermal-hydraulics, materials, and systems designs. The ability to accomplish that is driven by neutronics thus it becomes the starting point for design of such systems. In this study, the authors propose a step-wise method, using surface source writing and reading capability in MCNP, for deriving the subcritical multiplication. This method has been successfully verified by comparing the fission power distributions within the active region between the joint model and the surface source model.

When the subcritical facility with a k_{eff} of 0.97 or a k_{src} of 0.98, the fission power generated during actual operation is approximately 1 MW. This power level indicates more than 30% of that in the reference FHR. The results also show that source importance stays at a constant level as long as the system multiplicity is higher than 0.90. The neutronic effect of the reactivity control system has also been investigated. Four absorber rods are capable of reducing the system fission power by about a factor of 8. This creates a representative FHR decay power level and thus an excellent platform to demonstrate the decay heat removal without forced flow, i.e., under natural convection. At last, the neutronic impact of the subcritical facility on the MITR operation has been quantified. The MITR power deformation caused by activating the subcritical facility is found to be minor (by less than 1% at fuel element level) and resulting reactivity change is within 0.2% Δk/k.

6. Preliminary Drawings of MITR Subcritical Driven Facility

The system analysis and the engineering design of the subcritical facility are currently on-going at MIT. In Figs. 6 and 7, one can see the preliminary drawings of the primary vessel of the designed facility and the system arrangement in the reactor containment, respectively [9].

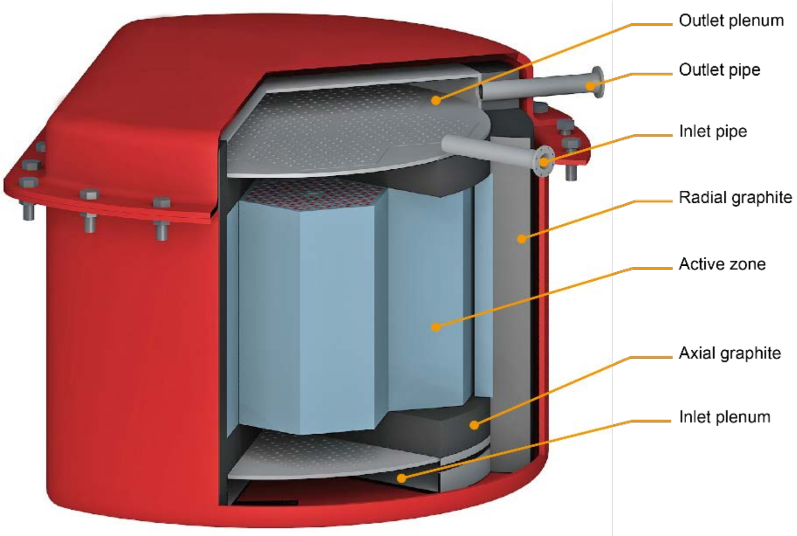

Fig. 6. Primary vessel of the MITR driven subcritical facility

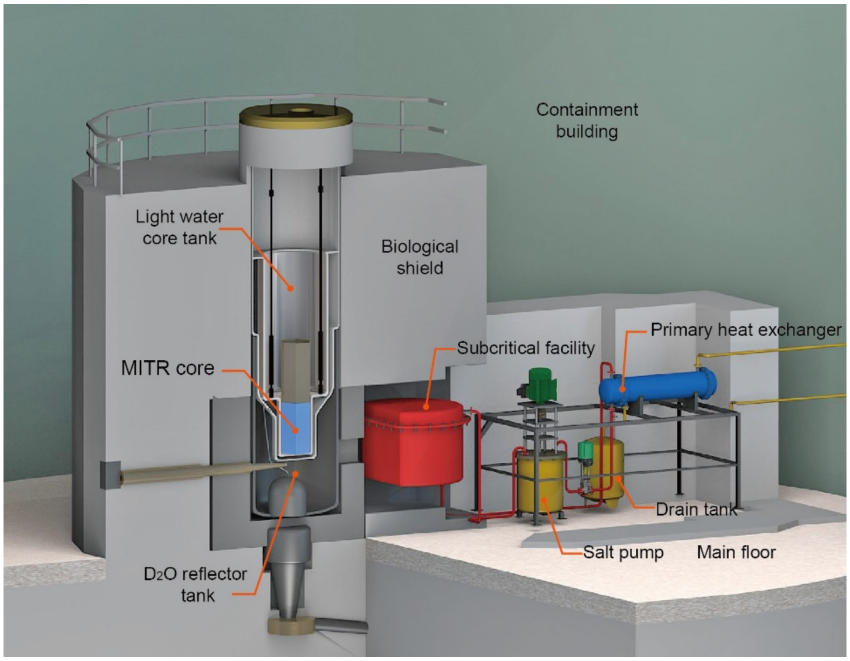

Fig. 7. System arrangement of the MITR driven subcritical facility

7. References

1. O. K. Harling et al., The Fission Converter–Based Epithermal Neutron Irradiation Facility at the Massachusetts Institute of Technology Reactor, Nuclear Science and Engineering, vol. 140: 223-240.

2. K. Sun, L. Hu, and C. Forsberg, Neutronic Design Features of a Transportable Fluoride-salt-cooled High Temperature Reactor, Journal of Nuclear Engineering and Radiation Science, Journal of Nuclear Engineering and Radiation Science, 2, (3), 031003 (2016)

3. Potter and A. Shenoy, “Gas Turbine-Modular Helium Reactor (GTMHR) Conceptual Design Description Report”, GA Report 910720, Revision 1, General Atomics, 1996

4. M. Sarotto et al., The MYRRHA-FASTEF Core Design for Caritical and Sub-critical Operational Modes (EU FP7 Central Design Team Project), Nuclear Engineering and Design, vol. 265 (2013) 184-200

5. A. Gandini and M. Salvatores, The Physics of Subcritical Multiplying Systems, Jouranl of Nuclear Science and Tchnology, Vol. 39, No. 6, p. 673-686 (June 2002)

6. K. Kobayashi and K. Nishihara, Definition of Subcriticality Using the Importance Function for the Production of Fision Neutrons, Nuclear Science and Engineering: 136, 272-281 (2000)

7. P. Seltborg, Source Efficiency and High-energy Neutronics in Accelerator-Driven Systems, Doctoral Thesis, Royal Institute of Technology, Stockholm, 2005

8. MITR-Staff, Technical Specifications for the MIT Research Reactor (MITR-II), Rev. 6, November 2010

9. K. Sun, L. Hu, C. Forsberg. Neutronics feasibility of an MIT Reactor–driven subcritical facility for the Fluoride-salt–cooled High-temperature Reactor. International Journal of Energy Research, 2017; 41:2248-2257

7. Commercialization Basis for Fluoride-salt-cooled High-Temperature Reactors (FHRs): Base-load Reactor with Heat Storage for Variable Electricity and High-Temperature Heat to Industry (MIT)[22]

Summary

The question for any advanced reactor is: *What is the compelling economic case to justify the development of the reactor?* For the FHR we examined an economic case based on the ability of a base-load FHR to provide (1) economic variable dispatchable electricity to the grid and (2) high-temperature heat to industry with high reliability. That case is based on the fact that salt-cooled reactors deliver higher average-temperature (~650°C) heat to the power cycle or industry relative to other advanced reactors.

Electricity markets are changing because of (1) the large-scale addition of wind and solar that results in times of low [excess wind or solar and/or low demand] and high [limited wind or solar and/or high demand] electricity prices and (2) the goal of a low-carbon economy. This creates incentives to operate nuclear reactors at base-load to minimize production cost while using heat storage to vary electricity output to match electricity demand. At times of low electricity prices, the minimum amount of heat is sent to the turbine to keep it operating for rapid return to higher power levels while the remainder of the heat goes to storage. At times of high electricity prices, all heat from the reactor and heat from storage go to the power cycle to produce peak power that is above the base-load electricity output of the reactor.

Heat storage costs are lower for reactors that deliver high-temperature heat to storage than low-temperature heat. The capacity of sensible heat storage systems depends upon the temperature swing from hot to cold that may be twice as large for an FHR compared to a light-water reactor (LWR); thus, reducing FHR heat storage cost for the same amount of stored heat. The heat-to-electricity conversion efficiency for stored heat from an LWR is 20 to 30% versus 40% or higher for an FHR because of the higher efficiency of converting high-temperature heat to electricity—reducing heat storage costs per unit of electricity. Heat storage can be incorporated (1) in the steam cycle with multiple options or (2) in the intermediate loop between the reactor and the power cycle using nitrate, chloride or other salts. Gigawatt-hour nitrate-salt heat storage is used in existing concentrated solar power systems and is proposed by several salt-cooled reactor startup companies. Very-low-cost chloride salts are being developed for the next generation of high-temperature (700°C) concentrated solar power systems with the same peak temperatures as an FHR. If heat storage is depleted, it can be backed up by a combustion heater to provide assured peak electricity generating capacity at a cost less than the alternative of a stand-alone gas turbine.

---

[22] C. W. Forsberg (cforsber@mit.edu)

Because of its high average temperature of delivered heat, the FHR can couple to Brayton power cycles with auxiliary-fuel (fossil fuels, biofuels, hydrogen or high-temperature stored heat) thermodynamic topping cycles. These power cycles have incremental heat-to-electricity efficiencies near 70%, greater than stand-alone gas turbines. The FHR provides heat to ~700°C for base-load electricity production with thermodynamic topping cycles using auxiliary fuel for peak power production that can raise peak turbine inlet temperatures to between 1100 to 1500°C. If there is excess low-price electricity, it can be converted into high-temperature stored heat for such topping cycles. Brayton power cycle options include (1) nuclear air-Brayton combined cycles and (2) nuclear steam-injected Brayton cycles.

Commercialization Basis for Fluoride-salt-cooled High-Temperature Reactors (FHRs): Base-load Reactor with Heat Storage For Variable Electricity and High-Temperature Heat to Industry (MIT)

1. Introduction

The central question for any advanced reactor is: *What is the compelling economic case to justify the development of a specific reactor relative to other (1) reactor options and (2) other electricity generating systems?* We conclude that a compelling economic case [1-4] can be developed based on the ability of base-load FHRs to provide (1) economic dispatchable electricity to the grid and (2) high-temperature heat to industry with high reliability. These capabilities are a consequence of the high average temperature of delivered heat from the FHR relative to other nuclear reactor types. The compelling economic case applies to all salt-cooled reactors that deliver high-temperature heat over a small temperature range: (1) FHRs with clean salt and solid fuel and (2) molten salt reactors (MSRs) with fuel dissolved in the salt. Some but not all of the options are applicable to high-temperature gas-cooled reactors (HTGRs).

There are other potential economic incentives for FHRs including lower capital costs because of low-pressure operation and safety characteristics (graphite-matrix coated-particle fuel and a coolant salt that dissolves fission products/actinides if released from the coated particle fuel) that can simplify the reactor plant. However, these depend upon future technology developments, the specific reactor design and licensing decisions. The commercialization basis described herein is not dependent upon the specifics of the reactor design beyond providing high-temperature heat.

The unique feature of salt-cooled reactors is the higher average delivered temperature of heat to the power cycle or industry: ~650°C (Table 1). In contrast the average delivered temperature of heat by the HTGR is ~550°C, by a sodium-cooled reactor (SFR) is ~500°C and by a light-water reactor (LWR) is ~280°C. HTGRs deliver some heat at higher temperatures than salt-cooled reactors but also deliver more heat at lower temperatures. High-temperature heat enables the use of efficient heat storage technologies with assured peak electrical generating capacity—replacing the role of fossil-fuel power plants in providing variable dispatchable electricity to the grid. The same set of technologies enables delivery of high-temperature heat to industry without the need for multiple reactors to meet high reliability requirements. Heat storage provides the backup heat source if a reactor is shutdown for any reason.

Table 1: Typical Reactor Coolant Temperatures

Coolant	Average Core Inlet Temperature (°C)	Average Core Exit Temperature (°C)	Average Temperature of Delivered Heat (°C)
Water	270	290	280
Sodium	450	550	500
Helium	350	750	550
Salt	600	700	650

2. Changing Electricity Markets and Requirements for Future Reactors

The traditional electricity grid has a mixture of electrical generating technologies [5-6]. Nuclear plants have high capital costs and low operating costs. Fossil plants have low capital costs and high operating costs where the electricity cost ($/kWh) is dominated by the fuel costs. The economic mode of operation to minimize total electricity costs is to operate the nuclear plants at base-load (full power) with fossil plants providing variable electricity to match electricity production with demand. In such a system the economic criteria for choosing a nuclear reactor is the reactor with the lowest levelized cost of electricity—total costs divided by total electricity production including the time value of money.

For an advanced reactor, the question is not the economics of the grid today but the economics of the grid when that reactor will be deployed. The electricity grid is changing rapidly in Europe, the United States, Japan, and China for two reasons. First is the addition of wind and solar with high capital costs and very low operating costs. The levelized cost of electricity from wind and solar is low in areas with good wind or solar conditions (Table 2); however, wind and solar are non-dispatchable. One requires another power source to provide electricity on an hourly to seasonal basis depending upon hourly to seasonal variations in wind and solar. While small-scale deployment of wind and solar can lower electricity prices to the consumer, the non-dispatchability of wind and solar is why large-scale deployment in locations such as Germany and California has resulted in increased electricity bills.

Table 2. Levelized cost of electricity for new plants (Lazard 2017) in $/MWe, unsubsidized cost and in parenthesis cost after U.S. federal tax subsidies.

Technology	Range of Levelized Cost of Electricity: $/MWh (Subsidized Cost in Parenthesis)
Solar PV: Rooftop Residential	187–319 (145–240)
Solar PV: Crystalline Utility Scale	46–53 (37–42)
Solar PV: Thin Film Utility	43–48 (35–38)
Solar Thermal Tower with Storage	98–181 (79–140)
Wind	30–60 (14–52)
Natural Gas Peaking	156–210
Natural Gas Combined Cycle	42–78
Nuclear (Existing LWR)	112–183

Because of their very low operating costs, in a free market wind and solar plants bid lower prices to sell electricity than other plants. Figure 1 (left) shows wholesale electricity prices in parts of California on a spring day in 2012 and 2017. Over a period of five years, large numbers of photovoltaic (PV) systems were installed that collapsed prices on days with good solar conditions and low electricity demand when the PV could meet much of the electrical load. The first month where the wholesale price of electricity was zero or below zero (negative prices) for more than 20% of the time (i.e., during the mid-day) has occurred. Revenue collapse limits solar even if there are large decreases in solar capital costs [7]. At the same time the price of electricity increases at times of low wind and solar because other plants must startup and shutdown to provide electricity at these times.

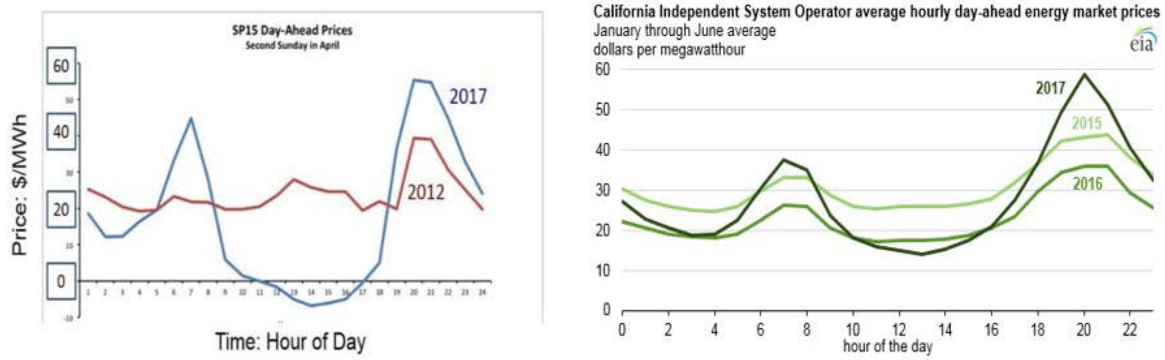

Fig. 1. Price Impact of Adding Solar PV (1) between 2012 and 2017 on a Spring Day in California and (2) Averaged Over Six Months for Different Years [8-10].

The average wholesale prices for electricity in California for the first six months of each year is shown in Fig. 1 (right) for the last several years. The price collapse is becoming larger at times of high solar output and wholesale electricity prices are increasing at other times because more PV is being added to the grid.

The same effect occurs with wind. Studies have quantified this effect in the European market [11, 12]. If wind grows from providing 0% to 30% of all electricity, the average yearly price for wind electricity in the market would drop from 73 €/MWh(e) (first wind farm) to 18€/MWh(e) (30% of all electricity generated). There would be 1000 hours per year when wind could provide the total electricity demand, the price of electricity would be near zero, and 28% of all wind energy would be sold in the market for near-zero prices. A similar effect would be seen in an electricity grid with only nuclear plants competing with each other. At times of low electricity demand the price would be driven to very low levels. This does not occur in markets dominated by fossil fuel generating plants where the minimum price is set by the cost of fuel. If electricity prices go below fuel prices, fossil plants shut down.

In such electricity markets, one wants a nuclear reactor with base-load reactor operation to minimize cost and variable output so (1) more electricity is sent to the grid when prices are high and a need for electricity and (2) less electricity is sent to the grid when prices are low and there is excess electricity production from wind and solar. In short, minimize production cost and maximize revenue.

Second, the electricity grid is changing because of the goal of reducing carbon dioxide emissions. The question then becomes what replaces fossil fuels in their role of providing dispatchable electricity to match electricity production with demand. Nuclear reactors in some countries such as France [13, 14] have operated with variable output for decades and thus provide dispatchable electricity. However, operating reactors at part load result in higher electricity production costs because expensive nuclear plants are not being used at full capacity.

To understand the impacts of reducing greenhouse gas emissions on the electricity grid and nuclear operations, several MIT studies [15, 16], including *The Future of Nuclear Energy in a Carbon Constrained World,* modeled the electricity grid in several parts of the United States to determine the optimum mixture of electricity generating technologies to minimize average electricity costs for different constraints on carbon dioxide emissions. This was done for carbon dioxide emission limits measured in grams of carbon dioxide per kilowatt-hour of electricity produced from 500 g CO_2/kWh to 1 g CO_2/kWh. The average emissions today in the U.S. from the electric sector are about 500 g CO_2/kWh. For each carbon dioxide emission constraint, the goal was to find the mixture of technologies that minimized the average cost of electricity. The analysis included existing fossil, nuclear, wind, solar and storage technologies (batteries and hydro pumped storage). There were several conclusions.

- *More nuclear if low-carbon constraints*. In every case, the optimum system included a larger fraction of electricity from nuclear power as carbon dioxide emissions constraints became tighter.
- *Electricity costs increase with tighter restrictions on carbon dioxide emissions because of the mismatch between electricity production and demand.* A low-carbon grid with existing technologies results in expensive electricity. To assure electricity supplies when needed (generating capacity) the system requires expensive batteries, overbuilding of wind and solar to reduce storage costs and nuclear plants operating at part load. That is because with tighter carbon constraints the use of low-capital-cost high-operating-cost fossil fuel electric generating plants is reduced.
- *Nuclear plants will need to operate with variable output.* As carbon constraints increase, nuclear reactors increasingly take on the role of providing variable electricity to the grid—not base-load reactor operation. They partly replace the role of fossil-fuel power generating systems.

Figure 2 and Figure 3 show how LWRs would be operated in such a world under different carbon emission constraints respectively for the Texas and New England electricity grids. The model assumes no transmission constraints or imports/exports of electricity from each region.

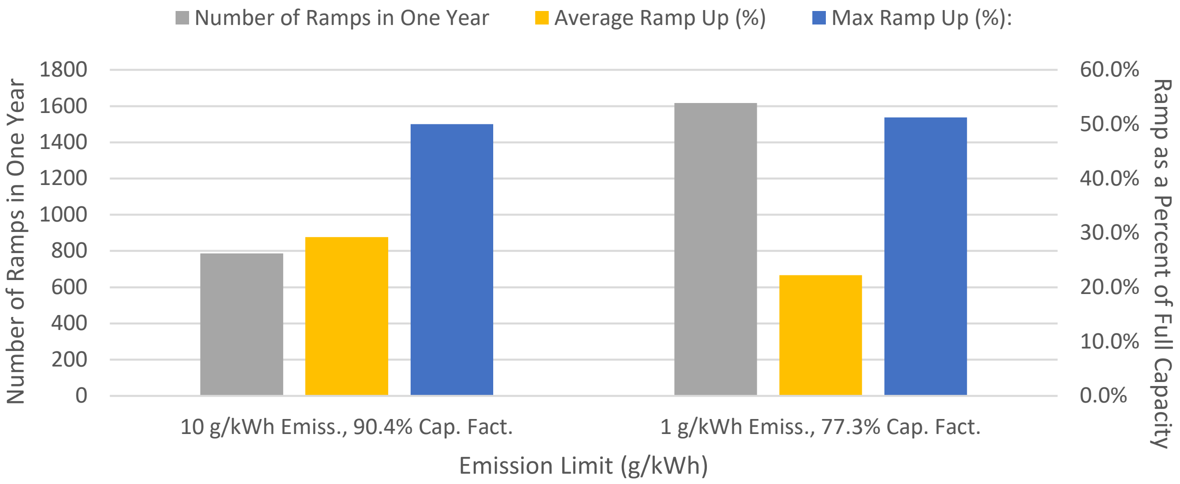

Fig. 2. Texas ERCOT: Characterization of Nuclear Plant Operations over a Year

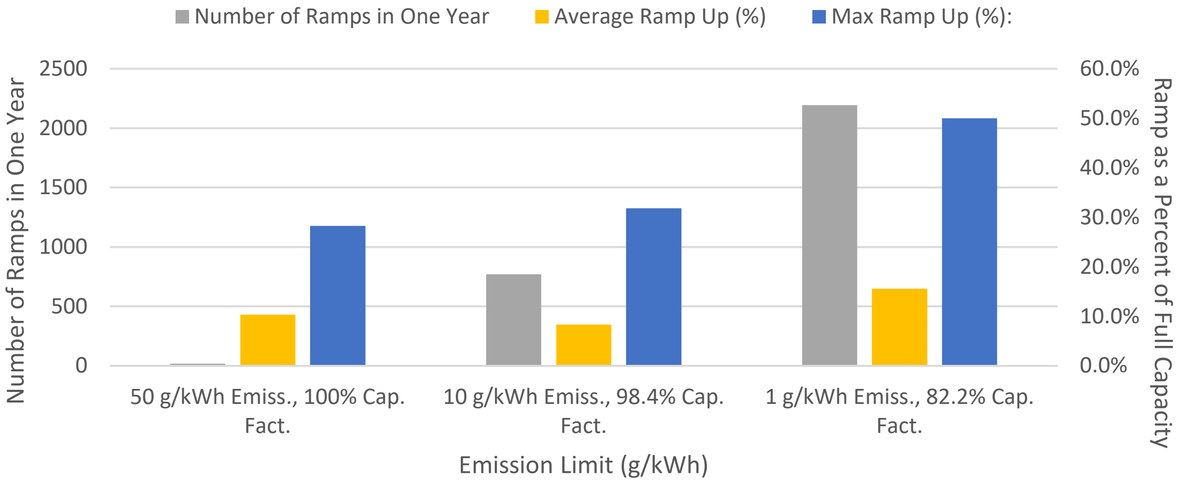

Fig. 3. New England: Characterization of Nuclear Plant Operations over a Year

There are several trends shown in the figures.

- *Number of ramps per year*. The model optimizes the system for each hour of the year—8760 hours. The number of ramps per year is the number of times the power level changes in a year. The number of ramps per year increases as the carbon constraints becomes more severe; that is, the nuclear plants do more load following and less time operating at base load. With tight carbon constraints, the reactor changes power levels a thousand or more times per year.
- *Average ramp up.* This is the average increase in power when the power level increases. This may occur over one hour or many hours. It ends when the next change in power level decreases power levels.

- *Maximum ramp up*. This is the largest increase in power over a year in any ramping event that could occur in an hour or over many hours. In this case the maximum ramping event is near 50% of full power.

The analysis assumes no heat storage associated with the reactors—only reactors doing load following using existing load-following operational constraints. If there were economic heat storage, the results would change because the reactors with heat storage would partly replace the use of other storage technologies such as batteries in the optimized system and many would operate at base-load with variable output.

The conclusion is that if the electricity grid has large installed capacities of wind or solar or the goal is a low-carbon grid, the levelized cost of electricity is not the proper metric to compare the relative value of different methods to generate electricity. *The reactors are not used for base-load electricity production*. The most economic reactor is the reactor that can provide variable electricity to the grid and heat to industry at the lowest cost—reactor plus storage system plus assured peak electricity generating capacity. This may or may not be the reactor with the lowest levelized cost of electricity production.

3. FHR Power Cycle and Heat Storage Requirements

Nuclear reactors are capital intensive with low operating costs; thus, the reactor should be operated at full capacity to minimize production cost. The electricity grid needs variable electricity. The addition of heat storage enables both goals to be met. There are several requirements (Fig. 4) for the heat storage system.

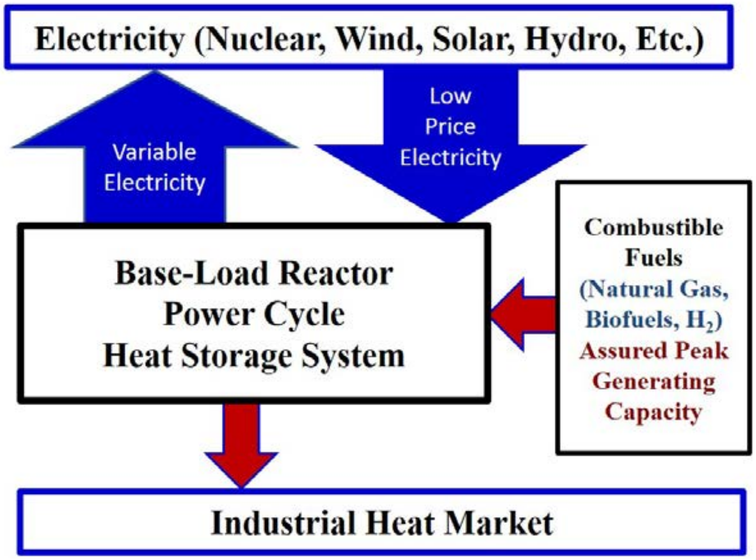

Fig. 4. Top-Level Reactor Plant System Design

- *Heat Storage*. Energy storage can be used to allow operation of nuclear, wind and solar at full capacity (lowest cost) with dispatchable electricity to the grid.

    - *Energy storage options*. Wind and solar photovoltaic produce electricity; thus, there is the option to include electricity storage in the system in the form of batteries, hydro pumped storage or other technologies. Nuclear reactors produce heat that is converted to electricity. At times of low electricity demand, some of the reactor heat output can be sent to storage while the reactor turbine-generator operates at minimum capacity. At times of high electricity demand, all reactor heat and heat from storage is used to produce peak electricity—more electricity than the base-load electricity production of the reactor above.
    - *Energy storage costs*. The cost of electricity storage systems (batteries, pumped hydro) is much higher than thermal (heat) storage systems. In the United States the U.S. Department of Energy goals are $150/kWh of electricity storage for batteries with the associated electronics doubling costs. A recent evaluation of the long-term costs of electricity storage estimated capital costs [17] of $340+/-60 per kWh when installed at the terawatt scale. In contrast, the DOE heat storage goal for concentrated solar power systems is $15/kWh. Heat storage at the gigawatt-hour scale is now used with some concentrated solar thermal power systems to enable solar power systems to sell electricity at times of higher prices. In the context of a nuclear reactor, the capital cost of heat storage for variable power is small relative to the cost of the reactor; thus, the economics favors adding storage to the reactor rather than building additional nuclear capacity that would operate at part load.

- *Assured Peak Generating Capacity with Heat Storage*. Storage systems cannot provide assured peak electricity generating capacity because they can become depleted by long periods of high demand or low wind/solar output. Assured peak generating capacity can be added to heat storage by a combustion heater burning natural gas, biofuels or ultimately hydrogen. The capital cost of the combustion heater is small because when one buys heat storage, the turbine generator and associated equipment was oversized for peak electricity production when the heat storage system was installed. The only added piece of equipment needed to provide assured peak generating capacity is the combustion heater to heat the fluid in the storage system. The combustion heater will seldom be used because most of the time heat from storage is used to provide peak electricity generating capacity. For assured generating capacity from electricity storage technologies (batteries, hydro pumped storage), the low-cost option is the backup gas turbine with a capital cost more than twice the cost of a combustion furnace to back up heat storage [3].

- *Use of Low-Price (Value) Electricity*. In any system with large-scale wind or solar capacity, there will be times of excess electricity production. If heat storage is available, one can convert excess electricity into stored heat using electric resistance heating. Because of the low cost of heat storage, this enables full use of excess electricity that may become available with large-scale wind or solar deployment.

4. Reactor and Heat Storage Economics

Recent studies for the United States [15] indicate that there is little difference in the capital costs of different advanced reactors. This reflects the large nuclear overhead (quality assurance, licensing, etc.) that is independent of the reactor technology. What does impact costs is the supply chain and experience in building reactors—the reasons why nuclear plant construction costs are much lower in South Korea and China for essentially identical plants. The cost breakdown of nuclear plants in different countries is similar as shown in Fig. 5. Most of the costs are associated with the reactor and associated structures—the cost of the turbine-generator power conversion block is small relative to the reactor.

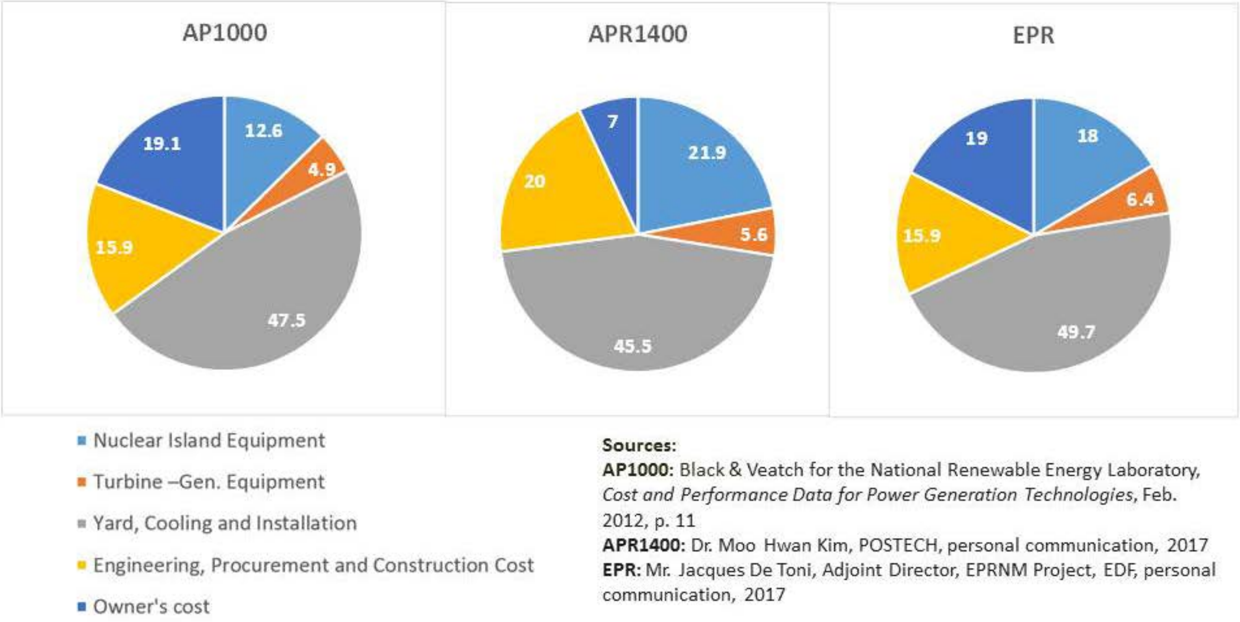

Sources:
AP1000: Black & Veatch for the National Renewable Energy Laboratory, *Cost and Performance Data for Power Generation Technologies*, Feb. 2012, p. 11
APR1400: Dr. Moo Hwan Kim, POSTECH, personal communication, 2017
EPR: Mr. Jacques De Toni, Adjoint Director, EPRNM Project, EDF, personal communication, 2017

Fig. 5. Capital Cost Breakdown for Several Advanced Light-Water Reactors

Our analysis concludes that the future market is for variable electricity. The question is then how does the addition of the heat storage system change the economics? U.S. capital costs for nuclear power plants are estimated at $5500/kW of electricity for a well-executed project. The DOE heat storage goal is $15/kWh(t) for concentrated solar power systems. The thermal-to-electricity efficiency depending upon the reactor type will be between 30 and 50%. This implies that heat storage costs per kWh electric will be under $50/kwh(e). If storing eight hours of electricity (solar induced price collapse), this is $400/kWe. The cost of heat storage relative to the cost of the reactor is small. Such analysis indicates that if one can come close to meeting DOE heat storage goals, a reactor with heat storage for variable electric production will be much more economic than a oversizing a reactor and operating it at part load.

The most economic reactor becomes the reactor with heat storage system with the above capabilities at the lowest cost. Heat storage economics can drive the choice of nuclear reactor. The economics of the storage systems strongly favors reactors that deliver high-temperate heat—such as the FHR.

- *Low-cost heat storage*. Heat storage costs are measured in dollars per kilowatt hour ($/kWh). Different heat storage technologies require heat input at different temperatures. Most storage systems have losses in efficiency through heat exchangers and other mechanisms where those losses are proportionally greater in low-temperature systems than high temperature systems. For sensible heat storage systems (hot rock, liquid salts, etc.) the heat capacity per unit volume of the storage material depends upon the temperature swing from hot to cold. If that temperature swing in storage is doubled, heat storage costs are reduced by a factor of two. High input temperatures enable larger temperature swings in the storage material resulting in lower-cost storage.
- *Efficiency in converting stored heat from the reactor into electricity*. The efficiency of converting stored heat to electricity depends upon the power cycle and the temperature of the stored heat. Higher temperatures increase efficiency. For LWRs the efficiency of converting stored heat into electricity will be between 20 to 30% depending upon the storage technology. For FHRs this heat to electricity efficiency may be above 40%. The cost of electricity using stored heat is reduced for high-temperature heat storage because of this efficiency effect.
- *Efficiency in converting auxiliary heat into electricity*. If heat storage is depleted, auxiliary combustion heaters can provide very high-temperature heat for assured electricity generation. If converting excess low-price electricity from the grid into stored heat, this heat can be stored at high temperatures.

    - *Efficient Power Cycle*. Higher-temperatures imply more efficient power cycles and less fuel to convert auxiliary heat to electricity.
    - *Brayton-cycle Topping Cycles*. These high-temperature heat sources in some Brayton power cycles enable incremental heat-to-electricity efficiencies greater than 70% by using thermodynamic topping cycles. In a thermodynamic topping cycle, the reactor initially heats the power cycle working fluid to between 600 and 700°C with the auxiliary heat source further heating the working fluid and producing additional electricity. Brayton power cycles enable peak temperatures as high as 1500°C. This is described below.

- *Assured peak electricity generating capacity*. High-temperature power cycles include options where the peak-to-reactor power output is much larger than for lower-temperature power cycles. This implies more assured generating capacity at low cost.

5. Heat Storage and Power Cycle Options

There are three technological pathways for FHRs to provide variable power to the grid while the reactor operates at full base-load capacity.

5.1. Steam Cycles

There is ongoing work by universities, vendors and utilities to incorporate heat storage with assured peak electricity generating capacity into light-water reactor (LWR) steam cycles [3, 18, 19]. The same systems apply to salt-cooled reactors except that one is using high-temperature steam rather than saturated steam. As previously noted, higher-temperature heat storage implies higher efficiencies in converting stored heat to electricity [4]. The changes in the electricity markets in the last several years makes this option potentially competitive today with LWRs; consequently, several utilities have begun plant-specific engineering studies as the first step for adding heat storage to existing reactors.

5.2.Brayton Power Cycles.

FHRs can couple to Brayton power cycles with the option of efficient peak electricity production via a thermodynamic topping cycle using an auxiliary combustion fuel such as natural gas, biofuels or ultimately hydrogen or high-temperature stored heat. The thermodynamic topping cycle implies higher incremental heat-to-electricity efficiency than a stand-alone gas turbine making such a system potentially competitive with today' gas turbines.

In a Brayton power cycle, air is compressed, heated, and goes through a turbine to produce electricity. With typical Brayton power cycles, the air temperature after compression is near 400°C. If nuclear heat is to be used, the temperature of the delivered heat must be considerably above this temperature—well above the temperatures of LWRs. FHRs couple efficiency to Brayton cycles whereas most other reactor designs do not (Table 1). That is not an accident. The original molten salt reactor was developed as part of the U.S. Nuclear Aircraft Propulsion program in the 1950s. The goal was a jet-powered aircraft. The requirements of the jet engine (Brayton power cycle) defined the requirements for the reactor that led to development of salt-cooled reactors. What has changed in 50 years are the advances in Brayton power cycles that make these power cycles practical for electricity production.

Brayton power cycles enable auxiliary fuel heat-to-electricity efficiency that is greater than any other technology. That is, more electricity is produced with less auxiliary fuel. In steam and supercritical power cycles, the peak temperature is limited by the heat exchanger that transfers heat from the reactor coolant to the power cycle. With high-temperature reactors, the practical limit due to the cost of materials is somewhere near 700°C. That implies peak efficiencies from 40 to 50%, depending upon the reactor and power cycle. Air Brayton power cycles are the most efficient power cycles because they can operate up to 1500°C with heat-to-electrical efficiencies above 60%. That is possible because with combustible fuels there is no heat exchanger limiting their peak temperature. Hot gases are created and go through turbine where the high-temperature turbine blades are cooled from the inside and have high-temperature ceramic coatings that limit heat conduction into the turbine blades.

This creates the option of using heat from a nuclear reactor at lower temperatures for base-load electricity production and using a combustible fuel (natural gas, biofuels, hydrogen) at higher temperatures—a thermodynamic topping cycle with auxiliary heat-to-electricity efficiency near 70%. In a combined cycle plant the overall efficiency may be 60%--made up of nuclear heat being converted with an efficiency in the mid 40% range and a toping cycle with the combustible fuel with an efficiency exceeding 70%. The total plant efficiency (electricity out/heat input) remains at 60% with low-cost uranium providing the “lower temperature” heat and the expensive combustible fuel providing the higher temperature heat.

Nuclear-reactor thermodynamic topping cycles are not new. In the 1960s the Indian Point I pressurized water reactor was built in the United States. The saturated steam from this reactor at 271°C was sent to an oil-fired super heater to raise the steam temperature to 540°C before going to the steam turbine—a topping cycle. At that time this was the most efficient power plant in converting incremental heat from oil into electricity. There are many Brayton power cycle design options—of which only one class of options has been examined in detail. Several of these options are described herein.

Nuclear Air-Brayton Combined Cycles (NACC)

Nuclear Air Brayton Combined Cycles (NACC) are a new technology [1-4, 20] under development that is enabled by advances in natural-gas-combined cycle (NGCC) power systems. The deployment schedule is driven by reactor development schedules, not the power cycle. Like NGCCs, a NACC couples a high-temperature Brayton power cycle to a lower-temperature Heat Recovery Steam Generator (HRSG)—a type of steam cycle. NACC can incorporate two types of internal heat storage [3]. One NACC system design with alternative operating modes is shown in Figure 6. This specific NACC design is based on the GE F7B NGCC and requires no advances in gas turbine technology. However, significant development work is required on the reactor coolant-to-air heat exchangers.

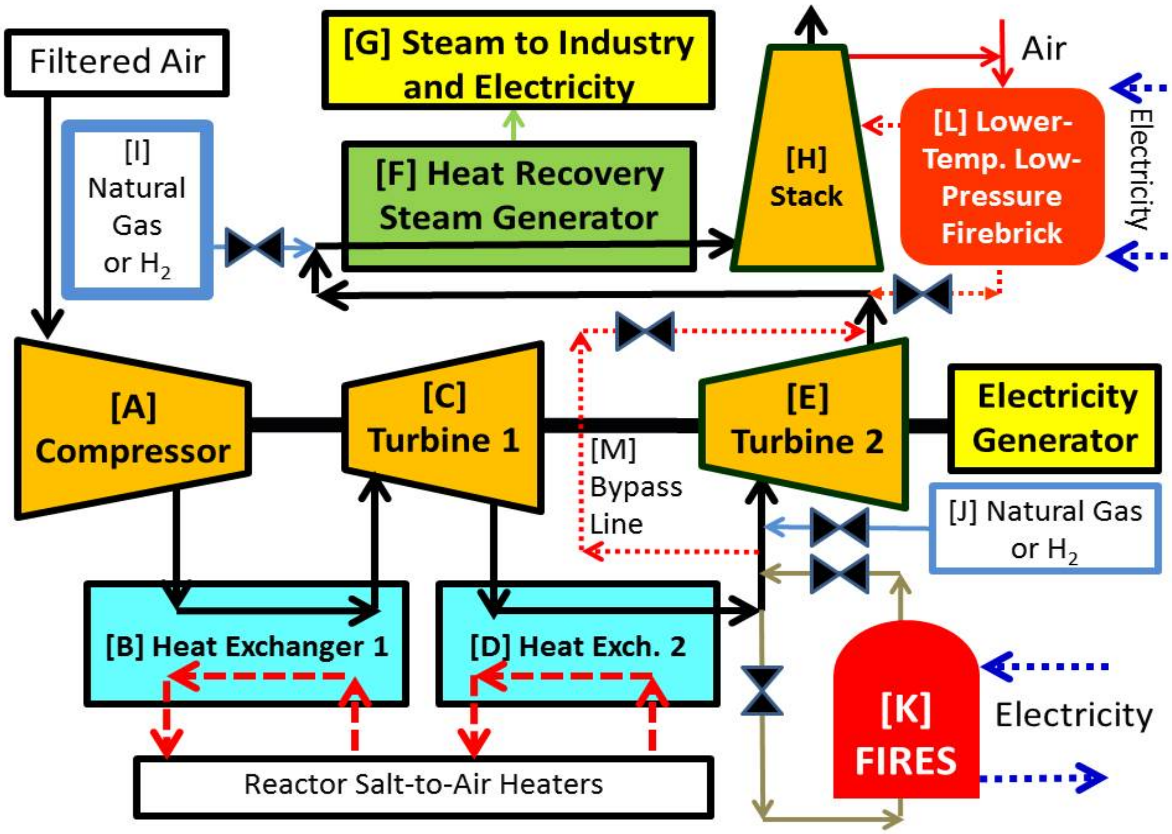

Fig. 6. NACC with Two Heat Storage Systems and Use of Auxiliary Fuels (Natural Gas, Hydrogen, Other).

During base-load operation (1) outside air is compressed [A], (2) heat is added to the compressed air from the reactor through Heat Exchanger 1 [B], (3) hot compressed air goes through Turbine 1 [C] to produce electricity, (4) air is reheated in Heat Exchanger 2 [D] and sent through Turbine 2 [E] to produce added electricity, (5) the warm low-pressure air exiting Turbine 2 goes through a HRSG [F] to generate steam [G] that is used to produce added electricity or sent to industry and (6) air and/or combustion gases exit up the stack [H].

Modern utility gas turbine compressors raise the gas inlet temperature to between 350 and 450°C. This requires that the nuclear heat input must be in the temperature range of 550 to 700°C. Almost all work to date in coupling NACC to a reactor has been with FHRs designed to deliver heat between 600 and 700°C to the power cycle. If NACC is coupled to an FHR, the base-load heat-to-electricity efficiency is 42% with the specific design described herein.

With a NACC there is the option of adding heat after the nuclear heating in Heat Exchanger 2 to further raise compressed gas temperatures before entering Turbine 2—a thermodynamic topping cycle. The added high-temperature heat can be provided by natural gas, hydrogen, another combustible fuel [J] or FIRES stored heat [K] (see below). Auxiliary heating the compressed air after nuclear heating up to 1065°C results in an incremental heat-to-electricity efficiency of 66.4%—the most efficient system using existing technology to convert heat to electricity. If the base-load output was 100 MWe, the added incremental heat will produce an additional 142 MWe. This design was optimized for base-load electricity. If optimized for peak power efficiency (radiant heat boiler section in HRSG, higher temperature gas turbine blades, etc.), the incremental heat-to-peak electricity efficiency would approach ~70%.

The GE 7FB combined cycle plant running on natural gas that was used in this analysis has a rated efficiency of 56.9%. The first of the General Electric H-Class NGCC plants are now being deployed with efficiencies in excess of 62%. NACC with H-Class technology would have significantly better performance with improvements in NGCC systems enhancing NACC performance. There are two heat storage options with NACC.

- *Firebrick Resistance Heated Storage (FIRES).* FIRES [K] is a new technology [21] that is under development to use this low-price electricity to replace natural gas in NACC and other applications. Electricity is bought whenever the electricity price is less than the price of natural gas and is used to heat firebrick up to temperatures that can approach 1800°C. Heating is done using either resistance heating of conductive firebrick or induction heating of conductive firebrick. FIRES is the only technology that can store high-temperature heat for the peaking cycle because heat is directly transferred from high-temperature firebrick to compressed air. Heat storage technologies using a heat exchanger and a secondary storage media such as molten salts will not work because of the temperature limits of the heat exchanger. When peak electricity is needed from NACC, the compressed air after nuclear heating in Heat Exchanger 2 is sent through FIRES to be heated to higher temperatures and then to Turbine 2. Exit temperatures from FIRES are controlled by either (1) adding cooler compressed air or steam from the HRSG to lower temperatures or (2) adding natural gas [J] (which self-ignites) to increase temperatures.
- *Firebrick Recuperator.* Heat storage can be added between Turbine 2 and the HRSG in the form of a firebrick recuperator [L]. If electricity prices are low or heat (steam) demand is low, the hot air exhaust from Turbine 2 is partly or fully diverted from the HRSG into a low-pressure (near atmospheric) brick recuperator [L] where it heats firebrick and then is exhausted to the stack [H]. At times of high electricity or heat demand, fans send cold air through the firebrick recuperator [L] that is heated to provide added hot air for the HRSG. There are several operational modes.

    - *Recycle Air*. If natural gas [I] is not being used as an auxiliary fuel for the HRSG, which requires oxygen, there is the option to use warm stack gas [H] rather than colder external air to transfer heat from the recuperator [L] to HRSG. This improves efficiency.

- *Bypass Turbine 2*. If the electricity demand is very low, there is the option of taking hot air exiting the salt-to-air Heat Exchanger 2 [D] and bypassing Turbine 2 [E] with that warmer air sent through a throttling valve directly to the recuperator [L] (dotted red line). This air will be at a higher temperature (670°C) than air exiting Turbine 2.
- *Resistance Heating*. If electricity prices are low or negative, there is the option to include electric resistance heaters to heat the recuperator firebrick [L] for later use to produce steam in the HRSG.

The recuperator operates at low pressure and relatively low temperatures enabling a low-cost heat storage system coupled to the HRSG. With large-scale deployment of wind or solar, there will be excess energy on weekends when the demand for electricity decreases with weekend price collapse. Very low-cost storage allows heat from the reactor and low-price electricity from the grid to be converted into heat on the weekends for production of added power during the five weekdays. However, the lower-temperature recuperator will have a lower heat-to-electricity efficiency than FIRES because lower-temperature heat is being delivered to the HRSG.

Nuclear Steam-Injected Brayton Cycles (NUSIB).

A Nuclear Steam Injected Brayton (NUSIB) cycle has two components. During base-load operations the reactor produces 650°C steam that uses a conventional steam cycle to produce electricity (solid lines). The current limit of steam cycles is near 650°C. For peak electricity production, some fraction of that steam is sent to a steam-injection air Brayton power cycle. A simplified schematic is shown in Fig. 7.

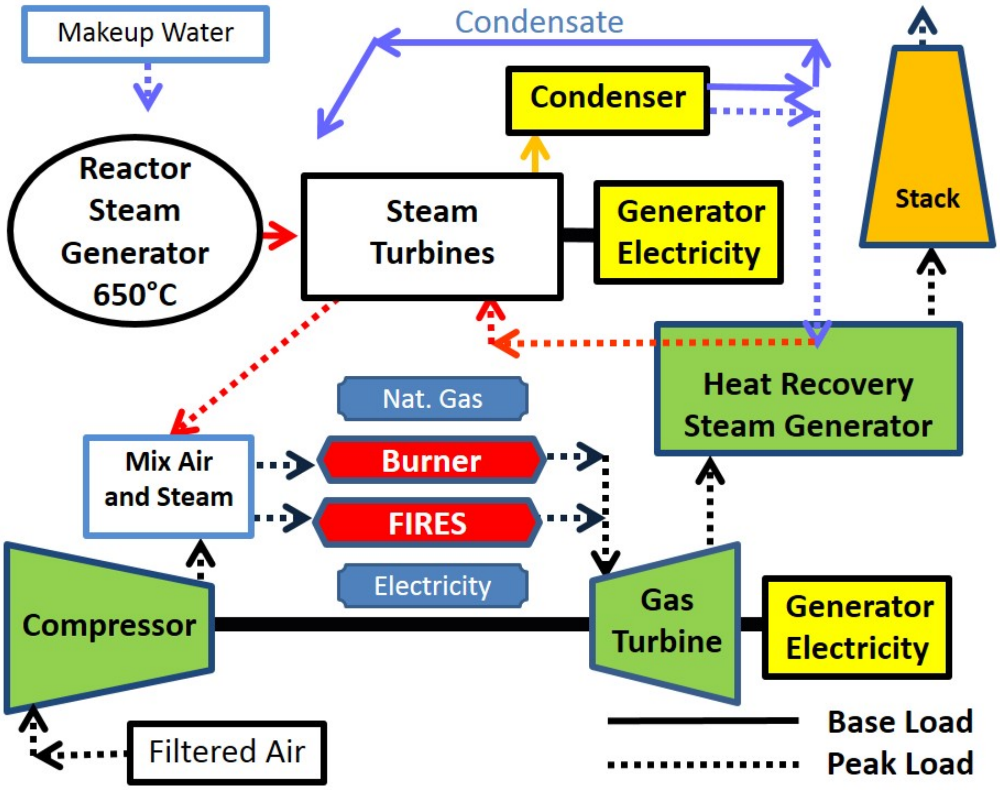

Fig. 7. Simplified Schematic of Base-load Steam Cycle with Steam-Injection Brayton Topping Cycle

For peak electricity production, a steam-injection Brayton cycle is used (dotted lines). In the example below this is a combined cycle plant. Stand-alone (non-nuclear) steam-injection Brayton power cycles are commercial products and there has been considerable work done on these cycles for different applications [22-24]. In a NUSIB cycle, air is compressed. The compressed air is mixed with fuel (natural gas, biofuels, hydrogen, etc.) and 650°C steam to produce a high-temperature gas. The heated compressed gas goes through the gas turbine generating electricity and then to a heat recovery steam generator (HRSG) and up the stack. Effectively the "low-temperature" 650°C steam is heated with compressed air to the peak gas turbine temperature—which with existing turbines could be as high as 1500°C. The limit to steam injection is the availability of oxygen in the compressed air to combust the fuel. Steam injection (650°C) is used to maximize power generation by the Brayton cycle. In peak power mode the plant is consuming water that exits the stack as steam. Like the NACC, there is the option to add FIRES to convert low-price electricity to high-temperature stored heat and replace the use of a combustion fuel.

There are several options for the steam cycle. Supercritical steam cycles are the most efficient at high temperatures. Water is compressed to above its critical pressure, goes through several feed-water heaters that raises the temperature, is heated by the reactor coolant in a heat exchanger, goes through a high-pressure turbine, is reheated by the reactor coolant in a second heat exchanger, goes through a second turbine (with the option of a third stage of reheat) before going to the lower pressure turbines as saturated steam. The initial pressures in supercritical steam cycles are extremely high—beyond that of typical gas turbines. However, the steam pressure decreases as it goes through each turbine. If such a steam cycle is used, steam can be diverted to the gas turbine after going through the first turbine and reheating where it will be at its peak temperature but at a lower pressure than the peak pressure of the supercritical steam cycle (or after the second turbine and reheating if three stages of reheat). There is also the option of operating a simple steam cycle that has no reheat and operates at lower pressures that match gas turbine requirements. There are many tradeoffs between steam cycle design and the gas turbine design that depend up design goals driven by specific markets: (1) peak to base-load electricity production and (2) efficiency of the base-load steam plant versus peaking efficiency.

NUSIB can be viewed as the high-temperature steam version of that used at the Indian Point I nuclear power plant in the 1970s—a nuclear plant with a thermodynamic topping cycle. The cycle in Fig. 7 is conceptually similar—a reactor provides "low-temperature 650°C" heat and the combustible fuel raises the steam temperature to as high as 1500°C. From the perspective of the Brayton cycle, steam impacts efficiency of the Brayton cycle in multiple ways.

- The 650°C steam heats the air exiting the compressor—a way of adding nuclear heat without the expense, loses or complications of a heat exchanger.
- The high-pressure steam reduces the amount of air that must be compressed in the gas turbine for the same gas flow through the turbine. The end result is the efficiency of converting incremental natural gas-to-electricity is higher than it would be in a stand-alone plant.
- There is a reduction in efficiency because the injected steam goes up the stack at a temperature above 100°C. In a steam cycle the water is condensed at sub-atmospheric pressure at perhaps 30°C. The heat rejection temperature is increased relative to a steam cycle. There are more complicated steam injection Brayton cycles that partly avoid these losses by expansion of the gas from the turbine into a condenser that condenses most of the steam with a compressor that then brings the non-condensable gases back to atmospheric pressure for release via the stack.

There are many variants, most options have not been analyzed. NUSIB can be coupled to other salt-cooled reactors or HTGRs. It would not couple efficiently to an LWR because LWR steam temperatures are significantly below the exit temperatures of the gas turbine air compressor. There is the option of adding a FIRES heat storage system, as in NACC, where electricity is converted into high-temperature heat that is used to heat the gas flowing through NUSIB. There is the option to have a simple cycle gas turbine with no HRSG. This option would have very low capital costs ($500/kWe). The economic case for NUSIB is based on several considerations.

- *Capital costs*. A nuclear plant costs about \$5500/kW (U.S.) and thus should be operated at base-load at all times. A combined cycle gas turbine costs about \$1000/kWe and a simple gas turbine about \$500/kWe. One wants to use the lower-capital-cost gas turbine for peaking power.
- *Natural gas-to-electricity efficiency*. A NUSIB cycle is more efficient than a stand-alone natural gas plant or gas turbine using another combustible fuel (biomass, hydrogen, etc.)
- *Capital cost of steam plant*. To minimize capital costs one wants to use the same steam cycle for base and peak power production. However, there may be efficiency advantages with two steam turbine plants, one set optimized for steam from the reactor and the other optimized for steam from the HRSG. If the second option is chosen, the combined cycle plant would be a stand-alone gas turbine with only a steam line from the reactor to steam injection.

The limit of steam injection depends upon the desired peak gas turbine temperature and available oxygen. As one raises the allowable peak gas turbine temperature, more natural gas is required to heat the compressed gas to this temperature. For natural gas at atmospheric pressure, the adiabatic combustion temperature is 1960°C. Steam injection reduces the oxygen content of the compressed air. If too much steam injection, there will not be sufficient oxygen to burn sufficient natural gas to reach desired peak gas temperatures. In most designs, the steam injection rate will be chosen so all the oxygen is consumed to reach the peak gas turbine temperature. There is one other effect that is highly beneficial. If one maximizes steam injection one can operate with near zero oxygen in the combustion gas that minimizes NO_X production.

Economic Implications of Topping Cycles

Energy markets pay per unit of electricity (MWh) delivered to the grid. In deregulated electricity markets, electricity generators bid a day ahead on the price that they are willing to sell electricity into the market—typically for each hour of the day. Generators bid their short-run operating cost to produce electricity, including fuel costs and variable operations and maintenance (O&M) costs. The grid operator accepts electricity bids up to the expected electricity demand for each hour. The accepted bid (\$/MWh) with the highest electricity price sets the price for that hour, and everyone who bids below that price gets the same marginal price.

In such energy markets, economic assessments indicate that an FHR with NACC as described above after paying for the natural gas (NG) will have 50% or more revenue in states such as Texas and California than a base-load nuclear plant. The FHR with NACC as described earlier has a base-load reactor heat-to-electricity efficiency of 42%. When operating with auxiliary natural gas, the incremental topping-cycle efficiency in converting NG heat-to-electricity is 66.4% versus an efficiency of ~56% for the same gas turbine incorporated into a stand-alone natural gas combined cycle plant and less than 40% for a stand-alone natural gas turbine. That implies the first "natural gas" plant that is dispatched by the grid to produce electricity is the FHR with NACC operating with peak electricity production (66.4% incremental NG heat-to-electricity efficiency) because it burns less natural gas per unit of electricity, followed by stand-alone natural gas combined cycle plants followed by the simple natural gas turbine. In today's market where natural gas plants are operating most of the time, the FHR with NACC would be operating in "peaking" mode most of the time. With newer gas turbines, the peak efficiencies would be higher.

As long as the FHRs with NACC do not dominate the market, electricity prices for each hour in a competitive electricity market will be controlled by stand-alone less-efficient natural gas plants that set higher electricity prices because of their lower natural gas-to-electricity efficiencies. The higher efficiency in peak power mode of NACC provides massive added revenue because all plants are being paid the same for electricity but the NACC uses less natural gas to produce a MWh of electricity. For every 100 MWe of base-load electricity, NACC produces an added 142 MWe of electricity with natural gas. The gain in revenue from that added 142 MWe for more efficient use of natural gas goes to the nuclear plant—the enabling technology for the thermodynamic topping cycle. This creates incentives to design topping cycles with (1) incremental heat-to-electricity efficiencies much higher than stand-alone gas turbines and (2) peak power production that is much larger than base-load electricity production.

Electricity markets also pay for assured generating capacity ($/kw-y). Wind, solar and batteries can't generally provide assured generating capacity. Today simple gas turbines with efficiencies of ~40% are the low-cost option for assured capacity. The capital cost of the added peaking capacity of NACC and other such systems is less than a stand-long gas turbines.

With more restrictive carbon dioxide emissions there is the option of using low-carbon biofuels and hydrogen. Because of the high-efficiency of converting heat to electricity, this technology may be the preferred option if using combustible fuels for peak electricity production because of the very high incremental heat-to-electricity efficiencies. This creates a trade-off between the cost of these fuels and heat storage. For short storage times, heat storage is likely to be the economic option. For longer time periods, the use of a combustible fuel may be preferred for peak power.

5.3.Heat Storage in Secondary Loop

Some FHR designs have secondary heat transfer loops between the reactor and the power cycle. Heat storage can be incorporated into this loop rather than in the power cycle. The leading heat-storage candidates are nitrate and chloride salts—but there are other candidates including carbonate salts.

Many large concentrated solar power towers use nitrate salt mixtures to (1) collect heat, (2) store heat on a gigawatt-hour scale and (3) deliver variable heat to a steam cycle to produce electricity at times of higher prices to maximize revenue. Several existing solar power towers have more than a gigawatt-hour of heat storage in the form of hot nitrate salts. The same technology can be coupled to a salt-cooled reactor. In addition, nitrate salts trap any tritium (produced in the primary reactor coolant salt system) that diffuses through the heat exchangers from the reactor coolant. Tritium diffuses through heat exchangers in the hydrogen form. If it contacts nitrate salts that are highly oxidizing, it is converted to water that does not diffuse through heat exchangers—it is trapped in the nitrate salt system. The tritiated water can be removed from the nitrate salt[23]. Because the nitrate salt can be used for heat storage and as a tritium trap, several salt-cooled reactor startup companies have proposed using nitrate salt intermediate loops.

The three major salts [25] are solar salt (60 wt% $NaNO_3$- 40 wt% KNO_3), Hitec (40 wt% $NaNO_2$- 53 wt% KNO_3- 7 wt% $NaNO_3$) and HitecXL (48 wt% $Ca(NO)_2$- 45 wt% KNO_3-7 wt% $NaNO_3$). Solar salt is used in the Solar Two, Gemasolar and Crescent Dunes solar power systems [26, 27] as the heat transfer fluid and storage media with a temperature swing of 288 to 565°C. Within the solar power receiver, the peak salt temperature in some parts of the receiver are considerably higher although the average salt exit temperature is 565°C. The nominal upper temperature limits for these salts is 600°C [25, 28, 29] but this may be somewhat extendable with control of the atmosphere above the salt [30, 31].

Existing concentrated solar power systems with nitrate heat storage use two-tank systems that would be applicable to a nuclear reactor with salt storage. In a two tank system (Fig. 8) at times of low demand, just enough hot salt is sent to the power system to operate it at minimum load to keep the turbine-generator on-line for fast return to full power. The remainder of the hot salt goes to the hot-salt storage tank. Cold salt from the power cycle and cold salt from the cold-salt storage tank goes back to the reactor. At times of high power demand, hot salt from the reactor and from the hot-salt storage tank goes to the power cycle. Part of the cold salt from the power cycle goes to the reactor and part goes to the cold-salt storage tank.

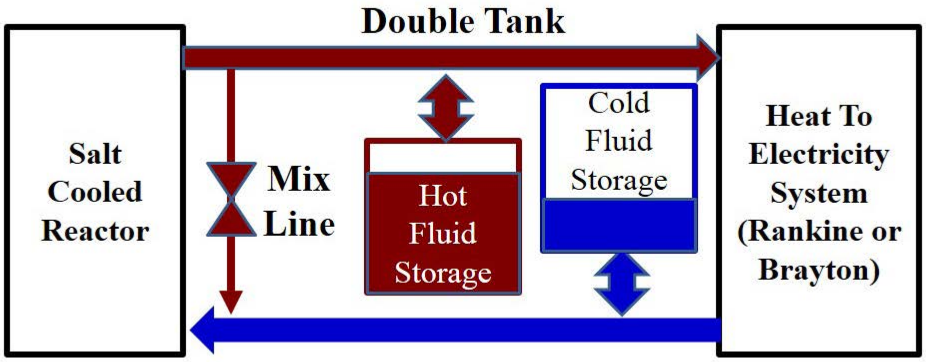

Fig. 8. Two-Tank Liquid-Salt Heat Storage

There are tradeoffs coupling salt-cooled reactors with nitrate systems.

---

[23] Nitrate salts are highly oxidizing; thus, oxygen enriched cover gases may be used to improve thermal stability. Tritiated water will gather in the gas space as steam. The quantities of tritiated water measured in grams are small; thus small amounts of normal water may be added to the nitrate salt to sweep out tritiated water and minimize tritium inventories in tanks. Nitrate salts were initially investigated in the 1970s as a tritium capture mechanism at Oak Ridge National Laboratory. Their use for heat storage was developed later by the concentrated solar industry.

- *Peak allowable nitrate salt temperature*. The peak allowable temperature is somewhat above 600°C—below the salt exit temperatures in many but not all FHRs. If the FHR has a second intermediate loop for radionuclide isolation, this is not a constraint.
- *Minimum salt-cooled reactor coolant temperature*. The minimum reactor salt temperature is somewhere near 550°C. A large temperature change in the nitrate salt minimizes heat storage costs. To minimize heat storage costs, the nitrate salt can provide heat to the power cycle down to its minimum temperature—typically near 280°C. This minimizes the cost of heat storage. However, if this is done, the return nitrate salt temperature will be significantly below the freezing point of the reactor salt. To avoid freezing the reactor secondary salt loop one can (1) design a heat exchanger with a very large temperature drop across the heat exchanger (very small heat exchanger) or (2) mix hot nitrate salt with cold nitrate salt to meet whatever temperature requirements are needed for the nitrate salt/reactor salt heat exchanger.

A longer-term salt option for secondary loop heat storage is the use of chloride salts. These salts have lower costs and can go to much higher temperatures than nitrate salts. The leading candidate for reactor systems in the U.S. is the same sodium-potassium-magnesium chloride salt that is the leading candidate [32, 33, 34] for advanced high-temperature solar power towers with operating temperatures above 700°C—significantly above the temperatures of solar power towers using nitrate salts. That commonality exists with nuclear heat storage systems because most of the requirements for an intermediate-loop coolant for a salt-cooled reactor and for a coolant in a high-temperature solar power tower are identical.

This salt has become the leading candidate for advanced high-temperature solar power tower systems because of (1) good physical properties including melting point and (2) very low heat-storage costs. There are significant uncertainties including controlling salt chemistry to minimize corrosion. The eutectic salt composition with a melting point of 383°C has a composition of 24.5 wt% NaCl, 20.5 wt% KCl and 55 wt% $MgCl_2$. If the temperature swing in storage is 200°C, the storage cost with this salt is estimated at $ 4.50/kWh—below that of nitrate salt storage or any other liquid heat storage system that has been identified to date.

The differences between chloride salts and nitrates salts is that the chloride salt (1) operates at higher temperatures (more efficient), (2) has the potential for much lower costs and (3) is not a commercial system. Significant R&D is required.

6. Heat Delivery to Industry

These systems have major implications for use of nuclear reactors to deliver heat to industry. Salt reactors have the advantage of delivering heat at higher temperatures and thus can meet a larger fraction of industrial heat demand. However, the major challenge in many cases is to provide heat to industry with very high reliability. For electricity production, high reliability is assured by the grid that connects together tens to hundreds of power plants. If one power plant is shut down, the grid continues to provide electricity. For industrial heat this is not an option. One strategy is to build more reactors at the industrial site than needed so to have backup reactors to enable delivering heat with high reliability. The other option is heat storage with assured heat delivery with combustion heaters. The technologies that enable variable electricity from a base-load reactor are the same technologies required for high reliability for delivery of heat to industry. Such systems can meet the very high requirements for reliability (99.9%) of steam supplies [35, 36].

Heat storage enables coupling the electricity market with the industrial heat market to store low-price energy when available from the electricity market for later use by the heat market. Coupling the electricity and industrial heat market should lower total costs to society.

7. Conclusions

FHRs have the potential to become the low-cost nuclear reactor for base-load electricity because of their low pressure operations, safety characteristics, fuel cycle characteristics and efficient power cycles. However, that will depend upon future developments and the specific reactor design. The alternative commercial strategy is to design the FHR power cycles with storage and peak power capability where they have two competitive advantages relative to other reactors: (1) lower-cost heat storage and (2) Brayton power cycles with thermodynamic topping cycles using stored heat or combustible fuels. These characteristics are a consequence of higher average temperatures of delivered heat by the FHR to the power cycle (including storage) and industry.

In a world with (1) large-scale deployment of wind or solar and/or (2) carbon emission constraints, the FHR with storage has potentially a large economic advantage. Such an FHR can provide the same service as fossil fuels provide today—dispatchable electricity to the grid and heat to industry. As such, the system is potentially the enabling technology for larger-scale wind and solar with the ability to buy and sell electricity to (1) reduce price collapse at times of high wind and solar electricity generation and (2) provide assured generating capacity at times of low wind or solar.

There are significant challenges. The large-scale changes in the electricity market have only occurred in the last five years. As a consequence there has been relatively little work on heat storage coupled to power cycles and the option space is not fully understood. There is technological overlap in these storage and power systems with concentrated solar thermal power systems. The near-term option heat storage option that has been adopted by several salt-cooled reactor startup companies is to include nitrate intermediate loops with the option of heat storage using the nitrate salt—the same option used by some concentrated solar power systems where heat storage has been deployed at the gigawatt-hour scale. The same systems in an FHR have lower costs than in concentrated solar power systems because of more storage cycles per year. In addition, nuclear generation can be more widely deployed—it is not dependent upon the availability of direct sunlight or distance from the equator.

8. References

1. C. ANDREADES, C., R. O. SCARLAT, L. DEMPSEY, and P. F. PETERSON, "Reheating Air-Brayton Combined Cycle Power Conversion Design and Performance Under Normal Ambient Conditions", *J. of Eng. for Gas Turbines and Power*, **136**, June 2014.
2. C. W. FORSBERG and P. F. PETERSON, "Basis for Fluoride-Salt-Cooled High-Temperature Reactors with Nuclear Air-Brayton Combined Cycles and Firebrick Resistance-Heated Energy Storage", *Nuclear Technology*, **196**, 13-31, October 2016.
3. C. FORSBERG, S. BRICK, and G. HARATYK, "Coupling Heat Storage to Nuclear Reactors for Variable Electricity Output with Base-Load Reactor Operation, *Electr. J.*, **31**, 23-31 (April 2018): https://doi.org/10.1016/j.tej.2018.03.008
4. C. W. FORSBERG, N. SEPULVEDA and K. DAWSON, *Commercialization Basis for Fluoride-salt-cooled High-Temperature Reactors (FHRs): Base-load Reactor with Heat Storage for Variable Electricity and High-Temperature Heat to Industry*, Center for Advanced Nuclear Energy Systems, MIT, Cambridge, MA, ANP-TR-178, August 2018
5. NATIONAL RENEWABLE ENERGY LABORATORY, *NREL Annual Technology Baseline*, 2018 https://atb.nrel.gov/
6. U.S. ENERGY INFORMATION AGENCY, *Annual Energy Outlook 2016: Levelized Cost and Levelized Avoided Cost of New Generation Resources in the Annual Energy Outlook 2015* (7 July 2016). http://www.eia.gov/forecasts/aeo/electricity_generation.cfm.
7. MIT ENERGY INITIATIVE, *The Future of Solar Energy: an Interdisciplinary MIT Study*, Massachusetts Institute of Technology, Cambridge, MA., 2015
8. CALIFORNIA ISO, "California ISO: Renewables and emissions reports," (9 April 2017): http://www.caiso.com/market/Pages/ReportsBulletins/RenewablesReporting.aspx.
9. CALIFORNIA ISO, Q1 2018, *Report on Market Issues and Performance* , July 10, 2018
10. ENERGY INFORMATION AGENCY, Today in Energy: California wholesale electricity prices are higher at the beginning and end of the day, July 24, 2018, http://www.eia.gov/todayinenergy/detail.cfm?id=32172
11. L. HIRTH, "The Market Value of Variable Renewables, the Effect of Solar Wind Power Variability on Their Relative Prices," *Energy Economics*, **38**, 218-236, 2013.
12. L. HIRTH, L., "The Optimal Share of Variable Renewables: How the Variability of Wind and Solar Power Affects their Welfare-Optimal Development, *The Energy Journal*, **36** (1), 2015.
13. INTERNATIONAL ATOMIC ENERGY AGENCY, *Non-Baseload Operation in Nuclear Power Plants: Load Following and Frequency Control Modes of Flexible Operation*, NP-T-3.23 (2018).
14. J. D. JENKINS, J. D., et al., "The Benefits of Nuclear Flexibility in Power System Operations with Renewable Energy", *Applied Energy*, 222, 872-884 (2018): https://doi.org/10.1016/j.apenergy.2018.03.002

15. D. PETTI et al., *The Future of Nuclear Energy in a Carbon-Constrained World*, Massachusetts Institute of Technology. September 2018.
16. C. W. FORSBERG, C., K. DAWSON, N. SEPULVEDA, M. CORRADINI, *Implications of Carbon Constraints on Electricity Generation Mix for the United States*, China, France and United Kingdom, Center for Advanced Nuclear Energy Systems, ANP-TR-179, Massachusetts Institute of Technology, September 2018.
17. O. SCHMIDT et al., "The Future Cost of Electricity Storage Based on Experience Rates", *Nature Energy*, **2**, July 10, 2017.
18. C. W. FORSBERG, et al., *Light Water Reactor Heat Storage for Peak Power and Increased Revenue: Focused Workshop on Near Term Options*, MIT-ANP-TR-170, Massachusetts Institute of Technology, Cambridge, MA., July 2017, http://energy.mit.edu/2017-canes-light-water-reactor-heat-storage-for-peak-power-and-increased-revenue
19. C. W. FORSBERG, "Variable and Assured Peak Electricity from Base-Load Light-Water Reactors with Heat Storage and Auxiliary Combustible Fuels", *Nuclear Technology,(In Press)*
20. N. FATHI, P. McDANIEL, C. FORSBERG, and Cassiano de OLIVERIA, "Power Cycle Assessment of Nuclear Systems, Providing Energy Storage for Low Carbon Grids," *J. of Nuclear Engineering and Radiation Science*, Vol. 4, ASME 020911, April 2018.
21. C. W. FORSBERG, D. STACK, D. CURTIS, G. HARATYK, N. A. SEPULVEDA, "Converting Excess Low-Price Electricity into High-Temperature Stored Heat for Industry and High-Value Electricity Production," **30**, 42-52, *Electricity Journal* (July 2017): https://doi.org/10.1016/j.tej.2017.06.009
22. BAHRAMI et al, 2015, Performance Comparison between Steam Injected Gas Turbine and Combined Cycle during Frequency Drops, *Energies*, **8**, 7582-7592; doi: 10.3390/en8087582.
23. E. H. BETELMAL, S. FARHAT, and B. AGNEW, "Exergy Analysis for Brayton and Inverse Brayton Cycles with Steam Injection", *J Appl Mech Eng*, **6** (6), 2017, DOI: 10.4172/2168-9873.1000292
24. K. JESIONEK. et. al., "Power enhancement of the Brayton cycle by steam utilization", *Archives of Thermodynamics*, **33** (*3*), 39–50, 2012.
25. GIL, A. et al., "State of the Art on High Temperature Thermal Energy Storage for Power Generation. Part 1—Concepts, Materials, and Modellization," *Renewable and Sustainable Energy Reviews*, **14**(1), pp. 31-35, 2010.
26. S. USHAK, A. G. FERNANDEZ and M. GRADEDA, 2015. "Using Molten Salts and Other Liquid Sensible Storage Media in Thermal Energy Storage (TES) Systems," *Advances in Thermal Energy Storage Systems*, pp. 49-63, 2015.
27. K. FEDERSEL, J. WORTMANN and M. LADENBERGER, "High-Temperature and Corrosion Behavior of Nitrate Nitrite Molten Salt Mixtures Regarding Their Application in Concentrated Solar Power Plants", *Energy Procedia*, 69, pp. 618-625, 2015.
28. M. M. KENISARIN, "High-temperature Phase Change Materials for Thermal Energy Storage," *Renewable and Sustainable Energy Reviews*, **14**(3), pp. 955-970, 2010.

29. M. MEDRANO et. al., “State of the Art on High-Temperature Thermal Energy Storage for Power Generation. Part 2—Case Studies”, *Renewable and Sustainable Energy Reviews*, **14**(1), pp. 56-72, 2010.
30. R. I. OLIVARES, “The Thermal Stability of Molten Nitrite/Nitrates Salt for Solar Thermal Energy Storage in Different Atmospheres”, *Solar Energy*, **86**(9), p 2576-2583, 2012.
31. ABENGOA SOLAR, Advance Baseload Molten Salt Tower, Sunshot CSP Program Review, DOE/GO-102013-3924, Phoenix, Arizona. 2013
32. M MEHOS et. al, *Concentrating Solar Power Gen3 Demonstration Roadmap*, NREL-TP-5500-67464, National Renewable Energy Laboratory (January 2017).
33. G. MOHAN, *Development of High-Temperature Sensible Thermal Energy Storage Systems for Advanced Concentrated Solar Power Generation*, PhD Thesis, Australian National University, June 2018
34. G. MOHAN, M VENKATARAMAN, J. GOMEZ-VIDAL and J. COVENTRY, “Assessment of a Novel Ternary Eutectic Chloride Salt for Next Generation High-Temperature Sensible Heat Storage”, *Energy Conversion and Management*, **167**, 156-164, 2018.
35. E. M. HERD and L. J. LOMMERS, "HTGR Strategies to Meet Process Heat Reliability and Availability Needs," *Proc. Int. Congress on Adv. in Nuclear Power Plants (ICAPP’10)*, San Diego, 2010.
36. E. HERD, L. LOMMERS and F. SOUTHWORTH, "Impact of Demand Load Size on Strategies for Reliable Process Heat Supply," *Nucl. Eng. and Design,* **251**, pp. 282-91, 2012.

8. Conclusions

The Integrated Research Project (IRP) made sufficient progress to begin the transition to a large-scale development program—as summarized in the Abstract and Executive Summary. That progress helped enable the launching of Kairos Power (https://kairospower.com), a startup company to commercialize the FHR that is building large-scale experimental facilities and includes many participants of this IRP. Kairos Power currently has 60 full-time employees.

The establishment of major experimental facilities is as important as the results. The experimental facilities enable future work. Equally important, the development, building, and operation of these facilities developed the knowledge and personal to build future facilities. It takes large amounts of time and effort to build and operate the first experimental facility of any type—there is a massive learning effort. Building the second such facility requires a small fraction of the effort and time required for building the first-of-a-kind facility. Three major sets of experimental facilities were developed as part of the first IRP and this second IRP.

- *Thermal hydraulic test facilities*. The University of California at Berkeley developed the Compact Integral Effects Test (CIET) facility that demonstrated the use of Dowtherm A as a realistic low-temperature simulant for understanding the thermal hydraulic behavior of liquid salts at scale.
- *Salt processing facilities*. The University of Wisconsin reestablished facilities to produce and purify salt coolants and corrosion test loops.
- *Materials irradiation in 700°C salt*. MIT established the capability to irradiate materials in salt—with the associated instrumentation to realistically test materials under prototypical conditions.